Chemical Engineering in Medicine

Published on June 1, 1973 on http://pubs.acs.org | doi: 10.1021/ba-1973-0118.fw001

Chemical Engineering in Medicine

A symposium sponsored by the
Division of Industrial
and Engineering Chemistry
at the 162nd Meeting of the
American Chemical Society,
Washington, D. C.,
Sept. 13-14, 1971.

Daniel D. Reneau

Symposium Chairman

ADVANCES IN CHEMISTRY SERIES 118

AMERICAN CHEMICAL SOCIETY
WASHINGTON, D. C. 1973

ADCSAJ 118 1–360 (1973)

Library of Congress Catalog Card 73–82786

ISBN 8412–0179–X

PRINTED IN THE UNITED STATES OF AMERICA

Advances in Chemistry Series

Robert F. Gould, *Editor*

Advisory Board

FOREWORD

ADVANCES IN CHEMISTRY SERIES was founded in 1949 by the American Chemical Society as an outlet for symposia and collections of data in special areas of topical interest that could not be accommodated in the Society's journals. It provides a medium for symposia that would otherwise be fragmented, their papers distributed among several journals or not published at all. Papers are referred critically according to ACS editorial standards and receive the careful attention and processing characteristic of ACS publications. Papers published in ADVANCES IN CHEMISTRY SERIES are original contributions not published elsewhere in whole or major part and include reports of research as well as reviews since symposia may embrace both types of presentation.

PREFACE

The period between 1960 and 1970 can be called the initiation of the Age of Space. We witnessed space spectaculars that climaxed with the landing of an American astronaut on the lunar surface. Equally possible is that we will look back and call the 1970's the initiation of the Age of Man. We will have witnessed spectaculars in environment, medicine, and the interaction between man and his environment. A large part of the Age of Man will belong to a new breed of professional—the biomedical engineer.

As a new profession, engineering in medicine is becoming more of a pronounced theme in today's academic and industrial society. Initial emphasis has been placed on the advancements that can result from the engineer's technical development ability. Already significant developments have resulted from applying quantitative engineering to the principles of physics. The development of sophisticated electronic monitoring equipment, biomedical instrumentation, and the optimum design of certain artificial devices are examples of areas generally associated with biomedical engineering.

Yet a field of engineering that perhaps offers more potential significance to medical and biological evolution than all others is that of fundamental, quantitative systems analysis of basic physicochemical biological processes. Likewise, overall design, development, and practical applied engineering in medicine and biology are confronted frequently with the need for a physicochemical systems approach.

Therefore qualitative and quantitative analysis of medical and biological processes requires cognition in terms of not only physics and mathematics but also chemistry. The uniqueness of chemical engineering as compared with other engineering disciplines (*raison d'etre*) is that in addition to mathematics, chemical engineering is based on two fundamental sciences—chemistry and physics. Of equal importance is that a chemical engineer is systems oriented instead of object oriented.

Consequently, the philosophy of chemical engineering combined with biological training is singularly adaptable today for a comprehensive investigation of fundamental biological processes heretofore impossible to analyze. Whether such development will occur remains to be seen. If developed, whether it will be in the name of chemical engineering or a new branch of biomedical engineering depends on the biological flexi-

bility of chemical engineering. It is said that chemical engineering would never have developed into a profession had mechanical engineers been willing to study chemistry.

The theme of the papers contained herein is closely allied to the systems analysis concept of chemical engineering in medicine. The papers are divided sequentially into four categories—general, engineering pediatrics, physiological control, and biochemical sensors. Each category emphasizes the diverse type of basic investigation and developmental design that is possible from an overall analysis using mathematics, physics, chemistry, and biology with the philosophy of chemical engineering.

DANIEL D. RENEAU

Ruston, Louisiana
August 1972

Blood Oxygenation by Liquid Membrane Permeation

NORMAN N. LI and WILLIAM J. ASHER

Esso Research and Engineering Co., Corporate and Government Research Laboratories, Linden, N. J. 07036

Blood oxygenation is one of the many potential applications of the separation technique using liquid membranes. In this particular application, the blood is oxygenated by contacting with oxygen bubbles pre-coated with the membranes. The oxygen in the bubbles diffuses through the membrane into the blood, whereas the carbon dioxide diffuses from the blood into the bubbles. The exploratory results show that stable fluorocarbon-type liquid membranes were formed around oxygen bubbles, and such membranes allowed opposite transfer of oxygen and carbon dioxide at substantial rates. Blood damage, which usually occurs in conventional artificial lung devices, should be greatly reduced as previous studies have indicated good and perhaps unique compatibility of the liquid fluorocarbon and blood interface. The potential advantages that this new and unique oxygenation technique can offer over the currently available techniques are discussed.

Blood oxygenation is one of the many potential applications of the separation technique using liquid membranes developed at Esso Research (*1*, *2*, *3*, *4*). In the presently available artificial lung devices, blood comes in contact directly with oxygen bubbles, with oxygen atmosphere, or with oxygen that has permeated through a solid polymeric membrane. These devices have served admirably for short times—*e.g.*, in surgery. However, they have had limited success for prolonged oxygenation, as might be used to aid patients with reversible respiratory insufficiency. The two primary problems for prolonged oxygenation are: (1) blood hemolysis—the rupture of red blood cells—and (2) denatura-

tion of proteins in the blood. Red cell ruptures and changes in the characteristic properties of blood proteins can occur easily when blood directly contacts oxygen or a non-compatible solid membrane surface.

In the blood oxygenation application of liquid membranes, the blood contacts fluorocarbon liquid membranes which encapsulate oxygen bubbles. The blood may be shunted from the body and passed through a contacting device before being sent back to the body. The contacting device can have many different types of structure. One type is a column in which the blood and the encapsulated oxygen bubbles flow countercurrently. The blood is the continuous phase in which the encapsulated bubbles are dispersed uniformly by the method they are introduced into the column and by the flow existing in the column. The liquid membranes encompass the oxygen bubbles completely, thus preventing the formation of a direct blood–oxygen interface while allowing oxygen to diffuse into the blood and carbon dioxide to diffuse from the blood to the gas bubbles. The liquid membranes are composed of fluorocarbon-type compounds because some seem to have good and perhaps unique compatibility with blood and no detectable chemical toxicity (*6*, *7*, *8*, *9*, *10*, *11*, *12*). Only fluorocarbon-type compounds, indicated to be bicompatible, were added to the blood and oxygen to form the liquid membranes of this system. Thus, the liquid membrane oxygenation method has the potential advantages of minimizing blood hemolysis and protein denaturation.

The resistance to O_2 and CO_2 transport of the liquid membrane should be minimal. The liquid membranes are typically quite thin. In systems where they have been measured, they are usually 1 μ or less, which is substantially thinner than polymeric membranes used for transport. The thinness of the membranes combined with the high solubility of fluorocarbons (*13*, *14*) for O_2 and CO_2 would be expected to lead to minimal liquid membrane resistance to transport.

The geometry for transport mimics that of the body. The gas encapsuled in the liquid membrane is the counterpart to the gas in the alveoli of the lungs in the body.

The normal transfer mechanism of oxygen in blood is different than in simple solutions (*15*, *16*). The quantity of oxygen carried in plasma at atmospheric pressure is very small, about 0.2 ml at STP/100 ml of plasma, expressed as a gas volume at standard conditions per solution volume. Whole blood, in contrast, can carry about 20 ml at STP/100 ml of blood. The larger load of oxygen is carried in chemical combinations with hemoglobin as expressed below:

$$\text{Hemoglobin} + \text{Oxygen} \longleftrightarrow \text{Oxyhemoglobin} \quad (1)$$

$$\text{Hb} + \text{O}_2 \longleftrightarrow \text{HbO}_2 \quad (2)$$

The hemoglobin becomes saturated at about 100 mm Hg O_2 partial pressure, and further oxygen has to be dissolved in the plasma.

Advantages of Liquid Membrane Oxygenation Over Other Methods

Presently available oxygenators can be divided into two categories. One is for blood to be in direct contact with oxygen; the other is for blood to be in contact with the oxygen that permeates through a solid polymeric membrane. Oxygenating blood in both types of oxygenator usually results in some degree of damage to blood proteins and red cells. There is no apparent improvement or remedy that can be made for the first method. For the second method, industrial and academic research has been carried out to modify or treat the polymeric surface, like chemically bond heparin to the membrane surface to make it more compatible with the blood. However, it has not yet been established that polymeric membrane oxygenators can operate over prolonged times with truly negligible blood damage. The liquid membrane technique has the potential advantages of presenting a blood interface minimizing hemolysis and protein denaturation and of using deformable liquid membranes.

The general advantages of liquid surfactant membranes over solid polymeric membranes have been discussed previously (*1*, *2*). They are summarized below:

(1) Greater surface area for permeation and separation because of high surface area of liquid membranes per unit volume

(2) Elimination of pinholes in imperfect solid membranes, which allow all components of a mixture to pass through, just as a broken liquid membrane would

(3) No membrane life problem since the liquid membranes are recovered after each separation and no deposit (for example thrombus) can accumulate with time to decrease performance

(4) A faster rate of permeation and separation since liquid membranes are much thinner than solid ones

(5) No need for a mechanical support, such as the frames that hold solid membranes in the mixtures being separated

(6) No minute flow channels to become blocked in time with solids (*e.g.*, thrombus)

Experimental

Philosophy. The exploratory results presented in this paper do not represent the best accuracy that could be obtained with the methods described, nor do the *in vitro* conditions used always most closely approach those which would be found *in vitro*. Also, the apparatus used was far from optimal for blood oxygenation. However, the representative data reported indicate strongly new phenomenon and application for

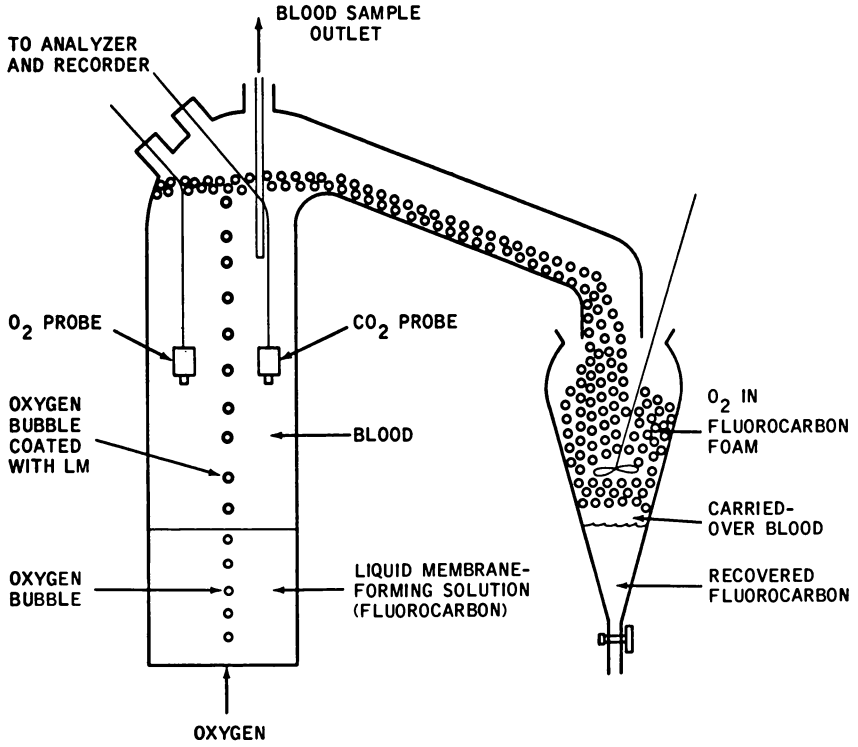

Figure 1. Liquid membrane (LM) blood oxygenator

liquid membranes and suggest several avenues for future investigations. For these reasons, the representative exploratory data are presented.

Apparatus. The liquid membrane oxygenator consists basically of a glass column of 11.5 inches in height and 1.25 inches in diameter (Figure 1). The bottom of the column was filled with the liquid fluorocarbon solution to a height of about 3 inches. The rest of the column was filled with blood all the way to the top. The oxygen and the carbon dioxide probes manufactured by Beckman Instrument and Variflo, respectively, were submerged in the blood phase. They were used in connection with a physiological gas analysis meter, manufactured by Beckman Instrument, to measure the oxygen and carbon dioxide partial pressures in the blood. A stainless steel tube went through the bottom stopper as the nozzle through which oxygen bubbles were formed in the liquid fluorocarbon solution. Two tubes of different size, 0.3 cm and 0.05 cm in diameter, were used in separate runs for forming oxygen bubbles of different size. A wet test meter was used to measure the rate of oxygen gas going into the oxygenator.

Materials. Bovine blood was used in the experiments within 24 hours after being obtained fresh from a nearby slaughter house. To each quart of blood, 5 cc of solution containing 5000 USP herapin units were added to prevent clotting. The liquid fluorocarbons used were manu-

factured by DuPont and 3M. The oxygen gas used was chemically pure (manufactured by Matheson Co.).

Procedure. The liquid fluorocarbon and blood were slowly introduced into the column just before the start of the run. The oxygen gas that had passed through the wet test meter was sent into the oxygenator through the stainless steel nozzle at low rate, such as 40 cc/min. When liquid membranes were to be made, the nozzle was submerged in a fluorocarbon layer. At such a low rate the oxygen gas emerged from the nozzle as individual bubbles rather than a continuous jet. The oxygen bubbles had an average diameter of about 0.4 cm for the nozzle size of 0.3 cm inner-diameter and an average diameter of about 0.10 cm for the nozzle size of 0.05 cm diameter. Provision was made to humidify the oxygen gas when necessary to equalize the partial pressures of water in the gas and in the blood.

The gas bubbles ascended through the fluorocarbon layer to the fluorocarbon–blood interface. As the bubbles ascended through this interface, a film of fluorocarbon remained around the gas bubbles, forming the encapsulating liquid membrane. The encapsulated bubbles then rose through the blood phase where the oxygen inside the bubbles permeated out into the blood and carbon dioxide in the blood permeated into the bubbles. Thus, the blood was changed from the state which was carbon dioxide-rich and oxygen-depleted to the state which was carbon dioxide-lean and oxygen-replenished. The oxygen and carbon dioxide partial pressures in the blood were monitored by the two probes, or electrodes, suspended in the blood phase. The encapsulated bubbles eventually emerged from the blood phase forming a phase which was apparently gas in a continuous fluorocarbon foam and moved down a slant glass tube of 1 cm in diameter and 16 cm in length into a receiving separatory funnel. In this slant glass tube there was an opportunity for a blood-gas interface to occur; however, obvious modification in the apparatus could eliminate this interface. The liquid membrane encapsulated bubbles collapsed with time in the separatory funnel, forming four phases. The top was the spent gas from the oxygenator which had reduced oxygen content and increased carbon dioxide content. Below this phase was the oxygen bubbles in a continuous fluorocarbon phase (oxygen in fluorocarbon foam). This phase isolated a blood phase below it from the potentially damaging gas phase. The third phase, oxygenated blood carried over by the oxygen in fluorocarbon foam, was usually very small in comparison with the quantity of blood oxygenated (about 1%). Since it was protected from directly contacting the spent gas, it should be recirculated to the patient. The fourth phase was the solution of fluorocarbon compounds which were reused to form liquid membranes encapsulating new oxygen bubbles. In all the runs the fluorinated-compound solution and blood carried over were measured. Samples of blood were taken directly from the column from time to time during the examination run.

Results and Discussion

Liquid Membrane Formation. The most important test of liquid-membrane oxygenation was determining whether stable fluorocarbon-

Table I. Transfer of Oxygen and Carbon Dioxide[a]

Time (Min.)	*O_2 Partial Pressure in Blood (mm Hg)*	*CO_2 Partial Pressure in Blood (mm Hg)*	*Accumulated O_2 Flow (liters at 1 atm, 25°C)*
0	17	17.2	0
2	18	17.2	0.08
5	19.2	17.2	—
10	21.0	17.2	0.31
12	24.5	16.4	0.38
14	27.0	16.4	0.46
17	30.5	16.4	0.59
22	32.4	15.0	0.63
37	39.0	15.0	0.88
43	44.0	15.0	1.10
47	49.5	15.0	1.3
58	62	15.0	1.84
70	76	15.0	2.4
76	84	15.0	2.65
85	99	15.0	3.10
125	350	15.0	5.58

Total amount of blood in foam coalescer after 125 min = 2 grams.
Total amount of fluorocarbons in foam coalescer after 125 min = 15 grams.

[a] Run No. = 10, temperature: 25°C, blood: 190 grams fresh bovine blood, hemoglobin content: 11.8 grams in 100 grams blood, fluorocarbon phase: 110 grams, oxygen nozzle size = 0.3 cm in diameter.

type liquid membrane can be built on the surfaces of oxygen bubbles. Fluorocarbons or their derivatives were used for making the liquid membranes because recent work (*6, 7, 8, 9, 10, 11*) has shown that several of this group of compounds cause minimal damage in contact with blood. The fluorocarbon solution was effective in forming stable membranes around oxygen bubbles. The presence of stable encapsulating liquid membranes during the rise of the bubbles through the blood is supported by the formation on top of the blood phase of a phase which seemed to be a foam of gas bubbles in a clear liquid. When this foam was removed from the top of the blood phase and allowed to collapse, it was dominately liquid fluorocarbon (*see* Table I). With the high density of the fluorocarbons (about 1.8 grams/cc) and the low gas flow rate (about 2 liters/hour), it is very unlikely that any substantial quantity of fluorocarbon thrown to or entrained to the top of the blood phase. The liquid membrane formation hypothesis was supported further when a substantial residence time was used for the gas in fluorocarbon foam on the top of the blood phase in the column. Under this condition some of the foam would collapse on top of the blood phase, resulting in the formation of fluorocarbon droplets. These droplets could be observed

to fall down through the column of blood counter to the rise of bubbles up through the column. This observed counter-flow of free fluorocarbon droplets down with continuous supply of fluorocarbon up the column is strong evidence for the fluorocarbons being carried up the column with the bubbles as liquid membranes.

Liquids (either solvents or solvents plus surfactants) other than fluorocarbons might be used to form liquid membranes for blood oxygenation. However, the following criteria must be satisfied:

(1) High-surface activity at the liquid membrane–blood interface—so that a liquid membrane can form around each gas bubble

(2) Insignificant solubility in water and in the much more complex fluid blood—so that objectionable quantities are not returned to the animal

(3) Good compatibility with blood—so that blood will not be significantly damaged or poisoned by contacting the liquid membranes phase

(4) High oxygen absorption capacity—so that it can rapidly transfer the oxygen from the bubble to the blood

(5) High carbon dioxide permeability—so that the liquid membrane it forms allows rapid transfer of carbon dioxide from the blood phase to the bubbles.

Oxygenation Rate. The progress of blood oxygenation in the glass column was indicated not only by the increase of oxygen partial pressure in blood (Table I and Figures 2 and 3) but also by the change of blood

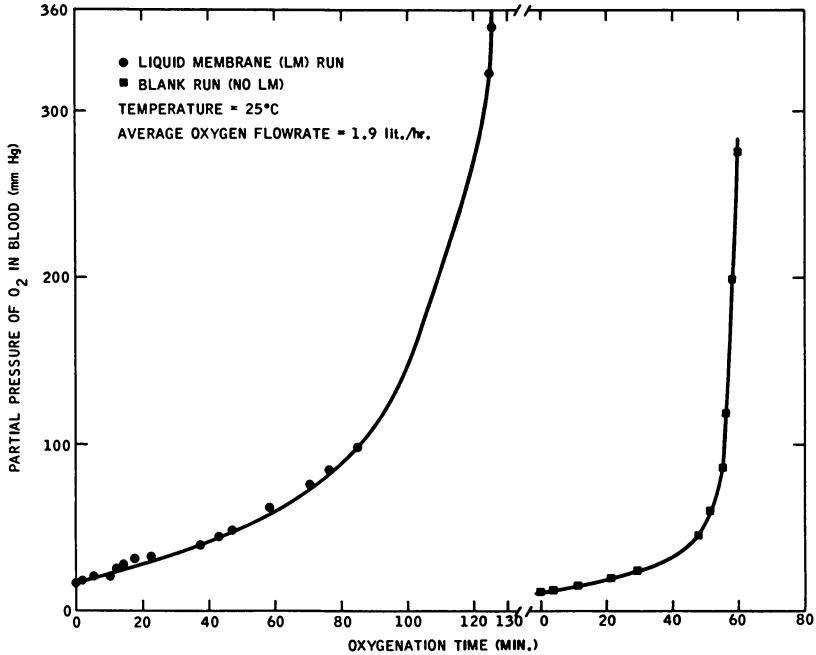

Figure 2. Blood oxygenation

color from dark red gradually to bright red when more and more oxygen molecules combined with hemoglobin as discussed before.

The oxygenation rate was measured; the initial slope of the curve using liquid membranes in Figure 2 is proportional to the rate of oxygen transfer. At about 100 mm Hg O_2 partial pressure, there is a sharp change in the slope of the curve. This corresponds to the partial pressure where the hemoglobin becomes saturated (*15*), and additional oxygen put into the blood must be dissolved largely in the blood. An additional mole of oxygen physically dissolved in the blood raises the oxygen partial pressure much more than an initial mole of oxygen which could be bound by the hemoglobin. Thus, the change in slope does not reflect a change in oxygen transfer rate.

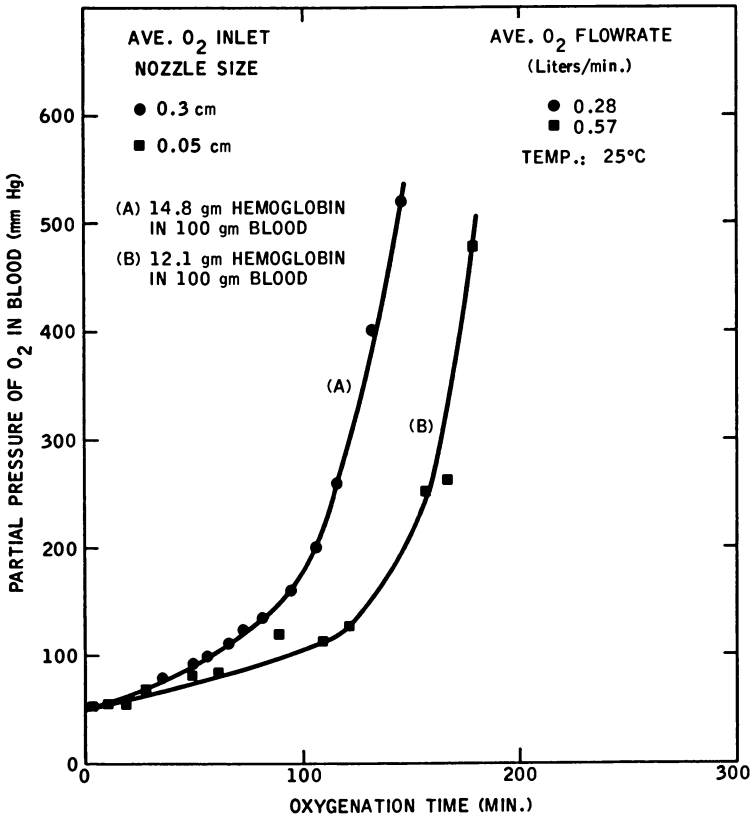

Figure 3. Blood oxygenation

The rate of oxygen transfer per unit area of liquid membrane was estimated. The rate of oxygen uptake was measured from the initial slope of the curve for liquid membranes in Figure 2 and the measured 13 gm/100 ml hemoglobin content of the blood. The volume formation

rate of liquid-membrane encapsulated bubbles was determined from the measured oxygen flow rate of 1.9 liters/hour. The encapsulated bubble diameter was estimated at 0.4 cm, and the rise velocity of the encapsulated bubbles in the blood was estimated at 0.15 ft/sec. The rough estimate of the rate of oxygen transport calculated from the above measurements and estimates was over 100 cc O_2/min/m^2. This rate does not differ within the confidence limits of the assumptions from the 30 to 80 cc O_2/min/m^2 measured in earlier fluorocarbon blood oxygenators (*6, 7, 8*). This is consistent with the major resistance to oxygen transport occurring in the blood phase as was thought to be the case in the earlier fluorocarbon oxygenator. The estimated rate of oxygen transport using liquid membranes is also consistent with the typical 40–60 cc of O_2/min/m^2 measured in polymeric membrane oxygenator using high transport membranes where the major resistance to transport was thought to be in the blood phase (*17, 18, 19*).

An attempt was made to determine experimentally if the liquid membrane was contributing a major portion of the resistance to oxygen transport or if, as suggested above, the major resistance to transport was in the blood phase. The experimental apparatus that was used with the liquid membrane was used, except that no fluorocarbons were introduced to the bottom of the column and the bubbles were formed directly in the blood. The rates of oxygen transport under 100 mm Hg of O_2 partial pressure were somewhat but not markedly higher without the liquid membrane, as shown in Figure 2. Figure 2 shows also that the times required to reach high oxygen partial pressure, with and without liquid membranes are substantially longer than with the developed oxygenators. This occurred because the very large bubbles (about 0.4 cm) used in the experiment expose a much smaller area of blood for oxygenation than the much smaller bubbles generated (on the order of 0.03 cm) in the developed oxygenators.

The lower rate with the liquid membrane might indicate some oxygen transport resistance of the liquid membrane. However, other factors could also account for the different rates. Subsequent experiments were performed using transparent plasma to allow visualization of the phenomena. In these experiments the oxygen bubbles formed from a nozzle submerged in the plasma were smaller than the liquid membrane-encapsulated bubbles formed at the plasma–fluorocarbon interface from a nozzle submerged in the fluorocarbon. The same phenomena of smaller bubbles being formed without the liquid membrane quite probably also occurred in the experiments with the opaque blood. The smaller bubbles without liquid membrane, which would provide more blood surface for oxygenation, is consistent with observed slightly more rapid oxygenation rate. In any case the small difference in rates of blood oxygenation observed

with and without liquid membranes would indicate the relative resistance to oxygen transport of the liquid membrane is small.

The diameter of the oxygen bubbles formed in the fluorocarbon was reduced from 0.4 cm to 0.1 cm for some experiments. This would be expected superficially to increase the surface area for transport and the oxygen transport rate particularly since a higher oxygen rate was used. However, the rate actually decreased a bit (Figure 3). Subsequent experiments using transparent plasma cast some additional light on this phenomenon. When small diameter nozzles were used in the fluorocarbon phase, small bubbles were formed, which rose to the fluorocarbon–plasma interface. The bubbles collected and coalesced on the fluorocarbon side of the interface until enough volume accumulated so that the buoyant forces exceeded the interfacial tensions, allowing the fluorocarbon-encapsulated bubble to rise into the plasma phase. Thus, smaller diameter nozzles in the fluorocarbon phase did not produce smaller diameter liquid membrane-encapsulated bubbles in the plasma phase. Using the small diameter nozzle at higher gas flow rates produced larger diameter liquid membranes. The gas bubbles actually formed clusters at the interface due to lack of time for coalescence. These clusters were larger than the individual liquid membrane encapulated bubbles formed at lower gas rates. This may be due to reduced buoyancy resulting from the additional fluorocarbon around each small bubble in the cluster. The above mentioned observations with plasma are consistent with the blood oxygenation results, specifically, the small diameter nozzle did not yield faster oxygenation and the higher oxygen flow rate produced a lower oxygenation rate.

It is desirable to use very small encapsulated bubbles for oxygenation. If 50 μ encapsulated bubbles, occupying 20 volume-% of a blood containing vessel, would be used effectively, only a 250 ml vessel would be required to give 6 square meters of interfacial area for oxygen transport. If based on the rate of oxygen transport per unit area previously measured at blood–fluorocarbon interfaces and rates estimated from this work, the 6 square meters would be adequate for the total rest oxygen requirements (of about 18 liters of oxygen per hour (*16*)) of a human. While it is unlikely that such a small oxygenator would be developed, the calculations indicate the potential for small volume. A method of generating and effectively using small diameter liquid membranes-encapsulated oxygen bubbles is needed. Perhaps, the methods used to make small diameter liquid membranes for other applications (*2*, *3*, *4*) could be used.

Carbon Dioxide Removal from Blood. Carbon dioxide was removed from blood by the liquid membrane-coated bubbles. The decrease of CO_2 partial pressure was from 26 mm Hg to 21 mm Hg in 12 min at an

oxygen flow rate 0.58 liters/min with the smaller diameter 0.05 cm nozzle. Similar results of CO_2 removal are shown in Table I at a different oxygen flow rate and bubble size. The CO_2 partial pressure in the blood, as withdrawn from the animal, should have been higher than the 26 mm Hg typically measured at the beginning of a run. The low CO_2 partial pressure was believed to result from CO_2 that escaped from the blood into the atmosphere resulting from the favorable CO_2 partial pressure difference between the blood and the atmosphere when the blood was stored in the refrigerator (*20*).

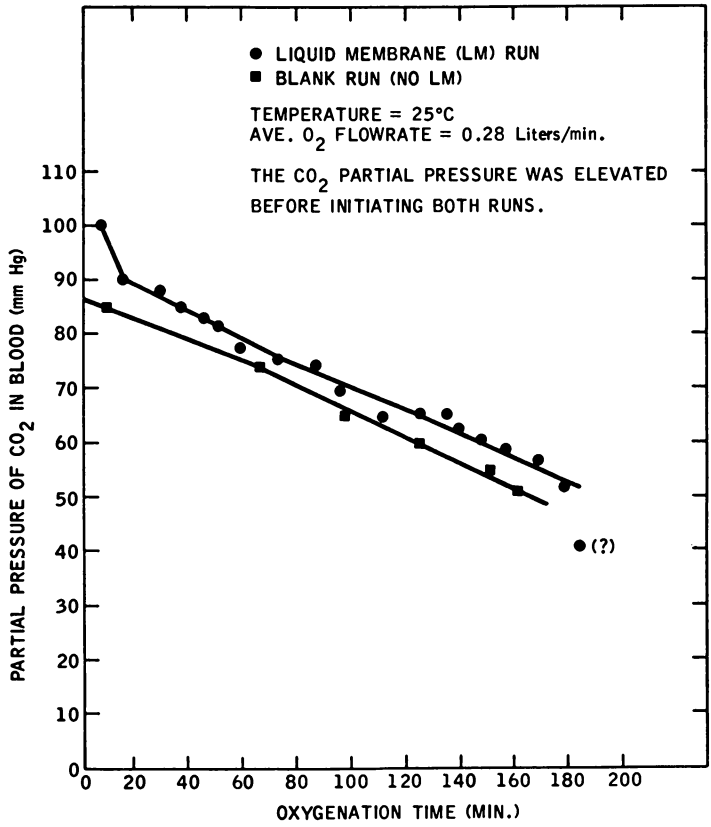

Figure 4. Removal of carbon dioxide from blood

To eliminate the possibility of a measurement artifact at low concentrations, the CO_2 partial pressure of some blood was increased to 100 mm Hg by bubbling CO_2 through the blood. The transfer of CO_2 from this blood is shown in Figure 4. Here the CO_2 partial pressure dropped from 85 mm Hg to 51 mm Hg in 154 min, using oxygen bubbles without liquid membranes (formed directly in the blood), and

from 100 mm Hg to 41 mm Hg in 176 min, using liquid membrane-encapsulated oxygen bubbles. This confirms CO_2 transport from the blood through the liquid membrane to the gas. Also, it is consistent with the above mentioned carbon dioxide removal through liquid membranes measured at lower partial pressure. The small, if not negligible, difference in rate of CO_2 removal with and without liquid membranes, shown by the parallel lines through the data in Figure 4, indicate that the resistance to CO_2 transport of the fluorocarbon liquid membranes is quite low.

The apparatus used for this study produced low transport rates for CO_2, as well as the previously discussed O_2, with and without liquid membranes compared with developed oxygenators. The reason for this slow transport is the very large (approximately 0.4 cm) liquid membrane encapsulated bubbles contrasted with the small bubbles of developed oxygenator. A means is needed to produce small fluorocarbon liquid membranes in blood so that the rapid transport achieved in other liquid membrane applications using small diameter liquid membranes can be achieved for transferring gases to and from blood.

Liquid Membrane Stability. While studies of other investigators have indicated that the blood has good compatibility with the liquid fluorocarbon surface, they also indicate that fluorocarbon droplets should not be introduced to the bloodstream of animals (*6*, *7*, *8*). Liquid membrane rupture in the oxygenator apparatus could produce droplets from the fluorocarbon which had formed the liquid membrane. These droplets would be entrained and returned to a test animal with the oxygenated blood. As a preliminary test for liquid membrane rupture and droplet formulation, the oxygen flow into apparatus was momentarily stopped, and blood samples were withdrawn for examination.

The blood samples were centrifuged at 20,000 rpm at a distance of 4.5 inches for 20 minutes in a centrifuge maintained at 20°C. After centrifugation the blood separated into two layers, a top layer of plasma and a bottom layer of red cells. Since the liquid fluorocarbon is immiscible with the blood and is much heavier than the blood, entrainment of fluorocarbon in blood should result in the formation of a small, third layer of the fluorocarbon at the very tip of the pointed centrifuge tubes after such intensive centrifugation. However, no such layer was found in the tubes for all the four blood samples tested. The blood samples were also examined carefully under microscope. No tiny droplets of fluorocarbon were noticed. While it is possible that a few liquid membranes ruptured and escaped detection and more definitive testing would be required before application, instability of the liquid membranes does not seem to be a major problem.

Conclusions

Liquid membrane of fluorocarbons can be formed encapsulating oxygen bubbles in blood. The transfer of oxygen and carbon dioxide through the liquid membrane to and from the blood, respectively, have been shown. Very similar transfer rates with and without liquid membranes indicate that the resistance of the liquid membranes is small.

The specific rate of oxygen transfer per unit of liquid membrane area seems to be quite reasonable. However, methods to form and utilize effectively much smaller diameter liquid membranes, perhaps similar to those used in other liquid membrane applications, would be required to obtain enough membrane area per unit blood volume for a practical blood oxygenator. The stability of the liquid membranes does not seem to be a major problem; however, more definitive liquid membrane stability information would be required before the blood oxygenator application.

Such a liquid membrane oxygenator would present a liquid fluorocarbon interface to the blood. Studies of earlier investigations have indicated good, and perhaps even unique, blood compatibility with these liquid fluorocarbon interfaces; however, more information is needed. In the liquid membrane blood oxygenator new blood–fluorocarbon interfaces are generated constantly as new liquid membranes are formed. The interfaces are collapsed returning materials held at the interface to the blood as the bubbles are collapsed. Additional blood compatibility study is needed in systems where the blood–fluorocarbon interface is generated continuously and then collapsed in long testing periods. For such information to be truly convincing, the experiments would have to be performed *in vivo*.

Presuming the successful investigations in the above mentioned critical areas, a liquid membrane blood oxygenator might be developed. Such an oxygenator would be unique and offer many potential advantages, including the possibility of long term oxygenation.

Acknowledgment

The authors would like to thank H. W. Wallace of the University of Pennsylvania, R. Ferguson of the National Heart and Lung Institute, and C. G. Young, R. P. Cahn, and A. L. Shrier of Esso Research and Engineering Co. for their helpful discussions. Also, the authors thank T. Hucal for his assistance with the experimental work.

Literature Cited

1. *Chem. Eng. News* (Oct. 5, 1970), 36; (June 7, 1971) 30.
2. Li, N. N., *A.I.Ch.E. J.* (1971) **17**, 459.

3. Li, N. N., *Ind. Eng. Chem., Process Res. Develop.* (1971) **10**, 215.
4. Li, N. N., Shrier, A. L., "Recent Developments in Separation Science," Vol. 1, p. 163, Chemical Rubber Co., Cleveland, 1972.
5. Li, N. N., Asher, W. J., U.S. Patent pending.
6. de Filippi, R. P., Nose, Y., *et al., Proc. Artif. Heart Program Conf.*, p. 381, June 9-13, 1969.
7. Anderson, R. M., Nose, Y., *et al.*, "Development of a Liquid-Liquid Blood Oxygenator," Annual Report, PH 43-68-1393 (July 24, 1969).
8. Anderson, R. M., Nose, Y., *et al., Trans. Amer. Soc. Artif. Intern. Organs* (1970) **16**, 375.
9. Pitzele, S., *et al., Surgery* (1970) **68** (**6**), 109.
10. *Chem. Week* (January 13, 1971), 42.
11. Sloviter, H. A., Petkovic, M., Ogoshi, S., Yamada, H., *J. Appl. Physiol.* (1969) **27**, 666.
12. Geyer, R. P., Monroe, R. G., Taylor, K., "Organic Perfusion and Preservation," J. C. Norman, Ed., p. 85, Appleton Century-Crafts, 1968.
13. Technical Bulletin, 3M Mfg. Corporation.
14. Technical Bulletin, Dupont Chemical Corporation.
15. Langley, L. L., "Physiology," 2nd ed., McGraw-Hill, New York, 1965.
16. Keller, K. H., Leonard, E. F., "Engineering Analysis of the Functions of Blood," American Institute of Chemical Engineers, New York, 1968.
17. Peirce, E. C., II, Mathewson, W. F., Jr., "Design and Fabrication of Blood Oxygenator for Circulatory Assist Devices," *Artif. Heart Prog. Conf. Proc.*, p. 450-416 (June 9-13, 1969).
18. Landé, A. J., Tiedeman, R. N., Subramanian, V. A., Fillmore, S. J., Lillehei, C. W., "Progress in the Testing and Development of Practical Flat Plate Membrane Oxygenators for Cardiopulmonary Assist," *Artif. Heart Prog. Conf. Proc.*, p. 417-430 (June 9-13, 1969).
19. Peirce, E. C., II, "A Comparison of the Landé-Edwards, the Peirce, and the General Electric-Peirce Membrane Lungs," *Trans. Amer. Soc. Artif. Intern. Organs* (1970) **16**, 358–364.
20. Levinson, S. A., MacFate, R. P., "Clinical Laboratory Diagnosis," Chap. 9, Lea and Febiger, Philadelphia, 1969.

RECEIVED November 22, 1971.

The Role of Inert Gas Exchange and Population Statistics in Studies of Decompression Sickness

RICHARD G. BUCKLES

Alza Research, 2631 Hanover St., Palo Alto, Calif. 94304

E. HARDENBERGH

Naval Medical Research Institute, National Naval Medical Center, Bethesda, Md. 20014

Mass transfer models were combined with dose–response analyses to yield more insight into the fundamental etiology of decompression sickness. Data are presented that would favor a four-tissue model of a hamster from an inert gas exchange point of view: (1) lung, (2) a fast tissue with a time constant corresponding to the cardiac output per gram of tissue, and (3, 4) two slow tissues (time constant 6.3 and 25.5 min) corresponding to those tissue sites susceptible to bubble nucleation.

Decompression sickness is a disease experienced by divers and airplane pilots. It can be avoided if one uses procedures based upon a mass transfer analysis. This type of analysis is very old, having been first carried out by Haldane *et al.* in 1908 (*1*). Recent modifications can only be viewed as empirical curve-fitting attempts based on an increased amount of data (*2*).

The studies reported here are oriented toward enunciating the basic mechanisms of the disease rather than improving the existing model by curve fitting. Because the population response to the disease exhibits wide variance, the dose–response characteristics of the animal must be incorporated into the model. This blending of pharmacokinetic models and dose–response models provides more insight into the etiology of the disease than has been available.

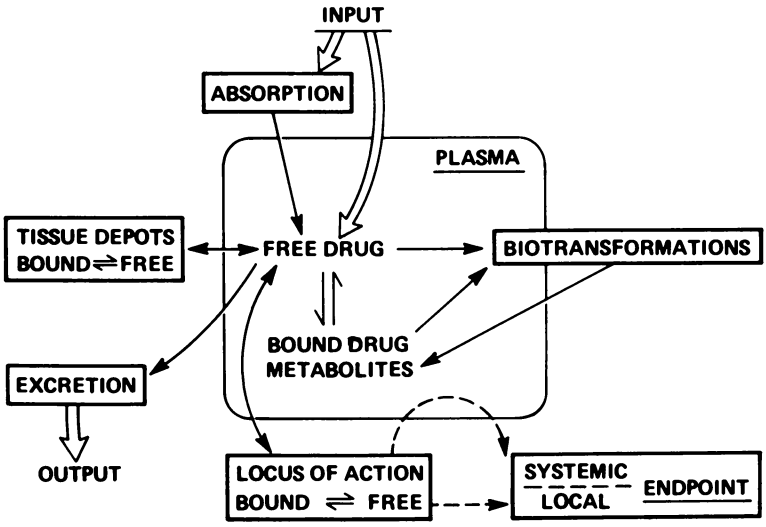

Figure 1. Drug distribution dynamics—i.e., *many processes can act on a drug from its point of input into the body to its output. Possible responses to the drug are also shown, indicating their (often) indirect relationship to the drug.*

Figure 1 summarizes the pharmacodynamacist's view of the flow of a material throughout the body from input to output, leading to a clinical endpoint. Through physiological measurements we can describe the transport of the material from input to the locus of action. We cannot confirm this process in decompression sickness because the locus is buried in peripheral tissue. Therefore, we must describe the population response (*i.e.*, endpoint) and make inferences about the process that occurs at the locus of action.

Decompression sickness represents the following simplifications of the general picture in Figure 1:

(1) The diffusing molecule is not protein bound.
(2) Time and dose are interrelated.
(3) Single route of introduction and excretion (the same route).
(4) No biotransformations occur.
(5) The locus of action is peripheral but random in location.

Since the action of the "drug" is a physical phenomena amenable to to mathematical description (*see* below), we hope that knowledge gained about the etiology of this disease in small animals can be scaled to larger animals and perhaps even to humans. The recent success of Bischoff *et al.* (3) in this type of scaling procedure for methadone provides increased confidence in the potential for applying the same scaling principles to decompression sickness.

Decompression Sickness

The symptoms of decompression sickness occur when bubbles form, grow, and circulate in the blood. The bubbles are generated when man goes from a high pressure to a low pressure environment, breathing some form of oxygen and "inert" gas. The inert gas is dissolved in all body tissues to a lesser or greater extent. (It is conventional to speak of the inert gas partial pressure, rather than its concentration, in these tissues [$P_{i\text{-tissue}} = C_{i\text{-tissue}} \div \alpha$]). When the hydrostatic pressure surrounding the animal is less than the partial pressure of the inert gas in any given tissue, there is a finite likelihood that nucleation of bubbles will occur, reducing the state of supersaturation in that tissue but leaving the tissue filled with bubbles. Divers enter this state of risk by breathing air at increased pressures while they are diving. They continue to absorb inert gas in various tissues while they are on the bottom. It is possible for divers to vary both the pressure and time of diving and end up with the same degree of risk. Because there has never been a satisfactory animal model for this disease, studies have been carried out on volunteer humans in simulated diving environments within steel chambers.

In 1966 experimental studies were initiated on the susceptibility of anaesthetized hamsters to decompression insult, attempting to utilize existing pharmacokinetic and toxicological modeling techniques to characterize the role of the inert gas in producing decompression sickness. The hamster model consisted of three discrete elements. First, a mass transfer model had to be developed that would describe the uptake,

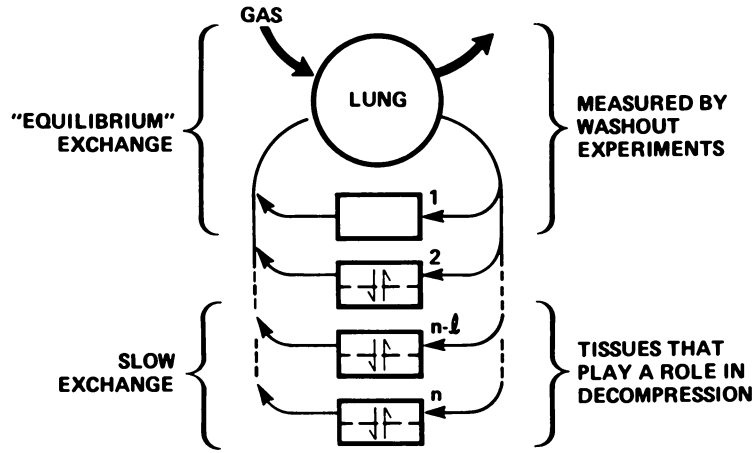

Figure 2. Generalized mass transfer model for the hamster
The model consists of n *tissues,* l *of which play a role in initiating decompression sickness. The first few tissues equilibrate with the rapidly circulating blood and have a high water content. The slower tissues may be characterized by two compartments coupled by inert gas diffusion.*

distribution, and elimination of nitrogen during exposure to high presssure air and a subsequent return to normal pressure. Secondly, the model had to take into account the response of the animal to supersaturation (*i.e., in vivo* nucleation had to be modeled). Finally, a population distribution based on the kinetics of bubble formation and growth would have to be superimposed upon the population response to bubbles.

Figure 2 describes the generalized mass transfer model based on the early work of Haldane (*1*). The region consisting of the lung and the fast tissue (No. 1) can be characterized by mass transfer studies of inert gas absorption and elimination. In these, it is assumed that Tissue 1 acts as a well-stirred chemical reactor so that the venous partial pressure of gas is equal to the average value for the tissue as a whole.

Somewhere in this model composed of *n* discrete tissues, it is postulated that the disease can be initiated by bubbles forming and growing. Evidence is presented here to indicate that it is the slow transport-limited tissues of the body that represent the tissues in which bubbles first nucleate. Mass transfer modeling of this sort postulates such tissues and then seeks experimental validation of their existence.

The population distribution elements of this model are described in Figure 3. Those distributions responding to a particular endpoint are plotted as a function of the inert gas tension in a characteristic tissue. This response would occur in an animal that had been exposed to a high pressure and then returned directly to 1 atm. Bubble formation begins when the tissue tension exceeds some lower limit and the population is

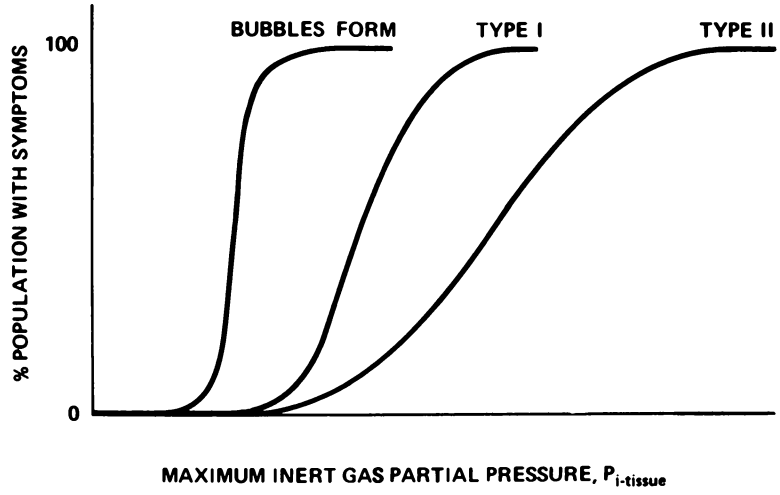

Figure 3. Generalized dose–response curves for decompression sickness As the tissue partial pressure ($P_{i\text{-tissue}}$) increases, the percentage of the population that exhibits a particular endpoint increases. The relative location of these three curves is the basis for much of the current controversy about modern diving practices.

distributed normally around a mean. Type 1 symptoms (itching, local pain, redness), those normally registered by divers, occur when the nitrogen tissue tension exceeds the level that just causes bubbles. This behavior is inferred from the many studies that have demonstrated the existence of circulating bubbles, even in humans, in the complete absence of clinical symptoms (*4*, *5*, *6*). Type 2 symptoms (paralysis, death), those exhibited by test animals in dose–response studies, occur at an even higher inert gas tissue tension.

The quantitative aspects of this type of population distribution study have never been characterized fully for animals or man. Recent trials by Flynn (*7*) and others (*8*) have at least demonstrated the qualitative aspects of this curve.

One fundamental assumption in explaining the etiology of decompression sickness is shown in Figure 4. This curve depicts the assumed behavior of small animals exposed to increasing insults of decompression risk. The percent mortality as a function of inert gas partial pressure in a characteristic tissue rises along an S-shaped curve and finally reaches a level of 100%.

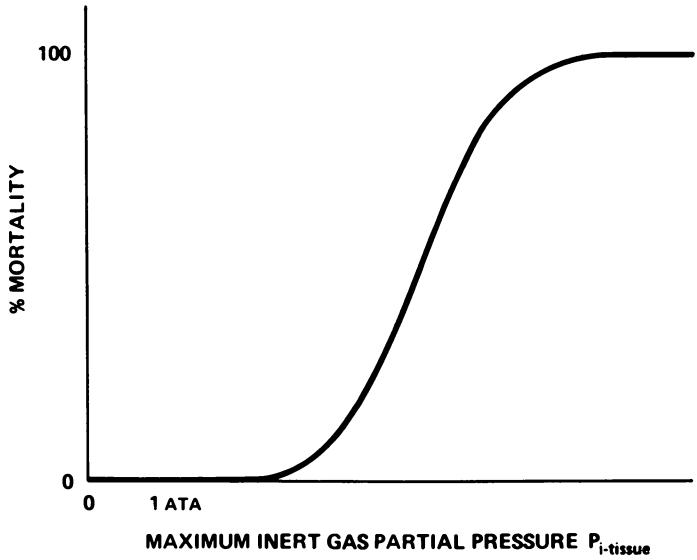

Figure 4. Assumed hamster dose–response curve
This curve exhibits a fundamental assumption about the occurrence of decompression sickness in hamsters: that they respond according to a normal dose–response curve and that mortality will go to 100%.

Experimental Studies

The experiments reported here were conducted according to the principles set forth in the "Guide for Laboratory Animal Facilities and

Care" prepared by the Committee on the Guide for Laboratory Animal Resources, National Academy of Sciences—National Research Council.

Our studies were carried out on male hamsters obtained from the NIH Breeding Colony, Bethesda, Md. They were anaesthetized with a chloralose urethane anaesthesia (1 cc/100 grams hamster with a solution containing 10 mg/cc chloralose, 10 mg/cc sodium borate, and 100 mg/cc urethane). Supplemental doses of 1/3 original dose were often required for long studies. The animals were kept a minimum of two weeks to stabilize dietary and environmental factors. An endotracheal tube, size PE60 or 90, was used in all cases, partly to eliminate the difficulty of respiratory stress, but more importantly in the gas washout studies to connect the animal directly to the breathing gas system.

Results

Two types of studies were carried out: the first, reported on a preliminary basis (*8*), involves the use of an endpoint—death—and is oriented towards the articulation of the receptor sites for bubble nucleation. The second study, reported here for the first time, involves a measurement of the fast inert gas exchange constants of the animal model. Both studies utilized air as a breathing mixture and were begun with the animal assumed to be in equilibrium with air at 1 atm ($P_{N_2} = 0.79$ ata).

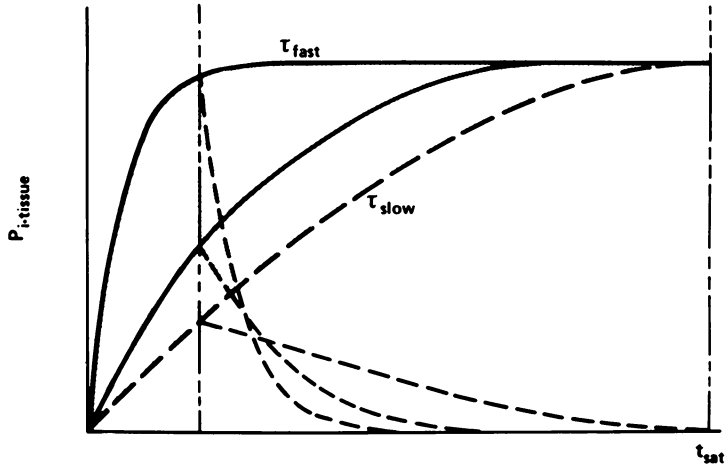

Figure 5. Inert gas partial pressure in the spectrum of hamster tissues during a simulated dive
The fast tissues (characterized by short time constants, τ_{fast}) rise rapidly to a level in equilibrium with the inspired air. In short dives, these tissues will be relatively more saturated than the slower ones (τ_{slow}). As the bottom time increases, the tissue partial pressures approach one another.

Dose–Response Curves. When the hamster is exposed to high ambient pressure, the partial pressure of nitrogen in its body tissues rises

along some form of exponential curve, ultimately reaching saturation (Figure 5). If at any time during this procedure the pressure is returned to 1 atm, the various body tissues are supersaturated with respect to ambient pressure and will attempt to return to ambient conditions (0.79 atm) along an exponential curve similar to that which they followed during the uptake portion of the dive. Short dives are characterized by high inert gas partial pressures in the tissues, represented by short time constants (τ_{fast}). However, long bottom time dives that show an ever-increasing degree of mortality, must reflect the gas uptake in the tissues with long-time constants (τ_{slow}).

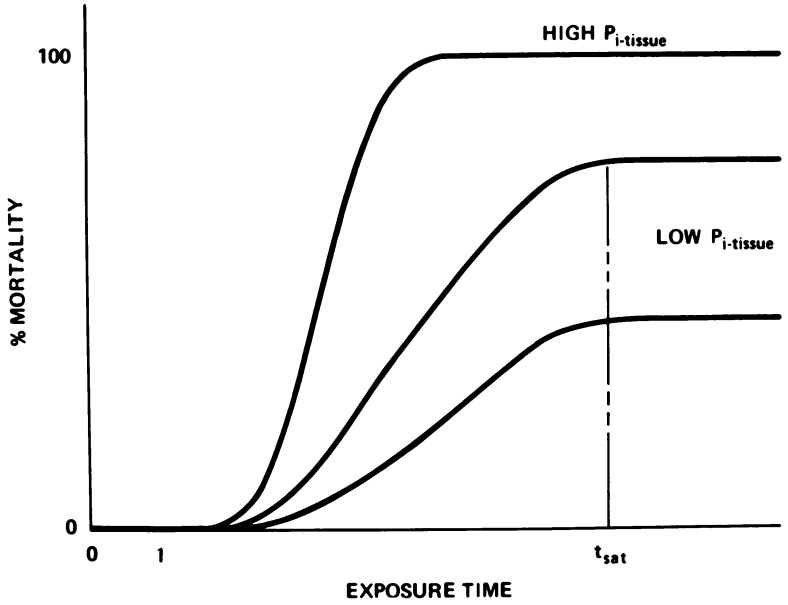

Figure 6. Generalized hamster dose–response curves
If the nitrogen partial pressure is high enough, the mortality will eventually go to 100%. However, with lower partial pressures the mortality rises to some asymptotic value after a constant time period. In this domain one can study the time effects independent of the nitrogen partial pressure.

Figure 6 shows three postulated dose–response curves that could be expected. In the curve marked high $P_{i\text{-tissue}}$, the ultimate response is 100% mortality because the inert gas partial pressure was so high that all animals were afflicted. If the depth of the dive is lowered (curves marked low $P_{i\text{-tissue}}$), the curve shifts to the right (towards increased exposure time) and flattens at a time (t_{sat}). In this range of pressures it is assumed that the time response is independent of the absolute pressure of the dive. Experiments of this kind are called time-based experiments (TB), and are used to characterize τ_{slow}, as defined in Figure 5.

Once τ_{slow} is determined, one may design an experimental dive sequence in which τ_{slow} will be the controlling tissue, regardless of depth. In these pressure-based trials (PB), one increases the absolute depth of the dive while maintaining the bottom time constant. An experimental dose–response curve similar to Figure 4 is then obtained and may be analyzed solely in terms of $P_{i\text{-tissue}}$, independent of time. $P_{i\text{-tissue}}$ can be calculated if one knows τ_{slow} and the time and pressure of a particular dive.

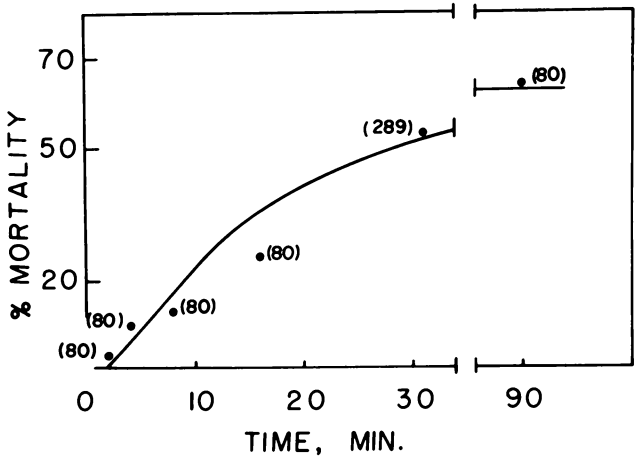

Figure 7. Hamster mortality as a function of time (8) *The hamsters were exposed to 11.2 ata of air for varying tissues. This graph exhibits the experimental results and the "best" line estimate of a normal mortality curve for the data. The numbers in parentheses indicate sample size*

The time-based and pressure-based studies were carried out in a small experimental chamber (8). The experimental results (% mortality as a function of time or pressure) were analyzed by the methods of probit analysis presented by Finney (9). The time-based studies were analyzed first (*see* Appendix I). A statistical best fit was applied to the data once it had been determined that the percent mortality that occurred at the longest bottom time (90 minutes) was the same as at the saturation level (*see* Figure 7). From the statistically best fit line of percent mortality *vs.* bottom time, the time associated with a mortality corresponding to 99% of saturation mortality was determined. Assuming that τ_{slow} characterizes a tissue that rises exponentially towards saturation, one may show that the time constant, τ_{slow}, is a simple multiple of the time to reach 99% of saturation (called t_{99}). From these experiments it was determined that $\tau_{slow} = 25.5$ minutes.

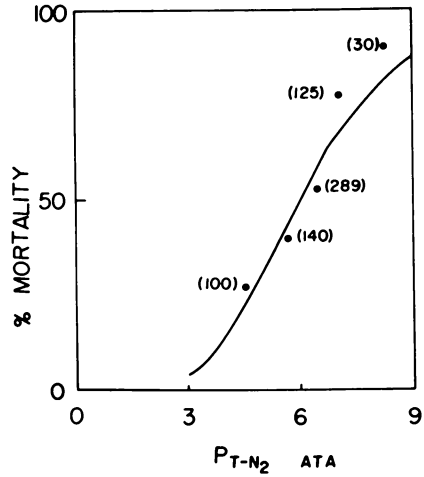

Figure 8. Hamster mortality as a function of maximum value of slow tissue nitrogen partial pressure (8)
The dives were carried out for 31 min in air (F = 0.79 *atm) and are related to the (assumed)* P_{T-N_2} *in the slowest tissue* (τ_1 25.5 *min). The partial pressure is related to dive depth,* P_{hyd}, *by:*

$$P_{T-N_2} = 0.79 + F(P_{hyd} - 1)(1 - e^{-t/\tau_1})$$

The numbers in parentheses indicate the sample size.

The pressure-based data were carried out by diving to increasing depths with a bottom time of 31 minutes. This time was determined from τ_{slow} so that the tissue controlling the mortality incidence would be the slowest tissue (τ_{slow}) under all conditions. Figure 8 is a plot of the percent mortality *vs.* the inert gas tissue tension in the slowest tissue for these PB data.

One may compute the inert gas tissue tension in the slow tissue at the end of the shorter bottom time dives in the TB series. These data points are plotted on Figure 9 where they are superimposed on the data from Figure 8. The dives corresponding to 2, 4, and 8 minutes fall significantly above the best fit curve based on the PB data.

Nitrogen Washout Curves. These studies were carried out to ascertain directly the rate of nitrogen elimination in anaesthetized hamsters at 1 atm. Hamsters that were initially equilibrated with air were attached to a breathing circuit, shown in Figure 10, through which an 80/20 helium oxygen gas mixture was passed at a constant flow rate. The gas passed through a sampling valve of a gas chromatograph so that one could take discrete samples at fixed intervals after the animal was at-

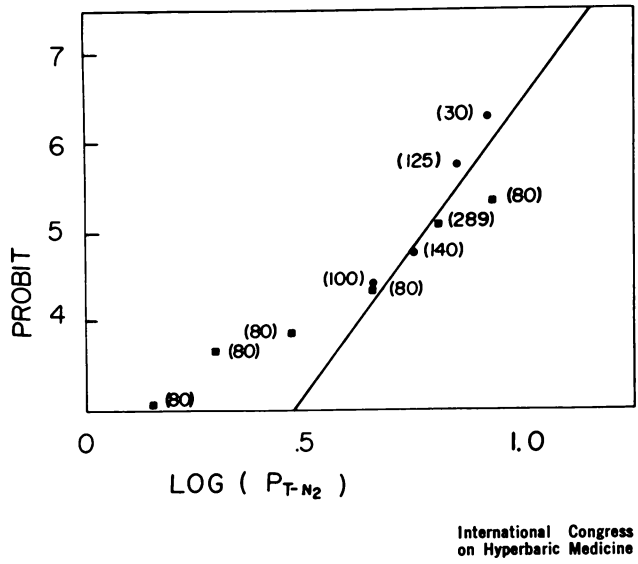

Figure 9. Hamster mortality as a function of P_{T-N_2} (8) *The data are plotted (for illustration) as the probit* vs. *log* P_{T-N_2}. The value of P_{T-N_2} *is computed from* P_{N_2t} *as in Figure 9, assuming* $\tau = 25.5$ *min. The solid line corresponds to a least-squares fit of the PB data. The TB data (■) fall significantly to the left of the line. The numbers in parentheses indicate the sample size* (see *Figure 8).*

tached to the system. Since the system could be calibrated with known gases, the acquired data were expressed in terms of nitrogen fraction (F) at discrete times during the washout. The dead space between the animal connection and the sampling loop was negligible.

The method of data analysis is derived in Appendix II. The animals were grouped according to weight, and the average data were plotted in terms of the log $[F\dot{Q}/W]$ as a function of time. The experimental parameters measured were nitrogen fraction (F), gas flow rate ($\dot{Q}$), and hamster weight (W). Figure 11 is a characteristic curve. Nitrogen excretion decreased rapidly during the first two minutes (pulmonary washout) and then more slowly. A best-fit line was drawn by eye, and the slope and intercept of that line were determined. Table I is a list of the intercept and slope (F_0 and τ).

A mass balance on nitrogen shows that

$$K = \frac{f_f \alpha_f}{\rho f} + f_w \alpha_w$$

where K is the ratio of total initial dissolved nitrogen to body weight. To determine K *a priori*, one must know the solubility coefficients for N_2

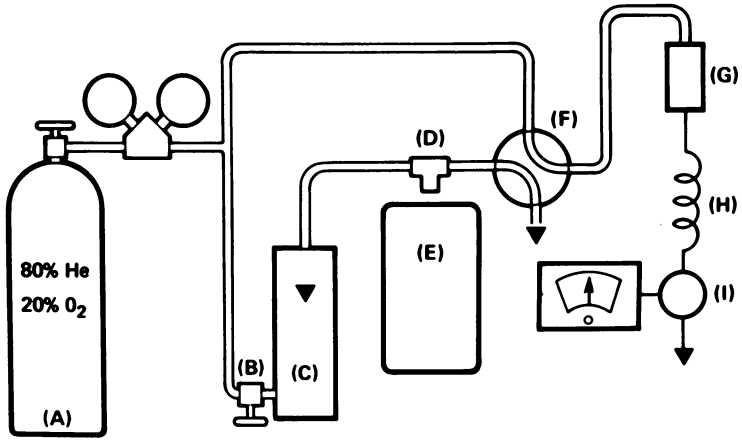

Figure 10. Hamster breathing loop for analysis of exhaled N_2 The system consists of: (a) compressed gas (80/20 He/O_2) and appropriate flow regulators; (b) fine flow rate control value; (c) rotometer; (d) T-joint with gas tight fitting for attaching hamster endotracheal tube; (e) heating pallet for hamster; (f) chromatograph sampling valve; (g) water and CO_2 absorbent bed; (h) chromatograph column; (i) thermal conductivity detector.

in fat and water (α_f, α_w), the density of body fat (ρf), and the fraction of body weight that is fat and water (f_f, f_w). K is measured experimentally by integrating the ($F\dot{Q}/W$) curve from time zero to infinity, neglecting the pulmonary contribution. A plot of K *vs.* body weight indicates that there is no statistical dependence on W (Table II). However, Figure 12 shows that τ, the time constant, is related to body weight. The time constants in these experiments are much shorter than the longest time constant determined in the dose–response experiments (25.5 minutes).

Discussion

The time-based dose–response curve yielded a slow tissue time constant of 25.5 minutes. This is significantly greater than any circulation time constants previously reported in small animals (7). The experiments cannot indicate the anatomical location or the mode of transport responsible for this slow time constant. Flynn's studies (7), which failed to show such a slow tissue, were performed on unanaesthetized mice so the conditions for comparison are not exact. Detection of this slow tissue by measurement of pulmonary gas washout is probably not feasible be-

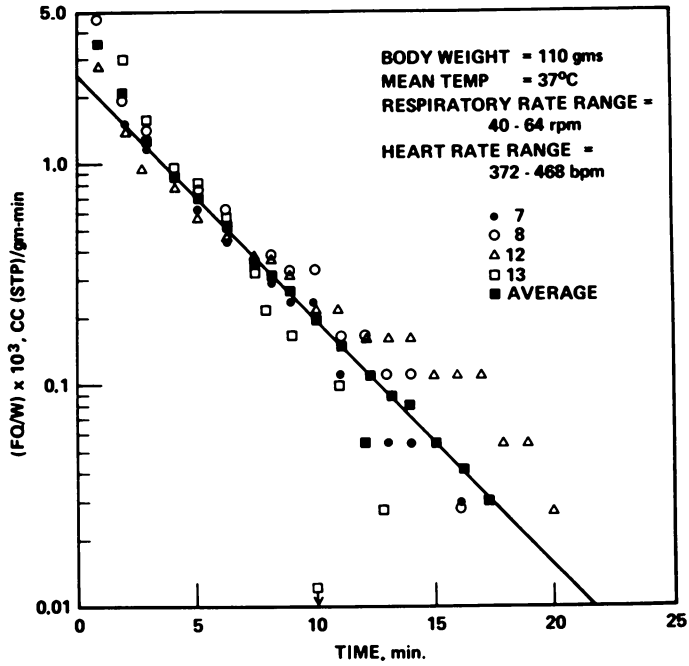

Figure 11. Exhaled N_2 $\frac{FQ}{W}$ as a function of time

Washout data from four, 110-gram hamsters with a mean body temperature of 37°C. The arithmetic average points (■) describe a simple exponential function of time.

Table I. Slope (τ) and Intercept ($FQ/W \times 10^4$) of Washout Curves

Total Body Weight, grams	τ, *minutes*	$(FQ/W \times 10^4)$, *cc/g-min*
75	.542	33.5
85	.875	25.0
88	.748	17.5
93	1.31	18.8
102	1.48	24.8
107	1.63	20.3
110	1.37	18.3
121	1.86	17.0

cause of the extremely low quantity of N_2 involved and the many sources of N_2 leaks that could yield this much nitrogen (diffusion through plastic tubing, transcutaneous N_2 transport, or leaks around seals).

If one extrapolates the pressure-based dose–response data to a 1% mortality level (a threshold for the disease), the inert gas partial pressure is 2.5 ata. Trials on humans have indicated a critical threshold for detecting decompression sickness at 2 ata, not too different from the value for

Table II. Experimental Values of $K \times 10^3$

Total Body Weight, grams	$K \times 10^3$, *cc/g-atm*
75	2.33
85	2.80
88	1.67
93	3.16
102	4.70
107	4.23
110	3.22
121	4.05

hamsters. This would imply that the population response curves for type 2 symptoms as measured on hamsters is not too different from the response curves for humans with type 1 symptoms at the low incidence level. This then suggests that the curves drawn in Figure 4 would be virtually coincident at the lower response levels. It is just this tendency for the curves to coincide that makes it so difficult to settle the arguments concerning the presence or absence of asymptomatic bubbles in human divers.

Figure 9 indicates that the slow tissue that was responsible for mortality in saturation dives could not be responsible for the high mor-

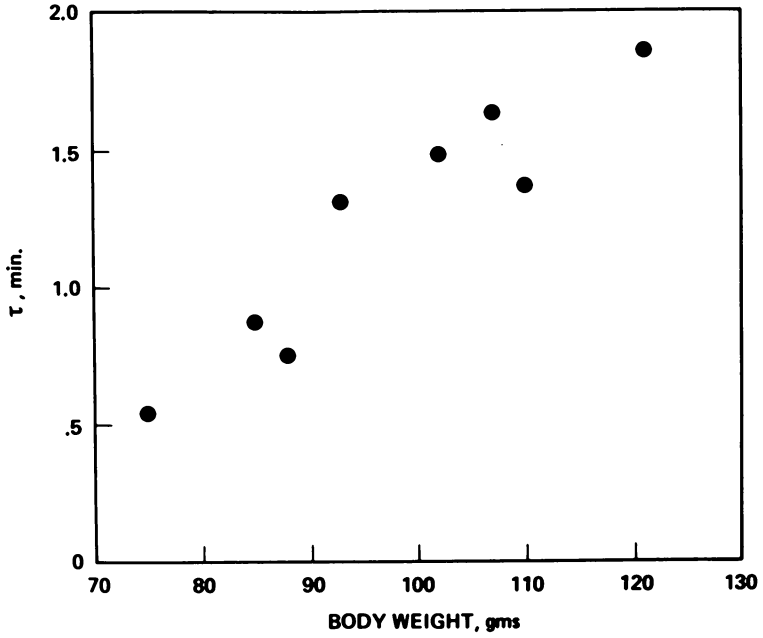

Figure 12. N_2 washout time constant (τ) as a function of body weight

tality in the shorter dives. That is, the experimental mortality was significantly greater than the least-squares line based on the slow tissue. One explanation of this would be that faster time constant tissues exist in the body and are responsible for the higher mortality in the shorter dives. Since we know from the N_2 washout studies that faster tissues do exist, it is worth trying to determine whether these faster tissues could be sites of nucleation for short dives.

If we assume that all tissues have the same susceptibility to bubble formation, their inert gas tissue tension should be the same as the best experimental line for the PB data. By this method we can calculate back to determine what the time constant of these faster tissues would be in order to acquire this level of inert gas tension. When this is done, the tissue time constant is 6.3 minutes for the two-minute bottom time experiments. While this is significantly faster than the 25.5-minute constant measured for the slow tissues, it is still significantly greater than the slowest time constant measured in the nitrogen washout studies (Figure 12). Thus, it is assumed that the well-perfused tissues of the body would never be the sites of bubble formation for dives greater than two minutes. These data also confirm experimentally the generally held notion that there is a spectrum of response time for the body tissues.

A range of physiologic responses was noted in hamsters exposed to the washout studies. Core temperatures as low as 30°C were measured. Heart rates ranged from 324 to 564 cpm, and respiration rates were 40–68 rpm. In spite of this, no significant systematic variation of time constants could be demonstrated. This is interpreted to mean that the time constants measured by this technique are for tissues that are so well perfused that they are independent of variabilities in the physiologic parameters measured. Peripheral tissues that are known to be sensitive to these parameters are obviously not measured by this method.

A comparison of the experimentally measured K value (Table II) and various theoretical K values is instructive. An average 100-gram hamster is 63.4% water, 17.4% fat, and 19.2% bone and other material (kindly determined by F. K. Millar, Laboratory of Physiology, NCI, NIH, Bethesda, Md.). Based on published values of solubility coefficients, one can compute a theoretical value of K of 26.2×10^{-3}. Thus, we must infer that only part of the total nitrogen washout was actually measured during the washout studies. At the other extreme, one could assume that we measured only the nitrogen dissolved in the bloodstream. When the average K value is converted to a fractional composition, assumed to be water, the fraction is 0.13. This is significantly higher than the known factor of blood ($\sim$.07) and much lower than the total water content. Thus, we must be measuring some volume greater than

the blood volume. It is inferred that certain tissues are perfused in an equilibrium fashion with the blood and are, therefore, washed out at the same rate as is the blood.

Various ways have been used to estimate the cardiac output per gram of tissue of animal species. Since direct information on cardiac output for hamsters is not available, different estimation procedures were used. These are summarized in Appendix III. The average value of cardiac output per gram of tissue is 0.64 cc/gram-min, based on a 100-gram hamster. Notice from Figure 11 that the inverse of the cardiac output per gram of tissue (1.6 minutes) is similar to the time constant for a 100-gram hamster. This lends strong credence to the observation above that the time constant measured for gas washout from hamsters in these experiments is essentially that of the gas dissolved in blood and the well perfused tissues of the body.

Summary

Arguments are presented that favor a four-tissue model of a hamster from an inert gas exchange point of view; (1) lung, (2) a fast tissue with a time constant corresponding to the cardiac output per gram of tissue, and (3,4) two slow tissues (time constant 6.3 and 25.5 minutes) corresponding to those tissue sites susceptible to bubble nucleation.

Acknowledgments

We express our appreciation for technical assistance in these experiments of L. Hardy, D. Bennett, L. Sutermeister, and J. M. Miles, Jr. F. K. Millar who graciously assisted us in determining hamster body composition.

Appendix I—Analysis of Time-Based Data by the Method of Probits

It is assumed that the time-based data fit a theoretical dose–response curve as shown in Figure 6. Analysis of such dose–response curves, first described by Bliss (*10*), consists of finding a convenient method to linearize the data. In such a linearized form, a least-squares regression line and standard estimates of data variance can be obtained.

However, the data are generally too sparse to permit simple analysis. Some judgment must be made of the several possible results to obtain one that is internally consistent. An example of this procedure is given here for the time-based data. The data are presented in Table I-A.

Table I-A. Time-Based Data

Bottom Time, min.	n	*Mortality, %*
2	80	2.50
4	80	8.75
8	80	12.50
16	80	25.0
31	289	52.9
90	80	63.75

The data are converted to the coordinate system of probits as a function of log (time). First the mortality data must be converted to response data. One may do this with one of two plausible assumptions: (a) that the mortality at 90 minutes corresponds to 100% response, or (b) that the mortality at both 31 and 90 minutes corresponds to 100% response, and one then lumps the data. The mortality data are converted to response data by expressing each as a percentage of the mortality selected as the 100% response. These data are plotted against the $\log_{10}$ (time). Data based on the two assumptions are given in Table I-B.

Table I-B. TB Data Expressed as Response Data

Bottom Time, min.	*$\log_{10}$ (time)*	*% Response (a)*	*Probit (a)*	*% Response (b)*	*Probit (b)*
2	.301	3.91	3.24	4.27	3.28
4	.602	13.7	3.90	15.0	3.96
8	.903	19.6	4.14	21.4	4.21
16	1.204	39.2	4.73	42.7	4.81
31	1.491	83.0	6.15	100.0	—
90	1.959	100.0	—	100.0	—

Although the data do not appear too different, logic leads us to select assumption (a). An approximate best fit to the data yields a time constant of about 30 minutes. If this is true, the data points of 31 minutes could not be at all representative of saturation data.

Since the data exhibits significant scatter, one must use a least-squares method to correlate probit with $\log_{10}$ (time) [*see* Finney (9), Chapter 4]. This is done in an iterative style of successively improving the approximation to the least-squares line. Four iterations were required to yield a least-squares lines given by:

$$\text{Probit} = 2.08 + 2.54 \log_{10} (\text{time})$$

A 99% response occurs when probit = 7.326. This yields a t_{99} (time when 99% response occurs) given by: t_{99} = antilog$_{10}$ (2.068) = 117 minutes.

Since we have assumed that this level of mortality is produced by a slow tissue reaching saturation with N_2 along an exponential curve, $e^{t/\tau}$, the time constant is related to t_{99} by:

$$\tau = t_{99} \div 4.61$$

Thus, $\tau = 25.5$ minutes.

Appendix II—Analysis of Nitrogen Washout Data

The nitrogen washout data consist of F, the fraction of nitrogen in exhaled air, measured as a discrete function of time after shifting to an 80–20 He–O_2 breathing mixture. When plotted as log F *vs.* time, the data fall along one line. Only the first one or two data points are above this "best" line. These presumably are caused by pulmonary and breathing loop dead spaces and are neglected hereafter.

To a first approximation:

$$[\text{Total } N_2 \text{ excreted}]\ t = n\Delta t = \sum_{j=1}^{n} F_j \dot{Q}_j \Delta t$$

where $\dot{Q}_j$ is the gas flow rate during the interval F_j is measured. When $n = \infty$, the total nitrogen excreted should equal the total nitrogen dissolved in the body at the start of the experiment (neglect skin transport of N_2 for this analysis). That is

$$V_{N_2\text{-TOT}} = \sum_{j=1}^{\infty} F_j \dot{Q}_j \Delta t = (V_f \alpha_f + V_w \alpha_w)\, P_{N_2\text{-air}}$$

where V_f (or V_w) is the volume of fat (or water) and α_f (or α_w) is the solubility coefficient for N_2 in fat (or water). This expression may be rewritten as:

$$V_{N_2\text{-TOT}} = W_{TOT} K P_{N_2\text{-air}}$$

where,

$$K = \left[\frac{f_f \alpha_f}{\rho f} + f_w \alpha_w\right]$$

ρf is the density of fat, and f is the weight fraction of fat or water.

Since we do not have data for $F\dot{Q}$ to infinity, it seemed desirable to derive a mathematical expression for it so as to convert the summation

to an integration. Consider the body as a lumped mass that transmits N_2 to the breathing loop at a rate

$$\dot{q} = k\overline{P}$$

where $\overline{P}$ is mean body N_2 partial pressure, and k is a transfer coefficient, and $\dot{q}$ is the nitrogen excretion rate.

Now,

$$\dot{q} = \frac{d}{dt}(V_{N_2\text{-TOT}}) = \frac{d}{dt}(KW_{TOT}\overline{P})$$

Rearranging,

$$\frac{k}{KW_{TOT}} = \frac{d \ln \overline{P}}{dt}$$

It is also true that $F = q/\dot{Q}$ if one can neglect variations in q_{O_2}, q_{CO_2}, and q_{H_2O}.

From this we obtain,

$$F = \frac{k}{\dot{Q}}\ \overline{P}$$

so,

$$\frac{dF}{dt} = \frac{k}{\dot{Q}}\ \frac{d\overline{P}}{dt}$$

and

$$\frac{1}{F} \cdot \frac{dF}{dt} = \frac{1}{P}\ \frac{d\overline{P}}{dt}$$

Thus,

$$\frac{d \ln F}{dt} = \frac{k}{KW_{TOT}}$$

Note also that: $\dfrac{d \ln (F\dot{Q}/KW_{TOT})}{dt} = \dfrac{d \ln \overline{P}}{dt}$

Hence, the slope of a line plotted through the data (log $(F\dot{Q}/KW_{TOT})$ *vs.* time) will yield a whole body mass transfer coefficient. It will then be possible to compute the experimental value of K by simple integration.

Appendix III—Estimation of Hamster Cardiac Output

Several methods are used to estimate cardiac output (CO), with data gathered from various animal species. Each is described, then an average value is taken. All data are based on a 100-gram hamster.

(A) $CO = \frac{(\text{Blood Volume})}{(\text{Circulation Time})}$

Blood volume $= f_B W_{TOT} = .074 \times 100 = 7.4$ cc
Circulation time: (Ref. *11*, p. 115)
man: 7–9 sec
dog: 10–11 sec
rabbit: 10.5 sec
If we assume for a hamster it is 10 sec, CO = 44.4 cc/min.

(B) CO = (Cardiac Index) × (Surface Area)

Cardiac index $= 1.6 \times 10^{-3}$ cc/min-sq m (Rat, Ref. *11*, p. 80)
Surface area $= .091 \times W_{TOT}^{2/3}$ (Rat, Ref. *11*, p. 80)
CO = 31.5 cc/min

(C) CO = (Cardiac Index) × (Surface Area)

Cardiac index $= 2.47 \times 10^3$ cc/min-in^2 [anesthetized ferrets (*12*)]
Surface area $= .001\ W_{TOT}^{2/3}$
CO = 53.2 cc/min

(D) $CO = \frac{(\text{Blood Volume})}{(\text{Circulation Time})}$

Blood volume = 7.4 cc (*see* III A)
Circulation time = 4.5 sec (*see* III C)
CO = 98.7

(E) $CO = \frac{(O_2 \text{ Consumption})}{(A\text{-}V\ O_2 \text{ Gradient})}$

O_2 Consumption = 2.3 cc/gram-hr (*see* III A)
A-V O_2 Gradient = 4.1 vol % [anesthetized dogs (*13*)]
CO = 98.7 cc/min

(F) The arithmetic average cardiac output is 64.3 cc/min. No weighing is given the various estimates because of uncertainties in all methods.

Literature Cited

1. Haldane, J. S. *et al.*, *J. Hygiene* (1908) **8**, 342.
2. Workman, R. D., "American Decompression Theory and Practice," in "The Physiology and Medicine of Diving and Compressed Air Work," P. B. Bennett, D. H. Elliott, Eds., pp. 252–290, Williams and Wilkins, Baltimore, 1969.
3. Bischoff, K. B. *et al.*, *Cancer Chemotherapy Repts. Pt. 1* (April 1970) **54** (2).
4. Oyama, Y., Spencer, M. P., *Physiologist* (1969) **12**, 320.
5. Gillis, M. F. *et al.*, *Nature* (March 1968) **217**, 965–967.
6. Smith, Kent H., Johanson, Dave, Virginia Mason Research Institute (Seattle, Wash.), *Tech. Rept.*, ONR Cont. N00014-69-C-0402 (1 June 1970).

7. Flynn, E. T., Lambertson, C. J., "Underwater Physiology," pp. 179–191, Academic, New York, 1971.
8. Buckles, R. G., Hardenbergh, E., *Proc. Intern. Congr. Hyperbaric Medicine, 4th, Tokyo* (1970), 109–115 (Igaku Shain Ltd.)
9. Finney, D. J., "Probit Analysis—A Statistical Treatment of the Sigmoid Response Curve," University Press, 1952.
10. Bliss, C. I., *Science* (1934) **79**, 38–39.
11. "Handbook of Circulation," WADC TR59-593.
12. *Proc. Soc. Exp. Biol. Med.* (1949) **72**, 711–714.
13. "Handbook of Respiration," WADC TR58-352, p. 58.

RECEIVED December 8, 1971. Studies carried out at the Naval Medical Research Institute, National Naval Medical Center, Bethesda, Md. under support from the Bureau of Medicine and Surgery, Navy Department, Research Task M4306, 01-1020B. The opinions and assertions herein are the authors' alone and do not necessarily reflect the views of the Navy Department or the naval service at large.

Respiratory Gas Transport in Brain under Normal and Pathological Conditions

J. GROTE, H. KREUSCHER, H. J. REULEN, P. VAUPEL, and H. GÜNTHER

Departments of Physiology, Anesthesiology, and Neurosurgery, University of Mainz, Mainz, West Germany

The oxygen supply conditions of cerebral tissue were studied in dogs and in patients under different physiological and pathological conditions. Under conditions of respiratory and nonrespiratory acidosis a decrease in pa_{O_2} *induced an increase of CBF when the oxygen tension in cerebral venous blood fell below 35–40 mm Hg. At the same time the cerebral glucose uptake, the cerebral lactate output, and the lactate–pyruvate ratio in cerebral venous blood increased. Critical conditions occurred for the oxygen supply of the brain when cerebral venous* p_{O_2} *fell below approximately 30 mm Hg. In edematous brain areas of patients, rCBF decreased with increasing brain water content. Theoretical analysis of oxygen diffusion in the brain tissue for the investigated conditions agreed with findings of regional metabolite concentrations.*

The problems of oxygen transport in the brain are investigated under different physiological and pathological conditions. The oxygen supply of an organ is determined by the relationship between the oxygen requirement of the tissue and the oxygen transport to the tissue cells by convection and diffusion. To maintain normal aerobic metabolism, a minimum oxygen tension of approximately 0.5–2.0 mm Hg must be maintained in the cells of cerebral tissue under conditions of an adequate substrate and ADP level (*1*, *2*, *3*). When oxygen tension in the mitochondria decreases below a critical value (0.2–3.0 mm Hg), the oxygen activating system begins to unsaturate, and aerobic cell metabolism decreases (*4*, *5*, *6*, *7*). Because the concentrations of respiratory enzymes are higher than necessary for the maximal mitochondrial respiration, the actual limiting

oxygen tension in the single cell can be smaller than the critical oxygen tension of the mitochondria (*4, 7*).

The quantity of oxygen transported per unit of time by convection to the brain is determined by the blood flow rate, the oxygen capacity, the oxygen affinity of blood, and the arterial oxygen tension. Under normal conditions the mean overall blood flow rate in cerebral tissue of dogs, monkeys, and humans ranges between 50 and 65 ml/100 g-min (*8, 9, 10, 11, 12, 13, 14, 15, 16, 17, 18*). Specific measured mean values of 80 to 110 ml/100 g-min were determined for cerebral cortex (*18, 19, 20, 21, 22, 23, 24, 25, 26, 27*), and 15 to 25 ml/100 g-min were measured for white matter (*20, 23, 26*).

In addition to blood flow rates, the oxygen capacity of blood is a major factor affecting the convective transport of oxygen to the brain. Oxygen capacity is the maximum oxygen uptake capability of the blood per defined unit of volume. Under physiological conditions it depends almost entirely on the hemoglobin concentration of the blood. The extent to which the oxygen transport capacity, determined by the blood flow rate and the oxygen capacity of the blood, can eventually be utilized is largely determined by the oxygen affinity of blood. The oxygen affinity of the blood is determined by the relationship between the oxygen tension and the oxygen saturation of the hemoglobin. This function is represented diagrammatically by the oxygen dissociation curve of the blood. Under the oxygen tension conditions present in the lung, the shape of the oxygen dissociation curve primarily determines the degree of hemoglobin saturation with oxygen. In tissue regions the blood oxygen affinity determines the oxygen tension decrease in blood during capillary passage and, consequently, the degree of oxygen exchange by diffusion between capillary blood and cerebral tissue.

Besides the oxygen transport characteristics of blood, important factors influencing oxygen transport by diffusion between blood and tissue cells are the oxygen tension and the acid–base status of arterial blood, kinetics of the intracapillary release of oxygen from oxyhemoglobin, tissue metabolism, oxygen diffusion coefficients of blood and cerebral tissue, capillary dimensions, and the anatomical structure of the supply area of single capillaries in cerebral tissue. Provided that all these biological data are known, it is possible to analyze the oxygen exchange processes between capillary blood and cerebral tissue and to predict by calculation the oxygen tension in tissue (*9, 28, 29, 30, 31, 32, 33, 34, 35, 36, 37, 38*).

Experimental

During our investigations of respiratory gas exchange in the brain, we combined experimental studies of the different parameters affecting oxy-

gen supply of cerebral tissue and theoretical analyses of oxygen diffusion between capillary blood and tissue cells (*31*, *32*, *33*, *39*, *40*, *41*). The present studies examined respiratory gas transport in the brain under normal conditions and under defined pathological conditions. Studies were conducted on dogs and humans.

During experiments on dogs, we studied the influence of arterial hypoxia on cerebral blood flow, cerebral oxygen supply, and cerebral metabolism under normal acid–base conditions as well as under conditions of respiratory and nonrespiratory acidosis. During investigations on patients, we studied the influence of local brain edema (in the periphery of brain tumors or brain lesions) on the cerebral blood flow, the oxygen supply, and the metabolite concentrations of the edematous tissue.

Experiments on Dogs. The influence of reduced arterial oxygen tensions on respiratory gas transport in the brain under different acid–base conditions were studied on 29 dogs during nitrous oxide anesthesia, muscle relaxation, and artificial ventilation. During the experiments ventilation conditions were changed in such a manner that arterial oxygen tension decreased but arterial carbon dioxide tension remained constant. Parameter studies were made at constant arterial carbon dioxide tensions. Mean arterial blood pressure and body temperature were kept in normal ranges. After constant conditions (steady-state) in arterial blood had been attained, total cerebral blood flow was measured using the dye dilution technique (*39*, *42*). In some cases regional cerebral blood flow of the cerebral cortex was measured, using the ^{85}Kr technique (*20*). The p_{O_2}, p_{CO_2}, and pH as well as the concentration of glucose, lactate, and pyruvate were determined polarographically, potentiometrically, and enzymatically (*43*), respectively, in simultaneously, anaerobically taken arterial (art. carotis communis) and cerebral venous (torcula) blood samples. The oxygen and glucose uptake and the lactate output of cerebral tissue were calculated. The EEG was recorded in some experiments.

Studies in Patients. Oxygen transport in cerebral edema were studied in 14 artificially ventilated patients during nitrous oxide anesthesia (*8*), halothane, nitrous oxide anesthesia (*2*), and neuroleptanalgesia (*4*). Arterial CO_2 tension as well as endexpiratory CO_2 concentration were regularly monitored. Arterial blood pressure was kept in normal ranges. Following craniotomy and opening the dura, regional cerebral blood flow in brain areas bordering brain tumors or brain lesions was measured by the ^{133}Xe clearance method, using a bolus injection of the radioisotope into the internal carotid artery. Following rCBF measurements, one or two brain tissue specimens including gray and subcortical white matter were removed, corresponding to the location of the respective scintillation probe, by means of a precooled rongeur (in an area which had to be extirpated later). Samples for analysis of metabolites were immediately immersed in liquid nitrogen. In each sample the content of tissue water, different electrolytes, and the tissue metabolites phosphocreatine, ATP, ADP, glucose, lactate, and pyruvate were analyzed (*44*). The p_{O_2}, p_{CO_2}, and pH were determined in the arterial blood immediately after rCBF measurements. Neither p_{O_2} in brain tissue nor p_{O_2}, p_{CO_2}, and pH in regional venous blood could be measured during the operative procedure. To obtain information about the local oxygen supply, the oxygen tension

distribution in the capillary blood and the brain tissue was predicted by calculation (*28, 31, 32, 33*).

Discussion of Results

Previous Work. As shown by the results of many experimentors, cerebral blood flow rate (under normal blood pressure conditions) is primarily determined by the CO_2 tension in arterial blood (*12, 14, 21, 22, 45, 46*). The pH value of the extracellular fluid in brain is regarded as an essential factor for regulating vascular diameter (*47, 48, 49, 50*). Cerebral hypoxia causes the CO_2-dependent regulation of the cerebral blood flow to change or vanish (*9, 21, 25, 40, 45, 46, 51, 52*).

If the oxygen tension falls below approximately 60 mm Hg in arterial blood and below approximately 25–28 mm Hg in cerebral venous blood, the cerebral blood flow increases. On the basis of numerous experimental investigations, Noell and Schneider defined a reaction threshold for a cerebral venous oxygen tension of 25–28 mm Hg and a critical threshold for a cerebral venous oxygen tension of 17–19 mm Hg (*46, 51*). If the oxygen tension in the cerebral venous blood falls below these values, an increased cerebral blood flow results in the first case; whereas unconsciousness and distinct changes in the EEG are observed when the critical threshold is reached (*25*).

It can be shown by theoretical and experimental investigations that, under normal acid–base conditions, hypoxia takes place in certain areas of the cerebral cortex or in other regions of the brain with high oxygen consumption rates when an oxygen tension of 27 mm Hg is reached in the cerebral venous blood. It can also be shown that anoxia occurs in the same sections of the brain at cerebral venous oxygen tensions of 17–19 mm Hg (*28, 31, 32, 33*).

Experiments on Dogs. Acidosis. Under respiratory and nonrespiratory acidosis the progressive lowering of arterial oxygen tension leads to an increase of the cerebral blood flow whenever oxygen tensions in cerebral venous blood fall below 35–40 mm Hg. Critical conditions for the cerebral oxygen supply occur when the oxygen tension in cerebral venous blood falls below 30–32 mm Hg. These reaction and critical threshold values are higher than those reported for conditions of normal acid–base status in arterial blood.

Respiratory Acidosis. Under conditions of respiratory acidosis with carbon dioxide tensions between 50 and 60 mm Hg the O_2-dependent elevation of cerebral blood flow is activated after reduction of cerebral venous oxygen tension to 35 mm Hg. Critical conditions of oxygen supply result from a further reduction of arterial oxygen tension when the cerebral venous oxygen tension falls below 30 mm Hg. With a cerebral

venous oxygen tension of 27 mm Hg, we observed a definite blood pressure fall and a pronounced bradycardia. Immediate elevation of the arterial oxygen tension restored the cerebral oxygen supply conditions to normal (Figure 1).

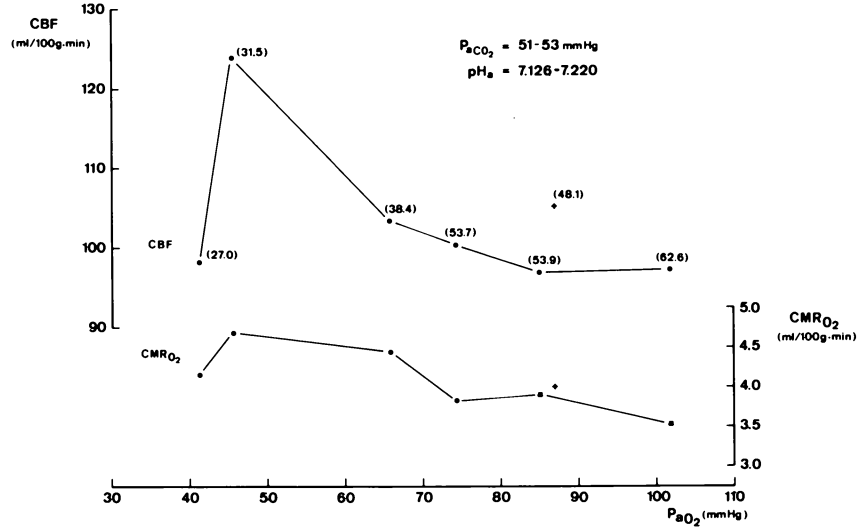

Figure 1. Effect of progressively decreasing arterial oxygen tension on cerebral blood flow and cerebral oxygen uptake under conditions of respiratory acidosis.

Values in parentheses are the pertinent O_2 tensions in cerebral venous blood. Values with a cross (+) indicate the cerebral blood flow rate and the cerebral oxygen uptake determined following return of ventilation conditions to normal.

NONRESPIRATORY ACIDOSIS. Under the combined conditions of nonrespiratory acidosis and arterial hypoxia, there was a large increase in cerebral blood flow and in the lactate–pyruvate ratio of cerebral venous blood. Also there was an increase in glucose uptake of the cerebral tissue. This occurred as soon as oxygen tensions below 38 and 40 mm Hg appeared in cerebral venous blood. When normal oxygen tensions in the arterial blood were adjusted again by changing the conditions of ventilation before reaching a cerebral venous oxygen tension of approximately 30 mm Hg, the values for the cerebral blood flow and the oxygen and glucose uptake of the cerebral tissue quickly returned to initial values (Figure 2).

When—under comparable conditions—the arterial oxygen tension was lowered to such an extent that values of oxygen tension below 30 mm Hg occurred in the cerebral venous blood, a decrease in arterial blood flow and in oxygen uptake was registered, whereas the glucose uptake of the cerebral tissue and the lactate–pyruvate ratio of cerebral venous blood continued to increase. In these experiments the return to initial

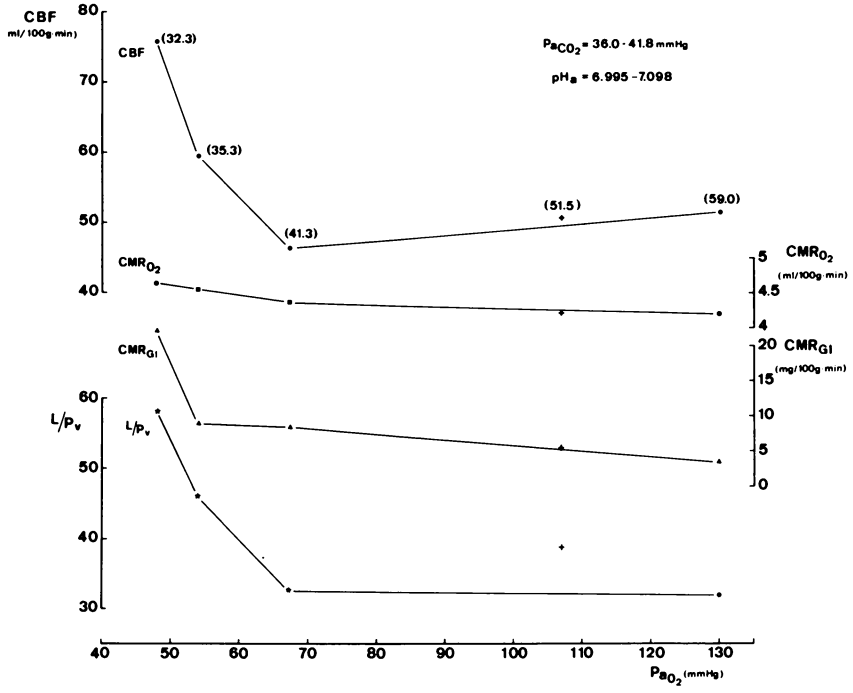

Figure 2. Effect of progressively decreasing arterial oxygen tension on cerebral blood flow, oxygen and glucose uptake of the brain tissue, and lactate pyruvate ratio of cerebral venous blood under conditions of nonrespiratory acidosis.

Values in parentheses are the pertinent O_2 tensions in cerebral venous blood. Values with a cross (+) indicate data determined following return of ventilation conditions to normal.

conditions did not lead to a complete normalization of the oxygen and glucose supply of the cerebral tissue if the cerebral venous oxygen tension was maintained below 30 mm Hg for about 10 min (Figure 3).

Similar trend recordings were observed during investigations on anemic dogs, which were under conditions of nonrespiratory acidosis. The values for the cerebral blood flow, however, were distinctly higher than for normal animals.

Under the conditions of cerebral edema and nonrespiratory acidosis, the cerebral blood flow rate did not increase as soon as the oxygen tension in cerebral venous blood decreased below the reaction threshold. During edema, a decrease of oxygen tension below the threshold value led to a slight decrease in cerebral blood flow and cerebral oxygen uptake; however, glucose uptake of the cerebral tissue and the lactate–pyruvate ratio of the cerebral venous blood increased. When arterial oxygen tensions were returned to normal, the cerebral blood flow and the cerebral

oxygen uptake did not return to initial values, and the lactate–pyruvate ratio increased further during the duration of the experiment (Figure 4).

Studies in Patients. During the investigations in patients with brain tumors or brain lesions, mean regional cerebral blood flow in the perifocal edematous areas amounted to 20.6 ml/100 g-min. These values decreased significantly in comparison with the mean hemispheric blood flow rate obtained with the same method in normal patients (50–55 ml/100 g-min) (27). The largest reduction in rCBF was encountered in patients with metastatic tumors and glioblastomas and may be related to the well-known tendency of these malignancies to develop brain edema.

To determine whether the local tissue water content exerts an influence on the blood flow rate, the rCBF values were plotted against the local tissue water content found in the corresponding brain biopsies. For comparison, the mean of the individual values of the water content of cortex and subjacent white matter were used. A linear regression, with

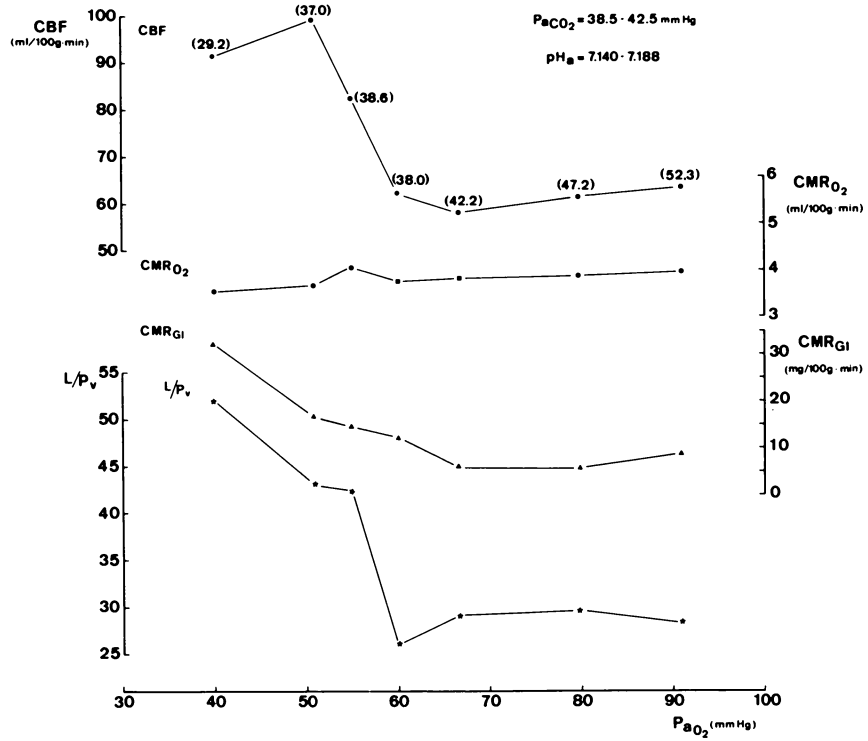

Figure 3. Effect of progressively decreasing arterial oxygen tension on cerebral blood flow, oxygen and glucose uptake of the brain tissue, and lactate pyruvate ratio in cerebral venous blood, under conditions of nonrespiratory acidosis.

Values in parentheses are the pertinent O_2 tensions in cerebral venous blood. Return to arterial normoxie failed to normalize the oxygen and glucose conditions of supply.

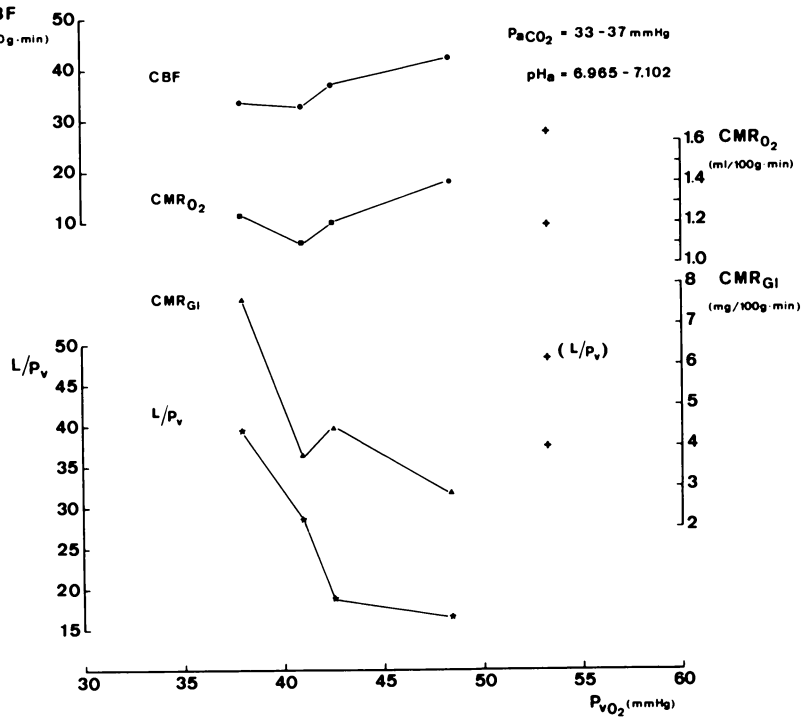

Figure 4. Effect of progressively decreasing cerebral venous oxygen tension on cerebral blood flow, oxygen and glucose uptake of the brain tissue, and lactate pyruvate ratio of cerebral venous blood under conditions of cerebral edema and nonrespiratory acidosis.

Values with a cross (+) indicate data determined following return of ventilation conditions to normal.

a high correlation coefficient ($r = 0.79$) exists between both parameters. Regional cerebral blood flow rates decrease with increasing local brain water (Figure 5). It seems, however, that the reduction of rCBF was related more to the increase in water content of the subjacent white matter than to the increase of water content of the gray matter.

The question of to what extent brain edema itself or increased intracranial pressure induced by edema and tumor are responsible for the depression in blood flow, is difficult to answer. The results indicate that the extent of local edema seems to be directly responsible for the reduction in regional blood flow. The influence of intracranial pressure may be partially neglected since the dura was open during the intraoperative rCBF measurements. Since the mean arterial blood pressure remained normal in these patients, the regional cerebrovascular resistance increased with increasing water content. It may be concluded that

pathological water accumulation in the tissue increases the local tissue pressure. Together with the increase in local tissue pressure, the pressure in the venules and capillaries probably rises and will consequently restrict the effective local tissue perfusion pressure and decrease the blood flow. In brain areas with pathologically increased water content, the lactate concentration is considerably higher than in areas with lower water content. However, no significant correlation could be found between the regional lactate concentration and the rCBF.

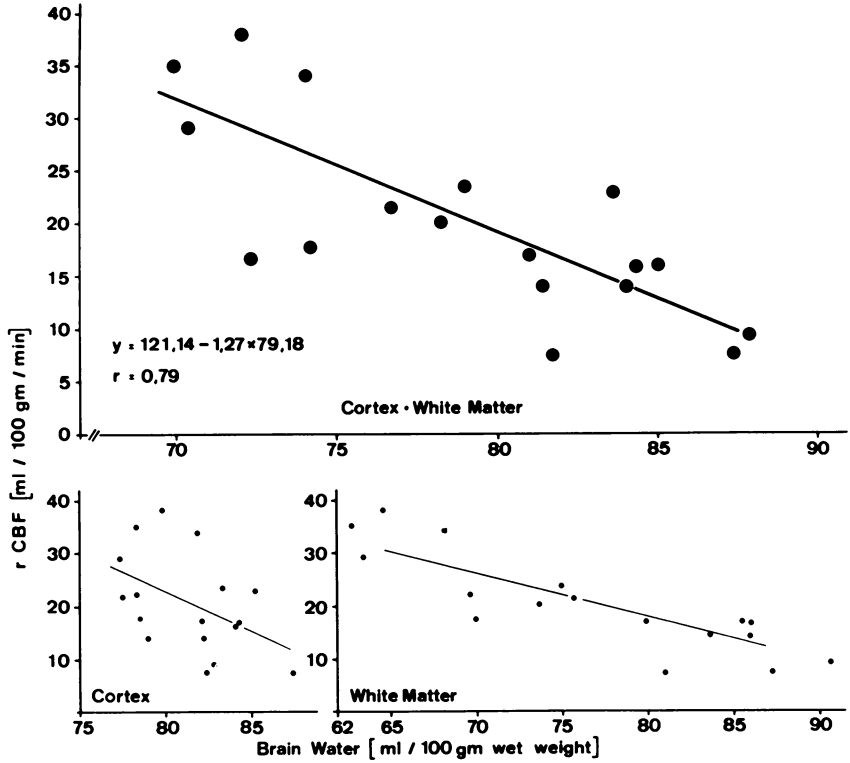

Figure 5. Correlation between regional water content and regional cerebral blood flow in cerebral edema adjacent to brain tumors and brain lesions

Attempting to answer the question of whether the reduction of rCBF in edematous brain tissue surrounding tumors and lesions causes a deficient oxygen supply of these areas, we predicted by calculation the mean oxygen tension decrease in the capillaries and the mean oxygen tension distribution in the tissue of these areas. Though the results of such a theoretical analysis of the oxygen tension distribution in the capillary blood and the brain tissue are rough approximations, they agree with finding of regional metabolite concentrations. We predicted tissue

hypoxia to be present in seven of 12 brain areas investigated. Simultaneously, metabolic changes characteristic of hypoxia alterations were obtained in the same areas. The mean concentrations of lactate and the lactate–pyruvate ratio were higher, and the concentration of phosphocreatine was lower than in areas with sufficient oxygen supply. Brain areas with estimated normal oxygenation or mild hypoxia showed normal or less alterated metabolite concentrations (Table I).

Table I. Metabolite and Water Content in Brain[a]

	A $n = 7$	B $n = 5$
Glucose	2.24 ± 0.32	2.07 ± 0.66
Lactate	6.71 ± 2.40	2.18 ± 0.70
Pyruvate	0.161 ± 0.017	0.169 ± 0.08
Lactate/pyruvate	39.02 ± 17.62	16.2 ± 3.79
CrP	1.44 ± 0.46	2.07 ± 0.45
ATP	1.20 ± 0.21	1.21 ± 0.07
ADP	0.72 ± 0.14	0.85 ± 0.13
Water	82.97 ± 1.44	75.87 ± 1.35

[a] Comparison of metabolite and water content in edematour brain areas with mathematically predicted tissue hypoxia (A) and mathematically predicted sufficient oxygen supply or mild hypoxia (B). Metabolite concentrations expressed as μmoles/gram wet weight, water content expressed as ml/100 grams wet weight.

In summarizing the results of investigations on patients with brain tumors or brain lesions, the following theory may be proposed. Increase in regional tissue water in edematous brain results in a rise in regional tissue pressure and a decrease in regional blood flow. This decrease in rCBF influences the respiratory gas exchange in the edematous cerebral tissue and may cause tissue hypoxia and characteristic metabolic changes.

Literature Cited

1. Silver, I. A., *Med. Electron. Biol. Eng.* (1965) **3**, 377.
2. Heidenreich, J., Erdmann, W., Metzger, H., Thews, G., *Experientia* (1970) **26**, 257.
3. Bicher, H. I., Bruley, D., Knisely, M. H., Reneau, D. D., *J. Physiol.* (1971) **217**, 689.
4. Chance, B., Schoener, B., Schindler, F., "Oxygen in the Animal Organism," pp. 367–388, F. Dickens and E. Neil, Eds., Pergamon, Oxford, 1964.
5. Schindler, F. J., "Oxygen kinetics in the cytochrome oxydase-oxygen reaction," Ph.D. Dissertation, University of Pennsylvania, Philadelphia, 1964.
6. Jöbsis, F. F., *MCV Quart.* (1967) **3**, 169.
7. Lübbers, D. W., Kessler, M., "Oxygen Transport in Blood and Tissue," pp. 90–99, D. W. Lübbers, U. C. Luft, G. Thews, and E. Witzleb, Eds., Thieme, Stuttgart, 1968.
8. Kety, S. S., Schmidt, C. F., *J. Clin. Invest.* (1948) **27**, 476.
9. Opitz, E., Schneider, M., *Ergebn. Physiol.* (1950) **46**, 126.

10. Lassen, N. A., *Physiol. Rev.* (1959) **39**, 183.
11. Gottstein, U., "Einzeldarstellungen aus der theoretischen und klinischen Medizin," Vol. 15, Hüthig, Heidelberg, 1962.
12. Alexander, S. C., Wollman, H., Cohen, P. J., Chase, P. E., Behar, M., *J. Appl. Physiol.* (1964) **19**, 561.
13. Wollman, H., Alexander, S. C., Cohen, P. J., Chase, P. E., Melman, E., Behar, M. G., *Anesthesiology* (1964) **25**, 180.
14. Reivich, M., *Amer. J. Physiol.* (1964) **206**, 25.
15. Harper, A. M., *Brit. J. Anaesth.* (1965) **37**, 225.
16. Meyer, J. S., Gotoh, F., Akiyama, M., Yoshitake, S., *Circulation Res.* (1967) **21**, 649.
17. Meyer, J. S., Gotoh, F., Akiyama, M., Yoshitake, S., *Circulation* (1967) **36**, 197.
18. Espagno, J., Lazorthes, Y., *Acta Neurol. Scand.* Suppl. (1965) **14**, 58.
19. Sokoloff, L., "Regional Neurochemistry," S. S. Kety and J. Elkes, Eds., Pergamon, Oxford, 1961.
20. Lassen, N. A., Ingvar, D. H., *Experientia* (1961) **17**, 42.
21. Häggendal, E., Johansson, B., *Acta Physiol. Scand.* Suppl. (1965) **258**, 27.
22. Harper, A. M., *Acta Neurol. Scand.* Suppl. (1965) **14**, 94.
23. Ingvar, D. H., Cronquist, S., Ekberg, R., Risberg, J., Höedt-Rasmussen, K., *Acta Neurol. Scand.* Suppl. (1965) **14**, 72.
24. Höedt-Rasmussen, K., Sveinsdottir, E., Lassen, N. A., *Circulation Res.* (1966) **18**, 237.
25. McDowall, D. G., "A Symposium on Oxygen Measurements in Blood and Tissue and Their Significance," pp. 205–219, J. P. Payne and D. W. Hill, Eds., Churchill, London, 1966.
26. Munck, O., Baerenholdt, O., Busch, H., *Scand. J. Clin. Lab. Invest.* Suppl. (1968) 102.
27. Paulson, O., Cronquist, S., Risberg, J., Jeppesen, F. J., *J. Nucl. Med.* (1969) **10**, 164.
28. Thews, G., *Pflügers Arch. Ges. Physiol.* (1960) **271**, 197.
29. Diemer, K., *Pflügers Arch. Ges. Physiol.* (1965) **285**, 99.
30. Diemer, K., *Pflügers Arch. Ges. Physiol.* (1965) **285**, 109.
31. Grote, J., "Hydrodynamik, Elektrolyt- und Säure-Basen-Haushalt im Liquor und Nervensystem," pp. 41–50, G. Kienle, Ed., Thieme, Stuttgart, 1967.
32. Grote, J., *Zool. Anz.* (1967) **179**, 330.
33. Grote, J., Der Einfluss der O_2-Affinität des Blutes auf die Sauerstoffversorgung der Organe, Habil.-Schrift, University of Mainz, 1968.
34. Grunewald, W., *Pflügers Arch.* (1969) **309**, 266.
35. Reneau, D. D., Bruley, D. F., Knisely, M. H., "Chemical Engineering in Medicine and Biology," pp. 135–241, D. Hershey, Ed., Plenum, New York, 1967.
36. Reneau, D. D., Bruley, D. F., Knisely, M. H., *A.I.Ch.E. J.* (1969) **15**, 916.
37. Reneau, D. D., Bruley, D. F., Knisely, M. H., *J. Ass. Advan. Med. Instrum.* (1970) **4**, 211.
38. Metzger, H., *Math. Biosci.* (1969) **5**, 143.
39. Grote, J., Kreuscher, H., *Zool. Anz.* (1967) **179**, 319.
40. Grote, J., Kreuscher, H., Schubert, R., Russ, H. J., In 6th Europ. Conf. Microcirculation, Aalborg, 1970, pp. 294–297, Karger, Basel, 1971.
41. Grote, J., Kreuscher, H., Vaupel, P., Günther, H., *Europ. Neurol.* (1971/72) **6**, 335.
42. Kreuscher, H., "Anaesthesiologie und Wiederbelebung," Vol. 21, Springer, Berlin, Heidelberg, New York, 1967.
43. Vaupel, P., Günther, H., *Pflügers Arch.* (1971) **323**, 351.
44. Reulen, H. J., Medzihradsky, F., Enzenbach, R., Marguth, F., Brendel, W., *Arch. Neurol.* (1969) **21**, 517.
45. Kety, S. S., Schmidt, C. F., *J. Clin. Invest.* (1948) **27**, 484.

46. Noell, W., *Pflügers Arch. Ges. Physiol.* (1944) **247,** 553.
47. Betz, E., Heuser, D., *J. Appl. Physiol.* (1967) **23,** 726.
48. Betz, E., Kozak, R., *Pflügers Arch. Ges. Physiol.* (1967) **293,** 56.
49. Kogure, K., Scheinberg, P., Fujishima, M., Busto, R., Reimuth, O. M., *Amer. J. Physiol.* (1970) **219,** 1393.
50. Wahl, M., Deetjen, P., Thurau, K., Ingvar, D. H., Lassen, N. A., *Pflügers Arch.* (1970) **316,** 152.
51. Fujishima, M., Scheinberg, P., Busto, R., *Arch. Neurol.* (1971) **25,** 160.
52. Noell, W., Schneider, M., *Pflügers Arch. Ges. Physiol.* (1944) **250,** 514.

RECEIVED August 4, 1972.

Pharmacokinetics and Cell Population Growth Models in Cancer Chemotherapy

KENNETH B. BISCHOFF, KENNETH J. HIMMELSTEIN,[a] ROBERT L. DEDRICK, and DANIEL S. ZAHARKO

School of Chemical Engineering, Cornell University, Ithaca, N. Y. 14850, Department of Chemical Engineering, University of Maryland, College Park, Md. 20742, Biomedical Engineering and Instrumentation Branch, DRS, and Laboratory of Chemical Pharmacology, NCI, National Institutes of Health, Bethesda, Md. 20014

The development of mathematical models to simulate cancer chemotherapy for ultimate use in optimizing treatment has two main requirements: prediction of the time course of drug distribution in the body, or pharmacokinetics, and quantitative description of the cancer cell growth and death as a function of the drug concentration in the local environment. The first has been determined for certain important cancer chemotherapeutic agents, yielding predictive, physiologically consistent models for several mammalian species. The second aspect is beginning; the basis for the models is a description of the cell population maturation and death where the loss term is a function of the drug concentration. Some available data for L1210 leukemia in mice will be used to illustrate the model predictions and compare these with experimental data.

The rational and reliable prediction of drug effects based on dosage regimen and concomitant biochemical events has been a long sought-after goal. Two necessary steps are involved: (a) prediction of the drug distribution, or pharmacokinetics, throughout the body, including the local concentration at the site of action; and (b) prediction of the actual drug action as a function of the local concentration. There is a great

[a] Present address: Dow Chemical Co., Midland, Michigan 48640.

similarity to chemical reactor analysis and design where the overall mass and energy balances and the local kinetics are used. There are no known examples where the complete task has been done in a truly quantitative and *a priori* fashion although this general type of reasoning is used by pharmacologists and clinicians to design therapeutic procedures. Because of the experimental and analytical difficulties involved in each phase, there may be some doubt that definitive predictions are feasible. However, the potential benefits to be obtained, especially for individuals, justify every reasonable effort that can help to simplify and reduce the typically extensive and somewhat risky clinical experimentation.

We will consider here this problem in the context of cancer chemotherapy. Since antineoplastic drugs by necessity are quite toxic, it would seem that meaningful mathematical models could be important guides in the optimization of various types of experimental and clinical trials. The mode of action of many of these drugs, at least semiempirically, is qualitatively and sometimes quantitatively known, and the pharmacokinetics of several types have been studied. More specific information seems to be available concerning the action on tumor cells than toxicity in critical normal cells such as bone marrow and gastrointestinal tract. However, to be useful in a clinical sense, both effects must be predictable since successful therapy is based on the balance between the cancer cell death and the toxicity.

This paper summarizes some recent work in each of the two areas of pharmacokinetics and local drug action and then illustrates an initial attempt at combining them to predict drug actions on mouse L1210 tumors.

Cell Kinetics

First consider the mathematical descriptions of cell kinetics which define the drug effects for cancer chemotherapy. Quantitative models to describe mammalian (or other) cell growth and death are still relatively crude. Although the complicated biochemical events leading to DNA and other chemical production, cell mitosis, and population growth have been studied qualitatively in some depth and quantitative aspects of some reactions are known, synthesis of this with a comprehensive description has not yet been completely accomplished.

The formal structure of various types of mathematical models has been summarized by Frederickson, Ramkrishna, and Tsuchiya (*1*) and Weiss (*2*). The various biological assumptions that are implicit in many simple models, such as the Michaelis–Menten formula, are discussed, and generalized approaches are suggested. Few specific actual examples

are known, however, where an analysis has been carried to completion. We will discuss here a fairly simple model, stating only the most important assumptions involved.

For many of the drugs of interest, action occurs presumably only during some fraction of the cell mitotic cycle. Most often this is considered to be the DNA production or S-phase of the total G_1-S-G_2-M cycle. A useful model, therefore, should at least be able to incorporate this type of information—*e.g.*, the structured models of Tsuchiya, Fredrickson, and Aris (*3*). This means that simple gross descriptions, such as Michaelis–Menten–Monod models are not sufficient, and some attention must be paid to the cells during growth. We assume here for a first approximation that a single cell age or maturation variable is sufficient.

Many investigators have studied models of the von Foerster type (*see* Trucco (*4*) for several references and properties), which belong to the general population balance category used in kinetic theory, particle agglomerization, crystallization, etc. (*see* Himmelblau and Bischoff (*5*) for a textbook treatment). We will use the model of Rubinow (*6*) for reasons discussed below.

Rubinow defined a normalized cell maturation variable, μ such that a cell will divide when $\mu = 1$. Now μ is related to the biochemical events occurring during the cell cycle in some undetermined fashion. It is, therefore, a semiempirical variable and is operationally defined in terms of measured cell cycle times. This implies that all cells divide after the cell cycle time of τ hours. It is observed, however, that cell division times are scattered about a mean value. This randomness must be accounted for suitably. Most models account for this with an explicit operation in the mathematical solution by averaging cell division times over the entire population. This scheme leads to the solution of a rather difficult integral equation (*see, e.g.*, Trucco (*4*)). Recently Subramarian *et al.* (*8*) have considered weighted-residual methods for more easily solving these problems.

Rubinow uses a simpler mathematical approach which assumes that groups of cells behave in a deterministic manner, all dividing when their $\mu = 1$, and then averages over a distribution of maturation rates for the entire population. Both approaches lead to similar final results although the fundamental biological assumptions are somewhat different.

Our purpose in this first attempt is to assess the feasibility of the fundamental approach, so we would prefer the simplest mathematical description. Ultimately, more involved models should prove useful, such as the comprehensive numerical model of Shackney (*7*); however, here we discuss only simple models.

With this description, then, the standard population balance equation describing the cell kinetics is:

$$\frac{\partial n}{\partial t} + \frac{\partial}{\partial \mu}(\upsilon n) = -\lambda n \tag{1}$$

where:

$n(\mu, t)$ = distribution function of cell maturation at time, t

$\upsilon(\mu, t)$ = maturation growth rate

$\lambda(\mu, t)$ = death or loss rate of cells

The pertinent boundary conditions for solving this partial differential equation are:

(a) initial state of system:

$$n(\mu, 0) = N_o\, g(\mu) \tag{2}$$

where N_o = total cell density

(b) mitosis boundary condition for binary fission:

$$\upsilon(0, t)\, n(0, t) = 2\,\upsilon(1, t)\, n(1, t) \tag{3}$$

In addition, the final solution can be averaged over the distribution function of maturation rates, $W(\upsilon)$.

It is not obvious exactly how the drug effect should enter the model since the maturation rate, υ, and the direct loss function, λ, could be affected. It is simplest to use only the second approach, and this will be done for the present. Also, if a constant maturation growth rate, $\upsilon = 1/\tau$, is used as a crude approximation to a more realistic function, Equation (1) reduces to:

$$\frac{\partial n}{\partial t} + \frac{1}{\tau}\frac{\partial n}{\partial \mu} = -\lambda(\mu, t)\, n \tag{1a}$$

and Equation (3) to:

$$n(0, t) = 2\, n(1, t) \tag{3a}$$

Relatively simple analytical solutions can now be obtained, and these are considered in more detail below.

The explicit variable usually observed is the total cell density since separating the cells into their cell cycle fractions would be difficult to

achieve. In terms of the model, this corresponds to adding all the μ-fractions, so that the total cell density is:

$$N(t) \equiv \int_o^1 \cdot \, n(\mu, t)\, d\mu \tag{4}$$

Finally, possible functional forms for $\lambda(\mu,t)$ should be discussed. This is how the drug effect is introduced into the model and is, therefore, the crux of the issue. One simple form is a direct first-order dependency on the local drug concentration, $C(t)$:

$$\lambda(\mu, t) = K(\mu, t)\, C(t) \tag{5}$$

where the rate constant, K, could depend on the cell cycle and also could be a function of time through deactivation or acclimatization effects. As an example of maturation dependency, the drug might only be effective during a certain fraction of the cell cycle, $a \leqslant \mu \leqslant b$, so that:

$$K(\mu, t) = \begin{cases} 0, & 0 \leq \mu < a \\ K, & a \leq \mu \leq b \\ 0, & b < \mu \leq 1 \end{cases}$$

The local drug concentration is given by the pharmacokinetics. A more realistic form takes into account commonly observed drug saturation effects:

$$\lambda(\mu, t) = \frac{K_1(\mu, t)\, C(t)}{K_2(\mu, t) + C(t)} \tag{6}$$

Loss functions defined by Equation (6) can be substituted into Equation (1a), and the solution obtained. Before this is done, however, the types of functions, $C(t)$, obtained from pharmacokinetics must be described.

Pharmacokinetics

If the intent is to develop a complete *a priori* description, the pharmacokinetics must be included. Several relevant studies have been done for some of the commonly used cancer chemotherapeutic agents; two are described here. The first is the folic acid antagonist, methotrexate (MTX); the second is cytosine arabinoside (ARA-C). Both are active against leukemia, which is of primary interest here.

A comprehensive pharmacokinetic model for MTX has been developed for wide ranges of doses, and for mammalian species from mouse

to man—*see* the papers of Bischoff, Dedrick, and Zaharko (*9, 10, 11, 12*) for detailed description of the models and references to prior work. Figure 1 shows a flow diagram that was adequate to represent many of the complicated phenomena occurring during the distribution of MTX in the body. It consists of discrete compartments representing basic functional plasma, highly perfused viscera, and poorly perfused tissues with the second of these further differentiated into the portal circulation because of the great importance of biliary secretion.

Transient mass balances for the various compartments can be written:

plasma

$$V_P \frac{dC_P}{dt} = (\text{injection}) + Q_L \frac{C_L}{R_L} + Q_K \frac{C_K}{R_K} + Q_M \frac{C_M}{R_M} - (Q_L + Q_K + Q_M) C_P \tag{7a}$$

muscle

$$V_M \frac{dC_M}{dt} = Q_M \left(C_P - \frac{C_M}{R_M}\right) \tag{7b}$$

kidney

$$V_K \frac{dC_K}{dt} = Q_K \left(C_P - \frac{C_K}{R_K}\right) - k_K \frac{C_K}{R_K} \tag{7c}$$

liver

$$V_L \frac{dC_L}{dt} = (Q_L - Q_G) \left(C_P - \frac{C_L}{R_L}\right) + Q_G \left(\frac{C_G}{R_G} - \frac{C_L}{R_L}\right) - r_o \tag{7d}$$

where

$$r_o \equiv \frac{k_L \, C_L/R_L}{K_L + C_L/R_L}$$

bile ducts

$$\tau \frac{dr_i}{dt} = r_{i-1} - r_i, \; (i = 1, 2, 3) \tag{7e}$$

gut tissue

$$V_G \frac{dC_G}{dt} = Q_G \left(C_P - \frac{C_G}{R_G}\right) + \sum_{i=1}^{4} \frac{1}{4} \left[\frac{k_G C_i}{K_G + C_i} + bC_i\right] \tag{7f}$$

gut lumen

$$\frac{dC_{GL}}{dt} = \frac{1}{4} \sum_{i=1}^{4} \frac{dC_i}{dt} \tag{7g}$$

$$\frac{V_{GL}}{4} \frac{dC_1}{dt} = r_3 - k_F V_{GL} C_1 - \frac{1}{4} \left[\frac{k_G C_1}{K_G + C_1} + bC_1\right] \tag{7h}$$

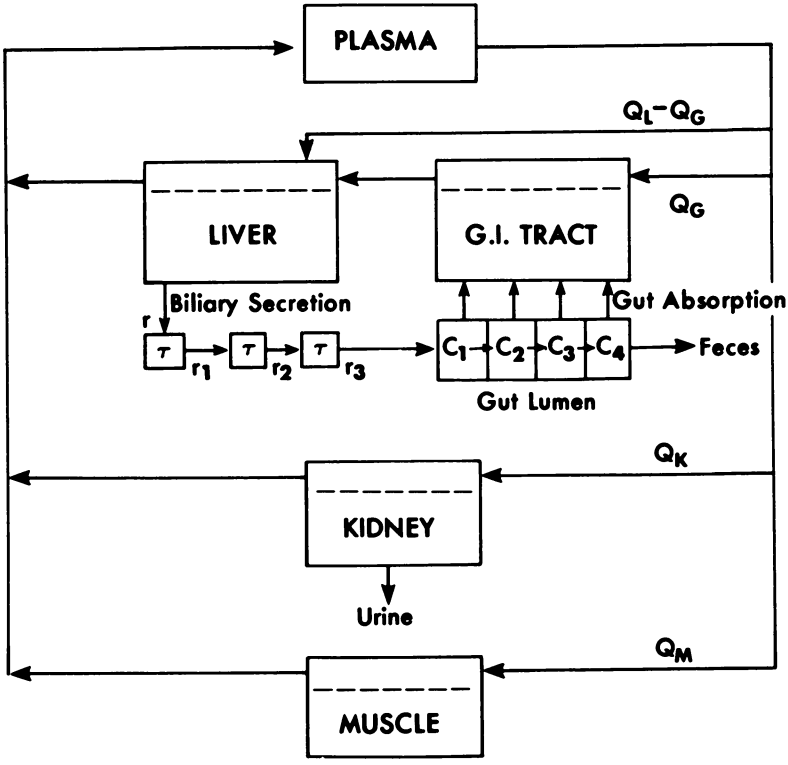

Figure 1. Compartmental model for MTX distribution

$$\frac{V_{GL}}{4}\frac{dC_i}{dt} = k_F V_{GL}(C_{i-1} - C_i) - \frac{1}{4}\left[\frac{k_G C_i}{K_G + C_i} + bC_i\right] \qquad (7i)$$

$$(i = 2, 3, 4)$$

These equations contain the usual input–output terms of compartmental mass balances and also a simple first-order renal clearance, which is close to inulin clearance for MTX. The R_i are tissue-to-plasma distribution ratios to account for protein binding. The volumes V, and flows, Q, are known from recorded anatomy and physiology. Other parameters are defined as follows: k_K, renal clearance; k_L, saturable rate of drug transport into bile; K_L, saturation constant for bile transport; k_G, saturable rate of intestinal absorption; K_G, saturation constant for intestinal absorption; b, nonsaturable rate of intestinal absorption; k_F, reciprocal of nominal transit time in small intestine.

Several complicating factors occur in the portal system balances. Equation (7d) contains a term, r_o, that represents the biliary secretion and could also model saturation effects. Equation (7e) approximates

distributed (*vs.* lumped) behavior by using three compartments-in-series. A similar scheme is used for the gut lumen, as indicated in the remaining equations. The latter also account for absorption through the gut wall by a saturable process. Further details of this aspect of pharmacokinetic modeling are given by Bischoff *et al.* (*13*).

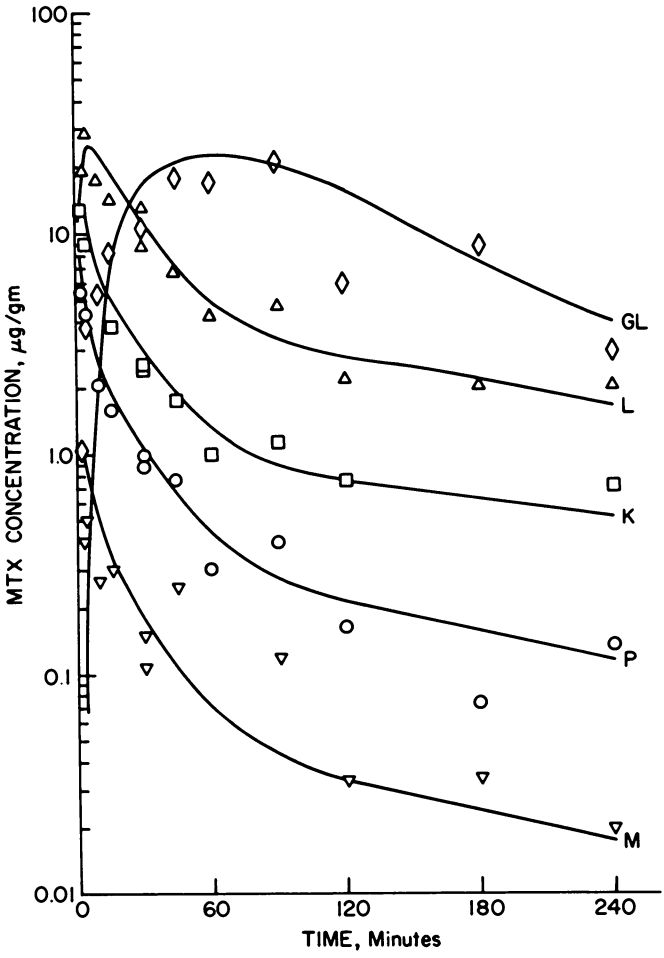

Figure 2. Comparison between curves predicted by model and observed data in mice at 3 mg/kg MTX

As described in detail in the above articles, the basic premise of the models is to utilize as much physiologic information as possible to approach an *a priori* predictive result. Therefore, all the flows, organ volumes, tissue binding, renal clearances, etc., are taken from standard physiological sources or are independently measured. These are incor-

porated into the model to attempt prediction of the experimental results obtained with intact animals. This approach deliberately focuses attention on the important physiologic and pharmacologic functions, thus leading to a more meaningful interpretation of experimental results and improved predictive models.

Figure 2 compares the model predictions with data from mice for each of the body regions, and excellent agreement is obtained. Figure 3 shows clinical plasma data in man. Although the time scale of events is quite different, the same pharmacokinetic model successfully predicts them.

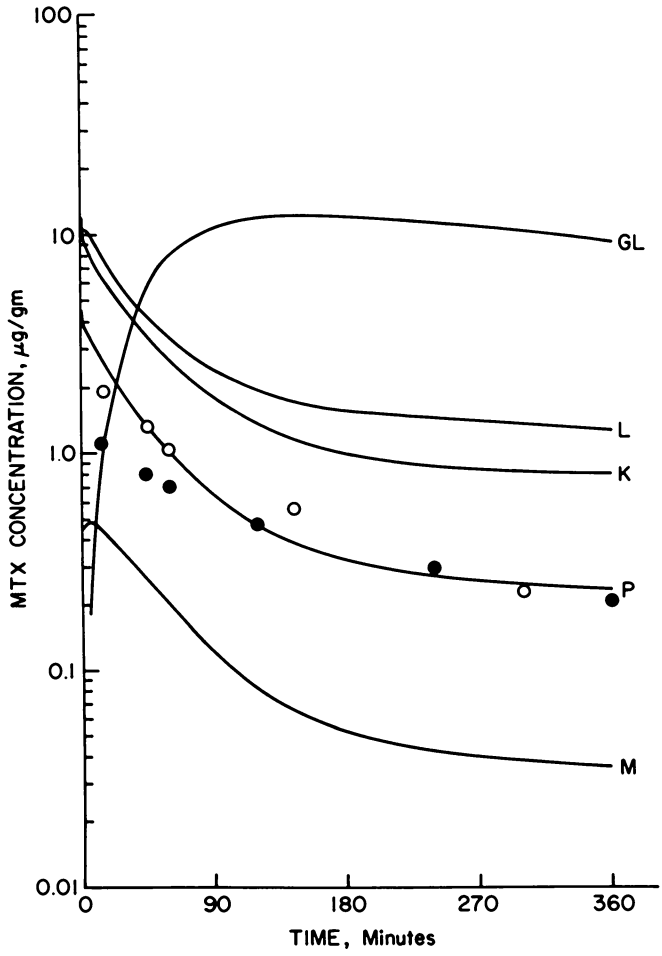

Figure 3. Comparison between curves predicted by model and observed data in man at 1 mg/kg (data from Reference 14)

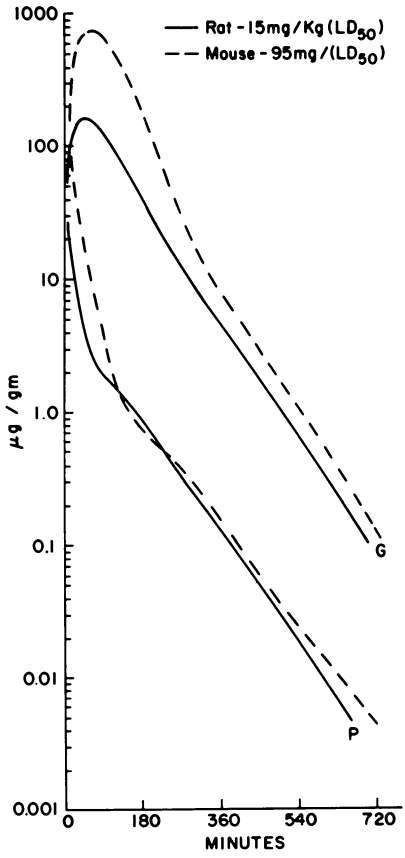

Figure 4. Model predictions in mouse vs. rat for observed LD_{50} doses

The potential importance of pharmacokinetic information is illustrated in Figure 4 where known LD_{50} (lethal dose) doses of MTX were simulated in the mouse and the rat. Despite the 6+-fold difference in LD_{50} doses, the model predicts quite similar time histories in the plasma at longer times. Therefore, searching for a biological reason for the different LD_{50} should certainly take into account the pharmacokinetics. The extrapolation of these ideas into the necessity for pharmacokinetic information in developing cancer chemotherapeutic drug dosage regimens should be clear.

The distribution of MTX is dominated by rather complicated biliary secretion phenomena with ultimate urinary or fecal excretion; it requires a detailed compartmental model for its description. The drug ARA-C is quite different since its distribution is dominated by rapid metabolism

in the liver and other organs of man. Dedrick, Forrester, and Ho (*15*) have shown how rather simple considerations can lead to a predictive model for ARA-C pharmacokinetics. Figure 5 shows a model that was devised to elaborate the detailed disposition of ARA-C.

Mass balances comparable with Equations (7) were used, but omitting the complications of biliary secretion and adding certain enzyme reaction rate terms. As an example the kidney balance [Equation (7c)] becomes

$$V_K \frac{dC_K}{dt} = Q_K (C_{\text{blood}} - C_K) - k'_K C_{\text{blood}} - \frac{v_{\text{max, } K} C_K}{K_{m, K} + C_K} V_{K, \text{ tissue}} \quad (8)$$

where

V_{max} = enzyme activity at saturation, μg/g min

K_m = Michaelis constant, μg/ml

The enzyme (pyrimidine nucleoside deaminase) levels in various body regions have been measured, and *in vitro* reaction rate studies give numerical values for V_{max} and K_m. Using all of this information together with physiological values for the organ weights and flows, Dedrick, Forrester, and Ho (*15*) were able to predict concentrations of ARA-C and its metabolite in the blood of human cancer patients; urinary excretion of the drug and its metabolite were also simulated.

A sample of the results is shown in Figure 6 where the lower curve is for ARA-C; the upper curve represents ARA-C plus metabolite, and the points are clinical data. Figure 6 shows that there is a very rapid drop in the drug concentration in the blood followed by a slower exponential phase. This behavior represents a complex interaction of physical and metabolic processes as discussed in the original source.

The model shown in Figure 5 has not yet been applied definitively to the mouse; however, Skipper, Schabel, and Wilcox (*16*), Mellett (*17*), Neil, Moxley, and Manak (*18*), and Borsa *et al.* (*19*) have presented data on plasma levels. The pharmacokinetics can be approximated by an exponential decay with a time constant of about 1/2 hour.

These examples show how description of the local drug concentration, $C(t)$, can be obtained for substitution into the loss function, $\lambda(\mu,t)$. For leukemias the plasma values may be what is required. For solid tumors, however, the local drug concentration would be of primary concern and would require a more comprehensive pharmacokinetics model.

Application to Cancer Chemotherapy

Since the necessary cell kinetics and the pharmacokinetics have been described, they can be combined in an attempt to show the results of drug treatment. Several general solutions to Equations (1a–3a) have been developed by Himmelstein (*20*); only one will be described here. A search for experimental data with which to test the models revealed that too little was available to utilize the full cell cycle specific provisions in the model. Computational comparisons (*20*) indicated that a time-dependent rate constant, $K_1(t)$, would give results similar to the cell cycle effects although much biological input might be lost with this semiempirical approach. For this case the loss function is a function only of time, $\lambda = \lambda(t)$, and the solutions to Equations (1a–3a) are par-

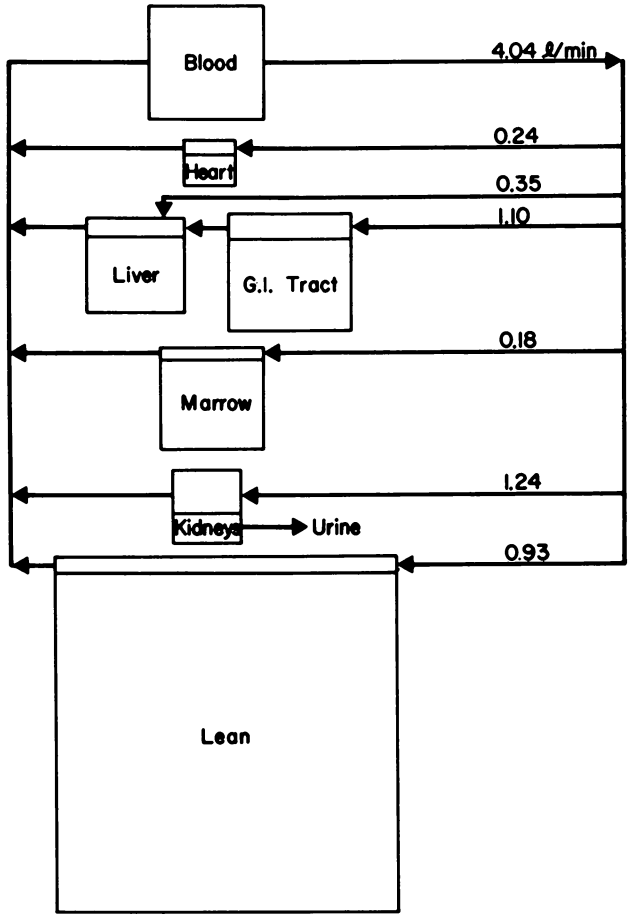

Figure 5. Compartmental model for ARA-C distribution

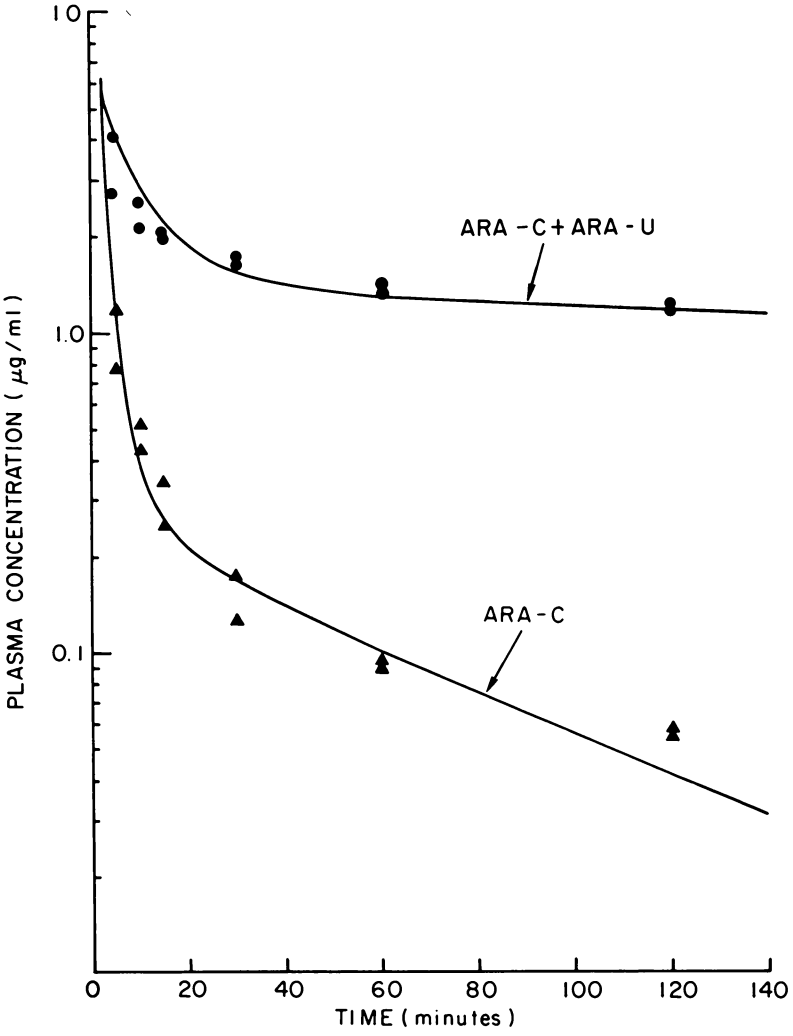

Figure 6. Comparison between curves predicted by model and observed data in man at 1.2 mg/kg ARA-C

ticularly simple. However, more general solutions are available for use when more complete data become available.

Our application is to mouse L-1210 leukemia cells where it is observed experimentally that essentially exponential growth occurs during the main middle portion of cell growth (*see* Reference *16*). An asymptotic solution for this case can be developed by assuming a functional form:

$$n(\mu, t) = N_o e^{\beta t} h(\mu) \exp[-\Lambda(t)]$$

where $h(\mu)$ = function of μ to be determined.

$$\Lambda(t) \equiv \int_0^t \lambda(t')\, dt'$$

Substituting this into Equation (1a), and using the mitosis boundary condition, Equation (3a), yields the final solution:

$$n(\mu, t) = N_0 (2 \ln 2)\, 2^{\left(\frac{t}{\tau} - \mu\right)} e^{-\Lambda(t)} \tag{9}$$

The total cell density is found from Equation (4):

$$N(t) = N_0\, 2^{t/\tau}\, e^{-\Lambda(t)} \tag{10}$$

Equation (10) is now used with the approximate exponential decrease of plasma ARA-C concentration in the mouse to describe observed drug effects on L-1210 cells. The exponential pharmacokinetics can be expressed by:

$$C = C_0\, e^{-t/t_d} \tag{11}$$

where t_d = time constant = (half-life)/(ln 2). Then the loss function can be determined as:

$$\begin{aligned} \Lambda(t) &= \int_0^t \frac{K_1 C_0 e^{-t'/t_d}}{K_2 + C_0 e^{-t'/t_d}}\, dt' \\ &= K_1 t_d \ln\left[\frac{K_2 + C_0}{K_2 + C_0 e^{-t/t_d}}\right] \end{aligned} \tag{12}$$

This can now be used in Equation (9) or (10).

With the mean generation time of L-1210 cells—about $\tau = 0.6$ day = 14.4 hours (*see, e.g.*, Reference *16*)—and the given pharmacokinetics, all of the information necessary to use Equation (10) is known except for the cell-killing kinetic parameters, K_1 and K_2. Saturation effects occur at a concentration of about 0.3–1.0 μg/ml (*16*), yielding an estimate of K_2. Curve fitting to the 24-hour *in vivo* data of Skipper *et al.* (*16*) shown in Figure 7 gives values for K_1 and K_2 which are then used in all subsequent calculations. The values are $K_2 = 0.25$ and a piecewise constant $K_1(t)$, $K_{11} = 0.7$ and $K_{12} = 0.35$, where the switching is done at a cumulative cell death of 0.01. The line on Figure 7 is computed from Equation (10); the scalloped shape is caused by pharmacokinetic effects.

At this point the model parameters are completely known, and if the model is to be useful, it should be able to predict the results of other types of experiments. Skipper *et al.* (*16*) give the results of extensive

tests where mice were inoculated with L-1210 cells and then monitored after various dosage regimens. Detailed cell counts are not available, but the death day of various groups was reported. This is operationally defined as the time when the number of leukemia cells reaches 10^9 although this is not necessarily the exact situation. Thus, the data essentially consist of the mean death days, defined as 10^9 cells, of groups of mice that were given no drug (control), one dose, two doses, etc., of ARA-C, and then monitored.

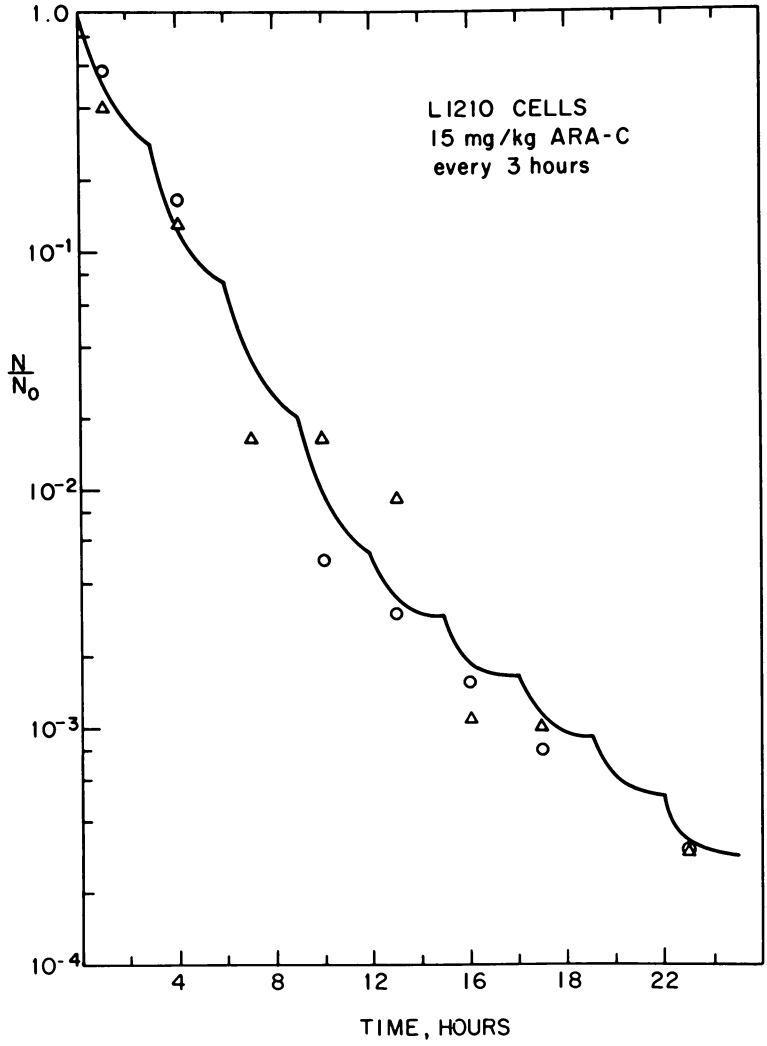

Figure 7. In vivo *cell count data and model results curve-fitted to points*

NO. OF INJECTIONS	0	1	3	6	9	12	15	24
EXPERIMENTAL MEAN DEATH DAY	9	10	11	13	16	18.5	20.5	24
MODEL DEATH DAY	9.0	10.5	12.5	14.0	16.0	18.0	20.0	26.0

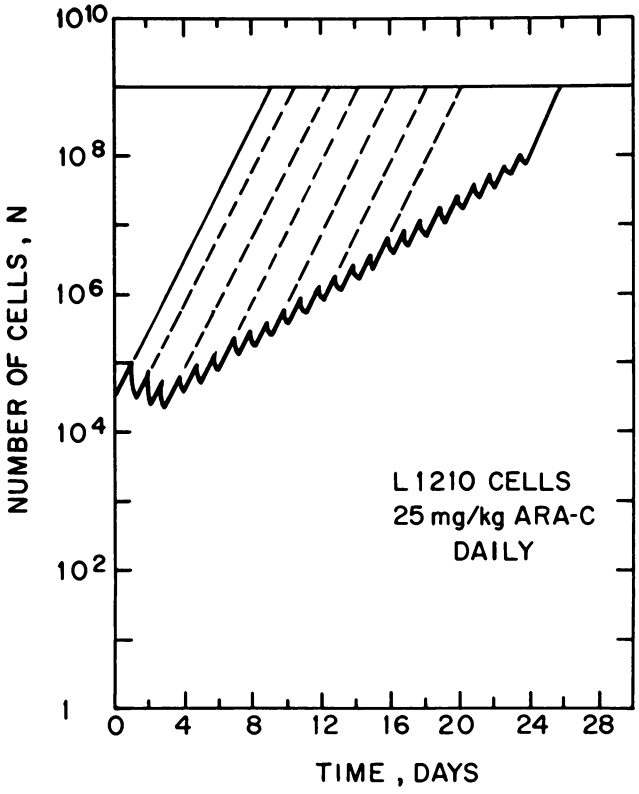

Figure 8. Cell density predicted by model and comparison with experimental mean death day for dosage regimen indicated

Figure 8 shows the model results for one such regimen. The heavy zig-zag lines are the model predictions for the drug effects from Equation (10). The same parameters as given above were used; the scalloped nature of the curves is not apparent on the graph scale. The table above the figure compares the model predictions for various doses, found from the dashed lines on the graph, with the experimental mean death days. Rather remarkable agreement is obtained. Because of the simplicity of the model and the various approximations used, this agreement is probably somewhat fortuitous.

However, Figure 9 shows a similar comparison for an alternative dosage regimen with different behavior. It appears, therefore, that models

of this type, even when oversimplified, may offer the ability to describe some of the overall events that occur when cancer chemotherapeutic agents are administered. Similar predictions of toxic effects on normal cells are also required before a true dosage regimen optimization can be attempted.

NO. OF INJECTIONS	0	1	2	3	4	5	6	7	8
EXPERIMENTAL RESULTS	8.5	9	10	13	14	14.5	15	16	17
MODEL RESULTS	9.0	10.5	11.7	12.9	14.1	15.0	15.9	16.8	17.7

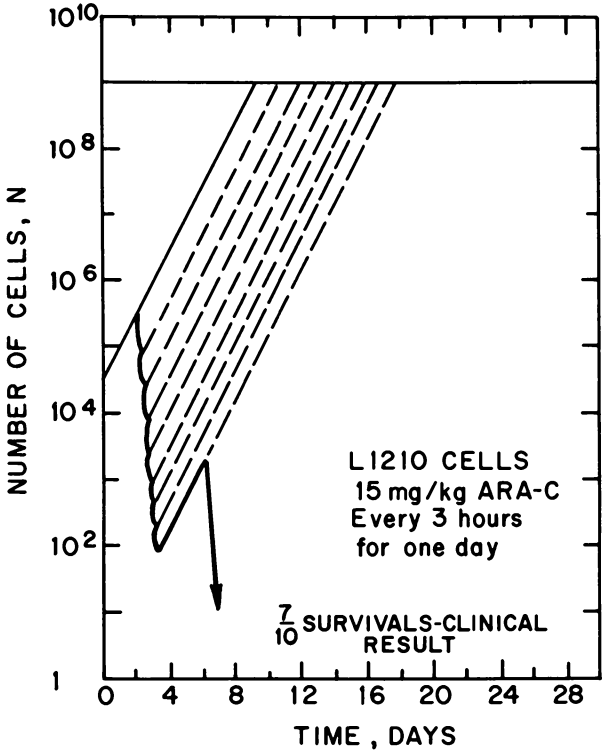

Figure 9. Cell density predicted by model and comparison with experimental mean death day for dosage regimen indicated

It seems justified to continue along this line with future work. As discussed above, more realistic loss functions already have simple mathematical solutions available and could be easily utilized if the specific data required to evaluate the model parameters were available. The direction of some interesting experimental work is indicated since a framework within which to place the results can be formulated. Although

much remains to be done before precise clinical results can be predicted, the simple models suggested here can offer significant guidance.

Literature Cited

1. Fredrickson, A. G., Ramkrishna, D., Tsuchiya, H. M., *Math. Biosci.* (1967) **1**, 327.
2. Weiss, G. H., *Bull. Math. Biophys.* (1968) **30**, 427.
3. Tsuchiya, H. M., Fredrickson, A. G., Aris, R., *Adv. Chem. Eng.* (1966) **6**, 125.
4. Trucco, E., *Bull. Math. Biophys.* (1965) **27**, 285, 449.
5. Himmelblau, D. M., Bischoff, K. B., "Process Analysis and Simulation," Wiley, 1968.
6. Rubinow, S., *Biophysical J.* (1968) **8**, 1055.
7. Shackney, S., *Cancer Chemother. Repts.* (1970) **54**, 399.
8. Subramanian, G., Ramkrishna, D., Fredrickson, A. G., Tsuchiya, H. M., *Bull. Math. Biophys.* (1970) **32**, 521.
9. Bischoff, K. B., Dedrick, R. L., Zaharko, D. S., *J. Pharm. Sci.* (1970) **59**, 149.
10. Dedrick, R. L., Bischoff, K. B., Zaharko, D. S., *Cancer Chemother. Repts.* (1970) **54**, 95.
11. Zaharko, D. S., Dedrick, R. L., Bischoff, K. B., Longstreth, J. A., Oliverio, V. T., *J. Natl. Cancer Inst.* (1971) **46**, 775.
12. Bischoff, K. B., Dedrick, R. L., Zaharko, D. S., Longstreth, J. A., *J. Pharm. Sci.* (1971) **60**, 1128.
13. Bischoff, K. B., Dedrick, R. L., Zaharko, D. S., Slater, S. M., *Proc. Ann. Conf. Eng. Med. Biol.* (1970) **23**, 89.
14. Henderson, E. S., Adamson, R. H., Oliverio, V. T., *Cancer Res.* (1965) **25**, 1018.
15. Dedrick, R. L., Forrester, D. D., Ho, D. H. W., *Biochem. Pharma.* (1972) **21**, 1.
16. Skipper, H. E., Schabel, F. M. Jr., Wilcox, W. S., *Cancer Chemother. Repts.* (1967) **51**, 125.
17. Mellett, L. B., "Progress in Drug Research," E. Jucker, Ed., Vol. 13, Birkhauser Verlag, Basel, 1969.
18. Neil, G. L., Moxley, T. E., Manak, R. C., *Cancer Res.* (1970) **30**, 2166.
19. Borsa, J., Whitmore, A. F., Valeriote, F. A., Collins, D., Bruce, W. R., *J. Natl. Cancer Inst.* (1969) **42**, 235.
20. Himmelstein, K. J., Ph.D. Thesis, University of Maryland (1971).

RECEIVED November 22, 1971.

Rapid Ion Exchanges across the Red Cell Membrane

EDWARD D. CRANDALL and ROBERT E. FORSTER

Department of Physiology, School of Medicine, University of Pennsylvania, Philadelphia, Pa. 19104

A stopped-flow rapid-reaction apparatus was used to measure the time course of pH changes in human erythrocyte suspensions. In one set of experiments a red cell suspension at pH 7.2 was mixed with an isotonic saline solution whose pH had been adjusted to a value between 2.1 and 10.4. Analysis of the results enabled computation of erythrocyte hydroxyl ion permeability as a function of pH. Further experiments were then performed in which erythrocyte suspensions at low p_{CO_2} were mixed with bicarbonate solutions at high p_{CO_2}. Analysis revealed that CO_2 equilibrium in the mixture was reached quickly, but pH equilibrium was delayed. Evaluation of the results indicates that variation in red cell OH^- permeability with pH is not compatible with a simple fixed-charge hypothesis of membrane permselectivity, and the uncatalyzed hydration-dehydration of CO_2 in extracellular fluid is required to produce pH equilibration after blood-gas exchange.

Diffusion across the red blood cell membrane may play an important, if not limiting, role in blood-gas exchanges, regulatory mechanisms, and other physiological processes. Accordingly, great efforts have been made to try to elucidate the determinants of these exchanges. The literature is filled with studies of the transmembrane movements of many different substances. In this work we have limited study to several ionic exchanges under special *in vitro* conditions, hoping to shed light on the movements of the ions, on properties of the membrane, and on some of the accepted notions of blood-gas exchanges. We have directed our attention to, in particular, the fixed-charge hypothesis of membrane perm-

selectivity and carbon dioxide–bicarbonate exchanges between red cells and plasma with their concurrent reaction phenomena.

We present first the equipment developed for the study of rapid pH changes in cell suspensions, and we then discuss the use of this equipment in studies of the hydroxyl ion permeability (p_{OH^-}) of the human erythrocyte membrane and in studies of pH equilibration between red cells and their environment during blood-gas exchanges. Finally, the implications of these studies, relative to previously presented hypotheses about anionic and blood-gas exchanges, are critically examined.

Rapid-Reaction Apparatus

Previous workers used continuous-flow (*1*) and stopped-flow (*2*) rapid-reaction instruments to follow fast pH changes by means of spectrophotometric measurements of indicator dyes. A pH-sensitive glass electrode was used successfully in a continuous-flow rapid-reaction apparatus to follow rapid pH changes (*3*) and rapid NH_3 exchanges (*4*) in red cell suspensions. The fastest device of the pH-electrode, stopped-flow type previously reported seems to have had a response time of less than 0.3 sec (*5*). An undocumented report of a system with a 60 msec response time has also appeared in the literature (*6*). We developed a stopped-flow rapid-reaction apparatus, using a commercially available pH-sensitive glass electrode, which can follow changes of ±0.02 pH units in less than 0.005 sec in a fluid volume of 0.1 ml and requires reaction solution volumes on the order of 1 ml.

Description. A schematic diagram of the stopped-flow equipment is shown in Figure 1. Reacting solutions in a pair of 3-ml syringes, A and B, are forced into a four-tangential-jet mixing chamber (~0.004 ml), out of which the mixture flows against the pH electrode in a 0.1 ml chamber and then out into the stop syringe (or a bypass). The mixing chamber and electrode assembly are attached to a Gibson–Milnes type instrument (*8*). The Ag–AgCl reference electrode and the glass electrode have maximal diameters of about 0.3 cm (commercially available as Leeds and Northrup #117233) with the pH-sensitive glass forming the conical tip of the glass electrode. The outputs from the glass and reference electrodes go directly into a high input impedance amplifier. Several different devices were tried, the best being a Transidyne General (Ann Arbor, Mich.) MPA-6 dc preamplifier (solid state) with its own power source.

The output from this impedance matching device is fed directly into a storage oscilloscope (Tektronix Type 564). It was possible to read the oscilloscope output to about ±0.01 pH unit, limited by 60 cps noise.

Response Characteristics. The pH electrode in the assembled apparatus was calibrated with standard buffer solutions. The electrode output

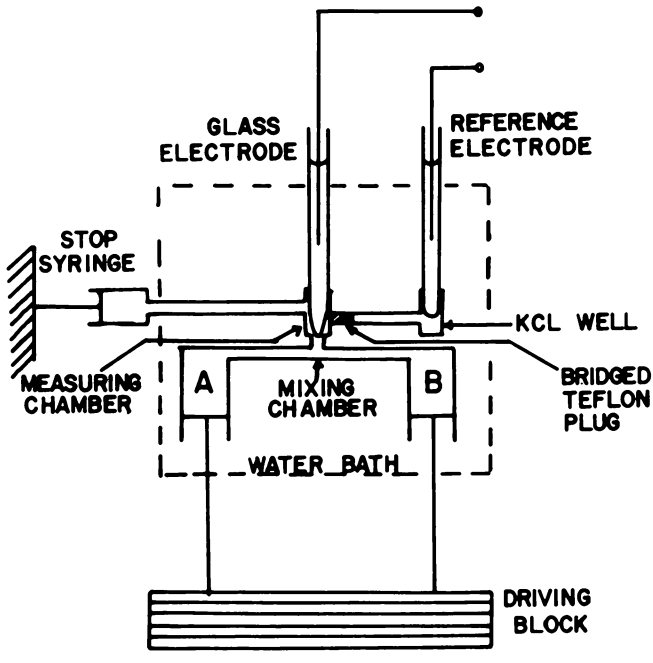

Journal of General Physiology

Figure 1. Schematic diagram of the stopped-flow rapid-reaction apparatus (7)

was linear with pH up to about 10.0 above which alkaline error became significant. The sensitivity of the electrode was usually about 56 mv/pH unit at 37°C.

To determine the speed of response of the instrument, a step change in the pH of the fluid around the electrode would have been ideal. It was not possible to do this experimentally in less than 0.030 sec, owing to the time required to wash out the electrode chamber. However, it was possible to estimate this speed using a ramp input, namely, the linear increase in pH produced by the dehydration of carbonic acid (*1*, *2*, *5*, *9*):

$$H^+ + HCO_3^- \underset{K_a}{\rightleftharpoons} H_2CO_3 \underset{k_u}{\overset{k_v}{\rightleftharpoons}} H_2O + CO_2 \qquad (1)$$

K_a is the true equilibrium constant for the first reaction, a neutralization which for practical purposes can be considered instantaneous (*10*). The forward (dissociation) and backward (association) rate constants for the second reaction are k_v and k_u.

When the reacting solutions are 0.01 N HCl and 0.02 M $NaHCO_3$, it can be shown (*11*) that

$$k_v (t_2 - t_1) = \left(1 + \frac{K_a}{b - a}\right) \ln \frac{[H^+]_2}{[H^+]_1} \quad (2)$$

where b is the total bicarbonate concentration and a is the total hydrogen ion concentration before neutralization. The pH therefore increases linearly with time at least until the back reaction

$$H_2O + CO_2 \longrightarrow H_2CO_3$$

becomes important.

A representative curve is shown in Figure 2. The rate constant k_v at 26°C was calculated from the initial slopes of this curve and others like it to be 24.1 sec^{-1}, comparable with the values of 25.5 sec^{-1} at 25°C reported by Rossi-Bernardi and Berger (*3*) and 20.0 sec^{-1} at 25°C reported by Khalifah (*9*).

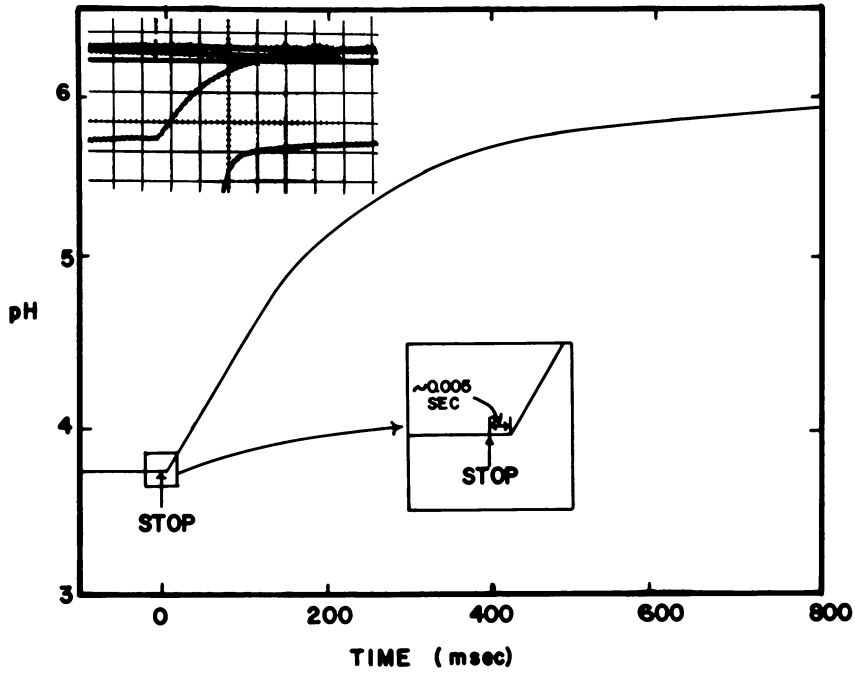

Figure 2. pH vs. time after mixing equal volumes of 10 mH HCl and 20 mM $NaHCO_3$ at 26°C. The original oscilloscope tracing is in the left upper corner (7).

The response time of the electrode system was estimated from Figure 2 by extrapolating the linear slope backward. It was estimated that the electrode system responds to a ramp change in pH in <0.005 sec, and this figure may be an overestimation owing to an imperfect stopping device.

This value for the speed of response is independent of the lag time between initial mixing and impingement of the mixture on the electrode tip. A realistic estimate of lag time was obtained by calculating the mixture pH immediately after neutralization (*i.e.*, at time zero) and comparing this value with the observed pH during flow. Lag time was then determined from the difference between the two pH values and the linear change of pH with time observed after stopping. The calculated pH of the particular neutralized mixture at time zero is very sensitive to the value used for K_a, varying from 3.51–3.82 as K_a goes from 3.5×10^{-4} (*12*) to 1.7×10^{-4} (*13*). An approximate value for the observed initial pH was 3.71; thus, an upper limit for lag time (using $K_a = 3.5 \times 10^{-4}$) was about 0.020 sec.

Exchanges Across the Red Cell Membrane

Exchange of CO_2 with red cells and plasma necessarily involves movements of CO_2 as well as of ions such as Cl^-, HCO_3^-, and OH^- across the cell membrane to achieve final equilibrium. Carbonic anhydrase is an important factor in the kinetics of these exchanges, and the confinement of this enzyme to the inside of the red cell limits its effectiveness as a catalyst in a cell suspension (*14*).

Preliminary analysis of the exchange of Cl^- for HCO_3^-, the chloride or Hamburger shift, brought us to the conclusion that this well-known process could not alone produce electrochemical equilibration in blood. Qualitatively, adding CO_2 to blood leads to diffusion of the gas into red cells as an unionized molecule. Inside the cells, CO_2 hydrates rapidly because of the catalytic action of carbonic anhydrase to increase $[H^+]$ and $[HCO_3^-]$, the latter ion diffusing out of the cell in exchange for Cl^- (Figure 3). At the eventual equilibrium the following relationships must obtain:

$$\frac{[OH^-]_o}{[OH^-]_i} = \frac{[H^+]_i}{[H^+]_o} = \frac{[HCO_3^-]_o}{[HCO_3^-]_i} = \frac{[Cl^-]_o}{[Cl^-]_i} = r \qquad (3)$$

The subscript i refers to the inside of the cell and the subscript o to the extracellular fluid; r is a function primarily of the net charge and concentration of the hemoglobin and of the plasma proteins. There must eventually be a finite increase in extracellular $[H^+]$ to reach equilibrium, but the addition of HCO_3^- to the plasma *via* the Hamburger shift will, if it alters the pH at all, increase it. The cell membrane is considered

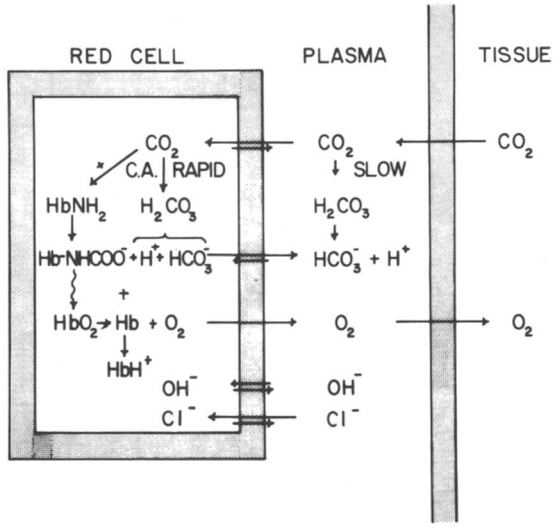

R. E. Forster, "Oxygen Affinity of Hemoglobin and Red Cell Acid–Base Status," Academic, New York, 1972

Figure 3. Schematic diagram of the blood-gas exchanges in tissue (15)

impermeable to H^+ and H_2CO_3 (*16*), so the flux of OH^- and/or the uncatalyzed hydration of CO_2 in the extracellular fluid would appear to be the most likely mechanisms for the addition of H^+ outside the cell. The limitations of the HCO_3^- exchange for Cl^- in producing chemical equilibrium between plasma and red cells following CO_2 exchanges were noted previously by Roughton (*16*).

To be able to evaluate quantitatively the phenomena occurring during CO_2 exchange between red cells and plasma (as shown in Figure 3), it is necessary to know reaction rates (which in fact are generally known) and membrane permeabilities (known for Cl^- only). Therefore, we first evaluated the red cell permeability to OH^- and then used this data to evaluate the importance of OH^- fluxes in CO_2 exchanges. The former was easily done by using the scheme shown in Figure 3 without O_2 exchange and without significant CO_2 in the system.

Hydroxyl Ion Movements

Estimates of the hydroxyl ion permeability (p_{OH^-}) of human erythrocytes were calculated from observations of rapid pH changes in red cell suspensions under conditions where only chloride and hydroxyl ion fluxes were significant. The experimental design used was similar to procedures reported previously by Maizels (*17*) Wilbrandt (*18*), and others.

Anion movements across the red cell membrane are much faster processes than cation movements. For example, potassium ion permeability has been reported to be about 2.2×10^{-11} cm/sec at 23°C and low ionic strength (*19*), while that for chloride ion calculated from the data of Tosteson (*20*) is about 10^{-4} cm/sec at about 23°C. The half-time for this chloride exchange is about 0.2 sec, so rapid that special techniques had to be devised to follow its time course. The same held true for the study of OH^- movements, necessitating development of the apparatus described above.

Methods for OH^- Permeability Experiments. Freshly drawn heparinized blood from five normal subjects was centrifuged for 25 min at 2750 g. The supernatant was discarded, the cells were washed with ten times their volume of 150 m*M* NaCl and recentrifuged, this procedure being repeated three times. After the last wash, the cells were resuspended in 150 m*M* NaCl to a hematocrit of about 18% to form suspension A, the pH of which was always about 7.2 at 37°C.

Solution B was 150 m*M* NaCl with pH adjusted as desired to any value between 2.1 and 10.4 by the addition of small amounts of either HCl or NaOH. Suspension A and solution B were almost CO_2-free

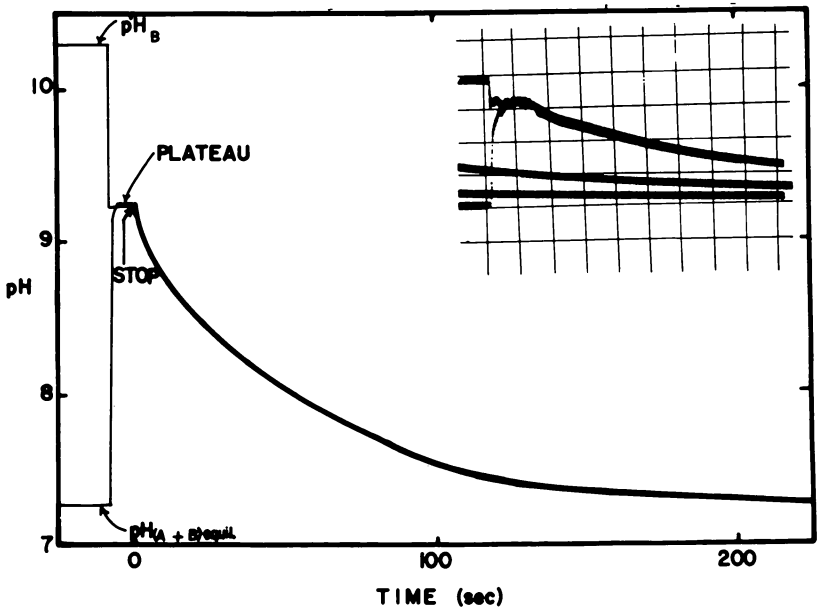

Figure 4. Extracellular pH vs. time after mixing equal volumes of suspension A and solution B at pH 10.26. The original oscilloscope tracing is in the right upper corner (7).

($[CO_2] < 0.02$ mM), as confirmed by the method of Van Slyke and Neill (*21*).

Total hemoglobin was measured as cyanmethemoglobin (*22*). Trace concentration of hemoglobin, such as that in the extracellular fluid of suspension A, was measured using a modified benzidine method (*23*).

The procedure for a specific experiment was as follows. Total hemoglobin concentration, supernatant hemoglobin concentration, hematocrit, and independent pH and cell lysate pH (utilizing a different pH electrode) measurements were made on suspension A. The driving syringes A and B were then filled, the experiment carried out at 37°C, and the effluent mixture collected and analyzed for total hemoglobin, supernatant hemoglobin, hematocrit, and pH. The experiment was then repeated with supernatant from an aliquot of the same suspension A used in the previous experiment in place of suspension A.

Experimental Results. pH as a function of time after mixing equal volumes of suspension A with solution B at pH 10.26 is shown for two experiments in Figure 4 while that for mixing suspension A with solution B at pH 3.42 is shown in Figure 5.

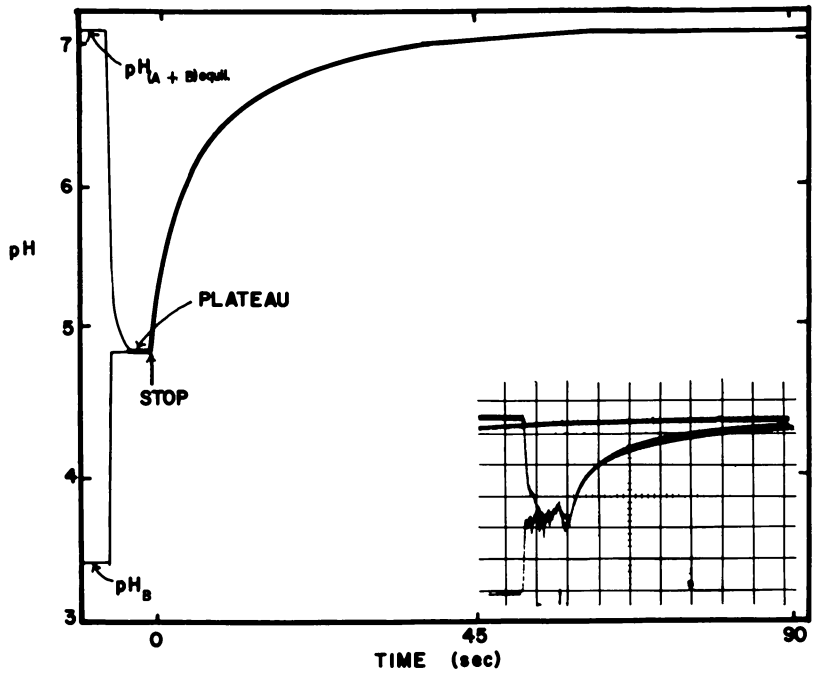

Journal of General Physiology

Figure 5. Extracellular pH vs. time after mixing equal volumes of suspension A and solution B at pH 3.42 (7).

The initial pH levels at the extreme left side of the records were those of the solutions in the electrode chamber before flow started (either the equilibrated mixture or solution B). Thus, in Figure 4 the initial pH was 10.26 for one curve and 7.26 for the other. While flow occurred, the pH reached a plateau at about 9.21, representing the essentially instantaneous neutralization of the suspending fluid in suspension A by solution B plus that portion of the red cell exchange that had taken place in 0.20 sec (or less). At time zero stoppage occurred and exchanges across the red cell membrane continued, returning the external pH toward the pH (7.2) of the original suspension A (ending with a quasi-equilibrium pH about 7.26 in Figure 4). In Figure 5 the starting pH values were 3.42 and 7.13, the plateau pH 4.86, and the end pH 7.13. The curves were approximately exponential, and a new quasi-equilibrium was reached in about 300 sec or less. There may be slower exchanges of cations occurring later which were not studied.

Computational Theory. Movement of univalent anions across a membrane can be described by (*24*):

$$\phi = \frac{uEA}{a} \frac{C_o - C_i e^{-EF/RT}}{1 - e^{-EF/RT}} = \frac{-V_o dC_o}{dt} = \frac{V_i dC_i}{dt} \qquad (4)$$

where ϕ is flux (mmoles/sec), u is ion mobility implicitly including a partition coefficient [cm/sec(mv/cm)$^{-1}$], E is membrane potential (millivolts), a is membrane thickness (cm), C_o is external concentration (M), C_i is internal concentration (M), F is the Faraday (96500 coulombs/mole), R is the universal gas constant (8314.4 mjoules/mole-°K), T is temperature (°K), A is membrane area (cm^2), V_o is extracellular solution space (cm^3), and V_i is intracellular solution space (cm^3). Implicit assumptions in Equation (4) are that (1) ions move under an electrochemical gradient; (2) the membrane is homogeneous; (3) the potential drop across the membrane is linear (25); and (4) there is one well-mixed intracellular compartment and one well-mixed extracellular compartment. In these experiments without significant CO_2 present, the only diffusible ions were chloride (Cl^-) and hydroxyl (OH^-), so Equation (4) could be written twice, once for each species.

It was also assumed that the flux of Cl^- was always equal and opposite to the flux of OH^- (after a very short transient period). Membrane potential was then given by:

$$E = -\frac{RT}{F} \ln \frac{u_{OH^-}[OH^-]_o + u_{Cl^-}[Cl^-]_o}{u_{OH^-}[OH^-]_i + u_{Cl^-}[Cl^-]_i} \qquad (5)$$

All concentrations in Equations (4) and (5) should be read as activity, and all pH electrode measurements were measurements of pa_H. The only correction necessary was to convert 150 m*M* (concentration) NaCl to 112.5 m*M* (activity) NaCl, assuming an activity coefficient of 0.75 (*26*). Since cation mobilities are so small relative to those for anions (*19*), cation contribution to membrane emf can be neglected.

The procedure used to solve Eqs. (4) and (5) was essentially as follows. Initial $[Cl^-]_i$ was computed from initial $[Cl^-]_o$ on the basis of the Donnan equilibrium laws. The Donnan ratio was determined from the measured initial intra- and extracellular pH. A value for u_{Cl^-} was calculated from the results of Tosteson (*20*), a value for u_{OH^-} was assumed, and the equations were integrated over one increment of time using a Runge–Kutta fourth-order method, assuming a to be 100 A. Intracellular and extracellular buffering systems were taken into account. The above steps were repeated over several time increments, using as initial values for each increment those concentrations computed at the end of the preceding increment. The computed pH was then compared with the experimental value at that time after mixing. If agreement was not satisfactory, the entire procedure was repeated using a new assumed value of u_{OH^-}. When satisfactory agreement was obtained, the assumed value of u_{OH^-} was accepted for that time interval. The entire procedure was then repeated for the next time interval, until the complete experimental curve was adequately simulated. In this way a set of values for u_{OH^-} as a function of pH was generated. All computations were performed on a PDP-6 digital computer.

A definition for membrane permeability is:

$$p = \frac{uRT}{aF} \tag{6}$$

With this definition p_{OH^-} was calculated from the hydroxyl mobility data computed as above. From the data of Tosteson (*20*), assuming cell water is 72% of cell volume (*27*), p_{Cl^-} is about 10^{-4} cm/sec and u_{Cl^-} is 4.0×10^{-12} cm/sec(mv/cm)$^{-1}$, the value that was used in the computations.

The internal and external buffering systems were included in the computations as follows. The important intracellular buffer is hemoglobin, and its buffer capacity under the conditions of these experiments was assumed to be 2.54 m*M* acid/m*M* Hb/pH (*28*, *29*). Extracellularly, hemoglobin concentrations were very low, and other buffers (water, lactate, phosphate, etc.) became important. Therefore, an empirical buffering curve for the extracellular fluid was determined by plotting concentration of acid added *vs.* the plateau pH values. Then, the buffering power of the extracellular fluid at any given extracellular pH was assumed to equal the slope of the curve at that pH.

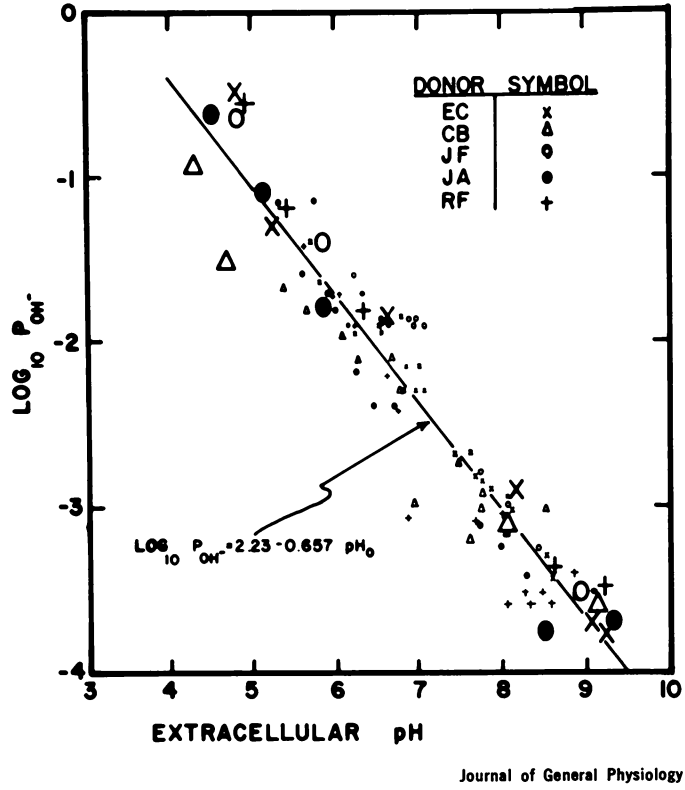

Figure 6. Log_{10} p_{OH^-} vs. *extracellular pH. The line is the linear regression line for all these points* [*Eq. (7)*] (7)

Although not necessary for solving the equations (unless solvent drag is considered a problem), net water movement was assumed to be zero to simplify the computations. Since all extracellular fluids were isotonic, this assumption should have been very close to fact.

Results of Computations. In Figure 6, the results from 23 experiments ($pH_B > 3$) are plotted as $\log_{10} p_{OH^-}$ *vs.* average extracellular pH for the time interval in which that p_{OH^-} was computed. The pH during an interval was never allowed to vary by more than 1.5 units. The larger symbols denote the p_{OH^-} values determined in the first time segment of each experiment. Also shown is the best straight line through all the points as determined by linear regression analysis. The equation for this line is:

$$\log_{10} p_{OH^-} = 2.23 - 0.657\ pH_o \qquad (7)$$

There were no appreciable differences in the dependence of p_{OH^-} on pH_o among individual bloods or between initial time segment values and all

values. The relationship between p_{OH^-} and extracellular pH can be seen to be qualitatively logarithmic.

Discussion. The computed magnitudes of hydroxyl ion permeability were generally consistent with permeability data for other chemical species with respect to the erythrocyte membrane. Figure 6 shows that the hydroxyl ion permeability at 37°C, pH 7.4, and an ionic strength of 0.150 is about 2.2×10^{-3} cm/sec. That for chloride at 23°C, pH 7.4 and similar ionic strength is about 10^{-4} cm/ sec (*20*). In view of the dependence of p_{Cl^-} on temperature (*30, 31*), it is probable that the two permeabilities are within an order of magnitude of each other. Furthermore, both are very much greater than cation permeabilities. This was not particularly surprising since the two ions have the same charge and not dissimilar ionic radii and hydration energies (*32*).

Fixed Charge Hypothesis. According to the computation described above, the movement of an ion across the red cell membrane is governed by its concentration gradient and the transmembrane potential. It has been suggested (*33*) that the membrane potential is one factor that, in addition to its direct effect on flux, is a determinant of ionic permeability. For cation movements over wide ranges of membrane potential, a relatively small dependence of permeability on potential has been demonstrated (*34*).

A presumably more important determinant of ion permeability is the concentration of fixed charges within the membrane. The evidence supporting a fixed cation hypothesis has recently been presented by Passow (*35*). The data reviewed by Passow suggest that anion and cation permeabilities are markedly affected by these charges, perhaps amino groups with a p*K* of 9 and a total concentration in the membrane of 2.5 *M*. The degree of dissociation of these groups would be expected to depend strongly on pH (internal and/or external). The reported experimental effects of these variables on cation and anion permeabilities have generally been consistent with the hypothesis.

Decreasing pH ($\sim 6.5 < \text{pH} < 8.0$) tends to increase the permeability to anions and decrease that to cations, presumably by increasing the concentration of the fixed positive groups in the membrane. Passow (*35*) and Deuticke (*36*) present evidence that while the rate-limiting barrier for cation movements is positive fixed groups, another site (perhaps negatively charged hydrophobic groups) limits anion movements.

The study of the fixed-charge hypothesis is ideally carried out by steady-state isotopic permeability experiments. These conditions are impossible to meet in the study of hydroxyl ion movements. Furthermore, net OH^- movements necessarily involve pH changes by their nature. Nevertheless, the experiments reported here can be used to determine the effects of external pH on OH^- permeability since temperature and

ionic strength were maintained constant and the calculated internal pH never varied by more than 0.13 unit within an experiment nor by more than 0.24 unit between experiments.

The effects of external pH on hydroxyl ion permeability have been shown in Figure 6 and summarized in Equation (7). There is an increase in p_{OH^-} with decreasing pH, as has been reported for other anions between about pH 6.5 and 8.0 (35), except that we found p_{OH^-} to be an exponential rather than an S-shaped function of pH. The actual experimental data reported by Passow (35) extend over a small range of pH and are not incompatible with our Equation (7). Our results, however, do not fit the concept of a single pK for the fixed dissociable group in the red cell membrane which determines permeability. It is, furthermore, difficult to reconcile them with the concept of a series of such dissociable groups of varying pK if the titration curve of these groups resembles those of red cell ghosts (33) or complex proteins (*e.g.*, hemoglobin), which are approximately linear with pH, while Equation (7) would suggest that the titration curve is an exponential function of pH (which is conceivable but unlikely). It is always possible that p_{OH^-} does not vary in the same way with pH as do the other anions studied previously, or that H^+, being such an unusual cation, does not behave as do other cations that have been studied relative to speed of penetration of the erythrocyte membrane.

HYDROGEN ION MOVEMENT. Jacobs and Parpart (37) in an experiment in which red cells were exposed to acid and the time of lysis observed concluded that the mechanism for acidity changes across the membrane was hydroxyl ion movement, not hydrogen ion movement. However, there was an implicit assumption that the permeability of the cell membrane to these two ions was constant despite changes in pH and ionic strength; our work invalidates this assumption. Recently, Scarpa *et al.* (38) studied the mechanism of pH equilibration in red cell suspensions by observing the response of intracellular pH to various acids added extracellularly. Their data can also be explained equally well by assuming either H^+ translocation or OH^- exchange. Thus the mechanism remains unresolved at this time. These two papers are the only ones addressed specifically to this question. This situation is not surprising since it may well be impossible to differentiate the effects of the two mechanisms.

With this in mind, the reasons that the data were interpreted and presented in terms of the movement of hydroxyl ions alone are twofold. The important consideration was the circumstantial evidence that anion movement across the erythrocyte membrane at normal temperatures is very much faster than cation movement for all ions studied to date. Sec-

ondly, it makes no difference relative to the pH behavior of membrane permeability which mechanism actually holds.

CHLORIDE PERMEABILITY. The value for p_{Cl^-} of 10^{-4} cm/sec was determined at 23°C and pH 7.4 (*20*). There is evidence, however, that it is somewhat temperature-dependent (*30*, *31*), and it is probably pH-dependent as well (*39*). Therefore, using this value with data obtained at 37°C and at widely varying pH was suspect. The computations of p_{OH^-} were insensitive to the value of p_{Cl^-} used over the range 10^{-6} to 10^{-1} cm/sec. The reasons for this lie in the swamping effects of the very high chloride concentrations relative to the hydroxyl ion concentrations (at least 500 times)—*i.e.*, so many chloride ions were readily available for movement across the membrane (relative to the number of hydroxyl ions) that chloride ion mobility could not become a limiting factor. Furthermore, the experiments were set up so that hydroxyl ion movement was driven by a large concentration gradient while there was approximately zero chloride concentration gradient initially. Thus, the chloride ion movement could be thought of as resulting solely from the membrane potential changes secondary to the altered OH^- gradients.

There is some recent evidence that the chloride permeability determined by exchange measurements is much greater than that determined by net translocation (*38*). However, throughout this work a counter-anion was always available, so the use of the high (10^{-4} cm/sec) permeability value seems justified since all movements of chloride ions occur under exchange conditions.

PRESENCE OF HCO_3^-. By the method of Van Slyke and Neill (*21*), we showed that we had $<2 \times 10^{-5}$ *M* total CO_2 in the reaction mixtures. However, in certain cases the gradient for OH^- was less than even this small number, so there was a possibility that a net transfer of H^+ across the red cell membrane was produced by the Jacobs–Stewart (*40*) CO_2 mechanism and that the calculated permeabilities for hydroxyl ions were in error. In this mechanism CO_2 is produced by the dehydration of H_2CO_3 on one side of the membrane, which diffuses across and rehydrates on the other side, producing a net transfer of H^+ (or OH^- in the opposite direction). HCO_3^- then exchanges for another anion, usually Cl^-, and the cycle is complete. The CO_2 reaction in the extracellular fluid is uncatalyzed and generally rate-limiting. To evaluate the possibility of significant CO_2 movement, we evacuated suspension A and solution B and flushed with N_2 containing less than 5×10^{-5} % CO_2 over several hours before performing the usual experiments. No significant change was noticed in the time course of pH after mixing. Thus, we conclude that CO_2 is either not present in our reaction mixture or that, if present, it is not contributing significantly (in these small concentrations) to the speed of pH equilibration.

Transmembrane Movements After CO_2 Exchanges

Our next step was to add CO_2–HCO_3^- to the experiments and computations performed above for the study of OH^- movements. Referring to Figure 3, we were able to do this by essentially retaining the same approach as that used for p_{OH^-} studies, removing O_2 from the system (preventing effects of O_2 exchange from influencing the situation), but adding CO_2 and bicarbonate ions to the suspensions and solutions.

Methods for CO_2 Exchange Experiments. All the experiments were performed in the stopped-flow rapid-reaction apparatus described above. Freshly drawn heparinized blood was added to ten times its volume of the standard buffer solution consisting of 30 m*M* $NaHCO_3$, 3.5 m*M* KCl, and 116.5 m*M* NaCl and equilibrated with 100% N_2 by bubbling the gas through the suspension for 2–3 hours at 37°C (suspension A). An equal volume of the standard buffer solution was simultaneously equilibrated with a 10% CO_2, 90% N_2 gas mixture, also at 37°C (solution B). Samples of the equilibrated reactants were analyzed for p_{CO_2} and pH. The individual experiments were then carried out exactly as above for the p_{OH^-} experiments, except that the initial driving force was now a change in p_{CO_2} (instead of pH) outside the red cells. The pH was measured as a function of time. The reactions were exactly similar to those studied earlier by Constantine *et al.* (*41*), except that they measured p_{CO_2} (by electrode) as a function of time after mixing in a continuous-flow rapid reaction apparatus.

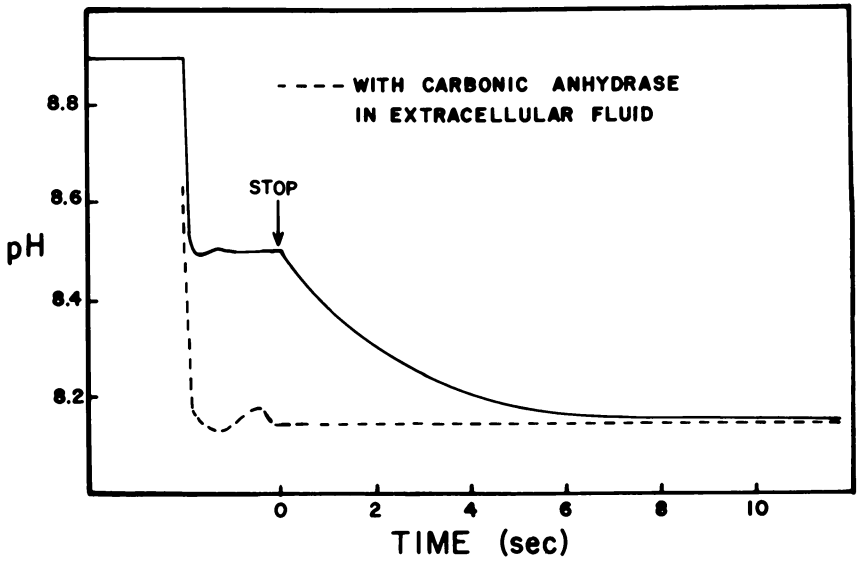

Figure 7. Extracellular pH vs. time after mixing equal volumes of suspension A ($p_{CO_2} \sim 0$) and solution B ($p_{CO_2} \sim 65$ torr) at 37°C

Experimental Results. The time course of pH after mixing suspension A with hematocrit of 4.5% and pH 8.88 ($p_{CO_2} \sim 0$) and solution B at pH 7.27 and p_{CO_2} of 65 torr is shown in Figure 7. A plateau pH of about 8.50 was seen, and the curve was approximately exponential. The most important fact is that the halftime of the process was about 2 sec, very slow for a biological process. When carbonic anhydrase was added to suspension A, the halftime of the pH change became <30 msec, also shown in Figure 7. The analogous results obtained by Constantine *et al.* (*41*) for p_{CO_2} *vs.* time are shown in Figure 8. This process had a halftime of 45 msec, about one-fortieth the halftime for pH equilibrium.

Further work in our laboratory has shown that there must have been some lysis of approximately 1% of the red cells in the reacting mixture of the experiment in Figure 7, which should have accelerated the CO_2 hydration–dehydration reactions about threefold. When the experiments were performed taking greater care to prevent lysis, the rate of extracellular pH equilibration did indeed slow down. Furthermore, using more precise data in the computations, the curve shown in Figure 10 also exhibited a lengthened half-time. We also discovered that the initial "plateau" pH of the flowing reaction mixture was significantly lowered through the formation of carbamate by the reaction of the CO_2 with diluted plasma protein. The presence of slight contamination with carbonic anhydrase in the older experiments (*41*) should not have significantly altered the uptake of CO_2 by the cell suspension (Figure 8), or the computation of the change in p_{CO_2} with time (Figure 9).

Theory of Computations. Basically, the computations performed were the same as those performed for the p_{OH^-} calculations, except that in this case only a forward integration was performed, using the value for p_{OH^-} in the appropriate pH range determined in the previous experiments. Here, Equations (4) could be written for three ionic species (OH^-, Cl^-, and HCO_3^-), only two of which are independent. OH^- and Cl^- were the species chosen since their permeabilities are better known than that of HCO_3^-. Equation (5) was used with all three ions, $p_{HCO_3^-}$ being taken as equal to p_{Cl^-} (*42*, *43*). The assumptions included those listed previously, and also

(1) we assumed that hydration–dehydration reactions of CO_2 and H_2CO_3 were catalyzed inside the cell and uncatalyzed outside

(2) membrane permeability to CO_2 was considered so great that intra- and extracellular p_{CO_2} were always equal

(3) the reactions of CO_2 with hemoglobin to form carbamate were neglected because this was an avoidable complication at this point and because we were not sure how the processes behave kinetically.

Two sets of computations were performed, one set trying to duplicate the experimental results reported above and thus obtain some verification of the validity of the model. The second (and more interesting) set of computations was performed to get as close as possible to *in vivo* conditions as (and after) blood passes through lung capillaries, within the limitations of the assumptions presented above.

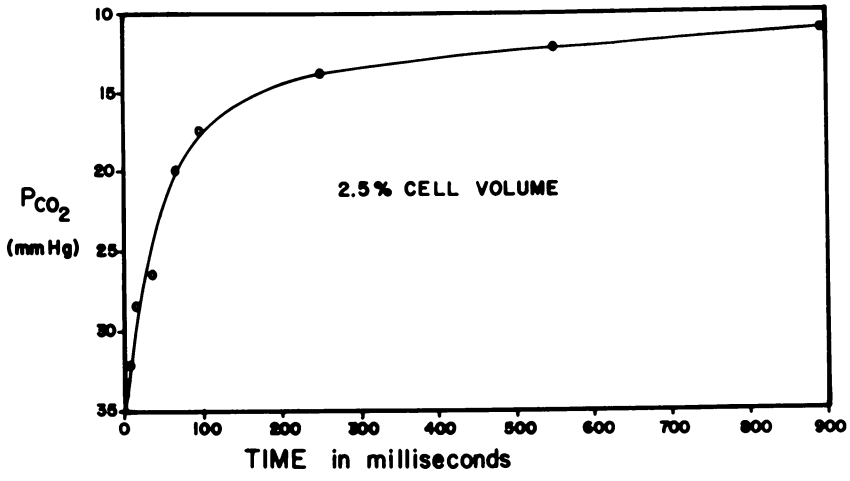

American Journal of Physiology

Figure 8. Change in p_{CO_2} with time after mixing equal volumes of suspension A ($p_{CO_2} \sim 0$) and solution B ($p_{CO_2} \sim 70$ torr) (41)

Results of Computations. We will first discuss the results of the computations simulating the experiment shown in Figure 7. The p_{CO_2} in this case increased from an initial value approximating zero to about 35 mm Hg and the initial pH was 8.65. The intracellular carbonic anhydrase was assumed to accelerate the CO_2 hydration by a factor of 5000. This value, instead of the experimentally determined value of 13,000 (*44*) was chosen in order to make the computations agree with the experimental results, and is another indication of the discrepancy between the apparent behavior of carbonic anhydrase within the cell and in a hemolysate. Figure 9 shows the time course of p_{CO_2}, which was always considered the same in cells and extracellular fluid, p_{CO_2} equivalent to intracellular $[H_2CO_3]$ and p_{CO_2} equivalent to extracellular $[H_2CO_3]$. By p_{CO_2} equivalent to $[H_2CO_3]$ is meant that value of p_{CO_2} which would be in chemical equilibrium with the existing $[H_2CO_3]$.

Figure 9 shows that the intracellular hydration of CO_2 produced nearly 90% chemical equilibration between p_{CO_2} and the cell contents within 0.1 sec, but that the analogous process in the extracellular fluid

took much longer. Once intracellular [H_2CO_3] reached quasi-equilibrium with p_{CO_2}, the rate of the hydration of CO_2 in the cells became entirely dependent on the rate of HCO_3^- movement out of the cell. The slowness of this equilibration in the extracellular fluid is brought out clearly in the graph of extracellular [H^+] *vs.* time in Figure 10, which is on a larger time scale. The half-time for the equilibration of intracellular [H^+] was 0.1 sec while that for the extracellular fluid was 0.9 sec.

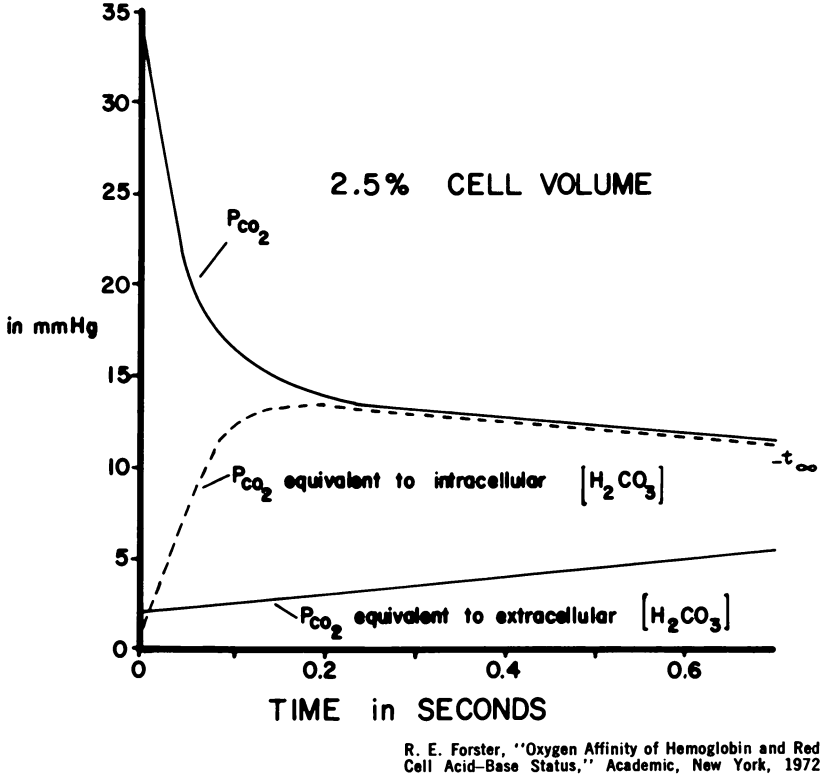

R. E. Forster, "Oxygen Affinity of Hemoglobin and Red Cell Acid–Base Status," Academic, New York, 1972

Figure 9. Computed curves of p_{CO_2} *vs. time after mixing equal volumes of a 5% erythrocyte suspension* ($p_{CO_2} \sim 0$) *and standard buffer solution* ($p_{CO_2} \sim 65$ *torr*) *at 37°C* (15)

The computed time courses of pH and p_{CO_2} after mixing were very similar to the experimental results. With carbonic anhydrase added to the extracellular fluid, the model computed a halftime that again agreed very well with the experimental results. Thus, we felt that while the model included several assumptions that were only approximations it was probably a reasonably good predictor of the behavior of the CO_2 exchange system and could be used to examine phenomena that have not yet been verified experimentally.

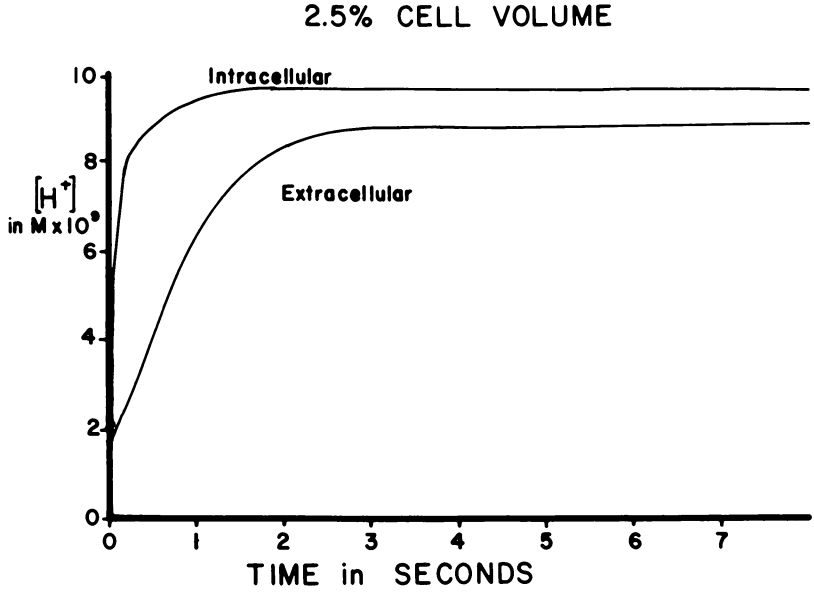

Figure 10. Computed curves of $[H^+]$ *vs. time after mixing equal volumes of a 5% erythrocyte suspension* ($p_{CO_2} \sim 0$) *and standard buffer solution* ($p_{CO_2} \sim 65$ *torr*) *at 37°C* (15)

The conditions for the second set of computations were more physiological, chosen to approximate the situation when blood with a 40% hematocrit, p_{CO_2} of 46 mm Hg, pH of 7.4, and temperature of 37°C was exposed to alveolar gas with a p_{CO_2} of 40 mm Hg for 0.6 sec. Allowance was made for the buffer power of plasma proteins. The effective catalytic factor of the intracellular carbonic anhydrase in this case was 13,000-fold. The p_{CO_2} (*see* Figure 11) started at 40 mm Hg (because it was assumed that alveolar capillary blood p_{CO_2} equals alveolar p_{CO_2}) and rose again when the blood left the alveolar bed and was allowed to equilibrate as a closed system. The intracellular $[H_2CO_3]$ was always in equilibrium with the p_{CO_2}, at least on the time scale used, but the extracellular $[H_2CO_3]$ took much longer to equilibrate. The time courses of intracellular and extracellular $[H^+]$ (Figure 12) were similar to those of the respective $[H_2CO_3]$, except for the first second, in which the diffusion of HCO_3^- into the red cells decreased extracellular $[HCO_3^-]$ without a significant effect on extracellular $[H^+]$. This meant that extracellular $[H^+]$ required about 7 sec to achieve half-equilibration, in spite of normal intracellular carbonic anhydrase activity. The pH of the extracellular fluid was falling from 2 sec on even though $[HCO_3^-]$ was approximately constant (not shown). This occurred by reason of the uncatalyzed dehy-

dration of H_2CO_3 to CO_2 in the plasma, the diffusion of the resulting CO_2 into the cell, its rapid rehydration there, and a final diffusion of HCO_3^- from the inside to the outside of the cell in exchange for Cl^-. This is the Jacobs–Stewart facilitated transfer of H^+ (*40*). This transport of HCO_3^- represents a reversal of the Hamburger shift.

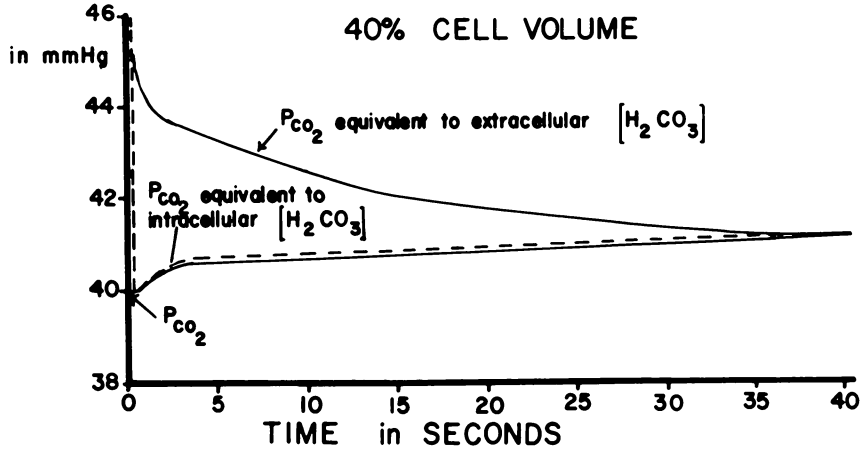

R. E. Forster, "Oxygen Affinity of Hemoglobin and Red Cell Acid-Base Status," Academic, New York, 1972

Figure 11. Computed curves of p_{CO_2} *vs. time following the exposure of whole blood (40% Hct) at* $p_{CO_2} = 46$ *torr to alveolar gas* ($p_{CO_2} = 40$ *torr) for 0.6 sec and then allowing the blood to equilibrate as a closed system* (15)

Discussion. From the experimental and computational results, it appears that blood can reach near-equilibration very rapidly with respect to CO_2 after exchange of CO_2 with its environment. The half-time is of the order of 0.1 sec. Furthermore, the Hamburger exchange of HCO_3^- for Cl^- produces an approximate HCO_3^- and Cl^- equilibrium within 1 sec. Since the removal of CO_2 from the tissues to alveolar gas is one of the most important functions of the circulation, it is appropriate that this be so.

However, H^+ equilibration seems to take a much longer time to be achieved. In the more physiological cases studied computationally, the necessary H^+ transfer across the red cell membrane was effected mainly by the CO_2–HCO_3^- cycle of Jacobs and Stewart (*40*) with OH^- transfer contributing very little to the final equilibration. The total flow through the CO_2–HCO_3^- cycle may have to be large to reach final equilibrium even though the net change in pH might be small. In addition, the more buffer present intra- and extracellularly, the longer the equilibration process will take although the total pH change might be smaller.

The extended length of time needed to reach H^+ equilibrium may have important physiological implications. For example, if a tissue is

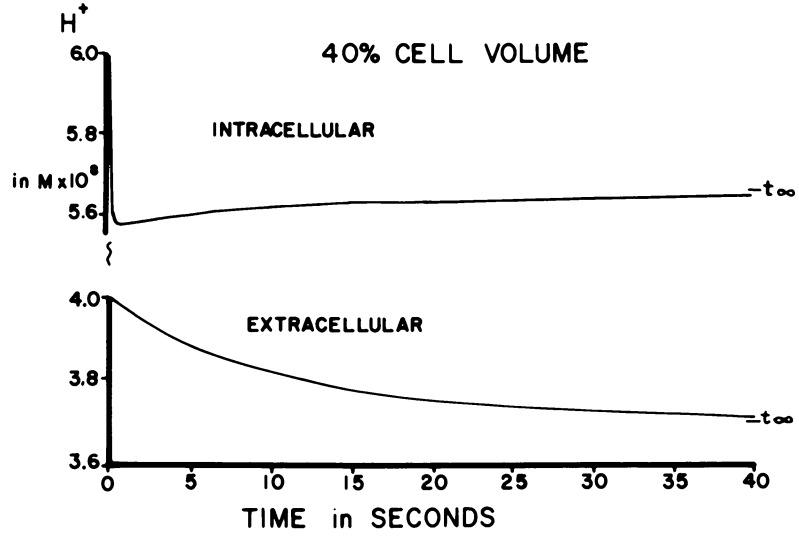

R. E. Forster, "Oxygen Affinity of Hemoglobin and Red Cell Acid–Base Status," Academic, New York, 1972

Figure 12. Computed curves of $[H^+]$ vs. *time following exposure of whole blood* ($p_{CO_2} = 46$ *torr) to alveolar gas* ($p_{CO_2} = 40$ *torr) for 0.6 sec and then allowing the blood to equilibrate* (15)

producing primarily CO_2 *via* aerobic respiration, the plasma of the blood draining that tissue would tend to become more acid with time, whereas if the tissue produces lactic acid, a substance which penetrates red cells slowly (*45*, *46*) *via* anaerobic respiration (as in exercising muscle), the plasma of the effluent blood would tend to get more alkaline with time. If a receptor is sensitive to plasma pH, measurements of the acidity of blood samples, which would reach total equilibrium before being measured, could give false values for the pH actually being seen by the receptors.

Summary

The p_{OH^-} of human erythrocytes varies markedly with extracellular pH. Our determination of p_{OH^-} *vs.* pH is not quantitatively compatible with a simple fixed-charge theory of membrane permselectivity. CO_2 equilibrium is rapidly achieved but pH equilibrium takes a much longer time to reach during CO_2 exchanges in blood. During CO_2 exchange, the unidirectional Hamburger shift cannot alone lead to complete equilibration between red cells and plasma. The mechanism for pH equilibration is the uncatalyzed CO_2 reactions occurring in plasma, rather than an OH^- flux, with a reverse Hamburger shift probable in many cases.

Acknowledgments

We would like to express our thanks to Joseph Pili, Dietrun Kamp, and Esther Chou for technical assistance with the equipment and experimental measurements. The availability of the Medical School Computer Facility under NIH Grant No. RR-15 is gratefully acknowledged. This work was supported by Grant No. 4108 from the National Heart and Lung Institute. E. D. Crandall was supported in part by PHS Special Fellowship No. 2-F03-GM-38, 982-02.

Literature Cited

1. Dalziel, K., *Biochem. J.* (1953) **55**, 79.
2. Gibson, Q. H., Roughton, F. J. W., *Proc. Roy. Soc. Ser. B. Biol. Sci.* (1955) **143**, 310.
3. Rossi-Bernardi, L., Berger, R. L., *J. Biol. Chem.* (1968) **243**, 1297.
4. Klocke, R. A., Rotman, H. H., Andersson, K., Forster, R. E., *Fed. Proc.* (1968) **27**, 286.
5. Sir, J. A., *Trans. Faraday Soc.* (1958) **54**, 207.
6. Love, W., "Technique of Organic Chemistry," Vol. VIII, "Rates and Mechanism of Reactions," S. L. Friess and A. Weissberger, Eds., Interscience, New York, 1953.
7. Crandall, E. D., Klocke, R. A., Forster, R. E., *J. Gen. Physiol.* (1971) **57**, 664.
8. Gibson, Q. H., Milnes, L., *Biochem. J.* (1964) **91**, 161.
9. Edsall, J. T., "CO_2: Chemical, Biological and Physiological Aspects," p. 15, NASA Spec. Publ. 188, 1969.
10. Eigen, M., Hammes, G., *Advan. Enzymol.* (1963) **25**, 1.
11. Brinkman, R., Margaria, R., Roughton, F. J. W., *Phil. Trans. Roy. Soc. London Ser. A. Math. Phys. Sci.* (1933) **232**, 65.
12. Roughton, F. J. W., "Handbook of Physiology," p. 767, Sect. 3, Vol. I, W. O. Fenn and H. Rahn, Eds., American Physiological Society, Washington, 1964.
13. Wissbrun, K. F., French, D. M., Patterson, A., *J. Phys. Chem.* (1954) **58**, 693.
14. Booth, V. H., *J. Physiol.* (1938) **93**, 117.
15. Forster, R. E., "Oxygen Affinity of Hemoglobin and Red Cell Acid–Base Status," Alfred Benzon, Symposium IV., P. Astrup, M. Rorth, O. Siggaard Anderson, Eds., Academic, New York, 1972.
16. Roughton, F. J. W., *Physiol. Rev.* (1935) **15**, 241.
17. Maizels, M., *Biochem. J.* (1934) **28**, 337.
18. Wilbrandt, W., *Pfluegers Arch. Gesämte Physiol. Menschen Tiere* (1940) **243**, 537.
19. Donlon, J. A., Rothstein, A., *J. Membrane Biol.* (1969) **1**, 37.
20. Tosteson, D. C., *Acta Physiol. Scand.* (1959) **46**, 19.
21. Van Slyke, D. D., Neill, J. M., *Internat. J. Biol. Chem.* (1924) **61**, 523.
22. Drabkin, D. L., Austin, J. H., *J. Biol. Chem.* (1932) **98**, 719.
23. Crosby, W. H., Furth, F. W., *Blood* (1953) **11**, 380.
24. Davson, H., "A Textbook of General Physiology," p. 390, Churchill (J. and A.), London, 1964.
25. Goldman, D. E., *J. Gen. Physiol.* (1943) **27**, 37.
26. Robinson, R. A., Stokes, R. H., "Electrolyte Solutions," p. 432, Butterworth, London, 1959.
27. Savitz, D., Sidel, V. W., Solomon, A. K., *J. Gen. Physiol.* (1964) **48**, 79.

28. German, B., Wyman, J., *J. Biol. Chem.* (1937) **117,** 533.
29. Rossi-Bernardi, L., Roughton, F. J. W., *J. Physiol (London)* (1967) **189,** 1.
30. Luckner, H., *Pfluegers Arch. Gesämte Physiol. Menschen Tiere* (1939) **241,** 753.
31. Wieth, J. O., *J. Physiol. (London)* (1970) **207,** 581.
32. Bull, H. B., "Physical Biochemistry," pp. 78, 85, 98, Wiley, New York, 1951.
33. Wilbrandt, W., Schatzmann, H. J., Ciba Found. Study Group Symp. No. 5 (1960), 340.
34. LaCelle, P., Rothstein, A., *J. Gen. Physiol.* (1966) **50,** 171.
35. Passow, H., *Prog. Biophys. Mol. Biol.* (1969) **19,** 425.
36. Deuticke, B., *Naturwissenschaften* (1970) **57,** 172.
37. Jacobs, M. H., Parpart, A. K., *Biol. Bull. (Woods Hole)* (1932) **62,** 32.
38. Scarpa, A., Cecchetto, A., Azzone, G. F., *Biochem. Biophys. Acta* (1970) **219,** 179.
39. Passow, H., "The Red Blood Cell," p. 71, C. Bishop and D. M. Surgenor, Eds., Academic, New York, 1964.
40. Jacobs, M. H., Stewart, D. R., *J. Gen. Physiol.* (1942) **25,** 539.
41. Constantine, H. P., Craw, M. R., Forster, R. E., *Amer. J. Physiol.* (1965) **208,** 801.
42. Dirken, M. N. J., Mook, H. W., *J. Physiol. (London)* (1931) **73,** 349.
43. Piiper, J., "CO_2: Chemical, Biological and Physiological Aspects," p. 267, NASA Spec. Publ. 188, 1969.
44. Kernohan, J. C., Forrest, W. W., Roughton, F. J. W., *Biochem. Biophys. Acta* (1963) **67,** 31.
45. Giebel, O., Passow, H., *Pfluegers Arch. Gesämte Physiol. Menschen Tiere* (1960) **271,** 378.
46. LaCelle, P., Passow, H., *Pfluegers Arch. Gesämte Physiol. Menschen Tiere* (1966) **219,** R15.

RECEIVED November 22, 1971.

6

Factors Affecting Placental Oxygen Transfer

LAWRENCE D. LONGO, ESTHER P. HILL, and GORDON G. POWER

Departments of Physiology and Obstetrics and Gynecology, School of Medicine, Loma Linda University, Loma Linda, Calif. 92354

The importance of factors affecting placental oxygen transfer has been studied theoretically by mathematical simulation and experimentally. The effects of varying uterine umbilical O_2 partial pressures, maternal and fetal hemoglobin flow rates, blood O_2 affinity, and placental diffusing capacity on the transient maternal and fetal placental end-capillary O_2 tensions and rate of O_2 transfer during a single capillary transit have been examined by varying each independently. The model predicts that transient fetal end-capillary p_{O_2} and O_2 exchange rates are most sensitive to uncompensated changes in umbilical arterial p_{O_2} and fetal p_{50}, somewhat less sensitive to maternal and fetal hemoglobin flow rate changes and changes in maternal p_{50}, and much less sensitive to changes in maternal arterial p_{O_2} or placental diffusing capacity. We have tested these predictions using an isolated perfused placenta cotyledon preparation.

The subject of fetal oxygenation has been of interest since earliest times. Hippocratic writers (*1*) as well as Aristotle (*2*) assumed that since adults would die without breathing, presumably the fetus also breathed. The precise nature of what actually was breathed was not determined until the discovery of oxygen by Scheele and independently by Priestley in the early 1770's. While the placenta apparently has been known since ancient times, it was not until the work of Harvey (*3*, *4*) that the independence of the fetal and maternal circulations was established. Further convincing experimental evidence for this independence was presented by William and John Hunter (*5*).

The fetus requires oxygen on a moment-to-moment basis. Assuming a fetal oxygen consumption of 6 ml/min/kg of fetal weight, a term fetus (weighing 3 kg) requires about 18 ml of O_2 per minute. In view of this

vital requirement, the fetal oxygen stores are surprisingly small. Assuming a blood hemoglobin concentration of 16.5 gram/100 ml of fetal blood (an O_2 capacity of 22 ml/100 ml of blood), a 3-kg fetus with a blood volume of 300 ml has a total oxygen capacity of 66 ml. Since the average saturation of fetal hemoglobin is about 60%, the fetal O_2 stores are only about 40 ml (66×0.60), barely a 2-min supply for the fetal tissues. This calculation assumes that blood is the primary reservoir of O_2 in the fetus. Although myoglobin acts as an oxygen store in the muscles of man and most mammals, recent evidence indicates little or no myoglobin in fetal skeletal muscle (unpublished observation). Nor could all of the oxygen be extracted from the blood since this would require that the oxygen tension (p_{O_2}) fall to zero—clearly impossible if the fetus is to remain alive. Thus, the fetal O_2 supply is rather large in view of its small stores and must be supplied without interruption. An uninterrupted maternal to fetal transfer of O_2 is clearly required.

Factors Affecting Placental O_2 Transfer

Several steps are involved in oxygen transfer from the ambient air to the cristae of the mitochrondria in fetal tissues where the O_2 is ultimately reduced. The transfer of oxygen across the placenta is only one link in this chain of sequential steps.

In the placenta a volume of oxygen sufficient for fetal needs must diffuse across the membranes from maternal to fetal blood during the short time the two circulations are in close contact. This oxygen transfer is a function of several factors which include uterine and umbilical arterial O_2 partial pressures, maternal and fetal placental blood flow rates, the O_2 capacity and O_2 affinity of maternal and fetal hemoglobin, the diffusing capacity of the placenta, the amount of CO_2 exchanged, and the vascular arrangement of maternal to fetal vessels.

The exchange process would ideally be studied by sampling the inflowing and end-capillary blood within a single exchange unit. However, it has not yet been experimentally possible to sample end-capillary blood directly or to study how these various factors affect O_2 transfer within individual capillaries. Several problems account for this. In the first place, the placenta may be compared with a black box with measurable maternal and fetal arterial inputs and mixed venous outputs. Venous outflow consists of blood from numerous exchange units in which O_2 partial pressures have reached different degrees of equilibration because of nonuniform distribution of maternal and fetal flows, nonuniform distribution of diffusing capacity to flow, and placental O_2 consumption. Also, there are probably vascular shunts in maternal and fetal placental circulations that contribute to the uterine and umbilical veins containing

a mixture of blood of various O_2 tensions. Another problem for the investigator is that when he changes a factor experimentally, various compensations mask its effect.

Normal values for the various determinants of O_2 transfer are necessary for quantitative analysis of the exchange process. Some values—*e.g.*, those for the maternal and fetal arterial O_2 tensions, O_2 capacities, and O_2 affinities—are fairly well defined. Others—*e.g.*, the diffusing capacity and maternal and fetal placental blood flows—are less well determined.

Placental Diffusing Capacity. The diffusion characteristics of the placental membrane may be described by Fick's first law (*6*):

$$\frac{dQ}{dt} = \frac{A \cdot K \cdot d \cdot \Delta C}{x} \tag{1}$$

where dQ/dt is the amount of a given substance (*i.e.*, oxygen) crossing the placental membrane per unit time, K is the permeability of the membrane, d is the diffusivity of the gas, ΔC is the concentration difference across the membrane, and x is the membrane thickness. The placental membrane, however, is a complex structure, having variable thickness and permeability. Since the area, permeability, diffusivity, and thickness are constants, these terms can be combined together into a single term which expresses the diffusion characteristics of the membrane:

$$\frac{dQ}{dt\Delta P} = D_p \tag{2}$$

where D_p is the placental diffusing capacity in ml/(min × mm Hg difference). For respiratory gases the partial pressure difference (ΔP) is used rather than the concentration difference (ΔC).

Barron and his co-workers first calculated the placental diffusing capacity (*7*, *8*). These investigators measured oxygen tensions in the uterine and umbilical artery and veins. They assumed that the uterine and umbilical venous oxygen tensions represented those in the placental end-capillaries and thus estimated that the mean maternal to fetal oxygen partial pressure difference was about 25 mm Hg. They calculated that the placental diffusing capacity for O_2, $D_{p_{O_2}}$ was about 0.5 ml (min × mm Hg) for a 3-kg fetus. However, their estimates of average O_2 gradients were probably incorrect for several reasons. These include the effects of placental oxygen consumption, vascular shunts, uneven distribution of maternal to fetal blood flow, and nonuniform distribution of diffusing capacity to blood flows. Consequently, their calculations of diffusing capacity based on venous p_{O_2} gradients were probably incorrect.

In the early part of this century the Kroghs recognized these problems in calculating the diffusing capacity for the lung and introduced the use of carbon monoxide, a diffusion-limited gas, to study the diffusion characteristics of the pulmonary membrane (*9*). Using a similar line of reasoning, we used carbon monoxide to measure D_p in sheep and dogs (*10*). The ewes were anesthetized with sodium pentobarbital (20 mm/kg) and tracheotomized. Polyvinyl catheters, 1.5 mm outside diameter, were introduced into the maternal femoral artery, a branch of the uterine vein; the abdomen was incised in the midline, and the fetus was exposed through an incision through the uterine wall. Fetal blood samples were obtained from a branch of the umbilical artery and vein. The ewes were placed on a closed rebreathing circuit and ventilated with a respiratory pump. This circuit included a carbon dioxide absorber and an oxygen supply. Following a control period of 20 min to 1 hour, a given amount of carbon monoxide (CO) was introduced into the circuit. Serial samples were taken to follow the time course of the change in maternal and fetal carboxyhemoglobin concentrations. Partial pressures of carbon monoxide (p_{CO}) in mm Hg were calculated from the Haldane relation (*11*).

$$p_{CO} = \frac{[COHb] \times p_{O_2}}{[O_2Hb] \times M} \tag{3}$$

where [COHb] and [O_2Hb] are carboxyhemoglobin and oxyhemoglobin concentrations respectively, p_{O_2} is the partial pressure of oxygen, and M is the relative affinity of hemoglobin for CO as compared with O_2. The fetal uptake of CO calculated from the change in fetal carboxyhemoglobin concentration, the mean maternal to fetal p_{CO} gradient, and the physicochemical relations of O_2 to CO were used to calculate $D_{pO_2} \cdot D_{pO_2}$ was 0.54 ml/(min $\times$ mm Hg $\times$ kg fetal weight) or, about 1.62 ml (min $\times$ mm Hg) for a 3-kg fetus (*10*). Thus the diffusing capacity for O_2 was appreciably greater than previously suspected. From these calculations the mean maternal to fetal p_{O_2} difference was calculated to be only 5–6 mm Hg, some threefold less than the previous estimates. While the diffusing capacity calculated from the CO data may not seem significantly greater than the 0.5 ml/min calculated from the O_2 data, there is an important difference. The higher value strongly suggests that there is no significant barrier to the diffusion of O_2 through the placental membrane as suggested by the former value. Furthermore, it suggests that the oxygen partial pressures equilibrate during the course of a single transit in the maternal and fetal placental exchange vessels.

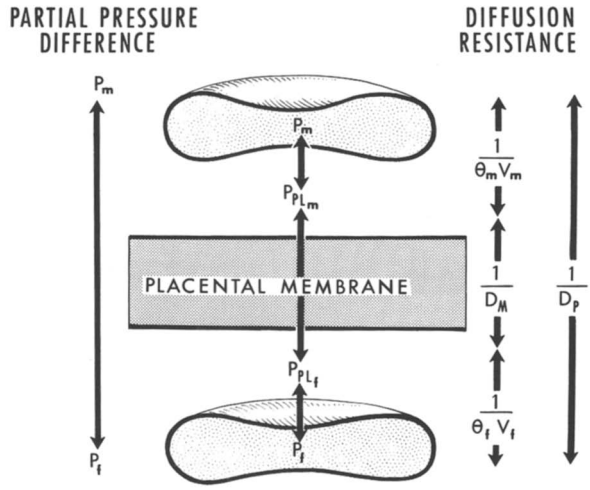

Figure 1. Schematic representation of the maternal to fetal partial pressure differences and resistances to diffusion.

The total p_{O_2} difference ($P_m - P_f$) consists of: (1) the difference from the interior of the maternal red blood cell to plasma ($P_m - P_{pl,m}$); (2) the difference across the membrane to fetal plasma ($P_{pl,m} - P_{pl,f}$); and (3) the difference from fetal plasma to the interior of the fetal erythrocyte ($P_{pl,f} - P_f$). The total resistance to diffusion ($1/D_P$) is the sum of the individual resistances: (1) the resistance of maternal blood ($1/\theta_m V_m$); (2) the placental membrane resistance ($1/D_M$); and (3) the reststance of fetal blood ($1/\theta_f V_f$) (see Equation 4).

Relative Resistance to Diffusion of Maternal and Fetal Blood and the Placental Membranes

A further consideration is the relative resistance to diffusion offered by maternal and fetal blood and the placental membranes. The total partial pressure difference between maternal and fetal blood is the sum of the pressure difference from the interior of the maternal erythrocyte to the maternal plasma, plus the pressure difference from the maternal plasma across the placental membrane to the fetal plasma, and the partial pressure difference from the fetal plasma to the interior of the fetal erythrocyte. These relations are diagrammed in Figure 1. The reciprocal of the diffusing capacity, the total resistance to diffusion, is the sum of the resistance of the maternal blood, the resistance of the placental membrane, and the resistance of the fetal blood (*12*). These resistances are depicted in Figure 1 and may be expressed as:

$$\frac{1}{D_P} = \frac{1}{\theta_m V_m} + \frac{1}{D_M} + \frac{1}{\theta_f V_f} \qquad (4)$$

where θ_m and θ_f are the diffusing capacities in ml/(ml × min × mm Hg) of maternal and fetal blood respectively, V_m and V_f are the blood volumes in milliliters in the maternal and fetal placental exchange vessels, respectively, and D_M is the diffusing capacity of the placental membrane in ml/(min × mm Hg). Although D_M remains constant, D_P varies along the capillary because θ_m and θ_f vary. The diffusing capacity of the red blood cells (θ) is a function of the rate of combination of O_2 with hemoglobin, which increases at higher oxygen tensions, and the concentration of reduced hemoglobin which decreases at increased oxygen tensions (*13*). The value of θ is relatively constant at low oxygen tensions but decreases rapidly at high oxygen tensions. By measuring the carbon monoxide diffusing capacity at various oxygen tensions, one may solve for the values of the maternal and fetal capillary blood volumes and the membrane diffusing capacity.

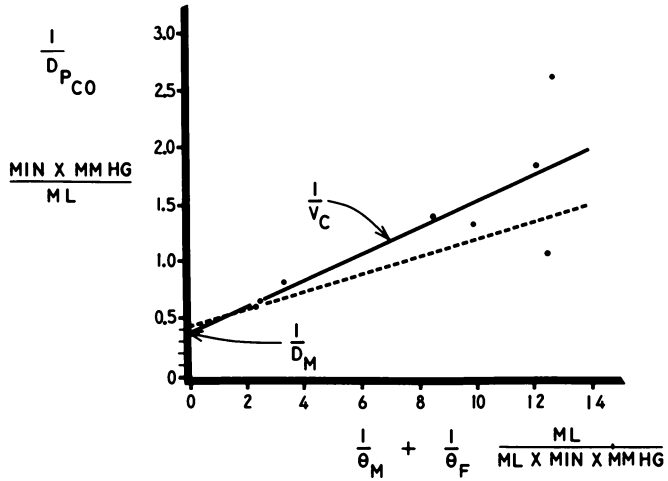

Figure 2. Plot of $1/Dp_{co}$ *(normalized to a fetal weight of 3 kg) as a function of* $(1/\theta m) + (1/\theta F)$*, assuming that* $V_m = V_f$*, and that the mean maternal placental* p_{O_2} *minus the mean fetal* p_{O_2} *equals that gradient during normal oxygenation. The closed circles represent measurements of individual animals except for the value 0.62 that is the mean of eight determinations at 1 atm* (10)*. The plot should give a straight line, the slope being equal to* $1/Vc$*, and the intercept of the vertical axis equal to* $1/D_M$*. The regression equation of the entire data is* $y = 0.375 + 0.116x$*. The values of* V_m *and* V_f *are about 9 ml each and* D_M *is 2.67 ml/(min × mm Hg). The dashed line represents the mean for the values of* $1/Dp_{co}$ *calculated assuming that the mean maternal placental* p_{o_2} *equaled the mean fetal* p_{o_2}*,* $Dm = 2.4$ *ml/(min × mm Hg) and* $Vc = 12$ *ml. The true values of* Vc *and* Dm *probably lie between these limits, namely 10 ml and 2.6 ml/(min × mm Hg), respectively.*

The CO diffusing capacity, $D_{p_{CO}}$, of sheep was measured at various O_2 tensions in a hyperbaric chamber using a method similar to that outlined above (*12*). $D_{p_{CO}}$ varied as a function of the oxygen tension. In Figure 2 the reciprocal of $D_{p_{CO}}$ is plotted as a function of the reciprocal of the diffusing capacity of the maternal and fetal red blood cells. From the plot the slope is the reciprocal of the value of V, the maternal and fetal capillary blood volume while the intercept is the reciprocal of $D_{M_{CO}}$. From these studies we calculated that the resistance of maternal and fetal red blood cells was approximately one-third of the total resistance while the resistance of the placental membrane *per se* was about two-thirds of the total resistance to O_2 diffusion (*12*). This is in contrast to previous studies which assumed that the placental membrane *per se* constituted the total resistance to diffusion.

Mathematical Model of Placental O_2 Transfer

With values for the various parameters affecting O_2 transfer, the exchange process occurring in the maternal and fetal exchange vessels (*14, 15, 16*) may be simulated mathematically. A mathematical model may be used to study how variations in individual parameters affect the O_2 exchange process and to calculate the relative importance of various factors affecting oxygen transfer (*15*). In turn the model can be a stimulus to design experiments to test the predictions of the model or to provide more exact values for the parameters affecting the exchange process.

The model uses values of the parameters affecting exchange such as inflowing oxygen tensions, flow rates of maternal and fetal blood, and the placental diffusing capacity in a forward integration procedure to calculate the time course of O_2 transfer (*14*). End-capillary O_2 tensions and contents are calculated as consequences of the exchange process, thereby avoiding the error of assuming that mixed venous oxygen values truly represent end-capillary values. The model predicts the extent of p_{O_2} equilibration in the capillaries under various conditions. It also permits study of the effects of placental tissue oxygen consumption vascular shunts, unequal maternal and fetal capillary transit times, and physically dissolved O_2 under high O_2 tensions. We recognize that the simplified model does not accurately represent the complexity of O_2 exchange *in vivo*. We further recognize that the model is no substitute for experimental measurements, but until these can be obtained from single exchange vessels in the placenta, it seems the best approach to study the transfer process.

Description of Model. Our model describes the diffusion of oxygen across a section of uniform tissue separating two parallel capillaries. The

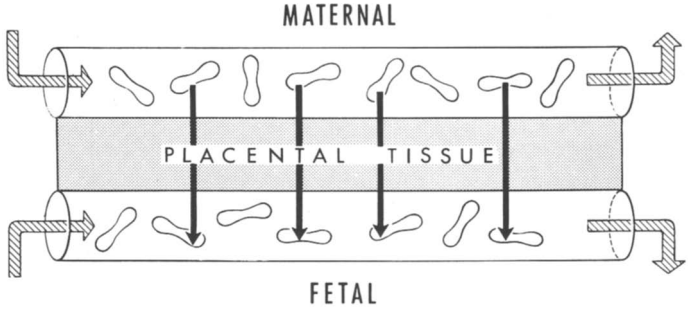

Figure 3. Diagrammatic representation of maternal and fetal placental exchange vessels with uniform dimensions and concurrent flows. As the blood flows along the capillaries, O_2 diffuses in a one-dimensional plane from maternal to fetal blood.

capillaries are assumed to have uniform diameter and equal length with concurrent maternal and fetal flow, as shown in Figure 3. Blood flow is assumed to be nonpulsatile with perfect radial mixing. The pH, p_{CO_2}, and temperature are assumed to be constant along the capillary. We represent the effect of all the capillaries in the placental exchange bed by a single unit with capillary volumes, V_m and V_f, and blood flow rates, $\dot{Q}_m$ and $\dot{Q}_f$, equivalent to that of the entire placenta. (The subscripts $_m$ and $_f$ refer to maternal and fetal sides of the placenta, and all references to diffusion refer to O_2.) As the blood moves along the capillaries, O_2 diffuses from the maternal capillary across the membrane to the fetal capillary. Thus the variation of O_2 partial pressures with distance along the capillaries is equivalent to the change in partial pressure in an element of blood with time, a simple one-dimensional diffusion problem. The small amount of diffusion occurring along the length of the capillaries is ignored (*14*). The capillary transit time is calculated as the capillary volume divided by the flow rate and is usually assumed to be equal in both vessels. Fick's first law of diffusion can be applied because the p_{O_2} remains constant (*i.e.*, steady state) at each point along the capillary.

The differential equations describing the change in oxygen content on the two sides of the membrane are:

$$\frac{d[O_2]_m}{dt} = \frac{-D_p(P_m - P_f)}{V_m} \tag{5}$$

and

$$\frac{d[O_2]_f}{dt} = \frac{-(V_m/V_f)\, d[O_2]_m}{dt} \tag{6}$$

where $[O_2]_m$ and $[O_2]_f$ are the O_2 contents (ml O_2/ml blood) in maternal and fetal blood respectively, P_m and P_f are the O_2 partial pressures (mm

Hg) at time t on the maternal and fetal sides, V_m and V_f are the maternal and fetal capillary blood volumes (ml) and D_p is the placental diffusing capacity for O_2 [ml/(min $\times$ mm Hg)]. While these equations ignore placental tissue oxygen consumption, this will be considered later.

The oxygen contents and partial pressures are related by the hemoglobin dissociation curves for maternal and fetal bloods. We used a modified Hill equation (*17*, *18*):

$$\log p_{O_2} = k_1 - k_2 (\text{pH} - 7.4) + k_3 \log_{10} [S/(100-S)] \tag{7}$$

where S is the percent saturation of the hemoglobin:

$$S = 100[O_2]/(O_2 \text{ capacity}) \tag{8}$$

The O_2 capacity equals 1.34 times the hemoglobin concentration, a variable in the model. The constants used in Equation 7 which fit experimental dissociation curves for sheep at 38°C (*18*) are for maternal blood: $k_1 = 1.544$ when $S < 81$, $k_1 = 1.585$ when $S \geq 81$, $k_2 = 0.456$, $k_3 = 0.346$ when $S < 81$ and $k_3 = 0.283$ when $S \geq 81$. For fetal blood: $k_1 = 1.20$, $k_2 = 0.464$, $k_3 = 0.348$. To obtain theta for Equation 4 we use an empirical equation which has been fitted to Staub's data (*13*) and scaled to correct for the difference of reaction rates in maternal and fetal human and sheep blood:

$$\theta = [k_1 (1 - e^{-k_2(100-S)}) + k_3 S - k_4] (O_2 \text{ capacity}/0.2) \quad (k'_c, \text{ sheep}/k'_c, \text{ human}) \tag{9}$$

where $k_1 = 3.287$, $k_2 = 0.1117$, $k_3 = 7.05 \times 10^{-3}$, $k_4 = 0.8142$, k'_c, sheep $= 130$ mM^{-1} sec^{-1}, for maternal blood and 151 mM^{-1} sec^{-1} for fetal blood (*19*), and k'_c, human $= 164$ mM^{-1} sec^{-1} (*20*). Figure 4 shows the variations in θ_m and θ_f and the resulting variations in D_P calculated with our model for a typical capillary transit.

Values of oxygen partial pressure in the plasmas, $P_{pl,m}$ and $P_{pl,f}$, can be obtained from the fraction of the total resistance resulting from the hemoglobin reaction rates:

$$P_{pl,m} = P_m - \frac{1/(\theta_m V_m)}{1/D_P} (P_m - P_f) \tag{10}$$

and

$$P_{pl,f} = P_f + \frac{1/(\theta_f V_f)}{1/D_p} (P_m - P_f) \tag{11}$$

In Equations 4 through 11, t is the independent variable and P_m, P_f, $P_{pl,m}$ and $P_{pl,f}$ the dependent variables. $[O_2]_m$, $[O_2]_f$, D_P, θ_m, θ_f are in-

termediate variables calculated during the solution of the equations. D_M, V_m, V_f, $\dot{Q}_m$, $\dot{Q}_f$, hemoglobin concentration and initial values of P_m and P_f are parameters which are varied in a systems analysis approach.

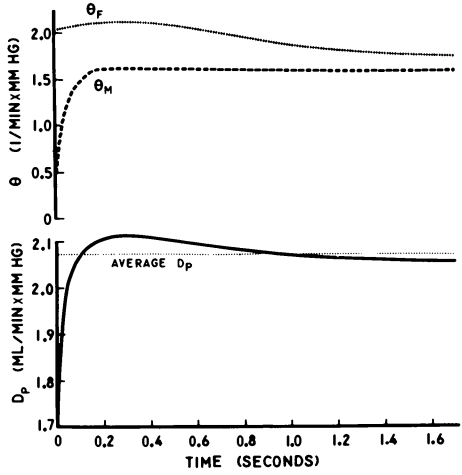

Figure 4. The calculated changes in diffusing capacity of fetal and maternal blood (θ_f,θ_m) and the placental diffusing capacity (Dp) *during a single capillary transit. θ_m is decreased during the first part of the capillary transit because percent oxyhemoglobin saturation in the maternal arterial blood is relatively high* (see *Equation 9*). *The change in* Dp *reflects the changes in θ_m and θ_f* (see *Equation 4*). *The average value of* Dp (*2.07 ml/min × mm Hg*) *is indicated by the dotted line and is obtained by summing the* Dp *values at each step and dividing by the number of steps.*

The above equations were solved with a fourth-order Runge–Kutta forward numerical integration technique on an EMR-6130 computer (*21*). The integration begins with initial values of P_m and P_f representing the arterial end of the capillary. The changes of these partial pressures are calculated during a small element of time. These changes are used to compute new values of P_m and P_f. After many such successive steps the cumulative time equals the capillary transit time, and the integration is terminated. The final P_m and P_f values represent those at the end of the capillary. The average D_P value is obtained by summing the D_P values at each step and dividing by the number of steps. The same procedure can be used to calculate average values of P_m and P_f.

Experimental Values Used in the Model. In using the model to simulate gas exchange *in vivo*, we try to choose values for $D_{p_{O_2}}$, p_{O_2} of inflowing blood, the amount of O_2 crossing the placenta, and flow rates through the exchange vessels that are self-consistent and agree with experimental values. $D_{p_{O_2}}$ may be estimated to be 2.04 ml/(min × mm Hg), D_M = 2.73 ml/(min × mm Hg), and $V_m = V_f$ = 10 ml, values

derived from $D_{p_{CO}}$ measured in sheep (*12*). The p_{O_2} values of 95 and 14 mm Hg for uterine and umbilical arterial blood are representative (*10*). The average rate of placental O_2 transfer is about 6 ml/(min $\times$ kg fetal tissue) (*22*). Although total placental flows have been measured by several investigators, the fractions which pass through exchange vessels are uncertain. An O_2 uptake rate of 18 ml/min for a 3-kg fetus and an arterial to end-capillary content difference of 7.14 vol % (estimated for an end-capillary p_{O_2} of 32 mm Hg) would require an effective flow of only 210 ml/min. Values of $\dot{Q}_m$ = 600–1000 ml/min (*23*, *24*) and $\dot{Q}_f$ = 450–600 ml/min measured experimentally probably include a considerable fraction that bypasses exchange areas through shunts (*25*, *26*) or is unevenly distributed (*27*). Assuming shunted fractions of 20–30% (*25*, *26*, *28*), calculations yield capillary flow rates of 400–500 ml/min, values much larger than the 210 ml/min calculated above. We chose an intermediate value of 350 ml/min for the capillary flow rates. Figure 5 shows the resulting p_{O_2} values in maternal and fetal red cells and plasma during the course of a single capillary transit. The values calculated for the first and last few steps during a typical forward integration have been presented elsewhere (*14*).

In the example shown in Figure 5, the end of a single capillary transit would come after 1.714 sec, the quotient of a V_f of 10 ml and $\dot{Q}_f$ of 350 ml/min. At this point the maternal and fetal end-capillary O_2 tensions equaled 32.26 mm Hg and 31.81 mm Hg, respectively. During the capillary transit, the average D_P was 2.074 ml(min $\times$ mm Hg), the mean maternal p_{O_2} was 38.63 mm Hg, the mean fetal p_{O_2} was 26.96 mm Hg, and 0.710 ml of O_2 was exchanged, giving an average O_2 exchange rate of 24.84 ml/min.

To assure sufficient accuracy of the numerical integration, we repeatedly halved the integration step size until no significant difference (0.1%) in solutions occurred. For the fourth-order Runge-Kutta method this required a step size of .04 sec (43 steps). An upper bound of the total error introduced by the numerical integration procedure can be obtained for the Runge–Kutta method (*29*). At a step size of 0.04 sec, the error estimate calculated is 0.004% (*14*).

Discussion of Assumptions of the Model. The pattern of maternal to fetal placental flow affects the amount of O_2 transferred. It seems unlikely that the simple concurrent system shown in Figure 3 accurately represents the placental capillaries in sheep, a species in which the exchange vessels interdigitate in a nonuniform and complex manner (*30*, *31*). The flow patterns are also complicated in humans where maternal blood enters the intervillous spaces from the base and flows upward and outward past fetal capillary loops in placental villi. Physiological studies also fail to reveal a simple geometric flow pattern. For

example, gas exchange in the sheep and goat behaves as either a concurrent exchange system with moderately uneven distribution of $\dot{Q}_m/\dot{Q}_f$ or a countercurrent exchange system with markedly nonuniform $\dot{Q}_m/\dot{Q}_f$ (*12, 25, 32, 33*).

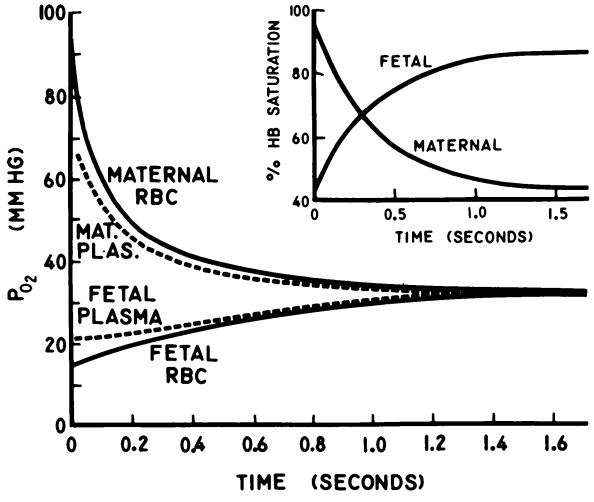

Figure 5. The time course of change in O_2 tensions during a single transit in placental exchange vessels. The p_{O_2} values in maternal and fetal red blood cells are shown by the solid lines. Using the indicated values (see text) the p_{O_2} in maternal and fetal end-capillary vessels barely reaches equilibrium (<0.5 mm Hg). The insert shows the change in maternal and fetal oxyhemoglobin percent saturation during the capillary transit. When maternal and fetal end-capillary p_{O_2} values are essentially the same, the percent O_2Hb of fetal blood is about twice that of maternal blood because of the higher O_2 affinity of fetal blood.

Several other workers have considered the effects of various blood flow patterns on placental exchange. Guilbeau, Reneau, and Knisely (*34*) analyzed the effects of fetal blood flowing concurrently within a cylinder of maternal blood and also a concurrent pattern with multivillous fetal flow. These authors solved partial differential equations to obtain the p_{O_2} changes in maternal and fetal blood during a single capillary transit. While these authors did not consider the finite resistances of hemoglobin reaction rates, the results of our analyses for concurrent flow in adjacent capillaries are somewhat similar and comparisons will be presented when appropriate. Faber (*35*) presented calculations and a graphical analysis of the effects of concurrent, countercurrent, and several other patterns of flow on placental exchange. It is

difficult to compare the results of our model with Faber's analysis, however, since his results are not expressed in terms of end-capillary partial pressures. Kirschbaum and Shapiro (*36*) considered O_2 exchange in a concurrent system with varying degrees of shunting, but neither end-capillary O_2 tensions nor mean O_2 exchange rates were presented for comparison. Chu (*37*) derived equations that consider the effects of oblique crossflow patterns on placental exchange, but results of the calculations were not presented. Van Liew (*38*) analyzed a model in which O_2 diffused from a subcutaneous gas pocket into several capillaries at various depths in a tissue block. An analogous situation in the placenta might be such that O_2 diffuses simultaneously from maternal vessels at various distances from the placental membrane to fetal vessels which are also various distances from the membrane.

Each of the flow patterns described may be present to some extent in various parts of the placenta. Ideally one should calculate the O_2 exchange that occurs with various vascular arrangements (*i.e.*, concurrent, countercurrent, crosscurrent, etc.) and sum the exchange of the various compartments to obtain the total. We have no data on the distribution of various flow pattern in the placenta, consequently such an approach is not possible at present. While we recognize that our model does not represent anatomical complexity and ignores pulsatile flow, it is simple, is compatible with physiological studies, and is convenient to study the effect of various parameters on O_2 exchange.

Additional determinants of the amount of O_2 transferred in the placenta are the amount of CO_2 exchanging and the temperature change during a capillary transit. The effects of p_{CO_2} and pH (Bohr effect) on O_2 exchange are significant and will be discussed in the presentation of a model of CO_2 exchange (manuscript in preparation). Since the temperature of the fetus is about 0.5°C higher than the maternal arterial blood (*39*, *40*), the maximum temperature change in each exchange vessel would be about 0.25°C. We consider this change small enough to be ignored.

Importance of Variation of D_P Along the Capillary. To study the importance of D_P as described previously (Equation 4 and Figure 4), we performed a Runge–Kutta integration using a constant value of $D_P = 2.074$, the average calculated from our sample calculation. Initially, D_P is less than the average D_P along the capillary, but later increases to a value greater than the average (Figure 4). Thus, at first the O_2 exchange rate is decreased slightly (1.2%) relative to what would occur at a constant D_P and as a result, the P_m and P_f values approach equilibrium more slowly than those calculated with a constant D_P. Later, the increased D_P increases O_2 exchange and compensates for the initial lag of p_{O_2} values relative to the constant D_P values, and the end-capillary p_{O_2}

values and average exchange rate calculated are insignificantly (<0.2%) different for the two cases.

O_2 Consumption. Our model predicts that the maternal and fetal end-capillary p_{O_2} difference would be less than 1 mm Hg. Experimentally the uterine vein to umbilical vein (V–v) p_{O_2} difference is from 10–15 mm Hg (*41, 42*). Possible explanations for the large V–v difference are placental O_2 consumption (*22*), uneven distribution of maternal and fetal placental blood flows (*27*), and vascular shunts (*25, 26*).

Equations 5 and 6 may be modified to allow for placental oxygen consumption by assuming the rate loss of O_2 to the tissues proportional to the partial pressure difference between the capillary blood and the surrounding tissue:

$$\frac{d[O_2]_m}{dt} = \frac{-D_p (P_m - P_f)}{V_m - k(P_m - P_t)} \tag{12}$$

$$\frac{d[O_2]_f}{dt} = \frac{-(V_m/V_f)\, d[O_2]_m}{dt - k(P_f - P_t)} \tag{13}$$

where P_t is the mean tissue p_{O_2} and k is a proportionality constant. This assumed a greater loss of O_2 by the maternal blood than by the fetal blood, especially near the arterial end of the capillary. Since the tissue surrounding any part of the capillary probably consumes O_2 at about the same rate, we wish to have the same rate of loss of O_2 at each step of the integration while weighting the amount coming from the maternal and fetal vessels according to their O_2 tensions. We do this by adjusting k at each step to give a total rate of O_2 loss to tissues of 0.066 ml/sec. This results in a total O_2 loss to the tissues of 4 ml/min, a figure chosen for a 0.5-kg placenta to agree with a placental O_2 consumption of 8 ml/(min × kg) (*22*). We assume P_t is constant throughout the placental tissue to maintain a one-dimensional diffusion problem. The value of P_t assumed has little effect on end-capillary p_{O_2} values (*14*). The consequences of placental oxygen consumption are that exchange is slowed slightly during the early part of the capillary since the pressure gradient is decreased, and the continuing loss of O_2 lowers the p_{O_2} all along the capillary (Figure 6). An alternative assumption would be that maternal and fetal blood would contribute the same quantity of O_2 to placental tissues. In this case the effects on the rate of gas exchange are slightly (0.2%) more pronounced.

In neither case would O_2 consumption explain the total uterine to umbilical vein oxygen tension difference. Equilibrium would merely occur at a lower p_{O_2}. If placental tissue were supplied with O_2 solely from fetal blood, the maternal to fetal end-capillary p_{O_2} difference would

be 5.6 mm Hg. Thus, placental O_2 consumption can explain at most only half of the total measured difference and is more likely to account for none or only a small fraction of the difference.

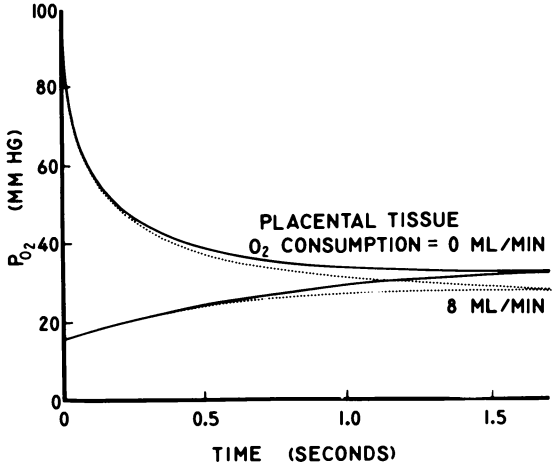

Figure 6. Effect of placental O_2 consumption on maternal (solid lines) and fetal (dashed lines) p_{O_2} during the capillary transit. While calculated fetal placental end-capillary p_{O_2} is 31.8 mm Hg in the absence of O_2 consumption, it is decreased about 14% (to 27.3 mm Hg) when placental O_2 consumption is 8 ml/min.

Calculation of Uterine and Umbilical O_2 Tensions with Vascular Shunts. Vascular shunting could also explain the p_{O_2} of uterine vein being greater than that of umbilical vein, despite equilibration in end-capillary blood predicted by our model. The equations allowing one to calculate the effect of shunts on the placental V–v difference are:

$$\frac{\dot{Q}_{s'm}}{\dot{Q}_{t'm}} = \frac{C_{v'm} - C_{c'm}}{C_{a'm} - C_{c'm}} \tag{14}$$

and

$$\frac{\dot{Q}_{s'f}}{\dot{Q}_{t'f}} = \frac{C_{v'f} - C_{c'f}}{C_{a'f} - C_{c'f}} \tag{15}$$

where $\dot{Q}_s$ and $\dot{Q}_t$ are the shunted flows and total placental flows respectively, C is the O_2 content, and the subscripts a, v, and c represent arterial, venous, and end-capillary values.

Using these equations one finds that a 26% shunt on maternal and fetal placental sides of the placenta results in values of uterine and

umbilical vein p_{O_2} of 39 and 25 mm Hg respectively, values close to those found experimentally. Anatomical shunts may be appreciably less than 26% since markedly uneven distribution of blood flows (uneven Q_m/Q_f) will also act as effective shunts (*27*).

Uneven Maternal and Fetal Capillary Transit Times. The standard values chosen for maternal and fetal blood flow rates are equal. In studying effects of variations of one of the flow rates (*15*), the maternal and fetal capillary transit times become unequal, and the time steps of the integration, Δt, do not correspond to the same distance along the capillary on each side. To prevent the integration from getting out of step (diffusion not occurring perpendicular to the membrane), Equation 5 must be modified (*14*) to:

$$\frac{d[O_2]_m}{dt} = \frac{-\beta D_P (P_m - P_f)}{V_m} \tag{16}$$

where $\beta = V_m\dot{Q}_f/V_f\dot{Q}_m$ = maternal transit time/fetal transit time.

Effects of Physically Dissolved O_2. In addition to the O_2 associated with the hemoglobin, physically dissolved O_2 is present in an amount proportional to the O_2 partial pressure: $[O_2]$ dissolved = αP, where α is the solubility of O_2 in blood (2.3×10^{-2} ml/(min $\times$ atm)) (*43*). At a p_{O_2} of 100 mm Hg, 0.132 ml O_2/ml blood is combined with the hemoglobin and 0.003 ml/ml (2% of the total O_2) is dissolved. Our calculations at normal p_{O_2} values ignore this small amount of dissolved O_2. However, at p_{O_2} values above 100 mm Hg the physically dissolved O_2 becomes increasingly important. In this case the conversion from O_2 content to partial pressure becomes much more complicated, and an iterative technique is used to calculate the p_{O_2} values (*14*).

At high oxyhemoglobin saturations, the hemoglobin reaction rates decrease, and θ, the diffusing capacity of the blood, becomes very small (Equation 9). The placental diffusing capacity, D_P, as calculated by Equation 4 would also approach zero. However, at very high tensions of O_2, much of the oxygen diffusing across the placental membrane is supplied by the dissolved O_2, so the effective D_P does not really approach zero. Equilibration occurs very rapidly (<1 mm Hg pressure difference after 0.1 sec with maternal arterial p_{O_2} = 3200 mm Hg). Therefore, Equations 4 and 10 must be modified to include the dissolved O_2 contribution.

When these modifications are incorporated (*14*), the integration time on the computer increases severalfold (from 0.15 to 0.95 sec per integration step), but the results obtained for a maternal arterial p_{O_2} of 95 mm Hg differed from those of Figure 5 by less than 3%. The simpler form of the equations ignoring physically dissolved O_2 was therefore

used in all cases except the series of studies at maternal arterial O_2 tensions above 100 mm Hg (*15*).

Results Using Human O_2 Dissociation Curves and Hemoglobin Concentration. Since no experimental data are available for values of D_p and capillary flow rates in humans, we assumed the same values as for sheep. Hemoglobin concentrations of 12.5 and 15.5 grams/100 ml for maternal and fetal blood were assumed. Data for maternal and fetal human dissociation curves (*17*) were fitted with least squares to Equation 7 to obtain the constants $k_1 = 1.421$, $k_2 = 0.456$, and $k_3 = 0.373$ for maternal blood and $k_1 = 1.302$, $k_2 = 0.464$, and $k_3 = 0.395$ for fetal blood. Human θ values were calculated from data on k'_c for adult (*20*) and fetal (*44*) blood.

Using these values the model predicts that equilibration is slightly less complete (1.4 mm Hg at the end of the capillary) than in sheep, and the end-capillary p_{O_2} values are lower [maternal end-capillary p_{O_2} of 28.0 mm Hg and fetal end-capillary p_{O_2} of 26.6 mm Hg (*14*)]. The O_2 exchange rate is only slightly greater than that for sheep (25.1 ml/min). These results are owing to the change in the oxyhemoglobin saturation curves and the increased hemoglobin concentrations.

Analysis of the Effects of Parameter Changes on O_2 Transfer

Effect of Varying Diffusing Capacity. The placental diffusing capacity for O_2 is a convenient index of the efficiency of respiratory gas exchange. It expresses the rate of O_2 transfer across the placenta for a given partial pressure difference between maternal and fetal blood. Its value depends upon the characteristics of the placental membranes, exchange vessels, and blood. Figure 7 depicts the change in O_2 tensions in maternal and fetal erythrocytes during the course of a single capillary transit for various values of D_P. Using a value of 2.04 ml/(min $\times$ mm Hg) for a 3-kg fetus, our model predicts that equilibration is 90% complete by 43% of a capillary transit and essentially complete when it reaches the end of the capillary. With lower values of D_P, however, oxygen equilibration would not be attained, and a measurable maternal-fetal end-capillary p_{O_2} difference would appear. This lack of complete equilibration is also demonstrated in Figure 8 which shows the increase in maternal end-capillary p_{O_2}, the decrease in fetal end-capillary p_{O_2} and the decrease in the mean rate of O_2 exchange as D_P decreases. This limitation of exchange rate and increase in maternal to fetal end-capillary p_{O_2} difference becomes increasingly significant as D_P decreases below normal values. Thus, while there is little limitation resulting from diffusing capacity under normal conditions, D_P is not so large that it may be regarded as infinite and equilibrium assumed for various clinical conditions.

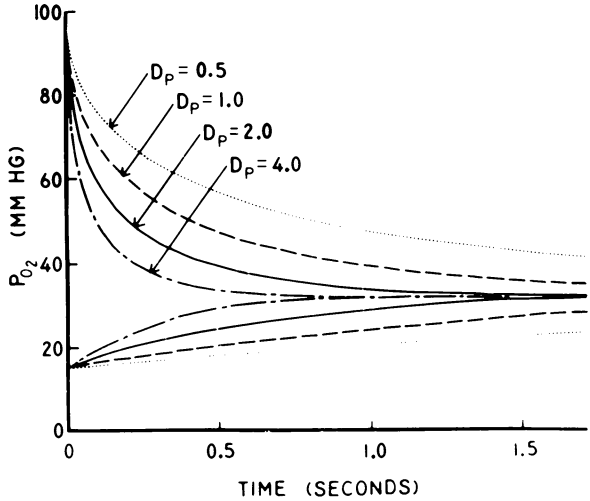

Figure 7. The change in O_2 partial pressure in maternal and fetal erythrocytes, during the course of a single capillary transit for various values of placental diffusing capacity, Dp. *The mathematical model was used for the calculations.*

Effect of Varying Maternal Arterial O_2 Tension. The dependence of O_2 transfer and the resulting end-capillary O_2 tensions on maternal arterial p_{O_2} (P_m) are shown in Figure 9. Maternal arterial p_{O_2} has relatively little effect until it drops below 70–80 mm Hg. However, further decreases become progressively detrimental to the fetus. For example, a decrease of maternal p_{O_2} to 50 mm Hg would cause a 19% reduction of placental O_2 exchange rate (from 24.8 to 20.0 ml/min) and of fetal end-capillary p_{O_2} (from 31.8 to 25.9 mm Hg) (Figure 9). Clearly, maintenance of normal maternal p_{O_2} is essential for fetal oxygenation. On the other hand, raising maternal arterial p_{O_2} above normal increases the exchange rate of O_2 only slightly. For example, increasing maternal arterial p_{O_2} to 600 mm Hg by administering 100% O_2 raises the fetal end-capillary p_{O_2} only 5.4 mm Hg and increases the exchange rate only 12% (to 27.7 ml/min). Administration of oxygen at 2 atm in a hyperbaric chamber increases the O_2 exchange rate across the placenta by 18% and increases the fetal end-capillary p_{O_2} to 43 mm Hg. As pressures increase above 2 atm, the end-capillary p_{O_2} values rise more rapidly because fetal hemoglobin becomes fully saturated.

Effect of Varying Fetal Arterial O_2 Tension. Placental exchange has usually been considered limited by either maternal and fetal blood flows or by diffusion. The present analysis suggests umbilical arterial p_{O_2} (P_f) is a third and very important factor, based on the observation

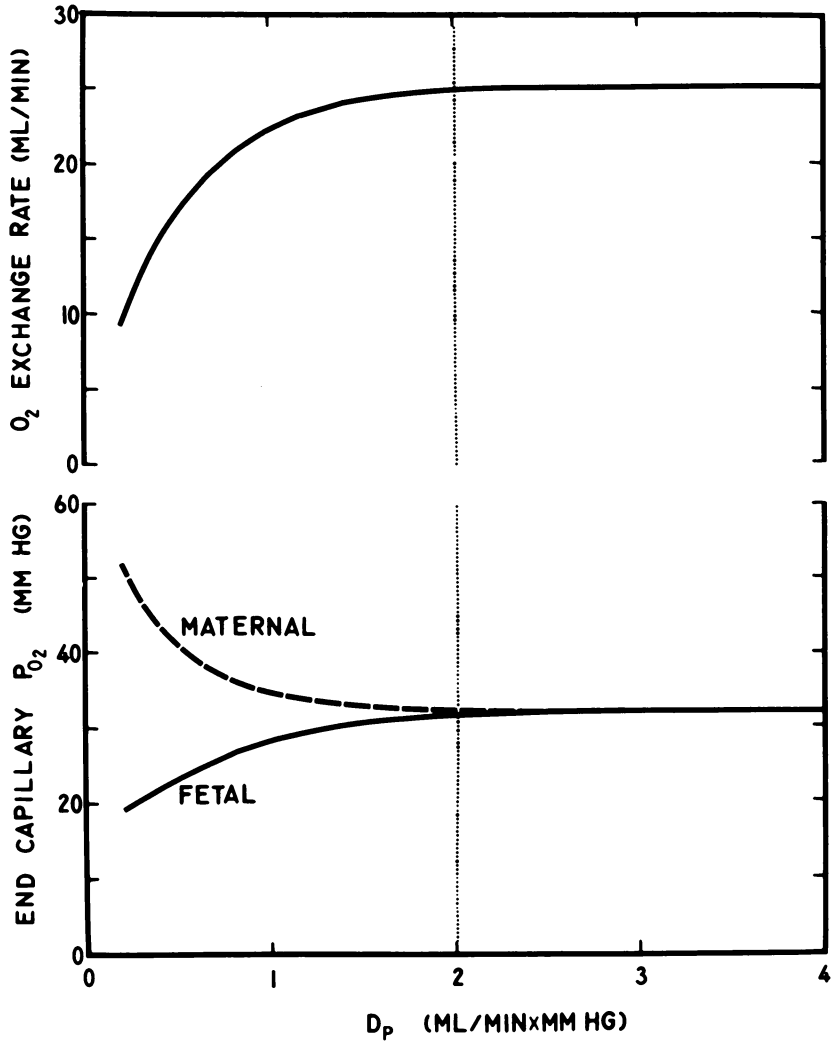

Figure 8. The change in maternal and fetal end-capillary p_{O_2} and the mean rate of O_2 exchange as a function of placental diffusing capacity. At values of Dp *less than 2.0 ml/(min × mm Hg) there is an increased maternal-fetal end-capillary difference and a decreased rate of O_2 transfer. The vertical interrupted line represents the assumed normal values of* Dp.

that both O_2 transfer rate and end-capillary p_{O_2} are more sensitive to a given percentage change in umbilical arterial p_{O_2} than to a similar percentage change in any other determinant of O_2 transfer.

Changes in umbilical arterial p_{O_2} will alter both end-capillary O_2 tension and O_2 transfer rate (Figure 10), but these two responses occur in opposite directions and offset one another to maintain O_2 transfer

consistent with fetal tissue needs. The operation of this mechanism is most clearly seen if we imagine that umbilical arterial p_{O_2} were to decrease for some reason. As P_f falls, the equilibrated end-capillary O_2 tension would decrease (Figure 10), as would the p_{O_2} of umbilical venous blood and that in the arteries supplying fetal tissues. This change would further aggravate fetal hypoxia. At the same time, however, the lower

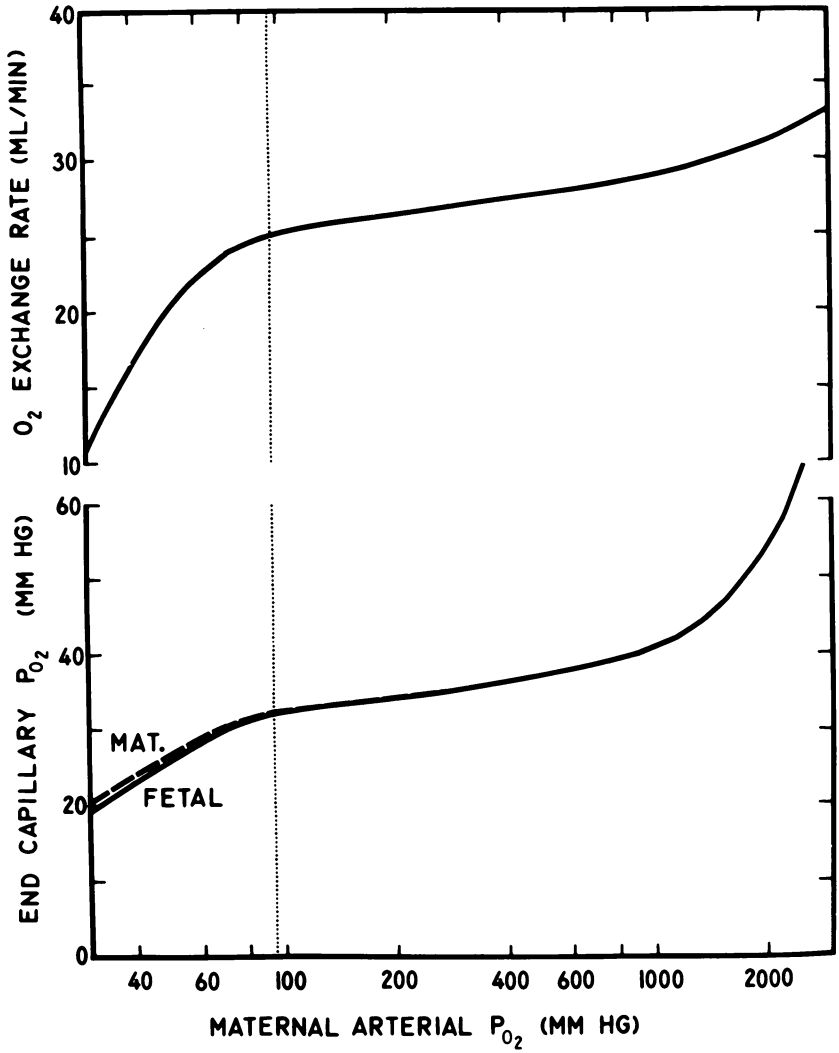

Figure 9. The effects of changes in maternal arterial O_2 tension on maternal and fetal end-capillary p_{O_2} and mean rate of O_2 exchange. Moderate increases in maternal arterial p_{O_2} above normal values (95 mm Hg) increase end-capillary p_{O_2} and mean O_2 exchange rate only slightly, but decreases in maternal arterial p_{O_2} produce substantial decrease in O_2 exchange and end-capillary values.

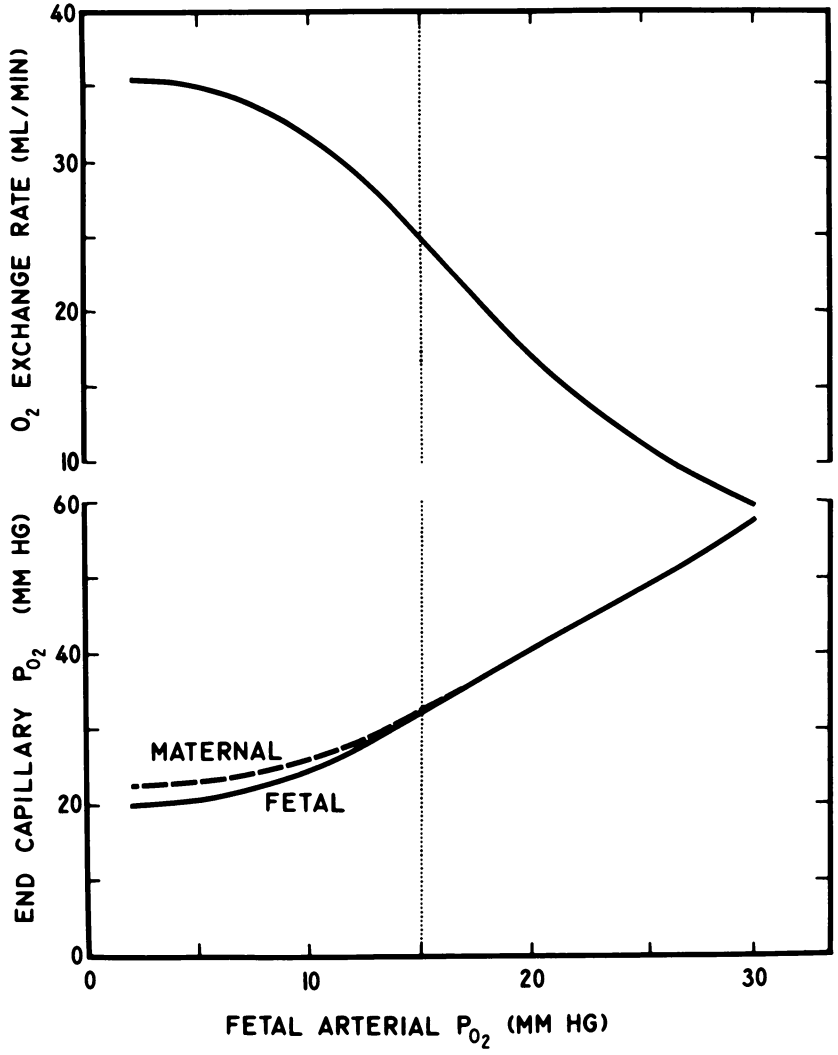

Figure 10. The effects of changes in umbilical artery p_{O_2} on end-capillary p_{O_2} and the mean rate of O_2 exchange. Changes in umbilical artery p_{O_2} from normal values result in increases in either end-capillary p_{O_2} or the O_2 transfer rate, but not both, and may serve to restore umbilical artery p_{O_2} to a normal value.

umbilical artery p_{O_2} causes a greater increase in O_2 content per milliliter of placental blood flow, principally because more exchange occurs on the steep part of the hemoglobin saturation curve. Not only is more O_2 transferred, but the rate of approach toward equilibrium is more rapid because the larger maternal to fetal p_{O_2} difference at the beginning of the capillary speeds transfer and placental diffusing capacity increases

slightly because of the increase in θ. Thus, more O_2 is loaded onto fetal hemoglobin. Then, provided fetal O_2 consumption and peripheral blood flow do not change, the p_{O_2} of blood leaving the fetal tissues will rise. This will eventually result in the placenta being perfused with blood at a higher p_{O_2}, thereby restoring umbilical arterial p_{O_2} toward its physiological level. Thus changes in O_2 transfer are minimized. The restoration cannot be entirely complete, however, and either transfer rate or p_{O_2} will remain below normal unless other compensations also play a part.

If umbilical arterial O_2 tension should rise above normal, the end-capillary p_{O_2} will increase, but this will be offset by less O_2 exchange per milliliter of blood. By the time inflowing O_2 tension rises from 15 to 34 mm Hg, the exchange rate would have decreased to one half of normal. The fetus seems to be as well guarded against the consequences of over-oxygenation as against underoxygenation.

This is a passive regulation system that does not require metabolic energy or changes in maternal and fetal placental blood flow. It maintains a rate of O_2 transfer closely linked with fetal tissue needs. Furthermore, the compensation is most effective within the physiological range. Figure 10 shows that when P_f decreases below about 8 mm Hg, further decreases in P_f are no longer so effective in increasing the transfer rate. The exact level of the critical p_{O_2} below which oxidative enzyme reactions begin to fail does not appear to have been measured for the fetus *in vivo* but may occur at about this level. Finally, the mechanism points out one of the most important respects in which placental O_2 exchange differs from that of the lung. In the lung when pulmonary arterial p_{O_2} decreases, the end-capillary P_{O_2} is maintained about constant because there is a large reservoir of oxygen in alveolar air. In the placenta when umbilical arterial p_{O_2} decreases, the end-capillary p_{O_2} also falls.

Effect of Varying Maternal Placental Blood Flow. Figure 11 shows the dependence of end-capillary p_{O_2} on maternal placental flow, $\dot{Q}_m$. At large flow rates the p_{O_2} of end-capillary blood approaches that of the maternal artery. At lower rates of flow the equilibrated p_{O_2} value decreases because less O_2 is available for exchange. The rate of O_2 transfer follows a trend similar to that of end-capillary p_{O_2}, except that increases in $\dot{Q}_m$ above 300–400 ml/min result in little additional O_2 transfer because the rise in mean maternal p_{O_2} adds little O_2 content to the flat part of the fetal oxyhemoglobin saturation curve.

In a different model of human placental O_2 exchange, Guilbeau *et al.* (*34*) predicted maternal end-capillary p_{O_2} would follow a trend similar to that shown in Figure 11. Their absolute values of p_{O_2} were several mm Hg less. This is not surprising since their model was based on different assumptions and used a different type of mathematical analysis.

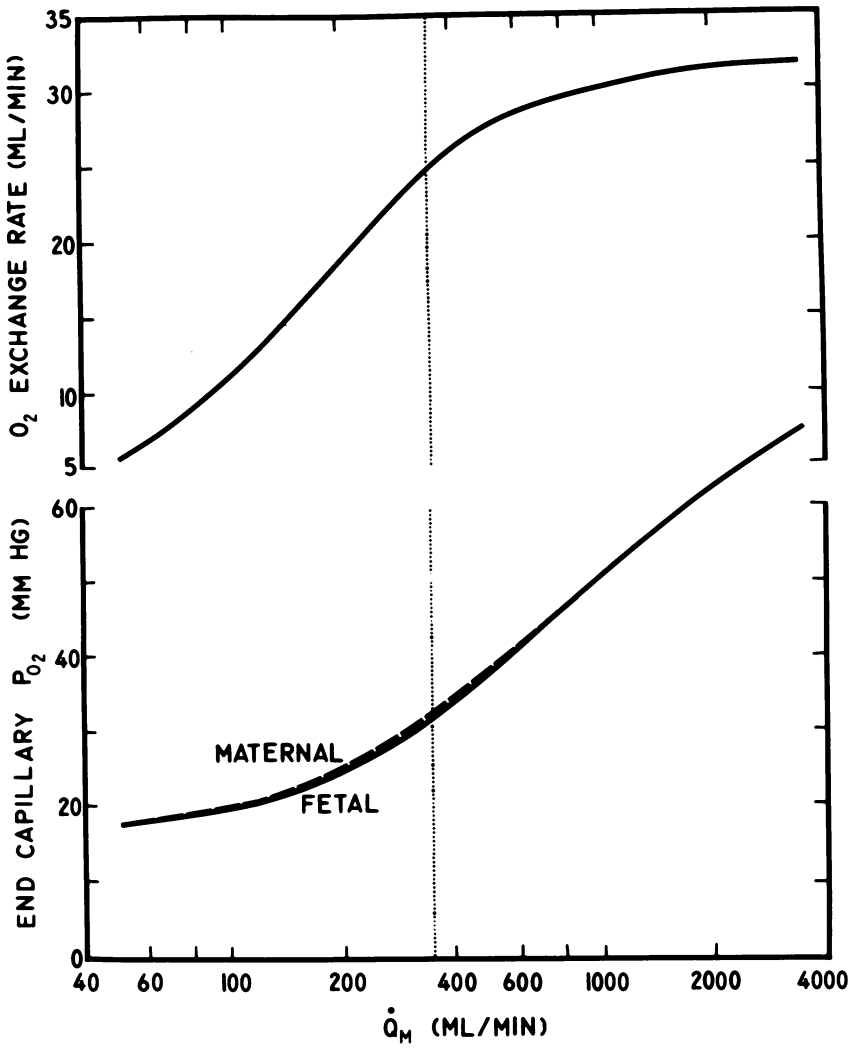

Figure 11. The effects of changes in maternal placental blood flow (Q_m) on maternal and fetal end-capillary O_2 tensions and average rate of O_2 exchange

Effect of Varying Fetal Placental Blood Flow. The effects of changes in umbilical flow, $\dot{Q}_f$, are shown in Figure 12. As umbilical flow increases, it can carry more O_2, and the end-capillary p_{O_2} decreases until finally at infinitely rapid flow rates the p_{O_2} approaches umbilical arterial p_{O_2}. A small end-capillary p_{O_2} difference becomes apparent at high values of $\dot{Q}_f$ because of a diffusional limitation. The O_2 transfer rate varies almost linearly with $\dot{Q}_f$ over the range from 100–400 ml/min. Above

about 500 ml/min the exchange rate no longer rises so steeply because additional O_2 is not available from maternal blood.

Guilbeau *et al.* (*34*) predicted a similar pattern resulting from a reduced fetal flow rate in their model but obtained lower absolute values of p_{O_2}. They also pointed out the rise in fetal p_{O_2} at slow flow rates could be attributed to less hemoglobin within the fetal capillaries per unit of time.

Effects of Changing Maternal and Fetal Placental Blood Flows Together. Figure 13 shows the effects of varying maternal and fetal blood

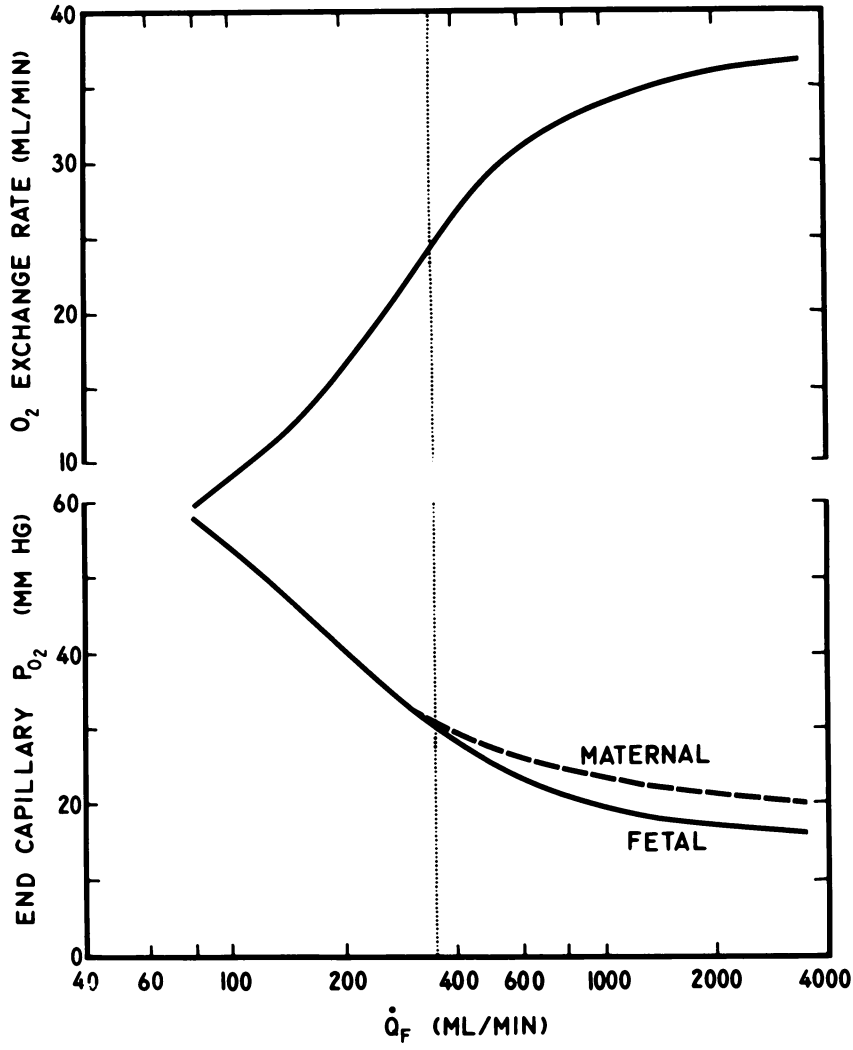

Figure 12. The effects of changes in fetal placental flow (Q_f) on maternal and fetal end-capillary O_2 tensions and average O_2 exchange rate

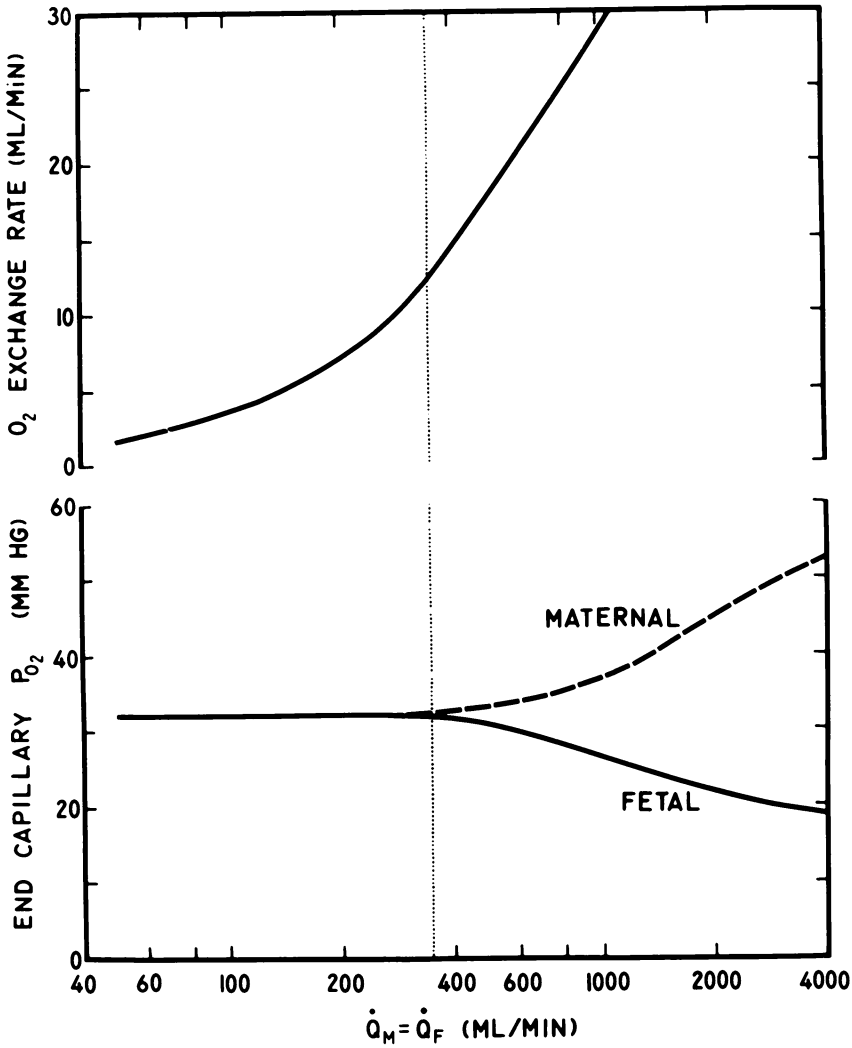

Figure 13. Effects of changes in both maternal and fetal placental flows ($Q_m = Q_f$) *on end-capillary differences appear when both flows become greater than 400 ml/min*

flow (with $\dot{Q}_m$ equal to $\dot{Q}_f$). Increases in total blood flows affect end-capillary O_2 tensions similar to a decrease in diffusing capacity (Figure 8) because the p_{O_2} of maternal and fetal blood does not attain equilibrium when there is a limited time for diffusion at rapid flow rates. A p_{O_2} difference between maternal and fetal end-capillary blood of greater than 2 mm Hg becomes apparent when flow rates exceed 500 ml/min. Increases in the transfer rate of O_2 are roughly proportional to increase

in flow rates, further emphasizing the importance of the transport capacity of maternal and fetal blood in limiting O_2 exchange.

Effects of Varying the Ratio of Maternal to Fetal Blood Flows. Not only may $\dot{Q}_m$ and $\dot{Q}_f$ vary, but the ratio of $\dot{Q}_m$ to $\dot{Q}_f$ may change as well (*27*). Figure 14 shows the effects of varying $\dot{Q}_m/\dot{Q}_f$, with the sum of $\dot{Q}_m$ and $\dot{Q}_f$ held constant. The p_{O_2} in maternal and fetal end-capillary blood is predicted to increase as a function of $\dot{Q}_m/\dot{Q}_f$ because more O_2

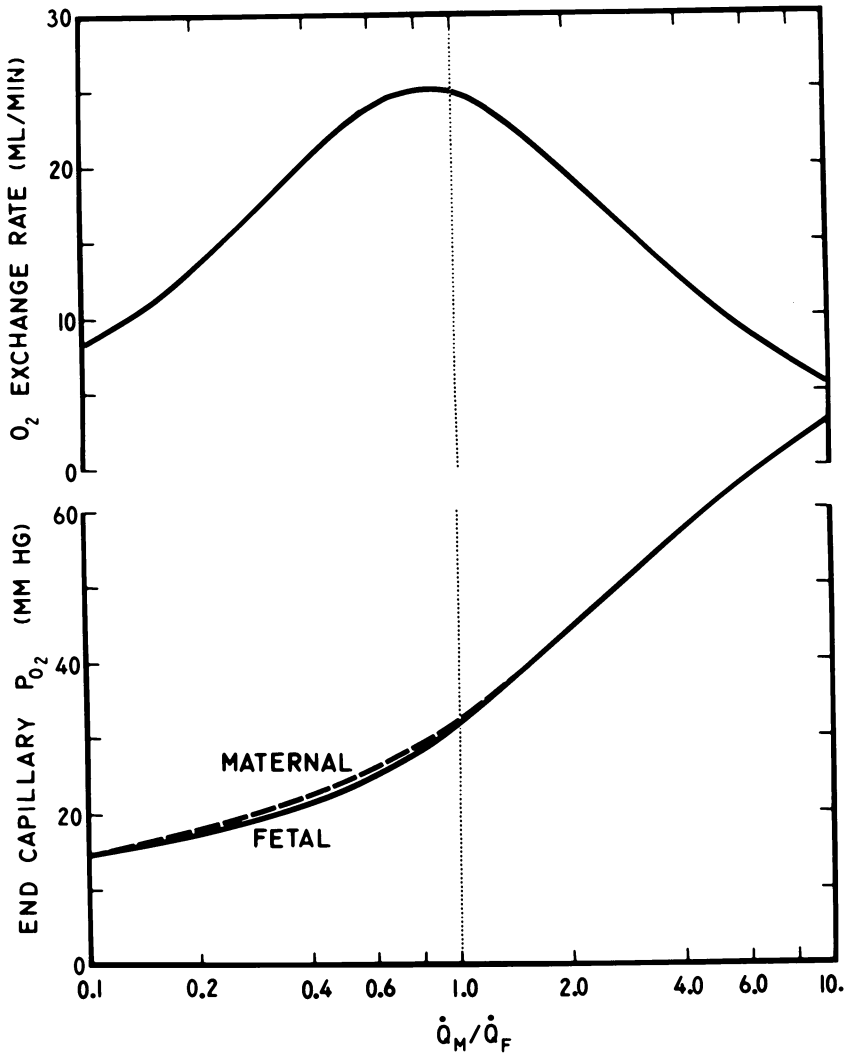

Figure 14. Effects of changes in the ratio of maternal to fetal placental blood flow (Q_m/Q_f) end-capillary O_2 tensions and average O_2 exchange rate. The optimum ratio of Q_m to Q_f for maximum O_2 exchange is about 0.9.

is delivered by maternal blood relative to the transport capacity of fetal blood when $\dot{Q}_m/\dot{Q}_f$ is high. Equilibration p_{O_2} values for various ratios of $\dot{Q}_m$ to $\dot{Q}_f$ can also be readily obtained by a graphical analysis of placental exchange (*45*). Figure 14 also shows that the rate of O_2 exchange is maximal when $\dot{Q}_m/\dot{Q}_f$ is about 0.9 and that it decreases as Q_m/Q_f increases or decreases from this ratio. Thus this ratio is optimal for gas exchange because it minimizes the total maternal and fetal blood flow rates required to deliver 1 ml of O_2 to fetal tissues. We previously reached a similar conclusion using a different analysis (*45*). Experimentally, it has not been possible to vary $\dot{Q}_m/Q_f$ while holding total flows constant.

Effects of Varying Maternal and Fetal Blood O_2 Capacity. At normal O_2 tensions most of the oxygen in the blood is combined with hemoglobin. Physically dissolved O_2 accounts for less than 2% of the total that is present and for less than 5% of the amount that crosses the placenta. The hemoglobin content determines the O_2 capacity of the blood (capacity = Hb $\times$ 1.34). It is not surprising, therefore, that the model predicts that a change in hemoglobin content affects O_2 transfer in almost precisely the same way as a change in blood flow. When maternal hemoglobin decreases 50%, for example (Figure 15), the effect on placental gas exchange is equivalent to a 50% reduction in $\dot{Q}_m$ (Figure 11). The same is true for changes in fetal hemoglobin (Figures 12 and 16). Thus it is readily apparent that the rate of hemoglobin flow, rather than blood flow *per se*, determines the amount of O_2 transported to and from the placenta.

This equivalency of flow and hemoglobin content is a convenient approximation. It is not strictly valid because alterations in hemoglobin content may alter O_2 exchange in other ways as well. These include changes in the buffer capacity of blood, which influences O_2 transfer through the Bohr effect, and changes in the distribution of blood flow brought about by changes in viscosity. Reduced hemoglobin content also lowers the placental diffusing capacity, but the effect is small and relatively unimportant.

Figure 15 shows that the rate of O_2 transfer and O_2 tension in fetal end-capillary blood decrease as maternal hemoglobin content falls. When maternal hemoglobin is 6 grams/100 ml, for example, the rate of O_2 transfer is decreased 24% (from 24.8 to 19 ml/min) and end-capillary p_{O_2} is decreased 21% (from 31.8 to 24 mm Hg). Guilbeau et al. (*34*) have also calculated that there is a marked decrease in the amount of O_2 transferred as maternal hemoglobin decreases below normal values.

Changes in fetal hemoglobin concentration will have several effects on placental O_2 exchange (Figure 16). The rate of O_2 transfer varies almost linearly with fetal hemoglobin concentration, as it does with $\dot{Q}_f$.

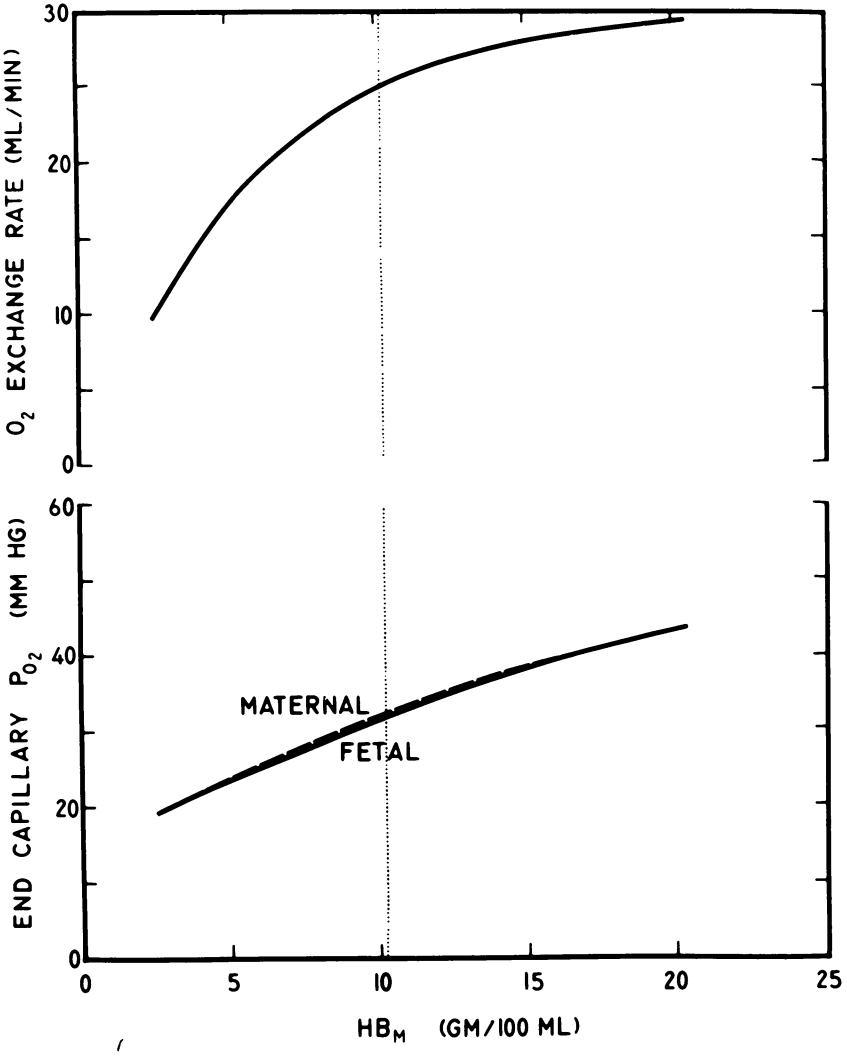

Figure 15. Effect of changes in maternal hemoglobin concentration (Hb_m) on end-capillary O_2 and average O_2 exchange rate. The effects are similar to those of maternal placental flow rate (Figure 11).

Equilibrated end-capillary p_{O_2} will vary inversely with fetal hemoglobin concentration since a larger quantity of fetal hemoglobin will lead to extraction of more O_2 from the maternal blood.

Comparison of the Importance of Various Parameters on O_2 Transfer. We compare the effects of all the above factors on fetal end-capillary p_{O_2} in Figure 17. The values of each of the factors are expressed as percentages of their assumed normal value so they may be compared

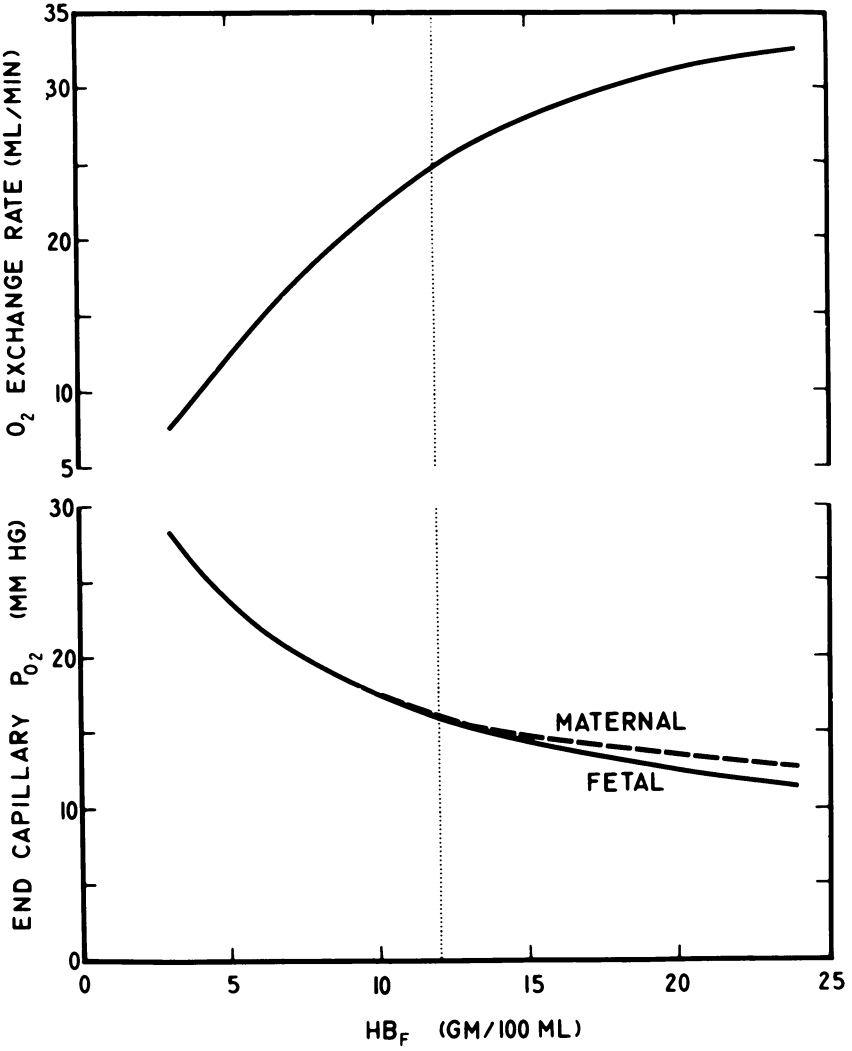

Figure 16. Effect of changes in fetal hemoglobin concentration (Hb_f) on end-capillary O_2 tensions and mean rate of O_2 exchange. The effects are similar to those of fetal placental flow rate (Figure 12).

conveniently with one another. We use the slope of each curve at 100% of normal to indicate the sensitivity of the p_{O_2} to a change in that factor (Table I).

Figure 17 shows that end-capillary p_{O_2} is most sensitive to changes in fetal arterial O_2 tension (P_f). It is less sensitive to maternal and fetal hemoglobin flow rates and the $\dot{Q}_m/\dot{Q}_f$ ratio. Changes in maternal arterial p_{O_2} (P_m), D_P, and the sum of ($\dot{Q}_m + \dot{Q}_f$) have little effect in the physio-

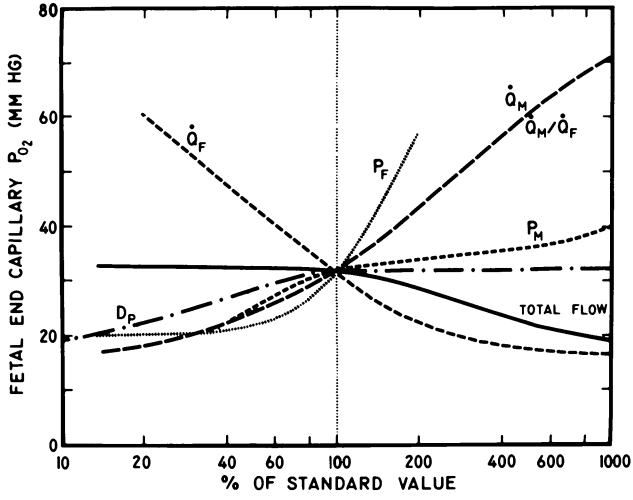

Figure 17. Effects of changes in various factors on fetal placental end-capillary O_2 tensions.
Plot is normalized by plotting fetal end-capillary p_{O_2} as a function of the percent change of the assumed normal values of a given factor. The slope of each curve at 100% of normal value indicates the relative sensitivity of the end-capillary p_{O_2} to that parameter. Fetal end-capillary p_{O_2} is most sensitive to changes in umbilical artery p_{O_2},P_f, slightly less sensitive to changes in maternal and fetal hemoglobin flow rates and the ratio of maternal to fetal flow. The curves for maternal and fetal hemoglobin are superimposed on the Q_m and Q_f curves. P_m and P_f represent the maternal and fetal arterial p_{O_2} values.

logical range. If the effects of changes in Hb were added to Figures 17 and 18, they would largely superimpose on the blood flow curves.

We compare the effects of various factors on the O_2 transfer rate in Figure 18. The O_2 transfer rate is most sensitive to fetal arterial p_{O_2} (Table I), only slightly less sensitive to the sum of $\dot{Q}_m + \dot{Q}_f$, followed by fetal and maternal hemoglobin flow. Changes in D_P, maternal arterial p_{O_2}, and $\dot{Q}_m/\dot{Q}_f$ have little effect in the physiological range.

The importance of a determinant of O_2 transfer depends on the sensitivity (the slope of the response curve) and its range of variation. For example, a two-fold increase in $\dot{Q}_f$ would increase O_2 transfer rate far more than a similar increase in $\dot{Q}_m$ (Figure 18). However, if $\dot{Q}_m$ could vary physiologically over a larger range than $\dot{Q}_f$, it might be a more important determinant of O_2 transfer rate.

A system to regulate O_2 transfer to the fetus would require a factor to which the body is sensitive and which varies over an appreciable physiological range and a mode of response. Many of the determinants of O_2 transfer are not likely to be active in regulation for different reasons. Changes in diffusing capacity, for example, would not affect

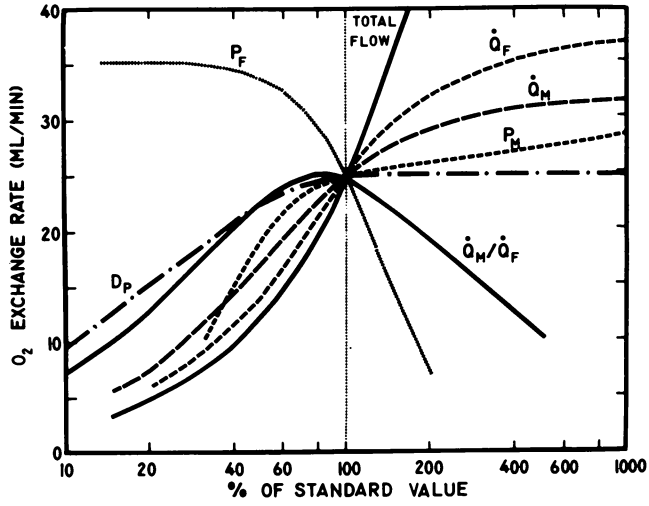

Figure 18. Effect of changes in various factors on the mean rate of placental O_2 exchange.
The plot is normalized by plotting percent change in value in O_2 exchange rate as a function of the percent change in the assumed normal values of a given factor. As in Figure 17, the slope of each curve at 100% of normal value indicates the relative sensitivity of the exchange rate to that factor. The O_2 exchange rate is most sensitive to umbilical arterial p_{O_2}, P_f, followed closely by the total flow and maternal and fetal hemoglobin flow rates. The curves for maternal and fetal hemoglobin are superimposed on the Q_m and Q_f curves. P_m and P_f represent the maternal and fetal arterial p_{O_2} values.

the transfer rate appreciably. Maternal arterial p_{O_2} is an unlikely factor since it does not vary more than a few mm Hg in the normal range. Maternal hemoglobin is also unlikely because there is no known mechanism for it to respond to the level of fetal oxygenation. Finally, fetal hemoglobin seems unlikely because its response would require at least several days.

The remaining determinants are maternal and fetal blood flows and their distribution and the umbilical arterial p_{O_2}. Experimentally, Dawes (*46*) demonstrated that the placental resistance to umbilical blood flow changes in response to maternal hypoxia during the last third of gestation in sheep. Power and co-workers (*27*) demonstrated that the distribution of $\dot{Q}_m/\dot{Q}_f$ became more uniform during maternal hypoxia in the same species, although Rankin *et al.* (*33*) reported relatively uniform distribution of $\dot{Q}_m/\dot{Q}_f$ with normal oxygenation. The role of fetal arterial p_{O_2} is somewhat different. Although exchange rate and end-capillary p_{O_2} are more sensitive to it than any other factor, its value depends on fetal

placental end-capillary p_{O_2}, peripheral blood flow, and O_2 extraction by fetal tissues.

The results of the theoretical studies above suggest that placental O_2 transfer should be particularly sensitive to changes in umbilical arterial p_{O_2}, somewhat less sensitive to changes in maternal and fetal hemoglobin flow rates, and much less sensitive to changes in maternal and fetal hemoglobin flow rates, and much less sensitive to changes in maternal arterial p_{O_2} and placental diffusing capacity. Experimentally, it is difficult to study the effects of individual factors. One reason for the difficulty is that when a given factor is changed, other parameters may change to mask the consequences of the change under study. When this occurs, the investigator misjudges the importance of the factor. Another reason is that, as noted above, umbilical venous blood represents a mixture from many placental exchange units with varying O_2 tensions caused by placental O_2 consumption, vascular shunts, nonuniform distribution of maternal and fetal placental blood flows, and probably nonuniform distribution of placental diffusing capacity to blood flow. While changes of a given factor will affect the placental end-capillary O_2 tensions, the change may not be accurately reflected by the umbilical venous p_{O_2} values.

We have tried to circumvent these problems by isolating a cotyledon of the placenta and perfusing its umbilical circulation *in situ* with blood of known and accurately controlled flow rates and O_2 tensions (*47*). We have also varied maternal arterial O_2 tension by administering various concentrations of inspired O_2.

Samples of blood flowing to and from the cotyledon were collected in glass capillary tubes of 0.18 ml volume. Maternal arterial samples were

Table I. Relative Sensitivity for Determining Fetal Placental End-Capillary p_{O_2} and Mean O_2 Exchange Rate (in Percent)[a]

Determinants of O_2 Transfer	*Fetal End-Capillary P_{O_2}*	$\dot{V}_{O_2}$
P_f	8	10.5
$\dot{Q}_m$	5	4
$\dot{Q}_f$	5	6
$\dot{Q}_m + \dot{Q}_f$	<1	10
$\dot{Q}_m/\dot{Q}_f$	5	<1
Hgb_m	5	4
Hgb_f	5	6
P_m	1	<1
D_P	<1	<1

[a] Calculated as percent change for a 10% change (over range 95 to 105%) in a given determinant of placental O_2 transfer.

collected in heparinized glass syringes. Samples were placed in ice slush and later analyzed for p_{O_2}, p_{CO_2}, and pH with a Radiometer blood gas analyzer (Model BM53). Control studies showed less than 1 mm Hg change in p_{O_2} per hour in the capillary tubes while awaiting analysis. This change was small because of the low range of p_{O_2} under study. Hemoglobin content was determined as cyanmethemoglobin. The net O_2 transfer rate across the placenta was calculated as the product of fetal perfusion rate and the arteriovenous O_2 content difference. Hemoglobin dissociation curves corrected for pH and temperature were used to convert p_{O_2} to oxyhemoglobin saturation and content. Experimental results were compared with the predicted results obtained using the mathematical model described earlier.

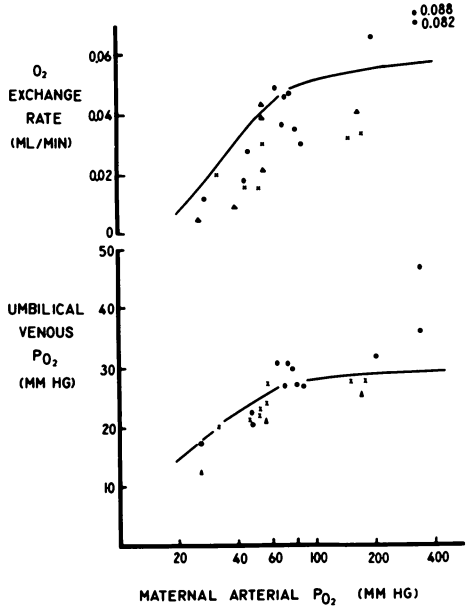

Figure 19. Relation of O_2 exchange rate (upper panel) and umbilical venous p_{O_2} (lower panel) to maternal arterial p_{O_2} in the isolated cotyledon. Data from four sheep are shown and may be compared with the solid curves which are predicted results from a mathematical model of O_2 exchange. Changes in maternal p_{O_2} are seen to become progressively more critical as values fall below about 70 mm Hg.

Effects of Varying Maternal Arterial Oxygen Tension. Oxygen, air, and various N_2-air mixtures were administered randomly to four ewes for 3–10-min intervals (*47*). The inspired gases achieved maternal arterial O_2 tensions ranging from 30–350 mm Hg. During this interval the isolated

cotyledon was perfused at constant flow rate (1.6 ml/min) with blood with a p_{O_2} of about 12 mm Hg. At the end of the interval, maternal arterial, umbilical arterial, and venous blood samples were taken almost simultaneously and analyzed for respiratory gases and pH.

The upper panel of Figure 19 shows the effect of varying maternal arterial p_{O_2} on the oxygen transfer rate. The lower panel shows the effect on umbilical venous p_{O_2}. Results for all experiments are shown, and those of individual sheep may be distinguished by different symbols. The oxygen transfer rate rose from 0.04 to 0.056 ml/min (about 40%) as maternal p_{O_2} increased from 90 to 300 mm Hg. This relatively slight change was not surprising in light of the shape of the oxyhemoglobin saturation curve, and the small quantities of O_2 carried by maternal blood in physical solution. Umbilical venous p_{O_2} rose from 29 to 34 mm Hg for the same maternal change.

Small decreases in maternal p_{O_2} from the normal level also had little effect, but larger decreases became progressively more significant. As maternal arterial p_{O_2} fell below about 70 mm Hg, umbilical venous p_{O_2} and the O_2 exchange rate both declined sharply (Figure 19). As maternal p_{O_2} approached 50 mm Hg (73% saturation), for example, the umbilical venous p_{O_2} decreased from 29 to 23 mm Hg, and the O_2 exchange rate decreased from 0.040 to 0.027 ml/min. These changes are probably greater than the changes that would be observed in the intact animal or human since most of the compensatory mechanism which might tend to maintain O_2 transfer constant were not operative in the isolated cotyledon.

The results predicted by the mathematical model are shown by solid curves in the figures for comparison. In constructing the curves, averages of the experimental values for maternal and fetal hemoglobin concentrations (10.7 and 10.8 grams/100 ml, respectively), fetal perfusion p_{O_2} (12 mm Hg), and fetal flow rate (1.6 ml/min) were used, together with estimates for the single cotyledon of maternal blood flow (0.3 ml/min), capillary volumes (0.2 ml), and placental diffusing capacity (0.04 ml/(min $\times$ mm Hg)). These values were assumed to remain constant during an experiment. These estimates, especially of maternal blood flow, are uncertain and arbitrarily low (uterine surgery having been assumed to lower maternal flow) so that any agreement between experimental and theoretical curves is not meaningful in absolute terms. The trend of the plot is valid, however, and in general, the experimental data points follow reasonably closely the trend of the theoretical curves. Figure 19 suggests, in summary, that changes in maternal arterial p_{O_2} in the physiological range affect O_2 transfer and umbilical venous p_{O_2} moderately and about as would be predicted.

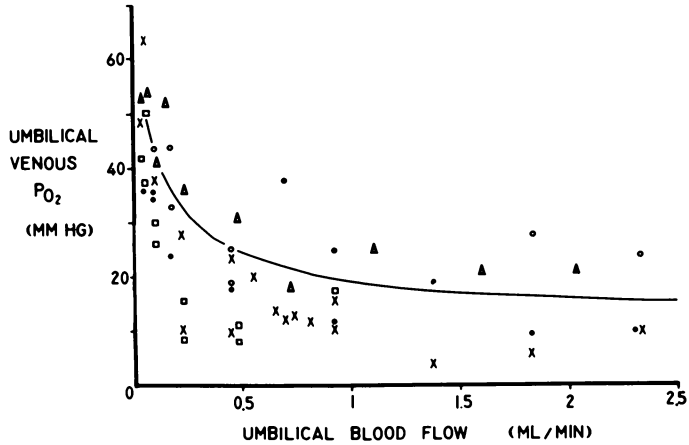

Figure 20. Relation of outflowing (umbilical venous) p_{O_2} *to the rate of blood flow. Data from five rabbit placentas perfused* in situ *through an umbilical artery with blood (Hb = 10.7 gram/100 ml) with an average* p_{O_2} *of 10 mm Hg. Maternal arterial* p_{O_2} *averaged 87 mm Hg. The solid curve shows results predicted by a mathematical model using experimental values and assuming a total maternal flow 1 ml/min and diffusing capacity [0.04 ml/(min × mm Hg)].*

Effects of Varying Umbilical Flow Rate. The fetal circulation of the cotyledon was perfused at flow rates from 0.22–2.6 ml/min in sheep and from 0.05–2.3 ml/min in rabbits. About ten different flow rates were studied randomly in each of five ewes and five rabbits (*47*).

Figure 20 shows the relation of umbilical blood flow and outflowing p_{O_2} for rabbits. The solid curve again shows results predicted by the model for comparison. The outflowing p_{O_2} tended to increase at slower flow rates. This was an anticipated finding since theoretical analysis had suggested that fetal placental end-capillary p_{O_2} values should increase as the ratio of maternal to fetal flow increases (*45*). More O_2 is supplied relative to the capacity of fetal blood to transport it away from the placenta; therefore, final equilibrium is attained at a higher p_{O_2}. Ignoring placental O_2 consumption, fetal outflowing p_{O_2} should approach maternal arterial p_{O_2} at very slow fetal flow rates, a trend suggested by results in Figure 20.

Outflowing p_{O_2} rose at low flow rates in two sheep cotyledons as it had in rabibts. In two other preparations, however, there was little change with flow while in the remaining animal outflowing p_{O_2} decreased measurably at the lowest flow rates that could be studied. These results may be reasonably attributed to a larger fraction of the O_2 deliv-

ered to the placenta being metabolized by placental tissue at low flows. An additional explanation would be more uneven distribution of fetal flow at low flow rates with a consequent fall in the efficiency of O_2 exchange. Thus a larger fraction of fetal flow might pass through regions remote from the areas of exchange.

Blood remains for a relatively short interval in the exchanging vessels at high flow rates. If a diffusional limitation to O_2 exchange were present, it should have become apparent by an abruptly decreasing p_{O_2} in fetal effluent blood once a certain flow rate had been exceeded (*15*). The present data gave no hint of such a change; thus, the present results do not support any diffusional limitation to O_2 transfer. The conclusion that placental O_2 transfer is limited by factors other than diffusing capacity now seems to be generally accepted (*48*).

Effects of Varying Umbilical Arterial O_2 Tension. The cotyledon was perfused simultaneously with blood from two infusion pumps. The output from each of the pumps was mixed together before entering the placenta. One syringe contained blood with a low oxygen tension (p_{O_2} = 10 mm Hg, p_{CO_2} = 40 mm Hg, pH = 7.4) and the other blood with a higher oxygen tension (p_{O_2} = 50 mm Hg, p_{CO_2} = 40 mm Hg, pH = 7.4). By varying flow rates of the two pumps independently, the p_{O_2} of the infusing blood could be varied while total flow and p_{CO_2} were held constant.

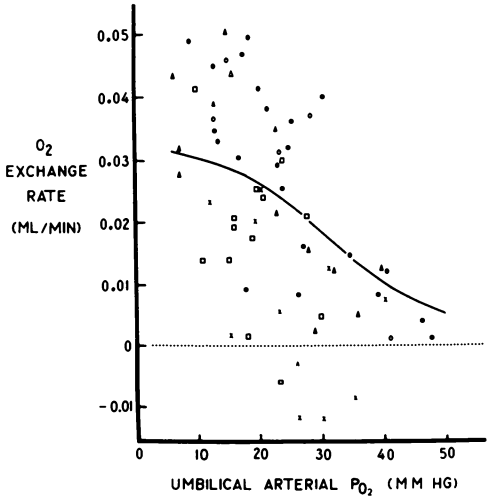

Figure 21. Relation of O_2 transfer rate to inflowing (umbilical arterial) p_{O_2} in five sheep cotyledons. Small changes in p_{O_2} are seen to be associated with relatively large changes in O_2 transfer in any given animal. The solid curve shows predicted results.

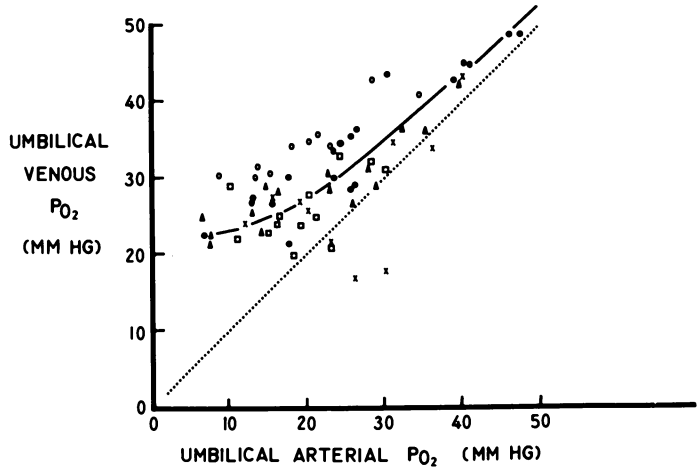

Figure 22. Relation of outflowing (umbilical venous) p_{O_2} *to inflowing* p_{O_2} *in five sheep cotyledons. The solid curve again shows predicted results.*

An average of 14 different O_2 tensions were studied in random sequence in each of five sheep (*47*). The effects of varying umbilical p_{O_2} on transfer rate are shown in Figure 21 and the effect on placental outflowing p_{O_2} in Figure 22. The solid curves show results predicted by the mathematical model, and there is generally good agreement with the experimental findings. Experimental O_2 transfer rate and outflowing p_{O_2} are quite sensitive to small changes in umbilical arterial p_{O_2}. To consider an example, a 20% fall in umbilical arterial p_{O_2} below a normal level of 14 mm Hg resulted in an average 20% increase in O_2 transfer rate. These results agree with the studies discussed which suggest that the umbilical arterial p_{O_2} should be the factor to which O_2 delivery to the fetus is most sensitive. Comparison of Figure 22 with Figures 19 and 20 show clearly that a given percentage change in umbilical arterial p_{O_2} affects outflowing p_{O_2} (also O_2 transfer rate) more than the same percentage change in either maternal arterial p_{O_2} or fetal flow rate. The present data suggest that the small day-to-day changes in umbilical arterial and venous p_{O_2} measured in unanesthetized sheep (*49*) are associated with sizable variations in the transfer function of the placenta for O_2. Moreover, changes in O_2 transfer resulting from changes in umbilical arterial p_{O_2} would have been even greater in the present studies if fetal blood, rather than material, had been used for the perfusion fluid. This is because the fetal oxyhemoglobin saturation curve is steeper in the physiological range.

It is interesting that changes in umbilical arterial p_{O_2} resulted in changes in O_2 transfer rate and outflowing p_{O_2} with the responses occurring in opposite directions. Thus, decreases in umbilical arterial p_{O_2}

increased O_2 transfer to the fetus, but only at the cost of lowering umbilical venous p_{O_2}. Conversely, increases in umbilical arterial p_{O_2} increased umbilical venous p_{O_2} at the expense of lowering the O_2 transfer rate. The same type of divergent response was noted with changes in umbilical flow rates. The only change in fetal hemodynamics which seems able to increase simultaneously outflowing p_{O_2} and O_2 transfer rate would be a more uniform distribution of fetal placental blood flow, such that it more closely parallels maternal flow distribution and/or the available surface for gas exchange.

Role of Various Factors in Placental O_2 Transfer. These experiments characterize the dependence of O_2 transfer and umbilical venous p_{O_2} on maternal arterial p_{O_2}, fetal placental flow rate, and fetal inflowing p_{O_2} on O_2 exchange in a single cotyledon of the sheep placenta and on fetal placental flow in the rabbit placenta. Each factor was studied individually while the fetal placental circulation was isolated and perfused *in situ*. The present findings do not apply for an intact fetus whose blood recirculates between peripheral tissues and the placenta because compensations would tend to maintain O_2 transfer equal to fetal O_2 consumption in this latter instance. The present data take account of changes in only a single variable.

One of the most striking conclusions of this study is that O_2 transfer depends to a greater extent on a specified percentage change in umbilical arterial p_{O_2} than on a similar change in umbilical blood flow. This is important because umbilical arterial p_{O_2} is a consequence of fetal tissue metabolism on one hand, and a factor which is important in determining placental O_2 transfer on the other hand. It thereby directly links fetal needs and O_2 delivery. Thus, small changes in umbilical arterial p_{O_2} will cause placental O_2 transfer to become equal to fetal O_2 consumption. This alignment can occur passively without any change in umbilical blood flow or other active response being required.

If it is true that the rate of umbilical blood flow remains constant in spite of spontaneous fluctuations in O_2 need and delivery, then there are important consequences for fetal homeostasis as recently discussed by Faber (*50*). A constant umbilical blood flow would assure that intravascular, hydrostatic pressures would remain constant in fetal placental capillaries, and the balance of maternal-fetal hydrostatic forces determining transplacental water movement would be maintained. The fetus would not gain or lose water as might otherwise happen if umbilical flow and pressure were to vary in response to different fetal O_2 needs. The fetus could avoid becoming dehydrated during periods of increased O_2 transport.

Some additional evidence supports the hypothesis that umbilical arterial p_{O_2} is the important physiological regulator of placental O_2

transfer. First, telemetry studies reveal that umbilical blood flow remains remarkably constant in the lamb of a pregnant ewe grazing quietly at pasture, running, and in various other circumstances (*51*). This constancy speaks against a significant regulatory role for umbilical blood flow in O_2 delivery. Second, as has been mentioned, small changes in umbilical arterial p_{O_2} accomplish sizable changes in O_2 transfer; a change of only 1 mm Hg causes a 6% change in transfer rate in the physiological range (Figure 21). Thus, the small day-to-day changes in umbilical arterial and venous p_{O_2} found in conscious sheep (*49*, *52*) are associated with significant differences in O_2 transfer. There may well be other fetal regulators of O_2 delivery, but many of them, such as changes in hemoglobin concentration or O_2 affinity of fetal blood, would require several days at least to affect O_2 delivery. Nor is there any presently known mechanism for maternal placental flow or other maternal adaptations to respond to the level of fetal oxygenation.

If umbilical blood flow is constant while O_2 requirements vary periodically, then fetal tissues would be required to withstand intervals of time in which they received blood with relatively low O_2 tension. One might suspect adaptations within fetal tissues to maintain O_2 utilization in vital organs which include changes in distribution of blood flow and in the number of functioning capillaries per unit of tissue. In contrast to adult tissues, these adaptations have not been extensively studied in the fetus.

Summary

We have discussed the factors affecting placental oxygen transfer. A mathematical model has been presented that uses equations describing one-dimensional diffusion between two parallel capillaries to calculate the oxygen tension changes during the course of a single transit in material and fetal placental vessels. Intracellular hemoglobin reaction rates and the placental membrane are sources of resistance and produces slight variation in diffusing capacity during the capillary transit. Consideration of these resistances permits calculation of oxygen tension values in plasma and red cells. Using representative values of diffusing capacity, uterine and umbilical arterial oxygen tension, and capillary flow rates, the model predicts that oxygen tension reaches 99.4% equilibration by the end of the 1.7 sec capillary transit. Moderate variation in almost any of these variables can increase the end-capillary pressure difference considerably, however. Thus while previous studies have indicated rapid and almost complete equilibration of inert gases, this model predicts that oxygen equilibration may not be so complete. The effect of placental tissue oxygen consumption is a lowering of end-capillary oxygen tensions

and a decrease in rate of oxygen exchange while the effect of shunts is a lowering of umbilical venous oxygen tension and elevation of uterine venous oxygen tension caused by mixing of the capillary blood with arterial blood that bypassed the exchange area. In the presence of 8 ml/min × kg) tissue O_2 consumption and 26% shunts, the venous oxygen tensions agree well with experimental values, but the oxygen exchange rate calculated is still much larger than experimental values. Thus, our concurrent flow model predicts a more efficient system than actually exists. Assuming either a countercurrent or crosscurrent flow pattern would produce even higher oxygen exchange rates. Probably some degree of uneven distribution of capillary flow rates and diffusing capacity exists in addition to a complex combination of flow patterns.

The main factors determining placental oxygen exchange are uterine and umbilical arterial O_2 tensions, maternal and fetal placental hemoglobin flows, placental diffusing capacity, characteristics of the oxyhemoglobin dissociation curve, the amount of carbon dioxide exchanged, and the spatial relation of maternal and fetal exchange vessels. The mathematical model was useful in studying the effects of isolated changes in the first five of these factors individually. End-capillary oxygen tensions and the oxygen exchange rate are most sensitive to changes in umbilical arterial oxygen tension, somewhat less sensitive to changes in maternal and fetal placental blood flows or hemoglobin concentrations, and relatively insensitive to change in maternal arterial oxygen tension or placental diffusing capacity.

The predictions of the model may be tested experimentally using an isloated placental cotyledon preparation. The O_2 transfer rate and outflowing oxygen tensions were most sensitive to changes in umbilical arterial oxygen tension; changes in maternal arterial O_2 tension and umbilical flow rate had less effect in the physiological range. Changes in maternal arterial oxygen tension, however, became progressively more critical to fetal oxygenation as the level fell. The pattern of results was similar to that predicted theoretically. Evidence is discussed suggesting that umbilical arterial oxygen tension, rather than umbilical blood flow, is the direct link maintaining the rate of placental oxygen transfer equal to the rate of fetal consumption.

Acknowledgment

The authors express their appreciation to John Bankhead and Peter Yuen for expert technical assistance. These studies were supported by the National Institute of Child Health and Human Development Grant No. HD 03807 and a grant from the Labor Foundation. Computation aid was given by the Scientific Computation Center, School of Medicine, Loma Linda University, which is partially supported by National Insti-

tues of Health Grant No. FR 00276. The program (Fortran IV) for performing these calculations is available on request. L. D. Longo is the recipient of USPHS Research Career Development Award No. 1-K4 HD 23, 676; E. P. Hill is supported by National Heart Institute Cardiovascular Physiology Training Grant No. HE 05171, and G. G. Power is the recipient of USPHS Research Career Development Award No. 1-K4 HD 20, 253.

Literature Cited

1. Hippocrates, "The Genuine Works of Hippocrates." Translated from the Greek, with a preliminary discourse and annotations by Francis Adams. 2 vols., London, Sydenham Society, 1849.
2. Aristotle, The Works of Aristotle Translated into English. J. A. Smith and W. D. Ross, Eds., 11 vols., Oxford, Clarendon Press, 1908–1931.
3. Harvey, William, "Exercitatio Anatomica de Motu Cordis et Sanguins in Animalibus," Francofurti; sumpt. Guilelmi Fitzeri, 1628.
4. Harvey, William, "Exercitationes de Generatione Animalium," Londoni, O. Pulleyn, 1651.
5. Hunter, John, "Observations on Certain Parts of Animal Oeconomy," London, 1786.
6. Fick, A., *Poggendorffs Ann. Physic* (Ser. 2) (1855) **94**, 59.
7. Barron, D. H., Alexander, G., *Yale J. Biol. Med.* (1952) **25**, 61.
8. Barron, D. H., Meschia, G., *Cold. Spr. Harb. Symp. Quant. Biol.* (1954) **19**, 93.
9. Krogh, A., Krogh, M., *Scand. Arch. Physiol.* (1909–1910) **23**, 236.
10. Longo, L. D., Power, G. G., Forster, R. E., II, *J. Clin. Invest.* (1967) **46**, 812.
11. Haldane, J., Smith, J. L., *Physiol. (Lond.)* (1897) **22**, 231.
12. Longo, L. D., Power, G. G., Forster, R. E., II, *J. Appl. Physiol.* (1969) **26**, 360.
13. Staub, N. C., Bishop, J. M., Forster, R. E., *J. Appl. Physiol.* (1962) **17**, 21.
14. Hill, E. P., Power, G. G., Longo, L. D., *Amer. J. Physiol.* (1972) **222**, 721.
15. Longo, L. D., Hill, E. P., Power, G. G., *Amer. J. Physiol.* (1972) **222**, 730.
16. Power, G. G., Hill, E. P., Longo, L. D., *Amer. J. Physiol.* (1972) **222**, 740.
17. Hellegers, A. E., Schruefer, J. J. P., *Amer. J. Obstet. Gynecol.* (1961) **81**, 377.
18. Meschia, G., Hellegers, A., Blechner, J. N., Wolkoff, A. S., *Quart. J. Exp. Physiol.* (1961) **46**, 95.
19. Lawson, W. H., Jr., *J. Appl. Physiol.* (in press).
20. Staub, N. C., Bishop, J. M., Forster, R. E., *J. Appl. Physiol.* (1961) **16**, 511.
21. Southworth, R. W., Deleeuw, S. L., "Digital Computation and Numerical Methods," pp. 455–462, McGraw-Hill, New York, 1965.
22. Campbell, A. G. M., Dawes, G. S., Fishman, A. P., Hyman, A. I., James, G. B., *J. Physiol. (London)* (1966) **182**, 439.
23. Dilts, P. V., Jr., Brinkman, C. R., III, Kirschbaum, T. H., Assali, N. S., *Amer. J. Obstet. Gynecol.* (1969) **103**, 138.
24. Ladner, C., Brinkman, C. R., III, Weston, P., Assali, N. S., *Amer. J. Physiol.* (1970) **218**, 257.
25. Metcalfe, J., Moll, W., Bartels, H., Hilpert, P., Parer, J. T., *Circ. Res.* (1965) **16**, 95.
26. Rankin, J. H. G., Peterson, E. N., *Circ. Res.* (1969) **24**, 235.
27. Power, G. G., Longo, L. D., Wagner, H. N., Jr., Kuhl, D. E., *J. Clin. Invest.* (1967) **46**, 2053.

28. Meschia, G., Battaglia, F. C., Bruns, P. D., *J. Appl. Physiol.* (1967) **22,** 1171.
29. Richardson, L. F., Gaunt, J. A., *Trans. Roy. Soc. London* (1927) **226A,** 300.
30. Makowski, E. L., *Amer. J. Obstet. Gynecol.* (1968) **100,** 283.
31. Steven, D. H., *J. Physiol (London)* (1968) **196,** 24.
32. Blechner, J. N., Makowski, E. L., Cotter, J. R., Meschia, G., Barron, D. H., *Amer. J. Obstet. Gynecol.* (1969) **105,** 368.
33. Rankin, J. H. G., Meschia, G., Makowski, E. L., Battaglia, F. C., *Amer. J. Physiol.* (1970) **219,** 9.
34. Guilbeau, E. J., Reneau, D. D., Knisely, M. H., ADVAN. CHEM. SER. (1973) **118,** 130.
35. Faber, J. J., *Circ. Res.* (1969) **24,** 221.
36. Kirschbaum, T. H., Shapiro, N. Z., *J. Theoret. Biol.* (1969) **25,** 380.
37. Chu, C., Oblique crossflow transfer (manuscript in preparation).
38. Van Liew, H. D., *Amer. J. Physiol.* (1968) **214,** 1176.
39. Abrams, R., Caton, D., Curet, L. B., Crenshaw, C., Mann, L., Barron, D. H., *Amer. J. Physiol.* (1969) **217,** 1619.
40. Hart, F. M., Faber, J. J., *J. Appl. Physiol.* (1965) **20,** 737.
41. Barron, D. H., *Yale J. Biol. Med.* (1951–2) **24,** 169.
42. Longo, L. D., Power, G. G., *J. Appl. Physiol.* (1969) **26,** 48.
43. Power, G. G., *J. Appl. Physiol.* (1968) **24,** 468.
44. Holland, R. A. B., *Resp. Physiol.* (1967) **3,** 307.
45. Power, G. G., Longo, L. D., *J. Appl. Physiol.* (1969) **26,** 38.
46. Dawes, G. S., "Foetal and Neonatal Physiology. A Comparative Study of the Changes at Birth," p. 72, Chicago, Year Book, 1968.
47. Power, G. G., Jenkins, F., *Amer. J. Physiol.* (submitted for publication).
48. Hellegers, A. E., *Yale J. Biol. Med.* (1969–1970) **70,** 180.
49. Comline, R. S., Silver, M., *J. Physiol. (London)* (1970) **209,** 567.
50. Faber, J. J., in "Respiratory Gas Exchange and Blood Flow in the Placenta," L. D. Longo and H. Bartels, Eds., U.S. Department of Health, Education, and Welfare, National Institutes of Health, Bethesda, 1973.
51. Elsner, R., personnel communication, 1971.
52. Meschia, G., Cotter, J. R., Breathnach, C. S., Barron, D. H., *Quart. J. Exp. Physiol.* (1965) **50,** 185.

RECEIVED January 21, 1972.

7

A Detailed Quantitative Analysis of O_2 Transport in the Human Placenta during Steady- and Unsteady-State Conditions

ERIC J. GUILBEAU and DANIEL D. RENEAU

Department of Chemical Engineering, Louisiana Tech University, Ruston, La. 71270

MELVIN H. KNISELY

Department of Anatomy, Medical University of South Carolina, Charleston, S. C. 29401

Distributed parameter, nonlinear, partial differential equations were solved to describe oxygen transport from maternal to fetal blood, which flows in microscopic channels within the human placenta. Steady-state solutions were obtained to show the effects of variations in several physiologically important parameters. Results reported previously indicate that maternal contractions during labor are accompanied by a partially reduced or a possible total occlusion of maternal blood flow rate in some or all portions of the placenta. Using the mathematical model, an unsteady-state study analyzed the effect of a time-dependent maternal blood flow rate on placental oxygen transport during labor. Parameter studies included severity of contractions and periodicity of flow. The effects of axial diffusion on placental transport under the conditions of reduced maternal blood flow were investigated.

The purpose of this and previous papers is an attempt to obtain a better quantitative understanding of oxygen transport from maternal to fetal blood in the human placenta by describing the process with detailed mathematical models. In a previous publication (*1*) a placental mathematical model was used to obtain a better insight into the effects of placental tissue oxygen consumption and the contractions of labor on

fetal blood oxygenation. Additional studies have now been made to show the effects on fetal blood oxygenation of changing specific physiological parameters under steady-state conditions. The results of several of these steady-state parameter studies and the results of unsteady-state studies which show the effects of axial diffusion during reduced maternal blood flow are presented in this paper.

The simulation applies to the microscopic transport unit of the human placenta, the terminal villus, during the latter stages of pregnancy and during the birth process. The study is mathematical and has been conducted as a prelude to experimental studies which will be based upon the insights gained in this theoretical analysis. The results should be interpreted as representing the proper trends since experimental validation is necessary before a complete quantitative interpretation is possible.

Engineers are well suited to combine theoretical prediction with experimental measurement. Previous investigators (*2, 3, 4, 5, 6, 7*) have had considerable success by first mathematically simulating complex biological systems and then conducting well-planned, experimental programs to combine theory with experimental results.

Chemical engineers have found that the fundamentals of chemical engineering systems analysis are applicable to the basic problem of determining how the organs of the body work and why at times they do not operate properly. This paper discusses a problem of this type.

The importance of maintaining normal placental function is easily understood since the placenta is responsible for the normal security and health of the unborn child during pregnancy. Many fetal deaths result from oxygen deprivation because of placental malfunction. Therefore, a complete understanding of the complex oxygen transport mechanisms of this biological organ is extremely important if the number of fetal deaths is to be reduced.

This paper reviews briefly those anatomical and physiological concepts required for the mathematical analysis and the mathematical model derived for the simulation. The mathematical techniques which were developed to obtain steady- and unsteady-state solutions of the model and the results of these steady- and unsteady-state studies are discussed.

Anatomy

In designing a mathematical simulation of any physical or chemical process, one must first determine an adequate geometric representation of the actual process. The success of the overall simulation depends often upon this initial step in the complete modeling process. When the physical or chemical process that is to be modeled is part of a physiologically and anatomically complex organ of the human body, the determination of a

suitable simulation geometry may become difficult. For this type of system the success one has in defining a suitable geometry depends directly upon the state of knowledge of the anatomy of the organ under investigation.

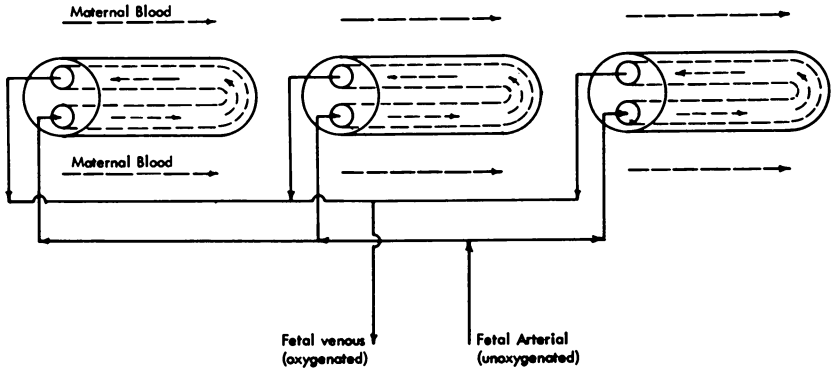

Figure 1. Terminal villi showing possibilities of concurrent and countercurrent flow within a terminal villus

The present study deals with the simulation of oxygen transfer in the human placenta at the microscopic level. The determination of the exact anatomy of the placenta has been the subject of intensive and exhaustive research for many years. For a detailed review of the present state of knowledge concerning placental anatomy, refer to the works of Ramsey (*8, 9*), Boyd (*10*), Arts (*11*), Corner (*12*), Crawford (*13*), Dawes (*14*), Freese (*15, 16*), and Barnes (*17*). Based on the placental anatomical description given by these and other authors, a simulation geometry for the microscopic transport unit of the human placenta has been developed. The rationale behind the development of this simulation geometry of the placental oxygen transport system has been discussed by Guilbeau, Reneau, and Knisely (*1*). For simulation purposes it is proposed that for the most part, in the microscopic capillary bed of the placenta where oxygen exchange occurs, maternal blood flows through a maze of closely packed, movable terminal villi. Fetal blood flows within looped capillaries contained within these terminal villi. This dual flow system may be diagrammed as in Figure 1. The looped configuration of the fetal capillary (*13*) within the fetal villi shows that fetal blood flowing within a fetal capillary in a single terminal villus may flow concurrently and countercurrently with respect to the maternal blood flowing past that particular villus. This anatomical representation of microscopic placental flow may be simulated by dividing the looped capillary into two straight capillaries, each equal in length to one-half of the length of the original looped fetal capillary (*see* Figure 2). A mathematical simu-

lation of oxygen transport between two streams flowing in this fashion requires a concurrent and a countercurrent solution of a system in which fetal blood flows within a bounded cylindrical capillary of radius R_1. This fetal capillary is exposed to maternal blood flowing longitudinally down the axis of the fetal capillary. Thus, each fetal capillary may be assumed to be supplied by an amount of blood flowing in a cylindrical annulus of radius R_2 much like the Krogh tissue cylinder concept (*18*). A small tissue thickness, the tissue of the terminal villus, separates the maternal and fetal blood streams. This microscopic exchange unit is shown in Figure 3 and is the basis for the derivation of the current mathematical model.

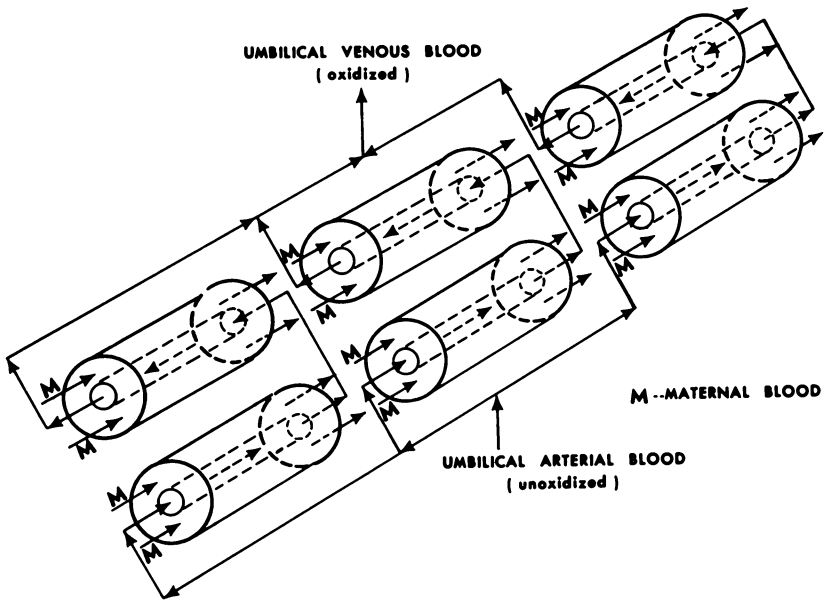

Figure 2. Straight capillary multivillous flow system, using a concurrent, countercurrent flow pattern

Physiology and Biochemistry

During pregnancy the fetus completely depends upon the maternal blood circulation for an adequate supply of oxygen and food nutrients and for the removal of metabolic wastes. Maternal blood flowing through the placenta carries oxygen in two forms—in the physically dissolved state and chemically combined with hemoglobin. A very small percentage of the total oxygen is physically dissolved. As maternal and fetal bloods enter the exchange area of the placenta, dissolved oxygen in the maternal blood begins to diffuse across a small thickness of tissue into the fetal

blood. As the concentration of dissolved oxygen in the maternal blood is reduced, oxygen is released from maternal hemoglobin, and similarly in the fetal blood stream as fetal blood oxygen concentration increases, fetal hemoglobin combines chemically with the oxygen in the fetal blood. This chemical relationship which exists between hemoglobin and oxygen in maternal and fetal blood streams results in the maintenance of a large radial oxygen diffusion gradient. The reaction kinetics between hemoglobin and oxygen are believed to be sufficiently fast so that the oxygen dissociation curve may serve as a reaction curve.

The rate of oxygen supply to the fetal blood depends upon the maternal and fetal blood flow rates, the dimensions of the oxygen exchange unit, the oxygen capacity of maternal and fetal blood, the oxygen concentration of maternal and fetal arterial blood, the oxygen solubility of maternal and fetal blood, the oxygen diffusivity of maternal and fetal blood, and the oxygen consumption, solubility, and diffusivity of placental tissue (for a detailed discussion of experimental values which have been determined for these parameters, *see* Guilbeau (*19*)).

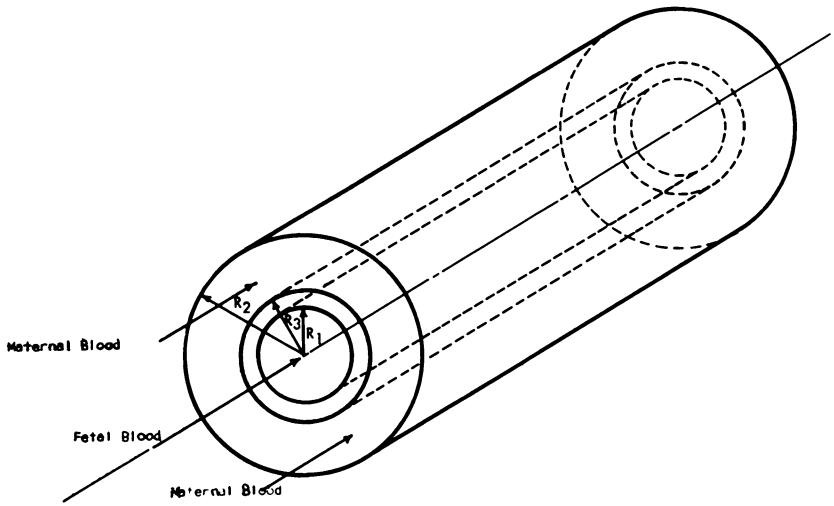

Figure 3. Fetal capillary–tissue–maternal blood, cylindrical arrangement

Mathematical Analysis

Assumptions. Derivation of the mathematical model for placental oxygen transport was based on the following assumptions:

1. The standard exchange unit (one-half of a looped capillary of the terminal villus as described earlier) is assumed to be a straight cylinder supplied by a cylinderlike quantity of maternal blood.

2. The terminal villi are assumed to contain only one fetal capillary. Shunts or alternate paths for the passage of fetal blood through the terminal villi are neglected.

3. The maternal blood space (intervillous space) between terminal villi is assumed to be of capillary size (*10*).

4. Eddy currents within the maternal and fetal blood stream are neglected.

5. The time of reaction for the release of oxygen from maternal erythrocytes is negligible compared with the time required for diffusion to the capillary wall (*20*). Similarly, the time of reaction for the combination of oxygen with fetal erythrocytes is negligible compared with the time required for diffusion from the capillary wall to the erythrocyte. This being true, mass transfer is the controlling factor, chemical equilibrium exists at all points in the system, and the oxygen dissociation curves serve as reaction curves.

6. The resistance to oxygen diffusion at the blood-tissue interface is negligible (*21*, *22*). The oxygen partial pressure profile is continuous at the blood-tissue interface, and transport across the blood-tissue interface can be described by Fick's first law (*22*).

7. For simulation purposes blood is considered a homogeneous solution.

8. Oxygen consumption is constant under a given set of conditions.

9. Oxygen consumption in the villus tissue is homogeneous.

10. Blood flow is laminar (*23*) and in the x-direction only. In fetal and maternal channels the velocity profile is assumed to be flat (*5*).

11. The system is axially symmetric.

12. Oxygen is transported in the capillary by blood flow and molecular diffusion.

The assumption that only one fetal capillary is contained within a terminal villus is contrary to the known anatomy of the placenta. In-flow and out-flow of fetal blood in the villus is not a matter of parallel one-way streets. Shunts and alternate paths are provided for and called into play, especially when the normal, physiological aging process causes deposition of fibrin in and around individual villi, thereby removing them from function (*10*, *24*). The effects of this assumption are possibly minimized by the method used in obtaining the standard length of the exchange unit (*19*, *25*).

The assumption that maternal blood flows in a cylindrical annulus of capillary size bounded by the surrounding terminal villi requires that the terminal villi be fixed in position. The actual position of the terminal villi and the space between them is highly variable. Many of the spaces between villi are of capillary size. At the point of entry of maternal blood, unattached villi are swept aside, and the space between them greatly enlarged. Also, there are several anatomical features which alter the size of the maternal stream—pools and lakes occur in the areas around the chorion or basalis or margin or septa, as well as placental caverns

of unknown origin (*10, 24*). The capillary space assumed may be taken as a gross average value of the order of magnitude that exists within a considerable portion of the intervillous space.

The assumption that the fetal capillary and the tissue surrounding this capillary is straight is contrary to the known anatomy of the terminal villus. This effect may be absorbed in the standardization of capillary length. In addition to an extremely torturous shape, the fetal capillary varies in size throughout the placenta. As for the maternal intervillous space, the radial dimensions of the fetal capillary are taken as gross average values of the order of magnitude that exists within a considerable portion of the placenta. The remaining assumptions are discussed by Guilbeau (*19, 26*).

Mathematical Model. Based on these assumptions and the geometrical arrangement, the following mathematical model was derived. (For details of derivation, *see* Reference (*1*).)

Fetal capillary equation:

$$K' \frac{\partial P}{\partial t} = D_1 \frac{\partial^2 P}{\partial r^2} + \frac{D_1}{r} \frac{\partial P}{\partial r} + D_1 \frac{\partial^2 P}{\partial x^2} - V_1 K' \frac{\partial P}{\partial x} \tag{1}$$

Fetal blood-tissue interface equation:

$$P_i \Big|_{\text{fetal blood}} = P_i \Big|_{\text{tissue}} \tag{2}$$

and,

$$\left(D_1 c_1 \frac{\partial P}{\partial r} \right)_i \Big|_{\text{fetal blood}} = \left(D_3 c_3 \frac{\partial P}{\partial r} \right)_i \Big|_{\text{tissue}} \tag{3}$$

Tissue equation:

$$\frac{\partial P}{\partial t} = D_3 \frac{\partial^2 P}{\partial r^2} + \frac{D_3}{r} \frac{\partial P}{\partial r} + D_3 \frac{\partial^2 P}{\partial x^2} - \frac{A}{c_3} \tag{4}$$

Tissue-maternal blood interface equation:

$$P_i \Big|_{\text{tissue}} = P_i \Big|_{\text{maternal blood}} \tag{5}$$

and,

$$\left(D_3 c_3 \frac{\partial P}{\partial r} \right)_i \Big|_{\text{tissue}} = \left(D_2 c_2 \frac{\partial P}{\partial r} \right)_i \Big|_{\text{maternal blood}} \tag{6}$$

Maternal intervillous channel equation:

$$K'' \frac{\partial P}{\partial t} = D_2 \frac{\partial^2 P}{\partial r^2} + \frac{D_2}{r} \frac{\partial P}{\partial r} + D_2 \frac{\partial^2 P}{\partial x^2} - V_2 K'' \frac{\partial P}{\partial x} \quad (7)$$

where:

$$K' = \left[1 + \frac{N_1 k_1 n_1 P^{n_1 - 1}}{c_1 (1 + k_1 P^{n_1})^2} \right]$$

$$K'' = \left[1 + \frac{N_2 k_2 n_2 P^{n_2 - 1}}{c_2 (1 + k_2 P^{n_2})^2} \right]$$

Divisions of Analysis. The preceding model describes conditions within a single fetal capillary surrounded by a thin tissue cylinder and supplied by a cylindrical annulus of maternal blood, as shown in Figure 3. Since the numerical techniques required for the solution of such equations were not well defined, the determination of a steady-state concurrent solution was first obtained. Based upon the results of this work, an unsteady-state concurrent solution was assumed possible and feasible.

Specifically, the mathematical model was solved for the following three cases: Case 1, steady-state concurrent solution neglecting tissue effects and axial dispersion; Case 2, unsteady-state concurrent solution neglecting tissue effects and axial dispersion; Case 3, unsteady-state concurrent analysis neglecting tissue effects but including axial diffusion. In the unsteady-state analysis, transient conditions were created by applying velocity changes to the system.

For the Case 1 solution which neglected tissue effects and axial dispersion for steady-state conditions, the mathematical equations reduced to the following:

Fetal capillary equation:

$$O = D_1 \frac{\partial^2 P}{\partial r^2} + \frac{D_1}{r} \frac{\partial P}{\partial r} - V_1 K' \frac{\partial P}{\partial x} \quad (8)$$

Fetal blood-maternal blood interface equation:

$$P_i \Big|_{\text{fetal blood}} = P_i \Big|_{\text{maternal blood}} \quad (9)$$

and,

$$\left(D_1 c_1 \frac{\partial P}{\partial r} \right)_i \Big|_{\text{fetal blood}} = \left(D_2 c_2 \frac{\partial P}{\partial r} \right)_i \Big|_{\text{maternal blood}} \quad (10)$$

Maternal intervillous channel equation:

$$O = D_2 \frac{\partial^2 P}{\partial r^2} + \frac{D_2}{r} \frac{\partial P}{\partial r} - V_2 K'' \frac{\partial P}{\partial x} \tag{11}$$

For the Case 2 solution which neglected axial dispersion and tissue effects for unsteady-state conditions, the mathematical equations of the model reduced to the following:
Fetal capillary equation:

$$K' \frac{\partial P}{\partial t} = D_1 \frac{\partial^2 P}{\partial r^2} + \frac{D_1}{r} \frac{\partial P}{\partial r} - V_1 K' \frac{\partial P}{\partial x} \tag{12}$$

Fetal blood-maternal blood interface equations:

$$P_i \Big|_{\text{fetal blood}} = P_i \Big|_{\text{maternal blood}} \tag{13}$$

and,

$$\left(D_1 c_1 \frac{\partial P}{\partial r} \right)_i \Big|_{\text{fetal blood}} = \left(D_2 c_2 \frac{\partial P}{\partial r} \right)_i \Big|_{\text{maternal blood}} \tag{14}$$

Maternal intervillous channel equation:

$$K'' \frac{\partial P}{\partial t} = D_2 \frac{\partial^2 P}{\partial r^2} + \frac{D_2}{r} \frac{\partial P}{\partial r} - V_2 K'' \frac{\partial P}{\partial x} \tag{15}$$

For the Case 3 solution which included axial dispersion but neglected tissue effects, the mathematical equations reduced to the following:
Fetal capillary equation:

$$K' \frac{\partial P}{\partial t} = D_1 \frac{\partial^2 P}{\partial r^2} + \frac{D_1}{r} \frac{\partial P}{\partial r} + D_1 \frac{\partial^2 P}{\partial x^2} - V_1 K' \frac{\partial P}{\partial x} \tag{16}$$

Fetal blood-maternal blood interface equations:

$$P_i \Big|_{\text{fetal blood}} = P_i \Big|_{\text{maternal blood}} \tag{17}$$

and,

$$\left(D_1 c_1 \frac{\partial P}{\partial r} \right)_i \Big|_{\text{fetal blood}} = \left(D_2 c_2 \frac{\partial P}{\partial r} \right)_i \Big|_{\text{maternal blood}} \tag{18}$$

Maternal intervillous channel equation:

$$K'' \frac{\partial P}{\partial r} = D_2 \frac{\partial^2 P}{\partial r^2} + \frac{D_2}{r} \frac{\partial P}{\partial r} + D_2 \frac{\partial^2 P}{\partial x^2} - V_2 K'' \frac{\partial P}{\partial x} \quad (19)$$

Since the tissue effects are neglected, the geometric description of the basic exchange unit shown in Figure 3 must be changed to the one shown in Figure 4 for these solutions.

Solution Techniques. Because of the complexity and nonlinearity of the equations representing the interconnecting two-flow system, straightforward, analytical solution of the model was not considered feasible, and numerical differencing methods were developed to obtain the solutions.

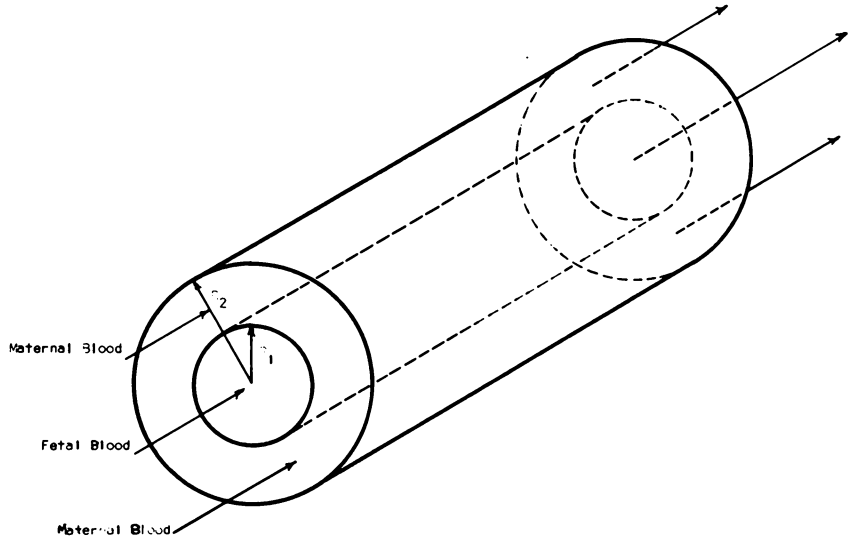

Figure 4. Fetal capillary–maternal blood, cylindrical arrangement

SOLUTION OF MATHEMATICAL MODEL FOR CASE 1. For the Case 1 solution iterative techniques were ruled unacceptable owing to the excessive time requirements of such methods. Several investigators (*27*, *28*, *29*, *30*) working with similar noncoupled systems found that the Crank–Nicholson 6-point implicit differencing method (*31*) provided an excellent solution. For the solution of Equation (8) we decided to apply the Crank–Nicholson method to the second-order partials and corresponding explicit methods to the first-order partials. Nonlinear coefficients were treated in a special manner outlined by Reneau *et al.* (*5*).

Since the term $1/r$ appears in Equation (8), special attention is required for the point where $r = 0$. Either a special equation is necessary

for this position (*29*), or a fictitious boundary (*27, 30*) is required. The special equation method was adopted and applied with L'Hospitals' rule.

Equation (11) represents steady-state conditions within the maternal intervillous channel and is a nonlinear, partial difference equation with two independent variables. Since the $\partial P/\partial r = 0$ when $r = R_2$, a special equation was also required at this position. The same techniques were used as in the fetal capillary equation.

The fetal capillary-intervillous channel arrangement is an interconnecting system with the values of the dependent variable in one of the phases being determined by conditions existing in both phases. A solution is possible only if the two phases are tied together in an appropriate manner. This is made possible by the adaptation of the interface equation. If the interface equation is differenced using a backward differencing scheme for the left-hand term and a forward differencing scheme for the right-hand term, and using the averaging technique of Crank–Nicholson for both, then the fetal and maternal equations are matched at the interface. The resulting system of equations was solved by the method of Thomas (*32*).

Solution of Mathematical Model for Case 2 and Case 3. For the Case 2 and Case 3 solutions, the technique developed for the Case 1 solution, which was based on the Crank–Nicholson implicit method, was unacceptable when the time derivative was included.

Peaceman and Rachford (*33*) and Douglas (*34*) developed an alternating-direction implicit technique to describe unsteady-state diffusion in two directions. Brian (*35*) later supplemented the work by expanding the procedure to describe unsteady-state diffusion in three directions. The procedure was then modified and applied to two-dimensional diffusion in laminar flow systems by Ananthakrishan, Gill, and Barduhn (*36*). Reneau, Bruley, and Knisely (*4*) developed a technique to solve nonlinear, unsteady-state equations representing an interconnected, convection–diffusion system composed of a laminar flow, cylindrical diffusion system coupled with a cylindical, solid diffusion system. The method used here is adapted from the technique outlined by Reneau *et al.* (*4*). This technique was adapted for this study to apply to equations which describe two interconnected, nonlinear, convection, diffusion systems. These methods are explained by Guilbeau (*19, 26*).

Discussion of Results

As stated previously, the mathematical model was solved for the following three cases: Case 1, steady-state, concurrent solution neglecting tissue effects and axial dispersion; Case 2, unsteady-state, concurrent solution neglecting tissue effects and axial dispersion; Case 3, unsteady-

state concurrent solution neglecting tissue effects but including axial diffusion. A discussion of the results of these three studies is presented below.

Steady-State Concurrent Solution Neglecting Tissue Effects and Axial Dispersion. In this steady-state analysis many parameter studies were made. The first study was a basic investigation in which linear velocities and channel lengths were standardized for maternal and fetal streams. The other studies investigated the effects of changing various physiological parameters on the transport of oxygen from maternal to fetal blood. The parameters investigated that are presented here are as follows: fetal and maternal blood volumetric flow rate, fetal and maternal oxygen capacity, oxygen diffusivity, oxygen solubility, and maternal blood arterial oxygen concentration. These studies are discussed below.

BASIC INVESTIGATION. A lack of experimental data reporting linear velocities and length of flow channels for maternal and fetal streams required that these values be standardized for the present study. Two types of flow variations are possible. The linear velocities of maternal and fetal blood may change in such a way that the ratio of maternal to fetal volumetric blood flow remains constant. Conversely, maternal and fetal linear velocities may change in a way that will alter the maternal to fetal flow ratio.

To determine the effects of changes in the maternal or fetal blood linear velocity on the partial pressure of oxygen at which the maternal and fetal blood streams equilibrated, a study was made in which the maternal and fetal blood linear velocities were varied while the maternal to fetal volumetric flow rate ratio was held constant. The partial pressure of oxygen at which the maternal and fetal blood streams equilibrated remained constant for all of the variations in maternal and fetal blood linear velocities which were studied. As the linear velocities were decreased, however, the capillary length required to obtain equilibration decreased. From this study it was concluded that one oxygen partial pressure equilibration value exists for a given maternal to fetal volumetric flow rate ratio if the only variables that are allowed to change are the maternal and fetal blood linear velocities. This equilibrium pressure may occur at different capillary lengths depending upon the magnitudes of the linear velocities which are used.

After it was determined that changing the linear velocity of the maternal or fetal blood stream did not affect the equilibration pressure, it was possible to determine the maternal to fetal volumetric flow rate ratio that would result in an equilibration pressure which matched experimentally determined values of umbilical vein and artery oxygen partial pressures (*37*). As the maternal to fetal volumetric flow rate ratio is increased, the partial pressure of oxygen at which equilibration

occurs is increased. The capillary length required for equilibration to occur in turn decreases. Based on this information, it was determined that the simulated volumetric flow rate ratio of maternal to fetal blood required to match experimental values was 2.1–1.0. This should not be interpreted as the maternal to fetal blood volumetric flow rate ratio for the gross human placenta. It is reasonable that many single exchange units within the placenta may operate under conditions of a 2.1–1.0 blood flow rate ratio, but for this study the value must be taken only as the value required for standardization of the mathematics against experimentally determined values of oxygen partial pressure. Linear velocities of a magnitude reported to occur in vessels the diameter of those in which the maternal and fetal blood is believed to flow were used, and the length of the exchange unit at which equilibration occurred was determined. These values of maternal to fetal blood volumetric flow rate ratio, maternal and fetal blood linear velocities, and capillary length were used as a basis for all other parameter studies. The following standardized values were used: maternal to fetal blood volumetric flow rate ratio of 2.1, standardized linear velocity of fetal blood of 0.00286 cm/sec, standardized linear velocity of maternal blood of 0.002 cm/sec, and a standardized capillary length of 800 μ. Using these values of maternal and fetal linear velocity and the standardized capillary length of 800 μ, capillary transient times of 40 sec and 28 sec are obtained for maternal and fetal bloods, respectively. These capillary transient times seem long when compared with capillary transient times in other organs of the body, and they lead to the question of whether the model is at all relevant. Borell *et al.* (*38*) using radioangiographic technique found that dye injected into the femoral artery of pregnant women required 20–30 sec after its first appearance to be cleared from the intervillous space. Freese *et al.* (*39*) in a later study using x-ray cinematographic techniques found that in dye-injected rhesus monkeys about 1½–2 sec following dye injection were required for the first appearance of dye in the cotyledons of the intervillous space. All entries were demonstrated not later than 8–8½ sec after injection if the uterus was not contracted, but about 90 sec were required for complete clearance of the intervillous space. In relation to these findings, a 40-sec transient time for maternal blood may be reasonable. For a given maternal-to-fetal blood volumetric flow rate ratio, only one equilibration partial pressure is possible. The capillary length required to yield this equilibration pressure depends on the linear velocities of the maternal and fetal blood streams, as well as the radial dimensions of the capillary. Similarly, the capillary transient time depends on the linear velocity. For a given maternal to fetal blood volumetric flow rate ratio if the linear velocity of maternal and fetal blood is increased in the same proportions and if results are presented in

dimensionless form, the response of the model in both cases will be identical. Since literature values for maternal and fetal capillary linear velocities in the placenta were not available, results have been presented in dimensionless form in this investigation. Axial capillary length is given by dimensionless capillary length, X' = variable length divided by total capillary length. Time is given by dimensionless time, τ = number of residence times = total time/one residence time.

These standardized values are not meant to represent actual conditions within the placenta. They are standardized so that a concurrent flow arrangement may be used in the simulation. These standardized dimensions result in the same exit oxygen partial pressures in the concurrent arrangement as would exist if the actual dimensions were used with the flow pattern that actually exists within the placenta.

FETAL VOLUMETRIC FLOW RATE. During pregnancy the umbilical cord of the fetus may become partially or totally occluded if it becomes knotted or compressed against the body of the fetus. A study was made

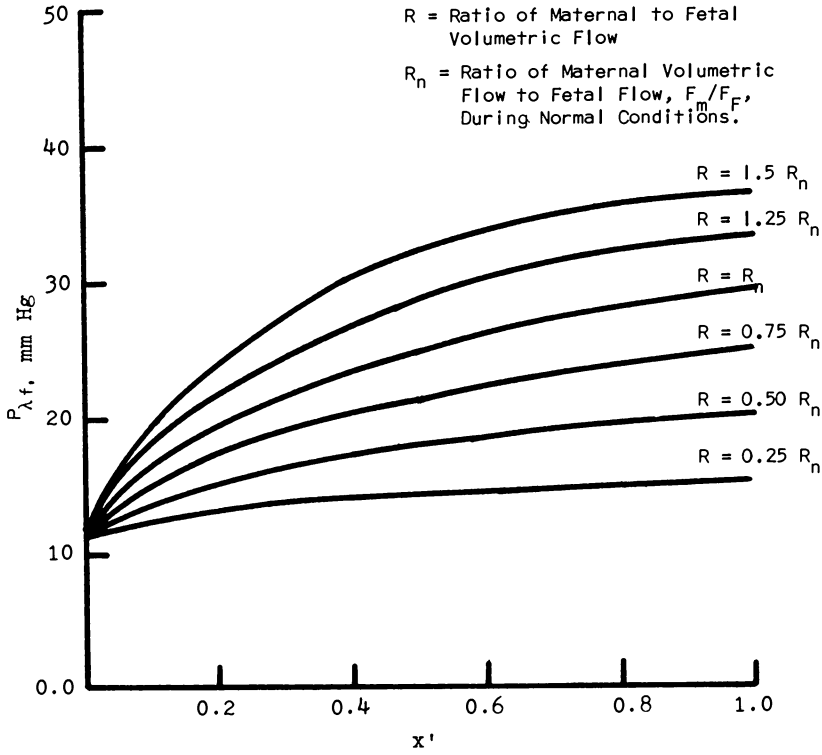

Figure 5. Axial partial pressure profiles in the fetal capillary for various maternal to fetal volumetric flow rate ratios. Maternal volumetric flow rate held constant.

to determine the effects of reducing fetal blood flow rate while the maternal blood flow rate was held constant at the normal value.

Figure 5 shows the results of reducing the fetal blood flow rate on the fetal capillary axial oxygen partial pressure profile. As the fetal blood flow rate is decreased, axial oxygen partial pressure profiles in the fetal capillary are shifted upward. Examination of the axial oxygen partial pressure profiles in the fetal capillary shows that at reduced fetal blood volumetric flow rates the initial slope of the profile is increased as fetal blood oxygen partial pressure values rise above those of the normal. This increase in fetal blood oxygen partial pressure is caused by the decrease in the amount of hemoglobin present within the capillaries per unit of time. Thus, if the initial rate at which oxygen is transferred remains the same as in the normal case, the fetal hemoglobin becomes saturated more quickly and fetal P_{O_2} increases at a faster rate.

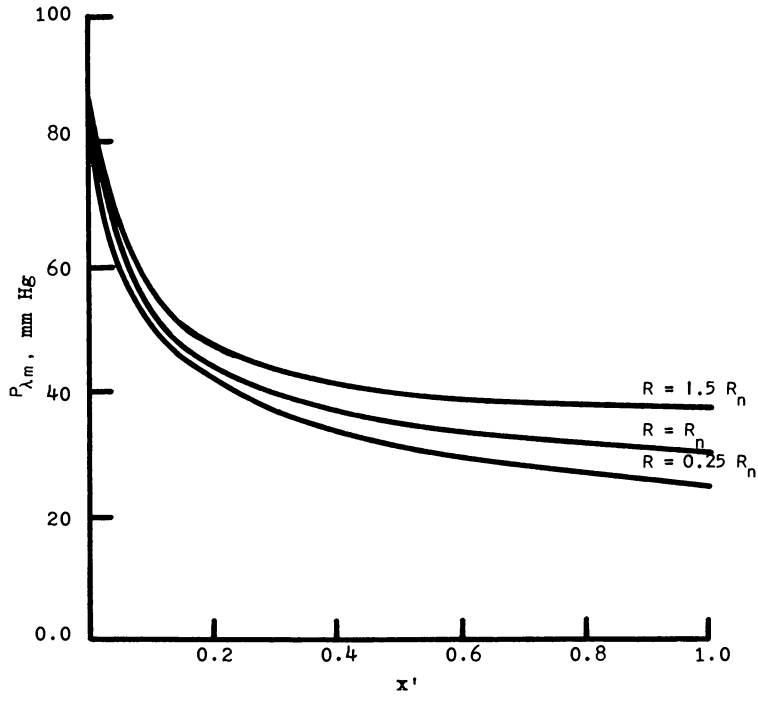

Figure 6. Axial partial pressure profiles in the maternal channel for various maternal to fetal volumetric flow ratios. Maternal volumetric flow rate held constant.

Figure 6 shows the effects of reduced fetal blood volumetric flow rate on the maternal blood axial oxygen partial pressure profile. As fetal blood flow rate decreases and fetal blood oxygen partial pressures increase,

equilibration occurs at higher oxygen partial pressures. If the fetal blood flow rate is allowed to increase indefinitely, the quantity of oxygen transferred asymptotically approaches a constant value above the normal. However, if the fetal blood flow rate is allowed to approach zero, the amount of oxygen transferred approaches a very small value.

A decrease in fetal blood flow rate leads to an increase in the oxygen partial pressure of fetal blood returning to the fetus if all other variables remain constant. This is misleading since it appears that the fetus will be better oxygenated than under normal conditions. However, it should be remembered that the quantity of oxygen returning to the fetus per unit of time is considerably less than under normal conditions. Therefore, high oxygen concentration levels resulting from reduced fetal blood flow are quite misleading and cannot be used as an indication of fetal health.

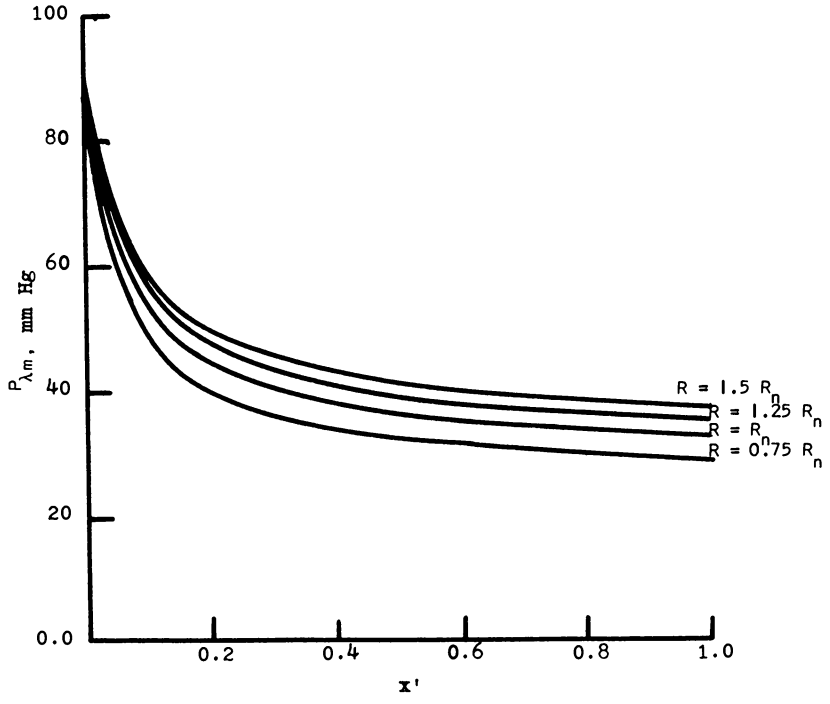

Figure 7. Axial partial pressure profiles in the maternal channel for various maternal to fetal volumetric flow rate ratios. Fetal volumetric flow rate held constant.

MATERNAL VOLUMETRIC FLOW RATE. During pregnancy the mother may contract any of several pathological conditions that can alter the rate of maternal blood flow. For example, a decrease in the maternal

blood flow rate may result from intravascular erythrocyte agglutination. In intravascular agglutination the smallest capillaries become plugged, and the blood flow rate through others becomes greatly reduced. This effect is felt throughout the entire circulatory system, and it is not probable that the placenta is an exception.

A study was made to determine the effects of reducing the maternal blood flow rate on maternal and fetal blood oxygen partial pressures. Figure 7 shows that as maternal blood flow rate decreases, the maternal blood axial oxygen partial pressure profiles are shifted downward. This results in oxygen partial pressures that are lower than the normal at all points along the exchange unit length.

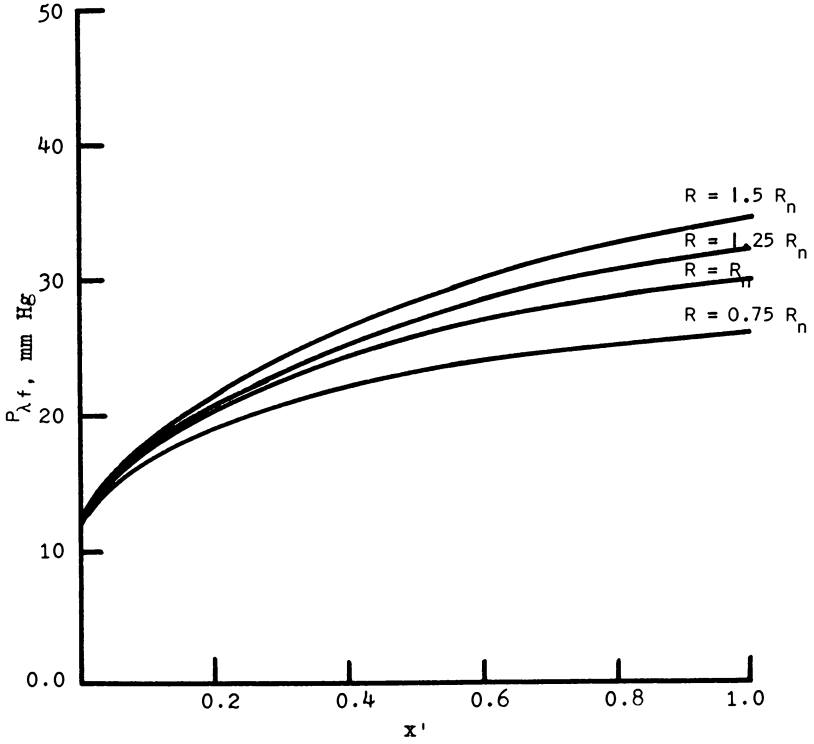

Figure 8. Axial partial pressure profiles in the fetal capillary for various maternal to fetal volumetric flow rate ratios. Fetal volumetric flow rate held constant.

Figure 8 shows the effects on the fetal blood axial oxygen partial pressure profile when the maternal blood flow rate is decreased. As the maternal blood flow rate decreases, the fetal profile is shifted downward, resulting in fetal blood oxygen partial pressure values in the fetal capillary that are lower than normal.

These changes may be explained in the following manner. As the maternal blood flow rate is reduced, the quantity of blood, and consequently, the quantity of oxygen flowing past the exchange area per unit of time, is reduced. Thus, the amount of oxygen available for transfer per unit of time is decreased. The amount of oxygen removed is reduced but not to the same degree as the maternal blood flow rate. Consequently, the percent of oxygen removed from each milliliter of maternal blood in the reduced flow rate state is greater than that removed in the normal flow rate state. This is shown by a decrease in maternal blood oxygen concentration to values that are below the normal values as shown in Figure 7.

However, since the total quantity (not percent) transferred to fetal blood is less, the oxygen partial pressure within the fetal capillary decreases as shown in Figure 8. This analysis was confirmed by additional calculations which determined the total quantity of oxygen transported.

Calculations show that if the maternal blood flow rate is allowed to increase indefinitely while fetal blood flow rate is maintained constant, the quantity of oxygen transferred increases asymptotically toward a value above the normal. Reductions in maternal blood flow rate in the normal region ($F_m/F_f = 2.1$) result in only small decreases in the amount of oxygen transferred.

During fetal anoxia or hypoxia, an increase in the maternal blood volumetric flow rate not only results in an increase in the amount of oxygen transferred, but also increases the oxygen partial pressure in the fetal blood leaving the placenta. Oxygen partial pressure and oxygen content are increased. A larger gradient is present for diffusion of oxygen between fetal blood and fetal tissue. In the previous study it was shown that a similar increase in fetal blood flow increased the quantity of oxygen transferred but decreased fetal oxygen partial pressure values. Consequently, from a control viewpoint it is probably better to have an increase in maternal blood flow rate rather than an increase in fetal blood flow rate.

OXYGEN CAPACITY OF MATERNAL BLOOD. Certain types of anemia decrease the oxygen capacity of blood. Since the oxygen capacity of blood is a measure of the amount of oxygen that can be carried by blood, any decrease in the oxygen capacity will result in a decrease in the oxygen available for diffusion. During pregnancy the degree of oxygenation of fetal blood depends on the amount of oxygen carried to the placenta in the mother's blood. Thus, maternal anemia is a possible hazard to the welfare of the fetus.

Figure 9 shows the effects of decreasing the oxygen capacity of maternal blood on the maternal axial oxygen partial pressure profile. In the normal case (N_2 = 16 ml oxygen/100 ml blood) maternal arterial blood enters the exchange unit at an oxygen partial pressure of 90.5 mm

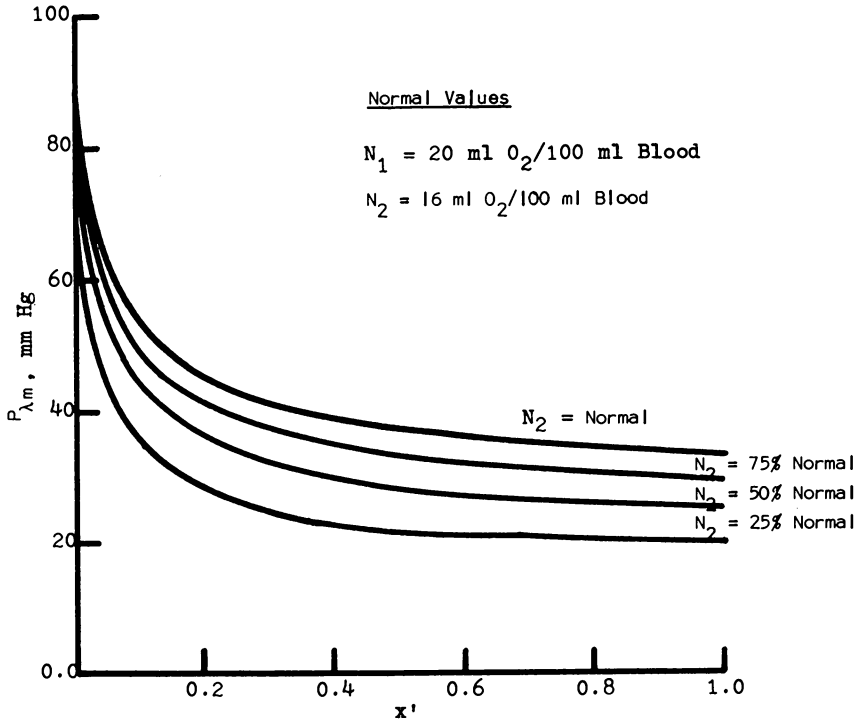

Figure 9. Axial partial pressure profiles in the maternal channel for various maternal blood oxygen capacities

Hg and leaves at a pressure of about 33 mm Hg. The initial rapid drop in the curves can be explained if the oxygen dissociation curve of maternal blood is examined. Maternal arterial blood enters at an oxygen partial pressure of 90.5 mm Hg. At this oxygen partial pressure the hemoglobin in maternal blood is almost saturated. The first oxygen which diffuses to the fetal blood is that which is physically dissolved in the maternal blood. As this oxygen diffuses, the oxygen partial pressure in the maternal channel decreases, and chemically combined oxygen is released from hemoglobin. In the 60–95 torr range on the oxygen dissociation curve, however, a given decrease in oxygen partial pressure results in a smaller amount of oxygen being released from hemoglobin than the same change yields on the linear portion of the curve. This partially accounts for the initial rapid drop in the profiles of Figure 9. As the maternal oxygen partial pressure drops below 60 mm Hg, the vertical position of the oxygen dissociation curve is reached and large amounts of oxygen are released to the system for small changes in maternal oxygen partial pressure. The amount of oxygen released approaches that which is removed,

resulting in the small slope and straight line appearance of the curve. As maternal and fetal blood flows down the exchange unit, the radial oxygen concentration gradient decreases, producing a reduction in the rate of oxygen transfer. This also accounts for the decrease in the slope of the axial oxygen partial pressure profile.

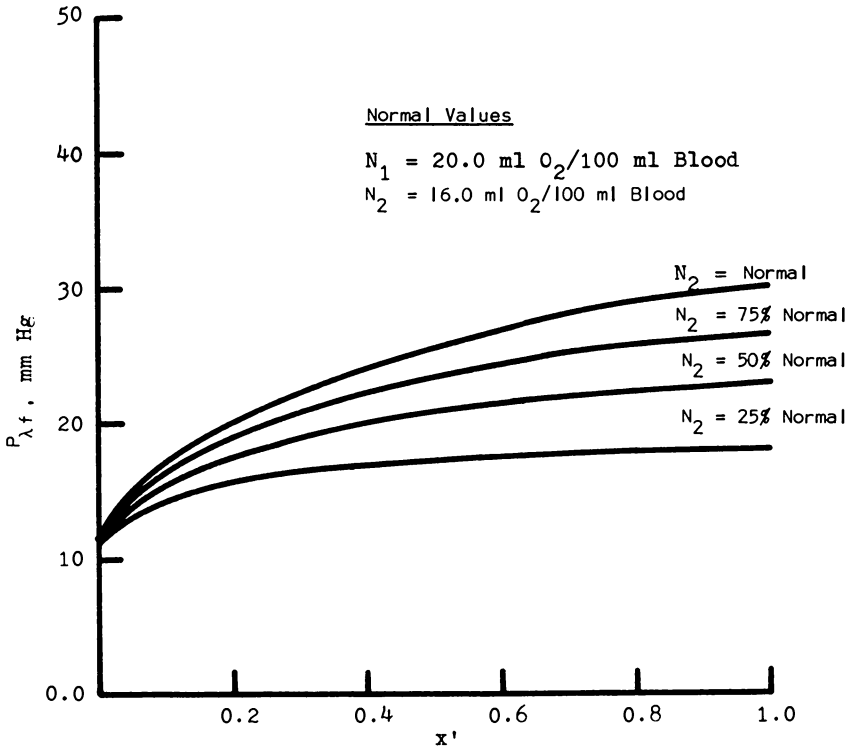

Figure 10. Axial partial pressure profiles in the fetal capillary for various maternal blood oxygen capacities

The effects of decreasing the maternal blood oxygen capacity on the fetal blood axial partial pressure profiles are shown in Figure 10. As the oxygen capacity of maternal blood decreases, the fetal axial oxygen partial pressure profile is shifted downward.

Fetal blood enters the placenta with an oxygen partial pressure of about 10.9 mm Hg. At this fetal blood oxygen partial pressure, the steep portion of the fetal oxygen dissociation curve is being used. The majority of the oxygen diffusing into the fetal stream combines with fetal hemoglobin, resulting in the slow increase in fetal blood oxygen partial pressure.

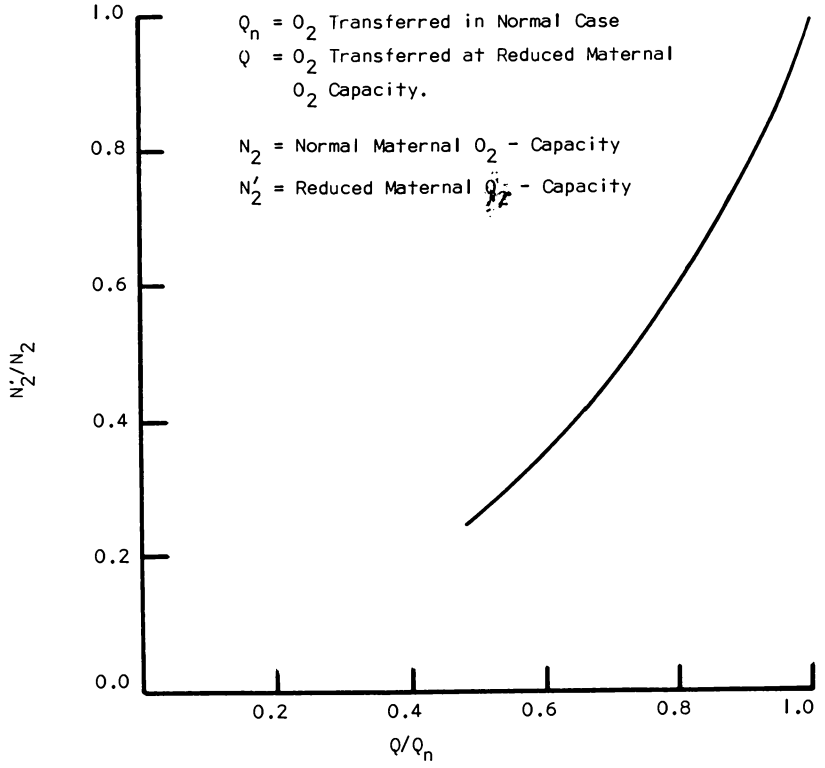

Figure 11. Fractional reduction in maternal oxygen capacity vs. *fractional reduction in oxygen transferred*

The fetal blood oxygen partial pressure values in the first half of the fetal capillary increase more rapidly than those in the second half. This results from the large pressure gradient initially present between maternal and fetal streams rather than the slope of the dissociation curve. As the last half of the exchange system is reached, maternal and fetal values approach each other, the gradient is decreased, and the rate of oxygen transfer decreases.

Figure 11 shows the effects of decreasing maternal blood oxygen capacity on the amount of oxygen transferred from maternal to fetal blood. The shape of the curve is interesting in that rather large reductions in maternal blood oxygen capacity are required in the normal region before a significant reduction in the amount of oxygen transferred occurs. In the lower region of the curve (below 40% of the normal value) small decreases in maternal blood oxygen capacity result in large decreases in the amount of oxygen transferred.

Oxygen Capacity of Fetal Blood. The effect of decreasing the oxygen capacity of fetal blood is presented in Figures 12, 13, and 14.

Figure 12 shows the effects of decreasing the fetal blood oxygen capacity on the fetal axial oxygen partial pressure profile. The lower curve is that of the normal with $N_1 = 20$ ml oxygen/100 ml blood. As fetal blood oxygen capacity decreases, the initial change in the fetal blood oxygen partial pressure becomes much more rapid. In the most extreme case studied (oxygen capacity equal to 20% of normal) the exit fetal blood oxygen partial pressure increased to a value of 60 mm Hg for a 100% increase over the normal value of 30 mm Hg.

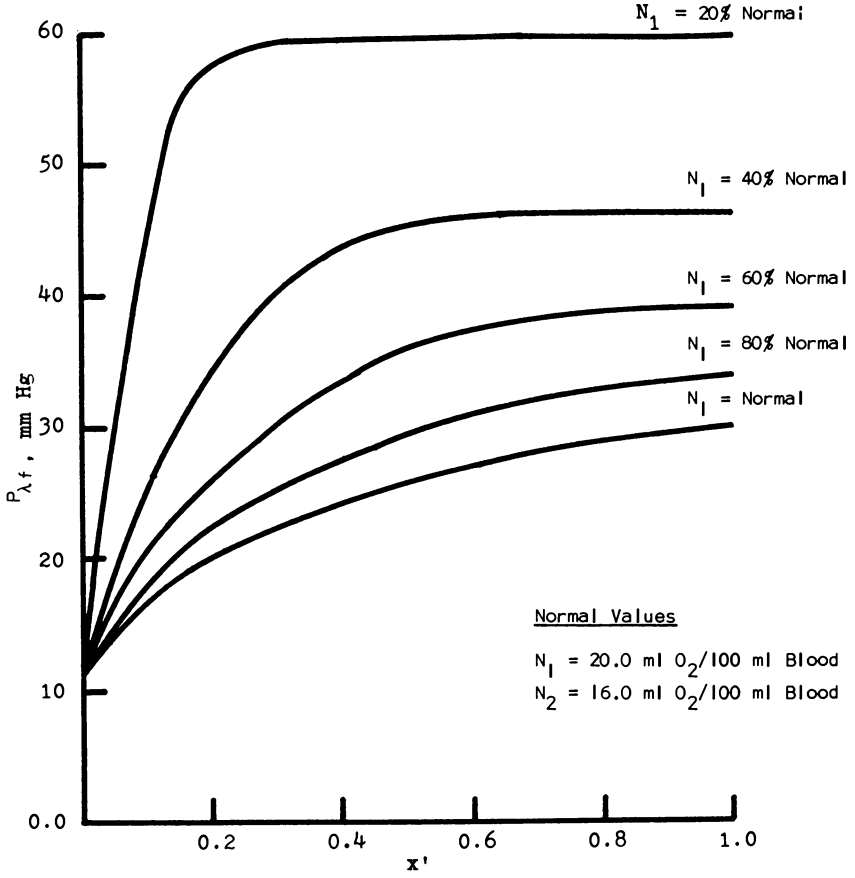

Figure 12. Axial partial pressure profiles in the fetal capillary for various fetal blood oxygen capacities. Maternal blood oxygen capacity held constant.

Since the calculated fetal blood oxygen partial pressure leaving the placenta is higher during the simulated anemic conditions, it may appear that the fetus is better oxygenated. This is not the case. As the oxygen capacity of fetal blood decreases, the total quantity of oxygen that can combine with fetal hemoglobin decreases. Fetal hemoglobin saturates

quickly, which results in an increase in the amount of oxygen physically dissolved in the fetal blood plasma. This causes a rapid increase in the fetal blood oxygen partial pressure. As the oxygen partial pressure in fetal blood increases, the radial maternal to fetal oxygen partial pressure gradient decreases, and the total quantity of oxygen transferred decreases.

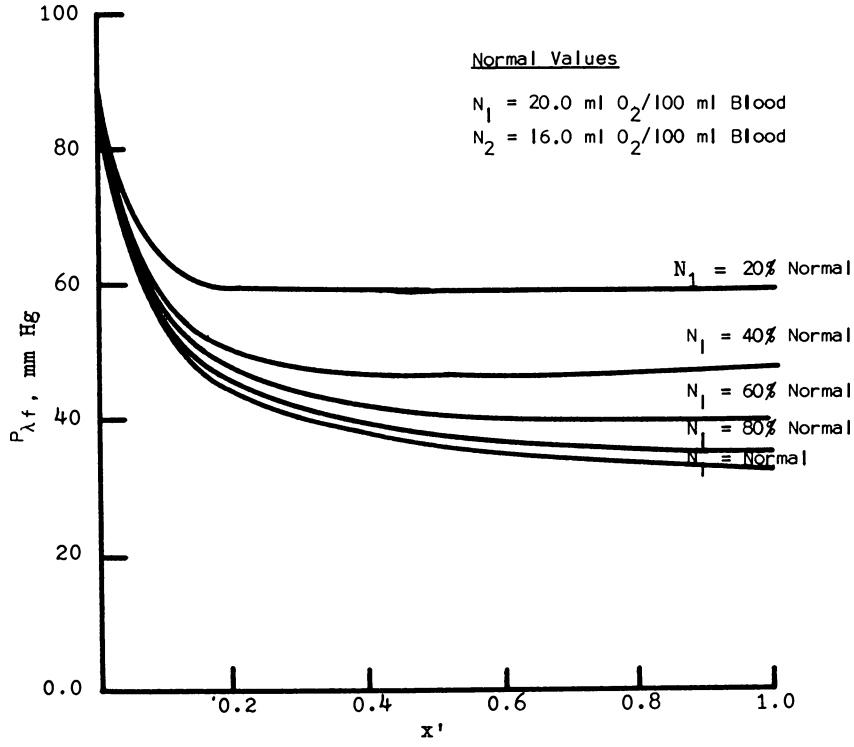

Figure 13. Axial partial pressure profiles in the maternal channel for various fetal blood oxygen capacities. Maternal blood oxygen capacity held constant.

Figure 13 shows the effects of decreasing fetal blood oxygen capacity on the maternal blood axial oxygen partial pressure profiles. As the fetal blood oxygen capacity decreases, the maternal oxygen partial pressure at the exit of the exchange unit increases. The maternal oxygen partial pressure reaches a constant value at increasingly shorter distances down the exchange path. The same effect was observed in the fetal capillary. If the maternal and fetal profiles are compared as the fetal oxygen capacity is decreased, the equilibration of oxygen partial pressures occurs at higher and higher values and at increasingly shorter distances down the exchange unit length. In the case where the fetal oxygen capacity is 20% of the normal value, equilibration has occurred at an oxygen

partial pressure of 60 mm Hg after the blood has traveled less than 20% of the entire exchange unit length. At this point diffusion has stopped since there is no longer a radial gradient, yet the maternal blood has released only a small amount of its total oxygen supply.

Figure 14 shows the effects of fetal blood oxygen capacity on the quantity of oxygen transferred from maternal to fetal blood. As the fetal blood oxygen capacity decreases, the amount of oxygen transferred decreases. Large reductions in fetal blood oxygen capacity are required in the normal region before a significant reduction in the amount of oxygen transferred occurs.

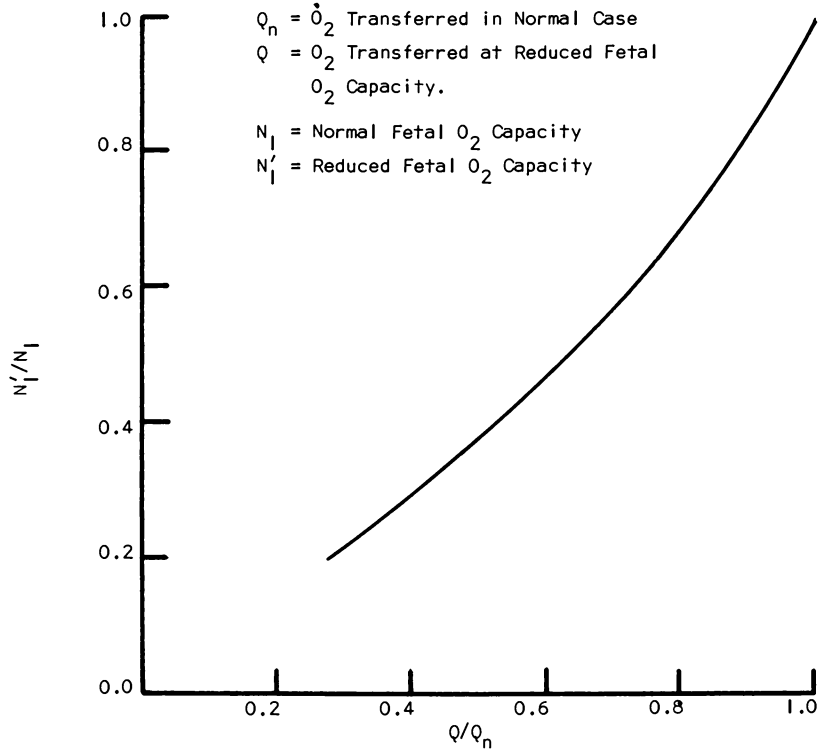

Figure 14. Fractional reduction in fetal oxygen capacity vs. *fractional reduction in oxygen transferred*

OXYGEN DIFFUSIVITY. A study was also made to determine the effects of simultaneously decreasing the oxygen diffusivity of maternal and fetal blood. Figures 15 and 16 show the effect on the maternal and fetal axial oxygen partial pressure profiles, respectively. For comparison purposes, normal conditions are represented by a blood diffusivity of $D = 0.112 \times 10^{-4}$ cm^2/sec.

If the maternal and fetal curves are compared as the diffusivity decreases (diffusion resistance increases), the fetal blood oxygen partial pressure values at the end of the fetal capillary decrease, whereas the maternal oxygen partial pressure values increase. The decrease in the amount of oxygen diffusing out of the maternal stream per unit of time is paralleled by an equal decrease in the amount of oxygen diffusing into the fetal capillary. Thus, as diffusivity decreases, the initial slope of the fetal oxygen partial pressure profile decreases, resulting in decreased fetal values. Very significant changes occur for a tenfold decrease in diffusivity.

Oxygen Solubility in Blood. In addition to the diffusivity study, an investigation was made to determine the effects of simultaneously decreasing the solubility of oxygen in maternal and fetal blood on the fetal and maternal blood axial partial pressure profiles. Comparison of the results of this study showed that a tenfold decrease in oxygen solubility had essentially the same effect on the axial oxygen partial pressure profiles as a tenfold decrease in oxygen diffusivity. Examination of the equations for the fetal capillary and maternal channel offers an explana-

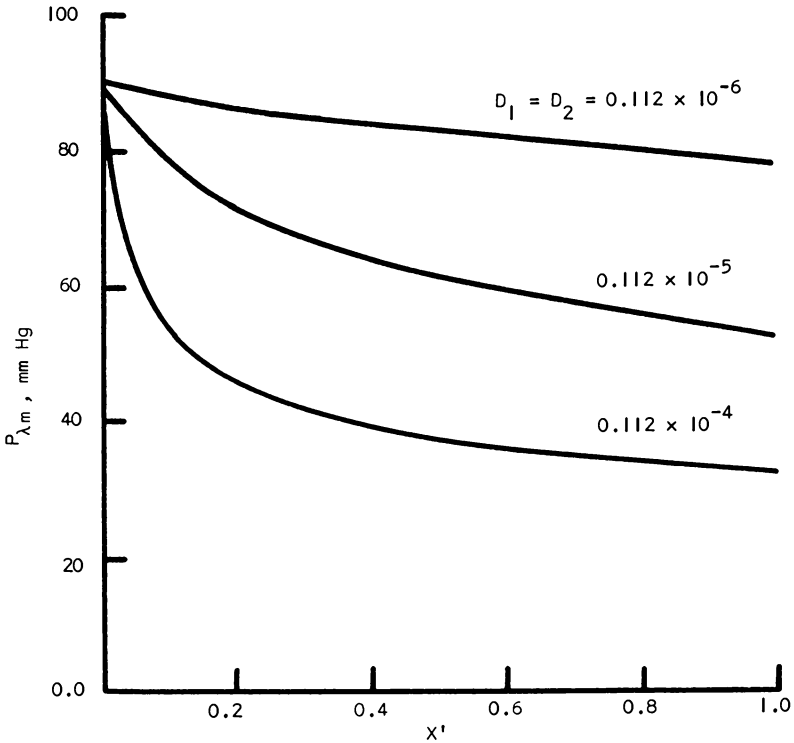

Figure 15. Axial partial pressure profiles in the maternal channel for various oxygen diffusivities

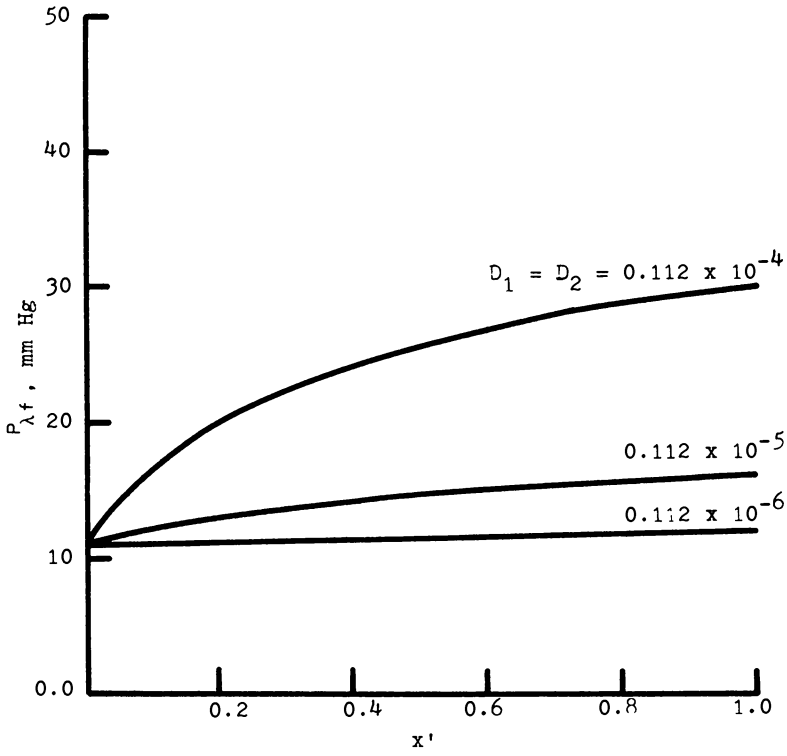

Figure 16. Axial partial pressure profiles in the fetal capillary for various oxygen diffusivities

tion. If the maternal channel equation is rearranged, it may be shown that for the steady state,

$$0 = \frac{\partial^2 P}{\partial r^2} + \frac{1}{r}\frac{\partial P}{\partial r} - \frac{V_2}{D_2}\frac{\partial P}{\partial x} - \frac{V_2 N_2 k_2 n_2 P^{n_2-1}}{D_2 c_2 (1 + k_2 P^{n_2})^2}\frac{\partial P}{\partial x}$$

Similarly, the fetal capillary equation may be rearranged to give,

$$0 = \frac{\partial^2 P}{\partial r^2} + \frac{1}{r}\frac{\partial P}{\partial r} - \frac{V_1}{D_1}\frac{\partial P}{\partial x} - \frac{V_1 N_1 k_1 n_1 P^{n_1-1}}{D_1 c_1 (1 + k_1 P^{n_1})^2}\frac{\partial P}{\partial x}$$

The last two terms in each equation represent the oxygen transported in the capillary by the convective flow of blood. The terms

$$\frac{V_1}{D_1}\frac{\partial P}{\partial x} \text{ and } \frac{V_2}{D_1}\frac{\partial P}{\partial x}$$

represent the transport of dissolved oxygen in the fetal and maternal plasma, respectively. The terms containing the nonlinear coefficients rep-

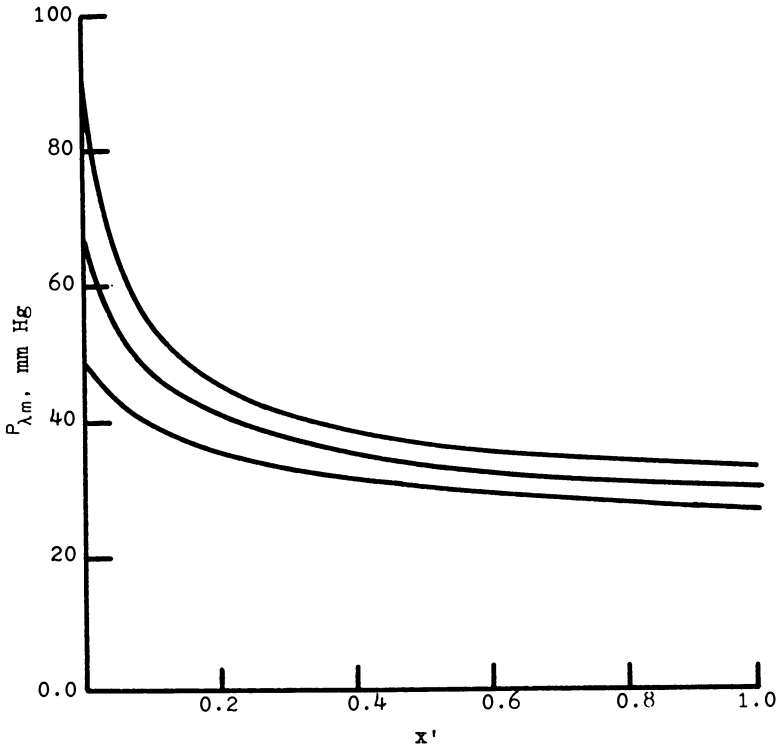

Figure 17. Axial oxygen partial pressure profiles in the maternal capillary for various maternal entrance oxygen partial pressures

resent the convective transport of oxygen chemically combined with hemoglobin. Since under conditions of normal hematocrit the amount of oxygen chemically combined with hemoglobin is much larger than that physically dissolved in the plasma, the effect of the convective transport term for chemically combined oxygen is much larger than that of the term for the convective transport of physically dissolved oxygen. The convective transport terms for physically dissolved and chemically combined oxygen are affected by the diffusivity (D_1 or D_2) while only the convective transport term is affected by the solubility. Since the overall effect of the term for the convective transport of physically dissolved oxygen is small in comparison to that for chemically combined oxygen, the effect of diffusivity on that term is of small consequence. Thus, diffusivity and solubility changes produce essentially the same results. Although small differences do exist, they are too small to be represented graphically. (Under extreme conditions of anemia and hyperbaria results would be different.)

MATERNAL ARTERIAL PARTIAL PRESSURE OF OXYGEN. At high altitudes the oxygen partial pressure in air is decreased. This results in a decrease in the saturation of the hemoglobin in the blood. Certain pathologic conditions may occur which can also decrease the lungs' ability to saturate hemoglobin with oxygen. A study was made to determine the effects of such conditions on the oxygenation of fetal blood.

Figures 17 and 18 shows the effects produced on maternal and fetal blood when the arterial oxygen partial pressure of maternal blood is decreased.

Calculations on the total quantity of oxygen transported indicate that small increases or decreases in the arterial oxygen partial pressure of maternal blood have little effect on total oxygenation. Decreases in maternal arterial oxygen partial pressure are relatively insignificant until an arterial oxygen partial pressure of 60 mm Hg is reached. Small reductions below 60 mm Hg result in significant reductions in oxygen transported.

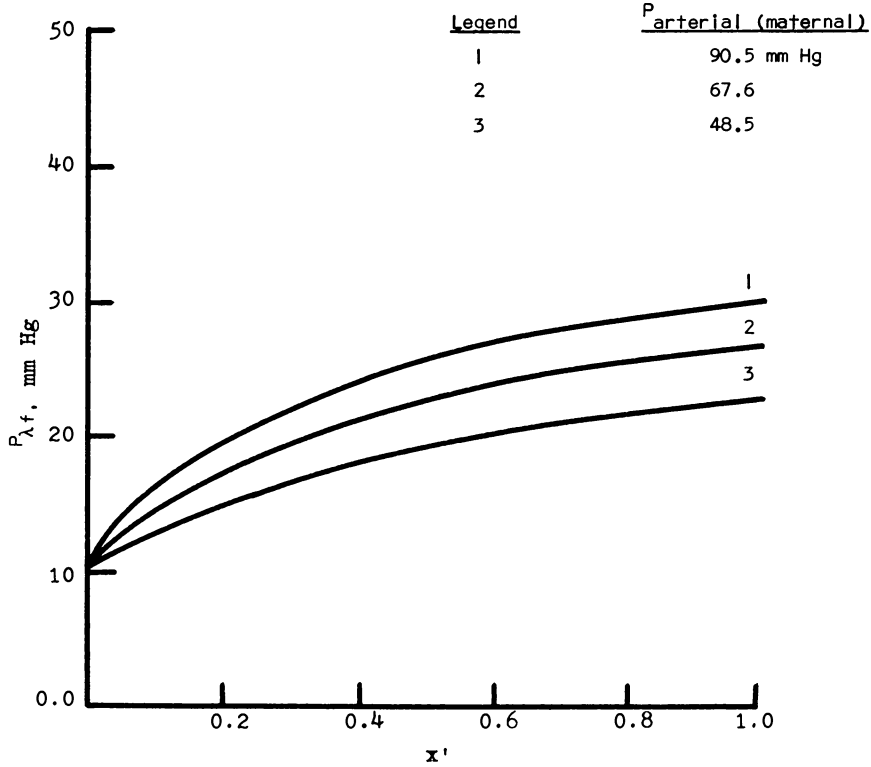

Figure 18. Axial oxygen partial pressure profiles in the fetal capillary for various maternal entrance oxygen partial pressures

The trend of the study indicated that unusually high hyperbaric conditions are required to increase significantly fetal oxygenation.

Unsteady-State Analysis Neglecting Axial Dispersion and Tissue Effects. In this unsteady-state analysis of the model, two specific studies were conducted for a single exchange unit. The first study consisted of determining the response of the end capillary fetal oxygen concentration after step changes on the maternal blood velocity were placed on the system. (End capillary maternal and fetal oxygen concentrations are the oxygen concentrations of maternal and fetal blood at the exits of the maternal and fetal channels of the basic exchange unit shown in Figure 3.) The second study involved the determination of the transient response of fetal end capillary oxygen concentration after a maternal velocity change given by a sinusoidal function was placed on the system. A detailed discussion of these studies follows.

STEP CHANGE ON MATERNAL VELOCITY. During pregnancy, especially during the latter stages of labor, the flow of blood on the maternal side of the placenta may be significantly reduced owing to increased amniotic pressure resulting from uterine contractions (*9, 38*). The response of the fetal blood concentration to these changes in maternal blood flow is not completely known at present. To obtain some idea of the magnitude of the reduction in the oxygen concentration of fetal blood leaving the placenta and the time required for this change to occur, several step changes in maternal blood velocity were placed on the system. The effects of these step changes in maternal blood velocity on the fetal end capillary oxygen concentration are shown in Figure 19. Figure 19 is a plot of fetal end capillary oxygen concentration *vs.* the time that has elapsed since the initiation of the step change on maternal velocity. This time is expressed in terms of the number of times the fetal blood has passed through the exchange unit—the fetal blood residence time.

Figure 19 shows that as the magnitude of the given step change on maternal velocity decreases (from 0.75 normal to 0.125 normal) the concentration of oxygen in the fetal end capillary blood is reduced. For the step change in maternal blood velocity where the new velocity is 0.75 times the normal velocity, the decrease in oxygen concentration is small. If the maternal blood velocity is reduced to one-half the normal value, the reduction in fetal oxygen concentration is greater than that experienced in going from a normal flow to 0.75 times the normal flow. The same trend is observed as the maternal blood velocity decreases from 0.5 normal to 0.25 normal and is a result of the nonlinearity of the oxygen dissociation curve at low oxygen partial pressures.

Since the consumption of oxygen by the fetus is not considered in this study, a maternal blood velocity change to a zero velocity would result in a fetal end capillary oxygen concentration that is equal to the

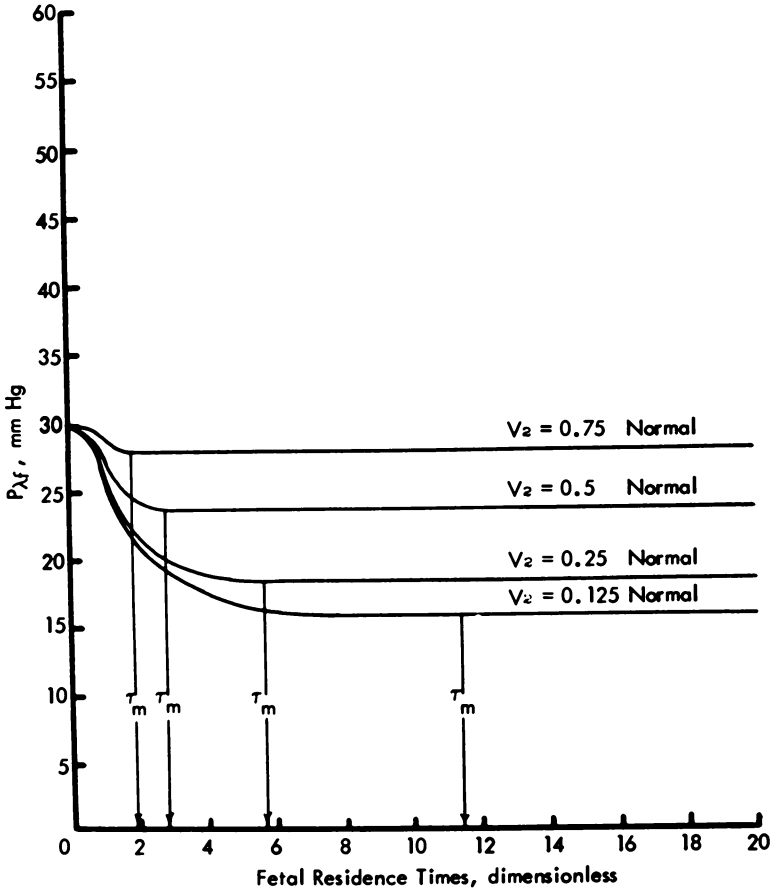

Figure 19. Fetal end capillary response to step change on maternal velocity

oxygen concentration of fetal arterial blood (for this study the normal fetal arterial oxygen concentration was taken as about 11 mm Hg). If the effects of fetal oxygen consumption were included in the model, the fetal venous end capillary oxygen concentration would approach zero as the maternal blood velocity became zero. For the present study, it must be recognized that the oxygen concentrations of fetal blood predicted by the model are higher than those that would be predicted if the model included fetal oxygen consumption. The values predicted may then be taken as safe estimates since the given step changes on maternal blood velocity would result in lower fetal end capillary oxygen concentrations if the oxygen consumption of the fetus was included.

The time required for the given change on the system to occur increases as the magnitude of the velocity change increases. For a step change in maternal blood velocity to a velocity that is 0.75 times the normal, the total change in fetal blood end capillary oxygen concentration occurs in approximately two fetal residence times. That is, the fetal blood has made two complete passes through the system. For a step change in maternal blood velocity to one-half the normal flow, about three fetal residence times are required for the change to be complete. However, in all cases the total changes occurred in approximately one maternal blood residence time. These maternal blood residence times are indicated on Figure 19 by the vertical lines labeled τ_m. These results, if compared on a dimensionless basis, are of the same order of magnitude as those of Longo and Power (*40*), who found that inert gases equilibrate between maternal and fetal exchange vessels within the time of a single capillary transient.

If a modified time constant (the time required for 62.3% of the total change to occur) is calculated for the responses of the fetal and maternal blood oxygen concentrations for the case where the step change was to a new velocity of 0.25 normal, values of 2.8 and 2.6 fetal blood residence times, respectively, are obtained. This means that the time required for 62.3% of the total change to occur is less in the fetal capillary than in the maternal channel at the exit of the exchange unit. At first examination this seems contradictory since changes in the fetal stream result from a velocity change in the maternal channel. The explanation is contained in the fact that for these studies the fetal blood velocity was taken as larger than the maternal blood velocity. After a step change on maternal blood velocity is placed on the system, the oxygen concentrations at the entrance of the system respond more quickly than those at the exit. This is expected since there is a larger radial gradient for oxygen diffusion at the entrance of the system than at the exit. Since the fetal blood velocity is greater than the velocity of the maternal blood, the effects of this initial response show up more quickly at the fetal exit than at the maternal exit.

These relationships are more evident if the transient axial response of oxygen concentration resulting from a step change in maternal velocity is studied. A study of this type was conducted in the Case 3 solution and will be discussed in detail below.

Cyclic Changes on Maternal Velocity. During labor the contractions of the uterus create a rhythmical increase and a decrease of the amniotic pressure. Although no specifically determined relationship between amniotic pressure and maternal placental blood flow rate has been shown, it is well known that the maternal blood flow rate is retarded in

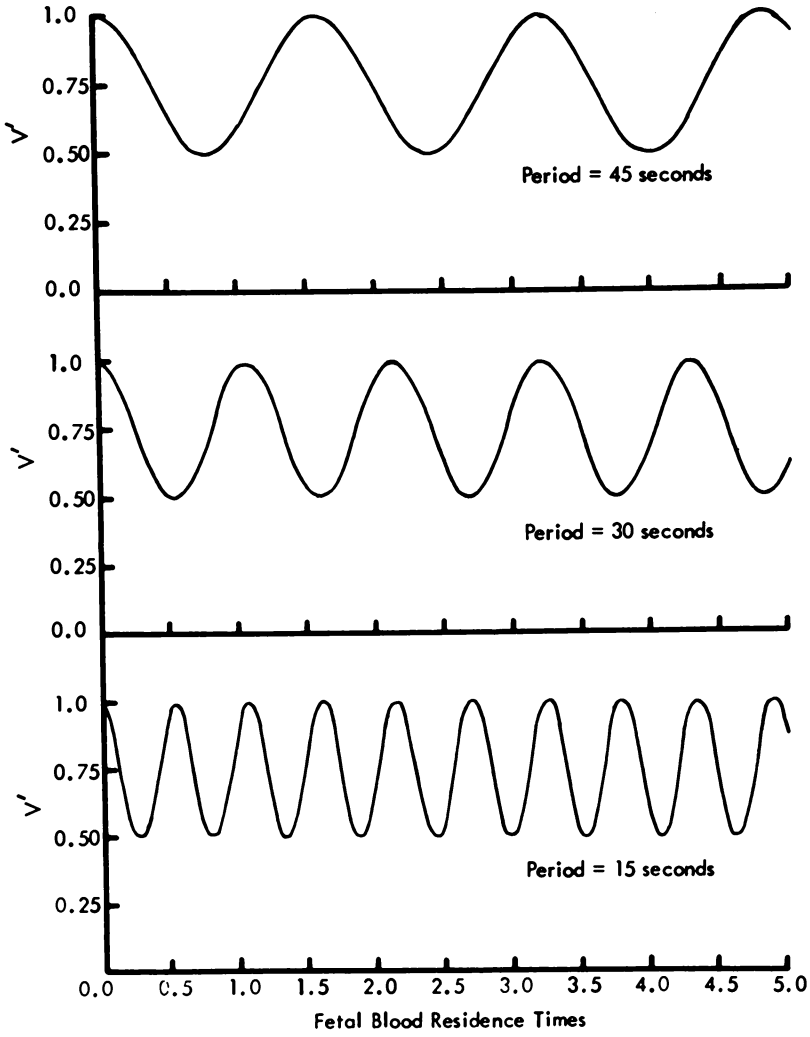

Figure 20. Plot showing sinusoidal maternal velocity functions used to create unsteady-state conditions

synchrony with uterine contractions (*9*). Since uterine contractions occur in a rhythmical fashion and since the cyclic variation of amniotic pressure resembles a series of peaks separated by a plateau, it is possible that the resulting variation in maternal blood flow rate follows the same type of relationship.

To study the effects of cyclic maternal blood flows (and consequently the effects of uterine contractions if the previous relationships exist) on the oxygenation of fetal blood in the concurrent exchange unit, the model

was solved using a sinusoidal velocity function of various periods for maternal blood flow. A sinusoidal velocity function was chosen for several reasons. During labor, amniotic pressure increases and decreases in a way which resembles a series of peaks separated by a plateau. Several investigators (9, 38) have shown that maternal blood flow into the intervillous space is reduced during the height of the contractions, but a definite relationship between amniotic pressure changes and maternal blood flow has not been determined experimentally although this relationship has been assumed to exist. The effect on fetal blood oxygenation of any number of different velocity functions might be investigated with the mathematical model. It is reasonable that maternal blood velocity will decrease during the height of a contraction (peak in amniotic pressure) and increase during relaxation (plateau region on amniotic pressure, uterine contraction relationship) and that this increase and decrease in velocity will not be so instantaneous a change as that shown by the amniotic pressure. Thus the change in velocity might resemble a sine wave. The sine wave also offered a more stable situation mathematically, and for these reasons was chosen as the velocity function for this initial study. As mentioned previously any number of different velocity functions might be studied by using the model, as well as the exact experimentally observed velocity function when it is defined by future experimental techniques. Figure 20 shows the three velocity functions which were used as input to the model. V' represents the fraction of the normal maternal blood velocity and is plotted *vs.* time expressed as number of fetal blood residence times. The velocity function shown in the top curve has a period of oscillation of 45 sec, the middle velocity function has a period of 30 sec, and the bottom curve has a period of 15 sec. All three velocity functions have an amplitude such that the minimum velocity is one-half of normal.

Figure 21 shows the response of the fetal blood end capillary oxygen concentration. Examination of these curves reveals several interesting facts. The decrease in fetal blood end capillary oxygen concentration for a sinusoidal maternal blood velocity change in which the minimum maternal velocity is one-half of the normal velocity is not as great as for a step change in maternal blood velocity to a new velocity of one-half normal. Figure 19 shows that for the step change to a new maternal blood velocity of one-half normal, the fetal blood end capillary oxygen concentration decreases to 23.6 mm Hg. For the sinusoidal case with a 45-sec period, Figure 21 shows that the fetal blood end capillary oxygen concentration decreases to only 26.3 mm Hg. This phenomenon may be explained by the period of oscillation for the velocity function. The velocity simply does not remain at its lowest value for a time long enough for the full effect of the reduced velocity to be felt.

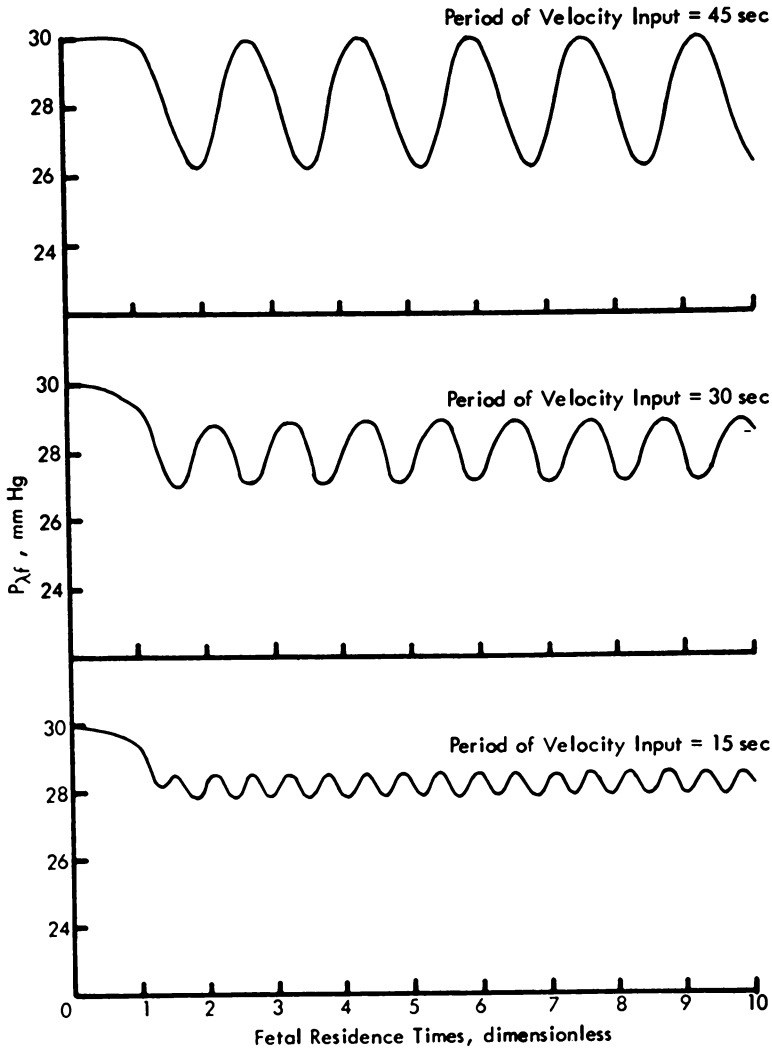

Figure 21. Plot of average concentration of fetal blood leaving exchange unit vs. *fetal residence times for sinusoidal maternal velocity changes*

Examination of the curves of Figure 21 shows that as the magnitude of the period of oscillation of the velocity function decreases (from 45 sec to 15 sec), the minimum fetal blood end capillary oxygen concentration increases from 26.3 mm Hg for a period of 45 sec to 27.8 mm Hg for a period of 15 sec. Additionally, the maximum fetal oxygen concentration decreases from 30 mm Hg (the normal value) for the 45-sec period to 28.6 mm Hg for the period of 15 sec. Thus, longer periods of contrac-

tion seem to result in more extreme reductions in fetal blood oxygen concentrations than shorter periods of contraction. The contraction of shorter period, however, maintains the fetal blood at an oxygen concentration that is constantly below the normal. During maternal sinusoidal velocity changes of long periods, the fetus may be exposed to more extreme reductions in oxygen concentration than during maternal velocity changes of shorter period, but these reductions occur only a short time. Also, with each cycle of the maternal blood velocity change, the blood oxygen concentration leaving the fetal side of the placenta returns to the normal value. Thus, at times, the fetus would be exposed to normal oxygen levels. However, during maternal blood velocity changes of short period, the fetus may be supplied with blood of oxygen concentrations

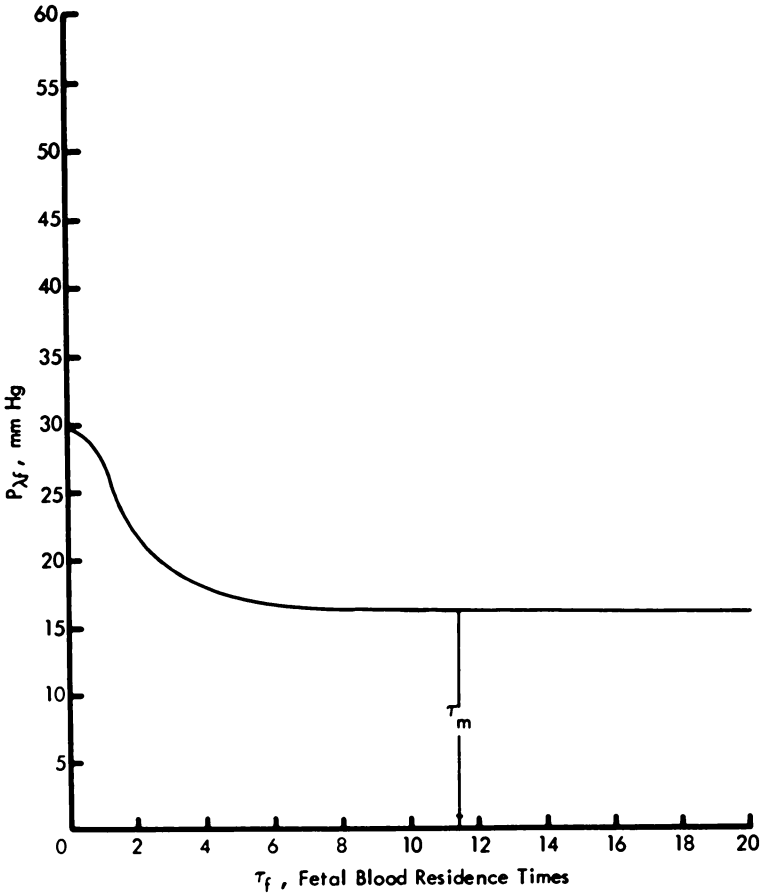

Figure 22. Fetal end capillary response to step change on the maternal velocity of $V_2 = 0.125$ *normal for the case in which axial dispersion is included*

which oscillate about a value that is lower than the normal value at all times. The question then becomes one of whether the extreme reductions of short duration are more damaging to the fetus than reductions that are less in magnitude but longer in duration. The reductions may be such that neither has a damaging effect on the fetus. Certainly, the possibility exists that velocity changes may be large enough to cause fetal distress. What the safe limits on velocity changes are cannot be quantitatively concluded by this study.

Unsteady-State Analysis Including Axial Dispersion. As in the previous unsteady-state analysis, the effects of placental barrier tissue oxygen consumption are neglected in this study. For the unsteady-state analysis of the model in which axial dispersion was included, one study was conducted. This study involved placing a step change on the maternal blood velocity to a new maternal blood velocity of 0.125 times the normal in an attempt to determine the effects of axial dispersion on the system at low maternal blood velocities. The discussion of this study is divided into the following two parts: first, the effect of axial dispersion on the response of the fetal blood end capillary oxygen concentration, and second, the effect on the transient axial profiles.

STEP CHANGE ON MATERNAL VELOCITY EFFECT ON RESPONSE OF END CAPILLARY OXYGEN CONCENTRATION. The effect of a step change on maternal blood velocity to a new velocity of 0.125 times the normal on the fetal end capillary oxygen concentration is shown in Figure 22. Figure 22 is a plot of the fetal blood oxygen concentration at the exit of the capillary system *vs.* the time that has elapsed since the initiation of the step change expressed in terms of the number of fetal blood residence times. As in the previous case which neglected the effects of axial dispersion, the reduction in maternal blood velocity causes a reduction in the fetal blood end capillary oxygen concentration. The bottom curve of Figure 19 represents the response of the fetal blood end capillary oxygen concentration to this same step change on maternal blood velocity but for the case where axial dispersion is neglected. Comparison of Figures 22 and 19 shows that the effects of axial dispersion at the reduced maternal blood velocity of 0.125 times the normal are very small.

In the fetal capillary it is not so easy to predict what the effects of axial dispersion will be. The direction of axial diffusion in the fetal channel is opposite to the direction of flow, namely from the exit of the channel toward the entrance. This should have the effect of reducing the oxygen concentration of fetal blood at the fetal capillary exit. Axial diffusion, if any, in the maternal channel, however, should increase the concentration of oxygen leaving the maternal channel. This would result in an increased radial oxygen concentration gradient between maternal and fetal blood at the exit of the system which would act to increase

the fetal blood end capillary oxygen concentration. Thus, the question of whether axial dispersion should increase or decrease the fetal blood end capillary oxygen concentration depends on whether axial diffusion in the fetal capillary has more effect than the increased radial gradient. Figures 22 and 19 show that the fetal end capillary oxygen concentration increased slightly, by about 0.5 mm Hg. This small increase may result more from the numerical error in the solution than from axial diffusion. (This error was found to vary from 1–4% depending upon the velocity change placed on the system.) The effects of axial diffusion at this level of reduced maternal blood flow appear negligible. In both cases the total change in the oxygen concentration at the exit of the maternal and fetal channels occurred in about one maternal blood residence time.

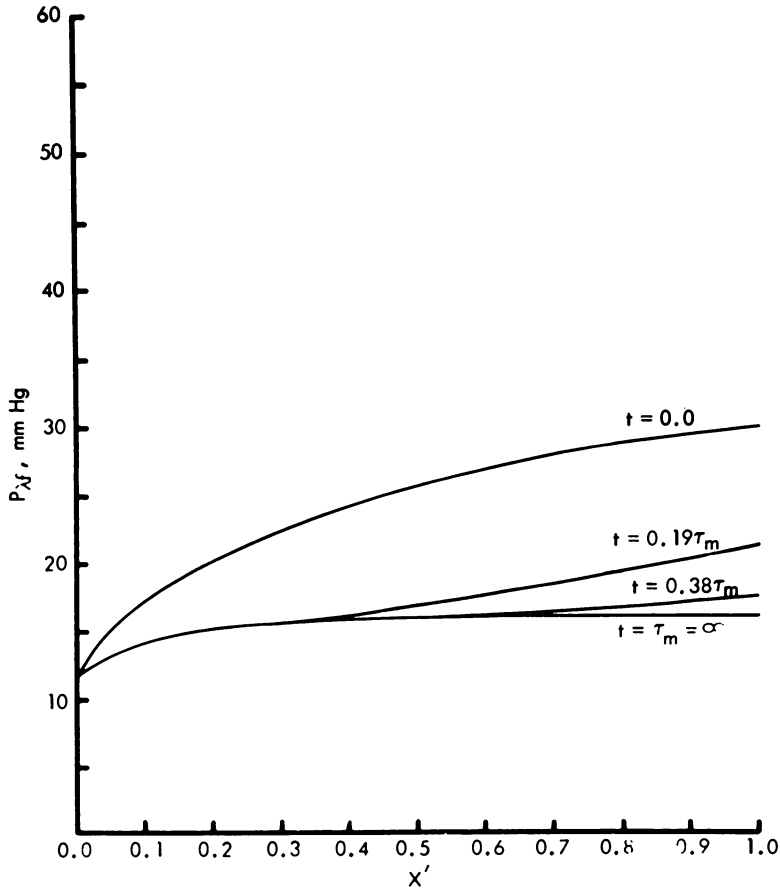

Figure 23. Axial oxygen concentration profiles for the fetal channel for transient conditions after step change $V_2 = 0.125$ normal for case including axial gradients

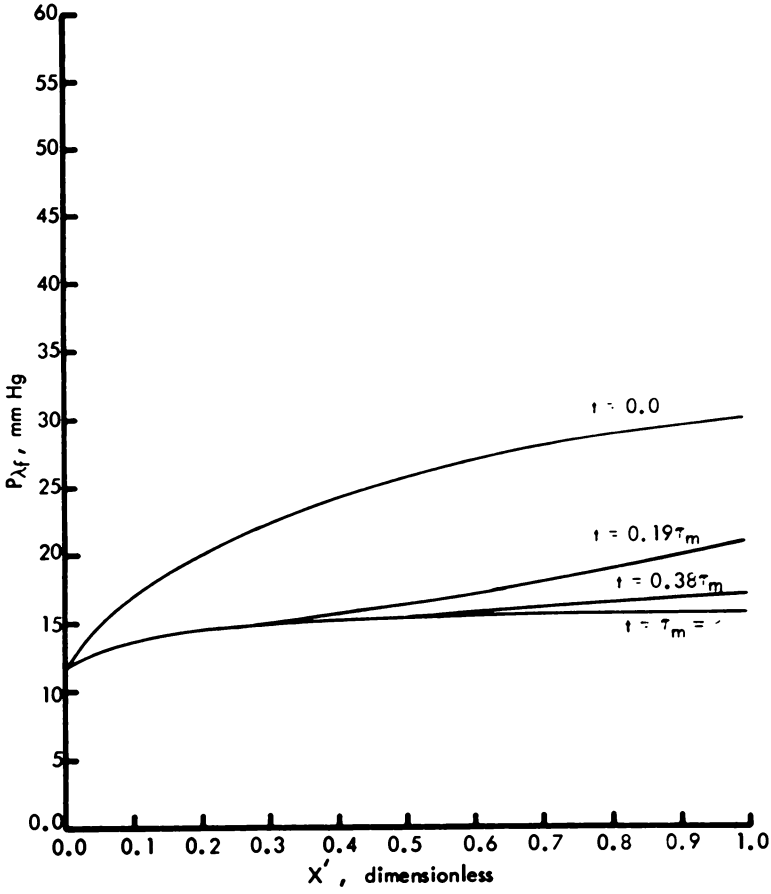

Figure 24. Axial oxygen concentration profiles for the fetal channel for transient conditions after step change $V_2 = 0.125$ normal for case without axial gradients

TRANSIENT AXIAL PROFILES. Although the effect of axial dispersion on the maternal and fetal end capillary oxygen concentrations was negligible, it is possible that the shapes of the transient axial profiles may have been affected. Figure 23 shows the axial oxygen concentration profiles for the fetal channel for transient conditions which resulted after a step change was placed on the maternal blood velocity ($V_2 = 0.125$ normal) for the case where axial diffusion was included. Examination of this figure shows that the response to the given step change occurs more rapidly at the entrance of the capillary system than at the exit. It is possible for a considerable relative time to elapse after changes occur at the entrance of the system before changes occur at the exit.

Figure 24 shows the axial oxygen concentration profiles for the fetal channel for the same transient conditions that were just discussed but for the case which neglected axial dispersion. These may be compared directly with the profiles in Figure 23 which represent the case which includes axial dispersion. As in the previous discussion, comparison of these figures shows that at this reduced maternal blood velocity the results are essentially the same, and the effects of axial diffusion are negligible.

Summary

This study was done for the specific purpose of gaining a better understanding of placental oxygen transport in the human by mathematical analysis. The assumption is often made that biological phenomena are far too complex for mathematical treatment; that they cannot be represented by equations. Knisely *et al.* (*41*) have pointed out, however, that equations are the only human device for accurate quantitative description of complex phenomena. Phenomena which have not been sufficiently analyzed (broken up into components) in one era often can be so described at some later time. The process of describing a process mathematically, then, is a continuing series of steps in which equations are added as new factors are discovered or as known factors are re-evaluated.

Serious mathematical analysis often reveals significant, previously unrecognized gaps in available biological knowledge. It is hoped that the mathematical analysis of placental oxygen transport presented in this paper will foster serious experimental investigation with regard to several areas. If serious mathematical analyses of this type are to continue, improve, and become quantitative, a means of measuring the anatomical dimensions of the placental exchange area must be developed. Other important parameters, presently believed impossible to measure, such as capillary blood flow rate, should be determined. The mathematical analysis showing the effects of reduced maternal placental blood flow during uterine contractions was based on inadequate biological data. Uterine contractions reduce maternal placental blood flow in a rhythmical manner. The authors have been forced to speculate that this variation in maternal blood flow may be represented as a sinusoidal relationship with amniotic pressure changes resulting from inadequate biological information. It is hoped that the analysis has shown that reduced maternal blood flow as a result of the uterine contractions of labor can reduce the oxygenation of fetal blood. Whether or not fetal distress can occur as a result of this reduced oxygenation can only be determined when the exact relationship between reduced maternal placental blood flow and uterine contractions is determined experimentally. Once the exact experimental

relationship is determined, the effect on fetal blood oxygenation may easily be determined with the use of the mathematical model.

The series of studies in which basic physiological parameters were varied may be used to point out which of these parameters most significantly affects placental oxygen transport. Additionally, these studies may be used with other solutions of the model in which several parameters are varied simultaneously to study possible control mechanisms which the mother–placenta–fetus system may have for maintaining adequate fetal oxygenation.

Nomenclature

A Constant metabolism of placental barrier tissue, cm^3 O_2/cm^3 tissue—sec

c_1 Oxygen solubility coefficient for fetal blood, cm^3 O_2/cm^3 blood—torr

c_2 Oxygen solubility coefficient for maternal blood, cm^3 O_2/cm^3 blood—torr

c_3 Oxygen solubility coefficient for placental barrier tissue, cm^3 O_2/cm^3 tissue—torr

D_1 Oxygen diffusivity in fetal blood, cm^2/sec

D_2 Oxygen diffusivity in material blood, cm^2/sec

D_3 Oxygen diffusivity in placental barrier tissue, cm^2/sec

k_1 Constant used in the Hill equation

k_2 Constant used in the Hill equation

K' Nonlinear coefficient $= \left[1 + \frac{N_1 k_1 n_1 P^{n_1 - 1}}{c_1(1 + k_1 P^{n_1})^2}\right]$ for fetal capillary

K'' Nonlinear coefficient $= \left[1 + \frac{N_2 k_2 P^{n_2 - 1}}{c_2(1 + k_2 P^{n_2})^2}\right]$ for maternal channel

L Length of capillary or tissue barrier, cm

n_1 Constant whose value depends on fetal blood pH

n_2 Constant whose value depends on maternal blood pH

N_1 Oxygen capacity of fetal blood at saturation, cm^3 O_2/cm^3 blood

N_2 Oxygen capacity of maternal blood, cm^3 O_2/cm^3 blood

P Oxygen partial pressure, torr

P_i Oxygen partial pressure at an interface, torr

$P\lambda$ Partial pressure of oxygen calculated from the space average fractional saturation of blood, torr

R_1 Radius of fetal capillary, cm

R_2 Radius of maternal channel, cm

R_3 Radius of tissue cylinder, cm

r' Dimensionless radial distance

r Variable radius, cm

t Time, sec

V_1 Local velocity of fetal blood in x-direction, cm/sec

V_2 Local velocity of maternal blood in the x-direction, cm/sec

V' Fractional change in velocity $= V_2/V_{\text{normal}}$, dimensionless

x Variable length, cm

x' Dimensioness axial distance

Subscripts

1 Fetal capillary value
2 Maternal channel value
3 Placental tissue barrier value
f Fetal capillary value
m Maternal channel value

Superscripts

$'$ Fetal capillary value
$''$ Maternal capillary value

Greek Letters

μ Microns
ψ Fractional saturation of blood
τ Number of residence times = time/residence time

Literature Cited

1. Guilbeau, E. J., Reneau, D. D., Knisely, M. H., "Respiratory Gas Exchange in the Placenta," L. Longo and Heinz Bartels, Eds., Department of Health, Education, and Welfare, United States Public Health Service, National Institute of Child Health and Human Development, in press.
2. Reneau, D. D., Bruley, D. F., Knisely, M. H., A Computer Simulation Showing Multiple Minute Hypoxic Areas in Cerebral Tissue As a Result of Sludged Blood, 5th European Conference on Microcirculation, Gothenburg, *Bibl. Anat.*, **10**, 540 Karter, Basel/New York, 1969.
3. Reneau, D. D., Bruley, D. F., Knisely, M. H., *JAMMI* (1970) **4**, 211.
4. Reneau, D. D., Bruley, D. F., Knisely, M. H., *A.I.Ch.E. J.* (1969) **15**, 916.
5. Reneau, D. D., Jr., Bruley, D. F., Knisely, M. H., "Chem. Eng. Med. Biol." Daniel Hershey, Ed., Plenum, New York, 1967.
6. Reneau, D. D., Bicher, H. I., Bruley, D. F., Reardon, W. C., Knisely, M. H., On-Line Computer Simulation of Oxygen Response in Brain During Anoxic-Anoxia and Hypoglycemia, *Biomedical Engineering Computer Simulation*, Preprint 20f, 69th National Meeting of A.I.Ch.E., Cincinnati, May, 1971.
7. Thews, G., Fischer, W. M., Vogel, H. R., *Pflugers Archiv.* (1965) **286**, 257.
8. Ramsey, E. M., *Amer. J. Obstet. Gynecol.* (1962) **84**, 1649.
9. Ramsey, E. M., Corner, G. W., Donner, M. W., *Amer. J. Obstet. Gynecol.* (1963) **86**, 213.
10. Boyd, J. D., Hamilton, W. J., *J. Obstet. Gynecol. Brit. Commonwealth* (1967) **74**, 161.
11. Arts, N. F. Th., *Amer. J. Obstet. Gynecol.* (1961) **82**, 147.
12. Corner, W. C., *Clin. Obstet. Gynecol.* (1963) **6**, 17.
13. Crawford, J. M., *Amer. J. Obstet. Gynecol.* (1962) **84**, 1543.
14. Dawes, G. S., "Foetal and Neonatal Physiology," Yearbook Medical Publisher, Chicago, 1968.
15. Freese, U. E., *Amer. J. Obstet. Gynecol.* (1966) **94**, 354.
16. Freese, U. E., *Amer. J. Obstet. Gynecol.* (1968) **101**, 8.
17. Barnes, A. C., "Intra-Uterine Development," Lea & Febiger, Philadelphia, 1968.

18. Krogh, A., "The Anatomy and Physiology of Capillaries," 1st ed., Yale University Press, New Haven, 1922.
19. Guilbeau, E. J., A Mathematical Simulation of Oxygen Transfer Across the Human Placenta, Masters Thesis, Louisiana Tech University, Ruston, Louisiana, 1968.
20. Thews, G., *Pflugers Archiv.* (1960) **271**, 197.
21. Blum, J. J., *Amer. J. Phys.* (1960) **198**, 991.
22. Pappenheimer, J. R., *Phys. Rev.* (1953) **33**, 387.
23. Bartels, H., Moll, W., *Pflugers Archiv.* (1964) **280**, 165.
24. Ramsey, E. M., personal communication.
25. Guilbeau, E. J., Reneau, D. D., Knisely, M. H., *Blood Oxygenation*, Proceedings of the International Symposium on Blood Oxygenation, held at the University of Cincinnati, December 1-3, 1969, Daniel Hershey, Ed., Plenum Press, New York, London, 1970.
26. Guilbeau, E. J., A Steady and an Unsteady State Mathematical Simulation of Oxygen Exchange in the Human Placenta, Dissertation, Louisiana Tech University, Ruston, Louisiana, 1971.
27. Bruley, D. F., Prados, J. W., *A.I.Ch.E. J.* (1964) **10**, 612.
28. Gonzales, L. O., Spencer, E. H., *Chem. Eng. Sci.* (1963) **18**, 753.
29. Lapidus, L., "Digital Computation for Chemical Engineers," McGraw-Hill, New York, 1962.
30. von Rosenberg, D. V., Durill, P. L., Spencer, E. H., unpublished paper, Esso Research Laboratories, Baton Rouge, Louisiana, 1960.
31. Crank, J., Nicholson, P., *Proc., Cambridge Phil. Soc.* (1947) **43**, 50.
32. Bruce, G. H., Peaceman, D. W., Rice, J. D., *J. Pet. Tech.* (1953) **5**, 70.
33. Peaceman, D. W., Rachford, H. H. Jr., *J. Soc. Indust. Appl. Math.* (1955) **1**, 28.
34. Douglas, J., *Trans. Amer. Math. Soc.* (1958) **89**, 484.
35. Brian, P. L. T., *A.I.Ch.E. J.* (1961) **3**, 367.
36. Ananthakrishnan, V., Gill, W. N., Barduhn, A. J., *A.I.Ch.E. J.* (1965) **11**, 1063
37. Wulf, H., *Amer. J. Obstet. Gynecol.* (1964) **88** (1), 38.
38. Borell, U., Ingemar, F., Ohlson, L., Wiquist, N., *Amer. J. Obstet. Gynecol.* (1965) **93**, 44.
39. Freese, Uwe E., Ranninger, Klaus, Kaplan, Howard, *Amer. J. Obstet. Gynecol.* (1966) **94**, 361.
40. Longo, L. D., Delivoria-Papadopoulos, M., Power, G. G., Hill, E. P., Forster, R. E., *Amer. J. Physiol.* (1970) **219**, 561.
41. Knisely, M. H., Reneau, D. D., Bruley, D. F., *Angiology* (1969) **20** (Suppl. to), 1–56.

RECEIVED November 22, 1972. Work supported by United States Public Health Service Grants NS-08228 and HE-04176.

8

Glucose Metabolism and Transfer in the Human Placenta

A. M. SOUCHAY, PHILIP A. RICE, J. E. ROURKE, and R. E. L. NESBITT JR.

Department of Chemical Engineering and Materials Science and Department of Obstetrics and Gynecology, State University of New York, Upstate Medical Center Syracuse, N. Y. 13210

In vitro *steady-state measurements of glucose metabolism and transfer have been made with a perfusion apparatus which simulates closely* in vivo *physiological conditions. The results suggest that glucose is metabolized by a first-order reaction in the range of 80–200 mg % and is transferred by simple diffusion. The rate constant is about 0.3/min, and the glucose metabolism rates at normal concentrations agree with metabolism rates observed in tissue studies. The glucose diffusion was determined to be about* 5×10^{-10} *cm²/sec. This value indicates that the diffusional resistance in the blood stream is negligible. The value of the diffusion observed under the conditions of the experiment is apparently not large enough to supply a mature fetus with all the glucose it needs.*

The placenta is the main organ of exchange between the mother and the fetus (Figure 1). It acts as a lung, an intestine, and a kidney and has important metabolic and endocrinologic activities. All transfer of oxygen and nutritive substances necessary to the growth and survival of the fetus, as well as the elimination of the fetal metabolic waste products, take place in the placenta.

To study some of the placental functions *in vivo* is difficult and dangerous. *In vitro* perfusion methods, provided they simulate closely enough the *in vivo* conditions, permit the study of numerous functions of the placenta in the laboratory. The placenta is one of the few human tissues available for such study.

In the earlier investigations, only the placental umbilical vessels were perfused (*2, 3, 4, 5, 6, 7, 8, 9, 10, 11, 12, 13*). In more recent studies

monitoring devices have been added to the mechanical apparatuses to depict arterial and venous flow rates, blood pH, gas concentrations, temperature, volume of perfusion fluid, pressures, etc. (*6*, *13*).

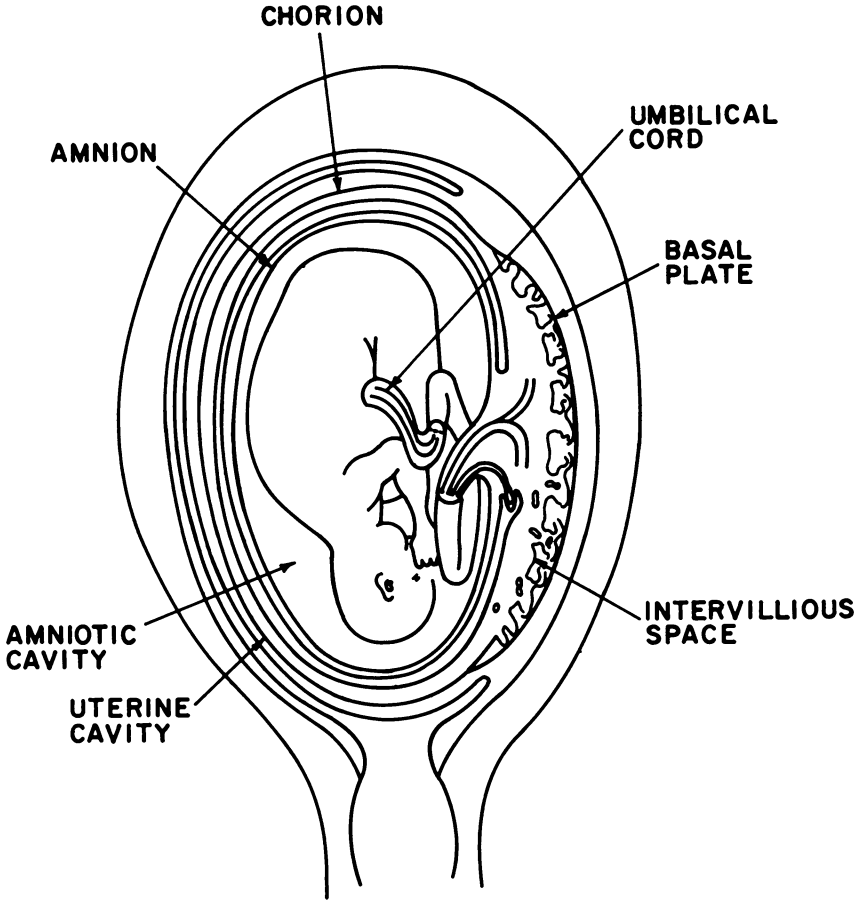

Figure 1. *A placenta* in vivo (1)
From Wilkin, "Le Placenta Humain," Masson et Cie, Paris, 1958.

Compared with the fetal side of the placenta, adequate perfusion of the material intervillous space, using extracorporeal circulatory techniques which suitably mimim physiological conditions, is difficult. Perhaps the best *in vitro* method of achieving adequate intervillous space perfusion uses semirigid polyethylene tubes fastened in the base of an artificial uterine chamber through the decidua basalis (*14*, *15*, *16*, *17*, *18*, *19*, *20*). The most sophisticated *in vitro* studies have resulted from successful perfusion of a single cotyledon through spiral arteries cannulated through their placental ends on the uterine surface (*12*).

In the experiments described here, the maternal and fetal sides of the placenta were perfused simultaneously by an apparatus in which maternal arterial inflow and maternal venous return occur through the base of the placenta, as they do *in vivo* (*20*).

A mathematical model of the transfer and metabolism of glucose in the placenta is used to interpret the experimental data. The close agreement between the results of the model and the experimental results supports these assumptions of the model and permits evaluation of diffusivity and a first-order reaction rate constant of glucose in the placenta.

Description of the Human Placenta

Morphology of the Placenta at Term. The placenta upon delivery appears as a thick (½ inch to ¾ inch), round (about 7 inches in diameter) disk, usually weighing about 600 grams. The fetal side or the chorionic plate is covered by two membranes, the amnion and the chorion, which extend from the periphery of the placenta and enclose the fetus during gestation. It thus presents a smooth aspect although the fetal vessels, filled with blood, can be seen through the transparent membranes. The umbilical cord, connecting the fetus to the placenta, usually stems from the center of the fetal side and contains two arteries and one vein for the fetal blood supply. The maternal side or basal plate looks spongy and is divided by furrows, called septa, into several roughly polygonal parts of different sizes, called lobes, numbering between 14 and 30. Those

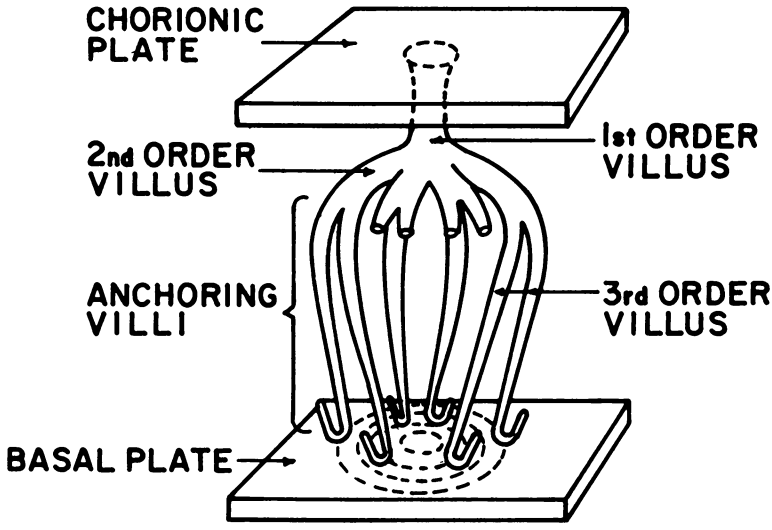

Figure 2. Schematic diagram of a chorionic tree (1)
From Wilkin, "Le Placenta Humain," Masson et Cie, Paris, 1958.

lobes, in turn, may be dissected into their constituent fetal cotyledons, each associated with a major artery and vein. There are about 200 cotyledons in an average placenta; of these, 10 are large and 50 are of medium size, constituting the bulk of the placenta (*21*). The space between the chorionic and basal plates is filled with maternal blood in which are immersed villous tufts stemming from the chorionic plate and attached to the basal plate. These villous tufts consist of small branching blood vessels which arise from the extensions of the umbilical arteries and veins lying in the chorionic plate. The interstices around the villous tufts are called the intervillous space.

The Maternal Circulation. The maternal blood flows into the intervillous space. It reaches the placenta through about 100 coiled arteries opening on the internal side of the basal plate. The outflow takes place through the veins opening from the floor of the intervillous space. Each cotyledon and its corresponding maternal bed constitute an independent unit (*22*). It is suggested in recent studies that the arterial openings lie at the center of the cotyledon, whereas the venous openings are distributed at the periphery of the cotyledon (*23, 24*).

Blood entering the placenta through the arterial openings is propelled by the maternal pressure toward the chorionic plate, the blood flowing in spurts. It circulates through the intervillous space and then is collected through the venous openings.

The Fetal Circulation. In the umbilical cord blood is conveyed from the fetus to the placenta by two arteries and from the placenta back to the fetus through a vein of larger cross section.

At the surface of the placenta, the two arteries and the vein divide into numerous branches supplying the different chorionic trees. The chorionic tree (Figure 2) is the most important structure inside the placenta. The treelike configuration of each fetal cotyledon is duplicated by the vascular system within the tree (*25*). In each cotyledon there is one chorionic tree, constituted of villi of a different order, in which the fetal vessels run.

The first-order villus is a single main stem arising from the chorionic plate in which runs one artery and one vein. Large stems (second-order villi) arise from the main stem and run parallel to the chorionic plate. They divide into 30–40 small stems (third-order villi) directed perpendicular to the plates and attached on the basal plate. From different points along these stems arise numerous smaller branches. The vascularization of the third-order villi (Figure 3) constitutes a capillary bed of arterioles and venulas which issue from the stem vessels lying just at the surface of the villi (*1, 23, 24*).

Another capillary bed called the superficial (or paravascular) network lies under the syncytial coat of the villi and is connected by a few

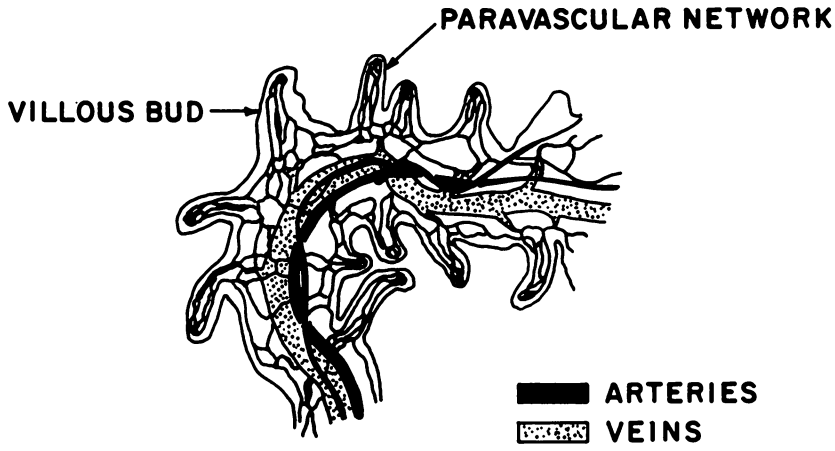

Figure 3. A tertiary villus (1)
From Wilkin, "Le Placenta Humain," Masson et Cie, Paris, 1958.

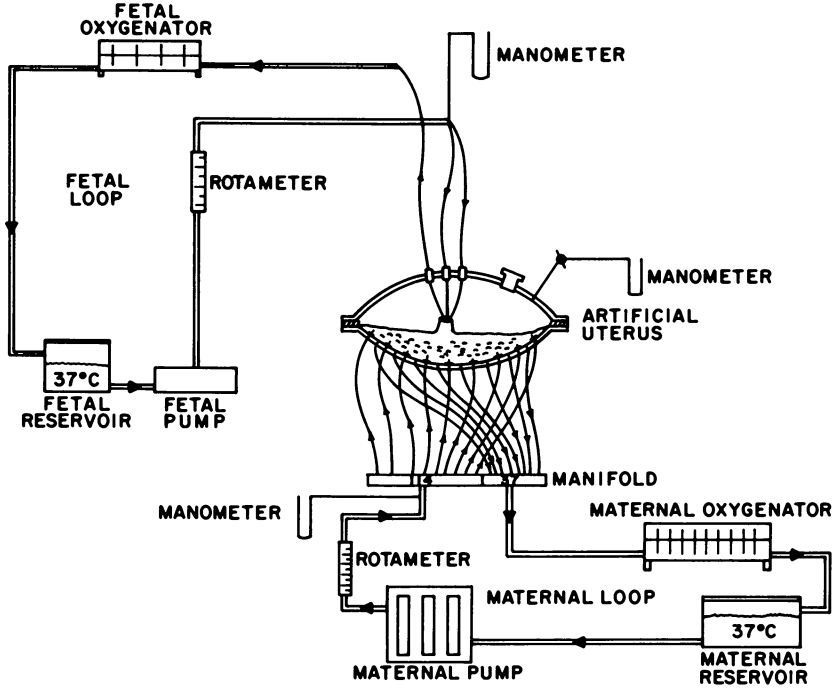

Figure 4. Schematic of the perfusion apparatus

branches to the main capillary bed. This paravascular network possibly acts as a shunt. The feto-maternal exchange takes place in the membrane between the fetal blood present in the main capillary bed and the maternal blood filling the intervillous space (*26*).

The capillary bed should be regarded as continuous in all three dimensions, and in the intervillous space the maternal blood channels resemble a labyrinth of canals with diameters of capillary dimensions (*27*). At the level of exchange, fetal and maternal blood may be considered to flow in similar channels, but the maternal channel is free of an enclosing membrane and is bounded by the villi of the capillary bed.

The Perfusion Apparatus and Perfusion Techniques

The Perfusion Apparatus. The perfusion apparatus was designed to simulate as closely as possible *in vivo* physical and physiological conditions: pressures, flow patterns, pH, temperature, oxygen pressure, etc. (Appendix IA, IB). The whole apparatus consists of three main parts: the artificial uterus which holds the placenta; the maternal circulatory loop, simulating the maternal circulation; and the fetal circulatory loop, simulating the fetal circulation (Figure 4).

The artificial uterus is made of two spherical sections of transparent Plexiglas representing the top and the bottom of the uterus (an emplacement ring is also sometimes used to hold smaller placentas in position).

The bottom of the uterus, connected with the maternal circulation through a manifold, is pierced by 151, 157-mm outside diameter (od) holes; 114 are used as arterial inlets. Through these inlets, sections of 18-gauge needles protrude 6-mm above the surface. Each of these needles is attached to a polyethylene tube. The other end of the tube is connected to the manifold (Figure 5).

Around the needle tips, 1/4-inch diameter, 1/16-inch thick rubber disks have been placed. By providing a seal for the placenta around the base of the needles, they prevent the short circuiting of the perfusion fluid and also, by slightly lifting the placenta above the surface, they permit an easier venous return through the other 37 holes flush with the uterine surface which serve as venous outlets. The return flow proceeds through polyethylene tubes to the venous compartment of the manifold.

This artificial uterus has a spherical shape approximating that of the uterus and conforming with the maternal side of the placenta. The distribution of the venous outlets as well as arterial inlets is on the base of the plate.

The placenta is connected with the fetal loop through openings in the top of the artificial uterus for the fetal arterial and venous cannulae made out of urethral catheter 8 Fr. 15 cm long. The top also contains an

amniotic fluid inlet and outlet, a manometer tap, and a plug for initially filling the amniotic fluid cavity. This cavity consists of the space left between the fetal surface of the placenta and the top of the uterus.

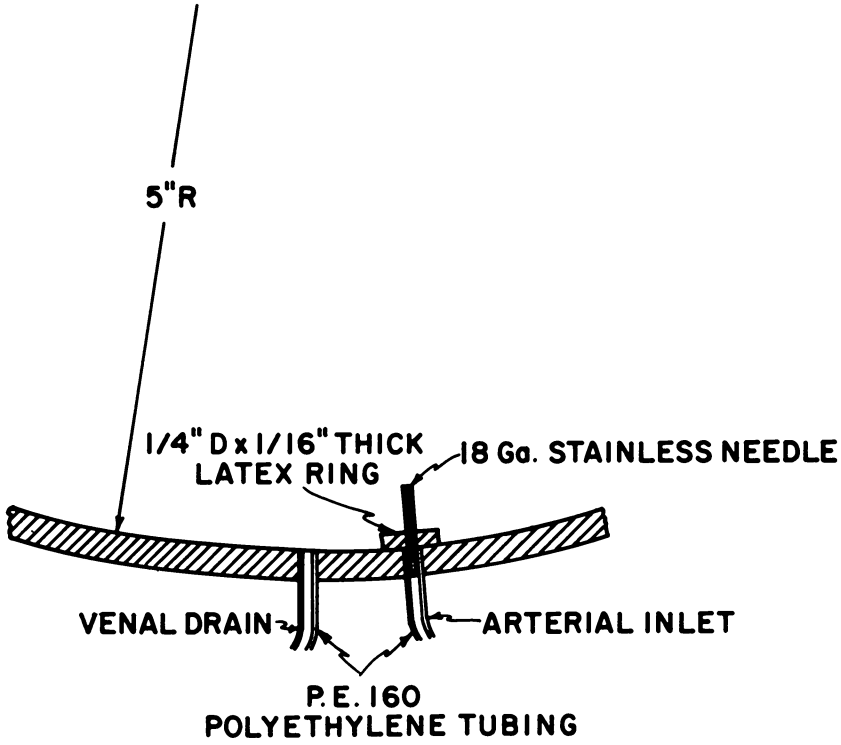

Figure 5. Detail of maternal artery and vein

The Circulatory Loops. Both loops include a reservoir, a pump, a flowmeter, and an oxygenator.

The Maternal Circulatory Loop. In the arterial circuit, maternal fluid perfusate is propelled from the maternal reservoir by a Bluemle–Holter triple chamber B-3 blood pump through a flowmeter (Gilmont Model J-228) to the arterial opening of the manifold, connected with the 114 arterial tubes. A manometer is connected just before the entrance of the manifold.

The blood, after perfusing the intervillous space, follows the venous circuit. It is first collected in the 37 venous tubes, then flows through a Tygon tube connecting the venous opening of the manifold to the disk oxygenator and back again to the maternal reservoir. The head difference between the oxygenator and the placenta approximately balances the frictional pressure drop through the tubes.

The Fetal Circulatory Loop. In the arterial circuit, blood is propelled from the fetal reservoir by the fetal pump (Masterflex No. 7545-15 variable flow), passes through a flowmeter (Gilmont Model J-288), and enters the placenta through the cannulated umbilical arteries.

In the venous circuit, the fetal blood collected in the cannulated umbilical vein flows down through the fetal oxygenator to the fetal reservoir. A positive pressure of about 15 mm Hg is maintained at the umbilical vein. A mercury manometer is connected just before the cannulae enter the amniotic fluid chamber.

The Reservoirs. The reservoirs are made from Plexiglas and are maintained at a constant temperature by a water bath. They have covers with openings for thermometers, pipettes, etc.

The Oxygenators. Both are disk oxygenators (*18*). The maternal one is used to oxygenate blood or sometimes to introduce CO_2 to regulate the maternal pH. The fetal one contains only five disks and is used mostly to introduce CO_2 into the fetal circulation at the beginning of the perfusion.

The Plexiglas Box. A Plexiglas box surrounds the artificial uterus and the manifold. Hot air is introduced through an opening in the side to maintain the placenta and the amniotic fluid at 37°C. Other equipment used included a Beckman pH meter, Beckman O_2 electrode, and CO_2 and CO_2–O_2 tanks.

Perfusion Techniques. Before the placenta can be perfused properly, it must be obtained immediately after delivery, be free from any abnormalities or lesions, have a sufficient amount of chorionic membrane to seal the placenta on the machine, and have a fairly straight umbilical cord since twisted vessels are very difficult or impossible to cannulate. Because of these requirements, only a small number of the total placentas received at the laboratory can be used for measurement (about 1 in 10).

If the above requirements are met, then the placenta is placed in the artificial uterus and perfusion by heparinized buffered solution (Appendix IA) is started as soon as possible to prevent clotting of the blood already present in the small capillaries. After the placenta is cleaned by perfusing with saline and the intactness of the placental membrane has been established, the blood perfusion is started. When the system has reached steady state (with regard to pressures, temperature, etc.) at physiological conditions, data are collected.

The final blood solution is about 1 part blood and 3 parts Krebs–Ringer bicarbonate solution. Ninety-five milliliters of 6% dextran is added to about 550 ml of the fetal blood solution to help prevent fluid from transferring from the fetal to the maternal circulations. The pH of the maternal and fetal solutions are initially in the physiological range

and are maintained there by using 5% CO_2 in the gas to the maternal oxygenator.

The fetal and maternal flow rates were set at 40–80 ml/min and 450 ml/min, respectively, and an amniotic fluid pressure of 15 mm Hg was maintained over the placenta throughout the experiment. Oxygen tensions were 60–160 mm Hg in the maternal artery and 14–28 mm Hg in the fetal vein. Glucose was added at the beginning of the perfusion to help maintain placental viability.

A summary of the operating conditions is given in Appendix IA and complete details of the operating procedure can be found in Nesbitt *et al.* (*20*).

Sampling. For steady-state experiments, glucose was added continuously to the maternal reservoir. The placenta was weighed before being placed in the artificial uterus, the rate of utilization of glucose by the placenta was then estimated, and the rate of glucose added was set approximately to the estimated rate of utilization.

Three milliliter samples were collected in both reservoirs as soon as the addition of glucose was started. Glucose concentration in the samples was analyzed by the Keston technique (*28*).

In many cases, the placenta was perfused with blood for more than 3 hours, sometimes up to 4 hours. Several tests were used to make sure that the perfusion on both sides was adequate and that the placenta was still viable at the end of our experiments.

Tests of Extent of Perfusion and Placental Viability. MATERNAL PERFUSION. The apparatus in almost all cases gave an excellent maternal perfusion. However, following a sudden decrease of the amniotic pressure, the placenta sometimes abrupted, and the maternal blood would short circuit directly to the base of the uterus. In doubtful cases maternal perfusion was checked after replacing the blood-saline solution by injecting and circulating fluorescein dye in the maternal circulation for 10 min under the same conditions of pressures and flow rates. After the placenta was removed from the uterus, it was cut, and the repartition of dye was checked under ultraviolet light. If the dye was completely spread through the intervillous space, then the perfusion was satisfactory.

FETAL PERFUSION. As soon as the saline perfusion is started, there are indications of the adequacy of the fetal perfusion: a high fetal pressure at a low fetal flow rate indicates that many capillaries are clotted. In this case, the remaining capillaries rupture and fluid transfers from the fetal to the maternal side at a high rate. Distribution of dye in the fetal circulation was also used to check the completeness of the fetal perfusion.

PLACENTAL VIABILITY. *Fluid Transfer.* Fluid transfer from the fetal to the maternal circulation of more than 2 ml/min of blood solution was

taken as an indication of deterioration of the placental cells. When fluid transfer is beyond the adopted limit, the experiment is concluded.

Fluid transfer is checked about every 15 min. In the experiments here it usually increased slowly during the first 2 or 3 hours, from approximately 0–1.5 or 2 ml/min, then increased rather quickly.

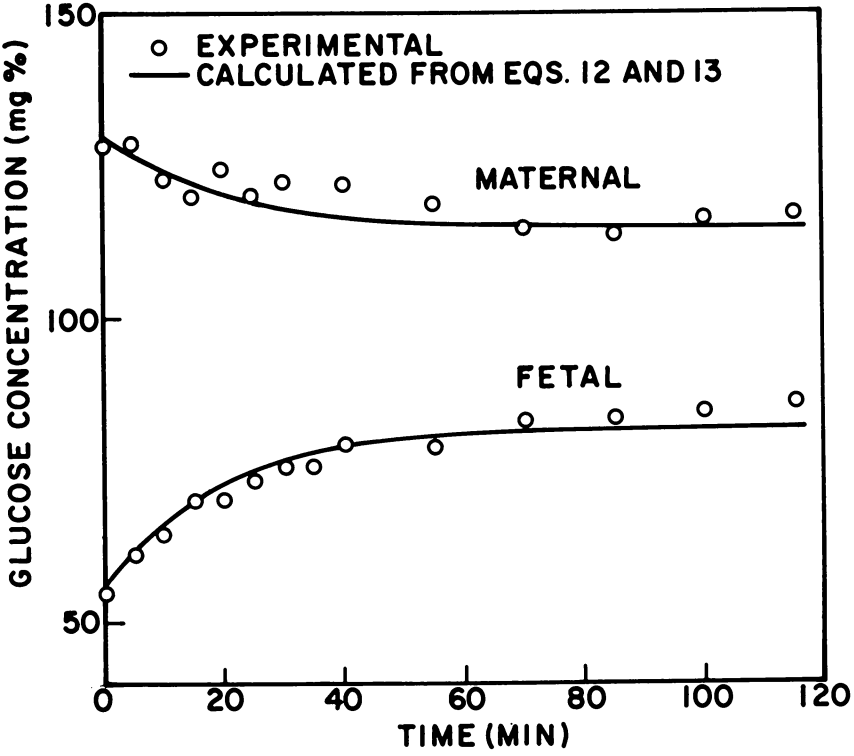

Figure 6. Steady-state experiment No. 1

A possible interpretation is that fluid transfer is related to the death of the cells constituting the membrane. As they die, they become permeable to the perfusate. This thesis is supported by the huge increase of fluid transfer which was recorded in a few experiments a few minutes after injection of cyanide, which "killed" the placentas.

Oxygen Transfer—O_2 and CO_2 Response. During the run, a fetal pO_2 dropping below 14 mm Hg seemed to indicate an inadequate perfusion. If the oxygen supply is eliminated on the maternal side, then resumed, the fetal oxygen tension was observed to successively decrease, then rise to its previous value. At the end of the run, the response of the fetal vessels to oxygen and carbon dioxide was checked to establish the

viability of the placenta at that time. Decreases in the fetal arterial pressure of the order of 10 mm Hg are observed if CO_2 is added to the fetal oxygenator. When the CO_2 is removed and oxygen added, the fetal arterial pressure rises again. This change in pressure has been observed *in vivo* and is attributed to changes in the diameter of the fetal vessels (*8*).

Glucose Transfer and Utilization. The fact that glucose is transferred from the maternal to the fetal side and utilized by the placenta indicates that the placenta is being perfused.

Since the apparent transport of glucose or oxygen could be owing to leakage of perfusate from one circulation to the other, the integrity of the two circulations was tested by injecting 0.5 ml of bromosulfthalein (BSP) at concentration of 50 mg/ml into the fetal circulation (*29*). BSP was used because in spite of the small size of this molecule; the intact placenta is impermeable to it.

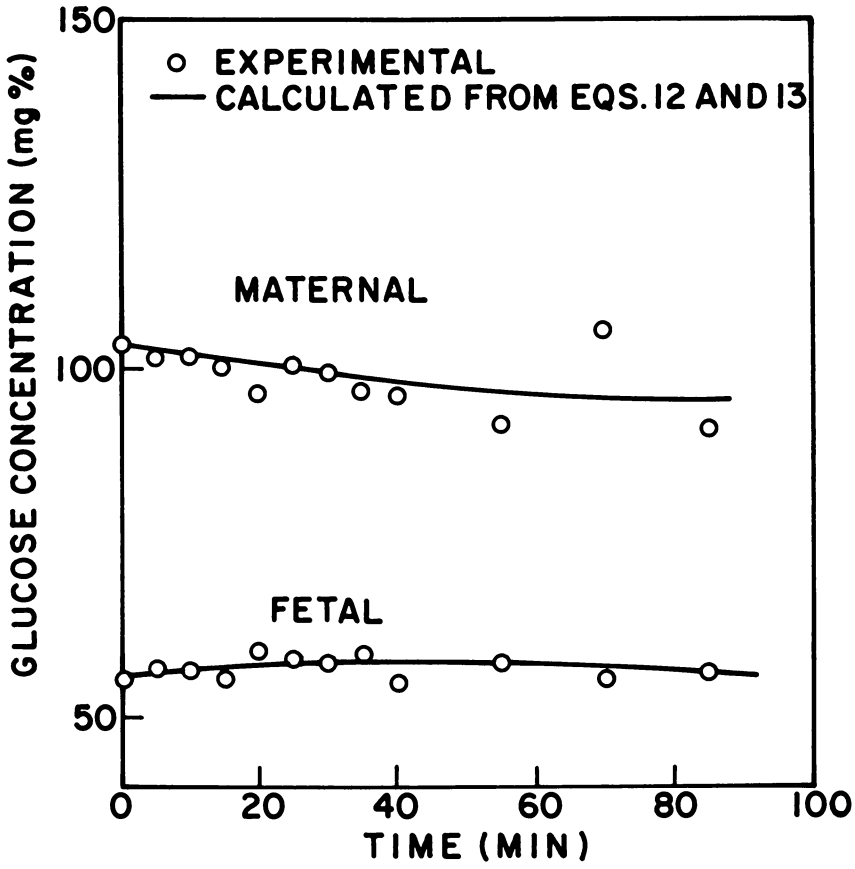

Figure 7. Steady-state experiment No. 2

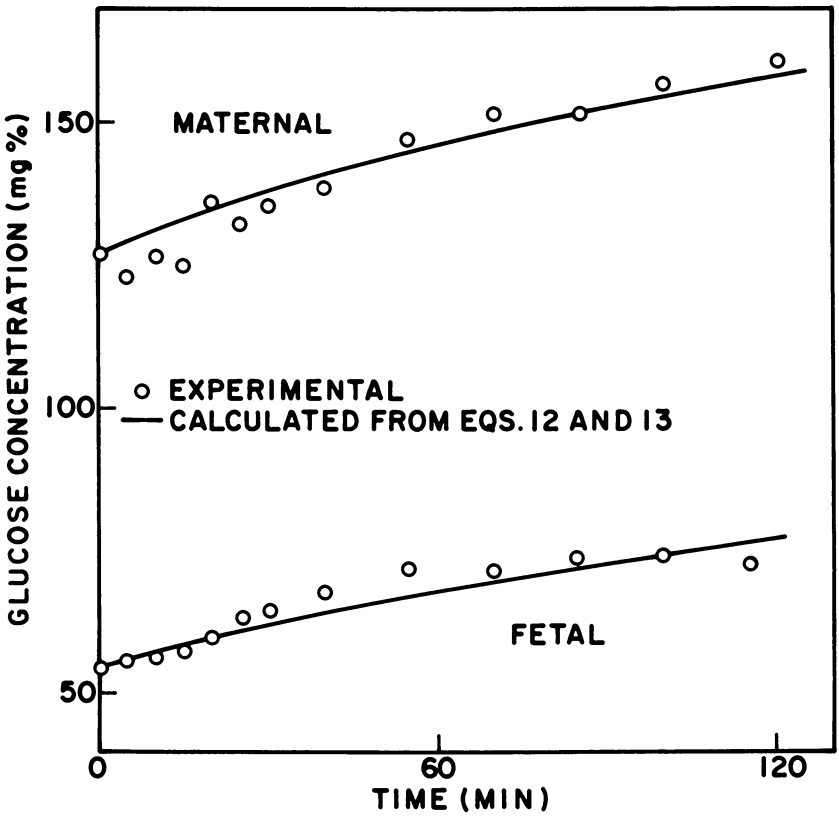

Figure 8. Steady-state experiment No. 3

The absence of BSP in the maternal reservoir throughout the run indicated in all these cases the intactness of the placental circulatory system.

Steady-State Glucose Transfer and Metabolism

General Considerations. Because conditions are constantly changing, the results obtained in unsteady-state experiments must be interpreted cautiously. Utilization rates will not necessarily equal metabolism rates because the quantity of glucose in the tissue changes with the concentration. In addition, the rate of transfer to or from the fetal circulation may depend upon the fetal flow rate if significant changes in concentration occur during the passage of fetal fluid through the placenta. This is much less likely to occur in the maternal circulation because the maternal flow rate is five times higher than the fetal rate. For these reasons, steady-state measurements of glucose transfer and metabolism were

made. After an initial dose to bring the maternal and fetal concentrations to approximate the correct values, glucose was added continuously at a steady rate.

Under steady-state conditions the problem of glucose uptake in the tissue disappears, and the rate of metabolism is exactly the rate of utilization. No significant difference in the results was observed or expected when the fetal flow rate was changed since with steady-state conditions in the system there is no net transfer at the fetal surface. The utilization rate depends upon the steady-state maternal and fetal concentrations. This rate is constant for a considerable time.

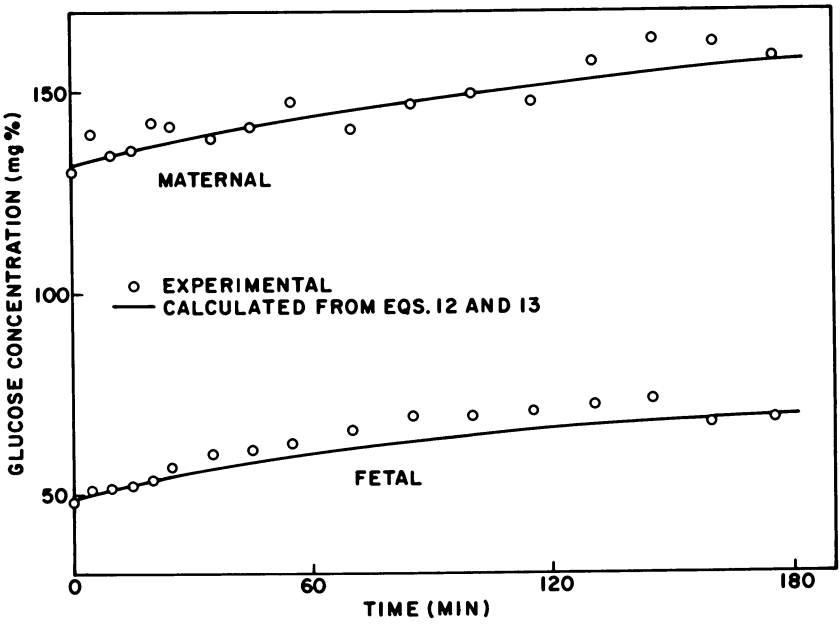

Figure 9. Steady-state experiment No. 4

Experimental Curves. To reach steady-state conditions, glucose was added at a constant rate in the maternal reservoir. The rate of glucose added was adjusted for each run, depending upon the mass of the placenta and the expected average concentration for the run. It appeared from preliminary runs that the average rate of utilization for initial concentrations of about 120 mg % on the maternal side and 50 mg % on the fetal side would be about 1.2 grams glucose/kg placenta/hour. By introducing glucose roughly at the same rate, a steady state after a short time was observed. The curves (Figures 6–14) show the different runs. Steady state was not always reached, since placentas, even under the same conditions, do not utilize glucose at the same rate, and

because the initial concentrations were not sufficiently close to the steady-state conditions to permit steady state to be reached during the course of the experiment. Thus, the curves may decrease or increase slowly. Steady state was reached almost immediately on the maternal side in a few cases when the rate of utilization was equal to the rate of glucose addition.

On the fetal side, the curves either level off after about 60 min when steady state is reached on the maternal side, or increase continuously if the maternal concentration increases with time.

Physical Model for Interpretation of Data. Glucose is assumed to transfer from the maternal to the fetal circulation through a membrane consisting of the walls of villous loops. The diameters of the villi are

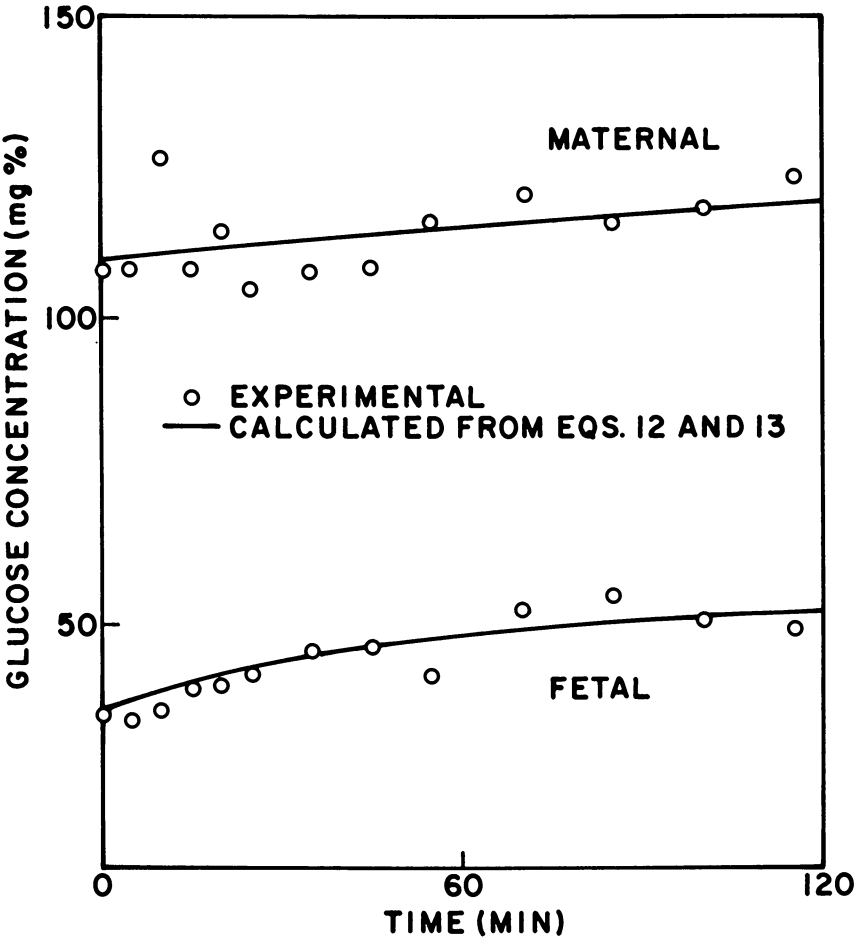

Figure 10. Steady-state experiment No. 5

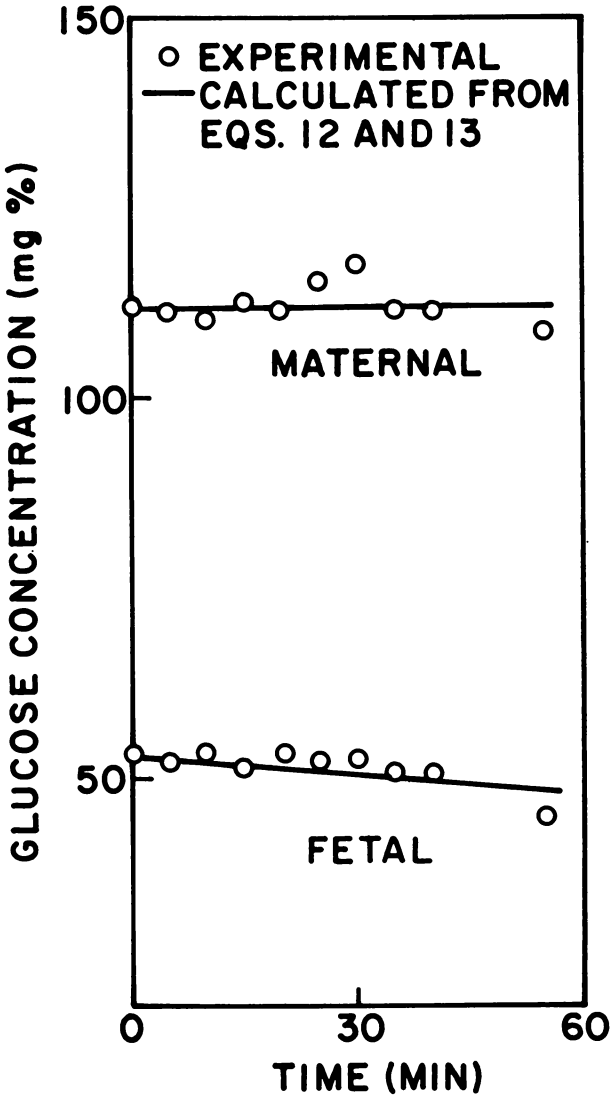

Figure 11. Steady-state experiment No. 6

assumed to be large compared with the thickness of the membrane, so that the entire villous surface can be treated as a flat membrane. Metabolism within the membrane is assumed to be by first-order reaction and transfer through the membrane is assumed to be by simple diffusion. The metabolism and transfer in general are more complicated than the models assume. Metabolism occurs by a long chain of enzyme-catalyzed reactions, any one of which may control the reaction rate. Over limited

concentration changes, however, any rate can be expressed approximately in first-order form. Transport, also, is more complex than simple diffusion, occurring probably in the form of a carrier–glucose complex (*16*, *30*). For the sake of simplicity and to keep the number of variables to a minimum, the simple diffusion model was used. This model should correspond closely to reality when the carrier molecules are far from being saturated. Under these conditions the carrier concentration at the tissue surface

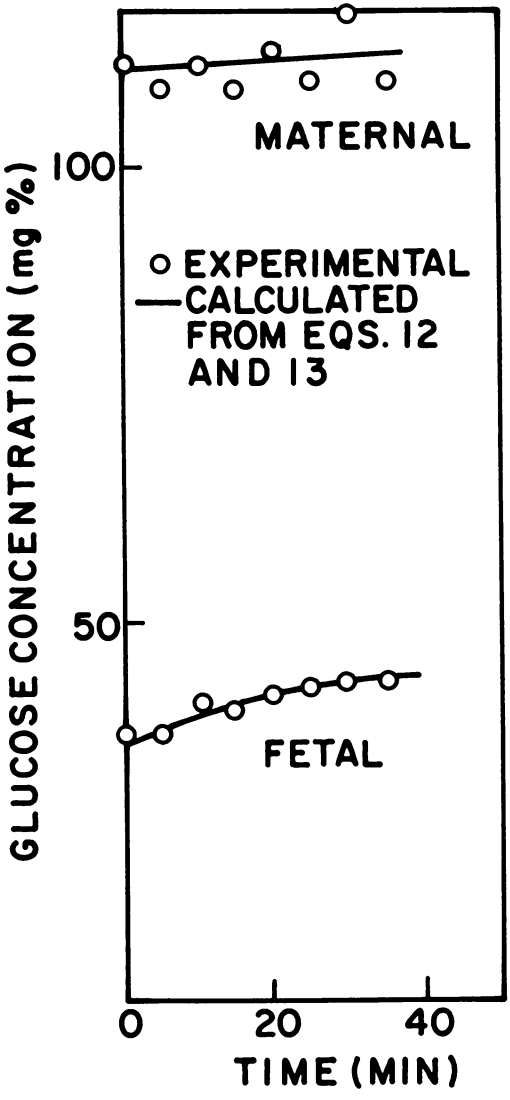

Figure 12. Steady-state experiment No. 7

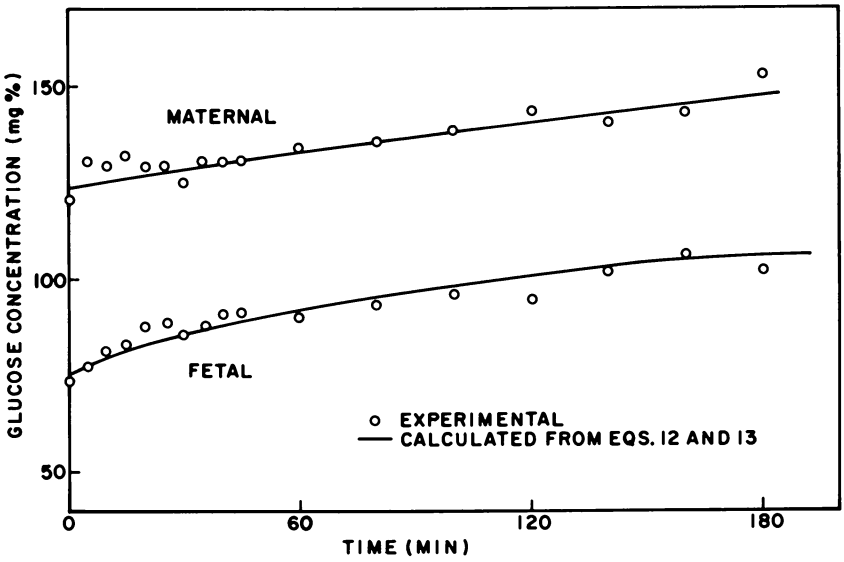

Figure 13. Steady-state experiment No. 8

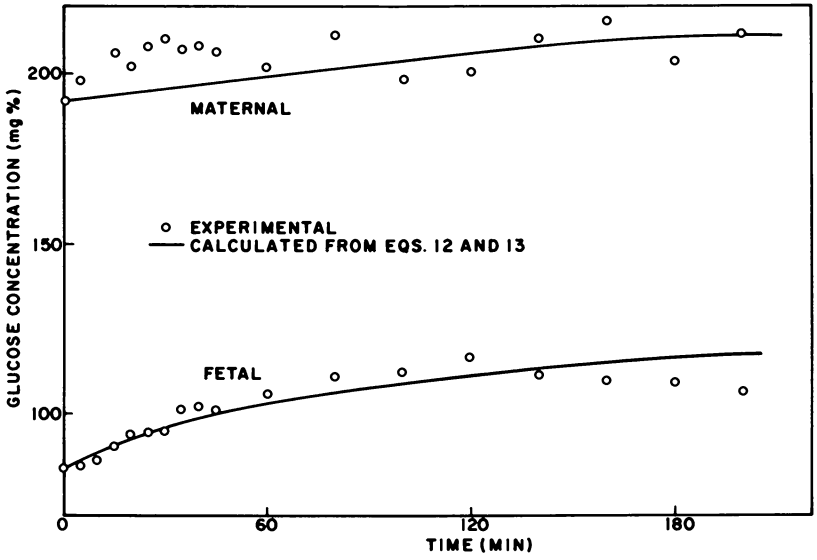

Figure 14. Steady-state experiment No. 9

equals the glucose concentration in the perfusate. The measured diffusion then would be the diffusion of the carrier–glucose complex.

The concentration change of the maternal fluid and fetal fluid during a single pass is assumed to be negligible. At steady state, this assump-

tion is necessary only for the maternal circulation since there is no net transfer to or from the fetal circulation. During the transient period while steady state is being established, the rate of concentration change in the maternal and fetal circulations is taken to be slow compared with the time required to establish steady state in the membrane. In addition, the volumes of fetal and maternal fluid are assumed to remain constant, and the concentrations at the membrane surface are taken to be the bulk concentrations in the circulations. Thus, during the transient period, the maternal and fetal reservoir concentrations are functions of time while the glucose concentration in the membrane is a function of the thickness of the membrane and the concentrations at the maternal and fetal surfaces. At steady state, the maternal and fetal concentrations are constant, and the membrane concentration varies with the membrane thickness.

From the mass balances on the maternal fluid, fetal fluid, and membrane, the following equations and the corresponding boundary conditions can be derived; ρ is the rate of glucose added per unit time.

$$V_m \frac{dC}{dt} - \mathrm{D}A \left.\frac{dm}{dz}\right|_{z=0} - \rho = 0 \tag{1}$$

$$V_f \frac{dq}{dt} + \mathrm{D}A \left.\frac{dm}{dz}\right|_{z=\delta} = 0 \tag{2}$$

$$\frac{\mathrm{D}d^2m}{dz^2} - Km = 0 \tag{3}$$

$$\text{B.C.} \begin{cases} t = 0 & C = C_o \quad q = q_o & (4) \\ z = 0 & \text{for all } t \quad m = C & (5) \\ z = \delta & \text{for all } t \quad m = q & (6) \end{cases}$$

Equation 3 can be integrated directly to find m in terms of C and q:

$$m = \frac{q \sinh \alpha z + C \sinh [\alpha(\delta - z)]}{\sinh \alpha\delta} \tag{7}$$

where

$$\alpha = \sqrt{K/\mathrm{D}}$$

Differentiating this expression and evaluating the derivative at $z = 0$ and $z = \delta$ yields,

$$\left.\frac{dm}{dz}\right|_{z=0} = \frac{\alpha}{\sinh \alpha\delta} [q - aC] \tag{8}$$

$$\left.\frac{dm}{dz}\right|_{z=\delta} = \frac{\alpha}{\sinh \alpha\delta}\,[aq - C] \tag{9}$$

Upon substituting these expressions, Equations 2 and 3 become

$$b\,\frac{dC}{d\bar{t}} - (q - aC) = \frac{\rho l}{V_f} \tag{10}$$

$$\frac{dq}{d\bar{t}} + (qa - C) = 0 \tag{11}$$

where,

$$b = V_m/V_f,\ a = \cosh \alpha\delta,\ l = \frac{V_f \sinh \alpha\delta}{DA\alpha},\ \text{and}\ \bar{t} = \frac{t}{\bar{l}}$$

These simultaneously can be solved for C and q with the result

$$q = A_1 \exp(R_1\bar{t}) + A_2 \exp(R_2\bar{t}) + \frac{\rho l}{V_f(a^2 - 1)} \tag{12}$$

$$C = A_1(a + R_1)\exp(R_1\bar{t}) + A_2(a + R_2)\exp(R_2\bar{t}) + \frac{a\rho l}{V_f(a^2 - 1)} \tag{13}$$

where,

$$A_1 = \frac{C_o - q_o(a + R_2) + \dfrac{R_2\rho l}{V_f(a^2 - 1)}}{R_1 - R_2}$$

$$A_2 = q_o - A_1 - \frac{\rho l}{V_f(a^2 - 1)}$$

$$R_1 = \frac{-a(b+1) + \sqrt{\Delta}}{2b},\ R_2 = \frac{-a(b+1) - \sqrt{\Delta}}{2b}$$

with

$$\Delta = \sqrt{a^2(b-1)^2 + 1}$$

At steady state, $\dfrac{dC}{d\bar{t}} = \dfrac{dq}{d\bar{t}} = 0$ and

$$q_s = \frac{\rho l}{V_f(a^2 - 1)} \tag{14}$$

$$C_s = \frac{a\rho l}{V_f(a^2 - 1)} \tag{15}$$

Also, at steady state, the two dimensionless parameters can be easily determined, since

$$a = \frac{C_s}{q_s} \tag{16}$$

$$l = \frac{V_f (a^2 - 1)\, q_s}{\rho} \tag{17}$$

Analysis. The shape of the concentration profiles is defined by the parameters a, b, and l. b was measured experimentally and values of a and l were chosen to give a minimum value for the expression

$$F = \sum_{i=L}^{n} [\, C_i - C(t_i)^2 + [\, q_i - q(t_i)\,]\,]$$

where C_i and q_i are the experimental values at t_i and $C(t_i)$ and $q(t_i)$ are the values of C and q calculated at t_i from Equations 12 and 13. The least square value was determined using the Gauss method (*31*). An outline of this procedure is given in Appendix B.

The initial values for the minimization for a and l were entered as

$$ao = \frac{C_s}{q_s} \text{ and } lo = \frac{V_f (a^2 - 1)\, q_s}{\rho}$$

A good approximation, when steady state was not reached, was to take C_s and q_s at the final concentrations of the run.

Results. Theoretical curves fit the experimental curves very well, both on the maternal and fetal side. Computed values for C and q are given in Figures 6–14. In all cases, the less square values of a and l were quite close to the initial values.

Evaluation of K and D. For each run, K and D were determined from the values of a and l. The placental membrane area was taken to be $A = A_o \times M/500$ where $A_o = 10^5$ cm^2 (*1*, *32*) and M is the mass of the placenta in grams. δ has been observed to vary between 2 μ and 6 μ (*32*, *33*) and an average value of 4 $\mu = 4 \times 10^{-4}$ cm was used here. The results are given in Table I. For the nine runs, K ranged from 0.22 to 0.43 min^{-1} and D ranged from 3×10^{-10} to 12×10^{-10} cm^2/sec.

Discussion of Results. The values of K and D determined here were about the same as the values obtained earlier on several unsteady-state decay experiments (*33*) in which a single dose of glucose was added at the beginning of the run and the changing maternal and fetal concentration profiles were observed. This agreement supports the assumptions that the concentration relaxation in the membrane is fast compared with the time required for significant concentration change in the circulations and that the diffusion resistances in the circulating maternal and fetal fluids are negligible.

Table I. Determination of K and D

Run No.	*1*	*2*	*3*	*4*
$a_{\text{steady-state}}$	1.38	1.78	2	2.28
$l(\text{min})_{\text{steady-state}}$	36.7	53.9	83.6	111.7
$a_{\text{least square}}$	1.40	1.85	1.89	2.15
$l(\text{min})_{\text{least square}}$	40.8	66	97	111
V_f(ml)	700	800	700	700
m(grams)	575	675	575	690
$K(\text{min}^{-1})$	.314	.430	.314	.264
D cm^2s^{-1}	11.1×10^{-10}	7.57×10^{-10}	5.35×10^{-10}	3.58×10^{-10}

The steady-state maternal glucose utilization rate can be calculated for a normal maternal glucose concentration of 120 mg % from the rate at which glucose diffuses into the placental tissue at steady state. This is given by:

$$r_m = -\mathrm{D}A \left.\frac{dm}{dz}\right|_{z=0} \text{steady-state} = \frac{\mathrm{D}A\,\alpha}{\sinh \alpha\delta}(aC_s - q_s)$$

$$= \frac{V_f}{l}\left(\frac{a^2-1}{a}\right) C_s$$

The average value for all nine runs for a normal maternal glucose concentration of 120 mg % is 1.24 grams glucose/hour/kg. This compares well with the value of 1.35 grams/hour/kg obtained in tissue studies (*34*) and is further evidence that the placenta is adequately perfused. It also agrees with the 1.25 grams/hour/kg observed by Howard and Krantz (*16*), but is about twice the rate observed by Krantz *et al.* (*19*) in a later study.

If a range for a is chosen ($1.4 < a < 2.3$ for almost all of our experiments), and if a physiological maternal concentration is maintained (90 mg % $< C <$ 125 mg %), then glucose transfer from the maternal to the fetal side will occur if $q < C/a$. Glucose transfer would take place if q is less than an upper limit ranging between 39 mg % and 89 mg %.

The normal fetal concentration values indicated by the literature (*35*) are higher: for a maternal arterial glucose concentration falling between 90 mg % and 125 mg %, q varies between 75 mg % and 104 mg %.

The rate of transfer can be calculated for any set of values of C and q by evaluating

$$r_t = -\mathrm{D}A \left.\frac{dm}{dz}\right|_{z=\delta} = \frac{\mathrm{D}A\,\alpha}{\sinh \alpha\delta}(C - aq)$$

$$= \frac{V_f}{l}(C - aq)$$

in Steady-State Experiments

5	*6*	*7*	*8*	*9*
2	2.13	2.5	1.44	1.89
68.2	92.5	77	45.6	112.5
2.18	2.36	2.21	1.35	1.75
94.4	117.6	111.5	49.9	101.9
650	700	700	750	650
650	800	650	580	600
.360	.425	.330	.274	.222
4.77×10^{-10}	5×10^{-10}	4.45×10^{-10}	8.1×10^{-10}	4.4×10^{-10}

For a value of $C = 130$ mg % and $q = 60$ mg %, r_t varies from approximately zero to a maximum of 0.47 gram/hour (Table II). The rate of glucose utilization by the fetus at term has been estimated to be about 1 gram/hour (*36*). The difference between what can be transferred across the placenta at term as inferred by the *in vitro* experiments and what is required by the fetus can be explained several ways. First, the condition of the placenta *in vitro* may not be the same as *in vivo*. Even if the placenta is adequately perfused, as evidence presented earlier suggests, a thin film of clotted blood which may have formed during the time between delivery and the beginning of perfusion (about 20 min) could increase significantly the diffusional resistance. This increased diffusional resistance, however, should not affect the placental utilization greatly and the first-order rate constant for glucose utilization. Diffusional resistance to glucose in the flowing maternal and fetal fluid apparently is not important since diffusion of glucose in plasma has been recently reported to be 0.4×10^{-5} cm/sec at 24°C (*37*), 10^4 times higher than the diffusions observed here.

The net rate of glucose metabolism by the placenta may also be affected by the rate at which glucose is being transferred. Under steady-state conditions, there was no net transfer of glucose because no glucose

Table II. Calculated Transfer Rates[a]

Run	*Rate of Transfer to Fetal Circulation (grams/hour)*
1	0.47
2	0.14
3	0.07
4	~0
5	~0
6	~0
7	~0
8	0.45
9	0.10

[a] $C = 130$ mg % $q = 60$ mg %

was being removed from the fetal circulation. Once glucose is removed from the fetal circulation at a rate necessary to sustain the fetus, a new mechanism of glucose transfer may come into play, increasing the glucose transfer rate above that indicated in our experiments.

Conclusion

The suitability of the apparatus to achieve adequate perfusion under physiological conditions has been established. It is a reliable basis for various future studies; these include the effects of different physiological, physical, hemodynamic, and pathological conditions on the formation, release, transfer, metabolism, and utilization of various substances, which may be foreign or intrinsic to the tissues.

Glucose metabolism in placental tissue can be described by a first-order reaction in the maternal concentration range of 80 to 200 mg %. The rate constant for the first-order reaction is 0.3 min^{-1}. The data are very limited above 150 mg %, so the first-order reaction rate may not apply at higher glucose concentrations. Glucose transfer also seems to be described in the concentration range studied by a simple diffusion model with a mean diffusion coefficient of 5×10^{-10} cm^2 sec^{-1}. This value of the diffusion does not seem to be sufficiently large to supply a term fetus adequately with glucose.

Nomenclature

A = total exchange surface area, assumed to be proportional to the mass of the placenta
A_1, A_2 = concentration constants
a = $\cos h\, \alpha\delta$ = parameter characteristic of the placenta
C = maternal glucose concentration
C_o = initial maternal glucose concentration
C_s = steady-state maternal concentration
$C(t)$ = computed maternal concentration at time t
D = diffusivity coefficient of the membrane with respect to glucose
K = rate constant of the chemical reaction
l = parameter characteristic of the placenta
M = mass of the placenta
m = glucose concentration in the membrane at time t and abscissa z
q = fetal glucose concentration
q_o = initial fetal glucose concentration
q_s = steady-state fetal concentration
$q(t)$ = computed fetal concentration at time t
R_1, R_2 = time constants
r_m = rate of metabolism of glucose
r_t = rate of transfer of glucose
t = time
$\bar{t}$ = dimensionless time

V_f = volume of the fetal circulation[1]
V_m = volume of the maternal circulation[1]
z = abscissa in the membrane

Greek Letters

$\alpha = \sqrt{\frac{K}{D}}$

δ = average thickness of the membrane
ρ = the rate of addition of glucose to the maternal circulation

[1] This takes into account the volume of the circulation inside the placenta, the volume of the tubing and the volume of the reservoir. V_m was estimated to be $V_{mat.res.}$ + 360 ml, V_f to be $V_{fet.res.}$ + 150 ml.

Appendices

A. Comparison of Reported Physiological In Vivo *Values with* In Vitro *Perfusion Values*

Maternal Circulation	*Accepted* In Vivo *Values*	In Vitro
Flow rate	600 ml/min	450-600 ml/min
Intervillous space blood pressure (resting)	10–20 mm Hg	
Temperature	37° C	37° C
pH	7.3–7.4	7.3–7.5
Arterial pO_2	90 mm Hg	60-160 mm Hg
Venous pO_2	33 mm Hg	
Fetal Circulation		
Flow rate	200 ml/min	60–90 ml/min
Umbilical artery pressure	88/54 mm Hg	35–110 mm Hg[a]
Umbilical vein pressure	22–34 mm Hg	15 mm Hg
pH	7.1–7.2	7.1–7.3
Arterial pO_2	14 mm Hg	
Venous pO_2	28 mm Hg	14–28 mm Hg
Amniotic Fluid		
Amniotic fluid pressure (resting)	10–20 mm Hg	15–20 mm Hg
Temperature	37° C	37° C

B. In Vitro *Conditions During Extracorporeal Perfusion*

Maternal Circulation	
Perfusion fluid	Buffered saline–blood 3:1
Volume	900–1100 ml
Flow rate	450–600 ml/min
Arterial pressure	50–100 (varies with amniotic fluid pressure)[b]

Maternal Circulation (Continued)

pO_2	60–160 mm Hg
pH	7.3–7.5
Temperature	37° C

Fetal Circulation

Perfusion fluid	Buffered saline–blood 3:1[c]
Volume	600–800 ml
Flow rate	60–90 ml/min
Arterial pressure	35–100 mm Hg (varies with flow rate and amniotic fluid pressure)[d]
pO_2	14–28 mm Hg
pH[2]	7.1–7.3
Temperature	37° C
Venous pressure	15 mm Hg

Amniotic Fluid

Fluid	Buffered saline pH 7.4
Volume	600–800 ml
Pressure	Adjusted as desired between 15 and 20 mm Hg
Temperature	37° C

C. *Composition of the Krebs Ringer Solution*

The Krebs-Ringer solution used in all the experiments is made out of the following solutions:

1–0.90% NaCl	(0.154 M)
2–1.15% KCl	(0.154 M)
3–1.22% $CaCl_2$	(0.11 M)
4–3.82% $MgSO_4$	(0.154 M)
5–2.11% KH_2PO_4	(0.154 M)
6–1.30% $NaHCO_3$	(0.154 M)

Mixed in the following amounts:

100 parts of solution 1
4 parts of solution 2
3 parts of solution 3
1 part of solution 4
1 part of solution 5
21 parts of solution 6

To prevent blood clotting, 10,000 USP units of heparin are added to each 4 liters of solution.

[a] Varies with flow rate and AFP.

[b] These values are corrected for the pressure drop through the maternal arterial and venous tubes. At 450 ml/min, the corrections were 8 mm Hg for the arteries and 24 mm Hg for the veins.

[c] 95 ml of a 6% dextran solution is added to the fetal reservoir.

[d] These values are corrected for the pressure drop through the cannulae. At a flow rate of 75 ml/min, the correction was 42 mm Hg for the arterial cannulae and negligible for the venous cannula.

Table AII. Appendix II

Determination of a *and* l *Gaussian Nonlinear Least Squares Fitting Method*

Given n couples of points (t_i, C_i) and (t_i, q_i), let's minimize

$$F = \sum_{i=1}^{n} [C_i - C(t_i)]^2 + \sum_{i=1}^{n} [q_i - q(t_i)]^2$$

with respect to a and l. Let

$$R_i = C^\circ(t_i) - C_i$$
$$S_i = q^\circ(t_i) - q_i)$$

where

$$C^\circ(t_i) = C(a^\circ, l^\circ)$$
$$q^\circ(t_i) = q(a^\circ, l^\circ)$$

$$F = \sum_{i=1}^{n} \left(\left[C_i - C^\circ(t_i) - \frac{\partial C(t_i)}{\partial A} \delta a - \frac{\partial C(t_i)}{\partial l} \delta l \right]^2 + \left[q_i - q^\circ(t_i) - \frac{\partial q(t_i)}{\partial a} \delta a - \frac{\partial C(t_i)}{\partial l} \delta l \right]^2 \right)$$

Let

$$\frac{\partial F}{\partial a} = \frac{\partial F}{\partial l} = 0$$

$$F = \sum_{i=1}^{n} \left\{ \left[R_i + \frac{\partial C(t_i)}{\partial a} \delta a + \frac{\partial C(t_i)}{\partial l} \delta l \right]^2 + \left[S_i + \frac{\partial q(t_i)}{\partial a} \delta a + \frac{\partial q(t_i)}{\partial l} \delta l \right]^2 \right\}$$

Thus

$$\sum_{i=1}^{n} \left\{ \left[R_i + \frac{\partial C(t_i)}{\partial a} \delta a + \frac{\partial C(t_i)}{\partial l} \delta l \right] \frac{\partial C(t_i)}{\partial a} + \left[S_i + \frac{\partial q(t_i)}{\partial a} \delta a + \frac{\partial q(t_i)}{\partial l} \delta l \right] \frac{\partial q(t_i)}{\partial l} \right\} = 0$$

and

$$\sum_{i=1}^{n} \left\{ \left[R_i + \frac{\partial C(t_i)}{\partial a} \delta a + \frac{\partial C(t_i)}{\partial l} \delta l \right] \frac{\partial C(t_i)}{\partial l} + \left[S_i + \frac{\partial q(t_i)}{\partial a} \delta a + \frac{\partial q(t_i)}{\partial l} \delta l \right] \frac{\partial q(t_i)}{\partial a} \right\} = 0$$

Let

$$\alpha = \begin{bmatrix} \delta a \\ \delta l \end{bmatrix}$$

$$A = \begin{bmatrix} \sum_{i=1}^{n} \left\{ \left[\frac{\partial C(t_i)}{\partial a} \right]^2 + \left[\frac{\partial q(t_i)}{\partial a} \right]^2 \right\} & \sum_{i=1}^{n} \left[\frac{\partial C(t_i)}{\partial a} \times \frac{\partial C(t_i)}{\partial l} + \frac{\partial q(t_i)}{\partial a} \times \frac{\partial q(t_i)}{\partial l} \right] \\ \sum_{i=1}^{n} \left[\frac{\partial C(t_i)}{\partial a} \times \frac{\partial C(t_i)}{\partial l} + \frac{\partial q(t_i)}{\partial a} \times \frac{\partial q(t_i)}{\partial l} \right] & \sum_{i=1}^{n} \left\{ \left[\frac{\partial C(t_i)}{\partial l} \right]^2 + \left[\frac{\partial q(t_i)}{\partial l} \right]^2 \right\} \end{bmatrix}$$

$$B = \begin{Bmatrix} -\sum_{i=1}^{n} \left[R_i \frac{\partial C(t_i)}{\partial a} + S_i \frac{\partial q(t_i)}{\partial a} \right] \\ -\sum_{i=1}^{n} \left[R_i \frac{\partial C(t_i)}{\partial l} + S_i \frac{\partial q(t_i)}{\partial l} \right] \end{Bmatrix}$$

Then, the above conditions can be written $A\alpha = B$ or $\alpha = A^{-1}B$.

The initial values *ao* and *lo* were found by APL. By the previous method, increments a and l are obtained and the iteration proceeds with

$$a_1 = ao + \delta a$$
$$l_1 = lo + \delta l$$

Literature Cited

1. Wilkin, P., "Le Placenta Humain," Masson et Cie, Paris, 1958.
2. Chesley, L. S., McFaul, I. E., *Amer. J. Obstet. Gynec.* (1949) **58**, 159.
3. Chesley, L. S., Alter, N. M., *Amer. J. Obstet. Gynec.* (1951) **61**, 1218.
4. Ciuchta, H. P., Gautieri, R. F., *J. Pharm. Sci.* (1963) **51**, 974.
5. Gautieri, R. F., Ciuchta, H. P., *J. Pharm. Sci.* (1962) **51**, 55.
6. Krauer, V. F., *Gynaecologia* (1968) **165**, 53.
7. Kustner, U., Siedentoph, H., *Arch. Gynaekol.* (1929) **138**, 131.
8. Nyberg, R., Westin, B., *Acta Physiol. Scand.* (1957) **39**, 216.
9. Page, E. W., "The Placenta and Fetal Membranes," pp. 195–199, Williams and Wilkins, Baltimore, 1960.
10. Page, E. W., *Amer. J. Obstet. Gynec.* (1957) **74**, 705.
11. Panigel, M., *Amer. J. Obstet. Gynec.* (1962) **84**, 1664.
12. Panigel, M., Pascuad, M., Brun, J. L., *J. Physiol.*, Paris (1967) **59**; Suppl., p. 277, No. 4125766.
13. Varangot, J., Cedard, L., Yannotti, S., *Amer. J. Obstet. Gynec.* (1965) **92**, 534.
14. Crist, R. D., Krantz, K. E., Warren, J. C., *Obstet. Gynec.* (1965) **25** (1), 89.
15. Hensleigh, P. A., Krantz, K. E., *Amer. J. Obstet. Gynec.* (1966) **96** (1), 5.
16. Howard, J. M., Krantz, K. E., *Amer. J. Obstet. Gynec.* (1967) **98** (4), 445.
17. Krantz, K. E., Panos, T. C., *Amer. J. Dis. Child.* (1959) **98**, 674.

18. Krantz, K. E., Panos, T. C., Evans, J., *Amer. J. Obstet. Gynec.* (1962) **83,** 1214.
19. Krantz, K. E., Blakey, J., Yoshida, K., Tromito, J. A., *Obstet. Gynec.* (1971) **37** (2), 183.
20. Nesbitt, R. E. L., Jr., Rice, P. A. Rourke, J. E., Torresi, V. F., *J. Gynec. Invest.* (1970) **1,** 185.
21. Crawford, J. M., *Amer. J. Obstet. Gynec.* (1962) **84,** 1543.
22. Brame, R. G., *et al., Obstet. Gynec.* (1969) **34,** 14.
23. Boe, F., *Cold Spr. Harb. Symp. Quant. Biol.* (1954) **19,** 29.
24. Wigglesworth, J. S., *J. Obstet. Gynec. Brit. Cmwlth.* (1969) **76,** 979.
25. Corner, W. C., *Clin. Obstet. Gynec.* (1963) **6,** 17.
26. Crawford, J. M., *J. Obstet. Gynec. Brit. Emp.* (1959) **66** (6), 885.
27. Bartels, H., Mall, W., *Pflügers Archiv.* (1964) **280,** 165.
28. Keston, A. S., Abstract of papers, 129th meeting, A.C.S., p. 31.C (1956).
29. Szabo, A. J., *et al., Metabolism* (1969) **18** (5).
30. Widdas, W. F., *J. Physiol.* (1952) **118,** 23.
31. Wilde, D. J., Beighter, C. S., "Foundations of Optimization," Prentice-Hall, Englewood Cliffs, N. J., 1967.
32. Aherne, W., Rurrill, M. S., *J. Path. Bact.* (1966) **91,** 123.
33. Torresi, V. F., Rice, P. A., Rourke, J. A., Nesbitt, R. E. L., "*In Vitro* Glucose Transfer and Metabolism in the Human Placenta," paper presented at the joint A.I.Ch.E.-I.Q.P.R. Symposium on Transport Properties in Biological Systems, San Juan, Puerto Rico, May 17-19, 1970.
34. Villee, C. A., *J. Biol. Chem.* (1953) **205,** 113.
35. Stenger, V., *et al., Amer. J. Obstet. Gynec.* (1966).
36. Adamson, Karlis, Jr., Birth Defects Original Article Series, Symposium on the Placenta, Vol. 1, pp. 27–33 (1965).
37. Colten, C. K., Smith, K. A., Merrill, E. W., Reece, J. M., "Diffusion of Organic Solutes in Stagnant Plasma and Red Cells Suspensions," Chemical Engineering Progress Symposium Series, No. 99, Vol. 66, p. 85 (1970).

RECEIVED November 22, 1971.

9

Oxygenators for Infants

ROGER G. SPRAGG[1] and THEODOR KOLOBOW

National Institutes of Health, Bethesda, Md. 20014

The need for infant heart–lung machines and their requirements are discussed. Bubble, disk, and membrane oxygenators are compared. Membrane oxygenators are essentially non-traumatic to blood and make possible extended perfusion of the hypoxic infant.

Six out of 1000 live infants born in the United States have congenital anomalies of the heart and great vessels (*1*). Of such infants who are symptomatic within the first 6 months of life, 80% have lesions amenable to surgery (*2*); at times the surgery cannot be delayed. Repair of defects such as total anomalous pulmonary vascular drainage, severe aortic stenosis, or a variety of intracardiac shunts frequently necessitates use of the heart–lung machine. Even with the use of the heart–lung machine, circulatory failure may occur during the induction of anesthesia, during thoracotomy, or during occlusion of any of the great vessels within the chest. For this reason some surgeons recommend having standby extracorporeal bypass equipment available for emergency use (*3*).

Extracorporeal blood gas exchange devices have been used on infants with the respiratory distress syndrome (RDS) (*4*, *5*). Twenty-five thousand newborns are estimated to die from this disease every year in this country (*6*). Though the causes of this disease are not clearly understood, it is hoped that supporting the infant with the aid of an extracorporeal gas exchanger will give his own lungs time in which to heal.

Extracorporeal blood gas exchange is only one method of treating the hypoxic infant. Hypothermia and hyperbaric oxygenation, alone and in conjunction with extracorporeal blood gas exchange, have been used to lower or to meet the metabolic requirements of the infant.

Lowering body temperature to 22°–25°C reduces oxygen consumption to approximately one-third of normal (*7*, *8*). It is at times possible

[1] Present address: University Hospital of San Diego County, 225 W. Dickinson St., San Diego, Calif. 92103.

to extend to 30 min the period of total circulatory arrest without using cardiopulmonary bypass (*9*).

Hyperbaric oxygen has been used during surgery with great success. Some workers believe that increased tissue oxygen availability decreases the incidence of hypoxic cardiac arrest (*10*). Others have pointed out the limitations of hyperbaric oxygenation (*11*): oxygen toxicity, a relatively slight increase in arterial p_{O_2} in the presence of significant venous admixture, and the hazards associated with environmental pressure changes. Additional limitations are imposed by the necessary equipment and length of depressurization. There seems to be no value in using hyperbaroxia to treat RDS (*12*).

Requirements of an Artificial Lung

The normothermic infant consumes 4.5–8 cm^3/kg/min of oxygen (*13*). At a respiratory quotient of 0.7 it is thus producing normally about 5 cm^3/kg/min of carbon dioxide (*14*). In the absence of cardiac anomalies, its cardiac output is about 210–240 cm^3/kg/min. In a 5-kg infant, therefore, it is necessary to provide 1200 cm^3/min of extracorporeal blood flow during total cardiopulmonary bypass, to provide about 35 cm^3 of oxygen per minute, and to remove about 25 cm^3 of carbon dioxide per minute. Hypothermia may lower these requirements by two-thirds, thus placing lower demands on the extracorporeal gas exchanger. Artificial lungs have been developed to handle the required blood flow and respiratory blood gas exchange. Such a device should be designed with the following principles in mind:

1. The extracorporeal oxygenator and circuit should have a low and precisely controlled priming volume. Every unit of whole blood used to prime the circuit introduces a finite risk of transmitting serum hepatitis virus to the patient. (It is estimated that 6% of the units of blood collected by the Red Cross in Washington, D.C. are so contaminated.) A device that uses little or no blood for a prime is therefore preferred. There are several advantages in using asanguinous priming solutions to effect hemodilution in the surgical patient. In a hypothermic environment lower viscosities are maintained than when whole blood prime is used (*15*). With hemodilution oxygen delivery remains adequate, and lactic acid production does not rise beyond levels present when hemodilution is not used (*16*). There is thought to be a decreased incidence of pulmonary complications following surgery when the intraoperative hematocrit is lowered to 60% of the preoperative value (*17*). Finally, a 5-kg infant with a blood volume of 400 ml can only tolerate a sudden gain or loss of 30–60 ml of blood without circulatory decompensation. Therefore, a device with highly accurate control of extracorporeal blood volumes is critical.

2. The extracorporeal gas exchanger should be atraumatic to blood. Ideally, there should be no rise in plasma-free hemoglobin secondary to

the destruction of red blood cells. Red cells should be handled gently so that their *in vivo* lifetime is not significantly diminished (*18*). An extracorporeal gas exchanger should be similarly atraumatic to platelets, and its use should not lower their circulating number. Soluble plasma constituents should likewise not be harmed.

3. Finally, an extracorporeal circuit including a blood gas exchanger should be construted out of biocompatible materials. Ideally, nonthrombogenic materials alone should be used. Since these are still in the developmental stage, materials with minimal thrombogenicity must be used. Heparinization, either regional or systemic, is necessary during the period of bypass to prevent coagulation. In long-term support of infants with RDS, the problems of bleeding associated with systemic anticoagulation are likely to be severe (*19*).

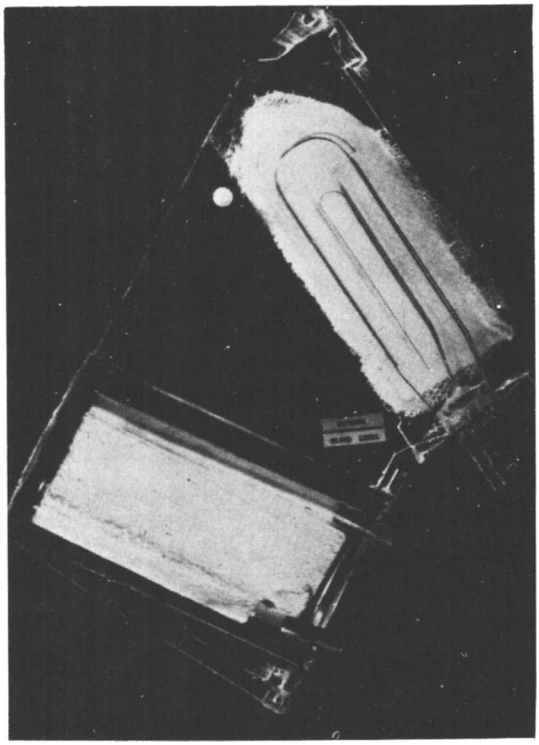

Journal of Thoracic and Cardiovascular Surgery

Figure 1. Cross section of the infant Temptrol oxygenator, Model Q 130 (28)

Blood Gas Exchangers

Blood gas exchange devices have either a gas–blood interface, as found in the disk and bubble oxygenators, or a membrane interposed be-

tween the gas and the blood, as in the membrane and the capillary oxygenators. The bubble oxygenator, represented by the Temptrol (*20*) (Figure 1) and Travenol (*21*) (Figure 2) models, is probably the most widely used gas exchanger for infants undergoing surgery. The Kay–Cross disk oxygenator (*22*) has been miniaturized and modified to be suitable for infant perfusion (*23*) (Figure 3). Membrane oxygenators suitable for infant use include the Kolobow spiral coil (*24*) and the Lande–Edwards (*25*) oxygenators.

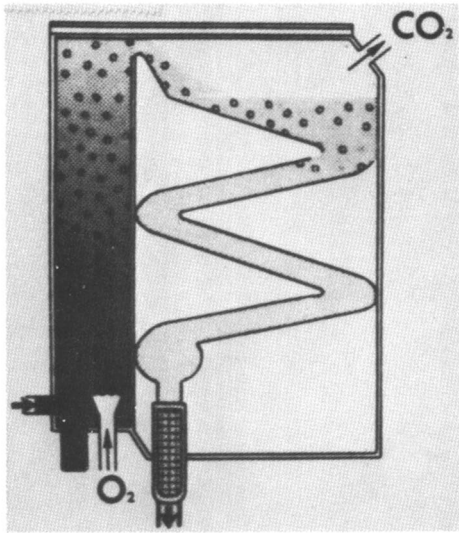

P. M. Galletti and G. A. Brecher, "Heart–Lung Bypass," Gune and Stratton, by permission

Figure 2. Infant bubble oxygenator (18)

Blood oxygenation in all these devices involves oxygen diffusion through plasma, diffusion through the red cell membrane and finally chemical binding with hemoglobin. In the membrane oxygenator an additional step is diffusion through the synthetic membrane interposed between the gas and the blood. The mass transfer of oxygen is limited by diffusion through plasma in all but a few experimental designs. Oxygen passage through plasma obeys Fick's law at 37°C; the permeation coefficient of oxygen in plasma approximates 6.5–10.1 $\times$ 10^{-11} ml cm/cm^2/sec/cm Hg. Within the red cell the permeation coefficient of oxygen is about one-half that of plasma (*26*). Therefore, to enhance oxygenation within a gas exchange device, it is necessary to maximize the oxygen

diffusion gradient. This is usually done by using oxygen concentrations of 90–100% (at 1 atm). Although applying oxygen to blood under hyperbaric conditions has been proposed (27), it has yet to find practical application. The rate of blood oxygenation can be further enhanced by mixing of the blood compartment; this is accomplished differently in various devices.

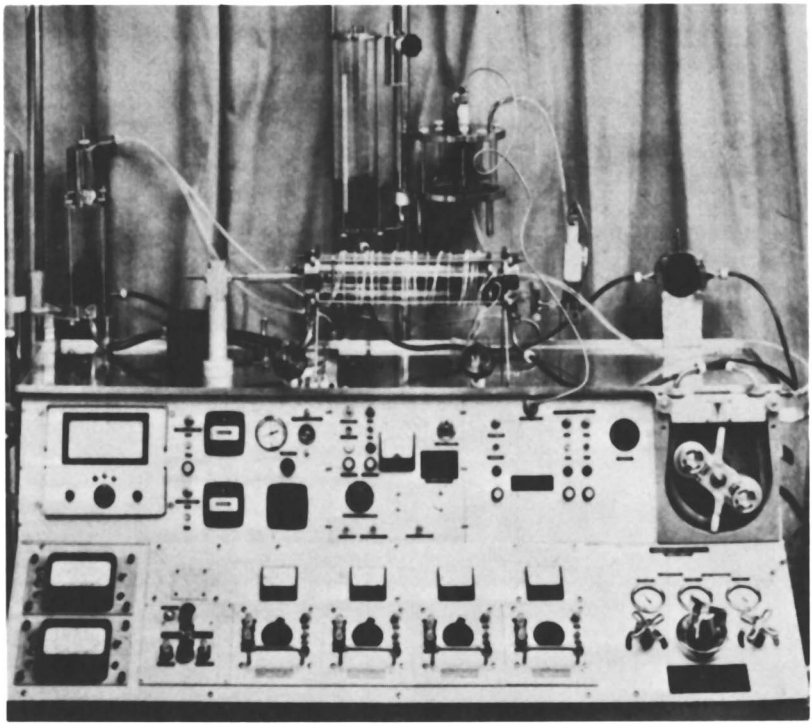

Diseases of the Chest

Figure 3. Infant perfusion apparatus with disk oxygenator (23)

Carbon dioxide also moves according to Fick's law. The carbon dioxide diffusion gradient is about 40–50 mm Hg (blood p_{CO_2} minus atmospheric p_{CO_2}). The rate of carbon dioxide diffusion in plasma is 15–20 times that of oxygen. Increasing the diffusion gradient is not possible, and mixing the blood phase does not increase significantly carbon dioxide removal. The area over which gas exchange takes place must be increased.

Bubble and Film Oxygenators. Numerous designs of bubble oxygenators have been proposed over the past 20 years; their history and evolution is reviewed by Galletti (*18*). All designs rely on introducing bubbles of gas into a column of blood and then removing the residual

foam and any remaining microbubbles that might cause embolic problems. Thus, most have three sections: a bubbling chamber, a defoaming chamber, and a settling chamber.

Transfer of oxygen to blood would be accomplished best by introducing into the blood microbubbles which would completely dissolve. Only the arterial–venous (A–V) oxygen content difference need be introduced, and provided the bubbles could completely dissolve under the limitations imposed by flow, defoaming would be unnecessary.

Requirements of carbon dioxide removal, however, dictate that high gas flow be used; if the A–V carbon dioxide difference is 4 vol %, then 4 cm^3 of carbon dioxide/100 ml of blood must be removed. The gas that carries carbon dioxide away will, at best, be fully equilibrated with the blood. At a blood p_{CO_2} of 40 and at normal barometric pressure, a minimum of 76 ml of gas is required to remove 4 ml of carbon dioxide from 100 ml of blood. Because full equilibration is highly inefficient, bubble oxygenation requires gas-to-blood flow ratios of 4:1–10:1. The choice of bubble size lies between the one extreme of small bubbles with a huge total surface area and a thick liquid film between bubbles and the other extreme of large bubbles with a much smaller total surface area but with a thinner film between them. Also, small bubbles are difficult if not impossible to remove completely from the blood. High gas-to-blood flow ratios are necessary to obtain adequate oxygen exchange with bubbles of a size easily removed from the blood; in achieving this, the blood may be actually purged of too much carbon dioxide. Therefore, it is not uncommon to use a 2–3% mixture of carbon dioxide in oxygen to establish a lower limit of outflow p_{CO_2}.

The defoaming of blood is usually accomplished with the aid of silicone-coated mesh. Dimethylpolysiloxane-based antifoams can be used to coat Teflon or steel or polypropylene mesh. A settling chamber is used separately or as part of the defoaming chamber to allow all residual bubbles to escape.

Advantages of the bubble oxygenator are simplicity of design with resultant low cost and assured function. Gaseous anesthetics may be administered *via* the oxygenator by adding appropriate amounts of the agent to the oxygenating gas.

The Temptrol oxygenator is an example of a commercially available bubble oxygenator suited for infant use (*28*) (Figure 1). The unit, formed of polycarbonate halves cemented together, contains an upper chamber (Figure 4) in which bubbling and defoaming over a silicone-coated polypropylene mesh occur, and a lower cylindrical chamber which acts as a settling chamber and contains a heat exchanger. The latter is a colloidal graphite-coated metal can in which flows thermostatted water.

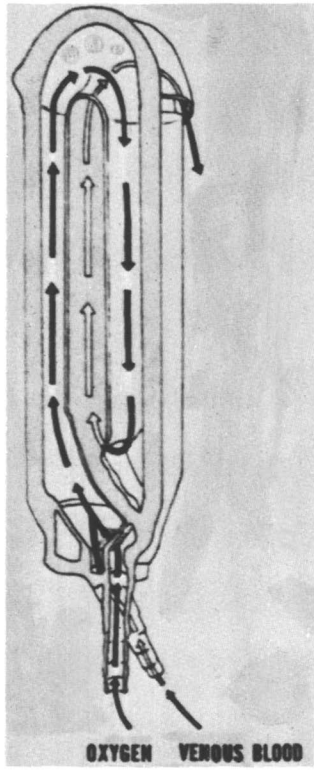

Journal of Thoracic and Cardiovascular Surgery

Figure 4. Cross sectional schematic view of the oxygenating column of the infant Temptrol oxygenator. Arrows indicate the pathway of blood flow (28).

The manufacturer recommends a maximum blood flow of 1500 ml/min, a maximum gas flow of 6 liters/min, and a prime volume of 500–1500 ml. The hole size in the bubbler is 0.007 inch.

Evaluating this unit *in vitro,* Clark and Mills found the maximal oxygen transfer rate to be 34 ml/min at a gas-to-blood flow ratio of 8:1 and at 1500 ml/min blood flow (Figure 5).

The dangers of gas embolization are substantially reduced when the blood is spread in a thin film on either a moving or a stationary support and ventilating gas is passed over it. The most commonly used oxygenator of this type is the disk oxygenator (Figure 6) in which rotating disks partially submerged in a reservoir of blood pick up a film of blood, carry it through the ventilating gas, and return it to the blood reservoir. Venous

blood flows in one end of the reservoir and oxygenated blood exits from the other. The factors influencing gas diffusion are the same as those described for the bubble oxygenator. The surface area available each minute for gas exchange is determined by the blood film surface area on each disk, the rate of disk rotation, and the total number of disks. Oxygen exchange may be enhanced by maximizing the diffusion gradient and the surface area. Carbon dioxide exchange may be similarly enhanced by increasing the ventilation through the device. Too rapid disk rotation may cause foaming and is to be avoided.

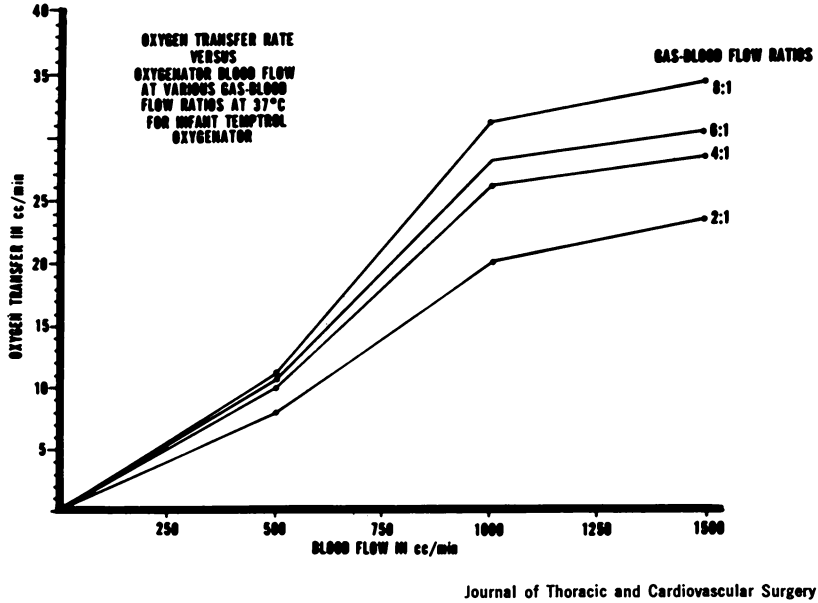

Figure 5. Oxygen transfer rate vs. *blood flow at various gas-to-blood flow ratios* (28)

The modified Kay–Cross disk oxygenator (23) (Figures 3 and 6) has disks that are flat stainless steel, 0.5 mm thick; the fewest number of disks used is 22. *In vitro* experiments establish a maximal oxygenating capacity of 0.690 ml of oxygen/min/disk at 100 rpm. Increasing the revolutions per minute by 20% increases the oxygen transfer by a similar amount. No increase in oxygen exchange is observed at disk rotations greater than 140 rpm. In clinical use, the oxygenating capability is assumed to be 0.5 ml of oxygen/min/disk, and the number of disks used is based on the patient's expected oxygen consumption. The advantage of disk oxygenation is the lack of foaming and the low risk of gas embolization.

Bubble and disk oxygenators share a number of disadvantages. Most importantly, one must remember that they can be lethal devices. Bubble or disk oxygenators are relatively safe only for a small number of hours after which patients (or animals) will not survive. The reasons for this appear to include the denaturation of blood proteins and protein complexes at the blood–gas interface (*29*, *30*). Bubble and film oxygenation of dog plasma has been shown to denature α-lipoprotein with accumulation of an abnormal insoluble phospholipid, cholesterol, triglyceride, and

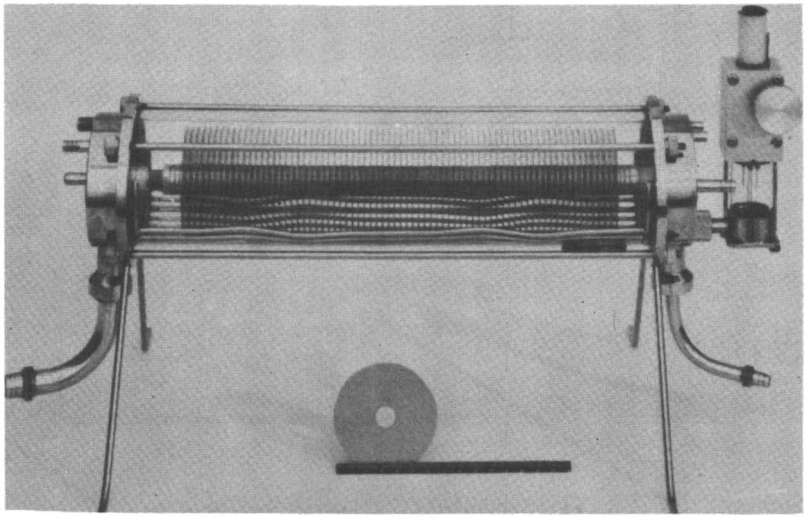

Diseases of the Chest

Figure 6. Infant disk oxygenator (23)

protein complex. These changes are detected after as little as 3 hours (*31*). Hemolysis is also appreciable in these devices, and hemaglutination of red cells with sludging can occlude the microcirculation (*29*).

When applied to infants, both disk and bubble oxygenators have the disadvantage of having an open or variable prime so that the venous inflow and the arterial outflow need to be precisely matched to avoid fatal shifts of fluid into or out of the patient.

Despite drawbacks, these devices can support infants through most cardiac surgery. For complex procedures the surgeon may desire an oxygenator which can function for long periods of time without doing harm. Also, in considering treatment of RDS with extracorporeal oxygenation, one must think in terms of prolonged gas exchange which is essentially noninjurious to blood.

Membrane Oxygenator. The problems of surface denaturation inherent in the bubble or film oxygenator are avoided by interposition of a

thin permselective membrane between the gas and the blood compartments of the oxygenator. This adds an additional barrier to the diffusion of oxygen and carbon dioxide. Carbon dioxide is usually about five times more permeable in a given synthetic membrane than oxygen. Permeabilities of a number of synthetic membranes to oxygen and carbon dioxide are shown in Table I. Silicone rubber has been chosen by the designers of most membrane oxygenators because of its high permeabilities, convenient physical properties, and biocompatibility. Oxygen permeability in silicone rubber is roughly 500 times greater than in plasma. Therefore, the blood plasma and particularly the stagnant layer of oxygenated plasma adjacent to the membrane provide a greater diffusion resistance to oxygen than does the synthetic membrane.

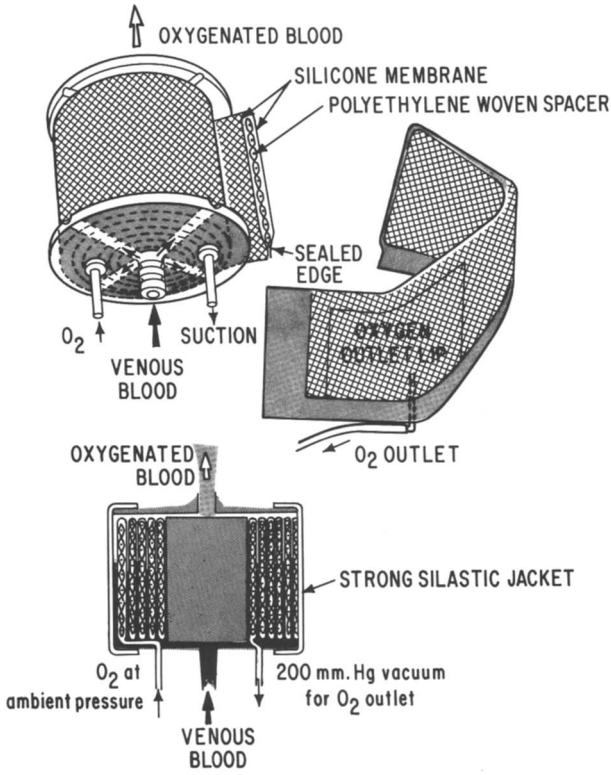

Figure 7. Schematic of the spiral coil oxygenator

Carbon dioxide, on the other hand, diffuses very rapidly through plasma, but less rapidly through silicone rubber. Because the diffusion gradient for carbon dioxide cannot be increased, it is necessary to increase

Table I. Approximate Permeation Coefficients of Materials Used to Manufacture Semipermeable Membranes[a]

Material	D'_{O_2}	D'_{H_2O}	$\frac{D'_{CO_2}}{D'_{O_2}}$
	ml cm/cm²/sec/cm Hg × 10^{-11}		
Polyvinylidene chioride (Saran)	0.05[1] 0.06[2]	0.01[2]	0.8[2]
Monochlorotrifluoroethylene (Trithene A)	0.09[2]	0.02[2]	10.7[2]
Polyester (Mylar)	0.22[1] 0.67[2]	0.09[2]	1.8[2]
Nylon 6	0.38[1]	—	—
Cellulose acetate	6.6[2] 6.0[3] 7.8[1]	5.4[2]	5.1[2]
Polypropylene	11.2[2]	0.04[2]	3.4[2]
Butyl rubber	13.0[1]	—	—
Polystyrene	18.6[2]	0.43[2]	4.9[2]
Polyethylene	35[4] 41[3] 55[1] 3.8–31.0[5] 8.5–34.4[2]	0.01–0.07[2]	 4–5[3] 2.6–4.6[2]
Tetrafluorethylene (Teflon)	66[2] 105[3]	0.02[2]	2.7[2] 2.6–4.0
Ethylcellulose (Ethocel)	96[2] 100[3] 265[4]	4.5[2]	4.1[2] 4.3[3]
Natural rubber	230[14] 327[3]	—	5[3] 5.6[3]
Silicone rubber (Silastic 50) (Silastic S–2000)	2600[4] 5890[2] 6500[3]	10.2[2]	4–5[4]
Microporous polyethylene (Permax)	130,000– 400,000[3]		
Blood plasma	6.5–10.1[6]	—	32–15

[a] From Galletti and Brecher (*18*) by permission of the publisher.

the diffusion area and this becomes the critical factor in determining the membrane area in a membrane oxygenator.

Blood phase mixing will maximize oxygen transfer and is accomplished in several ways. Membranes with rough surfaces will cause a turbulent flow of blood. Pulsing the blood flow or moving the membrane surface will provide further mixing. Shaking the entire device has been shown to introduce secondary flows within the blood phase of the oxygenator with such good mixing that oxygen transfer becomes membrane limited (*32*). Finally, minimizing the blood film thickness increases oxygen transfer.

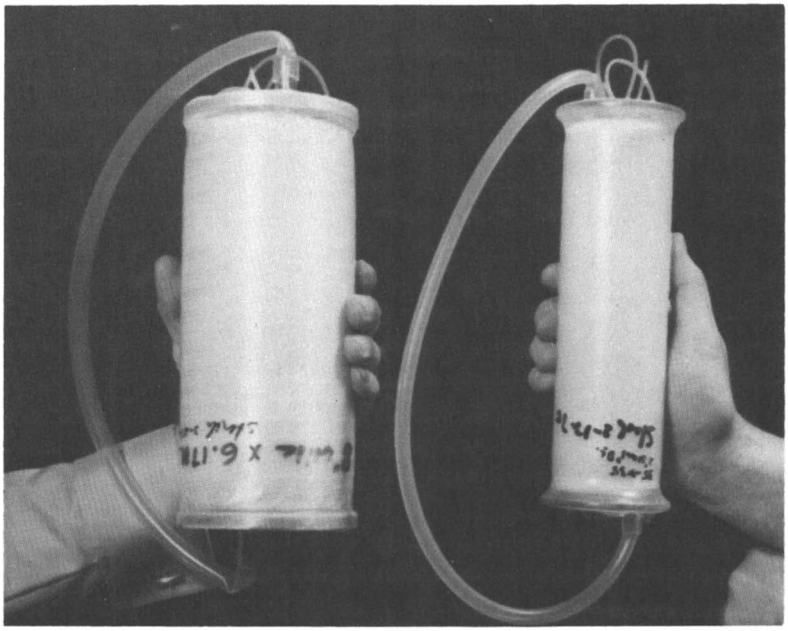

Figure 8. Spiral coil oxygenators: 2.5 m^2 and 1.5 m^2

There are three basic membrane oxygenator configurations: the stacked or layered devices, the spiral coil device, and the capillary design. The stacked devices include Lande–Edwards (*25*), the General Electric–Pierce (*33*), and the Travenol (*34*) oxygenators. A spiral-coil design has been developed in our laboratory at the National Institutes of Health and is commercially available (*24*). A capillary device is made by Dow Chemical Co.

The spiral coil oxygenator illustrates many of the problems and advantages of membrane oxygenators. It contains a sealed membrane

envelope enclosing a spacer screen and provided with oxygen inlets and outlets at appropriate intervals (Figures 7 and 8). The membrane envelope is constructed of cast silicone rubber film 0.005 inch thick which contains a reinforcing nylon mesh. The spacer screen within the envelope is Saran and has sufficiently close mesh to prevent the membrane sur-

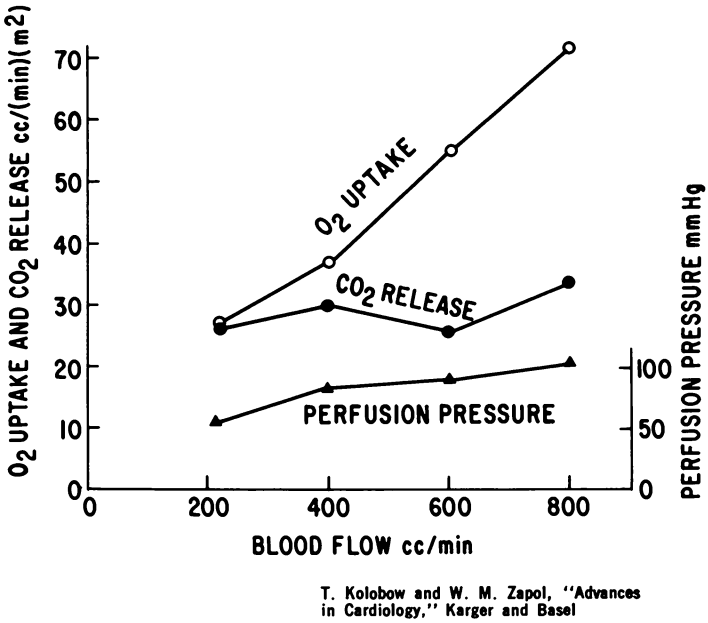

Figure 9. Gas exchange vs. blood flow in the spiral coil oxygenator (35)

faces from touching when deformed by subatmospheric pressure within the envelope. The membrane envelope is wound around a spool, and the envelope and spool are sealed within a tight-fitting silicone rubber jacket. Blood flows in a port on one end of the spool between the outer surfaces of the coiled membrane envelope and out a port on the other end of the spool. Subatmospheric pressure draws oxygen through the sealed membrane envelope while flattening the membrane onto the Saran screen, thus providing a space for blood passage. Using a subatmospheric pressure within the membrane envelope eliminates the danger of gas embolization into the blood should any hole develop in the membrane. The prime volume of the oxygenator is about 80 ml/m^2 of membrane used plus 25–60 ml for the headers.

Respiratory blood gas exchange occurs as the blood flows across the width of the spiral-wound membrane envelope; the blood film formed is about 160 μ thick. Blood oxygen saturation difference on passing through

the membrane lung increases with greater membrane width and decreases with increasing blood flow. The blood compartment is mixed by placing the rough fabric-containing membrane surface in contact with the blood and by pulsing the vacuum which draws oxygen through the envelope. This causes an in-and-out motion of the membrane surface and thereby increases blood mixing. Oxygen transfer is a function of blood flow, higher flows giving increasing transfers; oxygen transfer to blood with a hemoglobin content of 15 g % levels off at about 60 ml/min/m^2 independent of the width of the membrane envelope (Figure 9) (*35*).

Carbon dioxide transfer is maximized by ventilating the gas compartment with 2–2.5 liters O_2/min/m^2. With this ventilation the gas compartment p_{CO_2} is kept low, and about 45 ml/min/m^2 of carbon dioxide is exchanged.

For a patient with an A–V oxygen difference of about 5 vol % and an A–V carbon dioxide difference of about 4 vol %, about 1 square meter of membrane surface is necessary for each liter of blood flow. At this flow rate the blood perfusion pressure through the membrane long ranges from 30–150 mm Hg, depending on the width of the membrane envelope.

The Lande–Edwards gas exchanger contains plastic membrane support plates shaped so that under positive blood pressure the membrane is deflected into preformed grooves in the plates. Three-centimeter-long channels about 240–320 μ thick are formed. There are 1440 channels/plate (each plate = 1/19 m^2 membrane area). Because of the multiple short blood flow paths, resistance is low. Oxygen exchange increases with increasing flow in the 3-square-meter unit, reaching about 30 ml/min/m^2 at a blood flow of 1500 ml/min/m^2. Carbon dioxide exchange averages 21.6 ml/min/m^2 at a blood p_{CO_2} of 40 mm Hg (*36*). At 1500 ml/min/m^2 the pressure drop across the device is 20 mm Hg.

The capillary oxygenator attempts to minimize prime volume and to overcome the structural weakness of silicone rubber by using a tubular geometry (*5*). In most devices of this kind, blood flows through capillary tubes while the ventilating gas travels radially from the center to the outside of the capillary bundle. In one variant (*37*) the gas flows within the lumen of the tubes, and blood surrounds them. Oxygenation in the capillary lung is enhanced by using external vibration to mix the blood phase and by coiling the individual tubes into tight helices (*5*). Carbon dioxide transfer is limited by capillary wall thickness.

A capillary lung produced by Dow Chemical Co. (*38*) can pass 1.4 liters/min/m^2 of blood. It has siloxane–polycarbonate copolymer hollow fibers of 150 μ inside diameter, 25 μ wall thickness, and is 8.5 cm in active length. Prime volume is 100 ml/m^2. One square meter transfers 51 ml/min of oxygen and 66 ml/min of carbon dioxide at 1.4 liters/min/m^2

blood flow. At that flow, the pressure difference across the device is 180 mm Hg.

A capillary oxygenator has been used on a number of infants with good performance (*5*). Present difficulties with the capillary lung lie in the area of fabrication, particularly in the manifolding of blood into the capillary channels.

The chief advantage of a membrane oxygenator is its lack of damage to formed and soluble constituents of the blood. *In vitro* studies suggest this lack of toxicity (*31*), and *in vivo* studies have repeatedly confirmed it in animals (*39, 40*) and in man (*41, 42*). Free hemoglobin values remain within the normal range, and no disturbance of plasma lipoproteins is found. More to the point, the membrane oxygenator is not a lethal device. It has been used in animals for up to 16 days without the evolution of cardiopulmonary pathology (*19*). A further advantage of most membrane oxygenators is the relatively fixed prime volume which prevents fluid shifts into and out of the patient. No complicated sensing devices are necessary to ensure constant fluid volume in the extracorporeal circuit. Gas embolization is not seen when the gas exchanger is ventilated with gas at subatmospheric pressure.

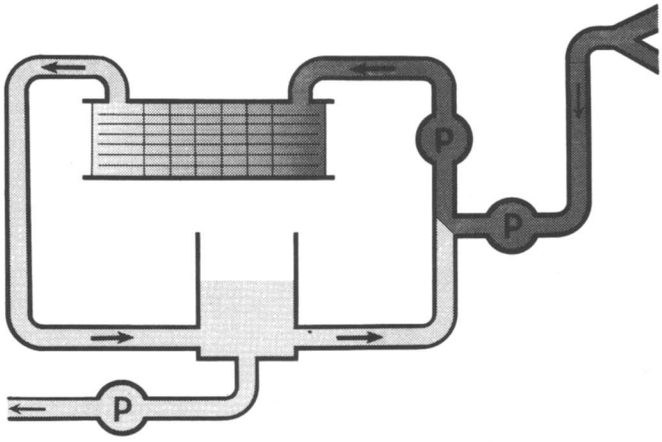

P. M. Galletti and G. A. Brecher, "Heart-Lung Bypass," Gune and Stratton

Figure 10. Blood circuit using recirculation (18)

For the membrane devices described, oxygen transfer increases within limits as blood flow increases. This has led some workers to use a recirculating technique (*43*), pumping a larger quantity of blood per minute through the blood gas exchanger than is being pumped to the patient. The excess flow is recirculated back to the venous inflow port of the exchange device (Figure 10).

The development of consistently strong, thin, inexpensive, pinhole-free membrane has lagged, and this fact, more than any other, has kept membrane oxygenators from wide clinical acceptance and application. Enthusiastic clinical reports (*4*, *43*) indicate that the potential use of membrane oxygenators with infants is great.

Another oxygenator, yet to see clinical use, is the liquid–liquid oxygenator which depends on the transfer of gases between blood and, most often, oxygen-saturated fluorocarbon fluid. In one design (*44*) oxygenated fluorocarbon is pumped up Teflon chimneys standing within a blood column. It spills over the edge of the tubes, and because of its high density, flows in a thin continuous sheet downward, collecting in the bottom of the chamber. The deoxygenated fluorocarbon fluid then flows to a bubble oxygenator where it is heated and reoxygenated. Such a device with a 0.25 m^2 exchange area and a prime volume of 450 ml has an oxygen transfer of 78 ml/min/m^2 at 1 liter blood flow. Carbon dioxide removal depends on the rapidity of circulation of the fluorocarbon and the solubility of carbon dioxide in it. The device has been successfully used for organ preservation.

In applying any of the devices mentioned to the infant, one practical problem encountered is how to remove enough blood from the infant to be oxygenated. For open heart surgery the large veins may be cannulated, but for prolonged support of the closed chest infant with pulmonary failure, the use of thin-walled (0.009–0.12 inch) conduits is imperative to maximize blood flow. Such catheters have been specifically designed and constructed of polyurethane with a steel spring reinforcement (*45*).

Perhaps the most pressing problem, however, is the development of nonthrombogenic surfaces to make the use of massive doses of heparin a thing of the past. The dangers of total anticoagulation, particularly in long-term support, are such that only the moribund patient is treated with a device which, if it could be applied earlier in the course of his disease, might exert a far more life-saving effect.

Literature Cited

1. Mustacchi, P., Sherins, R. S., Miller, M. J., *J. Amer. Med. Ass.* (1962) **183**, 241.
2. Malm, J. R., Bowman, F. O., Jesse, M. J., Blumenthal, S., *Amer. J. Surg.* (1970) **119**, 613.
3. Baffes, T. G., Fridman, J. L., Bicoff, J. P., *Ann. Thoracic Surg.* (1970) **10**, 354.
4. White, J. J., *Trans. Amer. Soc. Artif. Int. Organs* (1970) **16**, 357.
5. Dorson, W., Jr., Baker, E., Cohen, M. L., Meyer, B., Molthan, M., Trump, D., Elgas, R., *Trans. Amer. Soc. Artif. Int. Organs* (1969) **15**, 155.
6. Avery, M. E., "The Lung and Its Disorders in the Newborn Infant," p. 145, Saunders, Philadelphia, 1968.

7. Lundig, M., Rygg, I. H., *Scand. J. Thoracic Cardiovas. Surg.* (1968) **2**, 169.
8. Sevringhaus, J. W., *Ann. N.Y. Acad. Sci.* (1959) **80**, 384.
9. Swan, H., "Surgery of the Chest," p. 89, J. H. Gibbon, Ed., Saunders, Philadelphia, 1962.
10. Bernhard, W. F., "The Heart and Circulation in the Newborn and Infant," p. 379, D. E. Cassels, Ed., Grune and Stratton, New York, 1966.
11. Jacobson, J. H., Wang, M. C. H., Reich, T., "Cardiac Surgery," Ch. 12, p. 166, J. C. Norman, Ed., Meredith, New York, 1967.
12. Pittinger, C. B., "Hyperbaric Oxygenation," p. 70, Amer. Lectures in Anaes., J. Adriani, Ed., Charles C. Thomas, Springfield, 1966.
13. Cross, K. W., "Neonatal Respiratory Adaptation," p. 149, T. K. Oliver, Ed., U.S. Government Printing Office, Washington, D.C., 1963.
14. Cook, C. D., Cherry, R. B., O'Brien, D., Karlberg, P., Smith, C. A., *J. Clin. Invest.* (1955) **34**, 975.
15. Gollan, F., "Physiology of Cardiac Surgery," p. 53, Ryerson Press, Toronto, 1959.
16. DeWall, R., Lillehei, R. C., Sellers, R. D., *New Engl. J. Med.* (1962) **266**, 1078.
17. Roe, B. B., Hutchinson, J. C., Swenson, E. E., *Ann. Thoracic Surg.* (1965) **1**, 581.
18. Galletti, P. M., Brecher, G. A., "Heart-Lung Bypass," p. 313, Grune and Stratton, New York, 1962.
19. Kolobow, T., Spragg, R. G., Pierce, J. E., Zapol, W. M., *Trans. Amer. Soc. Artif. Int. Organs* (1971) **17**, 350.
20. DeWall, R. A., Bentley, D. J., Mitsuo, H., Beattung, V., Najafi, H., Roden, T., *Dis. Chest* (1966) **49**, 207.
21. Gott, V. L., DeWall, R. A., Paneth, M., Zuhdi, N., Weirich, W., Varco, R. L., Lillehei, C. W., *Thorax* (1957) **12**, 1.
22. Kay, E. B., Cross, F. S., *Surg. Gynec. Obstet.* (1957) **104**, 701.
23. Thompson, N. B., *Dis. Chest* (1965) **48**, 416.
24. Kolobow, T., Zapol, W. M., Sigman, R. L., "Blood Oxygenation," p. 306, D. Hershey, Ed., Plenum, New York, 1970.
25. Landé, A., Tiedeman, R. N., Subramanian, V. A., Fillmore, S. J., Lillehei, C. W., *Proc. Artif. Heart Prog. Conf.* (1969), 417.
26. Thews, G., Niesses, W., *Pflüger Arch. Ges. Physiol.* (1959) **268**, 318.
27. Weinreich, A., Lipton, B., Brondum, T., Jacobson, J. H., II, *Anaes. Analg.* (1970) **49**, 977.
28. Clark, R. E., Mills, M., *J. Thoracic Cardiovas. Surg.* (1970) **60**, 54.
29. Lee, W. H., Jr., Krumhaar, D., Fonkalsrud, E. W., Schjeide, O. A., Maloney, J. V., Jr., *Surgery* (1961) **50**, 29.
30. Owens, G., Adams, J. E., McElhannon, F. N., Youngblood, R. W., *J. Appl. Physiol.* (1959) **14**, 947.
31. Zapol, W. M., Levy, R. I., Kolobow, T., Spragg, R. G., Bowman, R. L., *Current Topics Surg. Res.* (1969) **1**, 449.
32. Drinker, P. A., Bartlett, R. H., Bialer, R. M., Noyes, B. S., Jr., *Surgery* (1969) **66**, 775.
33. Pierce, E. C., II, *Proc. Artif. Heart Prog. Conf.* (1969), 405.
34. Wildevuur, C. R. H., Kuipers, J. R. G., Spaan, J. A. E., Sugawara, H., Onodera, I., *Trans. Amer. Soc. Artif. Int. Organs* (1971) **17**, 362.
35. Kolobow, T., Zapol, W. M., "Advances in Cardiology," p. 112, R. H. Bartlett, P. A. Drinker, and P. M. Galletti, Eds., S. Karger, Basel, 1971.
36. Pierce, E. C., II, *Trans. Amer. Soc. Artif. Int. Organs* (1970) **16**, 358.
37. Zingg, W., *Canad. J. Surg.* (1970) **13**, 279.
38. Dutton, R. C., Mather, J. W., III, Walker, S. N., Lipps, B. J., Jr., Rudy, L. W., Sevringhaus, J. W., Edmunds, L. H., Jr., *Trans. Amer. Soc. Artif. Int. Organs* A1971) **17**, 331.

39. Kolobow, T., Zapol, W., Pierce, J., *Trans. Amer. Soc. Artif. Int. Organs* (1969) **15**, 172.
40. Landé, A., Fillmore, S. J., Subramanian, V., Tiedemann, R. N., Carlson, R. G., Bloch, J. A., Lillehei, C. W., *Trans. Amer. Soc. Artif. Int. Organs* (1969) **15**, 181.
41. Hill, J. D., Fallat, R., Cohn, K., Eberhart, R., Dontigny, L., Bramson, M. L., Osborn, J. J., Gerbode, F., *Trans. Amer. Soc. Artif. Int. Organs* (1971) **17**, 355.
42. Landé, A., Edwards, L., Bloch, J. H., Carlson, R. G., Subramanian, V., Ascheim, R. S., Scheidt, S., Fillmore, S., Killip, T., Lillehei, C. W., *Trans. Amer. Soc. Artif. Int. Organs* (1970) **16**, 352.
43. Baffes, T., *Trans. Amer. Soc. Artif. Int. Organs* (1971) **17**, 380.
44. Pitzele, S., Sze, S., Hagemann, A., Dobell, A. R. C., *Surgery* (1970) **68**, 1079.
45. Kolobow, T., Zapol, W. M., *Surgery* (1970) **68**, 625.

RECEIVED November 22, 1971.

10

Use of Systems Techniques in the Analysis of the Control of Erythropoiesis

KENNETH C. MYLREA

Instrumentation Systems Center, University of Wisconsin, Madison, Wis. 53706

PETER H. ABBRECHT

Department of Physiology, University of Michigan, Ann Arbor, Mich. 48104

A mathematical model of the control system for erythropoiesis is presented. It is postulated that the rate of erythropoiesis is controlled by a hormone, erythropoietin, which is released from the kidney in response to reduced renal oxygen supply. Equations are developed relating erythropoietin release to arterial oxyhemoglobin concentration, and hemoglobin production to plasma erythropoietin concentration, with appropriate time delays. Effects of plasma volume changes during hypoxia are included. The model simulates the dynamic response of the erythropoietic system to a step decrease in the pO_2 *of inspired air. Contributions of the parameters and relationships to the predicted response are analyzed. The model response compares favorably with experimental data obtained from mice subjected to different degrees of hypoxia.*

It is a complex and tedious task to understand completely the behavior and interaction of biological systems. Redundancies, interactions, and complexities are well beyond what might be imagined necessary for a physical or engineering system. Regardless of this, ideas are formed on the interaction of components, and theories are advanced to explain the behavior of biological systems. These ideas and theories constitute conceptual models which are evaluated and tested in experiments designed for that purpose.

Research in many areas of biology and medicine has progressed to the point where the basic operational concepts of specific physiological

systems are well understood. However, we should not underestimate the additional efforts needed before a complete understanding of these systems is attained. As the number of subsystem interactions increases, some mechanism is required to assist the researcher in understanding the complex interactions. Such a mechanism or tool should allow observation of the behavior of the system in response to a particular stimulus. An operational model developed from a mathematical description of a system can satisfy these requirements, and when used in a predictive role it can stimulate new research ideas.

One factor which might appear as a deterrent to the development and use of mathematical models is the requirement that the ambiguous, ill-defined relationships which are so often part of a conceptual model must be converted into quantitative equations. This procedure is a useful exercise since it distinguishes between what is known accurately and what is pure speculation.

Once a mathematical model has been formulated, the researcher has the means to test his ideas and evaluate his concept of the system. In addition, different experimental situations can be simulated to select optimal protocol for experiments.

The balance of this paper will be devoted to a model that has been used to facilitate the understanding of a complex biological control system. The erythropoietic system is relatively simple. However, when the interactions of associated physiological systems are considered, the control of erythropoiesis becomes highly interactive and complex.

The Control System for Erythropoiesis

The basic erythropoietic control system consists of the following. The kidney produces and releases a hormone—erythropoietin—in amounts that depend on the state of tissue oxygenation. This hormone is carried in the blood stream to the bone marrow where it stimulates the production of red blood cells. The increased concentration of red blood cells allows the delivery of more oxygen per unit time to the erythropoietin-producing tissue and thus reduces the stimulus for increased production of the hormone.

While this concept for the control of erythropoiesis is generally accepted, there are at present insufficient data to determine quantitative relationships among the variables involved. In addition, some auxiliary systems must be included to describe fully the erythropoietic response to stress such as hypoxia. The performance of the respiratory system and the relationships expressed by the oxyhemoglobin dissociation curve affect the oxygenation state of the blood. Blood volume, and in particular plasma volume, affect hemoglobin concentration which limits the amount

of oxygen that can be carried per unit volume of blood. Cell destruction along with production must be considered to determine the total circulating hemoglobin at any given time. All of these factors must be considered in predicting the behavior of the erythropoietic system.

A mathematical model was developed to facilitate studies of the system and to evaluate the effects of system parameters in response to various stimuli. The model and the derivation of parameters and relationships have been described in detail elsewhere (*1*), and only general characteristics will be repeated here.

The model was designed to simulate the response of the erythropoietic system to a step decrease in the pO_2 of inspired air. However, the response to other types of stimuli such as acute hemorrhage could also be evaluated.

Data for testing the model were obtained from mice which were subjected to three different step changes in ambient pressure representing mild, moderate, and severe hypoxia. At predetermined times after the beginning of hypoxia, samples of mice were selected, and measurements were made of hematocrit, hemoglobin concentration, red blood cell and reticulocyte count, blood volume, and mouse weight. Total circulating hemoglobin, total blood volume, total circulating red cell mass, and the red blood cell indexes were calculated from these measurements. A detailed description of the methods used and the resulting data have been published elsewhere (*2*). These experimental data as well as other data available in the literature were used to estimate parameter values in the model. Data shown on the figures here are the same as reported previously (*2*) and are repeated to allow evaluation of the model output using the new relationships and parameter values.

The Model

Major components of the model are shown in Figure 1. In the model the controlled variable is oxyhemoglobin concentration (the product of hemoglobin concentration and percent oxygen saturation). Erythropoietin is released from the kidney according to an exponential relationship (Equation 1) relating oxyhemoglobin concentration to the rate of erythropoietin release.

$$R(t) = K_1 e^{-K_2[HbO(t-T_1)]} \tag{1}$$

where

$R(t)$ = rate of erythroproietin release at the time t

$HbO(t - T_1)$ = oxyhemoglobin concentration at time $(t - T_1)$

K_1 and K_2 are constants

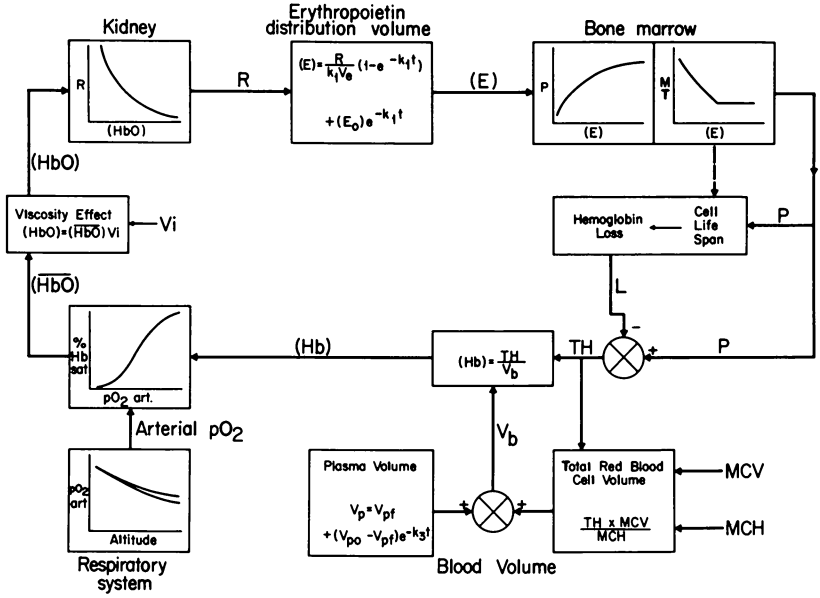

Figure 1. Block diagram of a model for the control of erythropoiesis (HbO), oxyhemoglobin concentration; Vi, viscosity factor; (HbO), effective oxyhemoglobin concentration; R, rate of erythropoietin release; (E), plasma erythropoietin concentration; E_o, normal plasma erythropoietin concentration; V_e, distribution volume for erythropoietin; P, rate of hemoglobin production; MT, erythrocyte maturation time; L, rate of hemoglobin loss; TH, total circulating hemoglobin; (Hb), blood hemoglobin concentration; V_b, blood volume; V_p, plasma volume; V_{po}, normal plasma volume; V_{pf}, steady-state hypoxic plasma volume; MCV, mean corpuscular volume; MCH, mean corpuscular hemoglobin; k, constant.

A delay of 4 hours (T_1) was incorporated into the model between changes in oxyhemoglobin concentration and subsequent erythropoietin release to account for the time required from release of the renal erythropoietic factor to the development of active erythroproietin in the blood stream (3). Values for K_1 and K_2 were estimated for the mouse by scaling a relationship derived from data in rats, relating oxyhemoglobin concentration to erythropoietin release (1). It was assumed that the released erythroproietin mixes instantly in a volume equal to twice the plasma volume and that the disappearance rate of erythropoietin is proportional to the plasma erythropoietin concentration with a disappearance constant of .130 day (4).

In the model, plasma erythropoietin concentration was used to determine the amount of hemoglobin produced and the time delay before new red blood cells (hemoglobin) are released into the blood stream. Equation 2 shows the postulated relationship between the rate of hemoglobin production and plasma erythropoietin concentration.

$$P(t) = Pm \{1 - K_3 e^{-K_4[E(t)]}\} \quad (2)$$

where

$P(t)$ = rate of hemoglobin production at time t

Pm = maximum rate of hemoglobin production

$[E(t)]$ = plasma erythropoietin concentration at time t

K_3 and K_4 are constants

The maximum rate of hemoglobin production is assumed to be seven times the normal production. The two constants, K_3 and K_4, were calculated using the conditions that (1) normal erythropoietin concentration results in normal hemoglobin production and (2) a basal hemoglobin production of .005 gram/day occurs when erythropoietin concentration is zero.

Two relationships were used to determine the time delay (maturation time) between the stimulation of red blood cell production by erythropoietin and the release of mature red blood cells (hemoglobin) into the blood stream. Normally cells are assumed to mature and enter the blood stream 3.75 days after stimulation by erythropoietin. However, this maturation time can vary from 2.5 to approximately 4.0 days, depending on the plasma erythropoietin concentration at the time of stimulation. This relationship is shown in Equation 3.

$$\begin{aligned} \text{Maturation time} &= 3.8\, e^{-K_5[E(t)]} && 0 < E(t) \leq E_k \\ &= 2.5 && E(t) > E_k \end{aligned} \quad (3)$$

where

$[E(t)]$ = erythropoietin concentration at the beginning of the maturation time

K_5 and E_k are constants

E_k is the arbitrarily selected value of erythropoietin concentration above which the maturation time will remain at 2.5 days. K_5 was calculated by assuming 3.75 days maturation time for normal erythropoietin concentration.

With very high concentrations of erythropoietin, a few of the cells skip one of the mitotic divisions during maturation and are released prematurely into the blood stream. In the model these early cells mature and enter the blood stream 1.5 days after stimulation by erythropoietin. Early cells are produced only when erythropoietin concentration is greater than a preselected value (E_e). The percentage of hemoglobin released in early cells is calculated as shown in Equation 4.

$$\text{Percent of hemoglobin released early} = 100 \left\{1 - \frac{(E_e)}{[E(t)]}\right\} \quad (4)$$

where

(E_e) = erythropoietin concentration below which no early cells are produced

$[E(t)]$ = erythropoietin concentration at the beginning of the maturation time

A characteristic of the early cells in the model is that they remain in the blood stream only 3 days. In the original model normal red blood cells were assumed to have a life span of 20 days (*1*). To account for normal variability in life span, cells were removed from the circulation according to a normal distribution centered at 20 days with a standard deviation of approximately 1 day.

Total circulating blood volume was calculated by summing plasma volume and total circulating red blood cell volume. Plasma volume changes in the model are represented by an empirically derived relationship. Upon application of a stimulus, plasma volume changes from the control value to an experimentally determined steady-state value in an exponential manner with a time constant of 1.5 days (*2*).

Total circulating red blood cell volume was calculated from experimentally determined values for mean corpuscular hemoglobin (*MCH*) and mean corpuscular volume (*MCV*) (*2*) and the model predictions of total circulating hemoglobin. In response to stimulus, *MCH* is assumed to remain constant while *MCV* changes from the control value to a steady-state value (predetermined from the data) in a linear manner during the first 5 days of stimulus.

Total circulating hemoglobin was calculated by continually integrating with time the difference between hemoglobin production and hemoglobin loss owing to the death of red blood cells. Hemoglobin concentration was calculated from total circulating hemoglobin and total blood volume. Oxyhemoglobin concentration, the controlled variable in the model, was calculated by multiplying hemoglobin concentration by the percent of hemoglobin saturated with oxygen (percent hemoglobin saturation). The oxyhemoglobin dissociation curve, relating arterial partial pressure of oxygen to percent hemoglobin saturation, was determined experimentally (*5*) and mathematically represented in the model. Changes in arterial partial pressure of oxygen in response to changes in pO_2 of inspired gas are represented in the model by a predetermined relationship. In response to sustained hypoxia, the arterial partial pressure of oxygen decreases suddenly to an acute value followed by an exponential rise with a 2-day time constant to an acclimatized value.

The acute and acclimatized values for each stimulus were determined from data available in the literature (*6*, *7*).

Since oxygen input to tissue depends upon tissue blood perfusion as well as oxyhemoglobin concentration, the latter was multiplied by a viscosity factor to account for perfusion changes resulting from the very high hematocrits that occur with severe hypoxia. Hematocrit was calculated from total red cell volume and total blood volume. The viscosity factor (Vi) was calculated from the relationship shown in Equation 5.

$$Vi = 1.1 - K_6 e^{-K_7 Hct} \quad (5)$$

where

Vi = the viscosity factor

Hct = hematocrit

K_6 and K_7 are constants

The constants K_6 and K_7 were selected to produce a viscosity factor of 1.0 for a particular hematocrit (Hct_k) and a preselected Vi when the hematocrit is 1.0. The viscosity factor has no effect when the hematocrit is less than Hct_k (normally 0.5) and maximum effect when the hematocrit equals 1. The viscosity effect was incorporated into the erythropoietic feedback system by multiplying Vi by the oxyhemoglobin concentration to produce an effective oxyhemoglobin concentration. This effective oxyhemoglobin concentration was then used to determine the rate of erythropoietin release as described earlier.

Computer Simulation

Simulation was carried out on a high speed digital computer. Initial values for each of the variables were calculated from a predetermined set of parameters. Subsequent values were calculated for 1-hour intervals of simulated time. Since shorter intervals between calculations did not appreciably change the results, it is believed that this method of simulation produces results which would compare favorably with a continuous model.

Results and Discussion

The results of the original model were compared with experimental data (*2*) in a previous publication (*1*). Although there is quite good agreement between the model output and the data, a number of discrepancies revealed some of the shortcomings in the estimated relationships of the model. Comparison of the model results with experimental data

led to a reevaluation of the conceptual relationships from which the model was created. The computer simulation was used to test different relationships in the model and to observe the effects of changes in various parameters (sensitivity). A summary of the findings from simulations using the original model (*1*) is included as background for modifications and tests.

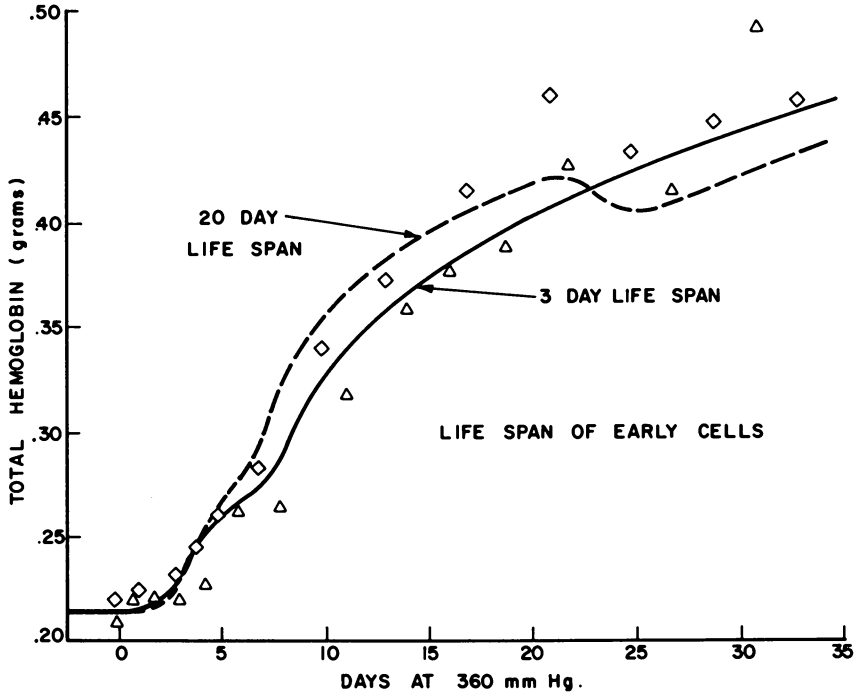

Figure 2. Experimental data (2) and the model results for mice exposed continuously to a total pressure of 360 mm Hg. Each data point is the average of values obtained from nine mice. Different symbols represent different runs. The model responses were obtained with the parameter values listed in Table I. The solid and broken lines were generated with the life span of early cells set at 3 days and 20 days respectively.

The life span of normal cells in the original model was estimated at 20 days because of a plateauing in the rate of increase of total hemoglobin 22 days after the beginning of stimulus at 360 mm Hg total pressure (*2*). Subsequent experimental data using the diisopropylfluorophosphate technique have shown that the life span of normal red blood cells for the strain of mice used is about 47 days (*8*). Therefore, the cells leaving the circulation 20 days after the beginning of stimulation at 360 mm Hg are older cells, which were left in the circulation for longer than 47 days, or

the new cells produced during the initial burst of erythropoiesis during extremely high plasma erythropoietin levels. The latter possibility was tested in the model with normal red blood cell life span set at 47 days and other modifications as described below. The results are shown in Figure 2. The parameters used in this and the following simulations are the modified parameters shown in Table I.

Table I. Parameter Values Used in the Model

Normal Erythrocyte Life Span, days	47
K_1, units erythropoietin/day	4.11×10^6
K_2, 100 ml blood/gm hemoglobin	1.35
K_3, gram hemoglobin/day	0.753
K_4, ml plasma/unit erythropoietin	20.2
K_5, ml plasma/unit erythropoietin	1.40
K_6	0.0068
K_7	4.48
T_1, days	0.167
P_m, grams hemoglobin/day	0.0116
E_k, units erythropoietin/ml plasma	0.30
E_e, units erythropoietin/ml plasma	0.20

Acute and Acclimatized Arterial pO_2

	Arterial pO_2, *mm Hg* [a]	
Total Pressure	*Acute*	*Acclimatized*
510	65	68
440	61	65
360	56	61

[a] The normal arterial pO_2 for the mouse was taken to be 78 mm Hg.

Figure 2 shows that a significant decrease in total circulating hemoglobin can occur when the early cells (cells that mature in 1 1/2 days in response to very high plasma erythropoietin) leave the circulation. The amount of decrease of total hemoglobin predicted by the model is controlled by the preselected parameter (Ee) which determines the number of early cells produced in response to a given plasma erythropoietin concentration. If the decrease in total hemoglobin in the experimental data represents a loss of cells from the circulation, at least two mechanisms are possible: (1) cells produced during the initial wave of erythropoiesis have a life span of approximately 20 days or (2) early cells and/or senescent cells are removed when the oxyhemoglobin concentration nears the level required to provide adequate tissue oxygenation. In the latter situation the system could selectively remove cells when the demand for oxygen approaches the normal. Such a mechanism might be partially

responsible for two other differences between model output and experimental data. The model response for total hemoglobin produced in response to 440 mm Hg total pressure is slightly higher than the experimental data (Figure 5), and the overshoot in total hemoglobin found experimentally in response to 510 mm Hg total pressure is not produced by the model (Figure 4). These factors point to a complication in the removal of cells from the circulation, which is not included in the model. The overshoot could also be caused by an overproduction of cells during the first few days of hypoxia followed by a sudden decrease in the rate of production. Additional experimental data are required to clarify the nature of the stimulus causing the removal of cells from the circulation.

In response to sustained hypoxia, the model predicts a sudden increase in plasma erythropoietin concentration followed by a rapid decrease with the maximum at approximately 12 hours. This type of response has been reported for man and animals (*9, 10, 11, 12*). However, in contrast to the reported experimental data, the erythropoietin levels predicted by the original model did not return to baseline levels after a few days of hypoxia. It appears that some mechanism not included in the model allows a continuing high level of erythropoiesis even after the plasma erythropoietin concentration has returned to near baseline levels. Such a mechanism has been proposed by Kretchmar in a model for the action of erythropoietin (*13*). His model predicts that the sensitivity of erythropoietin depends on the preceding level of stem cell differentiation. Increased erythropoietin concentration causes an immediate increase in stem cell differentiation as well as an increase in the effectiveness of erythropoietin during a subsequent period. His model also predicts a temporary reduction in the effectiveness of erythropoietin between an initial increase in erythropoietin concentration and the subsequent increase in erythropoietin effectiveness.

The effect of the Kretchmar hypothesis on the erythropoietin response of the model was tested by modifying the model in the following manner. A new variable was introduced to account for the increased effectiveness of erythropoietin subsequent to higher plasma erythropoietin titers. The new variable, called stem cell potentiation (*SCP*), is restricted to limits of 0.5 and 3.0 and is proportional to the average erythropoietin concentration during a 2-day interval centered at the third preceding day. The value of the variable was allowed to go to 0.5 to provide a decrease in potentiation when the erythropoietin titer is below normal. Hemoglobin production in the model was modified by multiplying the rate of hemoglobin production at time t [$P(t)$ in Equation 2] by *SCP*. The maturation time as calculated in the model is not affected by the variable *SCP*. To limit the maximum possible hemoglobin production to approximately seven times normal, the value of *Pm* in Equation 2 was set at 2.5.

This limits the maximum hemoglobin production to 7.5 when $P(t) = Pm$ and $SCP = 3.0$. Figure 3 shows the results from the model with the parameters listed in Table I (solid line) and when the stem cell potentiation variable is removed and Pm in Equation 2 is set to 7.0 (broken line). In the latter case total hemoglobin can be made to increase less readily by changing the relationship between erythropoietin concentration and hemoglobin production. The curves in Figure 3 were produced using a relationship such that hemoglobin production equals 90% of Pm when erythropoietin concentration is approximately ten times normal. A value 20 to 30 times normal would have to be assured to bring total hemoglobin levels close to the experimental data. The first assumption using a factor of ten is probably closer to the physiological situation.

Although inclusion of the variable SCP allows an increased hemoglobin production following high plasma erythrpoietin concentrations,

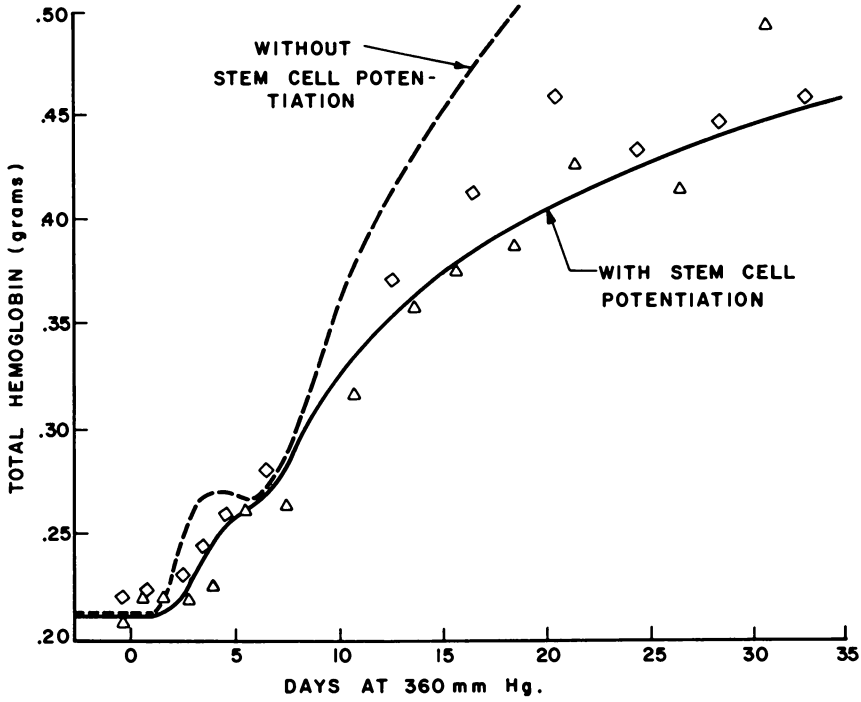

Figure 3. Experimental data (2) and the model results for mice exposed continuously to a total pressure of 360 mm Hg. Each data point is the average of values obtained from nine mice. Different symbols represent different runs. The model responses were obtained with the parameter values listed in Table I. The solid and broken lines were generated with and without stem cell potentiation (SCP) *included in the model.*

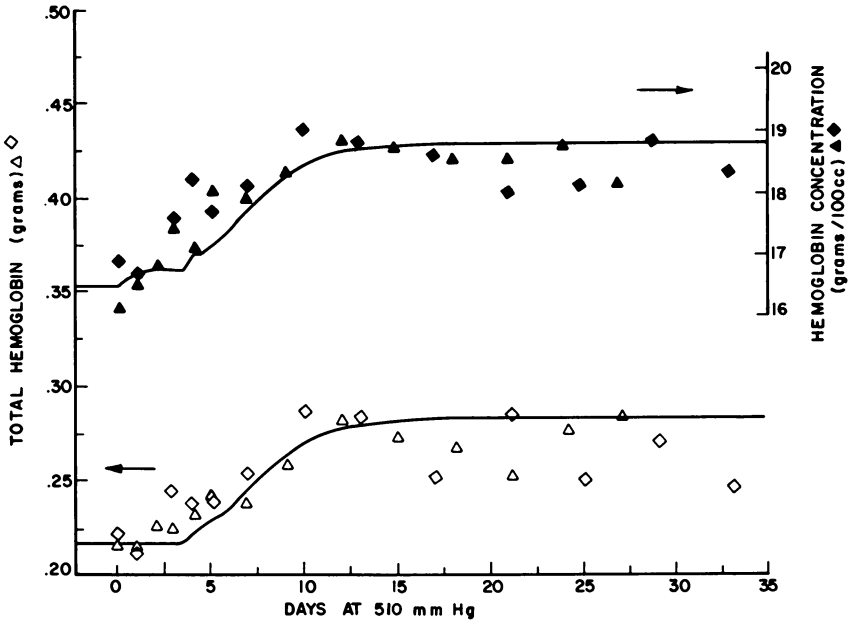

Figure 4. Experimental data (2) and the model results for mice exposed continuously to a total pressure of 510 mm Hg. Each data point is the average of values obtained from nine mice. Different symbols represent different runs. The model responses were obtained with the parameter values listed in Table I.

this variable will not significantly change the erythropoietin concentration during the first 2 to 3 days of hypoxia. It is during this time that erythropoietin concentration first increases to a maximum and then returns to near baseline levels. Three factors are responsible for the initial erythropoietin response: changes in plasma volume, changes in arterial partial pressure of oxygen, and the erythropoietin production–oxyhemoglobin concentration relationship. Since the first two factors are on firmer physiological grounds than the latter, it was decided to adjust the latter relationship to change the erythropoietin response to obtain closer agreement with physiological data. The erythropoietin response of mice to the three levels of stimuli used has been obtained (9) and the parameters for the relationship in Equation 1 were modified to produce close agreement between model results and collected data. The new values for K_1 and K_2 are shown in Table I.

With the relationship between oxyhemoglobin concentration and erythropoietin production selected to provide good agreement of erythropoietin concentration changes and experimental data, the constants in Equation 2 (hemoglobin production) were modified to produce a better total hemoglobin response. The conditions were that (1) normal plasma

erythropoietin concentration results in normal hemoglobin production and (2) a preselected level of plasma erythropoietin concentration results in a hemoglobin production rate of 0.9 the maximum rate. In addition, the minimum rate of hemoglobin production was set at one quarter of the normal rate. These conditions allowed additional flexibility in adjusting the relationship between plasma erythropoietin concentration and hemoglobin production. The values selected for constants K_3 and K_4 are shown in Table I.

The predictions for total hemoglobin and hemoglobin concentration from the modified model in response to continuous stimulation at 510, 440, and 360 mm Hg total pressure are shown in Figures 4, 5, and 6, respectively. The parameter values used in the simulation are shown in Table I. Although predictions are used to appraise the model's validity, it should be remembered that the purpose of the model is not to produce an optimal fit between experimental data and model output but to help understand the behavior and interaction of the components and subsystems.

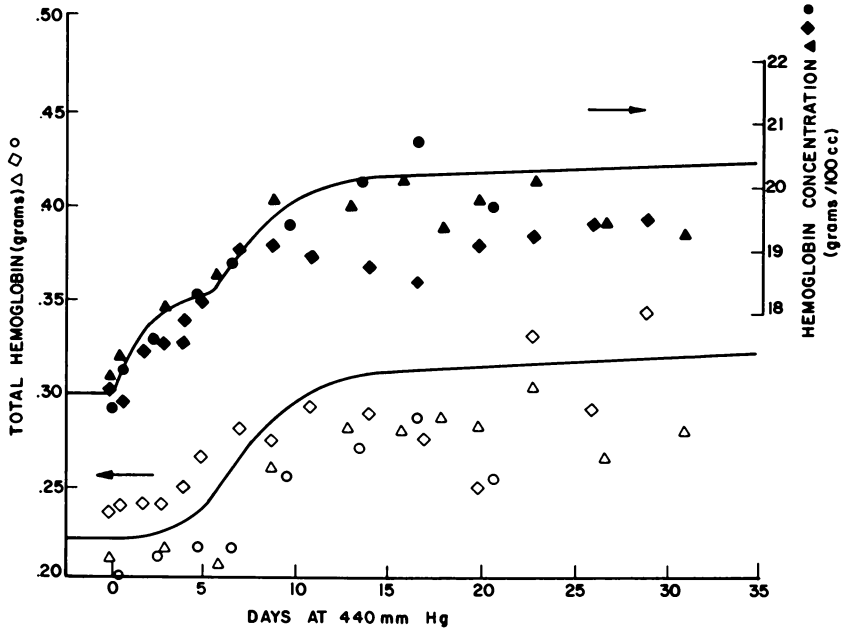

Figure 5. Experimental data (2) and the model results for mice exposed continuously to a total pressure of 440 mm Hg. Each data point is the average of values obtained from nine mice. Different symbols represent different runs. The model responses were obtained with the parameter values listed in Table I.

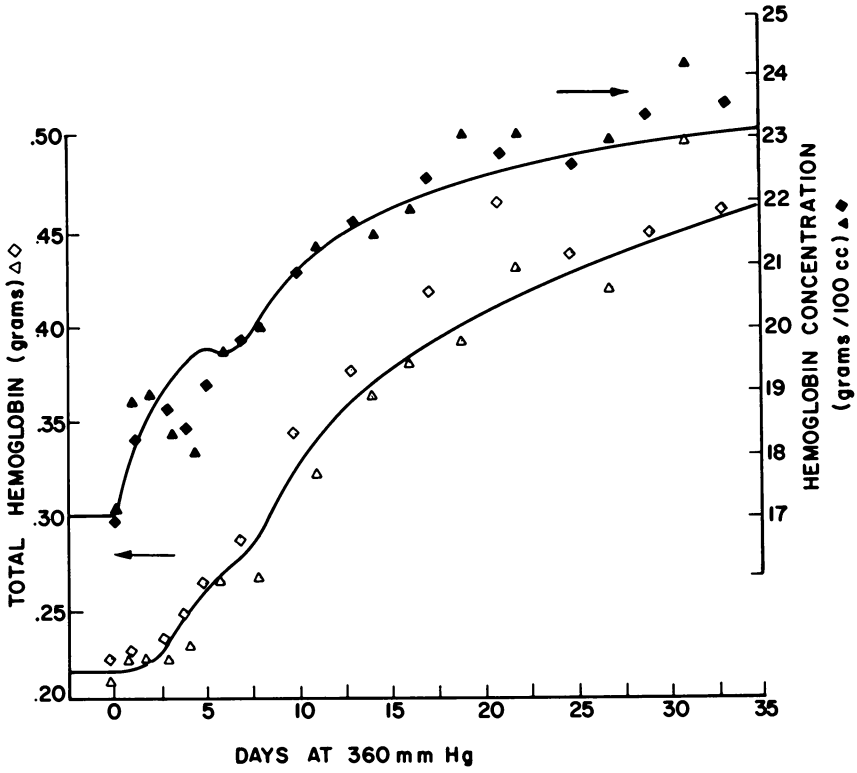

Figure 6. Experimental data (2) and the model results for mice exposed continuously to a total pressure of 360 mm Hg. Each data point is the average of values obtained from nine mice. Different symbols represent different runs. The model responses were obtained with the parameter values listed in Table I.

The effect on the model response of the subsystems can be demonstrated easily. For example, the effect of plasma volume changes on the behavior of the system can be seen by comparing the responses of the model with and without these changes. Figure 7 shows the total hemoglobin and hemoglobin concentration responses with and without plasma volume changes for a stimulus of 360 mm Hg total pressure.

Without a change in plasma volume in response to continuous hypoxia, hemoglobin concentration does not begin to increase until approximately 2 1/2 days after onset of the stimulus. Also, hemoglobin concentration remains below the levels found experimentally for the duration of the run. The delayed changes and decreased values for hemoglobin concentration in the model result in a higher erythropoietin concentration, increased rate of hemoglobin production, and higher total hemoglobin values as compared with the experimental data. This is clearly shown in the graph of total hemoglobin in Figure 7. Even the

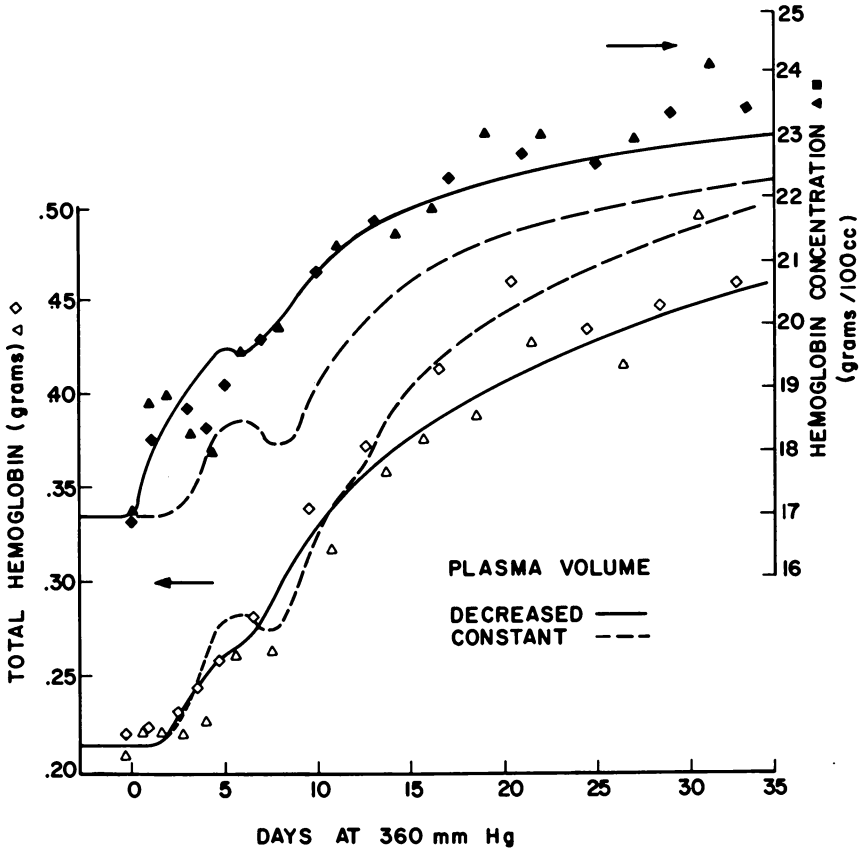

Figure 7. Experimental data (2) and the model results from mice exposed continuously to a total pressure of 360 mm Hg. Each data point is the average of values obtained from nine mice. Different symbols represent different runs. The model responses were obtained with the parameter values listed in Table I. The solid lines were obtained with the empirically determined plasma volume decrease included in the model. The broken lines were obtained when plasma volume was held constant at the control level.

increased level of total hemoglobin beyond 20 days of stimulus is not sufficient to maintain hemoglobin concentration at the experimental values. The predicted increase in erythropoietin concentration during the first few days of hypoxia results in the release of a greater number of early cells with a shortened life span. The removal of these cells from the circulation produces a dip in total hemoglobin and hemoglobin concentration 7 1/2 days after onset of stimulus. The magnitude of the dip can be varied by adjusting the value of (E_e) in Equation 4. The value of (E_e) is arbitrarily set with little experimental data for justification. However, regardless of the value selected for (E_e), the changes in plasma

volume play an important role in acclimatization during continuous exposure to decreased ambient pressure.

Operation of the model without plasma volume changes also provides an opportunity to appraise the effect of these changes on the erythropoietin concentration during the first few days of hypoxia. The predicted erythropoietin concentrations during continuous exposure to 360 mm Hg pressure, with and without plasma volume changes in the model are shown in Figure 8. With no change in plasma volume, erythropoietin concentration rises much higher but is reduced to experimentally determined levels within 4 days. The subsequent increase is produced by the decrease in oxyhemoglobin concentration when the early cells leave the circulation. Figure 8 also shows the erythropoietin response when plasma volume changes are included but arterial partial pressure of oxygen re-

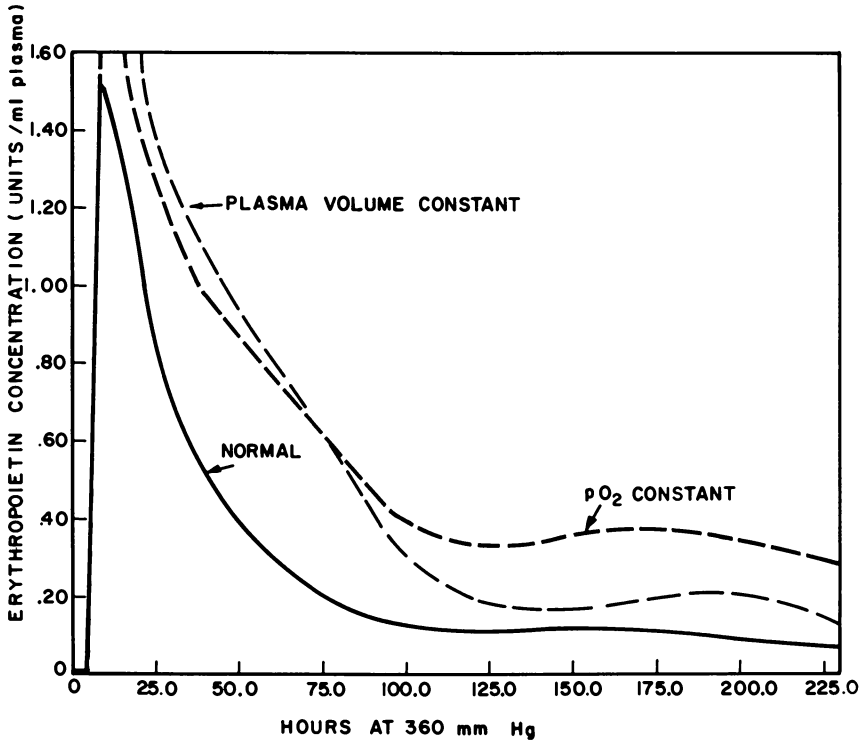

Figure 8. Model predictions for plasma erythropoietin concentration as a function of duration of hypoxic exposure at 360 mm Hg total pressure. The model responses were obtained with the parameter values listed in Table I. The solid line was generated with the changes in plasma volume and arterial p_{O_2} as described in the text and included in the model. The broken lines were obtained with either the plasma volume held constant or arterial p_{O_2} held at the acute level for the duration of hypoxic exposure.

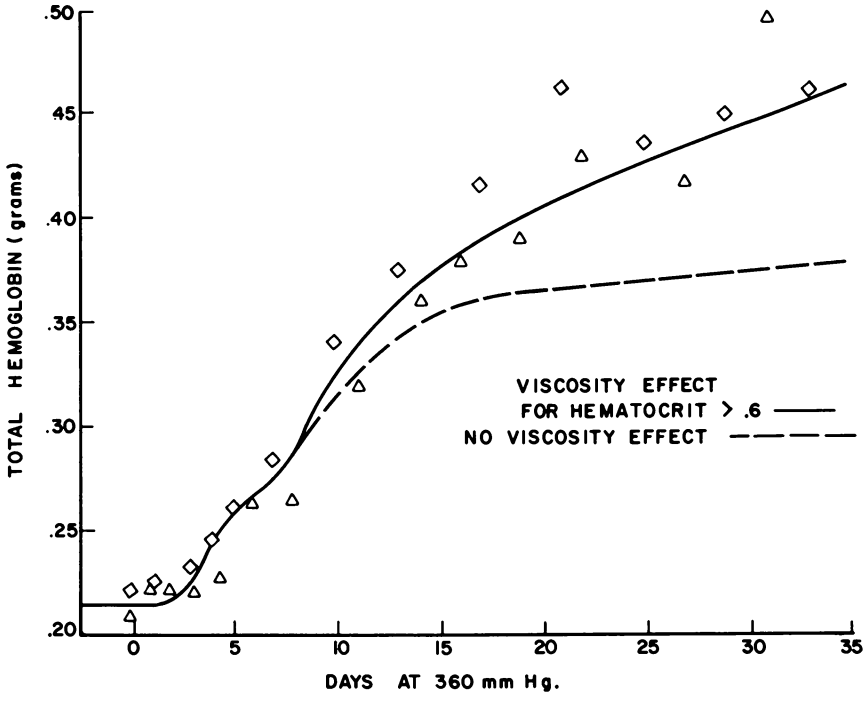

Figure 9. Experimental data (2) and the model results from mice exposed continuously to a total pressure of 360 mm Hg. Each data point is the average of values obtained from nine mice. Different symbols represent different runs. The model responses were obtained with the parameter values listed in Table I. The solid line was obtained with the viscosity factor effective only when hematocrit was greater than 0.6. The broken line was obtained with no viscosity effect in the model.

mains at the acute value. The two factors, plasma volume decrease, which causes an increase in hemoglobin concentration, and arterial pO_2 increase appear to be responsible for the major portion of the reduction in erythropoietin concentration within the first few days of hypoxia.

The most speculative of the relationships in the original model is the viscosity factor (Vi)—an oversimplification that accounts for a combination of effects. The inclusion in the model of the factor stem cell potentiation to allow for changes in the sensitivity of erythropoietin places less dependence on the viscosity factor to produce a reasonable fit between model response and experimental data. In the original model the viscosity factor took effect when hematocrit was greater than 0.5 (Hct_k) and resulted in a viscosity factor (Vi) of 0.8 when the hematocrit equaled 0.75. In the present model Hct_k was set at 0.6 so that no viscosity effect occurs until the hematocrit is greater than 0.6. In addition, K_6 in Equation 5 is set to produce a viscosity factor of 0.9 when the hematocrit is 0.75.

However, even this seemingly small effect, a reduction of only 10% for a hematocrit of 0.75, can have a profound effect on hemoglobin production when hematocrit is near this value. This is demonstrated in Figure 9, which shows the change in the response of the model with and without inclusion of the viscosity factor. Without the viscosity factor, total hemoglobin reaches a steady-state value considerably below the total hemoglobin found experimentally. Although the effect of the viscosity factor in the new model is closer to what might be expected physiologically, the possibility still exists that other parameter changes account for part of the effect currently attributed to the viscosity factor.

In summary, a mathematical model has been used to investigate the role of parameters and relationships in producing a response similar to available experimental data. As a result of this work, several questions have been raised concerning the behavior of various components of the system. Thus the model has successfully served as a tool to allow confirming some ideas, questioning of others, and stimulating thought on the various relationships and interaction of the components and subsystems involved in the control of erythropoiesis.

Literature Cited

1. Mylrea, K. C., Abbrecht, P. H., *J. Theo. Biol.* (1971) **33**, 279.
2. Mylrea, K. C., Abbrecht, P. H., *Amer. J. Physiol.* (1970) **218**, 1145.
3. Zanjani, E. D., Contrera, J. F., Gordon, A. S., Cooper, G. W., Wong, K. K., Katz, R., *Proc. Soc. Exp. Med. Biol.* (1967) **125**, 505.
4. Reissmann, K. R., Diederich, D. A., Ito, K., Schmaus, J. W., *J. Lab. Clin. Med.* (1965) **65**, 967.
5. Mylrea, K. C., doctoral dissertation, Rackham School of Graduate Studies, Univ. of Michigan, Ann Arbor, 1968.
6. Altland, P. D., Brubach, H. F., Parker, M. G., Highman, B., *Amer. J. Physiol.* (1967) **212**, 142.
7. Altman, P. L., Dittmer, D. S., Eds., "Blood and Other Body Fluids," p. 153, Fed. Amer. Soc. Exptl. Biol., Washington, D.C., 1961.
8. Abbrecht, P. H., "Erythrocyte Life Span in Mice Acclimatized to Different Degrees of Hypoxia," in press.
9. Abbrecht, P. H., Littell, J. K., *J. Appl. Physiol.* (1972) **32**, 54.
10. Siri, W. E., Van Dyke, D. C., Winchell, H. S., Pollycove, M., Parker, H. G., Cleveland, A. S., *J. Appl. Physiol.* (1966) **21**, 73.
11. Stohlman, F., Jr., *Ann. N.Y. Acad. Sci.* (1959) **77**, 710.
12. Prentice, T. C., Mirand, A. E., *Proc. Soc. Exp. Biol. Med.* (1961) **106**, 501.
13. Kretchmar, A. L., *Science* (1966) **152**, 367.

RECEIVED November 11, 1971. Work was supported by funds from the Wisconsin Alumni Research Foundation administered through the University of Wisconsin Graduate School Research Committee, by Grant GB 5874 from the National Science Foundation, and by U.S. Public Helth Service Grant AM 10395. Peter Abbrecht is the recipient of U.S. Public Health Service Research Career Development Award 1 KO4 GM 19289 from the National Institute of General Medical Sciences.

11

A Review of Thermal Control in the Human

EUGENE H. WISSLER

College of Engineering, The University of Texas at Austin, Austin, Tex. 78712

Physiological and physical factors which are important in thermoregulation in the human are described in general terms. Recent experimental studies are discussed from the point of view of obtaining quantitative relations for use in mathematical modeling. Two approaches to the development of useful models are presented. Several situations in which thermal effects are important are discussed. These include hypothermic anesthesia, open-heart surgery, and portable life support systems for astronauts and divers.

As man attempts to live and work in increasingly hostile environments and as new medical techniques involving the use of hypothermia are developed, the need to provide thermal control in human subjects also increases. Engineers and scientists are becoming increasingly involved with the design and development of life support systems which interact with the human thermal system. This paper summarizes the principal factors which must be considered in mathematically modeling such systems.

The literature dealing with thermal regulation in the human is very extensive but somewhat contradictory. Reviews (*1*, *2*, *3*) which cover earlier work in depth should be consulted for more information. Our attention will be focused on recent work in which quantitative results are developed in a form suitable for inclusion in mathematical models.

Factors involved in thermal regulation will be considered first for near-neutral environments. Then situations which involve greater thermal stress will be considered. Special life support systems designed to enable man to perform useful work in hostile environments will be discussed. Several examples of using deep hypothermia in surgery will be presented also. The paper will conclude with a discussion of mathematical simulation of the human thermal system.

Review of Thermal Regulation

The basic problem of thermal physiology is to define in adequate detail the mechanisms by which man maintains a tolerable central temperature under varying environmental conditions. To survive man must maintain a central temperature close to 37°C. Deviations of several degrees can be tolerated by healthy individuals. Increasing body temperature by 3°C does not impair performance, but higher temperatures can be dangerous, with death often occurring at 43°C. However, lowering the central temperature 3°C produces a state of semiconsciousness. Further cooling can be tolerated, but there is considerable danger of cardiac failure at temperatures below 26°C.

Although the neutral environment for a nude resting human is about 30°C, he can survive over a range 15° to 45°C depending on other environmental conditions. Man can remain comfortable under rather extreme conditions by using clothing or special protective garments to maintain his microenvironment near the neutral point.

Since metabolic reactions are exothermic, man's perpetual problem is one of transferring heat to his environment at an appropriate rate. Heat is generated in the basal man at the rate of roughly 72 kcal/hour. Since man weighs about 80 kg and has a mean specific heat of roughly 0.9 cal/(gram) (°C), his temperature would rise 1°C/hour if he were unable to transfer heat to the environment. In the resting man, 60% of the heat is generated in the trunk, principally in the liver and intestines; 20% is generated in the brain, and the remaining 20% is generated in the extremities. In the working man, the rate of heat generation is much higher; 900 kcal/hour is not an impossible figure. The rate at which heat is generated in the trunk and head remains relatively constant with the excess over basal being generated in the working muscles of the extremities. When subjected to a cold environment, the body tends to compensate by increasing the rate of metabolic heat generation. This is accomplished primarily by shivering, but it is argued by some physiologists that there is also a nonshivering component in the excess heat generation rate.

The external mechanisms by which heat is transferred to the environment are well known. These include convection, conduction, radiation, and evaporation. Although physiologists have been inclined to measure their own heat and mass transfer coefficients on living men and on mannikins, there is no reason to believe that standard engineering correlations are inadequate for this purpose. We will concentrate on the way in which the human body exploits various external heat transfer mechanisms in maintaining a constant central temperature.

One obvious mechanism available to the body is perspiration, which controls the wetness of the surface and, thereby, the rate of evaporation.

In hot environments evaporation is essential for survival. Heat is transferred away from the surface by evaporation alone, and the flow of heat by conduction is toward the surface from the environment. However, heat loss by evaporation is significant even when the subject is not perspiring noticeably. Not only is there a considerable amount of insensible evaporation from areas such as the palms of the hands, but there is also much evaporation in the upper respiratory tract. Nearly 20% of the total heat transferred to the environment in the resting state is transferred as latent heat of evaporation in the respiratory tract.

A more subtle internal mechanism available to the body is control of the vascular system through which blood circulates. Blood is pumped out of the left ventricle of the heart into the aorta at the rate of 5 liters/min in the resting man. The aorta branches into several smaller arteries, and if these branches are followed while moving away from the heart, one finds more and more arteries with smaller and smaller diameters. Ultimately, the smallest arteries become capillaries having diameters of 10–20 μ. It is flow out of these ubiquitous capillaries that one sees whenever he cuts himself. Blood leaving the capillaries flows into small veins, which merge into larger and larger veins as the heart is approached. In the right side of the heart, venous streams from various regions of the body are mixed together to form a single stream which is pumped into the capillaries of the lungs through the pulmonary artery. The flow returns to the left auricle of the heart through the pulmonary vein. In the resting man, roughly 20% of the cardiac output goes to the head; 60% goes to the trunk, principally to the liver, intestines, and kidneys; and the remaining 20% goes to the extremities. In the working man, cardiac output may be in excess of 35 liters/min with nearly all of the excess over the resting rate going to the working muscles of the extremities.

The rate at which heat is generated in the head and trunk is normally greater than the rate at which it is transferred to the environment across the surfaces of those elements. In the extremities the converse is normally true. Hence, the extremities are cooler than the head and trunk, and there exists a convective flow of heat from the head and trunk into the extremities. When the rate of heat generation in the arms and legs is greatly increased, as it is in the working man, the temperature of the extremities rises above the temperature of the head and trunk, reversing the direction of the convective flow of heat.

By controlling the rate at which blood flows to the superficial areas of the body, it is possible for the body to vary the surface temperature and, thereby, exercise some control over the rate at which heat is transferred from the surface to the environment. Since most humans are equipped with a fairly thick subcutaneous layer of fat with a relatively

low thermal conductivity, controlling the blood flow rate to the cutaneous capillaries is an effective means of controlling the surface temperature. When the body senses that it is necessary to conserve heat, it reduces the rate of blood flow to the capillaries in the skin, thus lowering the surface temperature. This is particularly noticeable in the fingers and toes where the constriction may be nearly complete in cold environments. However, the superficial capillaries are dilated in a warm environment to increase the surface temperature. The ratio of the maximum to minimum blood flow rates in highly vascular regions may be 100:1.

Although we have concentrated on heat transfer from the blood in small capillaries to neighboring tissue, heat transfer from larger vessels is also important. This is especially true because large arteries and veins tend to occur in adjacent pairs. Hence, there are many sites at which countercurrent heat exchange can occur between arterial and venous blood. It is postulated that this is an important mechanism for conserving heat in a cold environment, but the exact magnitude of the effect has never been determined.

The response of the human system to a given thermal stress is a complicated matter involving many factors. It is convenient to divide these factors into two classes: physiological and physical. Included in the class of physiological factors are the distribution of metabolic heat production rates, blood flow rates, and regional rates of sweating for a given situation. It is fair to say that these factors are understood imperfectly at the present time. Included in the class of physical factors are the temperature changes resulting from variations in the rates of heat generation, blood flow, and sweating. These factors are understood rather well in principle although their evaluation for a given system presents a formidable computational task.

Before the development of large high speed digital computers, one's ability to analyze the simultaneous interaction of so many factors was severely limited. Early thermal physiologists were very clever at devising experimental techniques for studying particular features of a very complex system. However, there is a limit to the amount of understanding that can be developed without recourse to mathematical modeling of the system. During the past ten years, development of adequate mathematical models has permitted achievement of a new level of understanding. This is especially true of transient responses which constitute the basis for thermal regulation.

One relationship which appears to be well established is that for any individual in equilibrium with his environment, the internal body temperature as measured rectally or in the esophagus is proportional to the metabolic rate and independent of the ambient temperature (*4*).

Individuals with varying levels of aerobic capacity can be compared on the basis of fraction of maximum oxygen uptake. Figure 1 shows data reported by Stolwijk and Cunningham (5) for two subjects. Data for two other subjects were also included in the program of 72 experiments. Ambient temperatures used were 10°, 20°, and 30°C. The solid line represents data reported for one subject studied at 22.3°C by Nielsen (3). Although Nielsen's experiments involved positive and negative work and, hence, considerable differences in the heat production rate at a given metabolic rate, the distribution of data points about the line was no greater than the scatter in Stolwijk's data. The values measured by Stolwijk appear to be consistently 0.4° to 0.5°C higher than Nielsen's. Stolwijk measured rectal temperatures, and Nielsen measured esophageal temperatures, which could account for 0.25°C of the difference (3), but the residual difference is still significant. The subjects studied by Stolwijk were somewhat larger than those studied by Nielsen (mean weight of 88 kg *vs.* 77 kg and mean skin surface area of 2.1 meter^2 *vs.* 1.99 meter^2). Expressing H_{met} as a fraction of the maximum metabolic rate does little to reduce the difference between individuals.

It has been observed also that the mean skin temperature is a linear function of the ambient air temperature and is relatively independent

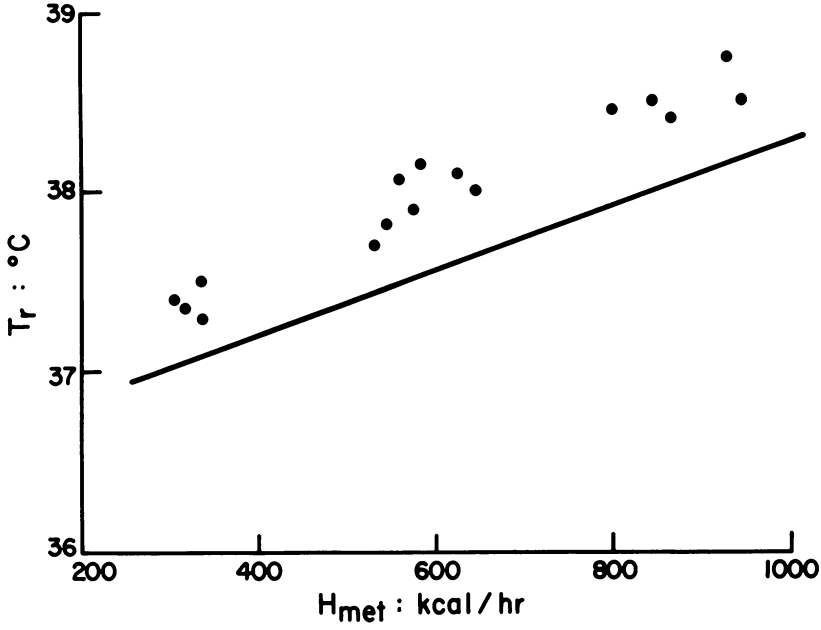

Figure 1. Relationship between rectal temperature and metabolic rate (Data points were taken from Stolwijk and Cunningham (5), solid line from Nielsen (4))

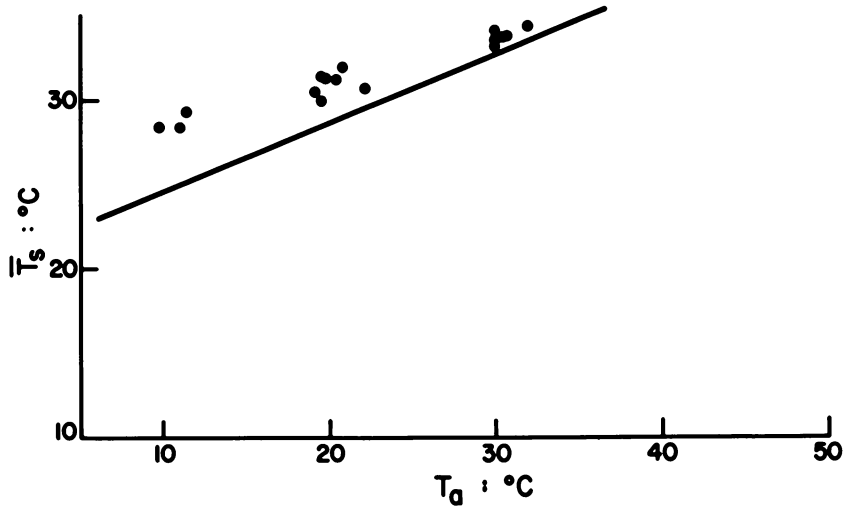

Figure 2. Relationship between mean skin temperature and environmental temperature (Data points were taken from Stolwijk and Cunningham (5), solid line from Nielsen (4))

of the level of exercise (*3*). Experimental data reported by Stolwijk and Cunningham (*5*) for a considerable range of metabolic rates are presented in Figure 2. Also shown is a solid line which described quite adequately the experimental data of Nielsen (*3*). There is clearly a significant difference between data taken in the two laboratories. A higher wind speed (50–100 cm/sec *vs.* 20 cm/sec) and a higher peddling rate (60 rpm *vs.* 50 rpm) were used in Nielsen's laboratory. Hence, the heat transfer coefficients should have been higher for Nielsen's subjects, which probably, at least in part, accounts for the lower skin temperatures she reported. The relationship established by Nielsen is between esophageal temperature and rate of metabolic energy liberation as determined by oxygen uptake and not between esophageal temperature and rate of total heat generation.

If the mean surface temperature is independent of metabolic rate, a heat exchange mechanism other than convection or radiation must be responsible for removing excess heat generated when a subject exercises. One's attention turns immediately to sweating, a phenomenon which has been studied in many laboratories. For subjects in equilibrium with the environment, the sweat rate is directly proportional to the total heat production rate. Perhaps this is expected because regulating central temperature by controlling the blood flow rate to skin, and, thus, the skin temperature is relatively ineffective. As the skin temperature rises, the difference between the central temperature and the skin temperature

decreases, which in turn reduces the efficiency for transferring heat from the core to the surface. Starting from a neutral condition, say $T_{env} = 30°C$, $T_{skin} = 32.5°C$, and $T_r = 37°C$, assume that the metabolic rate is doubled. In the absence of sweating, the mean skin temperature has to increase to 35°C, which reduces the central to surface temperature difference from 4.5°C to 2°C. Hence, the situation demands that approximately twice as much heat be carried to the surface when the temperature gradient is only 40% as great. To accomplish this, the blood flow rate to skin must increase about fivefold even for this relatively mild case. Working muscles also place a large demand on the heart during exercise, and excessive cardiac output would be required if convection and radiation were the only heat transfer mechanisms available.

Evaporation, however, can occur even when the environmental temperature exceeds the skin temperature. Hence, sweating is a means for cooling the skin and increasing the central to surface temperature difference, which is desirable when heat must be transferred efficiently from working muscles to the surface.

The mechanism by which sweating is regulated has not been established with certainty. Many attempts have been made to correlate the sweat rate with the central and mean skin temperatures. Recently, Nadel, Bullard, and Stolwijk (*6*) proposed the following relation for steady-state conditions.

$$E = [197\ (T_{central} - 36.7) + 23\ (T_{skin} - 34.0)] \times \exp\ [0.1\ (\Sigma \text{ weighted } T_{sl} - 34.0)] \quad (1)$$

in which E = maximum rate of heat transfer by evaporation, W/m^2

T_{sl} = local skin temperature, °C

Increasing the central temperature is much more effective in eliciting the sweating response than increasing the skin temperature. The equation also implies that one can inhibit sweating by lowering either the skin or central temperature. Although this equation did describe rather well experimental data obtained from steady-state resting and exercising exposures in a wide range of ambient conditions, it is not a complete description of the sweating mechanism.

Data reported by Nadel *et al.* show that the rate of sweating depends also on the time rate of change of mean skin temperature when the skin is cooled. During heating, a rate-dependent effect does not appear.

While a measure of success has been achieved in relating the rate of sweating to strictly thermal responses, there exists a considerable body of evidence which suggests that nonthermal responses may be involved

also. The necessity for such responses can be seen when one studies data involving positive and negative work. Forbes (*7*) found that men sweat less when walking up a grade than when walking on the level at the same metabolic rate. Since some of the energy generated metabolically is used to increase the potential energy of the subject during climbing, the net rate of heat production is less than the metabolic rate. Forbes' observation is consistent with the notion that skin temperature is independent of metabolic rate, as we noted earlier.

Other investigators have considered this matter also. Snellen (*8*) observed that the difference between metabolic heat production and heat loss by evaporation in walking up a grade was equal to the external work performed. Nielsen (*3*) found that the rate of sweating correlated with the net rate of heat production irrespective of whether the subject was performing positive, zero, or negative work. All of these experiments required that the subjects move more rapidly at a given metabolic rate when doing negative work than when doing positive work, which makes direct comparison questionable.

Smiles and Robinson (*9*) performed a series of experiments designed to evaluate the possible influence of walking speed on sweat secretion during positive and negative work. They found also that subjects sweated considerably more when walking downgrade than upgrade at a given metabolic rate. The rate of sweat secretion correlated well with the net rate of heat production, as others have noted, but it also correlated as well with the speed of walking and metabolic rate. Since it could not be correlated with the mean skin and rectal temperatures, the authors concluded that a stimulus of neuromuscular origin must be an essential part of the human thermoregulatory system during work.

Additional evidence to support this concept is given by Gisolfi and Robinson (*10*), who reported that sweating started to increase within 2 sec after work began when a subject had either a warm core (average of rectal, muscle, and femoral vein = 38°C), or a warm skin (35.5°C), or both before exercise started. When work stopped, the rate of sweating began to decline within 2 sec in two subjects and after a brief period of increasing sweat rate in a third subject. The only temperature that responds that rapidly is the muscle temperature, but other studies have shown that there is not a strong correlation between muscle temperature and sweat rate. This suggests also that neuromuscular reflexes participate in the regulation of sweating. Further evidence of a neuromuscular factor is given by the observation that the sweat rate depends on posture. A long delay in the decline of sweating occurred when the subjects stood after walking on the treadmill, and an immediate increase in the sweat rate occurred when they changed from sitting to an erect posture in the warm room.

Next we consider the manner in which man responds to cold. The body attempts to limit heat loss to the environment by reducing blood flow rate to the skin and lowering the skin temperature. However, the increase in tissue insulation that can be achieved by vasoconstriction is limited, and this mechanism must be augmented by increased heat production, either by shivering or by purposeful work. Shivering alone can increase the heat production rate to three to five times the basal rate, and work can increase it to ten times basal.

The number of quantitative studies devoted to shivering is much smaller than the number devoted to sweating. Even so, it is clear that the rate at which heat is generated by shivering depends on central and skin temperatures. It seems that there is a threshold of mean skin temperature above which shivering does not occur regardless of the central temperature. When the mean skin temperature falls below the set point, shivering will occur at a rate that depends on the central temperature. The following equation has been proposed by Nadel *et al.* (*11*) who induced independent variations in skin and central temperatures by having their subjects ingest ice cream or warm pudding.

$$\Delta M = 36\,(36.5 - T_{central})\,(32.3 - \overline{T}_{skin}) + 7\,(32.2 - \overline{T}_{skin}) \quad (2)$$

in which ΔM = increase in heat production rate over the resting rate, kcal/hour

$T_{central}$ = tympanic temperature, °C.

Since this equation was derived from quasi-steady-state data, it makes no allowance for a rate component in the control equation. However, the authors did comment that data derived from periods of rapidly changing temperature suggested the presence of a rate component in the regulatory mechanism. The equation will fail also at extremely low levels of skin temperature because of the inability of shivering metabolism to increase above a certain level. Shivering results in heat generation in the muscles that participate. In the appendages intrinsic heat production is so low that skin temperature can be maintained only by convective heating resulting from local vasodilation.

Blood perfusion rates in the skin, hands, and feet are influenced to a considerable extent by the general thermal balance of the body. Spealman (*12*) measured directly the blood flow rate to the hand immersed in water at various temperatures and showed that perfusion rate declined with declining bath temperature to 10°C. Below this temperature there was a striking increase in hand blood flow rate, which frequently attained values comparable with those observed in a water bath at 35°C. If the subject was comfortably warm except for the hand, alternating

periods of vasodilation and vasoconstriction (hunting) occurred. When the subject was chilled, a lower degree of increased blood flow occurred. If the subject was uncomfortably warm, the blood flow rate to the hand remained high even in water at 10°C.

Cutaneous veins also show responses that depend on central and skin temperatures. In a recent study, Rowell *et al.* (*13*) considered the relative influence of whole body skin temperature and occluded arm skin temperature on the venomotor state of superficial veins in the occluded forearm. Changes were elicited reflexly by cutaneous thermoreceptors located in portions of the body remote from the local region of interest. Such remote or general effects occurred with a short latency period (5–10 sec), and only small changes in skin temperature (1°C or less) were required to elicit the response. Changes in venomotor tone resulting from variations in the local skin temperature were characterized by a longer latency period (30–60 sec) and the requirement for a relatively large change in temperature (10–15°C).

The observations of Rowell *et al.* are consistent with the existence of two separate effects of cutaneous heating: (a) Altering body skin temperature changes the rate of adrenergic neural stimulation to cutaneous veins. When the body skin temperature is raised, the rate of sympathetic nervous stimulation of veins is reduced, and, even though local conditions allow maximal activity, no constriction occurs. (b) Altering local skin temperature alters the reactivity of cutaneous veins to any given level of reflex neural stimulation. This mechanism resembles closely that proposed by Webb-Peploe and Shepard (*14*) for the role of central *vs.* local blood temperature on the cutaneous venous responses in dogs. In addition to the thermal responses described, it was observed that all subjects showed venoconstriction in response to exercise at 300 kpm/min. When the work load was increased to 600 kpm/min after 1 min of work, additional venoconstriction was usually seen except in cases involving a very large initial response.

While the observations discussed before this point have pertained to healthy subjects, it is interesting to look at thermal regulation during fever in man. Von Liebermeister (*15*) was perhaps the first to suggest (1875) that the body temperature is regulated at a higher level during fever. Various studies made in recent times tend to confirm this early proposal. For example, Cooper *et al.* (*16*) measured digital vasomotor responses of febrile subjects into whom a measured amount of heat was introduced by immersing one hand and forearm in a warm, stirred water bath maintained at constant temperature by an electric heater. The rate of heat absorption by the arm was deduced from the power input to the heater. Cutaneous vasodilator response in the opposite hand was measured by finger calorimetry, and the results confirmed that the response

is mediated by central temperature receptors. The response to a heat load during fever was very similar to that when afebrile, provided that the temperature was stable. During the onset of fever, the response was diminished or absent, which is compatible with the view that fever represents a change in level of the regulated temperature.

Life Support Systems

There are several situations in which man could not survive long without special cooling or heating devices which compensate for the thermal stress imposed by a hostile environment. In the man-in-space program, it is necessary for astronauts to work very hard while isolated from direct heat exchange with the outside environment. Men working in certain industrial environments also require auxiliary cooling if they are to remain for a reasonable period of time. The situation may be such that protective garments which allow evaporation can be worn, but this is not always the case.

Shvartz and Benor (*17*) measured the tolerance time of subjects who walked on a treadmill at 3.5 km/hour while wearing a vapor barrier suit that covered the entire body. Environmental temperatures ranged from 25°C–50°C. The tolerance limit was reached when the subject described his discomfort as intolerable or when his rectal temperature reached 39°C. At 25°C subjects were able to complete a 2-hour work period, but at 30°C the mean tolerance time was reduced to 108 min, and at 50°C it was only 28 min. Cooling the subjects with a liquid-cooled garment containing 50 meters of polyvinyl chloride tubing through which chilled water circulated permitted them to complete the work assignment under all conditions. Subjects who were uncooled sweated at rates as high as 2 liters/hour in the 50°C environment. Skin and rectal temperatures rose to 40° and 38.3°C, respectively, at the end of the exposure. Cooling caused marked reductions in all three variables. The highest mean sweat rate was only 0.33 liters/hour, and the skin and rectal temperatures remained close to 30.4° and 37.1°C, respectively, regardless of the environmental temperature. To eliminate thermal stress, as indicated by sweat rate, it was necessary to increase the cooling power in proportion to the increase in environmental temperature. The combination of skin and rectal temperatures selected by subjects was just sufficient to suppress sweating as predicted by Equation 1. Generally, subjects overcooled and created a heat debt rather than storing heat.

These observations are consistent with those reported earlier by Waligora and Michel (*18*) who compared liquid and gas cooling in the Mercury pressure suit. They concluded that the liquid-cooled garment is far superior to the ventilated suit which was incapable of removing

the heat load generated by a subject working at 315 kcal/hour. Subjects lost 750 grams when wearing the ventilated suit compared with 150 grams when wearing the liquid-cooled garment. They concluded that the liquid-cooled suit was satisfactory when the metabolic rate did not exceed 500 kcal/hour. It is not clear whether the inability to remove heat adequately is caused by inadequate heat transfer from skin to the garment or by inadequate transfer from deep regions of the body to skin. However, a sensation of being hot internally while the skin was cool or cold was reported when the inlet water temperature was reduced to 6.7°C during a test conducted at a metabolic rate of 655 kcal/hour. This suggests that intracorporeal resistance is limiting.

At the other extreme, we have situations in which man is exposed to great cold. Two different cases must be considered, exposure to cold air and to cold water. In the first case, adequate protection is provided by suitable clothing and shelter, and men are able to work year round in arctic regions. However, the problems associated with diving to considerable depth in cold water are much more challenging and still in need of solution.

Exposure to cold water at depths of 600 feet or more causes great thermal stress for several reasons. One is that water is a more efficient heat transfer medium than air because its thermal conductivity is 25 times greater than that of air. This means that a surface at a given temperature relative to the environment will lose heat 25 times more rapidly to water than to air. It also means that special garments are required for diving because the displacement of air by water in any garment removes its insulating capability.

Other effects are related to depth. Protective garments which rely on entrapped gas for their insulating power lose much of their effectiveness at depth because the material compresses. For example, a 1/4-inch nylon-lined wet suit compresses to about 50% of its original thickness when subjected to a pressure of 4 atm (*19*). In addition to reducing the insulating power of the suit, compression also reduces the buoyancy. This can cause a serious problem for the diver when a thick foam suit is used to give thermal insulation.

Heat transfer through the respiratory system also increases markedly with immersion in cold water. Beckman (*19*) reports that lowering the environmental temperature from 35° to 10°C can increase the respiratory rate from 400 liters/hour to 3000 liters/hour. Increased gas density also causes greater heat loss through the respiratory system with increasing depth. Indeed, at 600 feet the respiratory heat loss nearly equals the metabolic rate over a range of activity levels.

The extreme thermal stress imposed by deep diving in cold water can result in unconsciousness and death for the diver if suitable equip-

ment is not used. McQueen (*20*) noted there are interpersonal differences in the deep body temperature at which changes occur in the central nervous system, but, in general, when the temperature of the brain falls below 34°C, one becomes amnesic and dysarthic. Pain is generally appreciated down to 30°C, where the ability to recognize associates and surroundings is also lost. Voluntary motion is lost below 27°C, as are the pupillary light reflexes and deep tendon and skin reflexes. Between 30° and 32°C cardiac irregularities, such as atrial fibrillation, ventricular ectopic beat, and ventricular rhythms, are likely to occur (*21*). Therefore, the diver whose central temperature falls below 34°C would have little recollection of ensuing events and would be incapable of taking actions necessary to save himself. Should his body temperature decrease to 32°C, it is likely that cardiac irregularities would terminate the operational mission.

To compensate for the large rate of heat loss experienced in deep diving in cold water, some form of auxiliary heating is required. Present technology provides a choice between two alternative systems. One consists of a wet suit heated by an open circuit hot water system. The hot water supply may be located either at the surface or at an underwater habitat. Tubing located within the loosely fitted wet suit distributes the hot water evenly over the diver's surface. After circulation, the water flushes to the sea. This system is inexpensive, easy to maintain, and relatively reliable. For shallow dives it is an excellent system but for deep diving it suffers from several disadvantages (*22*). Perhaps the most serious is that the diver will lose heat very rapidly if the hot water system should fail. This is particularly true if cold water flushes in from the sea because the sudden reduction in temperature can cause the diver to lose muscular control. This could happen within 1 or 2 min, and it is a very important consideration for divers who are working inside ships where 10–15 min may be required for escape.

The alternative arrangement consists of a dry suit and a closed-circuit hot water system. Warm water is circulated through plastic tubing sewn into an appropriate undergarment. Advantages of this system include the following:

(1) The diver is kept dry, which is of great importance when he returns to the personnel transfer capsule.

(2) If the hot water system fails, the diver will not cool too rapidly. This was demonstrated in the Navy 600-foot cold water dive conducted at Duke University (*22*). This test demonstrated that a diver could remain in 45°F water for 20 min after the hot water had been shut off.

(3) Hot water can be supplied from either a diver-carried heater or from an umbilical tube. The principal disadvantage is that the dry suit is not always dry.

When operating properly, wet and dry suits can adequately maintain central temperature. However, loss of heat from peripheral elements, such as the fingers, hands, and arms, can be the limiting factor in immersion tolerance. When these elements are cooled to 15.5°C, subjects develop increased reaction time, a decrease in muscle strength, a decrease in tracking efficiency, and a decrease in manual dexterity with a loss in tactile discrimination and kinesthetic sensation. The small diameter of these elements makes them difficult to insulate because the thermal resistance of a cylindrical shell increases as the logarithm of the outer diameter, not as the thickness of the wall as it does for a planar layer of insulating material. Furthermore, the necessity for maintaining a degree of dexterity limits the insulating thickness one can use. This combination of adverse factors makes protection of the hands and fingers from excessive cooling a difficult thing to accomplish.

Use of Deep Hypothermia in Surgery

As mentioned in the introduction, man's usual objective is to maintain central and peripheral temperatures within a rather narrow range. However, there are cases in which either general or local hypothermia is induced in patients before surgery.

At the University of Wisconsin, hypothermic anesthesia is being used currently for leg amputations (*23*), and improved equipment and techniques have made the procedure much more attractive than in the past. The leg is cooled using a double-walled Neoprene boot which surrounds the leg from toe to thigh. An ethylene glycol–water solution circulating through the boot is cooled by a conventional refrigeration system. Coolant flow rate is maintained high enough so that temperature rise through the boot is negligible. Pressure in the boot is held below 30 mm Hg to minimize the reduction in blood flow to the leg, but some reduction does undoubtedly occur. Cooling requires from 4–10 hours for legs which are to be amputated. The temperature at the center of the leg is lowered to 10°–15°C, which usually produces the desired anesthetic effect.

A mathematical model of the leg was developed to predict the cooling curve under various conditions. Factors which were important in determining the rate and final level of cooling include the diameter of the leg, blood perfusion rate, and the presence of subcutaneous fat. Metabolic heat generation and the presence of bone are relatively unimportant. Heat carried into the leg by incoming blood is sufficient to maintain a temperature of 8°–10°C at the center of the leg.

Hypothermia has been used also to permit periods of circulatory arrest during open-heart surgery. This technique is particularly advantageous when used for infants because they cool and rewarm readily, and

the alternative procedure using perfusion techniques has resulted in a high mortality rate. However, the development of suitable techniques followed a period in which attempts to use hypothermia were thwarted by the time limitations imposed and problems with ventricular fibrillation during cooling and rewarming.

In 1963 Horiuchi *et al.* (*24*) introduced a method of surface-induced hypothermia which allowed correction of ventricular septal defects in children younger than 1 year during periods of cardiac arrest of 12 min or less while the body temperature was 25°C. Dillard *et al.* (*25*) modified this technique to include intravenous low-molecular weight dextran, relative hyperventilation during cooling, and cardiac massage with electrical pacing during resuscitation. Deep ether anesthesia appeared to be critical in allowing deep levels of hypothermia to be achieved without ventricular fibrillation. Respiratory alkalosis was induced deliberately to counteract the metabolic acidosis resulting from cardiac arrest. These adjuncts permitted cooling to rectal temperatures of 17°–20°C, and extension of the period of circulatory arrest to 45 min.

Hypothermia was induced by immersing the deeply anesthetized child in a cold-water bath, with a plastic sheet separating the child from direct contact with the water. Additional cooling was accomplished by packing the infant with plastic bags containing crushed ice. During cooling, ventilation was maintained at normothermic levels which produced respiratory alkalosis. After approximately 30 min of cooling when the rectal temperature had fallen to 26°C, the child was elevated from the water bath, and cooling was discontinued while the chest was prepared, draped, and an incision made. During this period, the temperature continued to drift downward to 20°C, at which point the aorta was occluded and cardiac arrest was induced. Following correction of the defect, occluding tapes were removed, and cardiac resuscitation was accomplished by gentle massage with intermittent electrical pacing. The child was rewarmed by immersion in a warming bath, and when the child's temperature reached 35°C, the chest was closed. Rewarming required about 1 hour.

Induction of hypothermia in adults by surface cooling is much more difficult than in infants. The danger of ventricular fibrillation generally limits the degree of cooling to 30°C, which allows arrest of circulation for periods of time not greater than 8–10 min without cerebral damage. Treatment of secundum atrial defects is possible, but few other intracardiac procedures can be completed accurately and safely within that limitation. Hence, the development of relatively efficient blood oxygenators led surgeons to use cardiopulmonary bypass as the principal means of maintaining cerebral function during cardiac surgery. Readers who are interested in a historical account of use of deep hypothermia during

open-heart surgery should consult Boulton's paper (*26*), describing the use of Drew's method at St. Bartholomew's Hospital in London.

Mathematical Models

In the final section of this paper, we discuss mathematical models which have been developed for the entire human thermal system (*27*, *28*, *29*). In some cases, models have been used to gain greater understanding of thermal physiology and thermoregulation. At other times, they have been used to analyze the performance of systems involving thermal exchange between man and his environment. Work schedules for astronauts were checked to make certain that the heat removing capacity of the suit was not exceeded. Hence, such models have become tools for engineers who design life support systems.

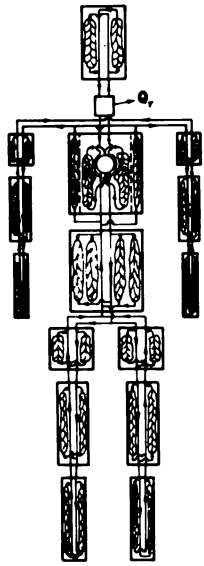

Bulletin of Mathematical Biophysics

Figure 3. Schematic diagram of the system on which a mathematical model has been based (28). *Shown are the geometric arrangement of elements and the circulatory system.*

Generally the model is based on a physical system similar to the one shown in Figure 3. It consists of several cylindrical elements representing longitudinal segments of the arms, legs, trunk, and head. Each element is assumed to possess axial symmetry, but properties such as specific heat, thermal conductivity, metabolic rate, and blood perfusion rate are functions of radial position and time. Three components of the vascular system, an arterial pool representing the large arteries, a venous pool representing the large veins, and a capillary bed, are distributed throughout each element. Blood flow follows that existing in the body in the sense that blood enters a given arterial pool from an adjacent pool closer

to the heart. Some of the blood entering each arterial pool flows into the capillary beds of that element; the remainder flows into another arterial pool. Blood leaving the capillary beds flows into the venous pool where it is mixed with venous blood from more distal elements. Direct heat exchange between blood in the arterial and venous pools and adjacent tissue is permitted.

It is assumed that there is perfect heat transfer between tissue and blood in the capillaries and the temperature of blood leaving the capillaries is equal to the local tissue temperature. This is not strictly correct, but it seems to be a reasonable approximation. Recently Keller (*30*) has pointed out that blood flowing through small vessels may serve as an effective heat transfer medium which, in effect, increases the apparent thermal conductivity of tissue.

Boundary conditions permit one to account for various heat transfer mechanisms at the surface of each element. Convection, radiation, and evaporation are incorporated into the model using standard correlations.

Allowance is also made for heat loss through the respiratory system. It is assumed that expired air is saturated with water vapor and that 25% of the heat loss through the respiratory system comes from the arterial pool in the head, 25% from the venous pool in the head, and 50% from the venous pool in the thorax.

Finite difference techniques are used to solve the equations which describe this system. Since approximately 250 equations must be solved for each time step, which may be no longer than 5–10 sec, this model can be used only when a high speed digital computer is available.

Simpler models can be used in certain cases, and especially those involving exercise in a warm environment when high tissue perfusion rates and elevated skin temperatures tend to reduce internal thermal gradients. This permits using rather large radial segments without introducing excessive truncation errors. However, using simplified models can introduce significant numerical artifacts when applied to situations involving large internal thermal gradients (*31*). The worst cases are those involving moderate exercise rates in a cold environment.

The relatively simple model, developed by Stolwijk and his associates (*5*, *29*), has been used extensively to study quantitatively various models of the human thermal system. In this model the body is subdivided into six segments, each having four layers. The segments represent the head, trunk, arms, hands, legs, and feet. Each layer is described in terms of heat capacitance, metabolic heat production rate, and heat exchange rates. In addition, a central blood compartment links the six segments together *via* appropriate blood flow to each segment.

The controller formulated initially by Stolwijk and Hardy (*29*) and modified by Stolwijk and Cunningham (*5*) receives from each layer the

instantaneous temperature and the rate of change of temperature. This set of thermal receptor outputs is then integrated according to the control equation and translated into effector command signals which may be modified locally when appropriate. Effector activities are translated into changes in the rates of metabolic heat production, blood flow, and sweating.

The controller model chosen by Stolwijk is based on the assumption that there exists a set point temperature for each layer. Effector signals are derived from error signals, which are the differences between instantaneous and set point temperatures in various layers. If a given error signal has a positive value, it represents an output from a warm receptor: negative values indicate outputs from cold receptors. The control equations used incorporate the adjustable set point concept formulated by Hammel *et al.* (*32*) and the nonlinear integration suggested by Hardy and Stolwijk (*33*). Blood flow rates to working muscles depend on the metabolic rate.

The control equations contain a considerable number of arbitrary parameters which can be adjusted to obtain reasonable agreement between experimental and computed results. Two kinds of experimental data have been used for this purpose. Steady-state data for different conditions involving various combinations of exercise rate and environmental temperature have been available for many years. Recently, good transient state data generated in response to a sudden change in exercise rate or environmental temperature have also become available (*34*). Variables measured in these studies include the rectal, mean skin, muscle, and esophageal temperatures, and the sweat and oxygen uptake rates. Parameters are usually evaluated using data from a limited number of experiments.

Results obtained using this approach represent a considerable improvement over those obtained using earlier models. However, problems still remain which require additional study. The greatest deficiency in the model stems from its inability to simulate adequately human behavior under conditions of low activity in cold environment. The model predicts that a rapid fall in rectal temperature will accompany the onset of exercise, which does not agree with experimental observations. One possible explanation is that blood flow to working muscles does not increase immediately upon exercise, which would allow the muscle temperature to increase before enhanced perfusion occurs. Another explanation is that heat transfer between blood in large vessels and the surrounding tissue, or countercurrent exchange, dampens the response seen in the central blood temperature.

Another unresolved question concerns the necessity for including nonthermal contributions in the equations which define sweat rate. This

problem was discussed earlier, and use of models such as those described in this section should help resolve the controversy concerning this subject.

Finally, control equations of the form proposed by Stolwijk have two characteristics; the use of a set point temperature for each layer tends to hold temperatures within a rather narrow range of values, and the model contains a very large number of adjustable parameters. Thus, one should be able to fit a limited amount of data rather well even if the model is invalid. Devising definitive experiments and adapting modern techniques for parameter estimation to this problem present a real challenge for engineers and scientists.

Literature Cited

1. Hammel, H. T., *Ann. Rev. Physiol.* (1968) **30**, 641.
2. Hardy, J. D., *Physiol. Rev.* (1961) **41**, 521.
3. Nielsen, B., *Acta. Physiol. Scand.* (1969), Suppl. 323.
4. Nielsen, B., *Acta. Physiol. Scand.* (1966) **68**, 215.
5. Stolwijk, J. A. J., Cunningham, D. J., Expansion of a Mathematical Model of Thermoregulation to Include High Metabolic Rates, NAS-9-7140, Final Report—A (1968).
6. Nadel, E. R., Bullard, R. W., Stolwijk, J. A. J., *J. Appl. Physiol.* (1971) **31**, 80.
7. Forbes, W. H., "Physiology of Heat Regulation and the Science of Clothing," p. 323, L. H. Newburgh, Ed., Saunders, Philadelphia, 1949.
8. Snellen, J. W., *J. Appl. Physiol.* (1960) **15**, 759.
9. Smiles, K. A., Robinson, S., *J. Appl. Physiol.* (1971) **30**, 409.
10. Gisolfi, C., Robinson, S., *J. Appl. Physiol.* (1970) **29**, 761.
11. Nadel, E. R., Horvath, S. M., Dawson, C. A., Tucker, A., *J. Appl. Physiol.* (1970) **29**, 603.
12. Spealman, C. R., *Amer. J. Physiol.* (1945) **145**, 218.
13. Rowell, L. B., Brengelmann, G. I., Detry, J. R., Wyss, C., *J. Appl. Physiol.* (1971) **30**, 72.
14. Webb-Peploe, M. M., Shepherd, J. T., *Circulation Res.* (1968) **23**, 693.
15. Von Liebermeister, C., "Hanbuch der Pathologies und Therapie des Fiebers," Vogel, Leipzig, 1875.
16. Cooper, K. E., Cranston, W. I., Snell, E. S., *Clin. Sci.* (1964) **27**, 345.
17. Schvartz, E., Benor, D., *J. Appl. Physiol.* (1971) **31**, 24.
18. Waligora, J. M., Michel, E. L., *Aerospace Med.* (1968) **39**, 485.
19. Beckman, E. L., "Proceedings of the Second Symposium—Underwater Physiology," C. J. Lambertson and L. J. Greenbaum, Jr., Eds., National Academy Science—National Research Council, Washington, D.C., 1963.
20. McQueen, J. D., "The Physiology of Induced Hypothermia," R. D. Tripps, Ed., Pub. 451, National Academy Science—National Research Council, Washington, D.C., 1956.
21. Virtue, R. W., "Hypothemic Amnesia," Thomas, Springfield, 1965.
22. Majendie, J. L. A., "Equipment for the Working Diver—1970 Symposium," 95–115, Marine Technology Society, Washington, D.C.
23. Mitchell, J. W., Galvez, T. L., Hengle, J., Myers, G. E., Siebecker, K. L., *J. Appl. Physiol.* (1970) **29**, 859.
24. Horiuchi, J., Koyamada, K., Matano, I., Mohri, H., *et al.*, *J. Thorac. Cardiov. Surg.* (1963) **46**, 180.
25. Dillard, D. H., Mohri, H., *et al.*, *Circulation* (1967), Suppl. I, Vols. XXXB and XXXBI, I-105.
26. Boulton, J. B., *Anesthesiol. Clin.* (1967) **5** (2), 381.

27. Wissler, E. H., *J. Appl. Physiol.* (1961) **16,** 734.
28. Wissler, E. H., *Bull. Math. Biophys.* (1964) **26,** 147.
29. Stolwijk, J. A. J., Hardy, J. D., *Arch. Ges. Physiol.* (1966) **291,** 129.
30. Keller, K. H., Seiler, L., *J. Appl. Physiol.* (1971) **30,** 779.
31. Wissler, E. H., *J. Physiol. (Paris)* (1971) **63,** 455.
32. Hammel, H. T., Jackson, D. C., Stolwijk, J. A. J., Hardy, J. D., Stromme, S. B., *J. Appl. Physiol.* (1963) **18,** 1146.
33. Hardy, J. D., Stolwijk, J. A. J., *J. Appl. Physiol.* (1966) **21,** 1799.
34. Stolwijk, J. A. J., "Expansion of a Mathematical Model of Thermoregulation to Include High Metabolic Rates," NAS-9-7140, Final Report—B (1969).

RECEIVED December 8, 1971.

12

An Elucidation of the Separate Effects Induced by Central and Peripheral Sensors in Human Thermoregulation

CHARLES E. HUCKABA, JOHN A. DOWNEY, and ROBERT C. DARLING

Department of Rehabilitation Medicine, College of Physicians & Surgeons, Columbia University, New York, N. Y. 10032

Engineering control concepts have been used to develop a comprehensive mechanism for human thermoregulation. Existing physiological evidence is accounted for by a feedback response induced by central sensors and feedforward anticipatory action generated by peripheral signals. The manner in which peripheral effects either can reinforce or inhibit the action of the central sensors is explained. A unique study procedure, using patients with spinal cord transactions, permits the proportioning of the total observed thermoregulatory response between the central and peripheral sensors respectively. These data provide the basis for evaluating the validity of mathematical functions proposed to represent the control elements under various physiological states and environmental conditions.

Thermoregulation in mammals has been the subject of widespread investigation for many years. Because of the many animal species and the almost limitless combinations of environmental and physiological conditions under which temperature regulation is of interest, the literature in this field is extremely broad and diverse.

Much of the previous work has been conducted on animals, often studied under anesthesia, even though anesthetic agents can grossly distort thermoregulatory response. Moreover, there are marked differences in some of the basic modes of thermal compensation between animals and man—in an attempt to relieve an excessive heat load, for instance, some mammals including man sweat, whereas others such as the dog pant. Animal studies can be valuable in developing general concepts,

but quantitatively precise, reliable data regarding human thermoregulation can be obtained only from studies on human subjects although such studies are subject to obvious constraints.

Recent reviews of thermoregulation by Hammel (*1*), Hardy (*2*), Downey and Darling (*3*), and Bligh (*4*), as well as a recent comprehensive compendium of papers edited by Hardy *et al.* (*5*) have helped to form a critical assessment of the present status of work in this field. Most of the work reported in the physiological literature has been experimental, and only during the past decade has any concerted attempt been made to interpret the data in view of postulated control mechanisms. An increasing number of papers are now appearing in which attention is directed to the possibilities of developing mechanisms which embody the basic concepts of engineering control theory.

The manner in which the human body controls temperature is important not only under normal conditions but also during exercise, fever, and trauma induced by injury, burns, surgery, etc. Over longer periods of time, hormones, adaptation, and acclimatization can exert significant effects. Although the work reported here is limited to normal short-term regulation, it is possible that the other situations can be explained in terms of modifications of the basic mechanism.

Control Mechanism

There is evidence that thermal sensors are distributed throughout the body. In animals sensors have been reported in the heart of the rabbit (*6*), the pulmonary vessels of sheep (*7*), and the spinal cord of the dog (*8*). However, it is agreed that some of the most important thermal receptors in the human are found in the anterior hypothalamus and the skin. The sensors at either of these locations can initiate thermoregulatory responses, and it is important that the action generated by each type of sensor be evaluated. However, most studies reported previously reflect the total response induced by both of these sources of sensory input acting together.

There have been several attempts (*9, 10, 11, 12*) to represent thermoregulatory action in a manner analogous to engineering control systems. For instance, the most frequent representation is the feedback loop, based on a hypothalamic temperature set point, which is the normal temperature (37°C) for the central part of the body under ordinary circumstances. Figure 1 shows in physiological terms the various elements of a conventional feedback control loop for sweating. Although this mechanism for representing central effects has not been proved, there is evidence which suggests that it is appropriate for use as a working postulate.

Several writers (*10–13*) have postulated a skin temperature set point, perhaps based on an average skin temperature which operates independently of that of the central hypothalamic temperature. However, since the skin is constantly exposed to a changing ambient temperature and since all parts of the body are in continuous thermal communication with one another, it is difficult to conceive that there is more than one independent set point serving as the objective of the human temperature control system. Once the set point for hypothalamic temperature is specified, all other temperatures throughout the body are dependent. If the body were to attempt to control simultaneously the central temperature to its set point and also some skin temperature to a second independent set point, the two control actions would be in conflict and an oscillatory, unstable situation would develop. Since human thermoregulation, even in the face of drastic changes in environmental temperature, occurs smoothly and at most with only minor instabilities, the evidence conclusively points to there being only the one central temperature set point. Moreover, this set point is appropriately located in the brain since this tissue should be given priority in protection against thermal damage.

To avoid the difficulties in using the same mechanism for skin temperatures as has been shown in Figure 1 for the central sensors, another type of control loop is postulated for the peripheral effects. There are several instances in the engineering field where a feedforward, anticipatory control action must be used to achieve precise specifications. Because of their location on the surface of the body in direct contact with the environment, it is logical for the skin sensors to serve such an anticipatory, "early warning" function. To visualize the basic action, in the absence of a skin temperature set point, one must look for an alternative activation potential that would serve the same purpose as an error signal. There is physiological evidence (*14*) that the thermal sensors located in the skin, although exhibiting some response as a function of static temperature

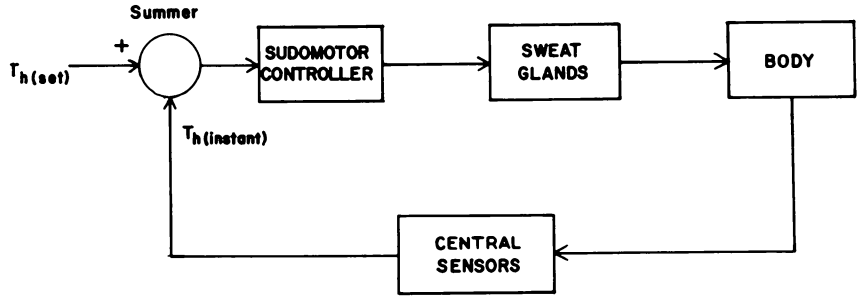

Figure 1. Feedback control of sweating

level, are activated primarily by rate of temperature change. Warm sensors and cold sensors are differentiated by whether they are activated by a rising or falling temperature. The magnitude of the firing frequency of these sensors seems to be almost directly proportional to the rate of change of skin temperature.

In view of this information, a feedforward control loop to account for the action generated by the peripheral sensors is shown in Figure 2, again using sweating for purposes of illustration. Except for the fact that there is no set point, and thus no need for a comparator to generate an error signal, the elements in this feedforward loop correspond exactly to those shown in Figure 1 for the feedback loop.

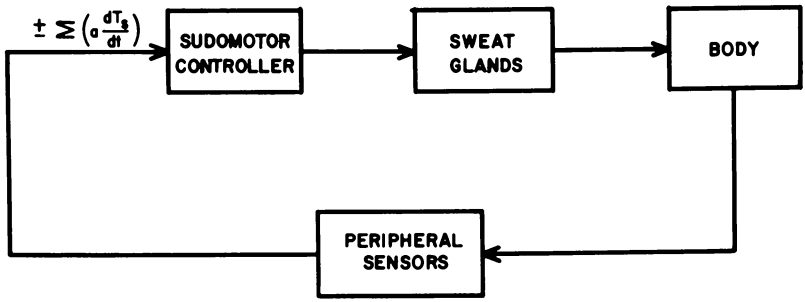

Figure 2. Feedforward sudomotor control

Even though we may account for the separate thermoregulatory responses which can be generated by either the skin sensors or the central sensors, there still remains the task of showing how the two loops are combined to produce a coordinated control action. Our attempt at formulating an overall mechanism is shown in Figure 3. This signal-flow diagram is comprised of a feedback loop and a feedforward loop for each of the three modes of thermal compensation: metabolic, vasomotor, and sudomotor. For the latter case the elements of Figures 1 and 2 are easily recognized in the overall mechanism, and metabolic and vasomotor actions are represented by analogous loops.

The signal modifier and summer combines the motivating potential produced by the central sensors in the form of an error signal based on the hypothalamic temperature set point with that generated by the peripheral sensors. Since this signal processing element is in continuous communication with each of the three controllers, it is possible, for instance, to activate a cooling response while inhibiting a heating response and vice versa. Moreover, the peripheral sensors can reinforce, attenuate, or even override a response being called for by the central sensors, depending upon environmental changes.

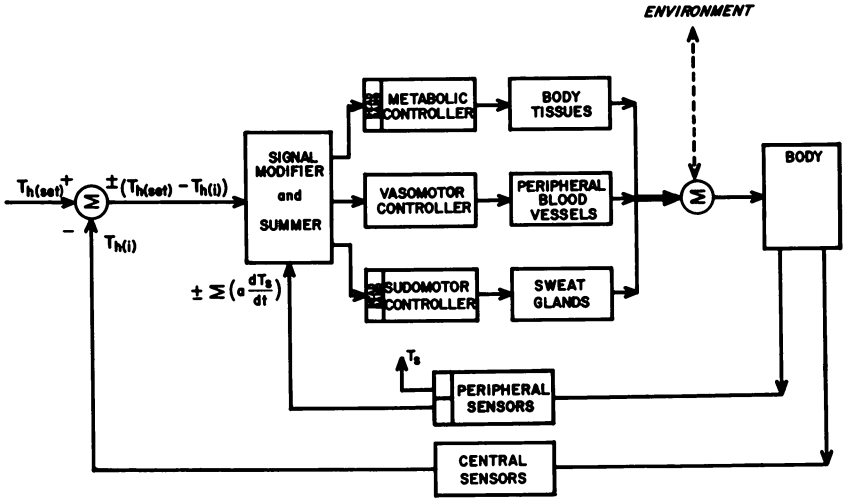

Figure 3. Human thermoregulation: normal short-term control

Physiological evidence (*15*) indicates that the vasomotor controller responds to even minor signals and thus can effect small adjustments in thermal balance. When the vasomotor action is unable to achieve the required compensation, the appropriate major control action, either metabolic or sudomotor, comes into play. Moreover, to prevent their needless activation by minor signals these controllers are protected by dead bands.

Although the skin temperature, T_s, in comparison with dT_s/dt, may play only a minor role in the activation of response mechanisms, it may well exert a significant effect on the dead bands of the metabolic and sudomotor controllers. Moreover, there is increasing evidence (*1, 5*) that T_s exerts local influences on the magnitude of the response of peripheral blood vessels and sweat glands. Whereas skin temperature effects have been elucidated for various animals (*1, 4*), further work is needed to define these effects quantitatively in the clinical human situation. For this reason in the signal-flow diagram (Figure 3) T_s is shown as being available but not specifically committed with respect to definite points of interaction.

Evaluation of Proposed Mechanism

There is evidence in the recent physiological literature which supports the postulated mechanism. Brown and Brengelmann (*16*) obtained data from water-bath studies which indicate that rate of change of skin temperature, dT_s/dt, is an important input which interacts with T_s and T_h to determine metabolic rate. They also concluded that magnitude

and direction (*i.e.*, whether + or −) of dT_s/dt seem important and that this dynamic factor may exceed the steady-state contribution of T_s. Data from these experiments show that a negative dT_s/dt increases metabolic rate above steady-state levels and a positive dT_s/dt decreases metabolic rate.

Bullard *et al.* (*12*), Banerjee *et al.* (*17*), and Nadel and Cunningham (*18*) in recent papers have emphasized the necessity of accounting for dynamic effects in studying rates of sweating. The most dramatic demonstration of the influence of dT_s/dt on sweating has been reported by Wurster and McCook (*19*). During a series of studies on ten male subjects they observed inhibition of sweating after transfer of subjects from hot to cool environments. This inhibition occurred while central core temperatures were rising and skin temperatures were falling.

The role of the central temperature-sensitive structures in human thermoregulation has been the subject of intensive study by many investigators as reviewed by Hammel (*1*). Downey *et al.* (*20*, *21*) obtained evidence that central cooling alone can initiate increased metabolism and shivering even when the sentient skin is kept above 34°C, which contradicts the conclusions of a previous investigator (*22*). There seems to be a consensus among workers in this field that the action elicited by central sensors can be approximated adequately by the feedback mechanism shown in our signal-flow diagram. For this reason it seems that attention should be directed for the present toward obtaining data for testing the feedforward loop as activated by the peripheral sensors.

Experimental Studies

Studies designed specifically to provide data for testing our proposed feedforward–feedback mechanism for human thermoregulation are in progress. The greatest need is to obtain information on the individual responses which can be elicited by either the peripheral sensors or the central sensors acting alone. Figure 4, showing one of our studies, is typical of the data on metabolic response found in the literature in which central and peripheral sensors fall simultaneously to produce a total combined oxygen response. It is impossible to determine from a plot of this type how much of the increase in oxygen consumption to attribute to the falling central temperature (T_{ear}) and how much was generated by the falling skin temperatures. This difficulty has been overcome in our studies by using patients with spinal cord transsections, as described by Downey *et al.* (*21*), in which the insentient portion of the body is used as a heat exchanger. While the sentient upper portion of the body is exposed to a falling ambient temperature, an equivalent amount of heat

is introduced into the insentient lower area by means of a surgical blanket. By this method it is possible to maintain a constant ear temperature while the skin temperatures fall. Oxygen consumption is measured by an open circuit technique (*21*), and thermocouples are used to indicate temperatures of the ear, mouth, rectum, nine skin locations and at multiple points in the environment. Hand blood flow is measured using a water-filled plethysmograph (*23*).

Figure 5 shows the oxygen response resulting from skin cooling alone which was obtained in a study on a patient with a T-10 lesion. In this instance the patient was subjected to a step change in ambient temperature by moving him quickly from a room at 30°C to a second room at 5°C. The curve shown for the anterior shoulder was typical of the rapid fall in skin temperatures. The ear temperature was maintained constant,

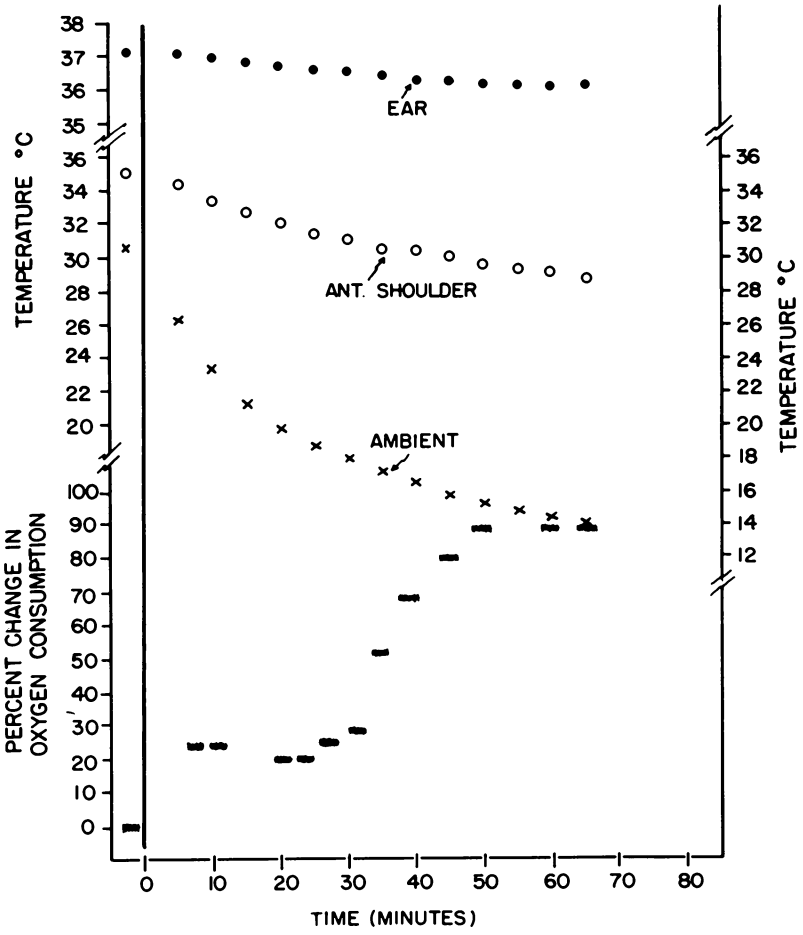

Figure 4. Response to falling ambient temperature (69 JW IV Level T-10)

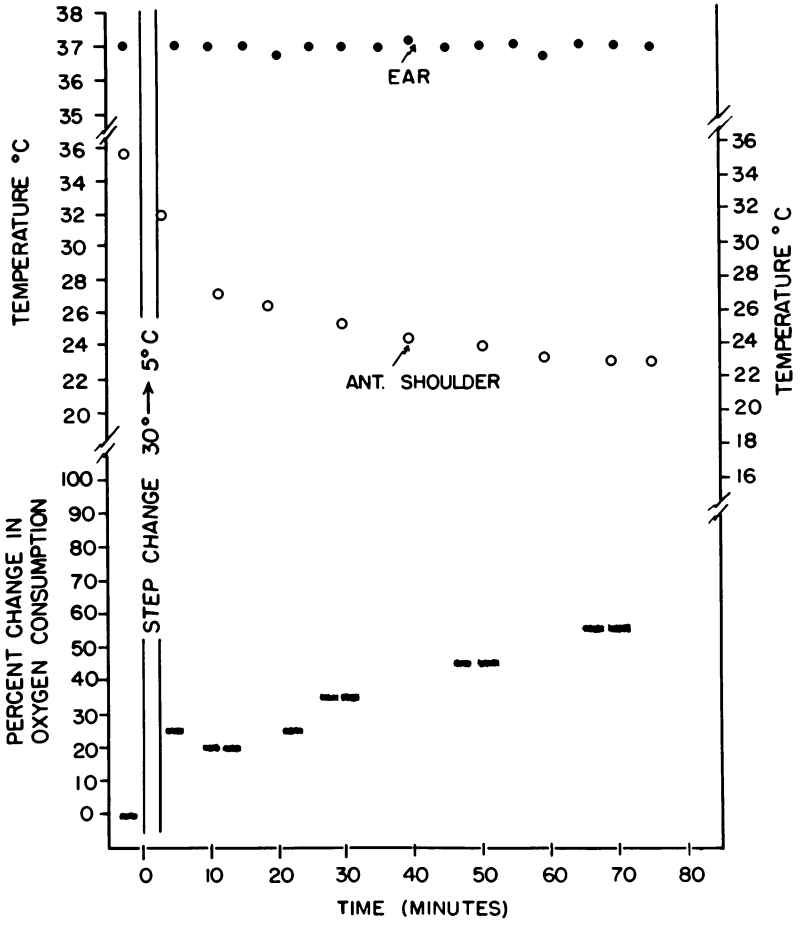

Figure 5. Response to step change in ambient temperature (70 JW II Level T-10)

using the techniques described above, so that the entire oxygen response can be attributed to the change in skin temperature.

Figure 6 shows the results of a two-part study in which, first, the ear temperature was maintained constant while the skin temperatures fell, and after 58 min the heating of the lower portion of the body was discontinued to permit the central (ear) temperature also to fall. This plot shows that a 35% increase in oxygen consumption was obtained by skin cooling alone and was further increased to 142% when the ear temperature was also allowed to fall. In terms of the proposed mechaism these results can be interpreted first as the response which was generated by the feedforward loop, followed by the enhancement caused by the activation also of the feedback loop.

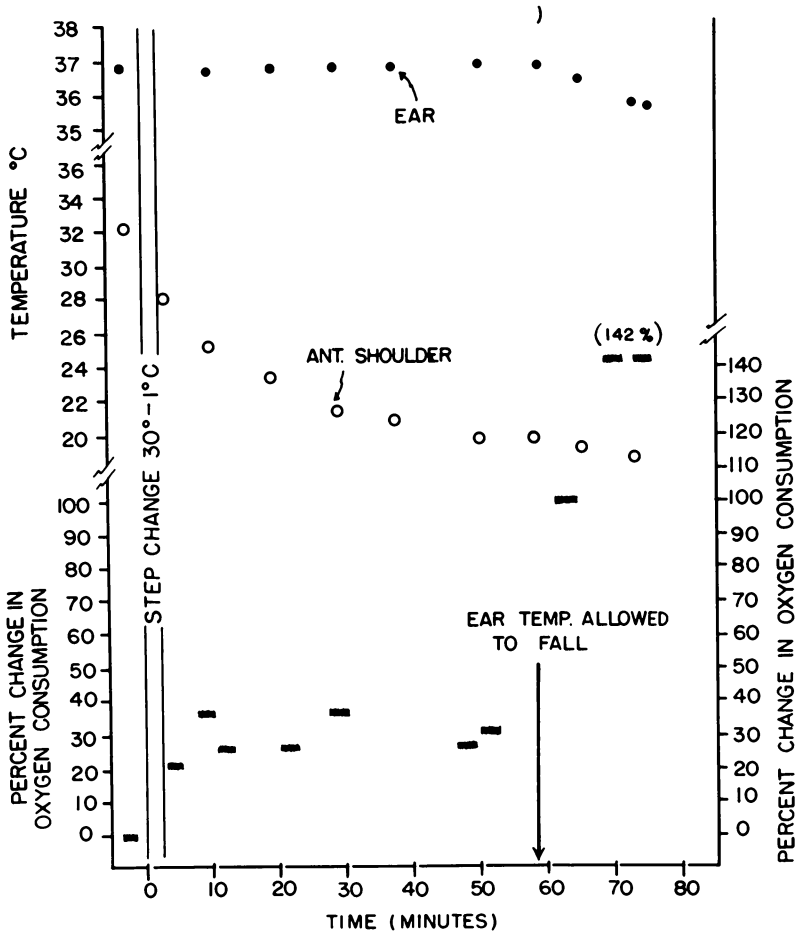

Figure 6. Response to step change in ambient temperature (70 JW III Level T-10)

The time sequence of initiation of vasomotor and metabolic responses is significant to the postulated mechanism. Figure 7 shows that vasoconstriction (reduced hand blood flow) has been completed before oxygen response starts. Moreover, the vasomotor response starts almost immediately upon application of a thermal stimulus. The dynamic effects of thermal stimuli are also seen in this plot as oxygen consumption and hand blood flow follow the ambient temperature variation.

Discussion

The proposed control mechanism for human thermoregulation as represented in Figure 3 by the signal-flow diagram seems to accommodate

presently available physiological evidence. At the same time this combined feedforward-feedback configuration agrees with the established engineering methodology where precise control specifications must be met. The data from our patient studies corroborate our postulated mechanism. These results, along with those reported by other investigators, supply evidence of the importance of evaluating under dynamic conditions the separate response which can be induced by central and peripheral sensors respectively.

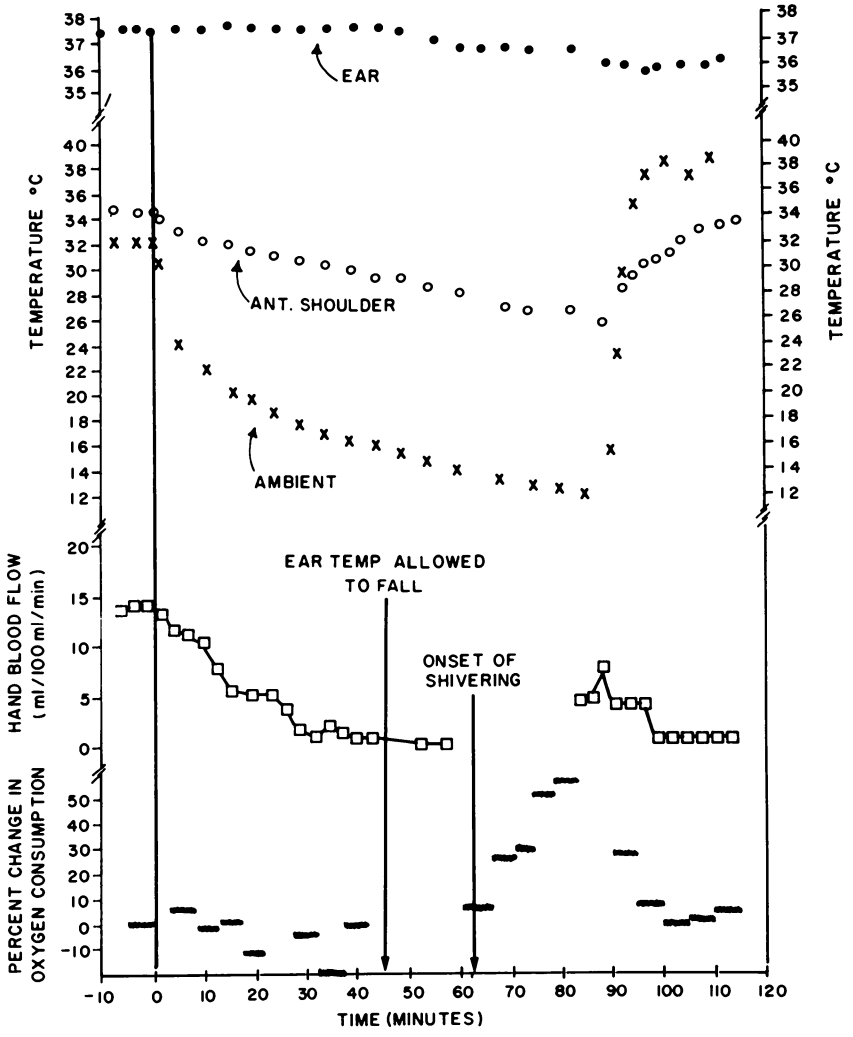

Figure 7. Response to changing ambient temperature (71 SC IX Level T-6)

As for the vasomotor response, the data confirm our theoretical postulation that this action is subject to only negligible, if any, dead band restraint. This is in distinct contrast to the situation for the metabolic controller where Downey *et al.* (*20*) demonstrated not only the existence of an appropriate dead band but also its functional dependence upon the level of skin temperature. They found that the higher the skin temperature, the lower the central temperature must fall to initiate the metabolic response.

Although the evidence presently available supports the control scheme shown in Figure 3, confirmation must await the accumulation of additional data on human subjects. Moreover, concurrent with the experimental program, a mathematical model corresponding to the control configuration of Figure 3 is being developed for making predictive computer computations. The ultimate test of the adequacy of a model for human thermoregulation will be in its ability to form the basis of predictive calculations of the thermal response of the body to the full range of physiological and environmental conditions of interest.

Although results of the work toward which these studies are projected hold potential benefits for the medical field, there is also perhaps an opportunity here for enhancing engineering control methodology. The human body is governed by a highly effective adaptive control system. As a better understanding of sophisticated physiological control mechanisms becomes available, a viable influence on engineering control system design becomes a possibility.

Literature Cited

1. Hammel, H. T., *Ann. Rev. Physiol.* (1968) **30**, 641.
2. Hardy, J. D., *Physiol. Rev.* (1961) **41**, 521.
3. Downey, J. A., Darling, R. C., *Amer. J. Phys. Med.* (1964) **43**, 265.
4. Bligh, J., *Biol. Rev.* (1966) **41**, 317.
5. Hardy, J. D., Gagge, A. P., Stolwijk, J. A. J., Eds., "Physiological and Behavioral Temperature Regulation," C. C. Thomas, Springfield, 1970.
6. Downey, J. A., Mottram, R. F., Pickering, G. W., *J. Physiol. London* (1964) **170**, 415.
7. Bligh, J., *J. Physiol. London* (1963) **168**, 747.
8. Simon, E., Rautenberg, W., Jessen, C., *Experientia* (1965) **21**, 476.
9. Hardy, J. D., Hammel, H. T., "Temperature—Its Measurement and Control in Science and Industry," Part III, Ch. 54, p. 613, Reinhold, New York, 1963.
10. Stolwijk, J. A. J., Hardy, J. D., *Pflügers Arch. Ges. Physiol.* (1966) **291**, 129.
11. Brengelmann, G. L., Human Temperature Regulation: Dynamic Characteristics of Metabolic Response, Ph.D. thesis, University of Washington (1967).
12. Bullard, R. W., Banerjee, M. R., MacIntyre, B. A., *Int. J. Biometeor.* (1967) **11**, 93.
13. Benzinger, T. H., *Sym. Soc. Expt. Biol.* (1964) **18**, 49.

14. Hensel, H., "Temperature—Its Measurement and Control in Science and Industry," Part III, Chpt. 19, p. 191, Reinhold, New York, 1963.
15. Snell, E. S., *J. Physiol. London* (1954) **125**, 361.
16. Brown, A. C., Brengelmann, G. L., "Physiological and Behavioral Temperature Regulation," Chpt. 47, C. C. Thomas, Springfield, 1970.
17. Banerjee, M. R., Elizondo, R., Bullard, R. W., *J. Appl. Physiol.* (1969) **26**, 787.
18. Nadel, E. R., Cunningham, D. J., paper presented at 54th Annual Meeting, Federation of American Societies for Experimental Biology, Atlantic City (April 1970).
19. Wurster, R. D., McCook, R. D., *J. Appl. Physiol.* (1969) **27**, 237.
20. Downey, J. A., Miller, J. M., Darling, R. C., *J. Appl. Physiol.* (1969) **27**, 209.
21. Downey, J. A., Chiodi, H. P., Darling, R. C., *J. Appl. Physiol.* (1967) **22**, 91.
22. Benzinger, T. H., *Proc. Intern. U. Physiol. Sci.* (1962) **1**, 415.
23. Greenfield, A. D. M., Whitney, R. J., Mowbray, J. F., *Brit. Med. Bull.* (1963) **19**, 101.

RECEIVED November 22, 1972.

13

Models of Respiratory Control

AKHIL BIDANI and RAYMOND W. FLUMERFELT

Department of Chemical Engineering, University of Houston, Houston, Tex. 77004

Recent advances in understanding and describing the control of the human respiratory system are discussed with particular emphasis on the mathematical models proposed. Important physiological observations relating to respiratory control are summarized, with a detailed review of the important models. The functional elements of these models are outlined as well as the predicted dynamic response to various forcing functions, the latter being compared with experimental observations. Respiratory control modeling is appraised, and suggestions for future study are given.

The basic function of the respiratory system is to maintain the respiratory gases, oxygen and carbon dioxide at levels which meet the demands of the metabolic processes and maintain the body acid-base balance. This is achieved through the regulation of ventilation in the lungs and the cardiac output and distribution of blood throughout the body. The levels of ventilation and blood flow, as well as the blood distribution, result from integration of many sensory inputs which may be chemical, mechanical, thermal, and neural in nature.

Because of the essential role that respiration plays in the overall body processes, physiologists and medical researchers have long been intrigued by this system and its regulatory mechanisms. As a result, numerous experimental studies have contributed to a rather advanced understanding of respiratory regulation. This information coupled with the rapid development of high speed computers has led to quantitative descriptions and representations of the respiratory process which have been used to predict steady state and dynamic behavior under various physiological conditions.

This article reviews and evaluates the existing work related to respiratory regulation with particular emphasis on the control models which

have been proposed and their relative success in predicting respiratory response over a wide range of physiological conditions.

This review is not an exhaustive survey, but rather focuses on principal advances and existing limitations. For additional insight there are several reviews on the physiological aspects of respiratory control (*1*, *2*, *3*, *4*, *5*) and respiratory control models (*6*, *7*, *8*). A brief review of the important physiological observations related to mechanisms of control, the stimuli, and the receptors is included. This information is the physiological background for the discussions of respiratory control models.

Physiological Observations

Mechanisms of Respiratory Control. To meet the metabolic demands of the body and to maintain the acid–base balance, ventilation is regulated by various stimuli acting at several locations in the body. Although the mechanism by which each stimulus acts in amplifying or diminishing ventilation is not well known, these stimuli clearly inhibit and excite the central respiratory centers in the medulla, either directly or indirectly. The electrical impulses generated in these centers are responsible for the motor activities which produce the ventilatory response.

In general, such electrical activity and the associated impulse traffic to the motor functions are affected not only by the chemical environment of the neurons in the central respiratory centers but also by reflex influences and voluntary drives. The principal afferent activity arises from stretch receptors in the lungs and aortic and carotid chemo- and baroreceptors. Other afferent stimuli to the respiratory centers include the protective reflexes—*e.g.*, coughing, sneezing, and other related actions—and reflexes from the joints, muscles, and tissues of the chest wall. Voluntary and emotional influences stem from neuronal activity in the cerebral hemispheres.

It is difficult to compare the relative quantitative effects of each type of reflex and voluntary action over the range of possible physiological conditions, but it is clear that during conditions of extreme physiological stress, such as vigorous exercise, all factors may influence the regulatory process. A complete analysis of respiratory response should include not only the chemically induced contributions but also those from mechanical, thermal, and neural influences. However, the lack of data on the relative contributions of these stimuli under various physiological conditions does not allow such a treatment. As a result, most analytical studies on respiratory control have been concerned with the relatively well-documented chemical regulation. Under normal conditions the results stemming from respiratory analysis in terms of the chemical stimuli seem to be consistent with those observed experimentally. It is only under more extreme con-

ditions, such as vigorous exercise, that mechanical reflexive effects and voluntary drives seem to be of comparable importance.

The Chemical Stimuli. The chemical stimuli of respiration have been known for many years. Before the start of the twentieth century there was some agreement on the important chemical components responsible for ventilatory control. As early as 1868 it was reported that hypoxia (abnormally low oxygen supply) stimulated ventilatory response beyond normal levels (*9*). This was followed by observations that acid perfusion also stimulates respiration (*10*). In 1892 J. S. Haldane and L. Smith (*11*) carried out a series of tests on the ventilatory behavior of subjects breathing in a closed chamber where the carbon dioxide accumulated with time. The observations were similar to those observed previously—*i.e.*, a small increase in CO_2 concentration resulted in significant increases in the ventilation. By using a CO_2 adsorber in the chamber, the breathing was unaffected until the O_2 content in air dropped from 21 to 15.5%. These tests showed that except for cases of low O_2 supply, CO_2 is the principal stimulus of respiration.

In 1911 Winterstein (*12*) proposed his reaction theory of ventilatory control. This theory, which has progressively evolved over the years with the accumulation of new experimental findings and interpretations (*13*, *14*), is based upon the idea that it is the hydrogen ion concentration $[H^+]$ in or near specific receptor cells which is the principal stimulus of respiration. Increased ventilation with increases in p_{CO_2} is explained on the basis that CO_2 has acid-forming properties in water—*i.e.*,

$$CO_2 + H_2O \rightleftharpoons H_2CO_3 \rightleftharpoons H^+ + HCO_3^- \quad (1)$$

with the result that increased concentrations of CO_2 in or near the receptor cells tend to form carbonic acid and thus H^+. The experimental observation that the addition of fixed acids to blood gives rise to smaller changes in ventilation than when CO_2 is added, both with equivalent increases in $[H^+]$, is explained by the comparatively rapid diffusion of CO_2 across the cell membranes of the chemically sensitive areas in the brain as opposed to the relative impermeability of these membranes to ions. Because of this, CO_2 penetrates to the chemoreceptor cells easily where it combines with water and alters the local $[H^+]$. However, H^+ concentrations associated with fixed acid addition would be confined largely to the blood. In this theory the effects of hypoxia are explained by the increase in acid products associated with anerobic metabolism.

Although the reaction theory has been continually updated to explain new experimental observations, it is not completely accepted, and there are still several theories as to how CO_2 might directly affect respiratory response. Regardless of the actual mechanisms taking place, CO_2, H^+, and O_2 are the important chemical stimuli to respiration.

Chemoreceptors. Early investigators assumed that the chemically sensitive areas controlling respiration were located in the brain. In 1926 De Castro (*15*) suggested that the carotid bodies, located near the carotid bifurcation of each common carotid artery, also could be important chemoreceptors. Shortly thereafter, Heymans and Heymans (*16*) found that ventilation was stimulated when the aortic arch of an animal was perfused with blood from an animal breathing a low oxygen air mixture. This study established the existence and general location of chemosensitive bodies in the aortic arch (the aortic bodies). Additional studies by Heymans and co-workers (*17*) delineated the location and function of the carotid bodies and demonstrated that they were stimulated by hypoxia and hypercapnia. The exact location and function of the aortic bodies was described by Comroe (*18*).

In general, these findings added a new dimension to the understanding of respiratory regulation and provided a basis for later studies which more clearly established the physiological role of the aortic and carotid bodies and the magnitude and nature of the effects of chemical stimuli. Most of these studies have been concerned with the carotid bodies since they can be isolated and perfused; their innervation in animals is readily accessible for recording with electrodes. The aortic bodies are fairly inaccessible, and much of the evidence for their function is indirect (*3*).

The chemosensitive cells of carotid and aortic bodies (the peripheral chemoreceptors) are stimulated by decreases in the O_2 tension of arterial blood perfusing the peripheral chemoreceptors and by increases in arterial p_{CO_2} or arterial $[H^+]$. The stimulation resulting from increased arterial p_{CO_2} is probably an indirect result of increased $[H^+]$ from the acidifying action of CO_2 in the vicinity of the chemosensitive cells. It now seems that these bodies respond to changes in their extracellular $[H^+]$ and can respond to even the most acute metabolic acid–base disturbance without significant delay (*19*).

The existence of areas in the brain which are highly sensitive to changes in CO_2 tension was established from extensive studies over many decades (*4*). Initially it was thought that these sensitive areas were located in the respiratory center of the medulla. More recent studies have shown the existence of such cell groups exterior to the medullary respiratory center (*2*).

In 1954 Leusen (*20*) demonstrated that the perfusion of the brain ventricular system with an acid fluid stimulated ventilation while perfusion with an alkaline fluid depressed ventilation. These ventilatory responses were assumed to be caused by direct stimulation or depression of chemosensitive elements within the respiratory center. Loeshcke and co-workers (*21*, *22*) were the first to present evidence that respiratory H^+ chemosensitivity might be located outside the medullary respiratory

center. Later, Mitchell *et al.* (*23*) delineated two areas on the surface of the medulla which produced changes in ventilation when the [H^+] of the bathing fluid was changed. Although the existence of chemoreceptor cells in these areas has not been verified by morphological evidence, there are clearly central chemosensitive areas (the central "chemoreceptors") which are influenced by changes in the chemical composition of the cerebrospinal fluid (CSF). It is not clear whether the ventilatory changes are caused by chemoreceptor cells or reflect the effects of diffused substances (from the CSF) on certain respiratory neurons located at some distance from the surface of the brain (*24*).

Regardless of the actual mechanism or precise location of the central chemoreceptors, these chemosensitive areas have the following important functional characteristics related to respiratory regulation:

(1) These areas are not stimulated by decreased pO_2.

(2) The [H^+] of the CSF fluid seems to be the important stimulus; however, a specific effect of CO_2 cannot be completely excluded.

(3) Increases in arterial p_{CO_2} result in central chemoreceptor stimulation mainly through the rapid diffusion of CO_2 into the CSF and the associated increase in [H^+] from the acidification of CO_2 with water.

(4) Arterial changes in [H^+] without accompanying changes in p_{CO_2} do not have significant effects because the H^+ and HCO_3^- do not readily diffuse into the CSF.

(5) Central chemoreceptors respond more slowly to p_{CO_2} and [H^+] changes in arterial blood than do the peripheral receptors.

In general, the principal function of the central chemoreceptors is to guard the [H^+] of CSF which bathes the central nervous system while the principal function of the peripheral chemoreceptors is to regulate p_{O_2} and, under extreme conditions, the p_{CO_2} and [H^+] of systemic arterial blood (*25*).

Respiratory Control Models

The accumulation of more detailed physiological data and information on respiratory regulation has led to the development of respiratory control models of varying complexity. In addition to providing insights into the interacting feedback mechanisms of respiratory control, such models provide the basis for analyzing and predicting ventilatory response under normal and abnormal conditions.

The underlying principle assumed to govern respiratory response is the tendency of the body to induce compensatory activity to neutralize or diminish the influence of any disturbance. This principle is implemented by feedback mechanisms where the controlled variables are kept within narrow ranges of certain set points (or reference) values (*see*

Figure 1). The disturbances (*e.g.*, changes in the chemical composition of inspired air or changes in metabolic activity) produce changes in the controlled system (the gas exchange and transport components of the respiratory and circulatory system) which in turn produce changes in the controlled variables (arterial p_{O_2}, p_{CO_2}, $[H^+]$, and CSF $[H^+]$). The deviation of the controlled variables from their reference values is sensed at various points (the central and peripheral chemoreceptors), and this signal is transmitted to the controller (the respiratory center in the brain) where it induces a change in the manipulated variables (ventilation, cardiac output, and blood distribution).

Although the assumption of such a control mechanism involving reference values for the controlled variables is intuitively attractive, the existence of such reference values is still questioned (*26*). However, in most respiratory control models to date such a servomechanistic regulation is generally used; only recently have other performance criteria been suggested (*26*).

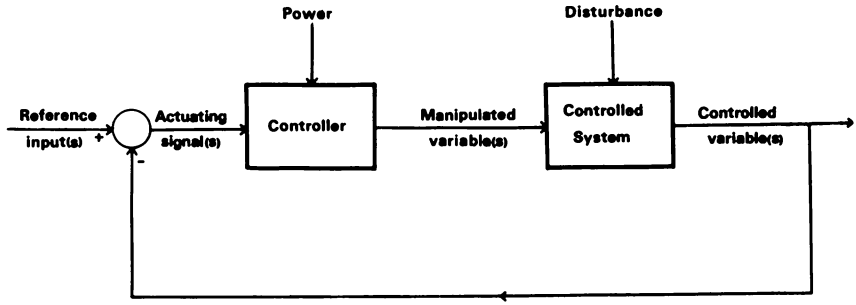

Figure 1. Block diagram representation of a negative feedback control system

Table I summarizes the important existing respiratory control models. Each model is made up of certain structural elements: (1) lungs, (2) body tissues, (3) blood–gas relations, (4) ventilatory control law, and (5) blood flow and blood flow distribution control laws. The models differ mainly in the treatment of the last four elements.

The first quantitative treatment of respiratory regulation, based upon a strictly chemosensitive viewpoint, was that of Gray (*27*) in 1946. The principal contribution of this study was the presentation of a multiple factor theory for ventilatory control. In particular, Gray proposed an empirical control law of the form

$$\dot{V} = k_1 [H^+] + k_2\, pCO_2 + k_3 (k_4 - pO_2)^{k_5} - k_6 \qquad (1)$$

which assumed that arterial $[H^+]$, p_{CO_2}, and p_{O_2} have simple additive effects on the ventilation V; the k_i's were specified constants. Gray used his model successfully to predict the ventilation at steady state corre-

sponding to various levels of CO_2 inhalation, hypoxia, and metabolic acidosis. This study was thus the first quantitative synthesis of information on ventilatory stimuli, pulmonary gas exchange, blood–gas transport,

Table I. Summary of

Investigator	*External Respiratory System (Lungs)*	*Internal Respiratory System (Tissues)*
Gray (*27*)	Internal and external respiratory systems are lumped.	
Grodins, Gray, Schroeder, Norins, and Jones (*28*)	Unsteady state lumped alveolar compartment with continuous ventilation; equilibrium between gas in lungs and arterial blood.	Lumped tissue compartment with equilibrium between tissue and venous blood.
Defares, Derksen, and Duyff (*29*)	Same as Grodins *et al.* (*28*).	Separated into a respiratory center (the brain) compartment and lumped tissue (nonbrain) compartment.
Grodins and James (*30*)	Similar to Grodins *et al.* (*28*) except with oscillatory ventilation.	Same as Grodins *et al.* (*28*) except with separate "brain" and "nonbrain" compartments.
Horgan and Lange (*32*)	Same as Grodins *et al.* (*28*).	Same as Grodins (*28*).
Horgan and Lange (*35*)	An incorporation of O_2 effects into previous model with more relatistic blood transit time delays and more complete blood-gas relations; the control law was taken to be that of Gray (*27*).	
Horgan and Lange (*36*)	Same as Horgan and Lange (*35*).	Separated into brain and nonbrain compartments. Brain compartments subdivided into a tissue compartment, ventrolateral surface compartment, and a CSF compartment with diffusion between each.
Clegg (*37*)	Same as Grodins *et al.* (*28*). except with the incorporation of O_2 effects.	Same as Grodins *et al.* (*28*) except with the incorporation of O_2 effects.

and blood buffer systems into a feedback regulator. Although Gray's model was very useful in steady-state calculations, by nature it was not applicable to analysis of dynamic respiratory response.

Respiratory Control Models

Blood–Gas Relations	*Controller*
Empirical chemical equilibrium relation between CO_2, H^+, and O_2 in blood.	Multiple factor theory used for ventilation which included arterial H^+, p_{co_2}, and p_{o_2}. Restricted to steady-state analysis.
Linear CO_2 absorption curves for CO_2 in blood and tissues.	Simple proportional control for ventilation in terms of tissue p_{co_2}. Effect of O_2 changes not considered. Cardiac output fixed.
Linearized blood CO_2 absportion.	Similar to Grodins *et al.* (*28*) except with control variable being arterial p_{co_2}. Effect of O_2 changes not considered. Blood flow to respiratory center related to arterial p_{co_2}.
Same as Grodins (*28*).	Controller involved proportional, rate, and integral elements. Inputs were arterial p_{co_2} and $\dot{p}_{co_2}$ and brain p_{co_2}. Effect of O_2 changes not considered. Cardiac output taken as linearly dependent on total CO_2 production with a first-order time lag.
Similar to Grodins *et al.* (*28*).	Nonlinear relations between ventilation and arterial p_{co_2}. Constant cardiac output.
Linearized CO_2 dissociation curves for blood and tissue.	Gray's equation; input being arterial p_{co_2} and ventrolateral surface p_{co_2}; constant cardiac output.
Simple treatment of CO_2 and O_2 dissociation effects; action of blood buffers included.	Empirical relation between ventilation and p_{co_2} and p_{o_2} at arterial and central chemoreceptors with appropriate time lags associated with diffusion at the receptors and blood transit times.

Table I.

Investigator	*External Respiratory System (Lungs)*	*Internal Respiratory System (Tissues)*
Milhorn, Benton, Ross, and Guyton (*41*)	Same as Grodins *et al.* (*28*) except arterial p_{o_2} was not taken to be in equilibrium with alveolar p_{o_2}.	Similar to Grodins and James (*30*) except blood and brain tissue are separated.
Longobardo, Cherniak, and Fishman (*43*)	Unsteady state lumped compartment made up of arterial blood and the functional residual capacity of lung.	In the case of CO_2, system was broken down into muscle and nonmuscle tissue compartments with unsteady lumped analysis being applicable in each. For O_2, only one tissue compartment was employed.
Grodins, Buell, and Bart (*46*)	Unsteady state lumped lung compartment with continuous ventilation with equilibrium between alveolar gas and arterial blood.	Separated into brain and other tissue; brain separated into lumped blood-tissue compartment and CSF compartment with diffusion between each.
Matthews, Lazlo, Campbell, and Reed (*48*)	Unsteady lumped similar to Longobardo *et al.* (*43*).	Internal system divided into arterial and venous blood compartments, a brain compartment, two separate compartments for the poorly perfused and well perfused tissues. The latter two compartments are subdivided into intracellular bicarbonate and total extracellular CO_2 (plus intracellular dissolved CO_2) pools. Kinetic rate expressions for the CO_2 hydration in these pools are included as well as balance equations for the ions.

Grodins and associates (*28*) in 1954 recognized that during inhalation of CO_2-enriched gas mixtures the human respiratory system shows characteristics of a negative feedback controller (*see* Figure 2). In particular, when the CO_2 content of the inspired air is altered, pul-

Continued

Blood–Gas Relations	*Controller*
Complete empirical blood–gas relations including O_2 and CO_2 dissociation effects as well as blood buffering relations.	Ventilation relation similar to Gray (*27*) with venous p_{CO_2} and arterial p_{O_2} taken as regulated variables; total blood flow was taken as constant; cerebral blood flow and tissue blood flow were regulated by both arterial p_{CO_2} and p_{O_2}.
Blood and tissue CO_2 and O_2 dissociation curves were assumed to be linear.	Empirical ventilation relation involving arterial p_{O_2} and p_{CO_2}; cardiac output and blood distribution assumed constant.
Complete blood–gas relations with Haldane and Bohr effects; modified buffer relation for CO_2 in brain-tissue compartment.	Used several empirical control laws; (a) simple proportional effects of H^+, p_{CO_2} (in brain), and (b) H^+ concentrations in CSF and arterial blood; effect of O_2 included as additive nonlinear term. Cardiac output treated in similar way as Grodins and James (*30*); variable blood transit times included.
Complete blood–gas, tissue–gas relations.	Ventilation assumed to be proportional to p_{CO_2} in brain pool minus threshold p_{CO_2}. Cerebral blood flow and muscle blood flow regulated by arterial p_{CO_2}.

monary ventilation changes in a manner suggesting that the basic mechanisms of the body are attempting to maintain the body CO_2 at some fixed value. Based upon these observations, the model shown in Figure 2 was proposed. Although the blood–gas relations were somewhat oversimpli-

fied and the blood transit times between compartments were negelected, the model was reasonably successful in simulating the relatively slow response associated with small step changes (increases) in CO_2 content in inspired air. The agreement between "on transient" predictions and experimental curves of ventilation *vs.* time was good. There were serious discrepancies in the off transient curves of p_{CO_2} *vs.* time. The model predicted much more undershoot than had been observed experimentally. Furthermore, Grodins noted certain high frequency oscillatory components in his experiments which could not be simulated.

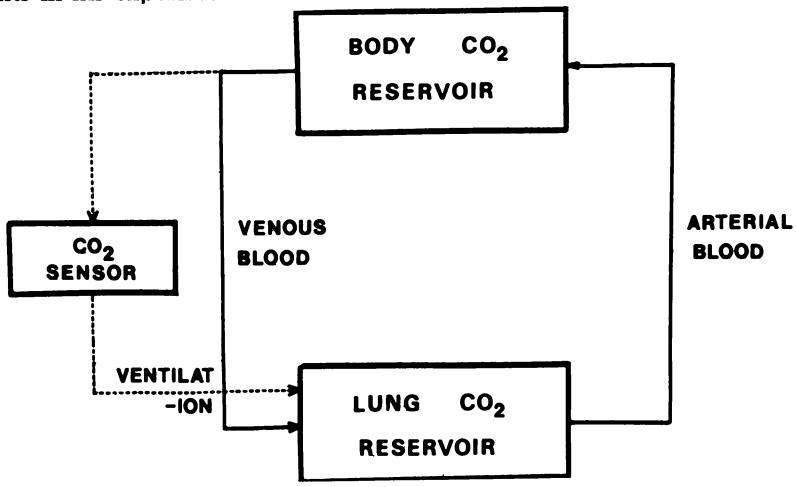

Figure 2. Block diagram of the respiratory control system, Horgan & Lange (6)

This very simple model in which all tissue CO_2 is lumped together leads to an abnormally large value for total labile CO_2 in the body since it does not take into account the much lower CO_2 concentrations in the intracellular fluid.

Additional refinements of the model were made by Defares *et al.* (*29*) and Grodins and James (*30*). Defares noted that the blood flow to the central respiratory centers increases monotonically with increases in local p_{CO_2}, independent of the cardiac output. Defares incorporated this effect into a model that treated the brain as a compartment separate from the other tissues. The response of this model differed somewhat from Grodins' model, and its transient response was in closer agreement with experimental data on CO_2 inhalation. The main drawback of Defares' work was the assumption that the pH of the blood varies passively with p_{CO_2}. Also, circulation time delays and the effect of arterial p_{O_2} were not included.

In a continuation of the early work of Grodins and co-workers, Grodins and James (*30*) presented a respiratory control model which like

that of Defares used the brain, nonbrain tissue representation. Among other modifications, ventilation in the lungs was allowed to oscillate, and a proportional-integral control law was used for the regulation of ventilation. The oscillatory behavior was introduced with the idea that an oscillatory signal might provide a higher ventilatory stimulus than a nonoscillatory one. The model was applied to conditions of CO_2 inhalation and exercise, and in the latter case was embarrassingly close to the experimental observations of Dejour (*31*). However, the neglect of blood flow transit times to the sensing regions makes such an agreement somewhat artificial.

In 1962, in an effort to gain a better understanding of periodic breathing, Horgan and Lange (*32*) presented a model in which ventilation was assumed to depend on arterial p_{CO_2}. Transport delay and mixing were introduced between lung and arterial chemoreceptors to simulate the flow of blood through the lung and left heart. This delay time was closely related to the period of Cheyne–Stokes respiration as had been observed in patients by Hetch (*33*). It was necessary to modify arbitrarily the chemoreceptor influences suggested by Gray (*27*) to demonstrate periodic breathing (such as Cheyne–Stokes behavior). The model successfully simulated the classic experiments of Douglas and Haldane (*34*) in which periodic breathing was induced in a normal individual by hyperventilation.

In 1963 Horgan and Lange (*35*) restored the chemoreceptor influence to Gray's form and added a second O_2 control loop. Other changes in the model included more accurate representations of the lung-to-artery time delay and the blood–gas chemistry relations. A further extension was introduced in 1965 (*36*) to include diffusion effects and associated time lags occurring between the blood, tissue, and cerebrospinal fluid of the brain. These refinements, prompted by the experimental work of Mitchell *et al.* (*4*) produced the model shown in Figure 3 which simulated the high frequency phenomenon associated with Cheyne–Stokes respiration and the low frequency phenomenon associated with CO_2 inhalation. At this point it was possible to simulate the experiments of Mitchell in which the CO_2 tension of mock cerebrospinal fluid was suddenly changed.

During the period in which Horgan and Lange were carrying on their studies, Clegg (*37*) presented a careful study of respiratory control which followed a more basic control approach than that used previously. The schematic representation of the system is shown in Figure 4. This work, which is seldom referenced, represented one of the first attempts at specifying the relative importance of the peripheral and central chemoreceptors to respiratory dynamics and stability. The model exhibited realistic transient and steady-state behavior under various conditions.

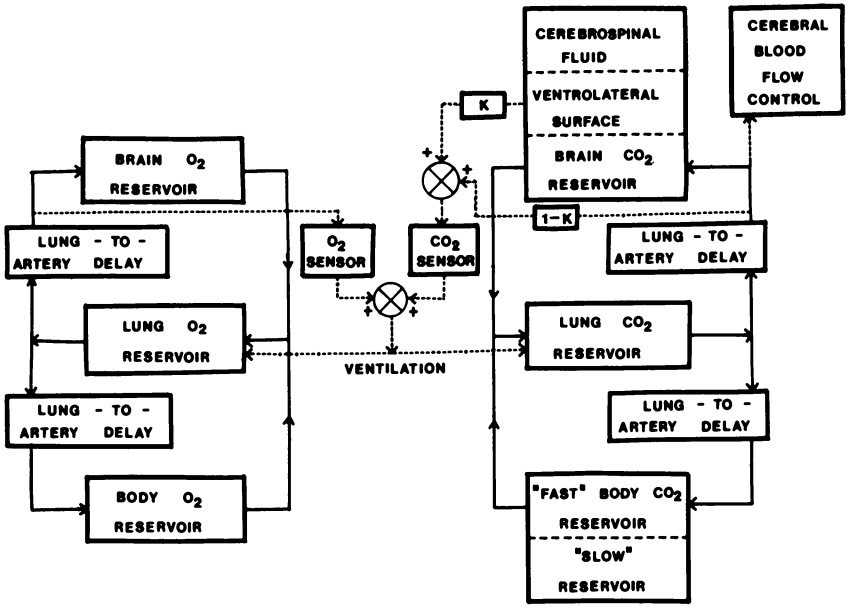

Institute of Electrical and Electronics Engineers

Figure 3. Block diagram of the respiratory control system, Horgan & Lange (6)

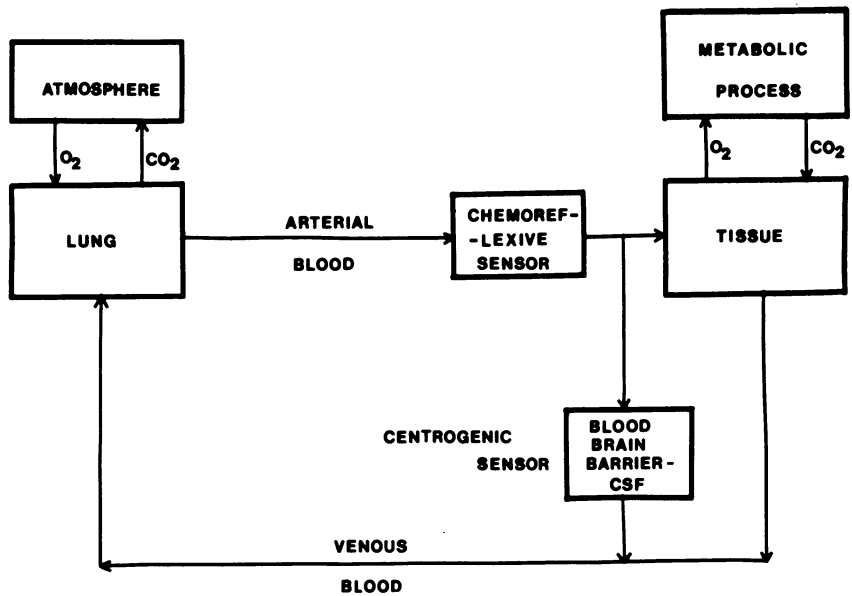

Figure 4. Block diagram of the respiratory control system—Clegg (37)

These included step changes in environmental CO_2 and O_2 concentrations and variations of several internal state parameters. Steady-state oscilla-

tions in normal ventilation, as well as Cheyne–Stokes respiration, were displayed over a range of temporal parameters and relative contributions of the aortic and medullary sensors.

In an extension of Gray's early work, Lloyd and Cunningham (38) tried to quantify the ventilatory response at steady state in terms of the alveolar O_2 and CO_2 tensions. By having subjects breath gas mixtures high in CO_2 at different alveolar oxygen partial pressures, the curves shown in Figure 5 were obtained. Based upon these observations, the steady-state ventilation was described by

$$\dot{V} = D\,(p_{ACO_2} - B)\left[1 + \frac{A}{(p_{AO_2} - C)}\right] \qquad (2)$$

for $p_{ACO_2} > B$, $p_{AO_2} > C$; where A, B, C, and D are constants. This representation differs from Gray's representation in four aspects:

(1) CO_2 and O_2 effects are multiplicative as well as additive.

(2) It is based entirely on experimental data.

(3) It is intended to cover only a portion of the physiological range ($p_{ACO_2} > B$ and $p_{AO_2} > C$); whereas Gray's was assumed to cover the entire range.

(4) $\dot{V}$ is the minute ventilation rather than the alveolar ventilation.

Milhorn and Brown (39) have reported the following values for the parameters in Lloyd and Cunningham's equation: $A = 13.6$ mm Hg, $B = 37.27$ mm Hg, $C = 25.0$ mm Hg, and $D = 2.0$ liters/min mm Hg.

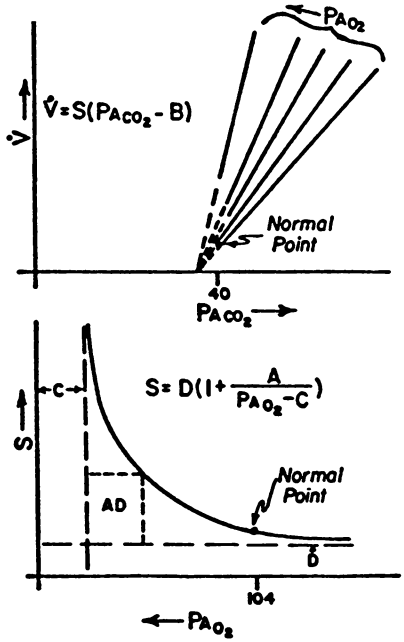

Computers and Biomedical Research

Figure 5. Diagram showing how Lloyd and Cunningham's controller equation was obtained (solid lines based on experimental data, dashed lines extrapolated, adapted from (39)

In 1965 Milhorn and Guyton (*40*) presented an analog computer analysis of Cheyne–Stokes respiration. The model used by these investigators was an extension of Grodin's earlier model with the addition of circulation times and ventilatory dead space. Like Grodins, it was assumed that the chemoreceptors were responsive to the tissue CO_2 tension rather than to p_{CO_2} in arterial blood. Thus, while the model could successfully simulate the relatively slow phenomenon observed in CO_2 inhalation, it could demonstrate Cheyne–Stokes breathing only when one or more parameters were adjusted to unusually high or low values.

In another study Milhorn *et al.* (*41*) provided a more detailed model of ventilatory control (*see* Figure 6) which included more general treatments of the behavior in the lungs (nonequilibrium between O_2 in lungs and O_2 in arterial blood was allowed), the blood–gas relations, and the blood flow variance and distribution. Whereas the previous studies of Grodins and others had lumped blood and brain tissue together, thereby creating a large capacitance and a slow change in the p_{CO_2} (or H^+) in these chemosensitive compartments, Milhorn separated these into two compartments with the blood compartment having a very low volume or capacitance for CO_2 accumulation. As a result, Milhorn's model, although more realistic, was more sensitive to transient changes in p_{CO_2} (or H^+) and showed a response to CO_2 inhalation which was too rapid. Milhorn suggested that this was attributable to the use of an oversimplified control law involving proportional elements with reference levels

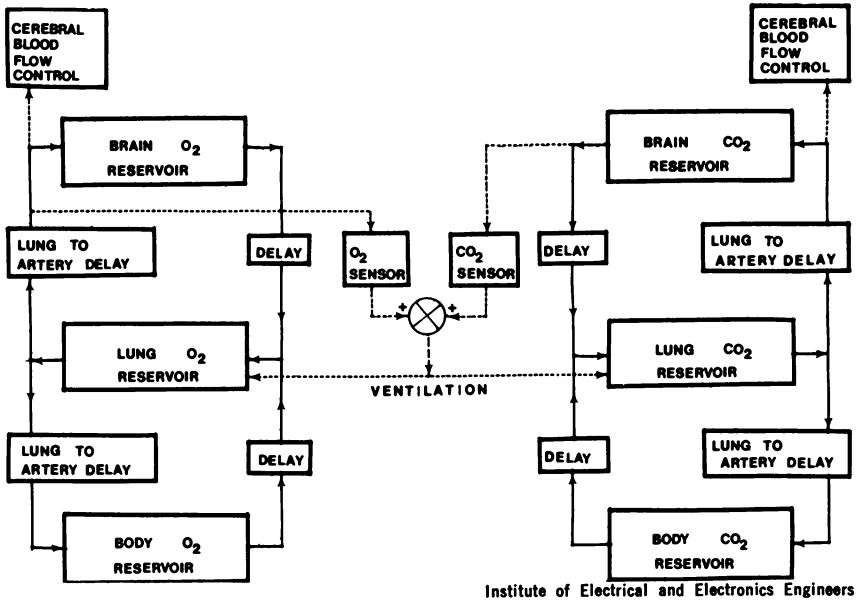

Figure 6. Block diagram of the respiratory control system—Horgan and Lange (6)

based upon steady-state observations. More likely, the principal problem was that the model did not include diffusional lag times in the brain. A more recent study by Milhorn and Reynolds (*42*) seems to bear out this latter observation.

Longobardo *et al.* (*43*) developed a model of ventilatory control which predicted the ventilation and blood–gas changes occurring during Cheyne–Stokes breathing in man and dog (*see* Figure 7). In this model the arterial p_{O_2} and p_{CO_2} were considered to determine the level of ventilation according to an equation based upon the ventilatory response to O_2 and CO_2 in the dog by Mitchell *et al.* (*44*) and in man by Nielson and Smith (*45*). The ventilation and blood–gas changes predicted by the model were compared with values actually measured by Longobardo in man and dog during periodic breathing, and the model reproduced the essential features of the changes. The usefulness of the model is limited by the inclusion of only peripheral chemoreceptors, as opposed to peripheral and central chemoreceptors.

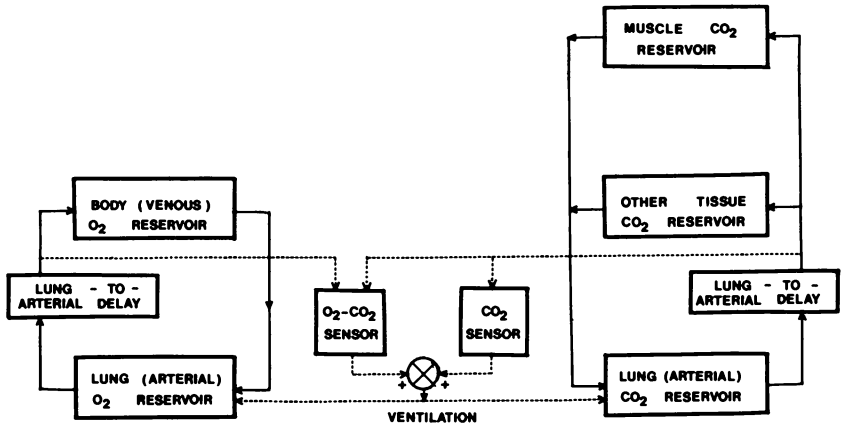

Figure 7. Block diagram of the respiratory control system, Horgan & Lange (6)

In 1967 Grodins and co-workers (*46*) presented one of the most complete model studies to date (*see* Figure 8). In this work the respiratory response was governed by CSF $[H^+]$, and arterial $[H^+]$ and p_{O_2} at the carotid chemoreceptors. Careful attention was given to the blood–gas relations as well as the transit delay times in the circulatory system. The movement of respiratory gases between a lumped blood–tissue compartment in the brain and the cerebrospinal fluid was governed by a simple diffusion representation, which effectively created an additional time lag. Grodins used this model to study the accuracy of several control models and to simulate ventilatory responses to various forcings including CO_2 inhalation, hypoxia at sea level, altitude hypoxia, and metabolic disturb-

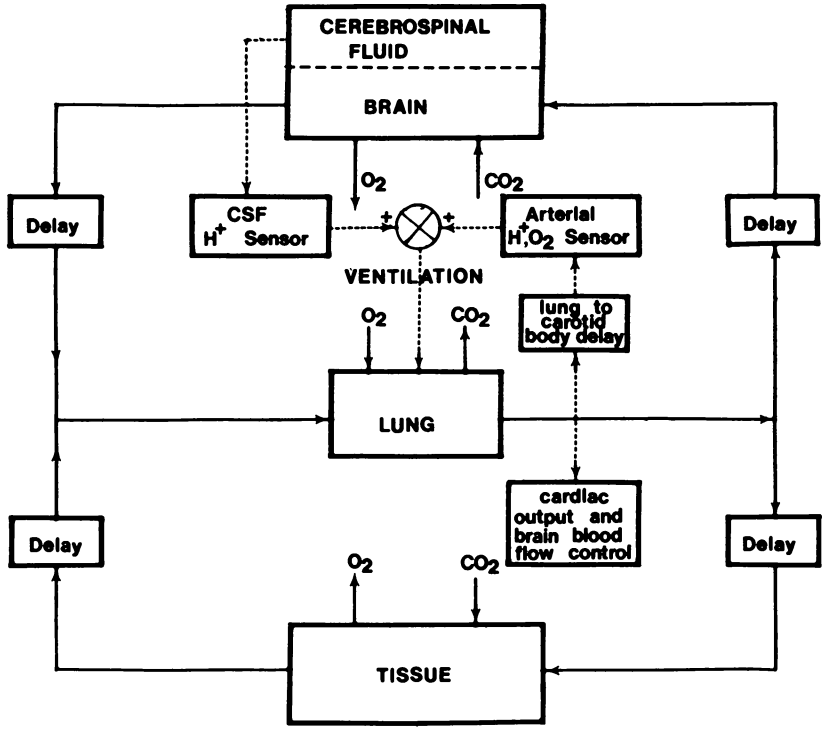

Figure 8. Block diagram of the respiratory control system—Grodins et al. (46)

ances in acid–base balance. For each, the general qualitative and quantitative behavior of the model was quite reasonable and was consistent with experimental observations of Mitchell (*4*) and Lambertson (*47*). Analysis of the dynamic behavior associated with various model modifications provided a number of insights into the relative importance of the different chemoreceptors, their time response, and their incorporation in ventilatory control laws.

Shortly after the publication of Grodins' work, Matthews *et al.* (*48*) presented a model in which the emphasis was placed on the blood–gas, tissue–gas relations, and the effects these have on respiratory response. This work was prompted by what these authors felt were inadequacies of previous models in the treatment of CO_2 dissociation and kinetics. The model proposed by these investigators is shown in Figure 9. The principal distinction of this model is the division of the tissue compartments (except brain) into intracellular and extracellular pools, thereby allowing a more detailed accounting of the equilibrium and kinetic relations between H^+, HCO_3^-, and CO_2 in the tissues. The control features were oversimplified and did not fully use available physiological information. In particular, the sensing portion was located in the lumped

brain compartment, and the peripheral receptors were effectively ignored (or at best the central and peripheral influences were crudely integrated). The simulation results for rebreathing and CO_2 inhalation were still in fair agreement with those experimentally observed with several subjects. A few discrepancies between experimental and computed values were noted by the authors, including a predicted ventilation which rose too rapidly during CO_2 inhalation. In general this work emphasized the importance of accurately representing the blood–gas equilibrium and kinetic relations.

Additional respiratory control models have recently been reported by Milhorn and Reynolds (*42*) and Duffin (*49*). Milhorn's model is similar to his previous model except that a peripheral sensor compartment is added, and the central H^+ sensor is located beneath the surface of the medulla. The depth of the central sensor was adjusted (effectively adjusting the diffusional time lag) to provide close agreement between computed and experimental ventilatory responses to CO_2 inhalation. When the model is applied to CSF perfusion, good agreement is reported.

Finally, we mention the respiratory control studies of Priban and co-workers (*50, 51, 52, 53*). In the models presented above, respiratory control is represented as a position control servomechanism, and as such the control variables are maintained near certain reference values (or set

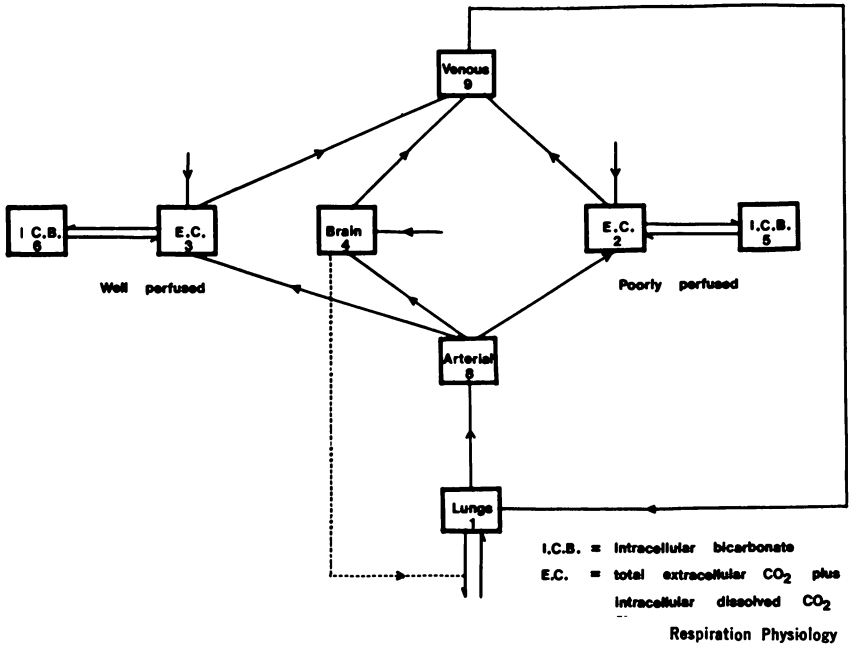

Figure 9. Block diagram of the respiratory control system—Matthews et al. (48)

points). Priban has questioned the applicability of this approach to describe the response of such a system involving a large number of interacting variables. Instead, it is suggested that a more realistic description is possible using recent concepts of control theory, in particular the theory of self-adaptive multilevel control systems.

In his studies Priban assumes that the respiratory control system consists of three interacting loops involving:

1. The control of the blood respiratory chemistry; the process by which for any given metabolic exchange requirement of oxygen and carbon dioxide the level of ventilation is kept at a minimum.

2. The control of the activity of the respiratory muscles; the process by which a pattern of activation (tidal volume, frequency of breathing) of the respiratory muscles is selected in which the average expenditure of energy is kept at a minimum for any level of ventilation demanded.

3. The control of airway dimensions; the process by which the energy required to ventilate is kept at a minimum for any alveolar gas exchange requirement.

The three processes are coordinated and controlled by the overall controller, which predicts the activity that will keep the overall energy expenditure of the respiratory system at a minimum. For this prediction the controller uses information fed back during previous breaths. In this sense, the model possesses predictive elements—*i.e.*, feed forward control with associated memory. As yet, extensive testing of the model with experimental data has not been reported.

In summary, two types of respiratory control models have been proposed. The first includes the so-called compartmental models in which the performance criteria is the close maintenance of certain respiratory variables at specified reference levels. Most models to date fall into this category and include the effects of CO_2, O_2, and pH of blood, and for Horgan and Lange, and Grodins *et al.*, the cerebrospinal fluid. These models include circulatory time delays as well as the storage effects of the lungs, the body tissue, the brain tissue, and the cerebrospinal fluid. The effect of CO_2 on cerebral blood flow is also included. In most cases the lungs are represented as a rigid compartment with continuous ventilation. Individual events of the respiratory cycle are not included nor are individual events of the cardiac cycle. The interaction between the respiratory and the circulatory system is not considered. Only James and Grodins (*30*) consider the analysis and description of the hypernea of exercise.

The second class of models is exemplified by the work of Priban and associates who use the work of breathing as a performance criteria in a self-adaptive control scheme. However, these workers do not include the representation of the central receptors whose physiological importance is now widely recognized. In addition, no information about the response

of this model to such well-known forcing conditions as CO_2 inhalation, hypoxia, and metabolic acidosis is reported.

Future Directions

The compartmental models have yielded modest agreement with experimental information on: (1) low frequency effects such as CO_2 inhalation, hypoxia resulting from low O_2 in inspired air, and changes in the p_{CO_2} of the cerebrospinal fluid (by perfusion of the medulla with mock CSF); (2) medium frequency effects such as Cheyne–Stokes respiration in normal subjects induced by hyperventilation and altitude, and in patients by increased circulation time (congestive heart failure), increased system gain (neurological disorders), and modified CO_2 dissociation (metabolic acidosis). However, none of the models has effectively analyzed the hypernea of exercise. Defares (*54*), reviewing the problem of exercise, proposes that during exercise the set point of p_{CO_2} is lowered by neural signals originating in the exercising muscles. As a result, the value(s) of the controlled variable(s) is forced back to the normal or resting value(s), despite the presence of the disturbing input caused by extra CO_2 production. To support this claim he cites experimental work in which exercise shifts the linear steady-state $V - p_{ACO_2}$ curve to the left. This is an interesting observation and needs to be incorporated and tested in future modeling of the human respiratory system.

Another approach to the problem could be the inclusion of terms involving the metabolic rate M as well as dM/dt in the control function. However, as noted by Grodins (*37*), the physiological isomorphism of such terms is still obscure.

A more fundamental approach to general respiratory control modeling, including the description of exercise, would seem to be that suggested by Priban. This approach integrates the effects of several separate control functions in a hierarchical scheme of respiratory control. The basic premise is that the body tends to minimize the work of breathing in a self-adaptive manner. The central receptors must be included in the analysis, however, if it is to simulate successfully chemical forcings such as changes in the CSF composition by mock perfusion of the medulla.

Stoll's work (*55*) on sinusoidal inputs of CO_2 fraction in inspired air is mentioned because it provides data for the testing of existing and future models. Such tests have suggested that nonlinearities and spontaneous periodicities (assessed by harmonic analysis and power spectrum analysis) are not severe enough to preclude linear analysis.

Finally, it must be mentioned that with modeling having attained a certain level of maturity, future studies should attempt to optimize the

parameters chosen in the analyses using techniques of system identification (*56*). Past studies have been somewhat lacking in this regard.

Literature Cited

1. Lambertson, C. J., "Medical Physiology," Chs. 38, 39, 40, V. B. Montcastle, Ed., C. V. Mosby, St. Louis, 1968.
2. Hornbein, T. F., "Physiology and Biophysics," Ch. 42, T. C. Ruch and H. D. Patton, Eds., Saunders, Philadelphia, 1965.
3. Sorensen, S. C., *Acta Physiol. Scand.* (1971) Suppl. 361, 1.
4. Mitchell, R. A., "Advances in Respiratory Physiology," pp. 1–47, C. G. Caro, Ed., Williams and Wilkins, Baltimore, 1966.
5. Leusen, I., *Physiol. Rev.* (1972) **52** (1), 1.
6. Horgan, J. D., Lange, R. L., *IEEE Trans. Bio-Med. Eng.* (1968) **BME-15,** 119.
7. Yamamoto, W. S., Raub, W. F., *Comp. Biomed. Res.* (1970) **1,** 65.
8. Cherniak, N. S., Longobardo, G. S., *Physiol. Rev.* (1970) **50,** 196.
9. Pflüger, E., *Pflüger Arch. Ges. Physiol.* (1868) 61.
10. Walter, F., *Arch. Exp. Pathol. Pharmakol.* (1877) **7,** 148.
11. Haldane, J., Smith, J. L., *J. Path. Bact.* (1892) **1,** 168.
12. Winterstein, H., *Pflüger Arch. Ges. Physiol.* (1911) **138,** 167.
13. Winterstein, H., Gokhan, N., *Pflüger Arch. Ges. Physiol.* (1952) **254,** 85.
14. Winterstein, H., *New England J. Med.* (1956) **255,** 216; *idem,* 272; *idem,* 331.
15. De Castro, F., *Trab. Inst. Cajal. Invest. Biol.* (1926) **24,** 365.
16. Heymans, J. F., Heymans, C., *Arch. Int. Pharmacodyn.* (1927) **33,** 272.
17. Heymans, C., Bouckaert, J. J., Dantrebande, L., *Arch. Int. Pharmacodyn.* (1930) **39,** 400.
18. Comroe, J. H., *Amer. J. Physiol.* (1939) **127,** 176.
19. Gray, B. A., *Resp. Physiol.* (1968) **4,** 229.
20. Leusen, I., *Amer. J. Physiol.* (1954) **176,** 39; *idem,* 45.
21. Loeschcke, H. H., Koepchen, H. P., Gertz, K. H., *Pflüger Arch. Ges Physiol.* (1958) **266,** 569.
22. Loeschcke, H. H., Koepchen, H. P., *Pflüuger Arch. Ges. Physiol.* (1958) **266,** 587; *idem,* 611; *idem,* 628.
23. Mitchell, R. A., Loeschcke, H. H., Massion, W., Severinghaus, J. W., *J. Appl. Physiol.* (1963) **18,** 523.
24. Pappenheimer, J. R., Fencl, V., Heisley, S. R., Held, D., *Amer. J. Physiol.* (1965) **208,** 436.
25. Comroe, J. H., "Physiology of Respiration," Ch. 3, Year Book Medical Publishers, Chicago, 1965.
26. Priban, I. P., "Encyclopedia of Linguistics—Information and Control," pp. 213–217, A. R. Meetham, Ed., Pergamon Press, New York, 1969.
27. Gray, J. S., *Science* (1946) **103,** 739.
28. Grodins, F. S., Gray, J. S., Schroeder, K. R., Norins, A. L., Jones, R. W., *J. Appl. Physiol.* (1954) **7,** 283.
29. Defares, J. G., Derksen, H. E., Duyff, J. W., *Acta Physiol. Pharmacol. Neerlandria* (1960) **9,** 327.
30. Grodins, F. S., James, G., *Ann. N.Y. Acad. Sci.* (1963) **109,** 852.
31. Dejours, P., "Handbook of Physiology, Section 3: Respiration," Vol. 1, pp. 631–648, American Physiological Society, Washington, D.C., 1964.
32. Horgan, J. D., Lange, R. L., *IRE Trans. Biomedical Electronics* (1962) **BME-9,** 221.
33. Hetch, H. H., Lange, R. L., *J. Clin. Invest.* (1962) **41,** 42.
34. Douglas, C. G., Haldane, J. S., *J. Physiol. Lond.* (1909) **38,** 401.

35. Horgan, J. D., Lange, R. L., *IEEE Int. Conv. Rec.* (1963) **II** (9), 149.
36. Horgan, J. D., Lange, R. L., *Biophys. J.* (1965) **5**, 935.
37. Clegg, B. R., "A Two Sensor, Lumped Parameter Model of Human Respiratory Regulation," Case Inst. of Techn. Report, Dec. (1963).
38. Lloyd, B. B., Cunningham, D. J. C., "The Regulation of Human Respiration," pp. 332–349, B. B. Lloyd and D. J. C. Cunningham, Eds., Davis, Philadelphia, 1963.
39. Milhorn, H. T., Jr., Brown, D. R., *Comput. Biomed. Res.* (1971) **3**, 607.
40. Milhorn, H. T., Jr., Guyton, A. C., *J. Appl. Physiol.* (1965) **20**, 328.
41. Milhorn, H. T., Jr., Benton, R., Ross, R., Guyton, A. C., *Biophys. J.* (1965) **19**, 503.
42. Milhorn, H. T., Jr., Reynolds, W. J., 24th Annual Conf. of Eng. in Med. of Biol., Las Vegas (1971) p. 30.
43. Longobardo, G. S., Cherniak, N. S., Fishman, A. P., *J. Appl. Physiol.* (1966) **21** (6), 1839.
44. Mitchell, R. A., Bainton, C. R., Edelist, G., *J. Appl. Physiol.* (1966) **21**, 1363.
45. Nielsen, M., Smith, H., *Acta Physiol. Scand.* (1951) **24**, 293.
46. Grodins, F. S., Buell, J., Bart, J., *J. Appl. Physiol.* (1967) **22**, 260.
47. Lambertson, C. J., "The Regulation of Human Respiration," pp. 257–276, B. B. Lloyd and D. J. C. Cunningham, Eds., Davis, Philadelphia, 1963.
48. Matthews, C. M. E., Laszlo, G., Campbell, E. J. M., Read, D. J. C., *Resp. Phys.* (1968/69) **6**, 45.
49. Duffin, J., 24th Annual Conf. of Eng. in Med. and Biol., Las Vegas (1971) p. 26.
50. Priban, I. P., *Nature (London)* (1965) **208**, 339.
51. Priban, I. P., "Breathlessness," pp. 115–122, J. B. Howell and E. J. M. Campbell, Eds., Blackwell, Oxford, 1965.
52. Priban, I. P., Fincham, W. F., "Theory of Self Adaptive Control Systems," pp. 57–63, P. H. Hammond, Ed., Plenum Press, New York, 1966.
53. Priban, I. P., "Encyclopedia of Linguistics—Information and Control," pp. 132–136, A. R. Meelham, Ed., Pergamon Press, 1969.
54. Defares, J. G., "Handbook of Physiology (Respiration I)," Ch. 26, American Physiological Society, Washington, D.C., 1964.
55. Stoll, P. J., *J. Appl. Physiol.* (1969) **27**, 389.
56. Bekey, G. A., *Simulation* (1970) **15**, 151.

RECEIVED November 22, 1971.

14

Studies of Cerebral Tissue Oxygenation and Related Autoregulation

DUANE F. BRULEY, Department of Chemical Engineering, Clemson University, Clemson, S. C. 29631

DANIEL D. RENEAU, Department of Chemical Engineering, Louisiana Tech University, Ruston, La. 71207

HIAM I. BICHER and MELVIN H. KNISELY, Department of Anatomy, Medical University of South Carolina, Charleston, S. C. 29401

The Krogh capillary-tissue cylinder arrangement has been modeled and solved to include interaction between the capillary and tissue. Sophisticated, distributed, and simple lumped parameter equations have been used to describe the system. Solutions have been investigated using digital, analog, and hybrid computer techniques. Results from the simulations have been compared with experimental tissue response data obtained with oxygen microelectrodes inserted in the brain of anesthetized, curarized cats. Comparisons indicate that autoregulatory mechanisms play an important role in determining the characteristic tissue oxygen tension response to arteriole oxygen tension upsets. Response curves also suggest the possibility of facilitated or active transport of oxygen in tissue and resistance to the back diffusion of oxygen from the tissue into the blood stream.

A vast amount of work is being done to describe quantitatively the transport of anabolites and metabolites in the microcirculation of the brain. The classical geometry for the capillaries and tissue has been the Krogh capillary-tissue cylinder. Recent investigations have considered other geometrical configurations to determine if other models derived for multicapillary systems are more descriptive than the single capillary structure used here.

Metzger (*1*) developed a capillary network model which allowed inhomogeneous blood flow and analyzed the inhomogeneous flow capillary

network system as well as homogeneous concurrent and countercurrent flow systems by calculating tissue oxygen histograms for normoxia and arterial hypoxia. Grunewald and Lubbers (*2*) compared asymmetric, concurrent, and countercurrent capillary flow models. Hutten, Thews, and Vaupel (*3*) modeled an array of capillaries and tissue with a transistor and resistor analog computer from which results were calculated for various capillary configurations. No conclusive evidence has established one configuration as more correct than the others.

Mathematical calculations (*4*, *5*, *6*), predicting rates of cerebral tissue oxygenation and deoxygenation with convection–diffusion models developed for Krogh capillary-tissue anatomical units (*7*), do not agree exactly with recently obtained experimental results using oxygen microelectrodes in brain tissue of living cats (*8*) (Table I). However, the theoretical calculations have been made using geometric, chemical, and physical parameters obtained for human brain (*9*, *10*), whereas the experimental results relate to cat brain. Therefore, correlations can be made only by comparing trends, and a true quantitative study cannot be done until microelectrodes are used in human brain with precise positioning.

Table I. Normal Values of Parameters and Variables for the Krogh Capillary–Tissue Cylinder

A	=	0.83×10^{-3} (cm^3O_2/cm^3 tissue − sec)
C	=	0.342×10^{-4} (cm^3O_2/cm^3 blood − mm Hg)
N	=	0.204 (cm^3O_2 sat./cm^3 blood)
Q	=	0.785×10^{-8} (cm^3/sec)
V_T	=	50.515×10^{-8} (cm^3)
V_c	=	0.353×10^{-8} (cm^3)
P_{c_1}	=	95 (mm Hg)
Pc	=	39 (mm Hg)
Ka	=	6×10^{-11} (cm^3O_2/sec − mm Hg)
n	=	2.20
k	=	0.001

Initial studies calculated response characteristics by solving a distributed parameter model consisting of a set of nonlinear, interacting, second-order partial differential equations.

The equation describing oxygen transport in the capillary is:

$$\frac{\partial P}{\partial t} = \frac{D_1}{\left[1 + \frac{N}{C_1}\frac{d\psi}{dP}\right]}\left[\frac{\partial^2 P}{\partial r^2} + \frac{1}{r}\frac{\partial P}{\partial r} + \frac{\partial^2 P}{\partial z^2}\right] - v\frac{\partial P}{\partial z} \quad (1)$$

At the interface the following two equations apply:

$$P_i \Big|_{\text{capillary}} = P_i \Big|_{\text{tissue}} \tag{2}$$

$$D_1 c_1 \frac{\partial P}{\partial r} \Big|_{\text{capillary}} = D_2 c_2 \frac{\partial P}{\partial r} \Big|_{\text{tissue}} \tag{3}$$

The following equation is derived for oxygen transport and consumption in the tissue cylinder:

$$\frac{\partial P}{\partial t} = D_2 \left[\frac{\partial^2 P}{\partial r^2} + \frac{1}{r} \frac{\partial P}{\partial r} + \frac{\partial^2 P}{\partial z^2} \right] - \frac{A}{c_2} \tag{4}$$

These equations must be solved simultaneously with the following boundary conditions:

$$\frac{\partial P}{\partial r} = 0, r = 0, 0 \leq z \leq L, t \geq 0$$

$$\frac{\partial P}{\partial r} = 0, r = R_2, 0 \leq z \leq L, t \geq 0$$

$$\frac{\partial P}{\partial z} = 0, z = L, 0 \leq r \leq R_2, t \geq 0$$

$$\frac{\partial P}{\partial z} = 0, z = 0, R, \leq r \leq R_2, t \geq 0$$

$$P = P(r), z = 0, 0 \leq r \leq R_1, t \geq 0$$

$$P = P(r, z), 0 \leq z \leq L, 0 \leq r \leq R_2, t = 0$$

Numerical alternating direction techniques required 10 hours of computation time on the IBM-7094 to achieve solutions with 80% convergence to the true steady state (*4*). Computation time was reduced to about 30 min per solution for triple the model time length, using Monte Carlo methods (*5*) to solve the deterministic model on an IBM-360 model 40 (the 7094 is about 10 times faster than the model 40). A digital computer solution of a three-component model (O_2, CO_2, and glucose) (*11*) and a hybrid computer simulation using the Monte Carlo technique (*12*) have recently been completed without significantly increasing computing speed.

Considering the need for multiple problem solutions for case studies involving autoregulatory effects as well as parameter sensitivity studies and the analysis of pathological phenomena, we decided to simplify the mathematics by using lumped-distributed parameter approximations.

The lumped models correlate well qualitatively with the more sophisticated distributed models dynamically and achieve essentially the same values for venous oxygen tension at steady state after upsets. However, the lumped parameter approximations of the distributed system result in space-averaged oxygen tensions for the total system rather than determining point values as is achieved with the distributed parameter models. For studies involving the prediction of point values, such as the dynamics of oxygen supply to neurons located at the lethal corner during circulatory failure (*6*), it is necessary to use the distributed model. In the present study, however, we wish to determine the system transient behavior with the major interest focused on autoregulatory mechanisms and their influence on oxygen tension response in brain tissue. Therefore, a qualitative evaluation of performance can be obtained satisfactorily with the lumped parameter approximations in reasonable computation time. This approach seems plausible since the comparison of experimentally determined cat brain responses with theoretical calculations using human brain parameters limits the analysis to a qualitative study anyway.

The models were examined using analog and hybrid computers. Pure analog computation required variable diode function generators to produce the nonlinear functions representing the oxygen dissociation curve (*4, 13*) flow rate as a function of arterial or venous oxygen tension (*9*) and oxygen consumption rate as a function of a tissue oxygen tension (*8*). To accomplish the vast amount of nonlinear function generation, it was necessary to use a hybrid computer. Hybrid computation allowed almost unlimited nonlinear function generation on the digital computer while integrating on the analog computer. This capability made it practical to look at multiple lump models as well as single lump systems, thus giving a better approximation to point values of oxygen tension.

With the use of oxygen microelectrodes, experiments have been conducted measuring tissue and blood pO_2 in anesthetized, curarized cats under positive pressure breathing (*8, 14*). To create disturbances in the arterial blood, a step change in the oxygen level of the inspired gas was forced by switching from normal air (20% O_2) to pure nitrogen. This resulted in a continuously varying oxygen tension in the arterial blood after passing through the lung and the blood stream to the brain. The actual forcing function occurring at the brain capillary is a filtered rectangular pulse, displaced in time because of pure transport delay.

Oxygen deficiency of the arterial blood leads to tissue anoxia; however, compensatory autoregulatory mechanisms appear to postpone this condition for a period longer than if pure diffusion and convection were allowed to operate normally. The experimental strip chart recordings revealed that there is a possibility of at least two major autoregulatory

actions that function when low oxygen tensions are encountered. First, flow changes occur (*15, 16, 17, 18*), and then the tissue oxygen consumption rate seems to have a Michaelis–Menten behavior (*19, 20*).

Flow rate *vs.* arterial oxygen pressure data (*9*) are available for steady-state conditions only; however, when considering transient changes, flow dynamics must also be included to describe accurately the system response. Tissue oxygen consumption rate changes, related to tissue oxygenation levels, are incorporated because of experimental evidence showing a change in neuron activity as the tissue oxygen tension changes (*8*).

Models have been developed that consider these influences and examine feedforward and feedback autoregulatory action to simulate the transient responses of brain tissue to oxygen tension upsets. Controller dynamics are being proposed that give essentially the same responses as those obtained from *in vivo* cat experiments.

Theoretical

A model has been devised to simulate the dynamic functional relationship between oxygen levels of gas entering the lungs and the cerebral cortex tissue oxygen tension response. The developemnt and simulation of the model provides a convenient, practical way to gain insight about important physiological phenomena such as the transport of anabolites and metabolites in the capillary-tissue system and the influence of superimposed autoregulatory action. The model includes a lump for the lung, a transport delay element for the time needed to flow from the lung to the brain, and a process model for the capillary-tissue system.

Process Model. To simplify computational problems and to allow simultaneous examination of physiological control phenomena, it was necessary to approximate the actual distributed parameter capillary-tissue system with lumped parameter models.

A general model that considers nonequilibrium oxygen tension conditions between the erythrocytes and plasma has been derived. The rate of oxygen transport between the erythrocyte and plasma is assumed to be a function of the difference between the equilibrium and dynamic oxygen dissociation curves, and the rate of oxygen transfer to the tissue is based on the oxygen tension difference between the plasma and tissue. The three-lump model can be written as follows,

Erythrocyte

$$V_c N \frac{d\psi_c}{dt} = NQ\psi_1 - NQ\psi_c \pm G$$

Erythrocyte-plasma rate equation

$$G = K_E (\psi_E - \psi_c)$$

Plasma

$$bV_cC \frac{dP_c}{dt} = bQCP_1 - bQCP_c \pm G - R$$

Plasma-tissue rate equation

$$R = Ka (P_c - P_T)$$

Tissue

$$V_TC \frac{dP_T}{dt} = R - AV_T$$

By assuming that equilibrium exists between the erythrocytes and plasma, the three-lump model is reduced to two lumps. The system equations for the tissue lump-capillary lump model are developed by writing oxygen material balances for the tissue and capillary separately or by summing the erythrocyte and plasma equations for the three-lump model. The two-lump model (*21*) has been used in this investigation and can be represented by the following set of equations (Figure 1).

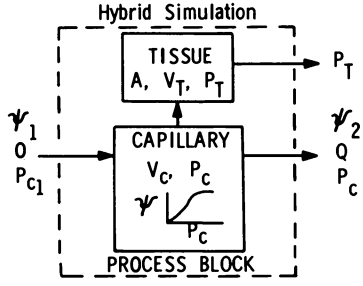

Figure 1. Tissue lump–capillary lump Krogh cylinder model

Capillary equation

$$-\left(\frac{N}{C}\right)\left(\frac{d\psi_c}{dt}\right) - \frac{dP_c}{dt} = \left(\frac{1}{V_c}\right) Q (P_c - P_{c1}) - \left(\frac{N}{V_cC}\right) Q (\psi_1 - \psi_2) + \left(\frac{R}{V_cC}\right) \quad (6)$$

$$\psi = \frac{kP^n}{1 + kP^n} \quad (\textit{see} \text{ Ref. 13})$$

and

$$\frac{d\psi_c}{dt} = \frac{\partial \psi_c}{\partial P_c} \frac{\partial P_c}{\partial t} = \frac{knP_c^{n-1}}{(1 + kP_c^n)^2} \frac{\partial P_c}{\partial t}$$

Interface equation

$$R = Ka\ (P_c - P_T) \tag{7}$$

Tissue equation

$$-\left(\frac{dP_T}{dt}\right) = -\left(\frac{R}{V_T C}\right) + \left(\frac{A}{C}\right) \tag{8}$$

The two-lump model was scaled using machine unit scaling and programmed on the hybrid computer. The most significant advantage of the tissue lump–capillary lump model over a single lump model is the possibility of observing tissue response characteristics separate from the blood response.

Autoregulatory Action

Because of discrepancies between experimental tests and predicted tissue oxygen response by convection–diffusion models, the influence of physiological control mechanisms was considered. It is proposed that a minimum of two autoregulatory actions (at least conceptually) are functional in helping prevent neuron damage when low blood oxygen tensions are encountered.

First, blood flow rate is regulated to achieve optimal tissue oxygenation. The exact mechanism and resulting flow rate changes as a function of oxygen tension are unknown; however, by carefully analyzing the experimental determinations, it is possible to postulate controlled dynamics along with the known steady-state flow rate as a function of oxygen pressure (*9*).

There is some dispute over exactly where oxygen tension measurements are made. Is the sensing done in the arteriolar blood, the venous blood, the tissue itself, or somewhere else in the complex physiological structure? Depending upon the location of sensing, the mechanism can be thought of in terms of feedforward or feedback control.

The second action that prevents neuron damage and which could be considered, at least conceptually, as feedback control is oxygen consumption rate. Even though the brain normally operates at a constant consumption rate, recent experimental results (*8*) indicate that the rate decreases when the tissue oxygen tension drops.

Flow rate and oxygen consumption changes have been superimposed on the capillary-tissue process block as automatic feedback and feedforward control loops (*see* Figure 2).

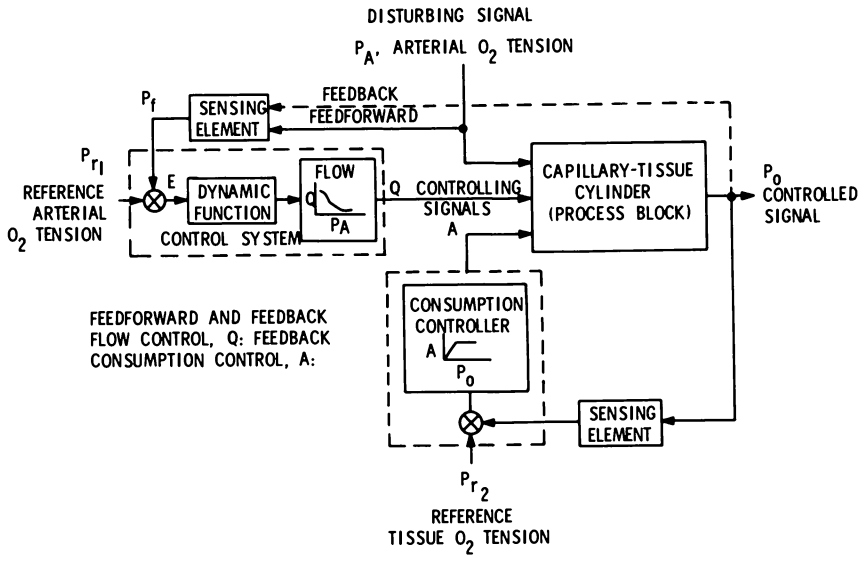

Figure 2. Lumped capillary–tissue cylinder with autoregulation

Discussion

As explained above, the comparison of experimental tissue response curves with theoretical predictions is purely qualitative at this stage of the research. The major considerations when examining Figure 3 are to observe the plateau at low oxygen tensions and the overshoot when oxygen tension is returning to normal in the tissue. These two characteristics initiated the proposal that autoregulatory action plays an important role in the *in vivo* experiments and that to predict the system behavior for living animals mathematically, it would be necessary to examine feedback and feedforward control loop dynamics. The experimental curve in Figure 3 is just one example of a response curve and should not be considered as a standard. Actually overshoot amplitudes covered an entire spectrum, from small magnitudes to very large as in Figure 3. No effort was made to obtain precise representations with the mathematical simulations since the fit would be fictitious (this could be accomplished by simply adjusting the system control parameters to give a close approximation to the experimental curve). The simulation has been used as a tool to demonstrate that plateau and overshoot characteristics, which could not be generated with a conventional convection–diffusion mathematical model considering constant flow and oxygen consumption, could be obtained with superimposed flow and oxygen consumption regulation.

The tissue lump–capillary lump approximation allows the tissue lump response to be investigated separately from the blood response. The

model contains blood–tissue interaction through the mass transfer rate expression. The mass transfer factor, *Ka*, was determined by trial and error until the outlet blood oxygen tension was normal at 39.0 mm Hg (space averaged) for normal blood tension input of 95 mm Hg. For this work *Ka* was assumed constant at that value even though it could vary when conditions deviate from normal.

The oxygen consumption rate as a function of tissue tension is considered to have a Michaelis–Menten form. [It has been shown (*8*) that neuron activity increases to a much higher rate as tissue oxygen tension decreases (injury potential) and then it drops off to essentially zero. This would indicate that a true Michaelis–Menten form would not be followed.] A zero-order reaction is assumed for high tissue tension; a first-order reaction is then imposed when the tension drops to a prescribed value, and then the consumption rate is set equal to zero at a second prescribed tissue tension (*i.e.*, $P_T > 30$ mm Hg, zero-order reaction, $20 < P_T < 30$ mm Hg, first-order reaction, and $P_T < 20$, zero consumption). When the consumption rate goes to zero, the model restricts oxygen transport in the reverse direction (tissue to blood) even if the blood tension drops below the tissue tension. This assumption was included to achieve a flat plateau like the experimental results; however, it is still open to speculation. Back diffusion can be considered in the model by simply removing a diode from the computer circuit. (This assumes a barrier to tissue washout.)

Conceptually, the oxygen consumption rate change can be superimposed as a negative feedback control loop in the total system block diagram (*see* Figure 2). The results of this control can be seen in Figure 3 by the plateau in the tissue tension curve as compared with the blood tension curve. The blood tension continues to drop even after consumption goes to zero because of capillary washout. A smooth curve results even when step changes of oxygen are forced because the lung was assumed to be a fifth-order filter with a 5-sec time constant.

The experimental curve in Figure 3 demonstrates overshoot in the tissue oxygen response. It was determined previously (*22*) that a term representing pure delay along with the steady-state blood flow *vs.* arterial oxygen tension data would cause overshoot. In this investigation it was found that a first-order time constant delay would also produce overshoot. Therefore, since exact controller mechanisms are not being postulated, the flow controlled dynamics used in this study include pure delay and time constant lag. To consider the problem of sensor location, feedback and feedforward control loops were superimposed on the capillary-tissue model.

With the disturbance function entering the system in the arterial blood and with known steady-state flow characteristics as a function of

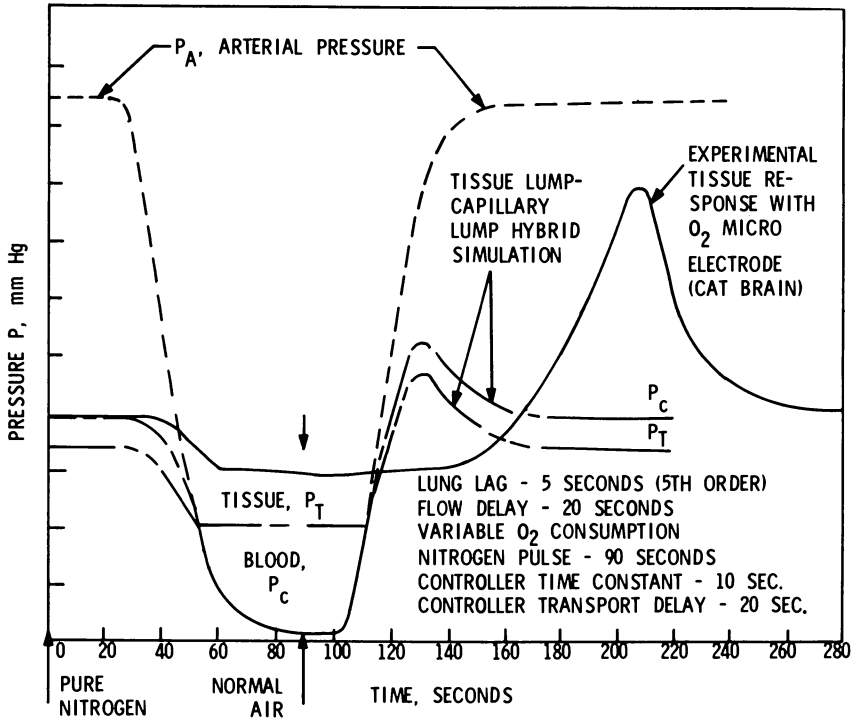

Figure 3. Krogh cylinder dynamics to step change in inspired air

arterial blood oxygen tension, the sensor was assumed located at the arterial end of the capillary, thus resulting in a feedforward control scheme. If the sensor is located at the venous end of the capillary, then the control configuration would be feedback control. To obtain steady-state flow *vs.* oxygen tension data to use with the feedback scheme (available experimental data being for Q *vs.* P_A only), the system was forced with the Q *vs.* P_A relationship and a plot of Q *vs.* Po backed out of the computer simulation.

It is possible that convection and diffusion contribute to the lags and delays that are apparently present in the regulation of flow. The sensor position would play an important role in the flow dynamics and more elaborate studies will have to be carried out to understand fully this physiological phenomenon.

Strangely enough, the flow rate delays and lags contribute to a more optimal operation when considering tissue oxygen tension. If flow rate increased as soon as low tension blood was sensed, then the system would be washed out more quickly and anoxic areas would form more rapidly. The same is true for decreasing flow rate when oxygen-rich blood is sensed after low tension blood has been flowing. The lags and delays

allow the blood to flow rapidly through the capillary-tissue system until it is filled with oxygen-rich blood, and then control reduces to the normal flow rate.

Figure 3 demonstrates the simulated tissue overshoot with a pure delay of 20 sec and time constant lag of 10 sec. Manipulation of the two variables yields overshoot peaks of various amplitudes and shapes.

The experimental response curves demonstrate a constant tissue tension for as long as 60 sec after a drop in arteriole tension occurs (*14*). When tissue tension begins to drop, the recordings show that flow rate increases. This characteristic response has not been explained at this time; however, it indicates that facilitated or active transport of oxygen in tissue might be present. Carefully planned experiments could elucidate this phenomenon.

Conclusions

Autoregulatory action helps to reduce nerve cell destruction resulting from brain tissue anoxia. Two possible mechanisms include flow controller dynamics in the form of pure delays and time constant lags and oxygen consumption control with Michaelis–Menten behavior. Response curves also suggest the possibility of facilitated or active transport of oxygen in tissue and resistance to the diffusion of oxygen from the tissue into the blood stream.

Nomenclature

Symbols

P = Pressure, mm Hg
t = Time, sec
D = Diffusivity, cm^2/sec
N = Oxygen capacity, cm^3O_2 sat./cm^3 blood
C = Solubility, cm^3O_2/cm^3 blood-mm Hg
ψ = Fractional saturation of erythrocytes
r = Radius, cm
z = Axial length, cm
v = Local velocity, cm/sec
A = Oxygen consumption rate, cm^3O_2/cm^3 tissue-sec
L = Total capillary length, cm
V = Volume, cm^3
Q = Flow rate, cm^3/sec
G = Mass transfer rate erythrocyte to plasma, cm^3O_2/sec
K = Mass transfer coefficient, $cm^3O_2/sec\text{-}cm^2$
b = Fractional volume of plasma in blood
R = Mass transfer rate plasma to tissue, cm^3O_2/sec
a = Area for mass transfer, cm^2
n = Constant dependent upon pH, dimensionless
k = Constant dependent upon pH, dimensionless

Subscripts

- i = Interface
- 1 = Capillary system or arterial input
- 2 = Tissue system or venous output
- c = Capillary
- E = Erythrocyte
- T = Tissue

Literature Cited

1. Metzger, H., PO_2 Histograms of Three-Dimensional Systems with Homogeneous and Inhomogeneous Microcirculation, a Digital Computer Study, Oxygen Transport in Tissue Workshop, Dortmund, Germany, July 1971.
2. Grunewald, W., Lubbers, K., Method for Comparison of Calculated and Measured Oxygen Distribution, Oxygen Transport in Tissue Workshop, Dortmund, Germany, July 1971.
3. Hutten, H., Thews, G., Vaapel, P., Some Special Problems Concerning the Oxygen Supply to Tissue, as Studied by an Analogue Computer, Oxygen Transport in Tissue Workshop, Dortmund, Germany, July 1971.
4. Reneau, D. D., Bruley, D. F., Knisely, M. H., *A.I.Ch.E. J.* (1969) **15**, 916.
5. Halberg, M. R., Bruley, D. F., Knisely, M. H., *Simulation* (1970) **15**, 205.
6. Bruley, D. F., Bicher, H. I., Reneau, D. D., Knisely, M. H., Dynamics of Tissue Oxygen Supply During Circulatory Failure—A Mathematical Analysis Using Monte Carlo Techniques, 6th European Conference Microcirculation, Aalborg, 1970, Karger, Basel, 1971.
7. Krogh, August, *J. Physiol.* (1918–1919) **52**, 409.
8. Bicher, H. I., Reneau, D. D., Bruley, D. F., Knisely, M. H., Effect of Intravascular Red Cell Aggregation and Its Counteraction by Anti Adhesive Drugs on Brain Tissue Oxygenation, 6th European Conference on Microcirculation, Aalborg, 1970, Karger, Basel, 1971.
9. Optiz, Erich, Schneider, Max, *Ergeb. Physiol., Biolog. Chem. Exper. Pharma.* (1950) **46**, 126.
10. Thews, Gerhard, *Pflügers Archiv.* (1960) **271**, 197.
11. McCracken, T. A., Bruley, D. F., Knisely, M. H., A Systems Analysis for the Transport of Oxygen and the Simultaneous Transport of Oxygen, Carbon Dioxide, and Glucose in the Capillaries and Tissue of the Human Brain, Report, Chemical Engineering Department, Clemson University, Clemson, S. C.
12. Hunt, D. H., Bruley, D. F., Knisely, M. H., Oxygen Transport in the Microcirculation Using Monte Carlo Techniques on the Hybrid Computer, Report, Chemical Engineering Department, Clemson University, Clemson, S. C.
13. Roughton, F. J. W., In "Oxygen," pp. 105–126, proceedings of a symposium sponsored by the New York Heart Association. Little, Brown, Boston, 1965.
14. Bicher, H. I., Bruley, D. F., Knisely, M. H., Reneau, D. D., *J. Physiol.* (in press).
15. Kety, S. S., In "Handbook of Physiology, Neurophysiology III," pp. 1751–1760, W. F. Hamilton and P. Dow, Eds., Williams and Wilkins, Baltimore, 1960.
16. Kety, S. S., Schmidt, C. F., *J. Clin. Invest.* (1948) **27**, 484.
17. Schmidt, C. F., In "Handbook of Physiology, Neurophysiology III," pp. 1745–1750, W. F. Hamilton and P. Dow, Eds., Williams and Wilkins, Baltimore, 1960.
18. Sokoloff, L., Kety, S. S., *Physiol. Rev.* (1960) **40**, 38.

19. Gonzolez-Fermandez, Jose M., Atta, Suzie E., *Math. Biosci.* (1968) **2**, 225.
20. Blum, J. J., *Amer. J. Physiol.* (1960) **198**, 991.
21. Bruley, D. F., Bicher, H. I., Reneau, D. D., Knisely, M. H., Chem. Engineering Progress Symposium Series, Advances in Bioengineering, Vol. 67, pp. 195–201 (1971).
22. Reneau, D. D., Bicher, H. I., Bruley, D. F., Knisely, M. H., In "Blood Oxygenation," pp. 175–200, Plenum Press, New York, 1970.

RECEIVED November 22, 1971. This work was supported by USPHS grants NB-06957, HE-04176, and NB 08228.

A New Method for Measuring Blood Gas Partial Pressures and Contents

DAVID KAVNER

Bio-Environmental Engineering Division, Rensselaer Polytechnic Institute, Troy, N. Y.

STEVEN F. DIZIO

Aero Vac Corp., Troy, N. Y.

SAMUEL R. POWERS, JR.

Albany Medical Center, Albany, N. Y.

A blood gas analyzer for the determination of partial pressures, contents, and the O_2 dissociation curve was constructed and tested. A membrane permeation cell was connected to the input of a mass spectrometer. During injection of the blood sample, the output of the analyzer was a function of the partial pressures. When injection ceased, gases were depleted from the blood sample. The area of the depletion curve was proportional to the original amount of gas in the sample. Any point on the depletion curve for O_2 in blood could be transformed to a point on the O_2 dissociation curve.

Blood gas analysis plays an important role in pulmonary research and clinical medicine. Knowledge of the blood gas partial pressures and contents is generally considered necessary for a complete description of the adequacy of pulmonary function and the transport characteristics of the blood.

Recently, evidence has accumulated that indicates that the position of the O_2 dissociation curve is subject to a physiological control mechanism involving an organic phosphate, 2,3-diphosphoglycerate (2,3-DPG). The concentration of this intermediate metabolite correlates with hypoxic conditions caused by lung function impairment and high altitude environ-

ments (*1*, *2*). The demonstrated shift of the O_2 dissociation curve to the right with increasing 2,3-DPG levels facilitates the release of the blood oxygen to the body tissues (*3*). Because of the physiological importance of this effect and its potential clinical manipulation, it can be expected that measurement of the O_2 dissociation curve in patients will be added to the burden of the hospital laboratory.

At present researchers and clinicians interested in complete blood gas analysis must resort to different sets of instruments and techniques for each of the three types of measurement. This chapter describes a membrane permeation cell connected to a mass spectrometer that can measure blood gas partial pressures, contents, and the position of the O_2 dissociation curve.

Previous Work

Partial Pressure Measurements. The measurement of the partial pressures of O_2 and CO_2 in blood has been facilitated by electrode techniques, introduced within the past few decades. The original Clark O_2 electrode (*4*) has undergone many improvements in design. The first electrodes had cathodes that consumed relatively large amounts of O_2, leading to discrepancies between readings in fluids and gases (*5*). The development of the microelectrode has done much to reduce the magnitude of this effect (*6*, *7*, *8*, *9*). An *in vivo* O_2 microelectrode has been described (*10*) though Schuler and Kreuzer (*11*) have shown theoretically that a residual flow dependence will always remain.

The CO_2 electrode as first described by Stow and Randall (*12*) is basically a pH electrode covered with a membrane. A bicarbonate solution reacts with the CO_2 permeating the membrane, giving a pH change that can be related to the P_{CO_2} with the Henderson–Hasselbalch equation (*13*). Because this measurement is based on a potentiometric technique, in which gas (CO_2) consumption does not play a role, no gas–fluid variations are observed.

The application of the mass spectrometer to blood gas analysis was demonstrated by Woldring *et al.* (*14*). They connected an *in vivo* catheter to the analyzing section of a mass spectrometer for continuous measurements of blood P_{O_2} and P_{CO_2}. Recently, Woldring (*15*) described a detailed and rigorous theoretical analysis of the design of the mass spectrometer *in vivo* blood gas analyzer. He showed that with highly permeable membranes, such as silicone rubber, the effective stirring rate must be great to reduce the boundary layer effects to a minimum. This effect was experimentally studied by Brantigan *et al.* (*16*). They emphasized the importance of heparinizing the catheter by the method of Grode *et al.* (*17*) to achieve satisfactory results.

Gas Content Measurements. The generally accepted standard procedure to determine O_2 and CO_2 in blood is the Van Slyke gasometric technique (*18*). This apparatus was modified by Roughton and Scholander (*19*) for use with blood samples in the microliter range. The principal drawbacks to the gasometric method center on the many steps required to complete an analysis. They are time-consuming, tedious procedures, needing a skilled operator to achieve optimum accuracy (*20*).

Spectrophotometers or oximeters are frequently used to determine the O_2 saturation in blood. These measurements are based on the light absorbing (*21*) or reflecting (*22*) properties of the hemoglobin molecule. An *in vivo* device has been described (*23*) that uses light-emitting diodes.

By chemically releasing the bound O_2 in a closed chamber, the initial content was proportional to the final partial pressure as measured with an O_2 electrode (*24*). This technique has been miniaturized to analyze blood samples down to 5 μl in volume (*25*, *26*). A continuous flow system based on this measurement was used to monitor continuously the O_2 content in dogs (*27*).

The gas chromatograph has been used to analyze the amount of gases in a sample of blood after they are chemically released (*28*). This method has the potential of measuring multiple gas species.

Dissociation Curve Analysis. Torrance and Lenfant (*29*) grouped the determination of the dissociation curve into three different methodologies. The first measures the O_2 content or saturation over a set of known p_{O_2}'s. The second approach measures the blood p_{O_2} using samples at known saturation. The most frequent determination is at the 50% saturation level described by Edwards and Martin (*30*).

Dynamic methods constitute the third category. Starting from desaturated blood, Duvelleroy *et al.* (*31*) measured the increasing p_{O_2} as O_2 was absorbed out of a closed gas phase. The partial pressure in the gas could be quantitatively related to the amount absorbed by the blood. Longmuir and Chow (*32*) further simplified this technique by generating O_2 by electrolysis, thereby reducing the need for the gas phase electrode.

Apparatus

Mass Spectrometer. The mass spectrometer used for this study was a Process Control Analyzer, Model 270, manufactured by the Aero Vac Corp. This residual gas analyzer is completely housed in a mobile cabinet and requires only electrical power for its operation.

There are several reviews in the literature on the theory and design of mass spectrometers (*33*, *34*). A brief description of the operation as it relates to the blood gas analysis cell is presented here.

At steady-state conditions, the rate of entry of molecules into the vacuum of the mass spectrometer, Q_v, determines the partial pressure P_{v_i}, according to the following relation,

$$P_{v_i} = \frac{Q_{v_i}}{S} \tag{1}$$

As the molecules pass by the ionization chamber, a fraction of them become positively charged by electron bombardment. These electrons are released from a heated filament and then accelerated across a constant 75-V potential. The electron current is kept constant at 0.8 mamp independent of the gas composition at the filament. The analyzer contains two filaments, so normal operation can be continued if one becomes inoperative. The production of positive ions is written as

$$P_i^+ = K_{I_i} P_{v_i} \tag{2}$$

The ionization constant, K_I, is assumed to be independent of the gas concentration, though it will vary with gas species. Other effects can occur during electron bombardment. These include dissociation and recombination phenomena along with the production of doubly charged ions.

The positive ions are drawn out of the ionization chamber and accelerated by an electrostatic field that can be varied from 75 to 450 V. These ions, collimated by a series of narrow slits, pass into the spectrometer tube. The rapidly moving positive ions pass through an orthogonal field of a permanent magnet where they are deflected according to the square root of the accelerating voltage times the mass/charge ratio.

Those ions that are deflected 60° pass through slits at the far end of the tube and impinge on a Faraday cup detector. The resulting current of about 10^{-12} to 10^{-9} amp is amplified by an electrometer providing an output of 0–10 mV over six input decades. The gas species that is to be monitored can be focused by varying the accelerating potential. This is done by manually switching to one of any four separate potentiometers located on the front panel of the mass spectrometer.

The output of the mass spectrometer, P_i^*, is proportional to the number of positive ions produced

$$P_i^* = K_{T_i} P_i^+ \tag{3}$$

K_{T_i} is a function of the ion beam dispersion, drawout potential (from the ion chamber), and amplifier gain. Equations 2 and 3 can be combined to obtain

$$P_i^* = (K_{I_i} K_{Ti}) P_{v_i} \tag{4}$$

This relates the output of the mass spectrometer to the partial pressure in the vacuum system. Using Equation 1, the important relation between the output and the input flow is obtained.

$$P_i^* = K_{Q_i} Q_{v_i} \tag{5}$$

where

$$K_{Q_i} = \frac{K_{I_i} K_{V_i}}{S} \tag{6}$$

Blood Gas Analysis Cell. The blood gases enter the mass spectrometer by permeation through a thin Teflon membrane enclosed in the blood gas cell (BGC). The design of the stirred BGC was determined by the following general requirements and constraints:

(1) adequate sensitivity,
(2) stability and accuracy of operation,
(3) minimal size of blood sample,
(4) separation of blood phase from the vacuum,
(5) limited boundary effects at the membrane–fluid interface, and
(6) simplicity of operation.

These conditions are often conflicting. Most noticeable is the attainment of the first requirement largely at the expense of the fifth. Yet this difficulty opened the way for a unique measurement of blood gas contents and the entire O_2 dissociation curve.

The diagram of the BGC shown in Figure 1 contains four main components. The cell is connected to a 3/4 inch steel tube protruding from the chamber of the mass spectrometer with mating Varian copper-gasketed flanges. The BGC is kept at a constant temperature of 37°C by enclosing the cell in a constant temperature bath. The water is recirculated and temperature controlled in an external circuit. Connecting tubes for fluid input and output and the stirring rod extension are fed to the cell through leak-tight fittings. Figure 2 gives two views of the BGC enclosed in the constant temperature bath.

The base of the BGC consists of a machined brass flange silver-soldered to a 2 3/4 inch od Varian flange. A threaded acrylic rim is epoxy cemented to the outside perimeter of the flange. This provides a way to attach the water bath shell. The brass face contains a 2-cm diameter well for insertion of the fritted glass. The medium porosity fritted disk, obtained from the Fisher Co., serves as a backing for the membrane. The disk was ground flat to the surface of the brass face. The outer rim of the brass flange is threaded to accept the retaining ring. The polymethyl methacrylic reservoir section defines the outer bounds of the fluid phase, furnishes a means of exciting the blood, and provides a mechanism to seal the membrane from air leaks. A groove machined

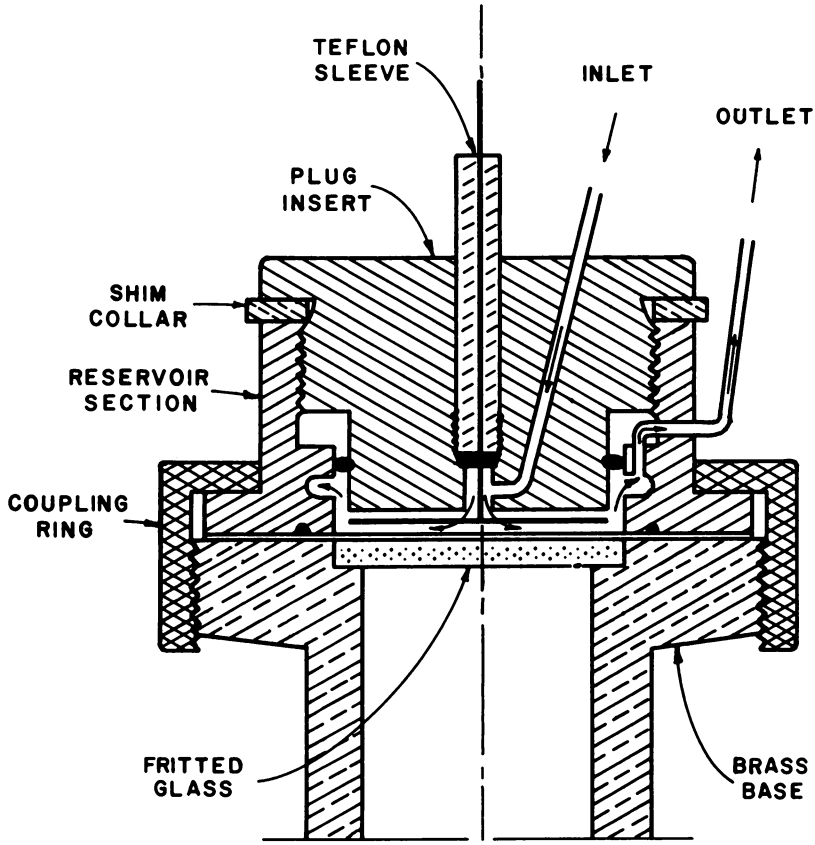

Figure 1. Blood gas analysis cell cross section (no scale)

in the inner surface of the reservoir collects the fluid that flows across the membrane. The fluid leaves the cell through an 18-gauge hypodermic needle cemented into this groove. A 1/8-inch wide, 1 1/16 inch od O-ring is fitted into a groove on the bottom face of the reservoir. When the coupling ring is tightly turned on the brass base, this O-ring squeezes against the membrane, creating a vacuum-tight seal.

The volume of fluid contained within the BGC is determined by the position of the plug insert in the reservoir section. The front surfaces of these two components are machined and polished so when they are fastened together a flat plane is achieved. By inserting a collar of brass shim stock between the edge of the reservoir and the flange extension of the plug, a gap of precisely that thickness is attained between the membrane and the plug face. This defines the thickness and volume of blood being analyzed in the BGC. The fluid phase thickness of 10 mils creates a volume of 80 μl in the 2-cm diameter reservoir.

The stirring apparatus is positioned in the well of the plug insert. The stirring rod is made from a 1 1/2 inch length of 21-gauge hypodermic tubing. The blades consist of two loops of 3-mil steel wire cemented to the lumen of the rod. These blades are bent perpendicular to the rod and extend to the side of the reservoir to ensure adequate mixing over the entire membrane area. A 1-inch Teflon sleeve is drilled along the center line with a No. 67 drill bit. The stirring rod fits snugly within the sleeve, yet can be easily rotated. A small piece of silicone rubber septum material is inserted in the bottom of the well. When the sleeve is squeezed against this rubber, no backflow is possible.

The fluid enters the cell through a 21-gauge steel hypodermic tube embedded off center in the plug insert. About 1/8 inch from the face of the plug, the tubing is bent toward the stirring rod. Fluid enters an annular space bound by the stirring rod on the inside and a No. 60 drilled hole on the outside. This relatively complex inlet system is designed to permit axial entry of fluid into the disk-shaped permeation region between the membrane and the plug face.

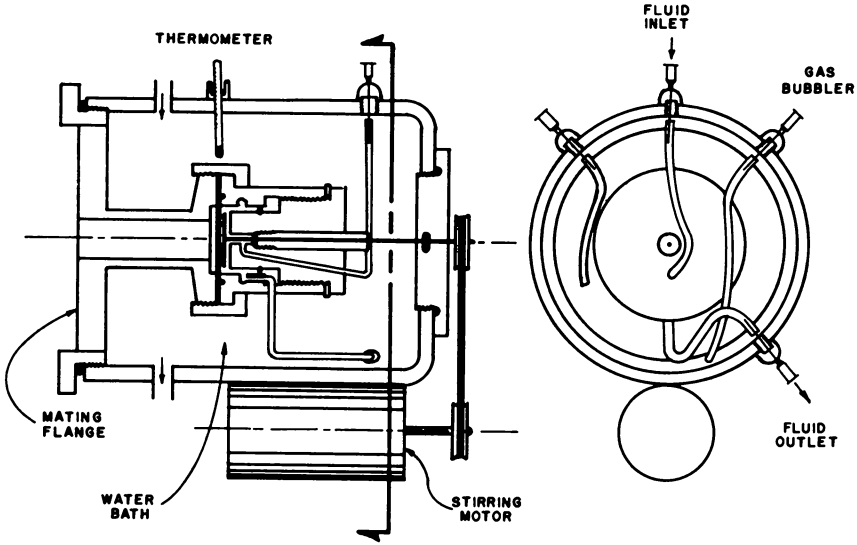

Figure 2. Diagram of BGC enclosed in water bath

The Membrane Inlet

Gas molecules must enter the mass spectrometer by permeating a thin plastic membrane. The theory of membrane permeation is well documented (*35*, *36*), and only a cursory discussion is presented here.

The fundamental driving force for diffusive transport is the gradient of the chemical potential. At low molecular densities this is proportional to the concentration gradient, C. The equation for the local steady-state diffusional flux, J, is

$$J = -D \nabla C \tag{7}$$

This is the familiar Fick's first law of diffusion. The phenomenological coefficient, D, is the molecular diffusivity of the gas species in the membrane. The gradient of the flux is equal to the negative time rate of change of the concentration. Thus, nonsteady diffusion is described by the following:

$$\frac{\partial C}{\partial t} = \nabla \times (D \nabla C) \tag{8}$$

If the diffusivity is not a spatially dependent property, Equation 8 can be written as Fick's second law,

$$\frac{\partial C}{\partial t} = D \nabla^2 C \tag{9}$$

Now consider a thin sheet of thickness N, whose concentration at surface $n = 0$ is $C(O)$, and $C(N)$ at $n = N$. For steady-state conditions, $\partial C/\partial t = 0$. Equation 9 can be solved to yield the linear concentration gradient

$$\frac{C(n) - C(O)}{C(N) - C(O)} = \frac{n}{N} \tag{10}$$

Equation 7 can now be integrated from $n = 0$ to give the flux through the membrane as

$$J = D \frac{C(N) - C(O)}{N} \tag{11}$$

For slightly soluble gases in membranes, the concentration is proportional to the partial pressure, P. The solubility coefficient, S, can be combined with the diffusivity to give the permeability coefficient, $[PM]$. Recognizing that at the surface, $n = 0$ and the membrane is in contact with a high vacuum, we reduce Equation 11 to

$$J = \frac{[PM]}{N} P(N) \tag{12}$$

Equilibrium thermodynamic considerations require that the partial pressure at $n = N$ be equal to the interfacial fluid partial pressure, P_{I_i},

Inserting this equality and multiplying Equation 12 by the membrane area gives the amount of gas species i entering the mass spectrometer, Q_{v_i}.

$$Q_{v_i} = \frac{[PM]_i \, A}{N} \, P_{I_i} \tag{13}$$

The rate of any gas entering the mass spectrometer is linearly related to the partial pressure at the membrane–fluid interface. The permeability coefficient is an intrinsic property of the membrane and is a function of the gas species and temperature.

Boundary Layers

The output of the mass spectrometer, P^*_i, is proportional to the rate of entry of a specific gas species into the vacuum system (Equation 5). At membrane steady-state conditions, the output of the mass spectrometer is also proportional to partial pressures at the membrane–fluid interface, P_{I_i}. A relationship between P_{I_i} and the partial pressure in the bulk fluid, P_{f_i} is needed. For $P_{I_i} = P_{f_i}$ a negligible rate of gas transport out of the fluid or a high degree of concentration uniformity within the fluid is required. The latter can be approached through vigorous convective mixing or by rapid fluid diffusing properties. Because of the sensitivity limitations of the mass spectrometer, the necessary membrane transport, Q_{v_i} is relatively fixed.

The existence of a mass transport resistance in the liquid phase can be shown experimentally. Water, equilibrated at 37° C with O_2 and CO_2, was pumped through the BGC with a Harvard syringe pump. Figure 3 shows the effect of flow and mixing on the output of the mass spectrometer. Even for high flow and rapid mixing, the difference between the gas phase outputs (P^*_g) and the fluid outputs (P^*_f) are significant. It is interesting to compare the O_2 curves with the CO_2 curves. Even though the fluid dynamics are identical, $P^*_{f_{CO_2}}$ approaches $P^*_{g_{CO_2}}$ much more closely than $P^*_{f_{O_2}}$ approaches $P^*_{g_{O_2}}$. Also, the $P^*_{f_{CO_2}}$ curves are flatter and depend less on the flow and stirring rates than the $P^*_{f_{O_2}}$ data. This predominantly results from the high solubility of CO_2 in water as compared with O_2.

To understand this data quantitatively and to predict other functionalities, the fluid and mass transport operations within the blood gas diffusion cell must be examined closely.

The equation of mass continuity for a region undergoing both molecular diffusion and convective transport is

$$\frac{\partial C}{\partial t} = D \, \nabla \, (\nabla C) - \overline{V} \times \nabla C \tag{14}$$

For the conditions within the BGC, the only component of transport that we are concerned with is in the negative z direction (toward the membrane). Assuming no time gradients, the material continuity equation reduces to

$$D_f \frac{d^2C}{dz^2} + V_z(z) \frac{dC}{dz} = 0 \tag{15}$$

The z directed fluid velocity was determined by modeling the complete flow pattern in the fluid region and then defining a turnover parameter. The effective z velocity was assumed to be linearly related to this parameter times a relative viscosity correction. The details of these computations are presented in the Appendix.

The boundary conditions on Equation 15 are determined at $z = 0$ (the membrane–fluid interface) and at $z = 2h$ (the face of the plug insert). Because there is no transport occurring at $z = 2h$, the concentration is assumed to be equal to the inlet fluid. At the membrane–fluid interface, the flux out of the fluid,

$$-D_f \left.\frac{dC}{dz}\right|_{z=0} \tag{16}$$

must be equal to the flux through the steady-state membrane described by Equation 12. This boundary condition is

$$D_{f_i} \left.\frac{dC_i}{dz}\right|_{z=0} = \frac{[PM]_i}{N} P_{I_i} \tag{17}$$

To evaluate the mass transport equation, MTE (Equation 15), with the proper boundary conditions, it is necessary to obtain a functional relationship between the concentrations and partial pressures of the gas dissolved in the fluid. For water, O_2, N_2, and CO_2 can be assumed to be linear—*i.e.*, have a constant solubility coefficient, S_i.

$$C_{w_i} = S_{w_i} P_{w_i} \tag{18}$$

The carriage of O_2 and CO_2 in blood is not a simple solubility process. The concentration curves are nonlinear and are functions of several parameters.

The MTE was solved using a finite difference technique on a digital computer. It was necessary to supply a constitutive relation for the gas–fluid pair that was being studied. For O_2-blood, the dissociation curve of Severinghaus (*37*) was used in a tabulated form. Because of its high solubility, CO_2 was assumed to be physically dissolved in blood without considering its dissociation curve.

The usefulness of the MTE depends on its ability to predict the actual data obtained from the BGC. The solid lines in Figure 3 were obtained from the solution of MTE. Comparison with the data points shows the reasonably good agreement and reinforces our confidence in the mathematical model and its predictive capabilities.

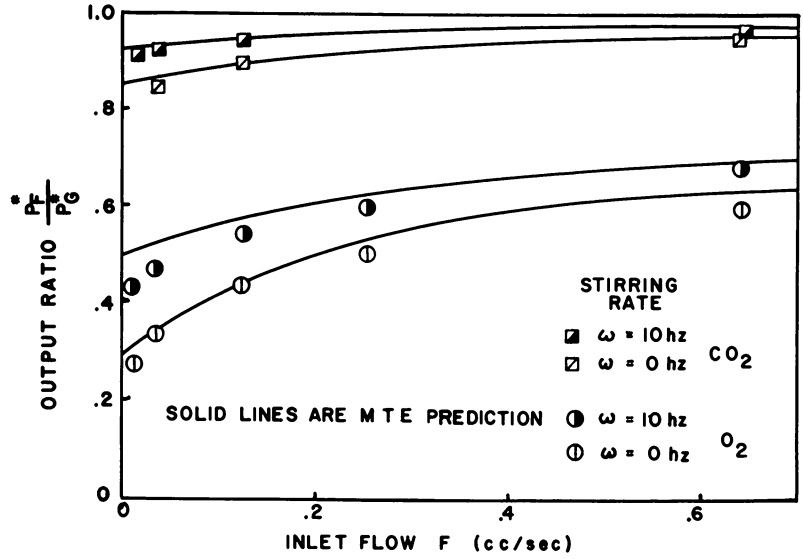

Figure 3. Effect of flow and stirring on output

Measurement of Partial Pressures

The partial pressures of CO_2 and O_2 are determined during constant injection of the fluid through the BGC using either a syringe pump or hand pump. Two ml of fluid injected at about 0.5 ml/sec are required to flush the 80-μl cell volume adequately. Calibration is performed using water at 37°C, equilibrated at a known partial pressure.

For CO_2 the solution to the MTE predicts that a simple proportionality relation can be used to relate the water calibration to the determination of P_{CO_2} in blood. The circles in Figure 4 represent blood samples equilibrated at four different P_{CO_2}'s. The corresponding water samples are represented by the crosses. The dashed line is the predicted gas phase output of the BGC. The linear correlation exceeded 0.98 for the water and the blood data. The standard error of measurement for blood was 0.57 mm Hg and 0.42 mm Hg for the water data.

The measurement of P_{O_2} in blood requires a more complex procedure. Figure 5 plots the predicted value of the mass spectrometer output, $P^*_{O_2}$, for gas, water, and blood. Though the gas phase and water

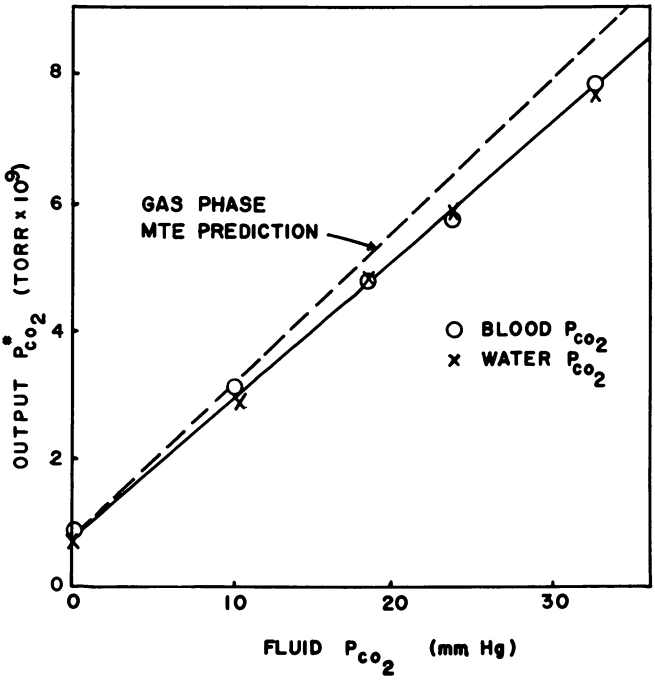

Figure 4. Determination of P_{CO_2}

output are linear, the prediction for blood indicates a substantial non-linearity. At low P_{O_2}'s this curve approached the gas phase output. As the P_{O_2} increases, the predicted output decreases to less than the water value. This can be understood by considering the sigmoid shape of the dissociation curve. At partial pressures less than 60 mm Hg, the effective solubility of O_2 in blood is great, thus diminishing the effect of the fluid boundary layer. At high P_{O_2}, where the hemoglobin is largely saturated, the blood O_2 solubility is similar to that of water, but the blood viscosity is greater (38). This enhances the fluid boundary layer.

It is necessary to construct a calibration curve that relates the true blood P_{O_2} to the estimated value based on a linear ratio with the water calibration. Figure 6 is a calibration curve for O_2-blood. The circles represent samples of blood equilibrated at known P_{O_2}'s. The average percent deviation from the calibration curve was −4.5%.

Depletion of the Gas

Theoretical Basis. The partial pressures of the dissolved gases are measured when the fluid is being injected through the BGC. If the flow is suddenly stopped at $t = 0$, the mass spectrometer output gradually

decreases to zero. This decline is caused by depletion of the gas in the fixed fluid volume, V_f, because of the outward gas transport through the membrane.

Assuming a homogeneous fluid phase and a pseudo steady-state membrane (a linear but changing concentration gradient), we can write a material balance of species i for the fluid phase,

$$V_f \frac{dC_{f_i}}{dt} = -Q_{v_i} \tag{19}$$

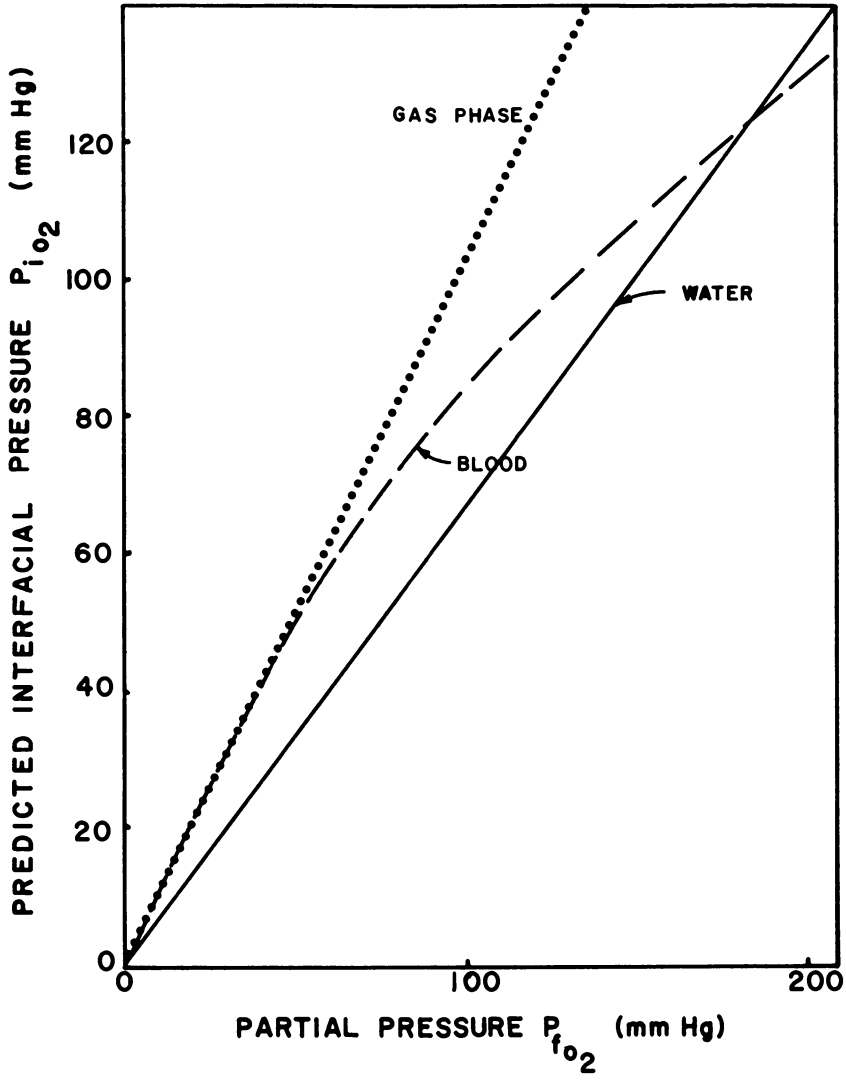

Figure 5. MTE predicted interfacial P_{CO_2}

Using Equation 5 relating Q_{v_i} to the output, P^*_i, and integrating Equation 19 from $t = 0$ to any time t gives

$$\int_{C_{f_i}(t)}^{C_{f_i}(0)} dC_{f_i} = \frac{1}{V_f K_{Q_i}} \int_0^t P^*_i(t)\, dt \tag{20}$$

As the time approaches infinity, the bulk fluid concentration goes to zero. Thus, the integral of Equation 20 shows the initial fluid concentration to be proportional to the time integral of the output curve.

$$C_{f_i}(0) = \frac{1}{V_f K_{Q_i}} \int_0^\infty P^*_i(t)\, dt \tag{21}$$

Integrating Equation 20 to time t and substituting Equation 21 yields

$$C_{f_i}(t) = \frac{1}{V_f K_{Q_i}} \int_t^\infty P^*_i(t)\, dt \tag{22}$$

Dividing Equations 22 and 21 to eliminate the system constants gives

$$\frac{C_{f_i}(t)}{C_{f_i}(0)} = 1 - \frac{\int_0^t P^*_i(t)\, dt}{\int_0^\infty P^*_i(t)\, dt} \tag{23}$$

So the fractional gas concentrations in the fluid at any time can be determined solely by integrating the output curve during depletion. The output of the mass spectrometer is a function of the partial pressure in the fluid. Therefore, it is possible to obtain continuously the relationship between the concentration and partial pressure. This defines the solubility curve.

The form of the depletion curve can be predicted if the constitutive equation of the dissolved gas in the fluid is known. For water a linear relation exists between the partial pressure and concentration of the dissolved gases. Also, the MTE predicts a constant ratio between the bulk and interfacial partial pressures, R_{IB}. The relation between C_{w_i} and P^*_i can be shown to be

$$C_{w_i} = \frac{S_{w_i} N}{R_{IB}\,[PM]_i\, A\, K_{Q_i}} - P^*_i \tag{24}$$

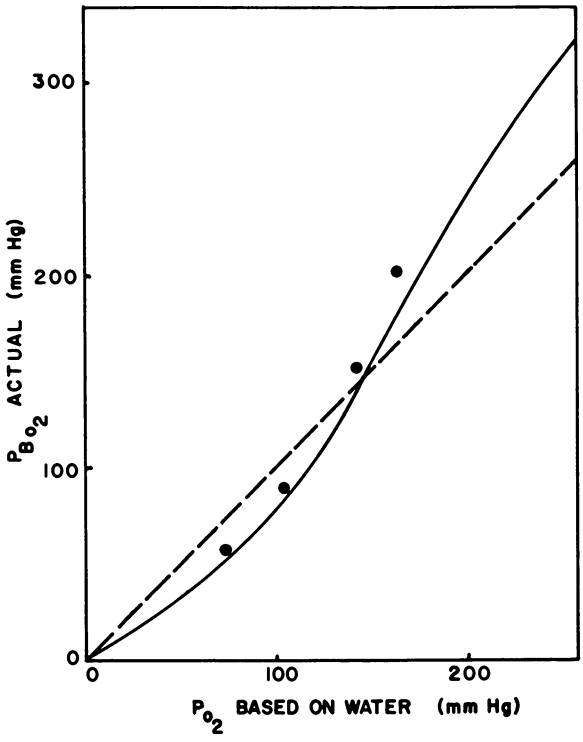

Figure 6. O_2-Blood calibration curve

The solution to this first-order ordinary differential equation can be written as

$$\frac{dP^*_i}{dt} = \frac{[PM]_i \; R_{IB}}{S_{w_i} \, 2Nh} \, P^*_i \tag{25}$$

Substituting this relation along with Equation 5 into Equation 19 gives

$$\frac{P^*_i(t)}{P^*_i(0)} = \exp - \left\{ \frac{[PM]_i \; R_{IB}}{S_{w_i} \, 2Nh} \right\} t \tag{26}$$

Verification of Theory. The solid line in Figure 7 is the relative mass analyzer output plotted as a function of time for the O_2-water depletion curve. The dotted line is the numerical evaluation of Equation 26 using the material properties published by Schuler and Kreuzer (*11*). R_{IB} was determined to be 0.63 by the MTE equation. The initial deviations can arise from two sources. At $t < 0$, the ratio R_{IB} is 0.68 owing to the reduced boundary layer from the added flow function. When the

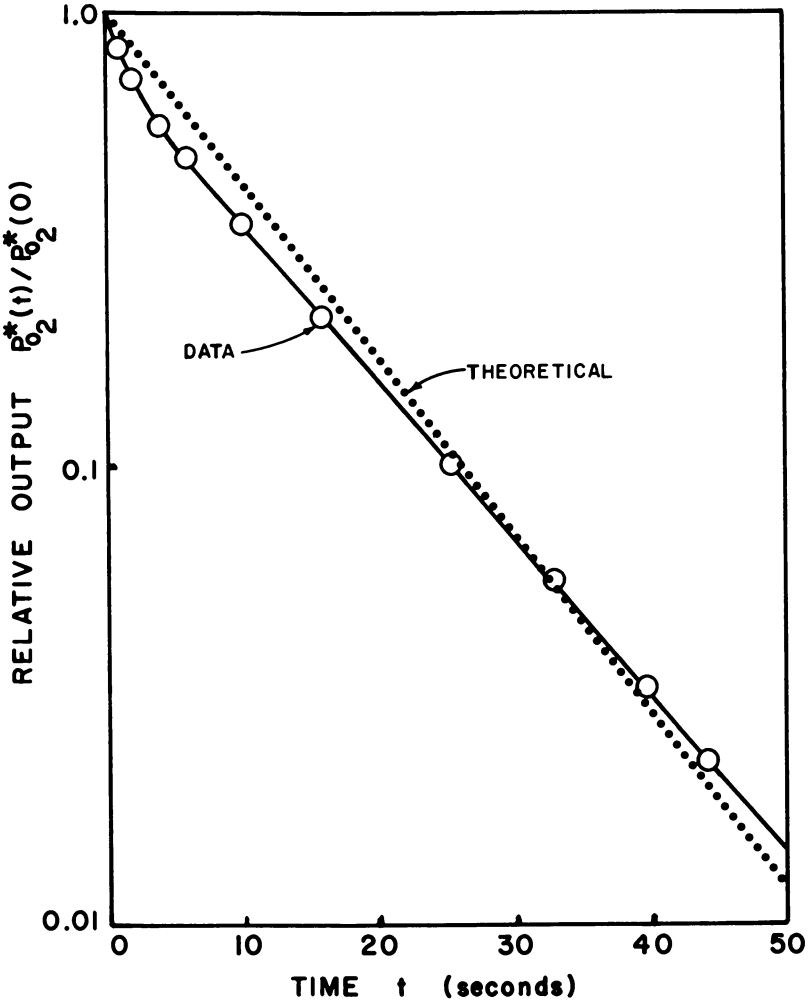

Figure 7. O_2 Depletion curve

injection is suddenly terminated, the fluid boundary layer must undergo a finite change. The other source of difference is brought about by the relatively rapid initial concentration changes. The assumption of continuous linear concentration gradient in the membrane with a 90% time response of 0.5 sec may cause some initial variations.

There is an 11.3% difference between the areas of these two curves (based on the theoretical area). This results from a flaw in the assumption of the pseudo steady-state membrane. For this to be true, the gas flux at the fluid interface must always equal the flux on the vacuum side of the membrane. The integration of the flux at the interface gives the initial amount contained in the fluid. A similar integration at the mem-

brane–vacuum interface adds the gas initially contained in the membrane to the fluid. On this basis, we can correct for the O_2 dissolved in the Teflon using the relative volumes of the fluid and membrane with their solubilities. Equation 21 becomes (for the O_2–water–Teflon system),

$$C_{w_{O_2}}(0) = \frac{1}{1.10\, V_w K_{Q_{O_2}}} \int_0^\infty P^*_i(t)\, dt \qquad (27)$$

This corrects the areas in Figure 7 to within 1.3%. For the CO_2–water, CO_2–blood, and the O_2–blood systems, this correction is negligible. Figure 8 presents the CO_2–water depletion curve with its prediction. As

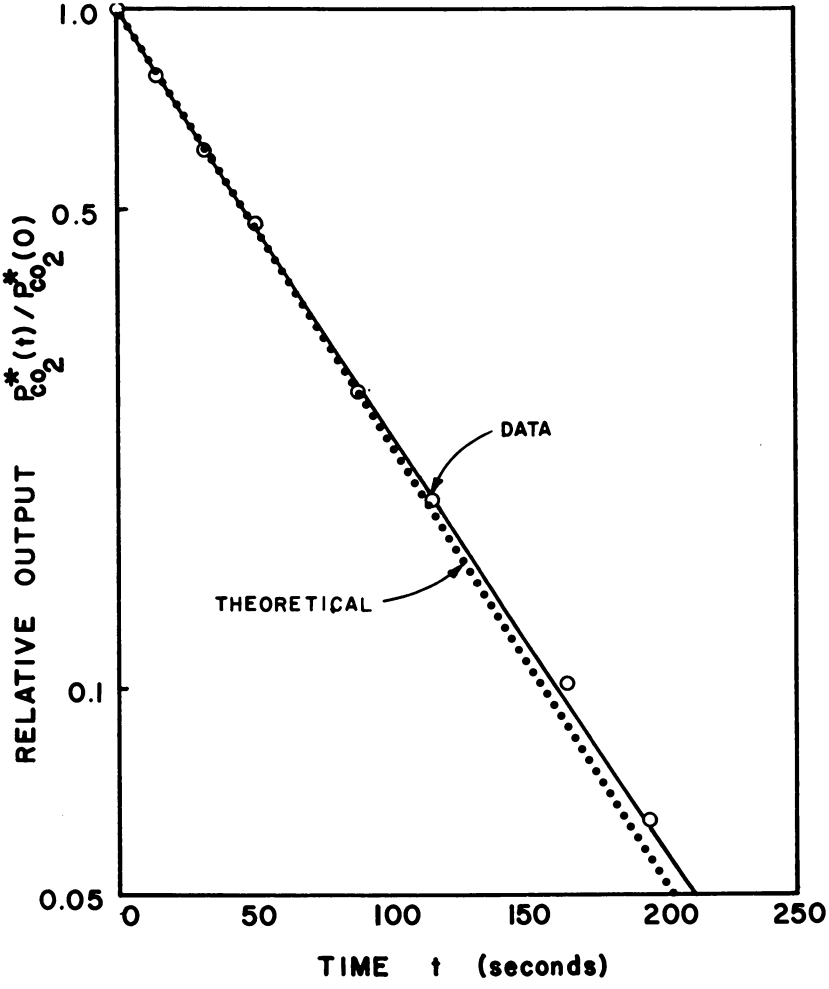

Figure 8. CO_2 Depletion curve

expected, the time response is much slower and less deviation from the form of Equation 26 occurred. The areas agreed to within 6%.

The Oxygen Dissociation Curve

The numerical evaluation of the actual concentration curve involves determination of several internal system constants. To simplify this procedure and to avoid time variations, the calibration of the blood O_2 content will be relative to a previously determined O_2–water curve. Writing the integral of the output curves as $A^{\infty}{}_o(f) = \int_o^{\infty} P^*(t)dt$ where f designates the fluid type, the system constants in Equation 27 become

$$\frac{1}{V_w K_{Q_i}} = \frac{P_{w_{O_2}}\ 1.10\ S_{w_{O_2}}}{A^{\infty}{}_o(w)} \tag{28}$$

Substituting this into Equation 21 gives the initial O_2 concentration in blood relative to that for water.

$$C_{B_{O_2}}(0) = 1.10\, S_{w_{O_2}} P_{w_{O_2}} \frac{A^{\infty}{}_o(B)}{A^{\infty}{}_o(w)} \tag{29}$$

Similarly, for Equation 23, the O_2 content in blood at any time can be represented as

$$C_{B_{O_2}}(t) = 1.10\ S_{w_{O_2}} P_{w_{O_2}} \frac{[A^{\infty}{}_o(B) - A^{\infty}{}_o(B)]}{A^{\infty}{}_o(w)} \tag{30}$$

These two equations are the working relations for the determination of the O_2 content in blood. The calibration requires the integrated output of O_2 in water, initially at a known P_{O_2}.

The values of the $P_{B_{O_2}}(t)$ corresponding to the decreasing blood O_2 concentration must also be ascertained for the construction of the O_2 dissociation curve. This is accomplished using the method described previously involving the comparison of the $P^*_{B_{O_2}}(t)$ with known values of $P_{w_{O_2}}$ and $P^*_{w_{O_2}}$. The calibration derived from the MTE is used to correct for the blood–water boundary layer differences.

The depletion by membrane permeation of CO_2 in blood introduces cause for concern. This affects the evaluation of $P_{B_{O_2}}$ and also shifts the position of the O_2 dissociation curve. The correction for this effect requires the continuous evaluation of the acid–base status of the blood sample. Using an initial reference point obtained from a separate pH measurement and P_{CO_2}, the variation in pH during the withdrawal process can be determined with incremental measurements of $P_{B_{CO_2}}(t)$.

Assuming a constant base excess, the pH can be continuously determined using the Henderson–Hasselbalch nomogram presented by Severinghaus (*39*). The corrected pH values are inserted into the input of MTE, and the shift in the dissociation curve can be determined using standard techniques (*37*).

Figure 9 is an O_2 depletion curve for a blood sample initially equilibrated at a P_{O_2} of 605 mm Hg. The rapid decrease in the output at small times is caused by O_2 leaving the blood primarily from the dissolved phase. When the blood P_{O_2} fell to about 80 mm Hg, the curve leveled, and the combined O_2 began to be released. The O_2–water depletion curve used for calibration is shown in Figure 10. The total O_2 concentration of the blood was 0.216 cm^3 O_2/ml. Subtracting the initial dissolved portion gave a figure of 0.201 cm^3 O_2/ml. Assuming the hemoglobin was initially completely saturated with O_2, we can calculate the hemoglobin content to be 14.5 grams/100 ml blood.

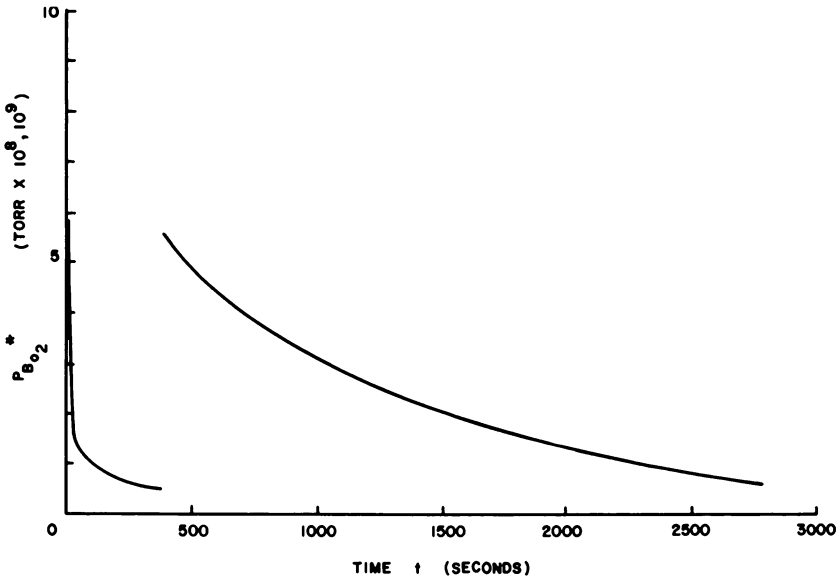

Figure 9. O_2-Blood depletion curve

Construction of the dissociation curve required that the O_2 content be determined for a set of points on the depletion curve. This was done using Equation 30. Table I contains the results of calculations necessary to determine the curve. The pH was calculated at each point using the CO_2 depletion curve (not shown) and the Henderson–Hasselbalch nomogram. Figure 11 contains the data points with the curve obtained

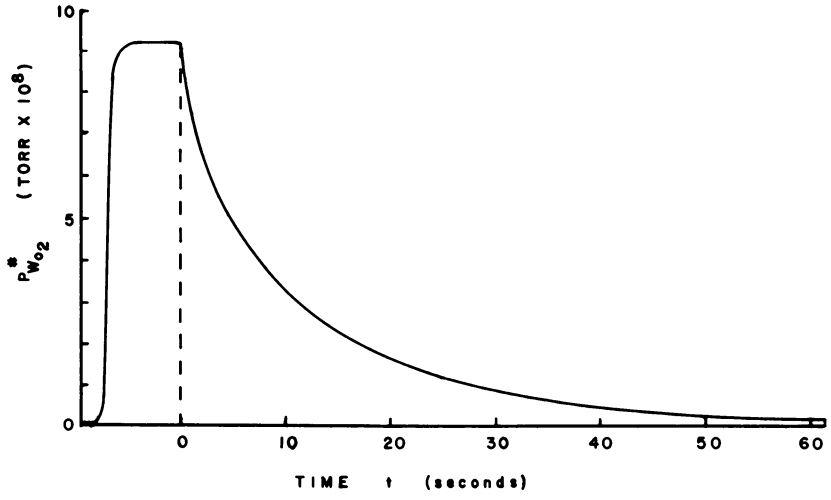

Figure 10. O_2-Water depletion curve

Table I. Construction of the O_2 Dissociation Curve

% Saturation	$p_{B_{O_2}}$ *(water ratio)*	$p_{B_{O_2}}$ *(from calibration curve)*	*pH*	$p_{B_{O_2}}$ *(corrected to pH = 7.4)*
100	386	480	7.41	480
99.5	252	312	7.41	312
97.2	128	120	7.42	121
92.3	74.7	58.2	7.43	60
88.6	62.5	45.6	7.45	48.2
75.2	45.7	33.0	7.50	37.8
63.6	37.5	25.1	7.53	32.0
58.4	31.1	23.0	7.60	28.6
41.5	25.0	18.0	7.65	23.7
34.0	23.7	14.0	7.74	20.4
9.72	12.5	9.7	7.82	16.1
6.85	6.25	4.3	7.85	10.2

from Severinghaus' data (*37*). The P_{50} was 25.7 mm Hg which agreed well with established values.

Discussion

These mass spectrometer techniques for determining blood gas partial pressures, contents, and the O_2 dissociation curve contain both improvements over existing methods and disadvantages.

One of the principal objections centers on the nonlinear calibration curve for the determination of blood oxygen partial pressures. This resulted from the formation of an oxygen-depleted boundary layer near

the gas permeation membrane. The calibration curve (Figure 6) becomes a secondary function of the dissociation curve. The magnitude of this effect can be appreciated by performing a variation analysis on the calibration curve parameters. For a Δ pH = 0.10, centered at 7.4, a maximum potential error of 5 mm Hg can occur for an uncorrected estimate of P_{O_2}. The most sensitive area for this interaction centers around 150 mm Hg. The errors decrease as the P_{O_2} ranges from this region.

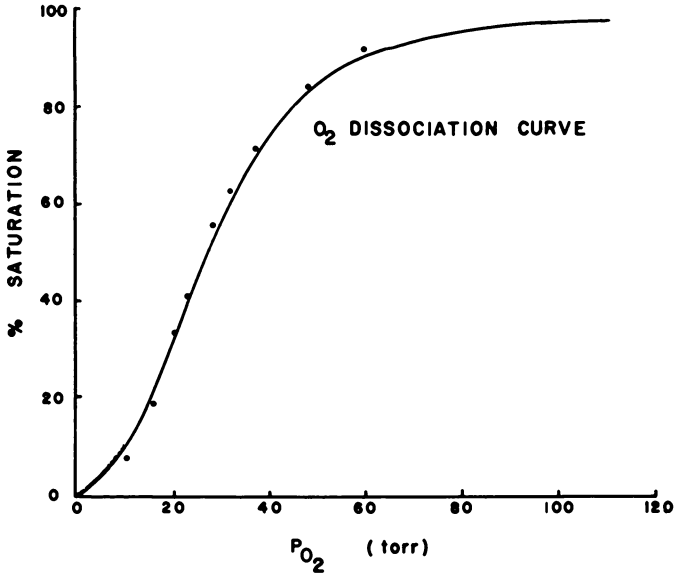

Figure 11. O_2-Dissociation curve

Though the most direct application of the analysis system is determining gas contents, the construction of the O_2 dissociation curve requires computation of P_{O_2}'s at several positions. This can introduce errors of the type mentioned. We feel that the potential of rapidly obtaining a dissociation curve for clinical use will more than balance these discrepancies.

For research applications, where maximal accuracy is desirable even at the expense of time and effort, two maneuvers are possible. The first involves derivation of the initial dissociation curve using the standard calibration curve. A second computation follows, using the derived curve for calibration. This process is repeated until the derived and calibrating dissociation curves match each other. This method requires considerable calculations, but it is theoretically valid even for abnormal hemoglobins. The other technique for accurate dissociation curve analysis is simply a variation on the traditional method of carefully equilibrating aliquots

of blood at known P_{O_2}'s. The blood gas analysis cell is used only to determine the O_2 contents. Though more manual effort and blood are required, less interpretation is needed.

The blood gas cell can be modified to optimize either the measurements of partial pressures or contents. Decreasing the permeability of the membrane by an order of magnitude will effectively reduce all boundary layer effects, allowing a linear calibration for P_{O_2}. At the other extreme, increasing the membrane permeability (*e.g.*, silicone rubber membranes) would permit a rapid depletion of the blood gases, facilitating content measurements.

Nomenclature

A	= area of diffusion, cm^2
A	= output integral for depletion curve, division-seconds
C_i	= concentration of species i, cm^3/cm^3
C_{I_i}	= concentration of i at membrane–fluid interface, cm^3/cm^3
D	= molecular diffusivity, cm^2/sec
F	= flow rate through blood gas cell, cm^3/sec
Hb	= blood hemoglobin concentration, g/100 ml
Hct	= hematocrit, cell fraction of blood $\times$ 100
J	= diffusion flux through membrane, cm^3/cm^2, sec
K_I,K_Q,K_T	= constants relating mass spectrometer output to input
L	= thickness of fluid layer, cm
N	= membrane thickness, cm
P_i	= partial pressure of gas species i, torr (mm Hg)
P^*_i	= partial pressure output of mass spectrometer, torr
Q_V	= flow rate into mass spectrometer, torr liter/sec
R_{IB}	= ratio between interfacial and bulk fluid partial pressure
V_f	= volume of fluid space in blood analysis cell, cm^3

Appendix

Derivation of Equations for the Fluid Boundary Layer. The fluid region of the blood gas analysis cell can be represented as a short cylinder of length $2h$. The axial position in the fluid, z, varies from 0 at the membrane surface to $2h$ at the face of the male plug. The stirrer is located at $z = h$ and rotates at an angular velocity of ω rps. During injection, the fluid enters the permeation region coaxially with the arm of the stirrer and flows radially, leaving the cell at $r = R$. The stirrer imparts a tangential component to the fluid velocity, v_θ. It can be seen that v_θ will be a function of both the radial distance, r, and the axial position, z. Assuming linear superposition, the total fluid velocity is

$$v(r,z) = v_\theta(r,z) + v_r(r,z) \qquad \text{(A)}$$

For $z \geq h$, the motion of the fluid due to the stirrer will be assumed to be equal to the speed of the stirrer, $2\pi r\omega$. The tangential velocity pro-

file from $0 \leqslant z \leqslant h$ can be approximated using a modified von Karman approach. The constants of a four-term polynomial expression for $v_\theta(r,z)$ can be determined from the following boundary conditions;

$$\text{at } z = 0 \qquad v_\theta(r,z) = 0$$

$$\left.\frac{\partial^2 v_\theta}{\partial z^2}\right|_{z=0} = 0 \tag{B}$$

$$\text{at } z = h \qquad v_\theta(r,z) = 2\pi r\omega$$

$$\left.\frac{\partial v_\theta}{\partial z}\right|_{z=0} = 0 \tag{C}$$

The solution to the polynomial expression from $0 \leqslant z \leqslant h$ is

$$v_\theta(r,z) = 2\pi r\omega \left[\frac{3z}{2h} - \frac{1}{2}\left(\frac{2}{h}\right)^3 \right] \tag{D}$$

To determine the radial component of the fluid motion owing to injection at a flow rate F ml/sec, a parabolic velocity distribution in the z direction will be assumed. The maximum velocity occurs at $z = h$.

$$v_r(r,z) = v_r(r,h)\left[\frac{2z}{h} - \left(\frac{z}{h}\right)^2 \right] \tag{E}$$

The flow rate, F, is the integral of Equation E from $z = 0$ to $z = 2h$.

$$F = \int_0^{2h} v_r(r,z)\ 2\pi r\omega dz \tag{F}$$

Substituting Equation E into F and performing the integration gives the velocity at $z = h$ in terms of F.

$$v_r(r,h) = \frac{3F}{8\pi rh} \tag{G}$$

The equations for the total fluid motion can now be written as

$$0 \leq z \leq h \quad v(r,z) = 2\pi r\omega \left[\frac{3z}{2h} - \left(\frac{z}{h}\right)^3 \right] + \frac{3F}{8\pi rh}\left[\frac{2z}{h} - \left(\frac{z}{h}\right)^2 \right]$$

$$h \leq z \leq 2h \quad v(r,z) = 2\pi r\omega + \frac{3F}{8\pi rh}\left[\frac{2z}{h} - \left(\frac{z}{h}\right)^2 \right] \tag{H}$$

Examination of these equations shows no axial (z-directed) component of fluid motion. Yet, if convection is to augment molecular diffusion of gases toward the membrane, an effective z component of velocity must exist. To create this mathematically, let us define a turnover number, T, that is equal to the number of times a fluid particle travels a characteristic distance, $2\pi r$, each second.

$$T(r,z) = \frac{v(r,z)}{2\pi r} \tag{I}$$

Averaging T over the radial distance to obtain T only as a function of z yields

$$T(z) = \frac{\omega}{2}\left(\frac{3z}{h} - \frac{z^3}{h^3}\right) + \frac{3F}{8\pi R^2 h}\ln\frac{R}{R_o}\left(\frac{2z}{h} - \frac{z^2}{h^2}\right) \tag{J}$$

A viscosity dependence of the turnover number can be gained by multiplying $T(z)$ by the relative Reynolds number of blood compared with water. This becomes the kinematic viscosity ratio ν_W/ν_B. The z-directed mixing velocity $v_z(z)$ can now be written as

$$v_z(z) = T(z)\frac{v_w}{v_B}z \tag{K}$$

Literature Cited

1. Lenfant, C., Torrance, J. D., Woodson, R. D., Jacob, P., Finch, C. A., *Fed. Proc.* (1970) **29**, 1115.
2. Brewer, G. J., Ed., "Red Cell Metabolism and Function," Plenum, New York, 1970.
3. Benesch, R. E., Benesch, R., *Fed. Proc.* (1970) **29**, 1101.
4. Clark, L. C., Jr., *Trans. Amer. Soc. Art. Organs* (1956) **4**, 41.
5. Severinghaus, J. W., Bradley, A. F., *J. Appl. Physiol.* (1958) **13**, 515.
6. Torres, G. E., *J. Appl. Physiol.* (1963) **18**, 1008.
7. Rhodes, P. G., Moser, K. M., Scarborough, W. R., *Fed. Proc.* (1964) **23**, 468.
8. Moran, F., Kettel, L. J., Cugell, D. W., *J. Appl. Physiol.* (1966) **21**, 725.
9. Heitman, H., Buckles, R. G., Laver, M. B., *Resp. Physiol.* (1967) **3**, 380.
10. Charlton, G., Read, D., Read, J., *J. Appl. Physiol.* (1963) **18**, 1247.
11. Schuler, R., Kreuzer, F., *Resp. Physiol.* (1967) **3**, 90.
12. Stow, R. W., Randall, B. F., *Amer. J. Physiol.* (1954) **79**, 678.
13. Davenport, H. W., "The ABC of Acid-Base Chemistry," p. 30, Chicago Press, Chicago, 1958.
14. Woldring, S., Owens, G., Woolford, D. C., *Science* (1966) **153**, 885.
15. Woldring, S., *J. Ass. Advan. Med. Inst.* (1970) **4**, 43.
16. Brantigan, J. W., Gott, V. L., Vestal, M. L., Fergusson, G. J., Johnston, W. H., *J. Appl. Physiol.* (1970) **28**, 375.
17. Grode, G. A., Anderson, S. J., Fald, R. D., *Trans. Amer. Soc. Art. Int. Organs* (1959) **15**, 1.
18. Van Slyke, D. D., Neill, J. M., *J. Biol. Chem.* (1924) **61**, 523.
19. Roughton, F. J. W., Scholander, P. F., *J. Biol. Chem.* (1943) **148**, 541.
20. Hill, D. W., "Oxygen Measurements in Blood and Tissues and Their Significance," p. 63, J. P. Payne, Ed., Little, Brown, Boston, 1966.

21. Siggaard-Anderson, O., Jorgensen, K., Naeraa, N., *Scand. J. Clin. Lab. Invest.* (1962) **14**, 298.
22. Brinkman, R., Zijlstra, W. G., *Arch. Chir. Neerl.* (1949) **1**, 177.
23. Johnson, C. C., Palm, R., Boudon, A. K., *Proc. 23rd ACEMB* (1969) 1–6.
24. Laver, M., *J. Appl. Physiol.* (1968) **22**, 1017.
25. Tucker, V. A., *J. Appl. Physiol.* (1967) **23**, 410.
26. Tazawa, H., *J. Appl. Physiol.* (1970) **29**, 414.
27. Jellinek, M., Barner, H. B., Kaiser, G. C., *J. Appl. Physiol.* (1970) **29**, 398.
28. Wilson, R. H., Jay, B., Chapman, C. B., *Fed. Proc.* (1961) **20**, 422.
29. Torrance, J. D., Lenfant, C., *Resp. Physiol.* (1969/70) **8**, 127.
30. Edwards, M. J., Martin, R. J., *J. Appl. Physiol.* (1966) **21**, 1898.
31. Duvelleroy, M. A., Buckles, R. G., Rosenkaimer, S., Tung, C., Laver, M. B., *J. Appl. Physiol.* (1970) **2**, 227.
32. Longmuir, I. S., Chow, J., *J. Appl. Physiol.* (1970) **28**, 343.
33. White, F. A., "Mass Spectrometry in Science and Technology," Wiley, New York, 1968.
34. Jayaram, R., "Mass Spectrometry," Plenum, New York, 1968.
35. Crank, J., Park, G. S., "Diffusion on Polymers," 1968.
36. Tuwiner, S. B., "Diffusion and Membrane Technology," Reinhold, New York, 1962.
37. Severinghaus, J. W., *J. Appl. Physiol.* (1966) **21**, 1108.
38. Burton, A. C., "Physiology and Biophysics of the Circulation," p. 52, Year Book, Chicago, 1965.
39. Severinghaus, J. W., "Handbook of Physiology," p. 1481, W. O. Fenn and H. Rahn, Eds., Amer. Physiol. Soc., Washington, D. C., 1965.

RECEIVED November 22, 1971.

16

Polarographic Oxygen Tension Measurements in Microstructures of the Living Tissue

A Digital Computer Study on the Oxygen Tension Histogram

HERMANN METZGER

Department of Physiology, Johannes Gutenberg-University, Mainz, West Germany

An alternative to the Krogh capillary-tissue model for describing oxygen tension distribution in the microstructure of the organism is developed. The new three-dimensional network model covers the inhomogeneities in capillary blood flow in a relation of 27:1. Oxygen tension distribution (steady-state case) of the capillary network is compared with that of the con- and counter-current flow systems. This study was performed to obtain information about the dependence of the oxygen tension frequency distribution pattern on capillary arrangement. Theoretical oxygen tension frequency distributions are compared with experimental results from rat cortex. The frequently observed low oxygen tension values are probably caused by low flow velocities in some branches of the capillary network.

Some typical concepts that are well known in chemical engineering systems theory can be applied to elucidate processes in biological systems. Biological systems are characterized by several transport phenomena such as diffusion, convection, and chemical reactions which occur in capillaries and tissue.

In this study a simulation of such processes for various arrangements of capillaries was performed to attain a better understanding of oxygen supply conditions in the brain cortex. Oxygen tension values were calculated for steady-state conditions by numerical solution of partial differential equations for different capillary-tissue systems. The analysis helps to explain the experimental results obtained from the microstructure of rat

or cat brain cortex with small oxygen microsensors. In particular, an explanation has been sought for the frequently observed low oxygen tension values.

Geometrical Model of Capillary-Tissue System

The first mathematical treatment of oxygen exchange between capillaries and tissue was made by Krogh and Erlang (*1*). They assumed a parallel, equidistant arrangement for capillaries in which blood flows concurrently at a constant velocity while oxygen diffuses into the tissue and is consumed. This geometric arrangement has been the basis for numerous theoretical calculations of oxygen tension distribution values in the blood stream and tissue (*2, 3, 4, 5*).

To simulate the histological complexity of capillary-tissue arrangements in a better way and to develop an alternative concept to the Krogh model, a three-dimensional network system is suggested here, providing for differences in directions and flow velocities within the branches of the network (Figure 1).

A new inhomogeneously perfused tissue model is considered for a tissue cube with $3 \times 3 \times 3$ capillaries. Arterial inputs and venous outputs are located at opposite corners of the tissue cube. As a simplifying condition, it is assumed that the hydrodynamic resistances of all the capillaries are equal. Furthermore, Kirchoff's laws are assumed to be valid, and capillary blood flow rates and directions can be calculated theoretically. For symmetry, the analyzed tissue cube can be divided into 24 parts, where only one part, a tetrahedron, had to be considered in the final analysis (thick lines at the left-hand corner, lower part). Blood flow directions at the inputs and outputs as well as in the tetrahedron are marked by arrows.

This study is an extension of a series of papers for the two-dimensional case (*6, 7, 8*). Results from the three-dimensional case approximate the physiological system more accurately and compare better with experimental results.

The Oxygen Tension Histogram Concept

Using small oxygen tension microsensors (tip diameter = 1 μm) enabled oxygen tension values to be measured in the microstructure of different organs. As the small oxygen sensor is moved forward from the surface into deeper layers of the tissue, tremendous oxygen tension differences are encountered between capillaries and the oxygen consuming structures in the cell (*9, 10, 11*).

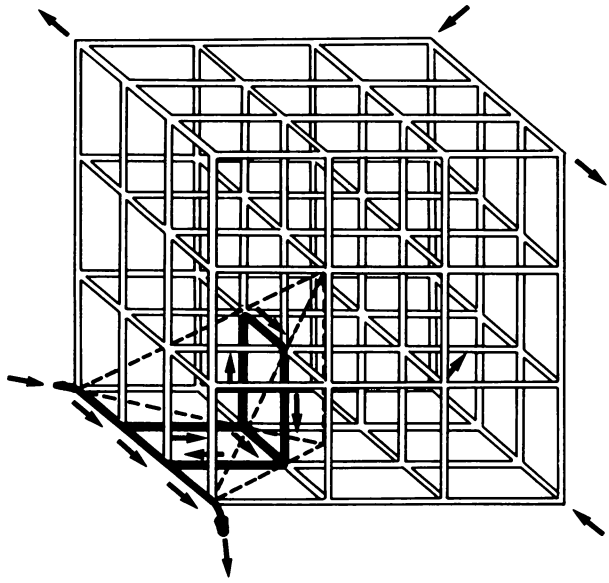

Figure 1. Capillary network system

From any oxygen sensor experiment in the animal tissue, a high data output was obtained, and hundreds of oxygen tension values were registered. To understand better the results, the frequency distribution of oxygen tension values (histograms) from a small tissue volume has been illustrated by numerous authors (*e.g., 12, 13, 14, 15*). Steady-state conditions of oxygen supply were usually assumed, resulting in an almost constant oxygen tension distribution independent of time (for method *see* Figure 2). The oxygen tension profiles measured with oxygen sensors were analyzed; a classification of 1 mm Hg was chosen. Results are from different experiments in a small volume of the occipital cortex of the anesthetized albino rat: Exp A: 898 measuring points. Exp B: 904 measuring points. Exp C: 840 measuring points. Exp D: 374 measuring points [according to (*15*)].

Questions arise as to what extent the experimental steady-state histograms depend upon the different physiological parameters—*e.g.*, as oxygen consumption rate, local blood flow velocity, capillary length and diameter, and capillary arrangement.

Here we make a first step toward providing an overall agreement between experimental and theoretical results. Oxygen tension values were calculated for different capillary-tissue arrangements, and the results were illustrated by histograms. A systematic investigation was performed by varying various physiological parameters and observing the histogram pattern.

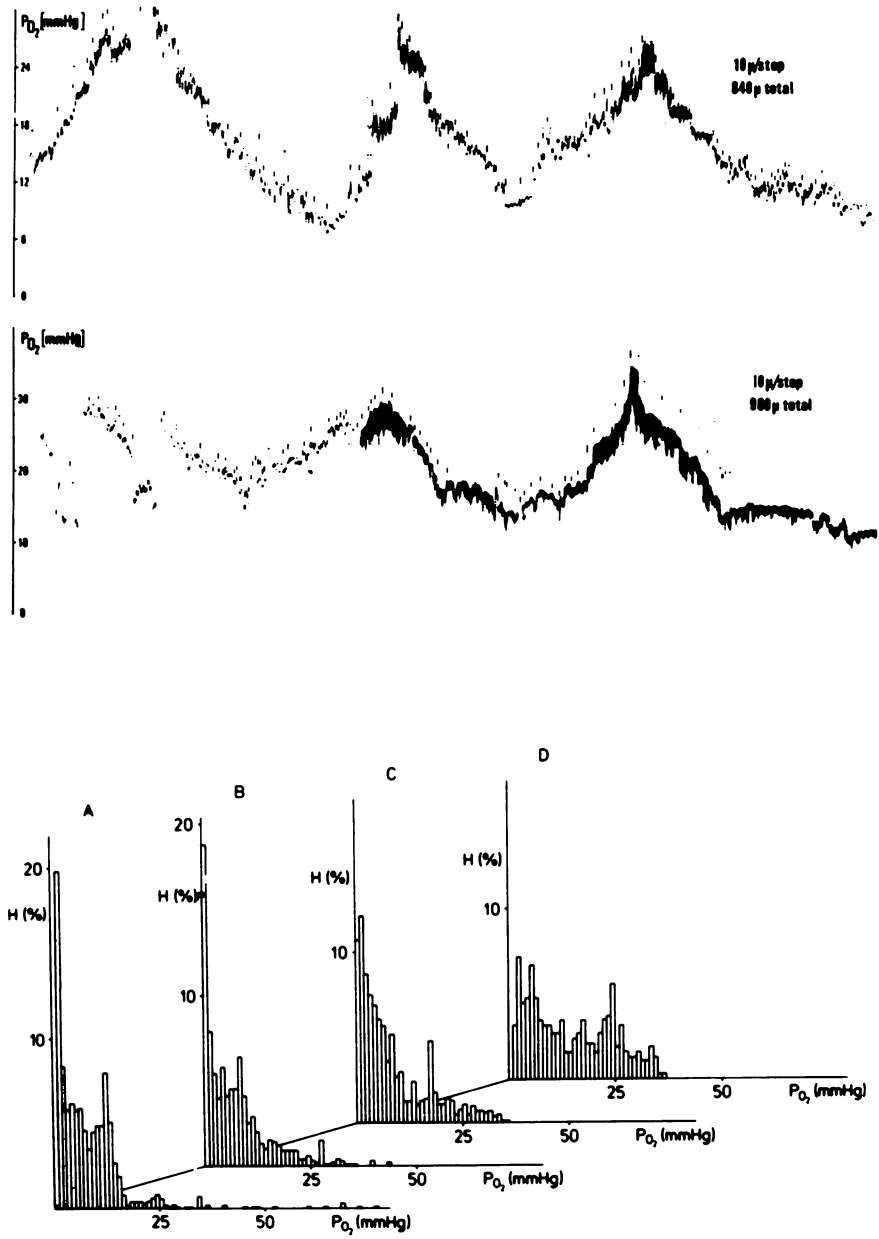

Figure 2. Typical oxygen tension profiles in the occipital rat cortex registered with an oxygen sensor of about 1 µm in diameter (according to (11) and (15)) (upper part). Steps of the micromanipulator are 10 µm (marked by thin lines). Frequency of oxygen tension values (H) (lower part).

Derivation of Capillary-Tissue Equations

In developing equations to describe oxygen transport in blood and tissue, several assumptions were used. The most important are summarized as follows:

List of Assumptions

1. Oxygen is transported in tissue by diffusion only and in capillaries by convection only.
2. Chemical reactions involving oxygen are assumed to take place at steady-state conditions and are described by Hill's law in the capillaries and by Michaelis and Menten's law in the tissue.
3. Oxygen consumption in the tissue is assumed to be homogeneous.
4. Flow velocity in the capillaries is calculated according to Kirchhoff's laws and is constant over the capillary cross section.
5. The diffusion resistance of the capillary wall is small compared with that of the tissue and can be neglected.
6. Oxygen concentration is continuous at the capillary-tissue interface, and transport across the interface can be described by Fick's first law.
7. The analyzed tissue area continues in the same way to infinity; the considered tissue volume is representative for the whole organ.
8. The differences of blood flow rate within the different capillaries are 27:11:4:3:1.

A mathematical description of the capillary-tissue model, based on assumptions 1-8, is possible and can be described by two coupled nonlinear differential equations.

Derivation of the Equations. The mass balance for oxygen in the tissue and capillaries is given by the equation of continuity for an element with volume V and surface F:

$$-\frac{\partial}{\partial t}\int_V c' dV = \int_F \vec{j}\, d\vec{F} + \int_V Q(c) dV \qquad (1)$$

where V is the tissue volume, $Q(c)$ is the oxygen consumption in terms of a chemical reaction per unit time and volume, and $\vec{j}$ is the oxygen flow through the surface element $d\vec{F}$. The first integral describes the temporal change of the oxygen quantity in volume V. The second integral summarizes the convection of oxygen at the volume surface F. The third integral represents the oxygen consumption in V. By applying Gauss's theorem and using differentiation according to the volume, we obtain the following partial differential equation

$$-\frac{\partial c}{\partial t} = \operatorname{div} \vec{j} + Q(c) \tag{2}$$

This differential equation is valid for both capillaries and tissue, but with different values. In the capillaries, $Q(c) = 0$; for the tissue we obtain

$$Q(c) = A \frac{c}{K + c} \tag{3}$$

(A = maximal respiration volume, K = kinetic rate constant). Only steady-state conditions are analyzed ($\partial c/\partial t = 0$). Furthermore, the validity of Fick's first law is assumed.

$$\vec{j} = -D \operatorname{grad} c \tag{4}$$

(D is the diffusion coefficient and is independent of position in the volume element.) We get

$$D\Delta c - A \frac{c}{K + c} = 0 \tag{5}$$

Equation 5 will be transformed into the dimensionless form

$$\frac{\partial^2 c_x}{\partial x^2} + \frac{\partial^2 c_y}{\partial y^2} + \frac{\partial^2 c_z}{\partial z^2} - AG \frac{c}{CH + c} = 0 \tag{6}$$

with

$$AG = A1^2/Dc_a \text{ and } CH = K/c_a \tag{7}$$

(Partial pressure values are calculated by dividing the concentration c by the solubility coefficient α). To obtain a differential equation for c' in the capillaries, we refer to Equation 1. For a stationary case and $Q(c) = 0$, we get

$$\int_F j dF = 0 \tag{8}$$

The integration is arrived at by a surface element of thickness ds:

$$Qv[c'(s + ds) - c'(s)] - d \times ds\, D \left[\left(\frac{\partial c}{\partial n}\right)_o + \left(\frac{\partial c}{\partial n}\right)_u + \left(\frac{\partial c}{\partial n}\right)_r + \left(\frac{\partial c}{\partial n}\right)_1\right] = 0 \tag{9}$$

This equation is already adapted to our three-dimensional model. Included are the additional assumptions that the capillary cross section Q is a square one ($Q = d^2$) and that c' can only change within the capillary in the capillary directions. The total concentration in the capillary interior c' is composed of a few physically dissolved molecules (c) and chemically bounded molecules

$$c' = 1.34 \frac{c_{Hb}}{100} \times \frac{s_T}{100} + c \tag{10}$$

with s_T, the saturation of oxyhemoglobin and c_{Hb}, the hemoglobin concentration. The saturation of hemoglobin depends on the oxygen concentration or tension p in the plasma and can be described by Hill's law

$$\frac{s_T}{100} = \frac{Kp^\gamma}{1+Kp^\gamma} \tag{11}$$

(K and γ are constants which are calculated from the actual dissociation curve.)

Furthermore, $j = c'v$ was placed in the capillary and Fick's first law applied to the areas bordering the tissue, the magnitude of which $d \times ds$ v is the velocity of blood in the different capillaries, which is calculated in the inhomogeneous model according to Kirchoff's laws. In the con- and countercurrent systems, the capillaries are perfused at the same velocity. The four differential quotients ($\partial c/\partial n$) at the areas bordering the tissue are taken in their normal directions.

After dividing by $d \times ds$ and after $ds \to o$, we obtain:

$$\frac{\partial c}{\partial s} = \frac{AK}{f(c)} \left[\left(\frac{\partial c}{\partial n} \right)_o + \left(\frac{\partial c}{\partial n} \right)_u + \left(\frac{\partial c}{n} \right)_r + \left(\frac{\partial c}{\partial n} \right)_1 \right] \tag{12}$$

with the expression

$$f(c) = \frac{c^{\gamma-1}}{(1 + K'c^\gamma)^2} \tag{13}$$

The constants AK and K' are defined as

$$AK = \frac{D}{dv} \frac{p_a \alpha 100}{1.34\, c_{Hb}\, \gamma K'} \tag{14}$$

and

$$K' = K_{p_a}{}^\gamma \tag{15}$$

(p_a is equal to the arterial oxygen tension.)

Equations 5 and 12 are two coupled nonlinear differential equations that completely describe the oxygen concentration in the three-dimensional model, provided that the influence of the capillary membrane as a diffusion barrier can be neglected.

Boundary Conditions. The equations for the blood–tissue interface are

$$c/_{\text{blood}} = c/_{\text{tissue}} \tag{16}$$

$$\frac{\partial c}{\partial n}\Big/_{\text{blood}} = \frac{\partial c}{\partial n}\Big/_{\text{tissue}} \tag{17}$$

The initial capillary point (arterial input) is

$$c_a = 1.0 \tag{18}$$

At the boundaries in the model, it is assumed that the oxygen tension field continues in the same way to infinity with the boundaries as symmetry lines. If, for example, the concentration of the boundary point with the coordinates x_o, y_o, z_o is to be calculated, concentrations at the points with the coordinates x_o, $y_o - h$, z_o or x_o, y_o, $z_o - h$ had to be considered. The following equations are valid

$$c(x_o, y_o - h, z_o) = c(x_o, y_o + h, z_o) \tag{19}$$

$$c(x_o, y_o, z_o - h) = c(x_o, y_o, z_o + h) \tag{20}$$

Similar equations have been derived for all the points at the boundaries of the same tissue block as well as the tetrahedron (Figure 3). (A representative tissue and a capillary point with the corresponding neighboring points necessary for calculation are marked in Figure 3. Only the two-dimensional case of the problem is shown to demonstrate the principle of calculation at the boundary lines.)

Special Equations. At special points of the network system a mixing of blood from two or more capillaries occurs and can be described by the equation

$$\sum_{\nu=1}^{6} c_\nu i_\nu = \bar{c} \sum_{\nu=1}^{6} i_\nu \tag{21}$$

with c_ν the concentration of the ν^{th} capillary with a blood flow rate i_ν and the mean concentration $\bar{c}$ at the mixing point.

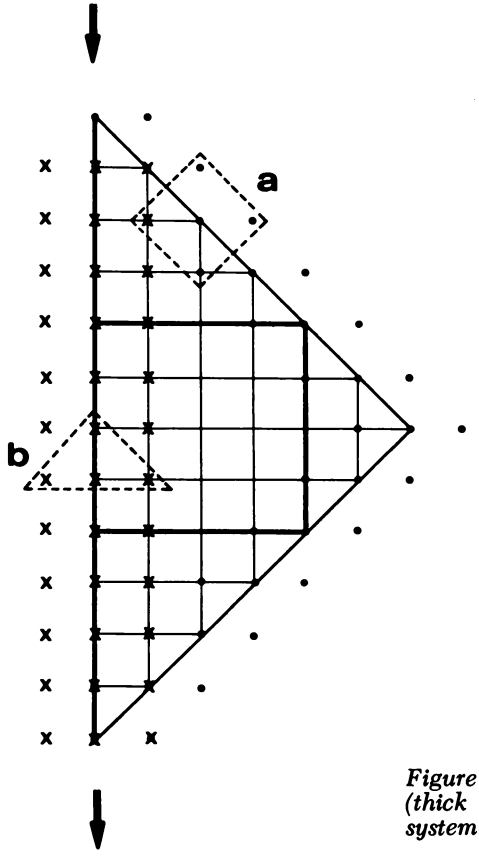

Figure 3. Basis area of the tetrahedron (thick lines: capillaries; thin lines: mesh system for calculation; arrows: blood flow input and output)

The values i_ν are calculated according to Kirchhoff's laws. At the nodes the equation

$$\sum_{\nu=1}^{6} i_\nu = 0 \tag{22}$$

is valid. For each mesh we arrive with the equation

$$\sum_{\mu=1}^{4} i_\mu W_\mu = 0 \tag{23}$$

The hydrodynamic resistances W_μ of the capillaries are assumed to be equal.

Transformation into Difference Form. The differential equations have been transformed into difference form and solved iteratively. The

function $c(x,y,z)$ was developed into a Taylor's series around the point x_o, y_o, z_o. Then we arrive at the following equations:

(a) Capillary equation:

$$c(l,m,n-1)^{(\nu)} - c(l,m,n)^{(\nu)} = AK/f[c(l,m,n)^{(\nu-1)}] \times [c(l,m+1,n)^{(\nu-1)} + c(l,m-1,n)^{(\nu)} + c(l,m,n+1)^{(\nu-1)} + c(l,m,n-1)^{(\nu)} - 4c(l,m,n)^{(\nu)}] \quad (24)$$

l,m,n are coordinates in capillary direction and perpendicular to the quadratic sides; ν is the iteration number.

(b) Tissue equation:

$$c(i,j,k)^{(\nu)} = c(i,j,k)^{(\nu-1)} + w[-c(i,j,k)^{(\nu-1)} + \bar{c}(i,j,k)^{(\nu)}] \quad (25)$$

$\bar{c}(i,j,k)^{(\nu)}$ is defined as

$$\bar{c}(i,j,k)^{(\nu)} = \frac{1}{6}\left[c(i+1,j,k)^{(\nu-1)} + c(i-1,j,k)^{(\nu)} + c(i,j+1,k)^{(\nu-1)} + c(i,j-1,k)^{(\nu)} + c(i,j,k+1)^{(\nu-1)} + c(i,j,k-1)^{(\nu)} - \mathrm{AG}\times h^2 \frac{c(i,j,k)^{(\nu-1)}}{CH + c(i,j,k)^{(\nu-1)}}\right] \quad (26)$$

i,j,k are the tissue coordinates; w is the relaxation parameter that affects the time for convergence tremendously. It was approximately calculated for the linear case of the difference equations according to Equation 16

$$w = 2\{1 + [1 - \cos(\pi/\mathrm{N})^2]^{1/2}\}^{-1} \quad (27)$$

with N the subdivision of one square of the network. For $N = 10$ as a typical example for the calculation, the relaxation parameter amounts to $w = 1.82$. In many cases the relaxation parameter was obtained after the first iteration steps by starting with $w = 1.0$ and improving the value by trial and error.

Results

The difference equations described above were solved numerically for the capillary network and for con- and countercurrent flow systems by using typical constants from the literature (*6*, *15*) (symbols and values of constants are listed below).

Similarly to the two-dimensional case, the convergence was improved by the method of successive overrelaxation (*8*). Between one-half to one-tenth of the original computer time for the successive displacement method was required to obtain an accuracy of 0.005%. Nevertheless, as

checked for the two-dimensional case, the computer time depended on the magnitudes of the parameters *AK* and *AG* (when *BN*, *BK*, and *CH* were left constant). Especially long running times for the computer calculations were obtained for normoxia: about 100 min for the con- and countercurrent flow systems and about 35 min for the network systems were necessary to obtain the prescribed accuracy. (The computer work was carried out using a CDC 3300 computer in the Computer Center of the Johannes Gutenberg University, Mainz, West Germany.)

There are four possibilities for representing the results:

1. Oxygen tension distribution. This graph consists of the iteratively calculated oxygen tension values. For one special case, at the base of the tetrahedron (capillary network), the oxygen tension distribution is plotted showing pronounced minima which were caused by the high oxygen consumption rate. Figure 4 shows the distribution of oxygen tension on the basis of the tetrahedron. The perfusion rate of the capillaries is characterized by different values having a ratio of 27:11:4:3:1. Typical oxygen tension decrease between arterial and venous end as well as between the different capillaries caused by metabolic rate of oxygen can be seen. Input parameter of the computer program for p_{O_2} calculation: $AG = 1.335$, $AK = 0.347 \times 10^{-3}$.

2. Isobars. Lines of equal oxygen tension values are plotted. The oxygen flux lines are shown at right angles to the isobars. This representation has been widely used in theoretical physics and the physiological phenomena are described completely by these plots.

3. Oxygen tension histograms. The frequency distribution of oxygen tension values is calculated from the oxygen tension field of the different capillary systems (Figure 5). The network system histogram has a broad oxygen tension spectrum. Countercurrent system shows a tremendous increase between 15 and 20 mm Hg. Input parameter of the computer programs: $AG = 0.91$, $AK = 0.63 \times 10^{-3}$ (con- and countercurrent systems); $AG = 0.91$, $AK = 0.17 \times 10^{-4}$ (network system). The oxygen tension histograms are important for understanding the experimental measurements which have been made by the oxygen microsensors.

4. Oxygen tension gradient histograms. Frequency distribution of the same oxygen tension differences between two points of the oxygen tension field are calculated. Oxygen tension gradient histograms were measured for skeletal muscle (*12*).

This study focused on the oxygen tension histogram pattern: the oxygen tension histogram of the inhomogeneously perfused network system is characterized by a broad spectrum of oxygen tension between 100 mm Hg and 0 mm Hg (Figure 5). The histogram has its maximum at low oxygen tension values. Small deviations from the monotonous shape of the curve are evident and might be caused by inhomogeneous blood flow in the different capillaries of the network.

The histogram of the countercurrent system shows a pronounced maximum of oxygen tension between 15 and 20 mm Hg with a steep decrease from the maximum value. The maximum value is in the range

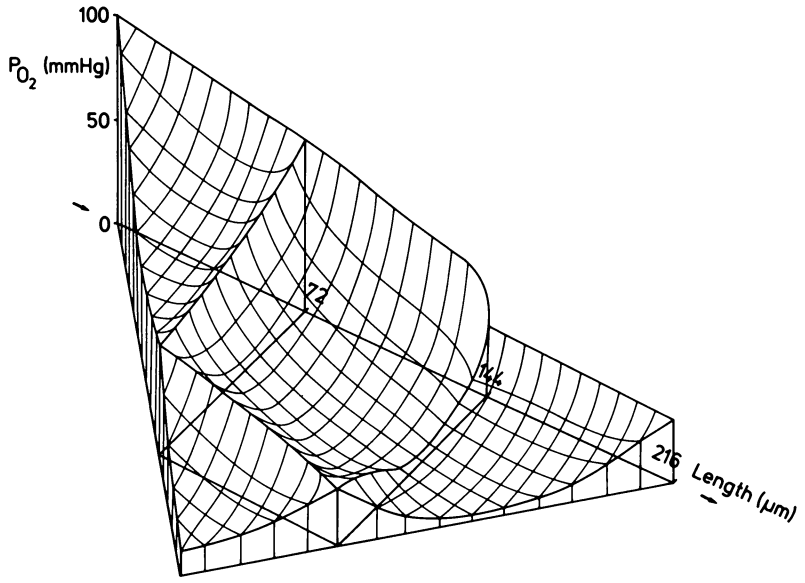

Figure 4. Oxygen tension distribution in the inhomogeneously perfused model

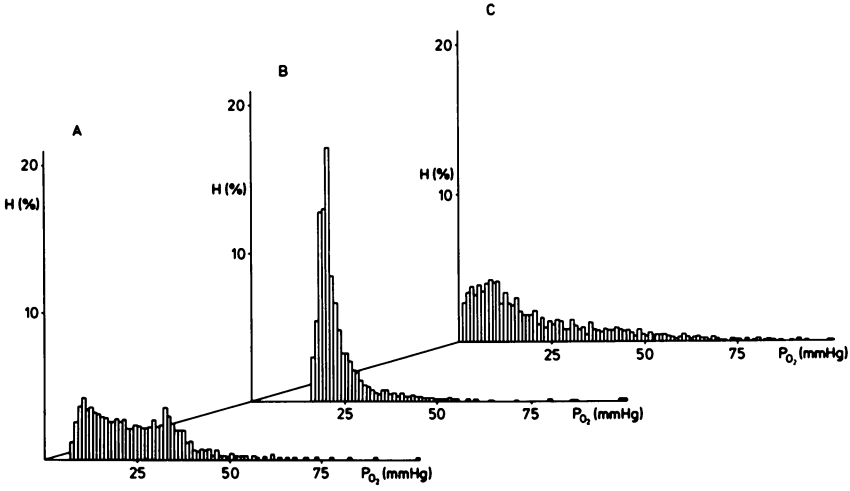

Figure 5. Oxygen tension histograms of the con- and countercurrent systems (A and B) and capillary network systems (C)

of the venous oxygen tension. Probably the oxygen tension values in the capillary countercurrent system can be detected with microsensors because of the characteristic shape of the histogram. In this case the oxygen microsensor experiments would give some information about flow direction within the capillary arrangement.

The same calculations of this type have also been performed for a set of parameters corresponding to arterial hypoxia ($p_aO_2 = 46$ mm Hg). Analysis of these results demonstrates that there exist only minute differences in the histogram patterns of the various capillary models.

Discussion

Mathematical analysis of oxygen tension values in the living organism gives better understanding of biological exchange and of regulatory systems. In analyzing diffusion, convection, and chemical reactions in the microstructure of the living body, the main problem arises from the geometric complexity of the capillary-tissue structure.

The basic assumption for all theoretical oxygen tension calculations was introduced by August Krogh. The organs, especially the muscles, are assumed to be composed of numerous, equal tissue cylinders with concentric capillaries. This rough assumption does not cover blood flow differences within the branches of the capillary bed which can be microscopically observed.

In our analysis the influence of blood flow differences in the different capillaries of the branched network were considered. A model structure was chosen which includes differences in capillary blood velocities in a ratio of 27:1.

The calculation results in a decrease in the oxygen tension values, and furthermore, the histogram shifts to lower values even under normoxic conditions. These results demonstrate that hypoxia might occur in brain tissue despite the presence of a high venous oxygen tension. A comparison of the oxygen tension distributions in the con- and countercurrent models with the network model leads to the conclusions that the venous oxygen tension provides some sufficient but not necessary information in diagnosing tissue hypoxia.

Oxygen tension histogram patterns were investigated to characterize oxygen supply conditions at the capillary and the cellular level. Histograms are important for interpretation of experimental results obtained with oxygen microsensors. As shown by different authors, the histogram pattern of the cerebral cortex is shifted to the left-hand side of the Figure (*12, 13, 14, 15*). This phenomenon cannot be explained by the countercurrent histogram which had been originally suggested as an important capillary arrangement within the brain cortex (*17, 18*). There is some histological evidence that network systems frequently occur in the brain cortex (*19, 20*). Thus we conclude that the network model might explain the great number of low oxygen tension values already measured under normoxia.

The inhomogeneously perfused network system might eventually be adapted to the capillary system of the kidney cortex. There the capillaries form a network which surrounds the tubuli in close proximity. Nevertheless, in the tubuli volume, there is no oxygen consumption. Therefore, the assumption of a homogeneous oxygen consumption within the tissue used by numerous authors had to be modified. This difficulty does not arise in brain cortex which is characterized by an almost homogeneous distribution of mitochondria.

Nomenclature

A = O_2 consumption rate of cerebral gray matter = 0.1 ml/g-min
l = capillary length of the network system = 60 (72) μm
l_c = capillary length of the con- and countercurrent system = 300 μm
d = capillary diameter = 6 μm
α = solubility coefficient of O_2 molecules = 0.025 ml/ml atm
D = diffusion coefficient in the tissue = 2×10^{-5} cm^2/sec
p_a = arterial oxygen tension = 100 mm Hg
K = Hill constant = 0.8575×10^{-4}
γ = Hill exponent = 4.04
Δs = change of saturation of oxyhemoglobin = 53%
p_K = critical oxygen tension = 1 mm Hg
v = flow velocity in the capillary
c = relative oxygen tension value normalized on arterial oxygen tension
c_a = initial oxygen tension at the arterial point = 1.0
$\bar{c}$ = relative oxygen tension at mixing points
i_ν, i_μ = capillary blood flow
ν, μ = indices
W_μ = hydrodynamic resistance of the capillary
s,m,n = coordinates
Δ = delta operator

Acknowledgments

My sincere thanks for improving the manuscript are due to M. Eitel, Department of Interdisciplinary Studies, Clemson University, Clemson, S. C.

Literature Cited

1. Krogh, A., *J. Physiol. (London)* (1918/19) **52**, 409.
2. Thews, G., *Acta Biotheor. (Leiden)* (1953) **10**, 105.
3. Blum, J. J., *Amer. J. Physiol.* (1960) **198** (5), 991.
4. Reneau, D. D., Bruley, D. F., Knisely, M. H., "Chemical Engineering in Medicine and Biology," W. Hershey, Ed., Plenum, New York, 1967.
5. Reneau, D. D., Bruley, D. F., Knisely, M. H., *A.I.Ch.E. J.* (1969) **15** (6), 916.

6. Metzger, H., *Kybernetik* (1969) **6**, 97.
7. Metzger, H., *Mathem. Biosci.* (1969) **5**, 143.
8. Metzger, H., *Mathem. Biosci.* (1969) **5**, 379.
9. Silver, I. A., *Med. Electron. Biol. Eng.* (1965) **3**, 377.
10. Lübbers, D. W., "Biochemie des Sauerstoffs," S. 67-92, Springer, Berlin, Heidelberg, New York, 1968.
11. Heidenreich, J., Erdmann, W., Metzger, H., Thews, G., *Experientia* (1970) **26**, 257.
12. Kunze, K., "Das Sauerstoffdruckfeld im normalen und pathologisch veränderten Muskel," Springer, Berlin, Heidelberg, New York, 1969.
13. Lübbers, D. W., "Oxygen Transport in Blood and Tissue," pp. 124–139, D. W. Lübbers, U. C. Luft, G. Thews, E. Witzleb, Eds., Thieme, Stuttgart, 1968.
14. Whalen, W. J., Nair, P., *Amer. J. Physiol.* (1970) **218** (4), 973.
15. Metzger, H., "Verteilung des O_2-Partialdruckes im Mikrobereich des Gehirngewebes," Habilitationsschrift, Mainz, 1971.
16. Forsythe, G. E., Wasow, W. R., Appl. Mathematics Series, I. S. Sokolnikoff, Ed., Wiley, New York, 1967.
17. Diemer, K., *Pflügers Arch. Ges. Physiol.* (1965) **285**, 99.
18. Diemer, K., *Pflügers Arch. Ges. Physiol.* (1965) **285**, 109.
19. Lockard, I., Barham, J. R., Forlidas, N. G., Myers, R. B., *J. Comp. Neurol.* **112**, complete issue (1959).
20. Lockard, I., *Anat. Rec.* (1960) **136**, 236.

RECEIVED November 22, 1971.

Problems in the Investigation of Tissue Oxygen Microenvironment

IAN A. SILVER

Department of Pathology, University of Bristol, England

There are two major categories of problems associated with measurements of tissue microenvironment. The first is concerned with the engineering and electro-chemical aspects of making suitable microprobes, and the second and more difficult one is the interpretation of the information obtained from the probes. These two broad divisions will be considered separately although inevitably at certain points they overlap.

Several problems are associated with oxygen microelectrodes. Tissue electrodes in this category may be regarded as those with a diameter of 0.1–5.0 μ although anything larger than 1.0 μ is likely to cause appreciable tissue damage. The ideal electrode must have a very sharp point to minimize the tissue distortion by forward pressure and especially to avoid capillary compression. It must be composed of a hard material to penetrate relatively tough biological structures, and its catalytic surface should be electrochemically stable and reasonably uniform. The shaft of the electrode should have the smallest diameter compatible with the necessary mechanical strength to minimize lateral pressure on small blood vessels. Additionally, electrodes with a large shaft, short taper, and small active area may mechanically alter the O_2 diffusion into the region being monitored, especially if the inter-capillary distance is large—*e.g.*, in resting voluntary muscle. This may be important in positions where the shaft occupies the region from which a major contribution of oxygen is usually derived by the cells at the electrode tip. The shaft in these circumstances produces a diffusion shadow which substantially alters the condition it is meant to measure. The O_2 uptake of the electrode should be small in relation to that of the cells in its vicinity. This is a particularly important requirement since O_2 electrodes strictly measure only the O_2 environment which they induce around themselves. They should therefore draw their

O_2 from a very small volume of fluid; preferably, their diffusion zone should be limited to within the barrier membrane with which they are covered. For bare electrodes the diffusion zone should be no greater than the thickness of the static fluid boundary layer which adheres to the catalytic surface. The diffusion zone around microelectrodes is a sphere whose diameter is of the order of six times the diameter of the electrode tip (*1*, *2*). Probes must not stimulate or depress tissue respiration either by mechanical irritation or by electrical stimulation from the polarizing voltage. The latter is one of the hazards of using pulsed electrodes in reactive tissue such as brain or muscle tissues (*3*, *4*), but is also a problem with constant voltage polarization in terms of effects on bioelectric membrane potentials. If such potentials are altered, then tissue respiration and activity may be affected drastically, giving rise to subsequent non-physiological changes in the local PO_2 (*5*).

Membrane material for covering electrodes may be a source of difficulty since many synthetics contain plasticizers which are highly toxic and diffuse out from the film very slowly, causing cellular embarrassment. This can clearly be shown by using tissue culture situations to test potentially useful materials. Rapid failure of cell respiration, followed by cell death, can often be observed around so called inert plastics. Even different batches of a normally safe plastic may be biologically dangerous.

The greatest hazards for tissue electrodes, besides mechanical damage, the unfortunate effects of protein deposition, and the formation of —SH complexes on the catalytic surface, is the hydration of the insulating material near the tip or a progressive change in its O_2 permeability. There seems to be no resin that is completely free from hydration problems, and none are superior to glass insulation (*2*, *6*). Even so, very thin glass will also hydrate and may crystallize or develop micro-cracks. It is perhaps unfortunate that the soft soda glasses, which are most compatible with platinum or platinum–iridium, are also the most inefficient insulators and the most liable to hydration.

The position of the reference electrode, although not usually critical, may be a source of error. Especially in the brain, local changes of cell membrane potential and redox potential may significantly affect the polarizing voltage between the microelectrode and the reference. An electrode with a poor current/voltage plateau and a short response time is thus liable to give a change of reading which may be falsely interpreted as a change of local PO_2 (*7*). On the other hand, if a silver reference electrode is too close to a microelectrode, electrolytic deposition of silver onto the noble metal surface can produce serious artifacts in the form of progressively increasing zero currents and loss of linearity in the current/O_2 relationship.

Microelectrodes are less sensitive than larger electrodes to fall off in current at very high oxygen tensions, but they tend to be somewhat unstable. It is not possible to relate the current–voltage polarogram with overall stability (*6*).

Poisoning. The poisoning of tissue electrodes has been a problem in relation to attempts to calibrate probes to obtain absolute readings of tissue PO_2. A commonly observed phenomenon, especially with larger electrodes, is that the current readings tend to fall progressively with time. This has been interpreted as (1) change in the surface properties of the electrode owing to chemical combinations of the catalytic surface with tissue products, especially —SH compounds and (2) change in the diffusion path near the electrode caused by protein deposition from blood or damaged cells onto the electrode either passively or by electrophoresis. The situation is complicated further by tissue reactions to the electrode, discussed below. Electrophoretic effects and —SH compound interference can be eliminated by using membranes (*2*, *8*, *9*, *10*) but passive deposition of protein and inflammatory tissue changes cannot.

The converse of poisoning is aging new electrodes in the electrolyte before use. This seems to involve a hydration process and may take many hours of soaking and polarization to achieve although the effect is soon lost. Electrodes which have been used beyond the optimum period can be revitalized by cleaning, drying and resoaking, and polarizing. The precise nature of the process awaits interpretation.

Lübbers (*6*) finds that for platinum–iridium microelectrodes the aging process reveals a plateau after 2–6 hours of polarization in physiological saline and that this plateau lasts for 10–20 hours before the characteristics of the electrode begin to change. Our experience has been similar with microelectrodes although large electrodes may require a much longer aging procedure.

Calibration. The calibration of microelectrodes presents many difficulties because of the individual variation between probes. Any microelectrode required for work in tissues should be membrane-covered to protect it and also to render it insensitive to stirring artifacts. Calibration fluids of varying viscosities, oxygen diffusion coefficients, oxygen capacities, and temperatures are necessary to check that the electrode output will be governed only by O_2 tension and temperature and is linearly related to these. A satisfactory method of calibration is to use a chamber, which can be flushed with fluids equilibrated with various known O_2 tensions and into which the electrode tips may be inserted. The chamber must contain a stirring device which does not give rise to electrical artifacts on the recording system and must have a provision for variable temperature control and monitoring. Our standard procedure follows:

(1) Clean, sterilized, membrane-covered electrodes are inserted into the chamber.

(2) Electrical output is monitored with the electrodes in physiological saline equilibrated with air. Probes giving readings in the order of 10^{-12}–10^{-14} amps/mm Hg O_2 are retained.

(3) The calibration fluid is stirred. Probes showing less than 0.5% change in reading are retained.

(4) The calibration chamber is flushed sequentially with fluid equilibrated with N_2, 10% O_2, air, 50% O_2, and 100% O_2; then with 50% O_2 and N_2 to detect hysteresis. Electrodes giving a linear response are retained providing the N_2 current is less than 0.5% of the reading in air.

(5) Air-equilibrated saline at 20°, 25°, 30°, 35°, and 40°C is flushed through the chamber. The temperature coefficient is noted; electrodes having a linear response are retained.

(6) The chamber is flushed with air saturated saline, blood, and 30% glycerol in water. Electrodes showing less than 0.5% difference in reading between different media are retained.

(7) A current/voltage polarogram between 0–1.1 volts is constructed. The best electrodes show a reasonably flat plateau between 0.6 and 0.75 volts, but lack of a flat plateau does not necessarily mean that the probe is faulty.

Shielding. Very small electrodes have inevitably a high impedance and are sensitive to electrical and magnetic interference. In many situations the tissue can be grounded to form an adequate shield for the electrode tip. High zero currents indicate often rectification of an ac field near the preparation. With ultramicroelectrodes such fields may completely submerge the oxygen signal, but backing off high dc signals is undesirable since the necessity to use such methods usually indicates that either the biological preparation or the electrode is faulty.

Movement Artifacts. Live tissues are never still since there is constant movement of intercellular fluid, intracellular cytoplasmic streaming, and passage of blood and lymph through vascular channels. In the vicinity of arteries and even arterioles there is pulsation transmitted from heart beats, and in certain organs there is constant gross movement which is either intrinsic or imposed from another actively moving organ. If an electrode is sufficiently small or has an adequate membrane coverage, micro-movements of fluids will not cause difficulties, but gross tissue movements—*e.g.*, as occur in voluntary muscles, heart, and liver (resulting from respiratory activity of the diaphragm)—can cause damage to the electrode directly or to the organ into which the electrode is inserted if the probe is rigidly held. This has led to the development of floating electrodes which move with the organ and are arranged to give minimum thrust at the tip (*11*). Even with the most careful floating, it is impossible to avoid some tissue damage, and by histological reconstruction of micro-

electrode sites in heart and liver, we showed that in at least 50% of such sites there is obvious hemorrhage at or near the electrode tip.

Response Time. Microelectrodes with tips of less than 5 μ should have a 97% response time of less than 1 sec when covered with appropriate diffusion membrane (*2, 9*) or when constructed with a slightly recessed (*4*) tip. These probes are potentially useful for investigating kinetics of local vascular changes and possibly O_2 diffusion. A problem arises here that the presence of minor hemorrhage at the electrode tips can alter the response time of the system by providing an oxygen storage facility in the region of the measuring device. Hemoglobin acts as a damping mechanism.

A simple example of this effect is given in the following experiment. Two microelectrodes were inserted at equal distances from a capillary in a 12 μ-thick tissue layer in a rabbit ear chamber. The response time of the two electrodes was recorded in relation to single breaths of pure O_2 and pure N_2 interpolated into normal air breathing. A capillary near one electrode (B) was then deliberately damaged so that red blood cells infiltrated around one electrode (B), but the original capillary was undamaged, and the second electrode (A) remained in blood-free tissue. The response to O_2 and N_2 breathing was again tested. The figures obtained are shown in Table I. The response time of the hemoglobin-enclosed electrode was lengthened considerably in both directions, whereas that of the other electrode was unaffected.

Table I. Effect of Local Hemorrhage on Electrode Response

		Electrode A		*Electrode B*	
		Before Hemorrhage at B	*After Hemorrhage at B*	*Before Hemorrhage*	*After Hemorrhage*
Lung to electrode time		8.7 sec	8.6 sec	8.5 sec	11.3 sec
Time for 97% change at electrode		2.3 sec	2.3 sec	2.4 sec	4.8 sec
Percentage change from 'Resting' PO_2	O_2	+22%	+25%	+26%	+8%
	N_2	− 9%	−10%	−10%	−3%

Pulsed Polarizing Systems. Intermittent pulsing of polarizing voltages has been applied successfully to tissue microelectrodes but has not been used widely owing to several technical problems (*3, 12*). Theoretically, pulsed voltages should be superior to continuously applied systems; since there is less O_2 utilized, the electrode should not interfere with the O_2 supply of the cell, and it should be relatively simple to obtain absolute values for O_2 levels in the vicinity of the electrode. One major difficulty that is encountered with pulsed measurements is the very high zero current. Kunze (*3*) has tried to compensate this by using two identical

electrodes, one held in nitrogen and the other in the test situation. The nitrogen current cancels out the zero current from the test system. The other problem is biological since the sweep potential may trigger membrane potential changes in the cells in its vicinity and stimulate them in some way, thus altering the conditions in the tissue.

Problems of Interpretation of Tissue O_2 Measurements

In most tissues there are steep oxygen gradients, and microelectrodes pick up their oxygen from some arbitrary point in the gradient (*12*, *13*). Thus, it is likely that the O_2 environment around the electrode is nonhomogenous and was that way even before any distortion which might have been produced by the probe. Albanese (*14*) argued on the basis of mathematical models that the presence of even a very small electrode distorts the oxygen diffusion field so much that errors of between 15–70% may arise in measuring local PO_2. Grünewald (*15*), also on the basis of computer models backed by *in vivo* behavior studies of electrodes, suggests that this view is unduly pessimistic.

We have attempted to assess this distortion in a flat plate of tissue 12 μ-thick, growing in a rabbit ear chamber, by direct measurement. Four, 1 μ electrodes were introduced into the tissue to form the corners of a square with sides of 50 μ. They were then each moved inwards towards the center of the square one at a time in steps of 5 μ until the side length was 10 μ. After this, one electrode only was moved to within 2–3 μ of the others in turn. No effect was seen of one electrode on the other in the first series of moves, but changes of up to 15% in current output occurred when the mobile electrode was brought to within 3 μ of the tips of the static probes. This suggests that electrode disturbance of the tissue environment is not a very serious hazard (at least to the tissue).

A more important problem is tissue reaction to the physical presence of the electrode. Most tissues respond rapidly to the presence of foreign bodies by developing an inflammatory reaction. This response is biologically complex, but its effects on the microelectrode are easily interpreted. The first part of the reaction involves changes in flow patterns in small blood vessels with concurrent increases in vessel wall permeability while the second part of the response involves cellular infiltration of the irritated area. Both parts of the reaction affect local PO_2 by altering the delivery of oxygen to the area, partly because of the blood flow change but also, and apparently very significantly, by increasing the diffusion distance from capillary to cell (and electrode) resulting from leakage of excess fluid into the perivascular spaces. At a latter stage cellular infiltration increases further the diffusion distance and adds an

oxygen sink in the form of very actively respiring phagocytic cells. We have observed by direct vision in transparent rabbit ear chambers, the development of inflammation in a thin layer of connective tissue and have measured the surface of such tissue with non-penetrating microelectrodes (*16*). We have also observed the vascular changes that occur when membrane covered electrodes of various sizes are inserted into a thin layer of well perfused tissue and have measured the PO_2 changes which accompany them. These are shown in Table II.

Table II. PO_2 Changes owing to Developing Inflammatory Response (PO_2 as a percentage of initial reading)

Electrode Size (*Tip Diameter*)	*Time* 0	*5 min*	*30 min*	*1 hour*	*3 hours*	*6 hours*
0.5 μ	100	105	101	98	93	90
1.0 μ	100	108	100	100	96	89
2.0 μ	100	103	105	93	96	92
5.0 μ	100	110	97	90	83	78
10.0 μ	100	105	94	93	89	81
25.0 μ	100	97	88	87	78	75

Thus very small electrodes, placed under direct vision to avoid damage to blood vessels, suffer little if any change resulting from inflammation, but reduction of up to 25% in the electrode reading may occur even in carefully placed electrodes of 5 μ or larger. It is reasonable to suppose that randomly inserted blind probes in normal tissue will cause greater damage and evoke a stronger inflammatory reaction. The brain has a rather poor inflammatory response and tolerates insult somewhat better than most tissues.

Before the development of microelectrodes numerous investigations were made with relatively gross (200–300 μ diameter) bare platinum or gold oxygen electrodes inserted into tissue of a type originally described by Montgomery and Horwitz (*17*). Such probes cause considerable tissue damage but may be useful for following major changes of O_2 availability in tissues since they draw their oxygen from a wide field which covers several capillary networks and cell populations. Attempts to calibrate such probes have been made (*18*), and although in favorable circumstances reproducible results may be achieved, the general experience with these electrodes is unsatisfactory in regard to reliability and to interpretation of results obtained in terms of real tissue environment. The steep gradients in tissues that are revealed by microelectrodes explain many of the more puzzling features of recordings from large electrodes.

A further difficulty in interpretation of changes in or a constant level of PO_2, as indicated by electrode current, is presented by tissue homeostatic mechanisms. The rate of tissue change and the electrode response

time may be critical in terms of the signal received. For instance, it is possible to use a system which allows the recording of oxygen tension and single unit action potentials concurrently from the same microelectrode in the brain (2, 9). If the spontaneous activity of a large neurone in the brain is recorded with the PO_2 at a point near its surface, one finds that while there may be rhythmic fluctuations in PO_2 these seem to be of vascular origin and not imposed by the cell's activity (2, 9). However, if the cell is caused suddenly to fire very fast by some distant stimulus—*e.g.*, cold on the skin—there is a lag phase of 1–1.5 sec, followed by a rapid fall in local PO_2 lasting 1–3 sec, and this is then compensated, and PO_2 returns to the original level until the cell firing pattern slows when there is an overshoot of PO_2 and again a return to the original level over 2–3 sec. This presumably represents local increased demand and supply of O_2, but what determines that the homeostatic mechanism adjusts to a particular level of PO_2? This type of change in O_2 environment can only be detected by systems with a reasonably rapid response and high spatial resolution, yet almost certainly our probes are not capable of seeing many adjustments of environment that are important to the cell.

We have some preliminary results on cell activity and microenvironment in different parts of the brain, suggesting that hypoxic damage to cortical cells can occur at extracellular PO_2 levels no different from those associated with full activity in hypothalamic cells (5). Do the cortical cells have a high critical PO_2 for their mitochondria, is there poor diffusion into them, or do they have some special component or anatomical configuration that makes them especially liable to damage? They seem to suffer irreversible damage at extracellular oxygen tensions which are sufficient to keep the flavoproteins and pyridine nucleotides fully oxygenated; yet brain stem cells remain electrically active for long periods even where the NAD is 20–30% reduced.

Conclusion

The investigation of tissue microenvironment is in an early phase of development, but the use of microelectrodes should provide useful data on the local conditions which affect cell activity.

Literature Cited

1. Fatt, I., *J. Appl. Physiol.* (1964) **19**, 326.
2. Silver, I. A., *Med. Electron. Biol. Eng.* (1965) **3**, 377.
3. Kunze, K., *Pflügers Arch. Gesamte Physiol.* (1965) **283**, 36.
4. Whalen, W. J., Riley, J., Nair, P., *J. Appl. Physiol.* (1967) **23**, 798.
5. Silver, I. A., "Oxygen Supply. Theoretical and Practical Aspects of O_2 Supply and Microcirculation in Tissue," *Proc. Int. Conf. Dortmund* (1971), M. Kessler *et al.*, Eds., Urban and Schwarzenburg, Munchen, 1972.

6. Lübbers, D. W., *ibid.*
7. Bicher, H. I., *ibid.*
8. Clark, L. C., *Trans. Soc. Art. Int. Org.* (1956) **2**, 41.
9. Bicher, H. I., Knisely, M. H., *J. Appl. Physiol.* (1970) **28**, 387.
10. Silver, I. A., "Oxygen Measurements in Blood and Tissues," J. P. Payne and D. W. Hill, Eds., Churchill, London, 1966.
11. Follert, H., "Oxygen Supply," *Proc. Int. Conf. Dortmund* (1971), M. Kessler *et al.*, Eds., Urban and Schwarzenberg, Munchen, 1972.
12. Davies, P. W., Brink, F., *Rev. Sci. Instrum.* (1942) **13**, 524.
13. Silver, I. A., *Prog. Resp. Res.* (1969) **3**, 124.
14. Albanese, A., *J. Theoret. Biol.* (1971) **33**, 91.
15. Grünewald, W., "Oxygen Supply," *Proc. Int. Conf. Dortmund* (1971), M. Kessler *et al.*, Eds., Urban and Schwarzenberg, Munchen, 1972.
16. Silver, I. A., Final Technical Report, U.S. Army Contract DAJA 37-69-C-1169 (1970).
17. Montgomery, H., Horwitz, O., *J. Clin. Invest.* (1950) **29**, 1120.
18. Cater, D. B., Silver, I. A., Wilson, G. M., *Proc. Roy. Soc. (B)* (1959) **151**, 256.

RECEIVED March 1, 1972. Work was supported by the U.S. Government funds under contracts DAJA37-70-C-2328 and DAJA37-72-C-0962.

INDEX

C

D

E

F

N

O

Q

R

S

T

U

V

W